Seismic structure and earthquake focal mechanisms of the Hengill volcanic complex, S W Iceland

Miller, Angus D.

Seismic Structure and Earthquake Focal Mechanisms of the Hengill Volcanic Complex, S W Iceland

Angus D. Miller

Abstract

Iceland provides a unique opportunity to study the processes that occur along mid-ocean ridges. In 1991, thirty temporary seismic stations were installed at the Hengill volcanic complex to record high-quality digital data from local earthquakes. From these data 449 earthquakes have been located, most of them beneath the geothermal area.

A local earthquake tomographic inversion was carried out to determine the three-dimensional V_P and V_P / V_S structure to 6 km depth, using P-wave travel times and S-P times from local earthquakes recorded in 1981 and 1991. The resulting models are smoothly varying and give a low data variance.

The V_P model is similar to that of a previous tomographic inversion in the area, although the models differ in detail. The main high-V_P features of these models are interpreted as solidified intrusions, and underlie extinct volcanic centres. A low V_P / V_S body (-4%) is detected from 0 to 3 km depth that correlates with the surface expression of the geothermal field and is probably due to a combination of effects that include a slightly lower pore fluid pressure (and thus a higher steam content), and rock matrix alteration.

Well-constrained moment tensors were determined for 70 local earthquakes by inverting the polarities and amplitude ratios of P and S arrivals. This method works well and is relatively insensitive to wave-speed model and attenuation variations. Most of the earthquakes are non-double-couple with explosive volumetric components.

Only 17 (28%) of the earthquakes are consistent with a double-couple model. The remaining earthquakes are modelled as a combination of an opening tensile crack and a shear fault. Two geometries are considered: (1) rupture on two separate fault planes aligned at 45°, and (2) opening-shear rupture on a single fault plane, which is equivalent to coplanar tensile and shear faults. Both models can give the same moment tensors, and the data cannot distinguish between them. They give a good fit to the data, with few polarity misfits for most of the earthquakes. Right-lateral opening-shear strike-slip faulting on near-vertical planes is consistent with the regional seismicity of the South Iceland Seismic Zone. The non-double-couple earthquakes may result from the regional stress regime interacting with the geothermal field.

Seismic Structure and Earthquake Focal Mechanisms of the Hengill Volcanic Complex, S W Iceland

Angus D. Miller

A thesis submitted in partial fulfilment of the requirements for the degree of Doctor of Philosophy

Department of Geological Sciences

University of Durham

February 1996

Dedicated to

my Parents

Acknowledgements

Thanks to:

- My supervisors, Gill Foulger and Bruce Julian for all their support and encouragement, and for all the hard work they put into this project.
- John Evans and other staff of the Branch of Seismology, U.S. Geological Survey, Menlo Park, California for warm hospitality and a stimulating working environment during my visits there.
- The Hengill 1991 project team— Gill Foulger, Bruce Julian, Rex and Mary Allen, Benni, Michelle and Kathleen, for employing superhuman data collection techniques and overcoming lots of obstacles.
- Steinunn Jakobsdóttir of Geophysical Division of the Iceland Meteorological Office, for supplying data from the SIL network and answering many questions.
- Staff of the Department of Geological Sciences, University of Durham.
- The Natural Environment Research Council, for financial support.
- Alwyn, Kathleen, Michelle, Simon and Anita for sharing the supervisory experience and much more.
- Fellow Durham students, especially Gail, Sarah, Giles, Zoë, Charlotte and all the other Friday Beer O'clockers.
- My friends in California: the Trail Builders, the hacky-sackers and the St. Mike's breakfast crew for making me feel at home in a strange country.
- My family, for all their support, even when they didn't quite understand what I was doing.

Chapter 2 of this thesis is based on two papers coauthored with my supervisors (*Julian et al.*, 1996; *Miller et al.*, 1996). Their input to this chapter is gratefully acknowledged.

And finally—

We may all be lying in the gutter, but some of us are looking at the stars.

Oscar Wilde.

Thanks to fellow star-gazers, especially Judith, Stephen, Chas, Cathy, Marcelle, Dr Mike, Mike and Andy, for enriching my life and being, always, the best of friends.

Contents

List of figures

List of tables

List of additional material

Copies of the following papers are contained in a pocket at the back of this thesis:

Foulger, G. R., A. D. Miller, B. R. Julian and J. R. Evans, Three dimensional V_P and V_P/V_S structure of the Hengill triple junction and geothermal area, Iceland, and the repeatability of tomographic inversion, *Geophys. Res. Lett.*, 22, 1309-1312, 1995.

Miller, A. D., G. R. Foulger and B. R. Julian, Non-double-couple earthquakes II. Observations, *Rev. Geophys.* (submitted), 1996.

Declaration

I declare that this thesis, which I submit for the degree of Doctor of Philosophy at the University of Durham, is my own work and is not substantially the same as any which has previously been submitted for a degree at this or any other university.

Angus D. Miller
University of Durham
February 1996

Chapter 1

Geology, tectonics and seismicity of Iceland and the Hengill area

1.1 Introduction

Iceland lies on the mid-Atlantic ridge, and is a product of the interaction of the spreading plate boundary and a mantle hotspot, which have formed a large volcanic pile and unique on-land exposure of an accretionary plate boundary. The island provides a rare opportunity to make detailed studies of the seismic and tectonic processes that occur at spreading plate boundaries. Temporary seismic stations were deployed in 1991 to record the continuous, low-magnitude geothermal seismicity that occurs in the Hengill volcanic complex, S.W. Iceland. The high-quality local earthquake data that were collected during this experiment have been used to determine the three-dimensional seismic structure of the area, and earthquake focal mechanisms.

1.2 Iceland

1.2.1 The geology of Iceland

1.2.1.1 Tectonic setting of the north Atlantic

The formation of Iceland and the development of the north Atlantic are closely related to the evolution of the Iceland hotspot. The hotspot has migrated eastwards relative to the North American plate over the last 70 Ma, and now lies at about 64°N 16°W, beneath Iceland (*Lawver and Müller*, 1994; Figure 1.1). The hotspot is thought to be a thermal anomaly within the mantle (a "mantle plume"), and to cause mantle melting beneath Iceland, the formation of a partial melt zone within the asthenosphere, and updoming of the asthenosphere. Low density within the mantle plume helps to compensate isostatically the Iceland topographic anomaly.

Iceland is part of an extensive transverse ridge, a topographic high which extends from Greenland to the Faeroe Islands (Figure 1.2). The Greenland-Iceland and Iceland-Faeroe ridges are submarine platforms composed of anomalously thick oceanic crust (*Vink*, 1984).

Spreading in the north Atlantic region first started at the beginning of the Tertiary period, at about 60 Ma, with the formation of Tertiary volcanic centres along the north Atlantic plate margins. Plate tectonic reconstructions show that spreading north of latitude 65°N started at about 54 Ma (*Bott*, 1985). At this time the mantle hotspot lay beneath the Greenland craton, and fed material laterally to the mid-Atlantic ridge, producing anomalously thick crust and forming the Iceland-Faeroe ridge (*Vink*, 1984).

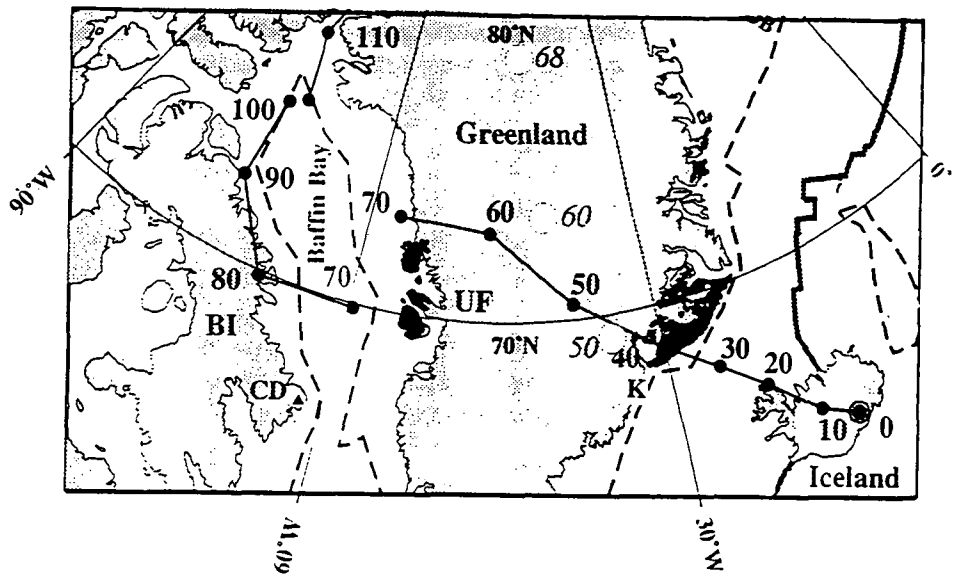

Figure 1.1: Map showing the migration path of the Icelandic hotspot. Solid dots show position, numbers are in Ma. Spreading in Baffin Bay occurred after the hotspot had passed through the area. Dashed line is the continent-ocean boundary (from *Lawver and Müller*, 1994).

At about 36 Ma the hotspot emerged from beneath eastern Greenland. Much of the Greenland-Iceland ridge was formed at this time. Latterly the locus of spreading has migrated eastwards with the hotspot, so that the plate boundary within Iceland is now offset by about 150 km to the east of the main trend of the mid-Atlantic ridge. Spreading along the mid-Atlantic ridge at Iceland occurs at a rate of about 1.9 cm/year at 104°N (*DeMets et al.*, 1990).

1.2.1.2 The evolution of Iceland

The oldest exposed rocks in Iceland date from about 16 Ma, and are probably underlain by rocks which date from at least 26 Ma (*Bott*, 1985). Tholeiitic basalts of Tertiary age (older than 3.1 Ma), in the east and northwest, form about 50% of the surface area of Iceland (Figure 1.3). Most of the basalts dip gently towards the centre of the island, with the steepest dips (up to 10°) found at the lowest stratigraphic levels. Individual units tend to thicken downdip, and most originated from central volcanoes, the majority of which are now extinct and eroded (*Walker*, 1974). The extinct central volcanoes exhibit major geothermal alteration with dyke swarms and, usually, large intrusive bodies of gabbro or granophyre that represent solidified magma chambers. There have been no major changes in the types of volcanic activity in the last 10 to 15 My (*Pálmason*, 1980). Since the onset of the Plio-Pleistocene (3.1 Ma) periods of glaciation have affected Iceland, resulting in subglacial volcanic products such as pillow lavas and "moberg" (hyaloclastite) mountains, and glacial rocks such as tillites that are inter-bedded with the extrusive volcanic rocks.

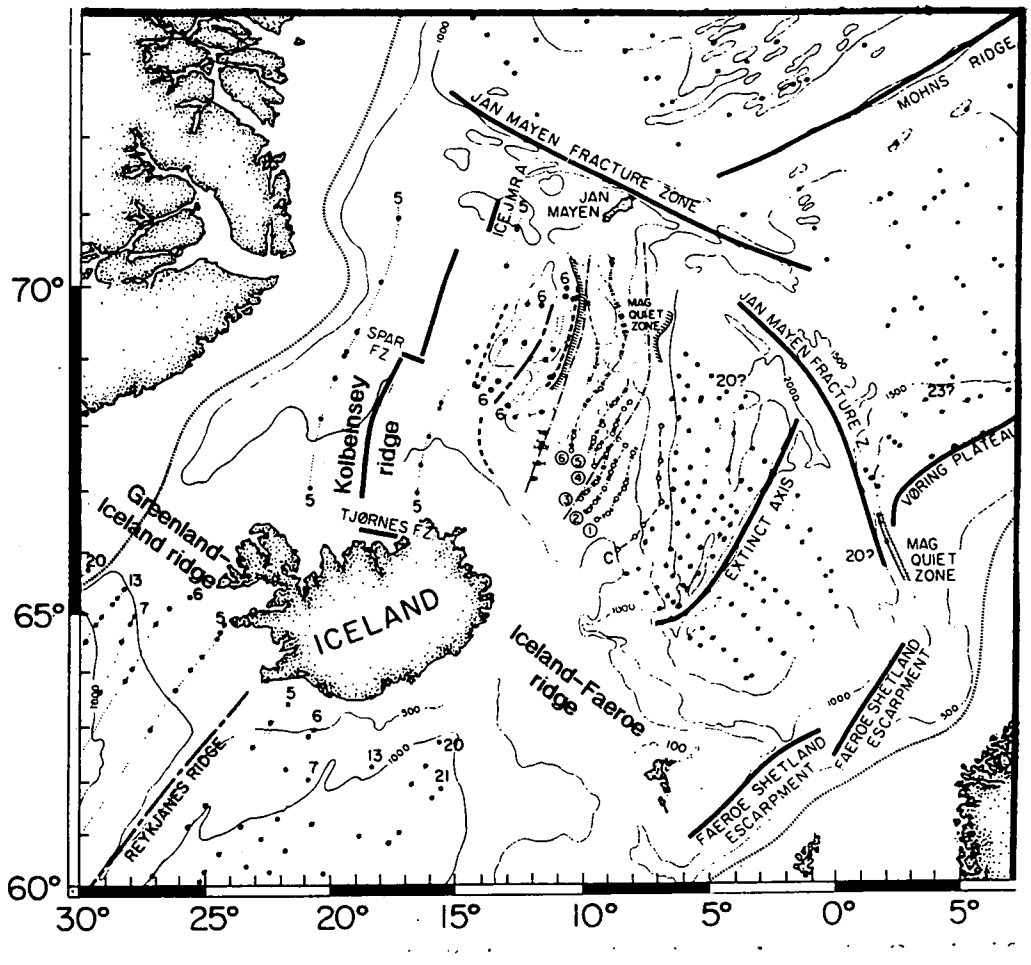

Figure 1.2: The tectonic setting of Iceland in the north Atlantic. Dots and thin lines show positions of magnetic anomalies (numbered) (from *Talwani and Eldholm*, 1977).

In the last 700,000 years (the Upper Pleistocene), volcanic and tectonic activity has been concentrated along the plate boundary, which comprises the neovolcanic zones and two transform zones (Figure 1.4). In the north, the Tjörnes Fracture Zone (TFZ) connects the Kolbeinsey ridge north of Iceland to the Northern Volcanic Zone (NVZ). South of latitude 65°N the plate boundary is split into the Western Volcanic Zone (WVZ) and the Eastern Volcanic Zone (EVZ). The South Iceland Seismic Zone (SISZ) joins the southern ends of the WVZ and EVZ. At its western end, the SISZ meets the WVZ and the Reykjanes Peninsula Volcanic Zone (RPVZ) at the Hengill triple junction.

There are two neovolcanic "flank zones", at Snaefellsness and south of the EVZ (Figure 1.3), that have been volcanically active only since the Plio-Pleistocene. The flank zones are characterised by transitional to alkali lava types and large cone-shaped

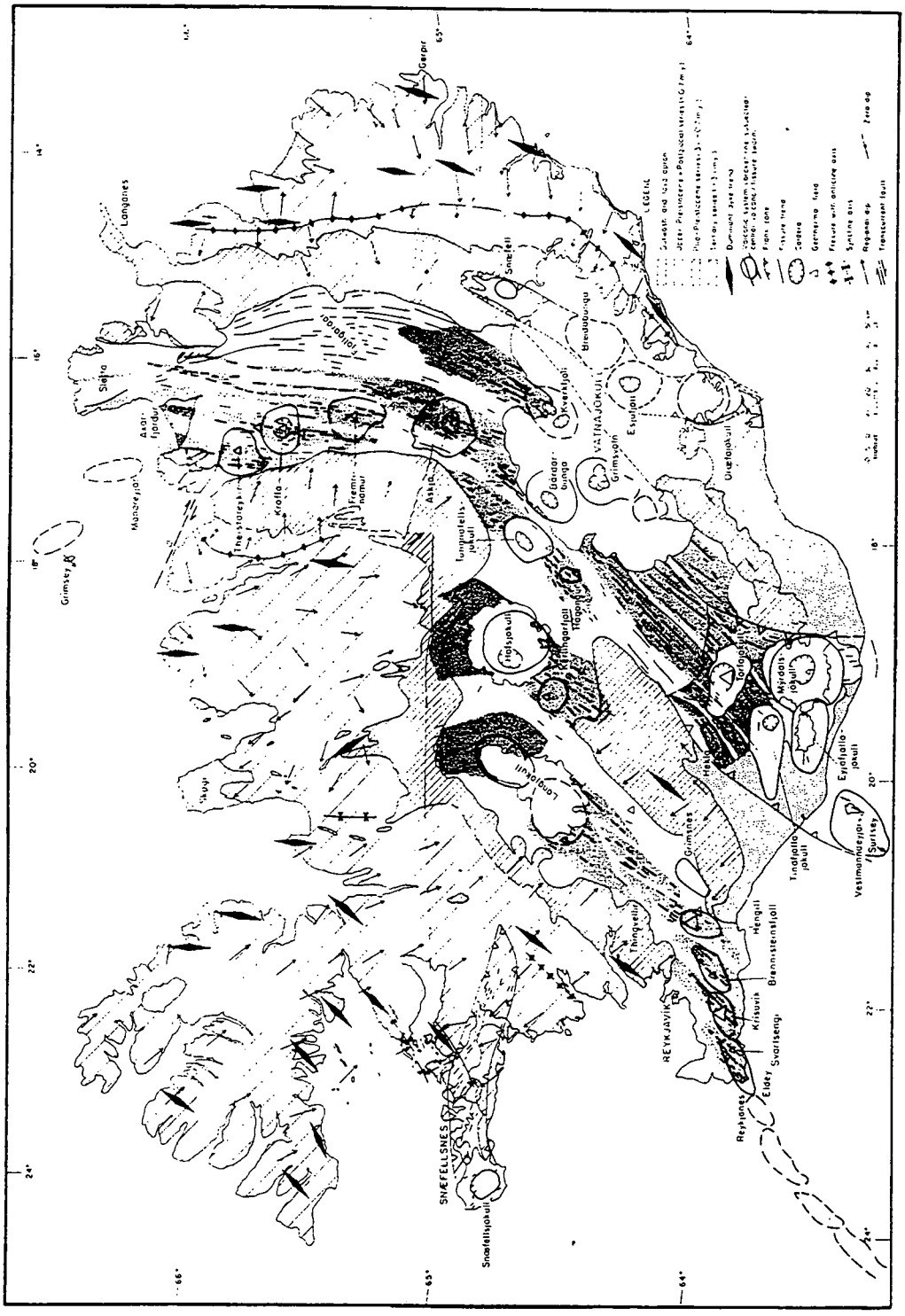

Figure 1.3: The geology and tectonics of Iceland (from *Sæmundsson*, 1979).

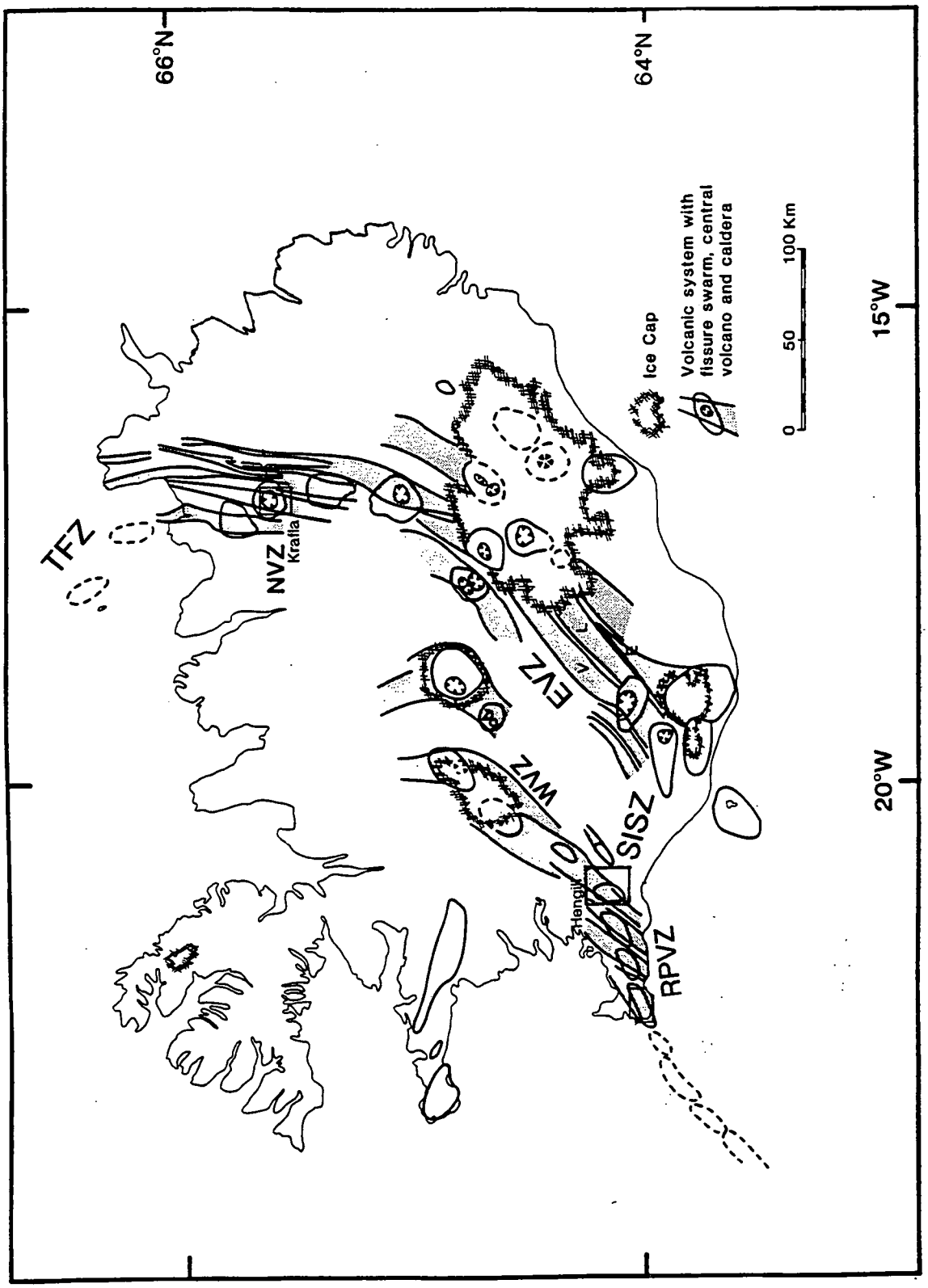

Figure 1.4: Map showing the plate boundary and volcanic systems in Iceland. NVZ: Northern Volcanic Zone; EVZ: Eastern Volcanic Zone; WVZ: Western Volcanic Zone; SISZ: South Iceland Seismic Zone; V, E, L: Sites of Vatnaölder and Veiðivötn, Eldgjá and Laki fissure eruptions (after *Einarsson and Sæmundsson*, 1987).

or elongated central volcanoes. They have much less extensional faulting and graben formation than the other volcanic zones, and their volcanic products lie unconformably on older, often eroded, rocks. The flank zone in southeast Iceland lies to the south of the junction of the EVZ and the SISZ.

Within the volcanic zones, activity is concentrated within discrete "volcanic systems" (*Sæmundsson*, 1978; 1979). Each volcanic system contains a fissure swarm that is 10 to 100 km long and up to 20 km wide. Fissure swarms contain open fissures, graben structures and crater rows. The trends of the fissure swarms tend to be uniform within each volcanic zone, and where the volcanic zone trends obliquely to the spreading direction, swarms are often *en échelon*. About 20 volcanic systems contain well-defined central volcanoes, which are loci of high lava production, geothermal alteration and evolved rocks. The central volcanoes sometimes have calderas, suggesting the existence of shallow crustal magma chambers.

Spreading along the plate boundary does not occur continuously. Instead, a volcanic system may be inactive for centuries before undergoing several metres of rapid rifting, accompanied by fissure eruptions. The presence of acid and intermediate rocks at central volcanoes suggests that at these locations magma is stored in crustal magma chambers, where it differentiates with time, leading to the formation of a wide variety of different igneous rock types.

Since the last glaciation, spreading in south Iceland has been partitioned approximately equally between the WVZ and EVZ (*Sigmundsson et al.*, 1995). In historical times, there have been few volcanic eruptions in the WVZ, and only one rifting event is known, which occurred in the Hengill fissure swarm in 1789 (Section 1.3.2.1). In contrast, there have been at least four major fissure eruptions in the last 1000 years in the EVZ, at Vatnaöldur and Eldgjá (about 900 A.D.), Veiðivötn (about 1480 A.D.) and Laki (1783 A.D.) (Figure 1.4). It is thought that current spreading in the WVZ is responsible for only 15±15% of plate divergence north of the SISZ (*Sigmundsson et al.*, 1995).

The mantle hotspot is thought to be currently centred beneath the EVZ (*Lawver and Müller*, 1994), and it is possible that spreading is being transferred to the EVZ, with activity in the WVZ decreasing, and that the southern tip of the EVZ, along with the SISZ, are migrating southwards. Estimates of the rate of this migration vary from 3.5-5 cm/yr (*Einarsson*, 1988) to about 1 m/yr (*Sigmundsson et al.*, 1995). Alternatively, the partitioning of spreading between the WVZ and EVZ may be irregular in time, because of variations in the magma supply rate to the two zones. If this is the case, the WVZ may be only temporarily magma starved (*Sigmundsson et al.*, 1995).

1.2.1.3 Crustal structure

The Iceland crust is composed of several kilometres of extrusive igneous rocks overlying intrusives, and has a similar structure to, but is much thicker than, oceanic

crust. Seismic wave speeds within the crust vary, reflecting the diverse structure of the crust in Iceland, with lower wave speeds and thinner layers beneath the neovolcanic zones. Wave speeds at the surface and at shallow depth vary depending on the degree of metamorphism of the rock and the amount of erosion. Most studies agree that the *P*-wave speed (V_P) at depths between 10-15 and 20-25 km is fairly constant at approximately 7.0-7.4 km/s (Figure 1.5).

Magnetotelluric (MT) soundings in Iceland detect a minimum in apparent resistivity that is equivalent to a low resistivity layer of unknown thickness between 10-20 km depth (*e.g.*, *Hersir et al.*, 1984; Section 1.3.3). The depth of this layer increases away from the neovolcanic zones.

The maximum depth of earthquakes may be used to constrain temperature at depth. Earthquakes occur down to about 7 km beneath the neovolcanic zones, and to a maximum depth of 12-14 km in certain areas, such as the eastern part of the SISZ (*e.g.*, *Stefánsson et al.*, 1993). Earthquakes are thought to occur down to the brittle-ductile transition which, depending on strain rate and lithology, may be at a temperature of 600-760°C (*Bjarnason et al.*, 1994; *Foulger*, 1995). Shear waves passing through the upper 16 km in south Iceland undergo very low attenuation, and most of the attenuation they do experience may be explained by small-scale heterogeneities in the upper 4 km (*Menke et al.*, 1995).

Three main models have been proposed for crustal structure in Iceland (Figure 1.5). The major difference between them is the nature of the V_P=7.0-7.4 km/s zone between about 10 and 20 km. An early model involves a 10-15 km thick crust underlain by a hot, partially molten basaltic layer in the upper mantle, with 10-20% partial melt, low resistivity and low V_P (*Pálmason*, 1971; *Gebrande et al.*, 1980). This model implies temperatures of about 1200°C at the crust-mantle interface. However, upper mantle peridotite at this temperature, and with >10% partial melt, is predicted to have a much lower V_P than the observed value of about 7.2 km/s in the 10-20 km depth range (*Bjarnason et al.*, 1994). Also, large amounts of partial melt would severely attenuate shear waves, and this is not observed, at least in south Iceland. Some of the evidence that supports this model comes from the interpretation of two long refraction profiles shot in 1977 (*Angenheister et al.*, 1980), which detected anomalously low *S*-wave speed (V_S) in the lower crust, with V_P / V_S values of about 2.0 (*Gebrande et al.*, 1980). These profiles have recently been reinterpreted, and augmented by data from a few regional earthquakes recorded in 1991 (*Menke et al.*, 1996). This reinterpretation suggests that $V_P / V_S \cong 1.76$ and that there is little attenuation of *S* waves in the upper 20-30 km.

An alternative crustal model involves a 10-15 km thick crust with a completely molten, thin, basaltic layer at the crust-mantle interface, underlain by 1200°C upper mantle with 1-4% partial melt. In this model, the molten basalt is the low resistivity

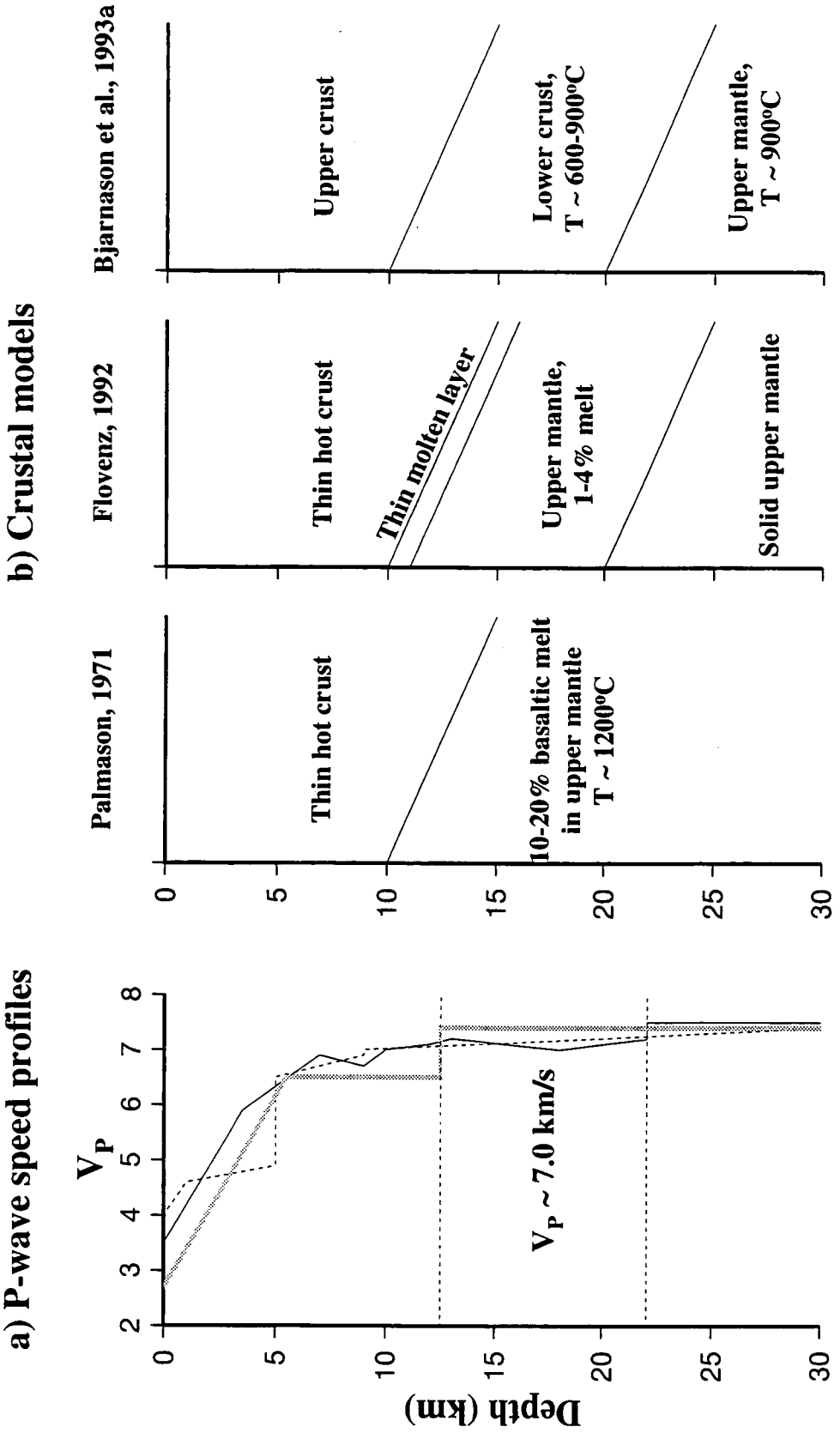

Figure 1.5: (a) *P*-wave speed profiles in Iceland from *Flóvenz* (1980) (grey line), *Gebrande et al.* (1980) (dashed line) and *Bjarnason et al.* (1993a) (solid line). (b) Crustal models proposed by *Pálmason* (1971), *Flóvenz* (1992) and *Bjarnason et al.* (1993a).

layer detected by MT. Mantle at this temperature and with a small volume of partial melt would have a V_P of about 7.2 km/s, which fits the observed wave-speeds for 10-20 km depth (*Flóvenz*, 1992).

Bjarnason et al. (1993a) detected a strong refractor at 20-24 km depth beneath south Iceland and interpret this as the Moho, which implies a much thicker crust than other models (Figure 1.5). It is suggested the lower crust has a V_P of around 7.2 km/s, which implies temperatures of about 900°C at the Moho, and thus no melting. These lower crustal temperatures are consistent with the lack of *S* wave attenuation (*Bjarnason et al.*, 1993a). However they leave the low-resistivity layer detected by MT unexplained. Similar low-resistivity layers are detected within continental crust in some areas, and are interpreted as graphite layers or interconnected saline pore fluids (*e.g.*, *Hyndman et al.*, 1993) but such explanations seem unlikely for the lower crust in Iceland. Alternatively the deep refractor detected by *Bjarnason et al.* (1993a) could be a transition from partial molten to normal mantle (*Flóvenz*, 1992).

The nature of the crust and upper mantle in Iceland is thus currently uncertain. It is known to vary greatly across Iceland and thus results from south Iceland, and especially the potentially anomalous crust in the SISZ, may not be representative of the rest of the island.

1.2.2 The tectonics and seismicity of Iceland

Almost all seismic activity within Iceland occurs along the plate boundary (Figure 1.6; *Einarsson*, 1991). The largest earthquakes in historical times have magnitudes up to 7.1 and occurred in the SISZ and the TFZ (*Einarsson et al.*, 1981; *Stefánsson et al.*, 1993).

The first Icelandic seismic station began operation at Reykjavik in 1930. The Icelandic regional seismograph network was established in the 1970s, with the installation of 30-40 short-period instruments that were located across Iceland to monitor the most seismically active areas (*Einarsson*, 1991). The South Iceland Lowlands (SIL) seismometer network was established as part of an earthquake prediction research project in the SISZ (*Stefánsson et al.*, 1993). The network became operational in 1990, and now has eleven three-component digital seismometers in south Iceland that are linked to a central processing point in Reykjavik.

In the neovolcanic zones, two types of seismicity are generally identified; small-magnitude activity in geothermal areas that is continuous on a daily basis, and "tectonic" earthquakes which often occur in swarms and are sometimes associated with rifting episodes. Most seismicity is associated with central volcanoes, but not all the volcanoes are seismically active. Earthquakes are common at volcanoes such as Krafla, Katla and central volcanoes underlying the Vatnajökull ice sheet (particularly Bárðarbunga and Grímsvötn). Many of the largest earthquakes in Iceland in the last 20

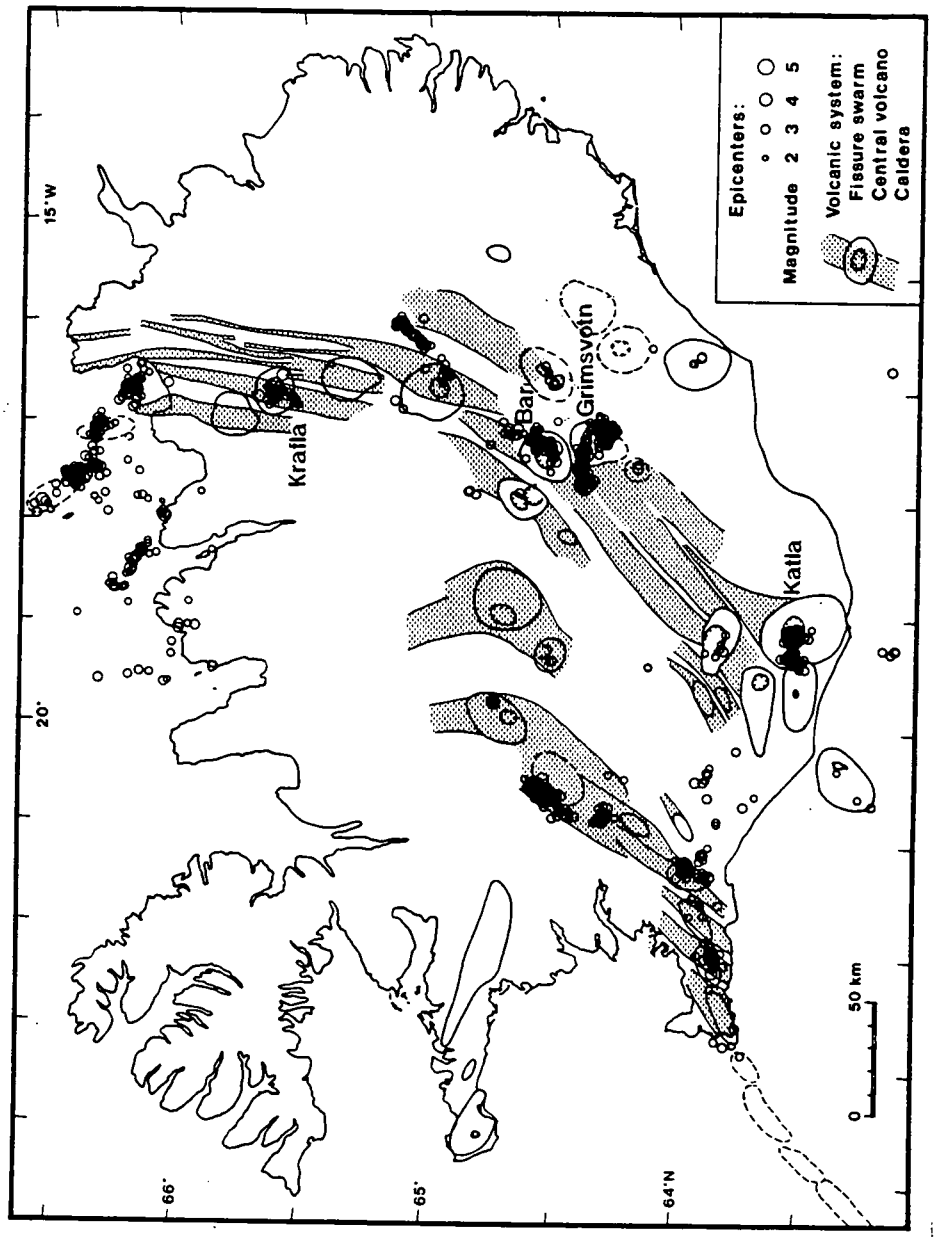

Figure 1.6: Map showing earthquakes with M_{IL}>2 in Iceland from 1982 to 1985, with the volcanic systems. Bar: Bárðarbunga (from *Einarsson*, 1991).

years have been at Bárðarbunga. Six large ($m_b \approx 5$) earthquakes from Bárðarbunga are listed in the Harvard moment tensor catalogue between 1977 and 1993. All these earthquakes have similar, non-double-couple moment tensors that have been interpreted as resulting from shear slip on a volcanic ring fault (*Ekström*, 1994; Section 2.4.12). The WVZ is also seismically active, with earthquakes occurring in swarms away from any central volcanoes (*Einarsson*, 1991).

Between 1975 and 1984 the Krafla volcano, one of the volcanic systems in the NVZ, experienced substantial crustal rifting and fissure eruptions. After the end of the rifting episode in 1985, the continuous background seismicity associated with geothermal activity was studied by a temporary radio-telemetered network of vertical-component seismometers with analogue recording (*Arnott and Foulger*, 1994a, b). During three months, 489 locatable earthquakes were identified. Most of the earthquakes occurred beneath two geothermal fields, at Krafla (within the volcano caldera) and Námafjall, to the southwest of the caldera, from the surface to 3.2 km depth. The magnitudes ranged up to M_{IL}=2.1.

Focal mechanisms derived from *P*-wave polarities of earthquakes recorded in 1985 are highly variable, with *P* and *T* axes distributed chaotically. This is different from other studies of the focal mechanisms of geothermal earthquakes at the Reykjanes Peninsula and the Hengill volcanic complex (Section 1.3.4.3.4), which found that mechanisms were highly regular, and consistent with horizontal *T* axes parallel to the local extension direction. This difference is attributed to the absence of an extensional deviatoric stress field at Krafla, probably because of the recent rifting episode (*Arnott and Foulger*, 1994b). Five of the earthquakes studied had *P*-wave polarities inconsistent with double-couple focal mechanisms (Section 2.4.4).

1.3 The Hengill area

1.3.1 The Hengill triple junction

1.3.1.1 Introduction

The Hengill triple junction is the junction of the RPVZ, the WVZ and the SISZ (Figure 1.4). The junction is thus of the ridge-ridge-transform type.

1.3.1.2 The Reykjanes Peninsula Volcanic Zone

The RPVZ is an obliquely-spreading zone that connects the offshore Reykjanes ridge to the Hengill triple junction. It contains four volcanic systems, dominated by normal faults and fissures that trend at about 45°N, and are arranged in a sinistral, *en echelon* pattern. There are four high-temperature geothermal areas located where the trace of the plate boundary crosses the fissure swarms.

A large earthquake swarm in the western Reykjanes Peninsula in 1972 was recorded by a temporary array of 23 one-component seismometers (*Klein et al.*, 1977). The swarm consisted of more than 17,000 earthquakes. Over 2500 of these were located, and defined a linear, 1-2 km wide band of seismicity at 2-5 km depth, with the seismicity concentrated within the volcanic systems. During the main, 8-day long swarm, earthquakes were clustered in space and time. Volumes of seismic activity grew or migrated laterally with time, at a rate of 1 to 2 km/day. Focal mechanisms were mainly normal and strike-slip, and consistent with the extensional tectonics of the region, with horizontal, NW-SE striking *T* axes. A small number of earthquakes, all in the same volume, had non-double-couple mechanisms (Section 2.4.2).

1.3.1.3 The Western Volcanic Zone

The WVZ strikes NNW from Hengill towards Langjökull, and is dominated by large hyaloclastite and shield volcanoes (*Sæmundsson*, 1992). It is not known to have been volcanically active in historical times, but generates earthquake swarms (*Einarsson*, 1991), and may take up only a small part of the tectonic spreading in south Iceland (*Sigmundsson et al.*, 1995).

1.3.1.4 The South Iceland Seismic Zone

The South Iceland Seismic Zone (SISZ) is a complex fault zone, oriented east-west, about 80 km long and 10-15 km wide. It connects the southern end of the WVZ at the Hengill triple junction to the EVZ (Figure 1.7). Many large historical earthquakes have occurred in the SISZ, with over 30 earthquakes between 1164 and 1912 described in written records (*Einarsson et al.*, 1981). The most recent large and moderate earthquakes are a magnitude 7.0 earthquake that occurred in 1912 and a M_W=5.9 earthquake at Vatnafjöll in 1987, both within the eastern section of the SISZ (Figure 1.7). Small-magnitude seismicity within recent decades has been distributed throughout the zone. Focal mechanisms are predominantly strike-slip, with north-south and east-west nodal planes (*e.g.*, *Einarsson*, 1991). The SISZ is undergoing left-lateral shear on a regional scale, and recent geodetic measurements suggest that is currently responsible for 85±15% of the transform motion across south Iceland (*Sigmundsson et al.*, 1995).

Despite the east-west trend of the SISZ, and the left-lateral motion measured along it, no major east-west strike-slip fault has been identified within the zone. Also, unlike transform faults along submarine sections of accretionary ridges, the SISZ has no major topographic expression. Historical earthquakes have damage zones elongated north-south, and north-south oriented surface ruptures (*e.g.*, *Einarsson et al.*, 1981). For example, the 6 May 1912 earthquake ruptured fresh basalt lava flows along a ~20 km long, north-south oriented, *en échelon* fracture system, with right-lateral slip of 1 to 3 m (*Bjarnason et al.*, 1993b).

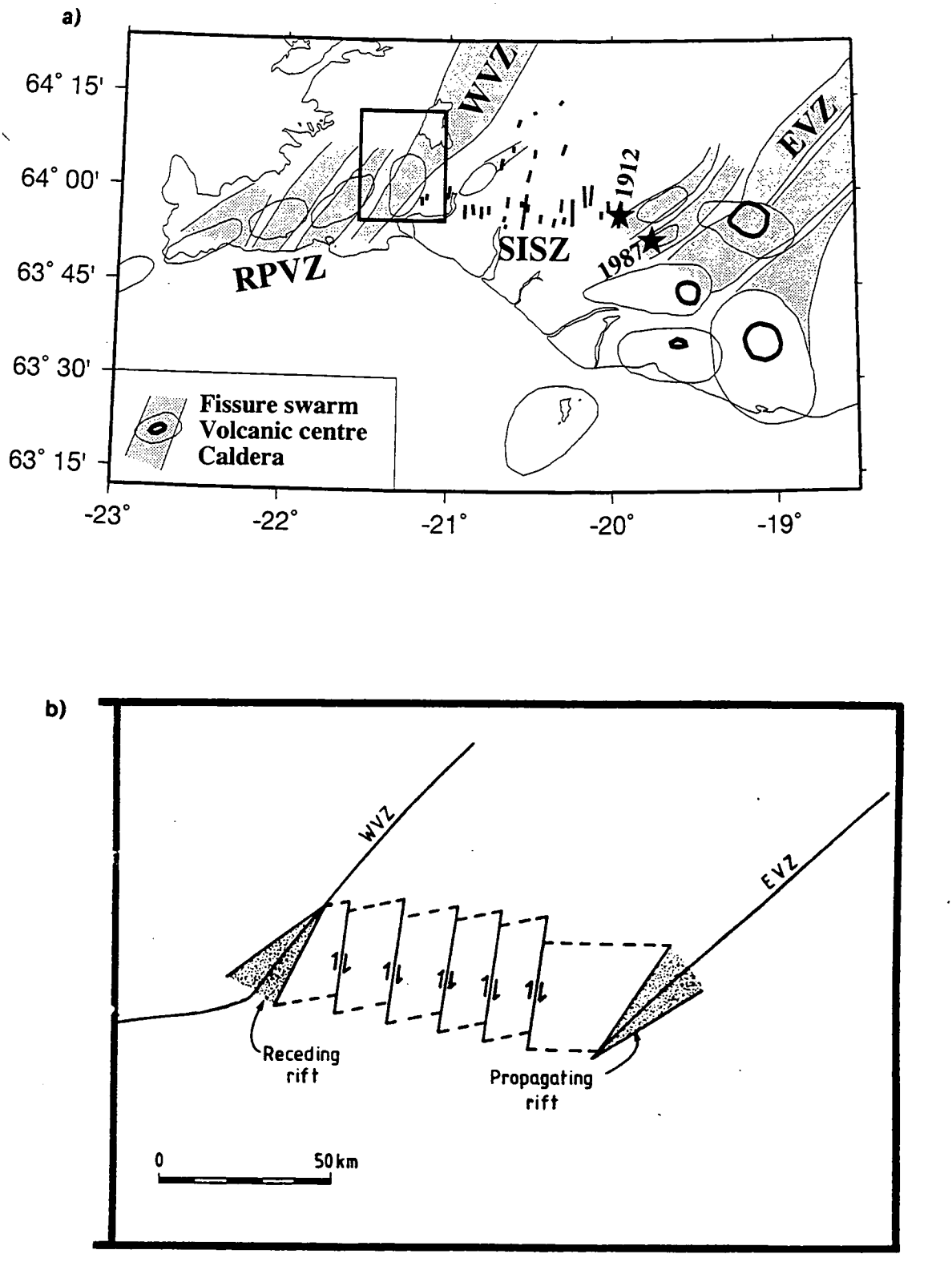

Figure 1.7: (a) Map showing the tectonics of south Iceland. Solid lines: mapped faults in the SISZ (after *Einarsson and Sæmundsson*, 1987). The box shows the position of the Hengill volcanic complex. Stars: epicentres of the 1912 and 1987 earthquakes. (b) The bookshelf tectonic model. Deformation within the SISZ occurs by right-lateral strike-slip motion on a series of north-south oriented faults (from *Foulger et al.*, 1993).

It has been proposed that faulting within the SISZ occurs on a system of closely-spaced, parallel, north-south oriented faults, with deformation occurring in a "bookshelf" tectonic style (*Einarsson*, 1991; *Foulger et al.*, 1993; *Sigmundsson et al.*, 1995; Figure 1.7). The bookshelf model predicts that crustal blocks 1-5 km wide are rotating anti-clockwise, and are bordered by north-south faults undergoing right-lateral shear.

The SISZ is probably migrating southwards, along with the propagating tip of the EVZ. The amount of slip on currently-active faults suggests that it has been in its present location for only about 25,000 years (*Sigmundsson et al.*, 1995). *Morgan and Kleinrock* (1991) suggest that in this situation, deformation along north-south fault planes is more likely, as such faults can grow and slip incrementally as the zone migrates southwards. The alternative situation, with slip on a major east-west fault, would require the creation of a series of entirely new east-west faults as the SISZ migrated southwards.

The SIL network (Section 1.2.2) detects up to 1700 earthquakes per month in the SISZ (*Stefánsson*, 1993). Earthquakes are distributed throughout the area covered by the network, but are concentrated along the SISZ (Figure 1.8). Maximum hypocentral depths increase away from the WVZ, from about 8 km at Hengill (21.5°W) to 12 km at 20°W.

The data collected by the SIL network show that there is strong *S*-wave anisotropy within the SISZ (*Menke et al.*, 1994). The anisotropy is estimated by measuring the amount of *S*-wave splitting, and the azimuth of the fast *S*-wave polarisation direction from three-component recordings of local earthquakes. Measured *S*-wave splitting times range from 0.1-0.3 s, suggesting that anisotropy varies from 7-12%, with the highest values recorded in the WVZ. The fast shear-wave azimuth is quite consistent across the area and is oriented northeast-southwest, parallel to the tectonic grain (Figure 1.9). *Menke et al.* (1994) suggest that the anisotropy is due to systems of parallel cracks in the shallow crust that strike northeast, with the crack orientations reflecting the direction of current extension.

Menke et al. (1995) found low values of attenuation for *P* and *S* waves in the lower crust in and around the SISZ, using data from the SIL network. Seismic attenuation is the decrease of amplitude of seismic waves with distance due to scattering and absorption. In the mid- to lower crust, from 8 to 18 km depth, $Q_P > 110$ and $Q_S > 250$, which implies that the temperature of the lower crust is between 700 to 775°C. Higher attenuation, with $Q_P \approx 60$ and $Q_S \approx 100$ occurs above 4 km depth. The lowest Q_P and Q_S values are found in the WVZ and EVZ. *Menke et al.* (1995) suggest that most of the attenuation is due to scattering from small-scale heterogeneities such as fissures, and porosity changes in the upper crust.

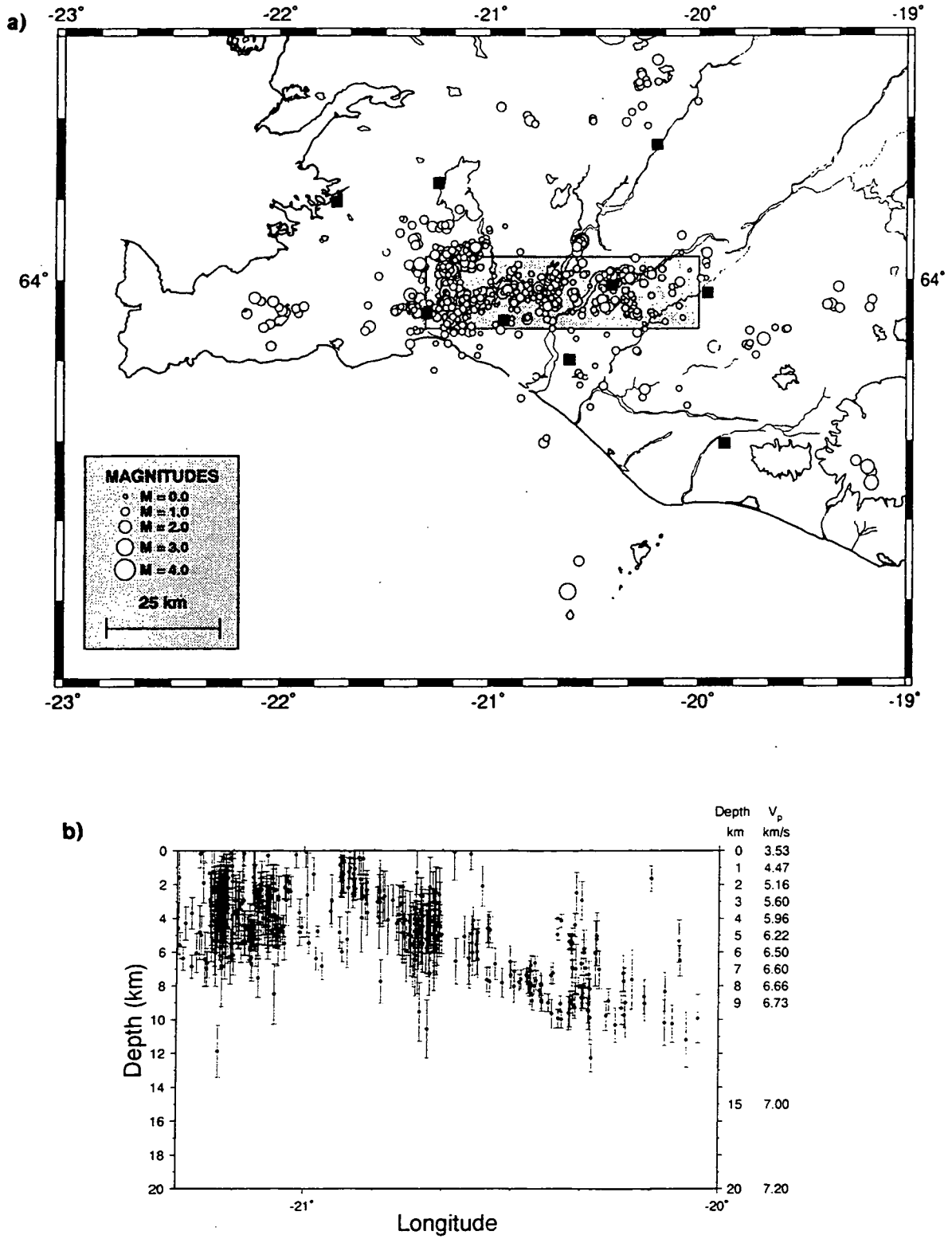

Figure 1.8: (a) Map of earthquake epicentres (circles) in the South Iceland Seismic Zone (box) and surrounding area, located by the SIL network from July 1991 to February 1992. Solid squares are stations of the SIL network. (from *Stefánsson et al.*, 1993). (b) A depth section of earthquakes within the SISZ, located using the one-dimensional v_P model shown at right. Error bars are 1σ (from *Stefánsson et al.*, 1993).

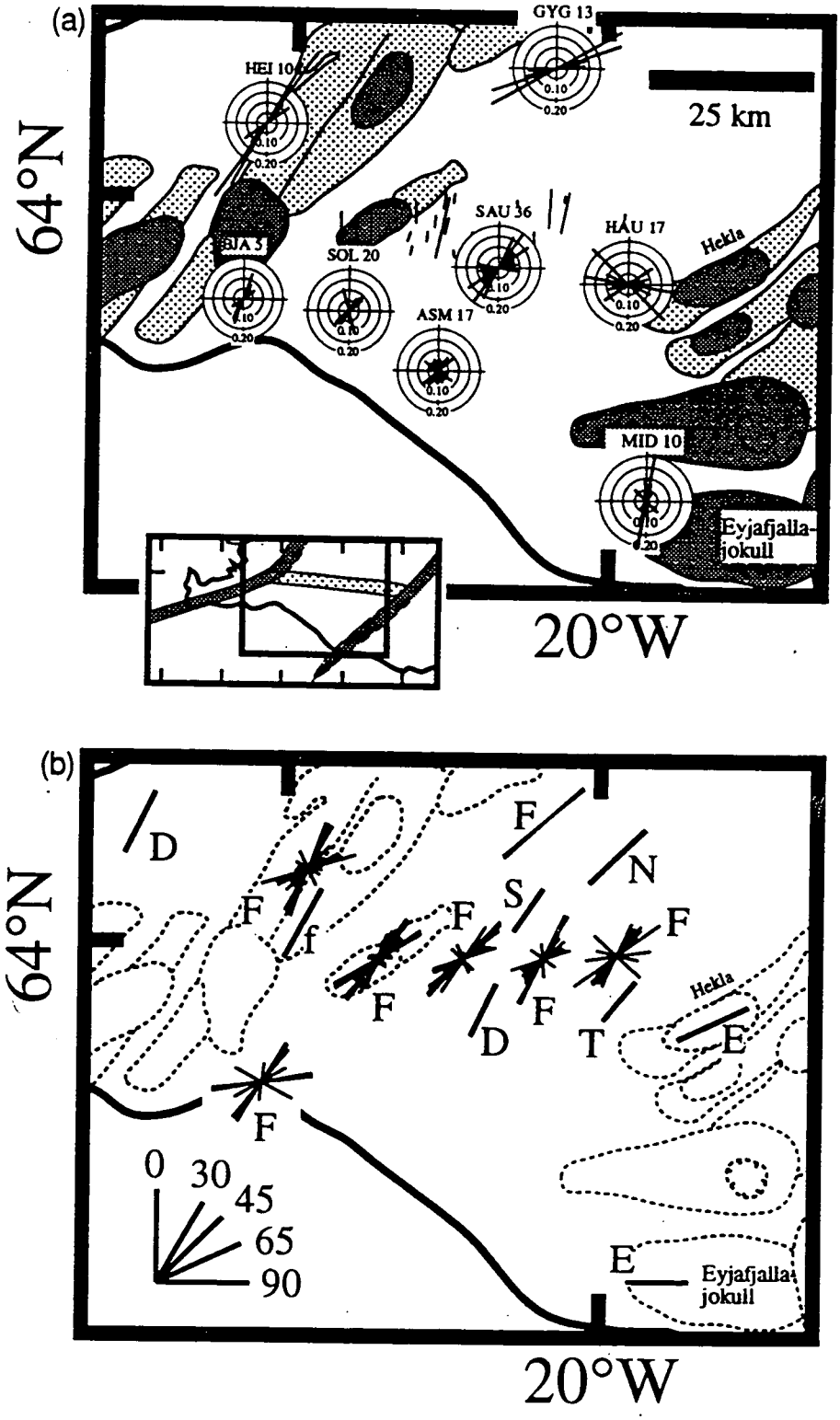

Figure 1.9: Seismic anisotropy within the SISZ. (a) Circles show anisotropy measured at each station. Orientation of line segments gives fast polarisation direction, length of line indicates amount of splitting. Station name and number of observations are printed above the station. (b) direction of maximum compressive stress determined from strike of dykes (D), eruptive fissures (E), fissures (f), normal faults (N), tension cracks (T) and focal mechanisms (F) (From *Menke et al.*, 1994).

1.3.2 The geology and tectonics of the Hengill volcanic complex

1.3.2.1 The volcanic systems

The Hengill area is dominated by three volcanic systems, the Hengill, Grensdalur and Hromundartindur systems, which are or were the discrete loci of spreading and/or volcanism (Figure 1.10). Activity has migrated westwards within the area since 0.7 Ma. The crust is mainly composed of eruptive units from these systems and a handful of small shield volcanoes.

The Grensdalur system is the oldest, and is now probably extinct. It was active from about 2.5 Ma, as a central volcano within a NNE-trending fissure swarm. The volcanic centre is now deeply eroded and is exposed in a topographic basin. Within the Grensdalur system, the oldest geologic units are aphyric (lacking phenocrysts), with the proportion of phenocrysts increasing with time. This suggests that the Grensdalur volcano had a crustal magma chamber (*Walker*, 1992).

The Hromundartindur volcanic system lies between the Grensdalur and Hengill systems. It became active at the same time as the Hengill system, and does not have a well-developed fissure swarm or rift. Mt. Hromundartindur is the highest mountain within the system and contains intermediate rocks, suggesting a fractionating magma chamber source. One minor post-glacial eruption has occurred within the system.

The Hengill volcanic system is now the locus of spreading and volcanic activity in the southern WVZ. Mt. Hengill comprises mostly one eruptive unit, and has not developed into a mature central volcano. It lies within a well-developed fissure swarm (Figure 1.10). Five post-glacial eruptions have occurred in the Hengill fissure swarm. Four of these occurred north of the Hengill volcano (*Sæmundsson*, 1992). There, the fissures are 5-10 km long, and have produced crater rows and aa lavas, with smaller quantities of pahoehoe lava. The most recent eruption is dated at 1880±65 years BP by ^{14}C dating, and formed the Nesjahraun lava, which covers an area of 10-11 km^2. The lava formed at the same time as ash eruptions from a tuff cone at Sandey, an island in Lake Thingvallavatn (Figure 1.10).

The Hengill fissure swarm is about 65 km long and trends 030°N through the Hengill volcanic centre, from near the south coast of Iceland to north of Lake Thingvallavatn. The swarm has nested graben structures, and appears to be active episodically. The Thingvellir section of the swarm has been active since the last ice age, as fissures dissect a 9000 year old lava to the north of Lake Thingvallavatn (*Gudmundsson*, 1987). This section has undergone a maximum of 70 m subsidence, and is delineated by two major fissures, Almannagjá (the site of the historic Icelandic parliament) and Hrafnagjá (Figure 1.10). The most recent rifting episode occurred in 1789, and involved activity along the entire fissure swarm. At Thingvellir farm new fissures formed that could be "crossed in one step". The Almannagjá and Hrafnagjá fissures were activated and

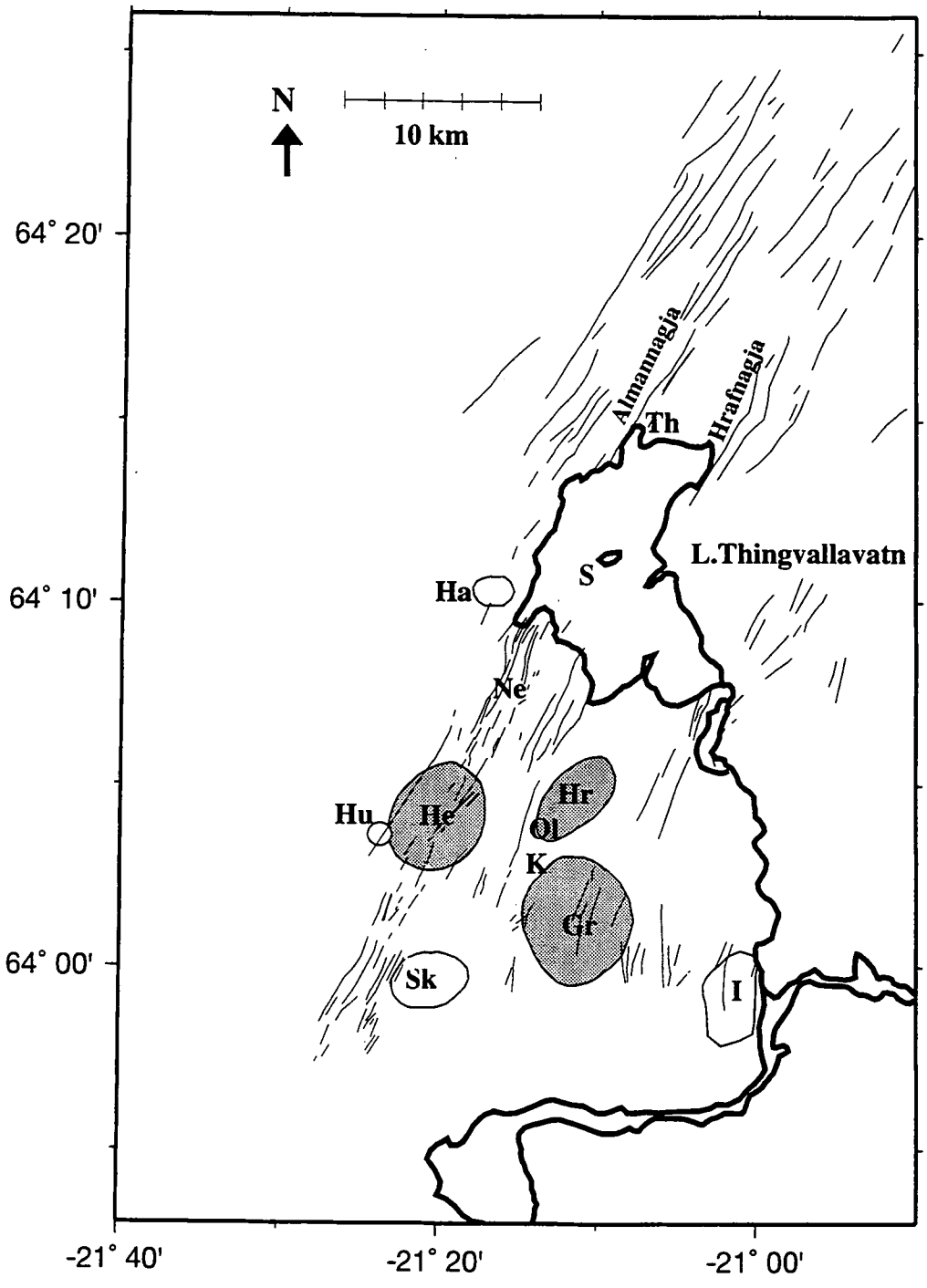

Figure 1.10: Map of the Hengill volcanic system and the Hengill area. Lines show main fissures and faults. Hengill (He), Grensdalur (Gr) and Hromundartindur (Hr) are volcanic centres. Húsmúli (Hu), Hæðir (Ha), Skálafell (Sk) and Ingolfsfjall (I) are shield volcanoes. Th: Thingvellir; S: Sandey; Ne: Nesjavellir; Ol: Ölkelduhals ; K: Klambragil.

became impassable to horses. A total subsidence of over 1 m occurred during the episode with the maximum subsidence in the centre of the graben (*Sæmundsson*, 1992). Geodetic measurements from 1967 to 1990 across the Thingvellir fissure swarm show only 10 mm of widening, a rate of 0.43 mm/year (*Tryggvason*, 1990).

Subaerial lava shields at Húsmúli, Hæðir, Ingolfsfjall and Skàlafell are compositionally distinct from the other volcanic rocks in the area and from each other. They were probably formed by magma supplied directly from the upper mantle over short time intervals, perhaps less than 50 years (*Walker*, 1992). These shields date from inter-glacial periods in the Upper Pleistocene.

The tectonic fabric changes abruptly about the 64°N line of latitude. North of this line, there is rugged topography, dominated by the volcanic centres with a high density of surface fissuring and faulting, and active surface geothermal features. South of 64°N and east of the Hengill fissure swarm is the flat raised beach of the Ölfus lowlands, with low-temperature geothermal features only, and little surface faulting.

1.3.2.2 Geothermal activity

The Hengill-Grensdalur geothermal area contains over 100 hot springs and fumaroles (Figure 1.11) that cover an area of 70 km^2 with a surface heat production of 350 MW (*Böðvarsson*, 1951). The springs are dominated by hot water production of approximately 200 kg/s, with steam production of 10 kg/s (*Arnason et al.*, 1986). The area has been extensively explored to analyse its potential for commercial heat and power production, with drilling in the upper 2 km and several geophysical surveys.

At Nesjavellir, 18 wells have been drilled and geothermal fluids are used to heat fresh water that is piped to Reykjavik for space heating. Temperatures of 250-380°C at 2 km depth and geothermal gradients of 300°C/km in the upper few hundred metres have been detected in boreholes (*Böðvarsson et al.*, 1990). The Nesjavellir field is partially two-phase (water and steam) and the remainder of the field is hot water saturated.

Fumarole gas geochemistry suggests that there are three separate geothermal reservoir maxima beneath the Hengill-Grensdalur geothermal area (*Torfason et al.*, 1983). Temperatures exceed 310°C beneath the southern section of the Hengill system, and peak at 300°C beneath Ölkelduhals, within the Hromundartindur system, and 270-280°C beneath the centre of the Grensdalur system (Figure 1.11). These separate maxima suggest that the geothermal area is supplied by at least three separate heat sources, rather than one large source.

1.3.3 Geophysical surveys of the Hengill area

In the 1970s, several resistivity soundings were carried out in the Hengill area, particularly to the south and west of Hengill. The results are summarised by *Hersir* (1980). A low-resistivity layer ($< 15\Omega$) was detected beneath most of the area, from

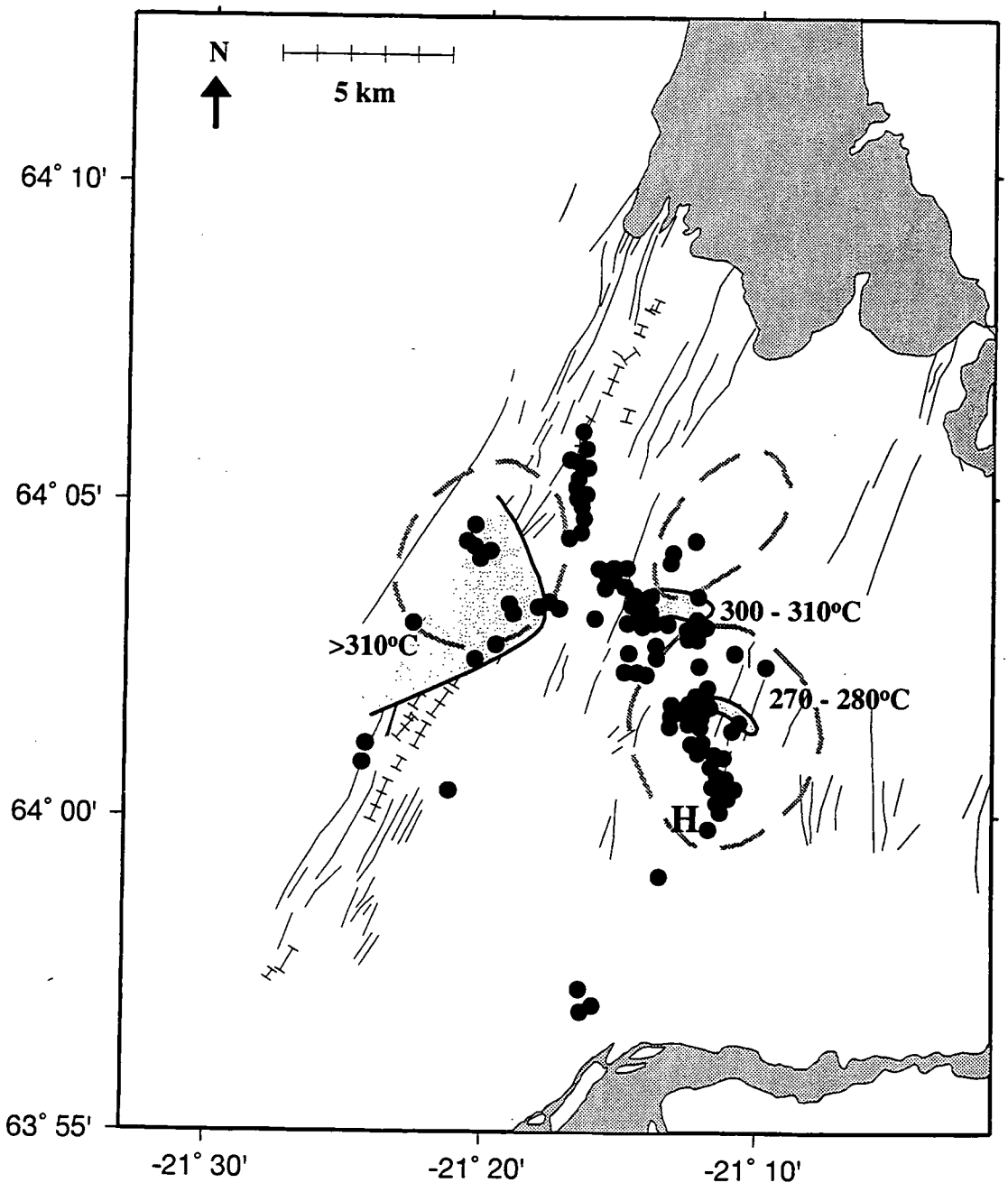

Figure 1.11: Geothermal features of the Hengill volcanic complex. Dashed lines: volcanic centres; thin lines: faults and fissures; solid dots: hot springs; H: Hveragerði; stippled areas show positions of temperature maxima in the geothermal field (from *Torfason*, 1983).

Hengill eastwards to Hveragerði (see Figure 1.11 for location). The layer is deepest beneath the Hengill fissure swarm, at about 400 m, and is bounded by the western margin of the fissure swarm. This low-resistivity layer is though to be caused by geothermal fluids.

A magnetotelluric profile was measured at 10 stations across the WVZ north of Lake Thingvallavatn in 1976 (*Hersir et al.*, 1984). This survey detected a persistent anomalous conductive layer ($< 5\Omega$) that deepened from 8 km at the WVZ to 30-40 km at the ends of the profile. The results from two stations in the Hengill area that were measured at the same time suggest that this layer is also present beneath Hengill, at a similar depth to the part of the profile that crosses the WVZ (*Hersir*, 1980).

A gravity survey was conducted in 1982 and 1983, and measurements were made at 315 stations with an average station spacing of 1.5 km (*Thorbergsson et al.*, 1984). The Bouguer anomaly field has a regional trend that increases from the northeast to southwest and is part of the Iceland-wide low gravity anomaly (Figure 1.12). Superimposed on this trend there is a general low along the Hengill fissure swarm, and high anomalies at the Grensdalur and Húsmúli volcanoes.

A 170 km long refraction / reflection profile was shot across the WVZ, passing to the north of the Hengill area (*Bjarnason et al.*, 1993a). *P*-wave data from 11 shot points and 210 receiver points were inverted to determine a two-dimensional wave-speed model along the profile, which was judged to be well-resolved down to 8 km depth. The depth to the 6.5 km/s contour varies from 4 to 8 km along the profile, and is deepest beneath the SISZ. The wave-speed profiles of *Bjarnason et al.* (1993a) agree with those obtained from earlier experiments (*e.g.*, *Pálmason*, 1971), although they have been interpreted in terms of different crustal thicknesses (Section 1.2.1.3).

1.3.4 The seismicity of the Hengill area

1.3.4.1 Historical seismicity

Three large earthquakes have occurred near the Hengill triple junction since 1700, in 1706, 1896 and 1935 (*Foulger*, 1984). The locations of these three earthquakes are not known precisely, but all are thought to have occurred close to or south of 64°N, and they caused damage to farm buildings there. The 1789 rifting episode was accompanied by a swarm of moderate earthquakes, distributed over a fairly large area. This swarm was erroneously interpreted as a single large earthquake in some early summaries of Icelandic seismicity.

1.3.4.2 Recent monitoring by permanent networks

The regional seismograph network has 8 stations within 80 km of Hengill. In the first seven years of operation of this network 1040 earthquakes, with $M_{IL} \leq 4.2$, were located near the Hengill area (*Foulger and Einarsson*, 1980; *Foulger*, 1988a). The

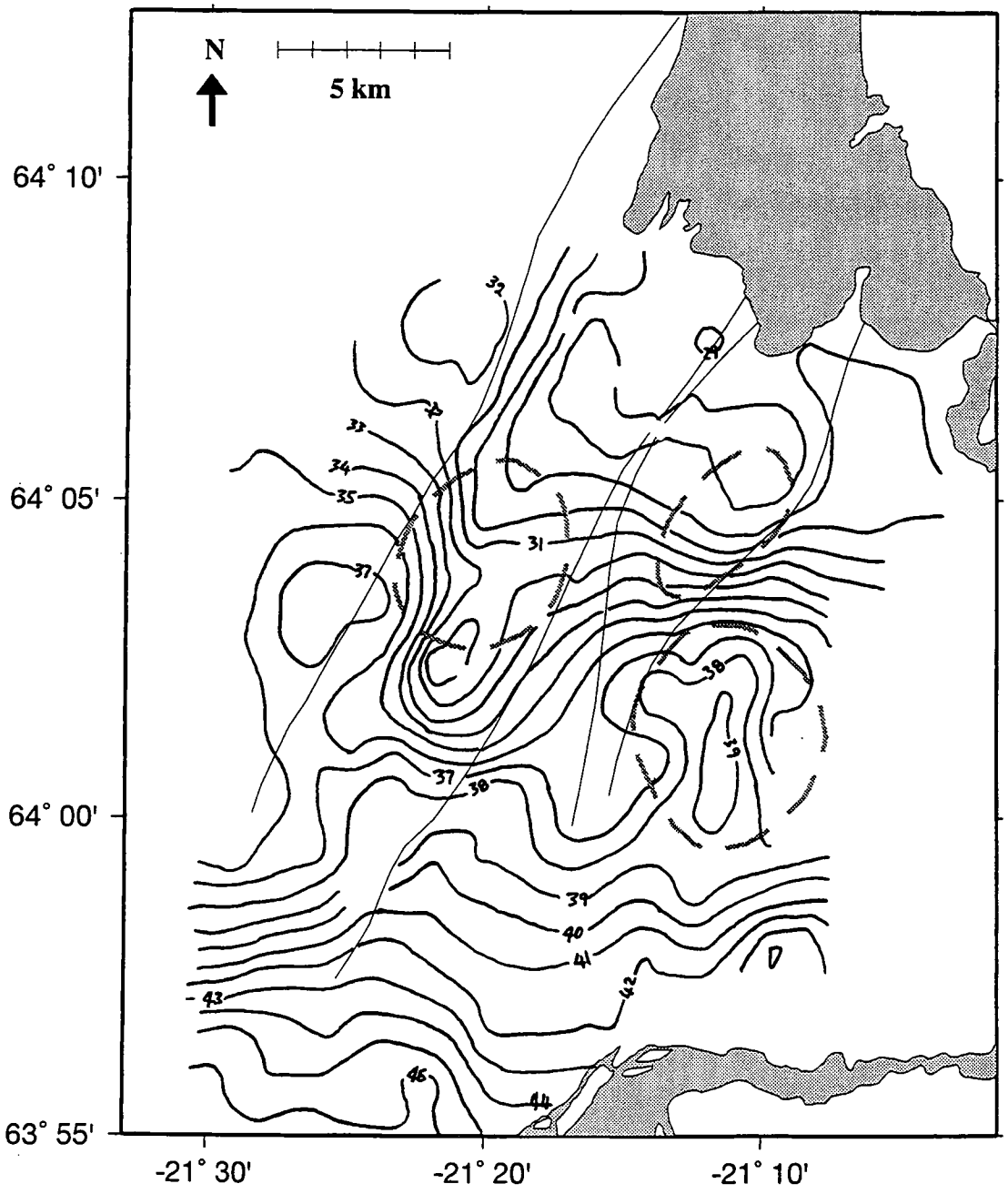

Figure 1.12: Map of the Bouguer anomaly field of the Hengill area, calculated using a density of 2450 kg/m^3. Contour spacing is 1 mGal. Dashed lines: volcanic centres; solid lines: outlines of the Hengill and Hromundartindur volcanic systems (After *Field*, 1994 and *Thorbergsson et al.*, 1984).

earthquakes were mainly located within the geothermal field, immediately west of the Hengill volcanic system, and in the Ölfus lowlands. Only a few earthquakes were associated with the Hengill volcanic system. Over a seven year period, the seismic rate was approximately one M_{IL}=1 earthquake per day. Monitoring by the SIL network since 1986 (Section 1.2.2) shows that the recent distribution of seismicity in the Hengill area is broadly similar to that recorded by the original permanent network, and thus the seismicity pattern has remained essentially constant for over 20 years.

1.3.4.3 The 1981 local earthquake monitoring experiment

1.3.4.3.1 The monitoring network A temporary network of 23 short-period, vertical-component seismometers was operated at Hengill-Grensdalur from July to September 1981 (*Foulger*, 1984; 1988a; Figure 1.13). The experiment was designed to study the continuous small-magnitude seismicity of the area and to evaluate the potential of using seismic studies for geothermal prospecting. Seismic recordings were transmitted by FM radio signal to three magnetic-tape recorders where the data were recorded in analogue. One-component, Wilmore Mk III seismometers were used, which had a natural frequency of 1 Hz.

Over 1900 earthquakes were identified from paper records. Each earthquake had 10-20 *P*-wave arrival times. The earthquakes were located using a one-dimensional crustal model derived from the modelling of explosion data in south Iceland. Local magnitudes were calculated using empirical coda length scales for several stations, and normalised to the Icelandic local magnitude scale. A b-value of 0.76±0.05 was calculated.

1.3.4.3.2 Spatial and temporal distribution of the seismicity Earthquakes recorded in the 1981 temporary experiment are distributed throughout the area encompassed by the array, to a depth of 8 km (*Foulger*, 1988a; Figure 1.14). Most earthquakes locate within clusters of intense seismicity. Many earthquakes are located beneath the Klambragil area from 2 to 6 km depth. A large number of earthquakes are located between 2.5 to 5 km depth to the west of the Hengill fissure swarm, in an area devoid of surface faulting or geothermal activity. The Hengill fissure swarm exhibited low seismicity during 1981, a pattern consistent with the seismicity recorded by the Icelandic permanent network (Section 1.2.2). Nesjavellir is the most active zone within the Hengill fissure swarm.

Three earthquake swarms have been described within the SISZ in the Hengill area. They lasted for 1-4 days and contained a number of spatially close earthquakes (Figure 1.15). Between 1974 and 1978, a number of earthquakes occurred near the village of Hveragerði. On 4-5 February 1977, a swarm occurred, including a magnitude 3.7 earthquake, within a NNE-trending, 8 km-long zone (*Foulger and Einarsson*, 1980). A major swarm at Kirkjuferjuhjáleiga on 19-22 September 1981 was recorded by the temporary network, although the earthquakes lay just outside the network so accurate

locations were not possible (*Foulger*, 1984). *Rögnvaldsson and Slunga* (1994) describe a swarm of 12 earthquakes at 63.96°N, 21.06°W that occurred on 22 October 1991, with $-0.3 \leq M_{IL} \leq 1.0$. All the earthquakes had similar waveforms at a close station. Accurate relative locations were achieved using a joint hypocentre location procedure and suggest that all the earthquakes occurred on a north-striking fault plane with a steep dip. The focal mechanisms of the largest earthquakes are compatible with right-lateral shear on a fault plane of this orientation.

Foulger (1995) mapped the maximum and minimum depths of seismicity across the area, using accurate hypocentral locations for the 1981 earthquakes. For a constant strain rate and uniform lithology, the maximum depth of seismicity gives an indication of temperature at depth. For assumed values of the strain rate in the Hengill area, and a lithology similar to diabase, the temperature at the maximum depth of seismicity is predicted to be 650±50°C.

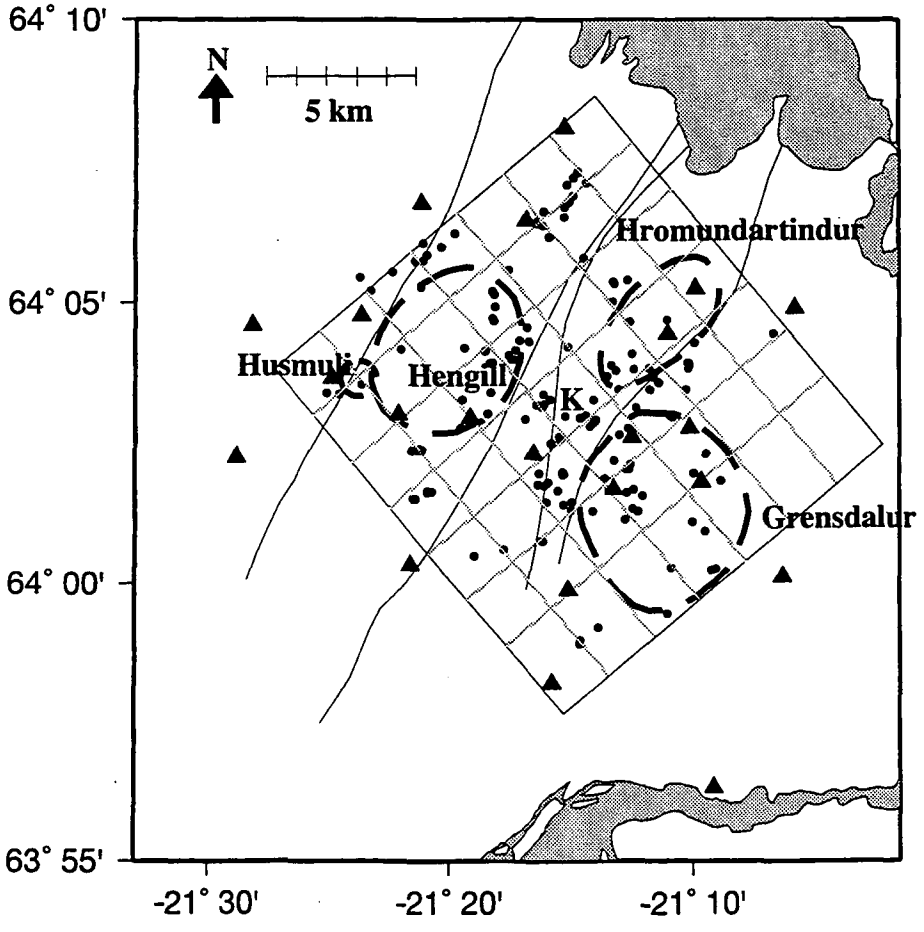

Figure 1.13: The temporary seismometer network deployed in 1981. Solid triangles are stations, dashed lines show main volcanic features, solid lines are outlines of the Hengill and Hromundartindur volcanic systems. Box shows area modelled using local earthquake tomography. *P*-wave speed values were calculated at intersections of light grey lines.

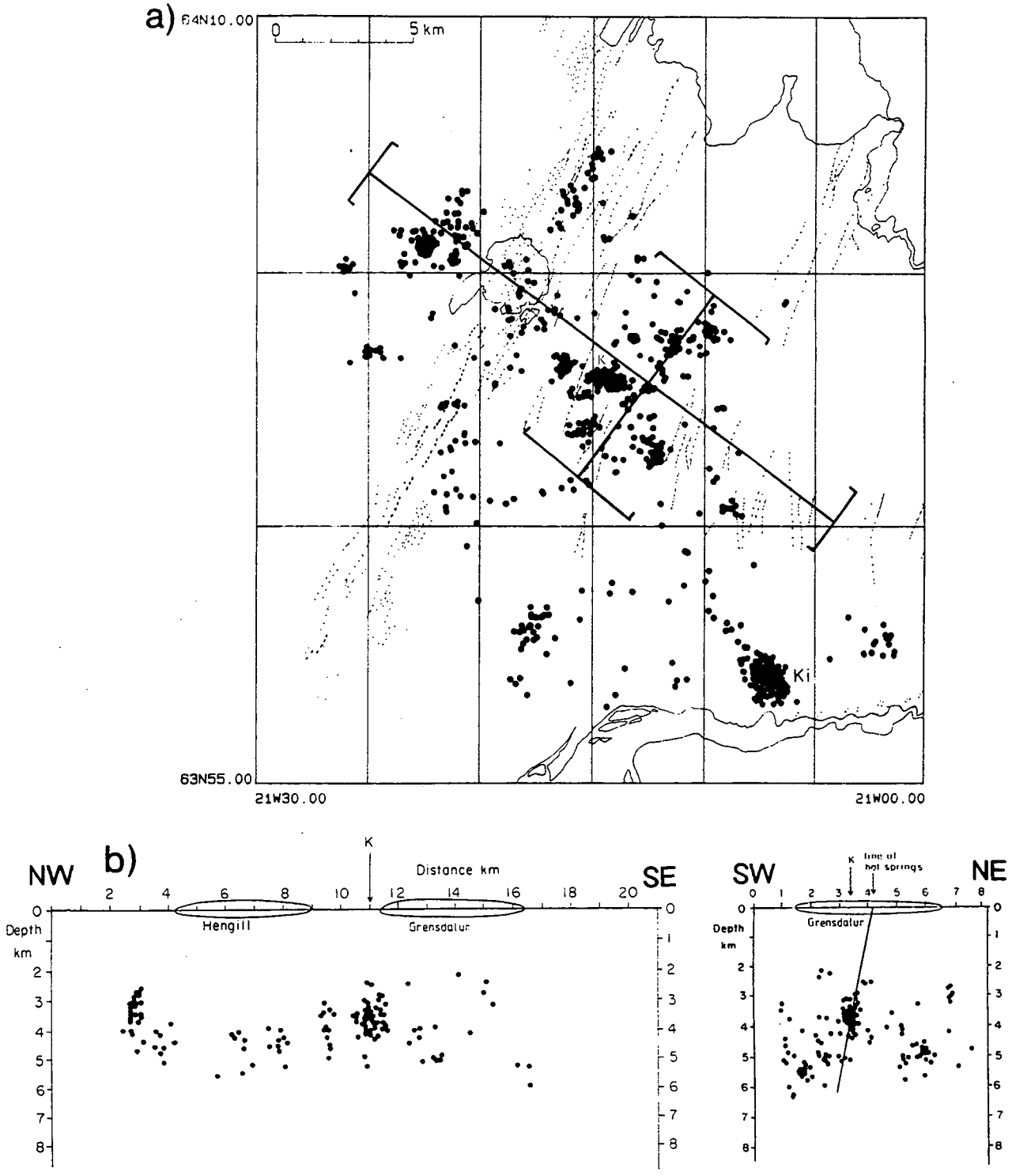

Figure 1.14: (a) Map of epicentres located using data from the 1981 temporary network. All events have horizontal errors less than 1.0 km and RMS travel-time residuals less than 0.1 s. K: Klambragil; Ki: Kirkjuferjuhjáleiga. Heavy lines show position of depth sections. (b) Depth sections along lines shown in (a). The positions of the Hengill and Grensdalur volcanic centres are shown (from *Foulger*, 1988a).

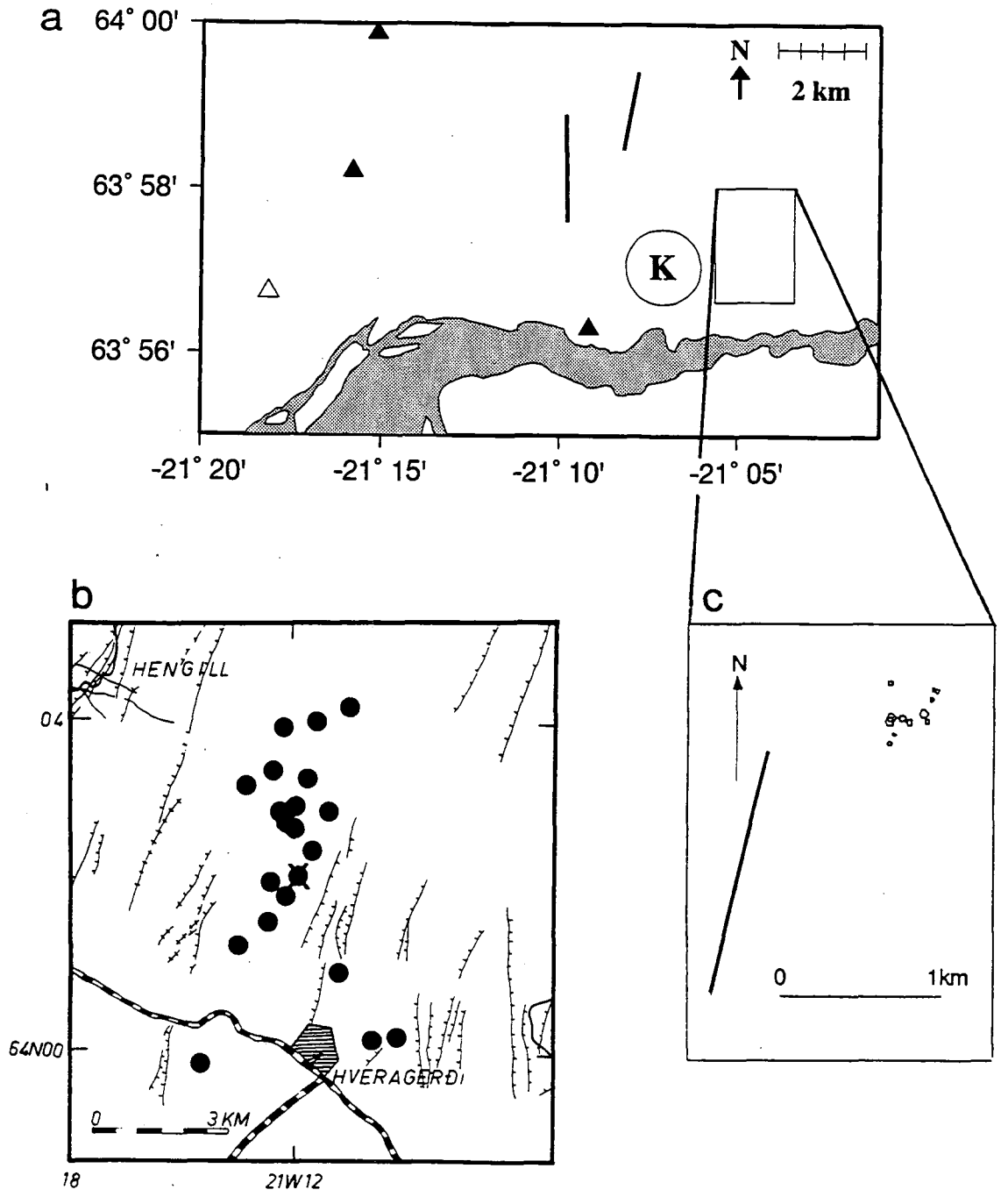

Figure 1.15: Earthquake sequences in the Hengill area. (a) map showing locations of the 1981 Kirkjuferjuhjáleiga (K) and the 1991 (box) swarms. Solid triangles: 1981 temporary stations; open triangle: SIL station bja; solid lines: major faults. (b) Location map of the 1977 mainshock sequence. Cross indicates M_{IL}=3.7 mainshock (from *Foulger and Einarsson*, 1980). (c) Detailed locations of earthquakes in the 1991 swarm. The earthquakes all lie within 5 m of a plane that dips to the ESE. Black line shows a nearby fault trace, which may represent the same fault plane (from *Rögnvaldsson and Slunga*, 1994).

The maximum depth of seismicity varied from 4-7 km, with the deepest earthquakes occurring in the Ölfus lowlands and the Hengill fissure swarm to the west and north. The shallowest well-constrained maximum depth of seismicity was at Ölkelduhals, the site of one of the reservoir temperature maxima (Section 1.3.2.2). These depths of seismicity correspond to average geothermal gradients of 84-138°C/km from the surface to the base of the seismogenic zone. The highest geothermal gradients were found beneath Ölkelduhals, and not, as might be expected, beneath the currently active Hengill volcanic centre. The seismogenic layer was of approximately constant thickness (3 km) across the area, except for the western part of the Grensdalur system and in the region north of Hengill volcano.

1.3.4.3.3 Local earthquake tomography The data set collected in 1981 is ideally suited for local earthquake tomography as the earthquakes had broad spatial distribution and were recorded by a uniform array, giving a set of diverse ray paths which sampled a crustal volume down to 6 km depth.

The simultaneous inversion method of *Thurber* (1981) was used to calculate the three-dimensional V_P structure of a 14 × 15 km area to 6 km depth (*Toomey and Foulger*, 1989; *Foulger and Toomey*, 1989; Figure 1.13). The method uses *P*-wave arrival times to simultaneously calculate changes to the V_P model and earthquake hypocentral parameters. The model is continuous and defined at nodes with linear interpolation between the nodes.

A subset of high-quality earthquakes was selected to give a set of ray paths that sampled the study volume as uniformly as possible. Each earthquake used had at least 9 *P*-wave arrival times, with a maximum gap in source-to-receiver azimuths of 180°. In volumes of intense seismicity, only the highest-quality earthquakes were used. The final data set consisted of 158 earthquakes and two explosions with 2409 *P*-wave arrival times (*Toomey and Foulger*, 1989).

The wave-speed model was defined at nodes spaced at 2 and 3 km horizontally (Figure 1.13) and 1 km vertically, from 0 to 6 km depth. The final three-dimensional wave-speed model had three discrete volumes with high V_P (where the difference from the regional wave-speed structure is greater than 7%). These volumes were located beneath Grensdalur volcano, from 0 to 3 km depth, beneath the Húsmúli shield volcano from 0 to 3 km depth, and beneath Ölkelduhals, from 3 to at least 5 km depth (Figure 1.16). The Húsmúli anomaly formed a narrow (2 km diameter) cylinder that curved towards the Hengill volcano at depth. A small volume of low relative wave speed (where the difference from the regional wave-speed structure is less than -7%) was imaged beneath the northern section of the Hengill volcanic system, at 3 km depth. Other, smaller volumes of both high and low relative wave speed were not considered significant (*Foulger and Toomey*, 1989).

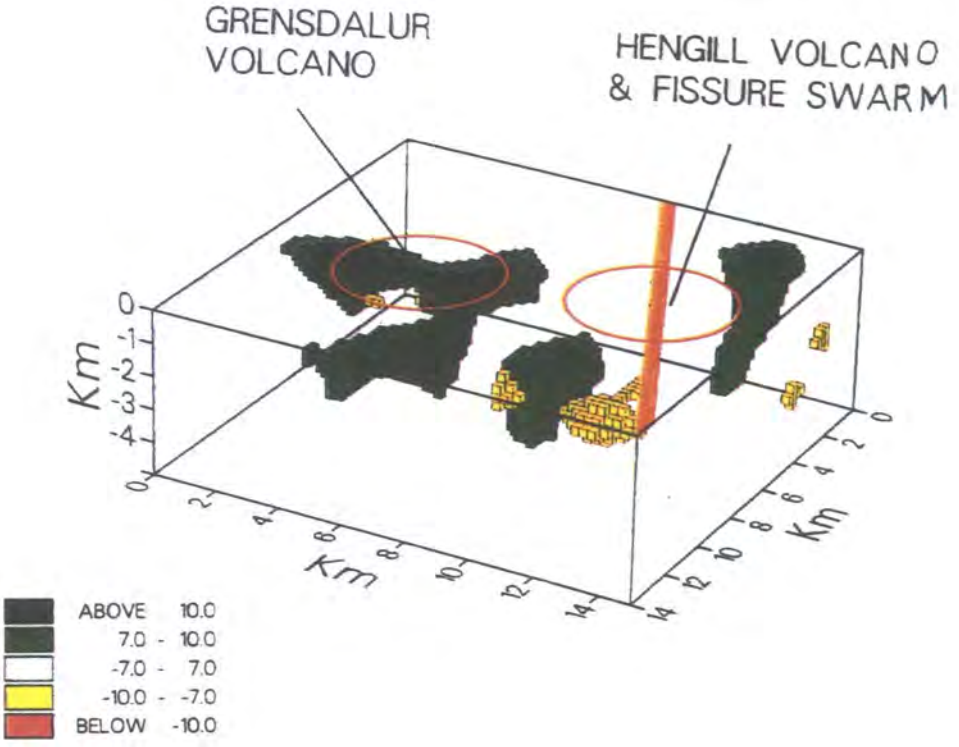

Figure 1.16: Image of three-dimensional *P*-wave speed model, viewed from the northeast. Colour scale shows percentage difference from one-dimensional starting model. *P*-wave speed is shown in cubes of dimension 0.25 km, although the actual model is interpolated linearly between nodes. Red circles show the Hengill and Grensdalur volcanic centres. Orange line represents the Hengill fissure swarm (from *Toomey and Foulger*, 1989).

The high wave-speed bodies were interpreted as volumes of high-density, solidified intrusions (*Foulger and Toomey*, 1989). The shape and orientation of the Húsmúli body with respect to the Hengill volcanic centre suggests that it represents a solidified conduit that supplied magma from beneath Hengill to the surface during the eruption of Húsmúli. The low wave-speed body beneath Hengill was interpreted as a volume that may contain partial melt (*Foulger and Toomey*, 1989).

1.3.4.3.4 Focal mechanisms Well-constrained focal mechanisms were obtained using *P*-wave polarities for 178 of the earthquakes recorded in 1981 (*Foulger*, 1988b). Almost 50% of these earthquakes have *P*-wave polarities incompatible with orthogonal nodal planes, and were classified as "non-double-couple" (non-DC) (*Foulger*, 1988b). Most of the non-DC earthquakes occurred in the geothermal area, and they comprised 60-90% of all earthquakes in some geographical clusters. The non-DC earthquakes were intermixed spatially with earthquakes compatible with DC focal mechanisms, suggesting that the non-DC earthquakes were not an artefact of anomalous ray

propagation due to heterogeneous structure. To confirm this, *Foulger and Julian* (1993) traced rays through the three-dimensional wave-speed model obtained using local earthquake tomography (Section 1.3.4.3.3). They determined that crustal heterogeneity does affect the locations of stations on the focal sphere, sometimes by large amounts, especially for earthquakes that experience large changes in focal depth when relocated using the three-dimensional model. However, 56 of 131 of the best-constrained earthquakes were found to still have non-DC mechanisms. These earthquakes were interpreted as tensile cracking, possibly accompanied by shear failure or an implosion due to pore fluid pressure reduction accompanying tensile failure (*Foulger and Long*, 1984; *Foulger*, 1988b; Section 2.4.3).

The focal mechanisms of the DC earthquakes observed in 1981 tend to be consistent within geographical clusters. The earthquakes had mostly normal or strike-slip mechanisms, with *P*-axes that dip from vertical to near-horizontal and strike northeast, and near horizontal *T*-axes that strike predominantly northwest (Figure 1.17). The normal-faulting earthquakes are consistent with faulting on planes with a similar orientation to faults mapped at the surface (*Foulger*, 1988b).

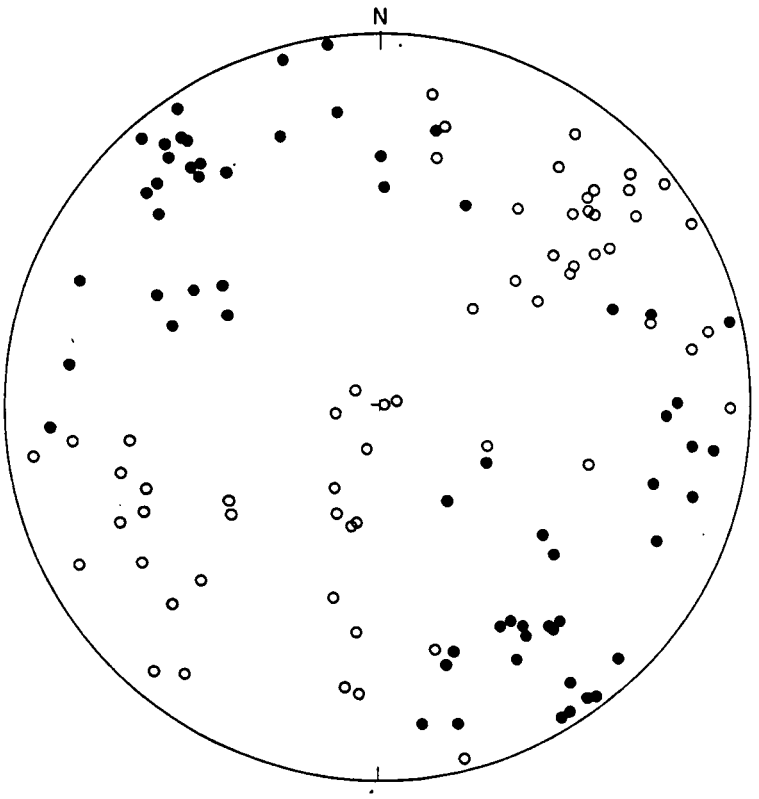

Figure 1.17: Stereographic projection of *P* (solid dots) and *T* (open dots) axes for all earthquakes with DC focal mechanisms recorded in the Hengill area in 1981 (from *Foulger*, 1988b).

1.3.4.3.5 Implications for processes in the geothermal area The geothermal seismicity in the area may be due to thermal fracturing of fresh rock in the cooling carapace around the still-hot cores of intrusions (*Foulger*, 1988a). As geothermal fluids circulate though the cooling layer, the rock will cool and contract, forming cracks that allow further penetration of fluid into the intrusion. This process was invoked to explain the longevity of seismic activity in the geothermal area around the Grímsvötn volcano (*Björnsson et al.*, 1982).

The high-V_P bodies beneath Grensdalur and Ölkelduhals are seismically active, which suggests that they are still cooling and supplying heat to the Hengill-Grensdalur geothermal system. Heat-balance calculations suggest that these bodies must have been replenished by fresh magma intrusions since the main focus of volcanic activity moved to the Hengill volcanic centre at 0.7 Ma, as a body the size of the Grensdalur V_P anomaly would cool in about 10,000 years at the present rate of heat loss (*Foulger and Toomey*, 1989).

1.3.4.3.6 Joint interpretation of the tomographic model and gravity data The three-dimensional model that resulted from the tomographic inversion of the 1981 seismic data (Section 1.3.4.3.4) was used to predict the Bouguer gravity anomaly field, which was compared with the observed field (Section 1.3.3) (*Field*, 1994). The V_P model was converted to a Bouguer gravity field by relating the seismic wave-speed to density using an empirical relationship developed for a range of Icelandic rocks. The simulated gravity field has similar characteristics to the observed field with the regional trend removed. The main features of both models are positive anomalies at Húsmúli and the north part of the Grensdalur volcanic centre, and a negative anomaly along the Hengill fissure swarm, although this is poorly predicted by the simulated field (Figure 1.18).

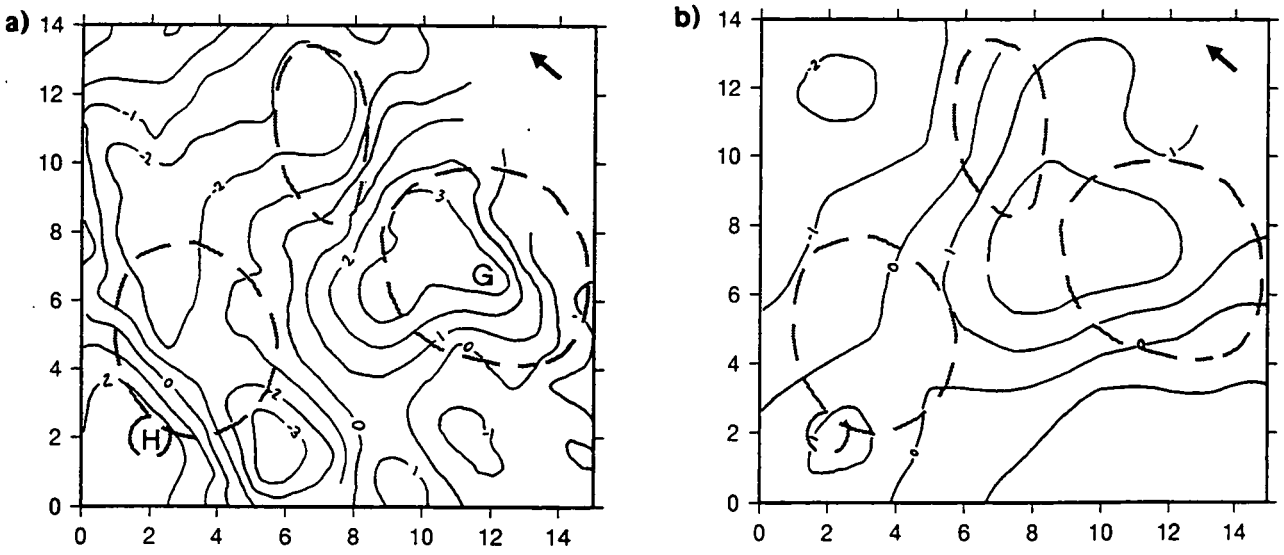

Figure 1.18: Maps of the Bouguer anomaly field. (a) The detrended real field, (b) the simulated field calculated from the tomographic model. The contour spacing is 1 mGal. Dashed lines: volcanic centres; H: Húsmúli; G: Grensdalur. The arrow points north (from *Field*, 1994).

There is a large misfit between the two models in an east-west trending zone from south Hengill to Hromundartindur. This zone corresponds to the north of the main area of geothermal activity (Figure 1.11). The simulated field gives larger Bouguer anomalies than the observed field, suggesting that (1) the tomographic method may not have detected a zone of near-surface low wave-speed in this area, or (2) that a different density / wave speed relationship applies for rocks in this part of geothermal area (*Field*, 1994).

1.3.4.4 *S*-wave anisotropy

High-quality digital local earthquake data collected in 1991 (Chapter 3) show that *S*-wave anisotropy exists in the Hengill area (*Evans et al.*, 1996). Three-dimensional particle-motion plots of 237 *S*-wave arrivals were used to determine the polarisation direction ϕ of the faster *S* phase. The horizontal seismograms were then rotated to this direction and the arrival times of the fast and slow arrivals measured. The measured time lags have a median of 40 ms, which was interpreted as representing 2-5% anisotropy, a value much lower than the 12% measured by *Menke et al.* (1994) for the WVZ. The smallest lag times are measured for stations close to the volcanic centres (Figure 1.19).

At most stations, ϕ values cluster well, and the mean ϕ varies from station to station (Figure 1.19). The median direction is 021°N, close to the strike of tectonic features in the area. The anisotropy is probably due to near-vertical fissures and micro-cracks that are perpendicular to the direction of minimum compressive stress, σ_3. A slight change from NE-trending ϕ in the NW to NNE in the south and east is apparent, suggesting that σ_3 varies across the area, as might be expected in the vicinity of an active volcanic centre. However, the general variability of ϕ means that this is a tentative conclusion.

1.4 Summary

The interaction of a mantle hotspot with the mid-Atlantic ridge has formed the volcanic pile of Iceland. The structure of the Icelandic crust and upper mantle is not well understood, and probably varies significantly across Iceland. The plate boundary within Iceland is complex, comprising four main volcanic zones and two transform zones. Seismic activity is mainly restricted to the neovolcanic zones, and is geothermal or tectonic in origin. The Hengill triple junction lies at the intersection of the WVZ, RPVZ and the SISZ. The SISZ is a transform fault zone, but is characterised by an array of parallel, north-south oriented, strike-slip faults rather than a single east-west transform fault. Earthquakes in the SISZ are right-lateral strike-slip, consistent with "bookshelf" tectonics. The Hengill area has three volcanic centres, two of which are inactive, and a geothermal field that has been investigated using several geophysical

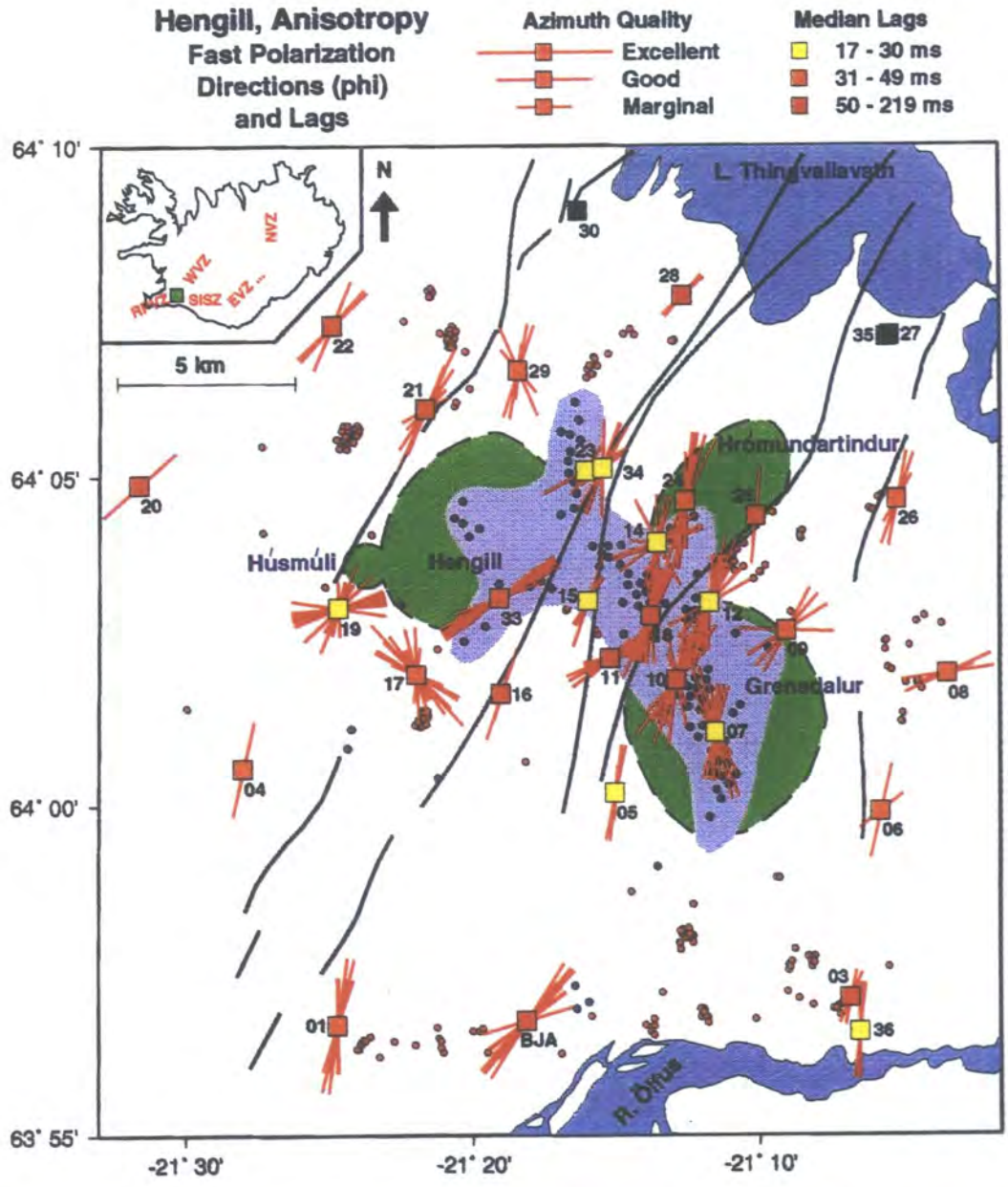

Figure 1.19: Results of shear-wave splitting analysis of data collected in 1991. Squares: stations used (colour depends on median lag); red lines: Fast *S*-wave polarisation direction (length depends on quality); light blue: geothermal field; blue dots: geothermal springs; red dots: earthquakes used; green shading: volcanic centres; black lines: outlines of fissure swarms; inset: regional setting and tectonics (from *Evans et al.*, 1996).

techniques. Large, historical earthquakes are restricted to the south of the area, and monitoring over the last 20 years by permanent networks shows that the pattern of small-magnitude, continuous geothermal seismicity has remained fairly constant. A temporary network of vertical-component instruments in 1981 recorded a large, local earthquake dataset. Most of the seismicity occurred in the geothermal field, and the Hengill fissure swarm was almost aseismic. Simultaneous inversion for wave-speed structure and earthquake locations showed that the upper 5 km has several volumes of high *P*-wave speed, thought to be solidified intrusions underlying the main volcanic centres. A small volume of relatively low wave-speed near the Hengill volcano may be partial melt. A synthetic gravity field produced from this model is similar to the observed Bouguer anomaly field, although the models differ in detail. Almost 50% of focal mechanisms studied were incompatible with DC sources, even when the three-dimensional wave-speed structure was taken into account. These earthquakes were interpreted as thermal contraction cracking in the cooling heat sources of the geothermal area. The DC mechanisms, corresponding to normal and strike-slip faulting, were generally consistent with the local spreading direction. Strong *S*-wave anisotropy was found using earthquake data collected in 1991, probably caused by NE-striking fissures.

Chapter 2

Non-double-couple earthquakes

2.1 Introduction

The idea that earthquakes are caused by faulting was first proposed by *Gilbert* (1884), and was supported by observations of surface breaks accompanying several earthquakes in India and Japan in the late 19th century (*e.g.*, *Richter*, 1958), and the 1906 San Francisco, California earthquake (*Lawson*, 1908; *Reid*, 1910). A much larger body of evidence connecting earthquakes with faulting comes from instrumental observations of seismic waves. In theory, compressional waves radiated by shear slip on a fault have a four-lobed pattern, with adjacent lobes alternating in polarity. Seismologists usually specify earthquake mechanisms in terms of equivalent force systems, and shear-fault mechanisms are called "double couples" (DCs). Instrumental determination of earthquake mechanisms became reliable in the 1960s, with advances in seismological theory and the introduction of a global network of standardised instruments that returned large amounts of data of unprecedentedly high quality. Fault-orientation and slip-direction determinations for thousands of earthquakes are now available, and these have played a central role in advancing understanding of tectonic processes (*e.g.*, *Isacks et al.*, 1968).

The hypothesis that earthquake source mechanisms are DCs has been so widely accepted as to have been treated as a fundamental law by many seismologists. Potential non-DC earthquake mechanisms have been given little attention because the DC model has adequately explained most seismic observations.

To a large extent, however, the success of the DC model has been a consequence of limitations in data quantity and quality. Recent improvements in seismological instrumentation and analysis techniques have now convincingly identified earthquakes whose radiated waves are incompatible with DC force systems, and thus with shear faulting. Well-constrained non-DC earthquakes have been observed in many environments, including volcanic and geothermal areas, mines and deep subduction zones. Non-DC earthquake processes that are applicable to volcanic and geothermal areas, and observations of non-DC earthquakes in volcanic and geothermal areas are reviewed here. *Julian et al.* (1996a) and *Miller et al.* (1996) review the theory and observations of non-DC earthquakes in all environments in more detail.

2.2 Describing non-DC earthquakes

Earthquake mechanisms are most often determined from compressional-wave polarities, under the assumption that the mechanism is a DC. Polarity observations are plotted on the "focal sphere", an imaginary sphere surrounding the earthquake focus, and orthogonal "nodal" planes sought that separate compressions and dilatations. For a shear fault, one of these nodal planes represents the fault. The assumptions that the nodal surfaces are planar and mutually orthogonal narrows the range of feasible solutions and makes interpretation using simple graphical methods possible. For general non-DC sources, however, the nodal surfaces are not necessarily planes, the range of possible interpretations is much wider, and manual solution is impractical. In other words, the rejection of the DC constraint on interpretations greatly exacerbates the classical inverse problem of earthquake mechanism determination.

To surmount this problem, and to resolve general non-DC source mechanisms, it is almost always necessary to use other data than just *P*-wave polarities, such as wave amplitudes. Virtually any kinds of seismic waves may be used, and they may be analysed by various methods.

Non-DC source mechanisms are almost always expressed as symmetric moment tensors. The moment tensor is a second-order tensor, which represents the force system of the source in terms of nine elementary force systems. The three diagonal components of the moment tensor are linear dipoles, while the off-diagonal elements are force couples. Under the assumption that the source exerts no net torque, the moment tensor is symmetric with six independent components.

Moment tensors can be transformed by rotations of the coordinate system and expressed as three orthogonal dipoles, and then the force system is completely described by the three principal moments, m_1, m_2 and m_3, and three values that specify the orientation. The source information is then independent of the orientation information, and the relative principal moments can be expressed in various ways to facilitate comprehension. First, m_1, m_2 and m_3 are written as a column vector, and the moment tensor is separated into volumetric and deviatoric parts:

$$\begin{bmatrix} m_1 \\ m_2 \\ m_3 \end{bmatrix} = m^{(V)} \begin{bmatrix} 1 \\ 1 \\ 1 \end{bmatrix} + \begin{bmatrix} m_1' \\ m_2' \\ m_3' \end{bmatrix}, \qquad 2.1$$

where the moment of the volumetric component $m^{(v)} = (m_1 + m_2 + m_3)/3$ and m_1', m_2' and m_3' are the principal moments of the deviatoric component (thus $m_1' + m_2' + m_3' = 0$).

The deviatoric component can itself be decomposed in many different ways, to give DC components with different orientations, or a DC component and a "compensated linear vector dipole" (CLVD) component (*Julian et al*, 1996a). Here, the scheme of *Knopoff and Randall* (1970) is followed, where the major principal axis of the CLVD component coincides with the same principal axis of the DC component:

$$\begin{bmatrix} m_1' \\ m_2' \\ m_3' \end{bmatrix} = m^{(DC)} \begin{bmatrix} 0 \\ -1 \\ 1 \end{bmatrix} + m^{(CLVD)} \begin{bmatrix} -\frac{1}{2} \\ -\frac{1}{2} \\ 1 \end{bmatrix}, \qquad 2.2$$

where the principal moments of the deviatoric part of the moment tensor are arranged so that $|m_1'| \le |m_2'| \le |m_3'|$.

The non-DC nature of a moment tensor can be quantified using two parameters; k, a measure of the volumetric component, and ε, with:

$$k \stackrel{def}{=} \frac{m^{(V)}}{|m^{(V)}| + |m_1'|} \text{ and } \varepsilon = \frac{-m_1'}{|m_3'|}, \qquad 2.3$$

The parameter ε is zero for a DC, and ± 0.5 for a CLVD.

The equivalent force system of an earthquake cannot uniquely identify the physical source process. The force system is a phenomenological description of the source, and is all that can be determined from seismological observations, but different physical interpretations are generally possible. For example, a DC could correspond either to shear slip on a planar fault or to opening of a tensile crack and simultaneous closing of an orthogonal crack (or to many other things). In discussing earthquake focal mechanisms, geology, rock physics, and other non-seismological disciplines therefore play essential roles.

2.3 Non-DC source processes

2.3.1 Introduction

Non-DC source processes and the necessary background theory are reviewed by *Julian et al.*(1996a). Here a brief synopsis of the non-DC source processes that may be relevant in volcanic and geothermal areas is given.

2.3.2 Processes involving net forces

Net forces and torques are usually excluded from source mechanisms, because they are thought to be inappropriate for real Earth processes. However, in cases where linear and angular momentum are transferred from the source to the rest of the Earth, the

include landslides, volcanic eruptions and unsteady fluid flow in channels (*Takei and Kumazawa*, 1994; *Ukawa and Ohtake*, 1987).

The eruption of volcanic material exerts a downward net force on the Earth, and this force can give rise to observable seismic waves. If a magmatic fluid flows through a volcanic conduit at a variable speed, a time-varying net force will be exerted on the surrounding rocks. This may be the process of volcanic tremor and "long-period" volcanic earthquakes (*Ukawa and Ohtake*, 1987; *Julian*, 1994).

2.3.3 Complex shear faulting

If earthquakes occur together in space and time, then observed seismic waves may not be able to resolve them, and they may be misinterpreted as a single event. The moment tensor of such a composite event is the sum of the moment tensors of the individual components. In general, the sum of two DCs is not a DC, and thus complex shear faulting can produce a non-DC moment tensor if individual shear-faulting components within a composite earthquake are not resolved (Figure 2.1).

Many DC combinations that are likely to occur add to give a composite DC. These cases include earthquakes with (1) parallel fault planes, (2) parallel slip directions or (3) parallel intermediate principal axes. This means that slip on listric faults, simultaneous slip on conjugate faults, or slip on cylindrical faults that have slip parallel or perpendicular to the rotation axis, will produce a composite DC (*Frohlich et al.*, 1989; *Frohlich*, 1990). Also, the addition of DC components can never give a composite moment tensor with a volumetric component, because the trace of a moment tensor is a linear function of its components.

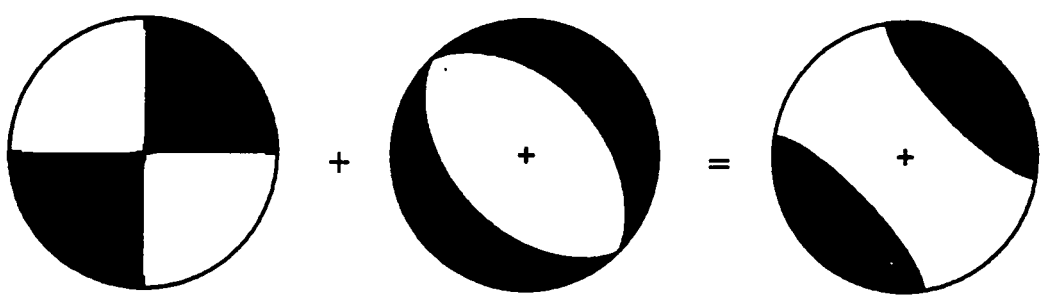

Figure 2.1: Combination of two shear-fault mechanisms to give a non-DC mechanism. Equal-area projections (which can be either upper or lower focal sphere) of the *P*-wave radiation patterns are shown. A strike-slip mechanism and a normal-fault mechanism with the same *T*-axes combine to give a CLVD.

Shear faulting on volcanic ring faults may have a non-DC mechanism. Two types of concentric dykes are often found in exhumed volcanic centres; inward-dipping "cone sheets" and vertical or steeply outward-dipping "ring dykes" (*e.g.*, *Clough et al.*, 1909). If dip-slip faulting occurs on a conical fault and spans a sufficient azimuthal range, then the resulting mechanism, considered as a point source, will be non-DC (Figure 2.2; *Ekström*, 1994).

2.3.4 Tensile faulting

A tensile fault has an equivalent force system with principal moments in the ratio $(\lambda+2\mu):\lambda:\lambda$. Tensile faulting can occur when the shear stress (the difference between the two extreme principal stresses) is low and fluid pressure is high so that much of the compressive stress caused by the overburden is cancelled. On a Mohr circle diagram, this is equivalent to a small-diameter circle that touches the failure envelope in the tensile failure zone (Figure 2.3).

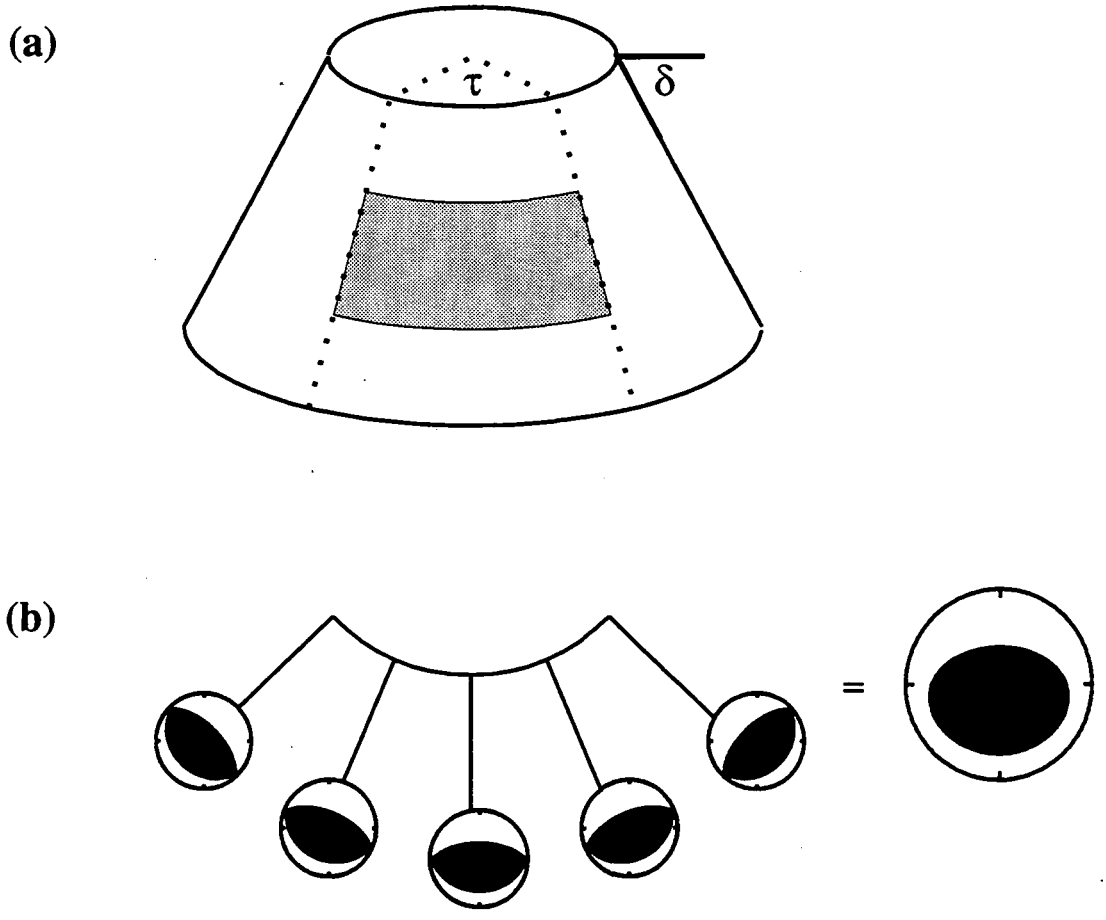

Figure 2.2: Slip on a ring fault is equivalent to the combination of many planar sub-faults. (a) the size of the non-DC component of a ring-fault earthquake depends on the fault dip (δ), the angle subtended by the rupture zone (τ) and the slip direction. (b) an example of the radiation pattern from a ring-fault earthquake with normal motion and $\tau = 90°$, $\delta = 60°$. The radiation pattern is the sum of the radiation from planar faults with a range in azimuths.

In theory, tensile cracks cannot propagate fast enough to radiate seismic energy, because the rate of propagation is controlled by the maximum speed that fluid can flow. Departures from heterogeneity, however, can allow tensile cracks to propagate unstably (*Sammis and Julian*, 1987).

The far-field *P*-wave radiation from an opening tensile fault is always positive, with the largest amplitudes in directions perpendicular to the fault. The subsequent migration of fluid into a crack may cause a dilatational signal, occurring after the arrival of the first compression. At long wavelengths, this dilatation may reverse the apparent first motion, giving dilatational arrivals for stations near to the plane of the crack. However, this theory is not supported by numerical models of tensile faulting, which show the dilatations caused by fluid flow are too weak to cause a reversal in the apparent first motion (*Chouet and Julian*, 1985; *Chouet*, 1986).

2.3.5 Combined tensile and shear faulting

If a tensile crack and a shear fault intersect, stick-slip instability could cause sudden episodes of crack opening or closing that radiate seismic energy (*Shimizu et al.*, 1987). The stress fields at the ends of both shear and tensile cracks favour this kind of pairing. A tensile crack alone, although it could open suddenly and radiate seismic energy (Section 2.3.4), would be expected to close slowly and aseismically.

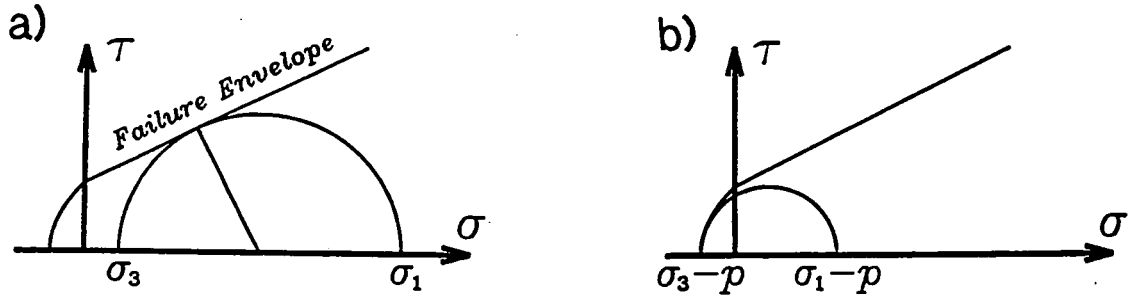

Figure 2.3: Mohr circle diagrams showing conditions for shear and tensile failure. The diagrams show the relationship between shear traction τ and normal traction σ across a plane at a point in a stressed medium. Locus of (σ, τ) points for different orientations of the plane is a circle of diameter $\sigma_1 - \sigma_3$ centred at $((\sigma_1 + \sigma_3)/2, 0)$. Failure occurs when the surface touches the "failure envelope", here shown corresponding to Griffith theory of failure as modified by F. A. McClintock and J. B. Walsh (*Price*, 1966). (a) At high confining pressure with no fluid pressure, shear failure occurs. (b) High fluid pressure lowers the effective confining stress, and tensile failure occurs at low stress differences.

The moment tensor and radiation pattern of combined shear and tensile faulting can be calculated by adding the moment tensors of the two components (Figure 2.4). The composite moment tensor is insensitive to the angle between the two faults, and the moment tensors for angles of $45 \pm x°$ are equal (*Julian et al.*, 1996a).

2.3.6 Opening-shear faulting

In laboratory experiments with foam rubber blocks, transient separation of fault surfaces is often observed during shear faulting (*Brune et al.*, 1993). If this mechanism occurs in nature, it would not be apparent in moment tensors of temporal order zero, because the fault surfaces are closed before and after the earthquake. If for some reason the fault surfaces separated and remained open during shear faulting (perhaps because of high fluid pressure), then the resulting moment tensor would be equivalent to the sum of coplanar tensile and shear fault moment tensors. This is a special case of combined tensile and shear faulting (Section 2.3.5), with an angle of 0° between the two faults (Figure 2.4b). It has been suggested that fault plane roughness could cause fault-normal motion during shear faulting (*Haskell*, 1964).

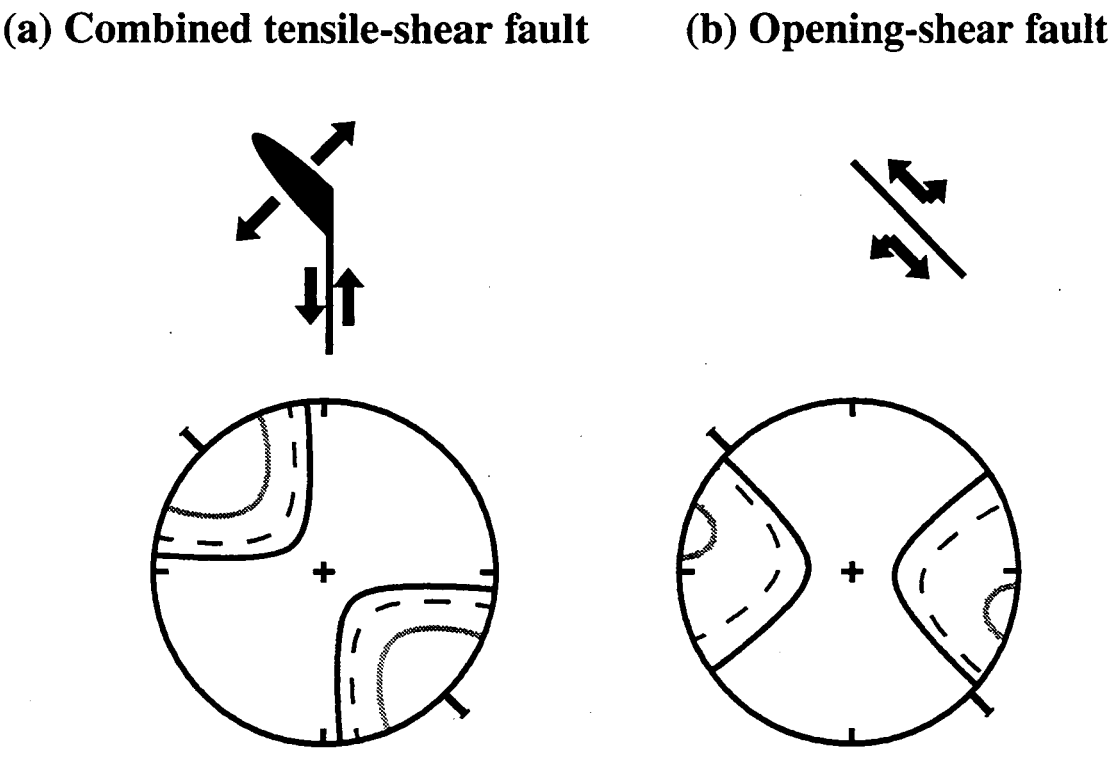

Figure 2.4: Two possible combinations of tensile and shear faults. (a) faulting on two separate planes with an angle of 45° between them. (b) coplanar tensile and shear faulting. The bottom panels show equal-area projections (which can be either upper or lower focal sphere) of the *P*-wave nodal lines, for R_{TF} values of 0.1 (solid line), 0.2 (dashed line) and 0.35 (grey line), where $R_{TF} = m^{(TF)} / \left(m^{(TF)} + m^{(SF)} \right)$.

2.4 Observations of non-DC earthquakes in volcanic and geothermal areas

2.4.1 Introduction

Observations from dense local seismic networks that give good focal sphere coverage have demonstrated that earthquakes in several volcanic and geothermal areas have non-DC mechanisms. Most well-constrained non-DC earthquakes have explosive volumetric components. So far, analysis of such earthquakes has mainly been restricted to study of the distributions of *P*-wave polarities.

2.4.2 The Reykjanes Peninsula, southwest Iceland

A few earthquakes recorded at the Reykjanes Peninsula, SW Iceland, in an experiment in 1972 had non-DC *P*-wave polarity distributions with small dilatational fields (*Klein et al.*, 1977). These events occurred within a large earthquake swarm that was recorded by 23 temporary stations. Most of the *P*-wave polarity distributions were consistent with DC mechanisms of normal and strike-slip type, compatible with the extensional tectonics of the region. The non-DC earthquakes had mostly compressional *P*-wave first motions, and the dilatational fields occupied less than half of the focal spheres. They were clustered in a small volume where seismicity was relatively low, and were intermingled spatially with DC events. This intermingling suggests that the non-DC mechanisms probably are not artefacts of propagation or instrumental effects. A source mechanism involving a tensile-faulting component could explain the observations (*Klein et al.*, 1977).

2.4.3 The Hengill volcanic complex, southwest Iceland

The Hengill volcanic complex has so far provided the largest number of well-constrained volcanic and geothermal non-DC earthquakes (*Foulger and Long*, 1984; *Foulger*, 1988b). Of the best-constrained earthquakes recorded by the temporary network in 1981 (Section 1.3.4.3), 56 out of 131 of the *P*-wave polarity distributions are inconsistent with orthogonal nodal planes, when the three-dimensional wave-speed structure is taken into account (Figure 2.5).

The non-DC earthquakes at Hengill are thought to be caused by thermal stresses induced in recent intrusions that are being cooled by circulating ground water (Figure 2.6). The regional extensional stress field, together with the availability of high-pressure geothermal fluids, enables tensile-mode failure to occur (*Foulger and Long*, 1984; *Foulger*, 1988b).

2.4.4 The Krafla volcanic system, north Iceland

A smaller number of non-DC earthquakes have also been recorded in the Krafla volcanic system in north Iceland. This system underwent a major dyke-intrusion

1.2.2; *Björnsson*, 1985). In 1985, a temporary network of 28 vertical-component seismometers recorded earthquakes for three months (*Foulger et al.*, 1989; Section 1.2.2). *Arnott and Foulger* (1994a, b) used numerical ray tracing in a tomographically-derived three-dimensional model to determine hypocentral locations and to map *P*-wave polarity observations onto focal spheres. The focal depths of the earthquakes at Krafla were unexpectedly shallow and thus focal-sphere coverage sufficiently good to distinguish between DC and non-DC mechanisms was obtained for only a few earthquakes. Nevertheless, five events have polarity distributions incompatible with DC mechanisms, and four of these have significant volumetric components (two implosive and two explosive) (Figure 2.7).

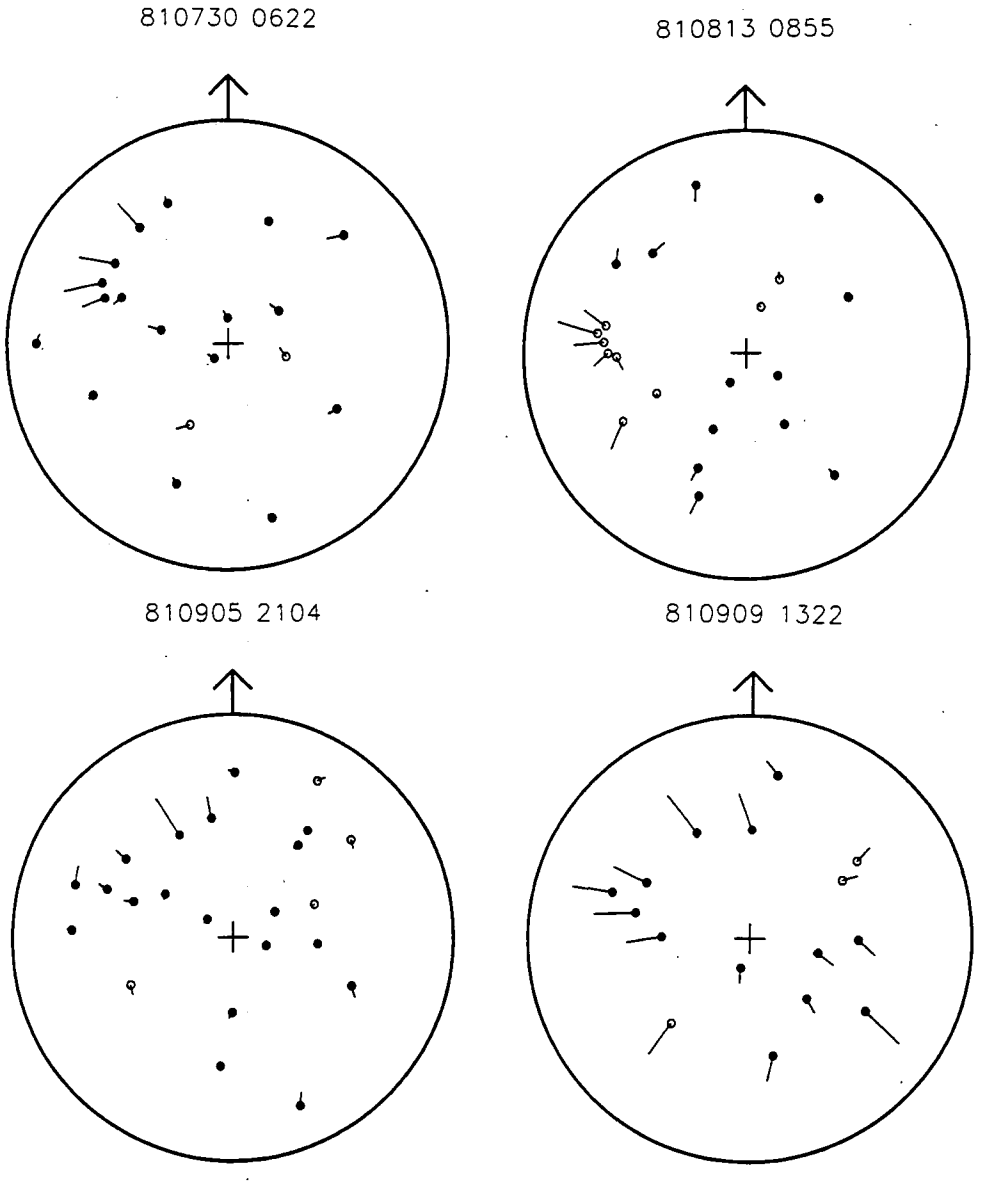

Figure 2.5: Observed *P*-wave polarities for four non-DC earthquakes in the Hengill area recorded by the temporary network in 1981. Symbols (solid: compressions; open: dilatations) are plotted at the station positions when the earthquakes are located and rays are traced through the three-dimensional model of *Toomey and Foulger* (1989). Lines show change in position from the one-dimensional model. Upper focal hemispheres are shown in equal-area projection (after *Foulger and Julian*, 1993).

It is thought that, as in the Hengill-Grensdalur area, earthquakes in the Krafla system are caused mainly by thermal stresses induced by cooling of geothermal heat sources by ground water. However, the stress field at Krafla is inferred to have only a small deviatoric component, on the basis of the unsystematic orientations of DC-earthquake principal axes (*Arnott and Foulger*, 1994b), a state that was probably caused by the recent rifting (*Foulger and Long*, 1992). Such a stress field is compatible with the occurrence of implosive and explosive volumetric earthquakes together.

2.4.5 Mid-ocean ridges (MORs)

The seismic and volcanic processes observed in Iceland have long been assumed to be similar to those at submarine spreading plate boundaries, and the recent discovery of many large geothermal areas along the MOR system suggests that small non-DC geothermal earthquakes may occur on MORs also. Unfortunately, studying small MOR earthquakes is hindered by a lack of data, as currently deployed stations on land record MOR earthquakes well only for $m_b > 4.5$. For smaller earthquakes, the difficult and expensive deployment of ocean-bottom seismometers (OBSs) or hydrophones (OBHs) is necessary. Several OBS experiments on different sections of the MOR system have investigated small earthquakes and earthquake swarms, but none has involved enough stations to allow accurate determination of focal mechanisms. For example, a microearthquake monitoring experiment at the Mid-Atlantic Ridge in 1982 recorded a maximum of 10 *P*-wave first motions per earthquake (*Toomey et al.*, 1985; 1988).

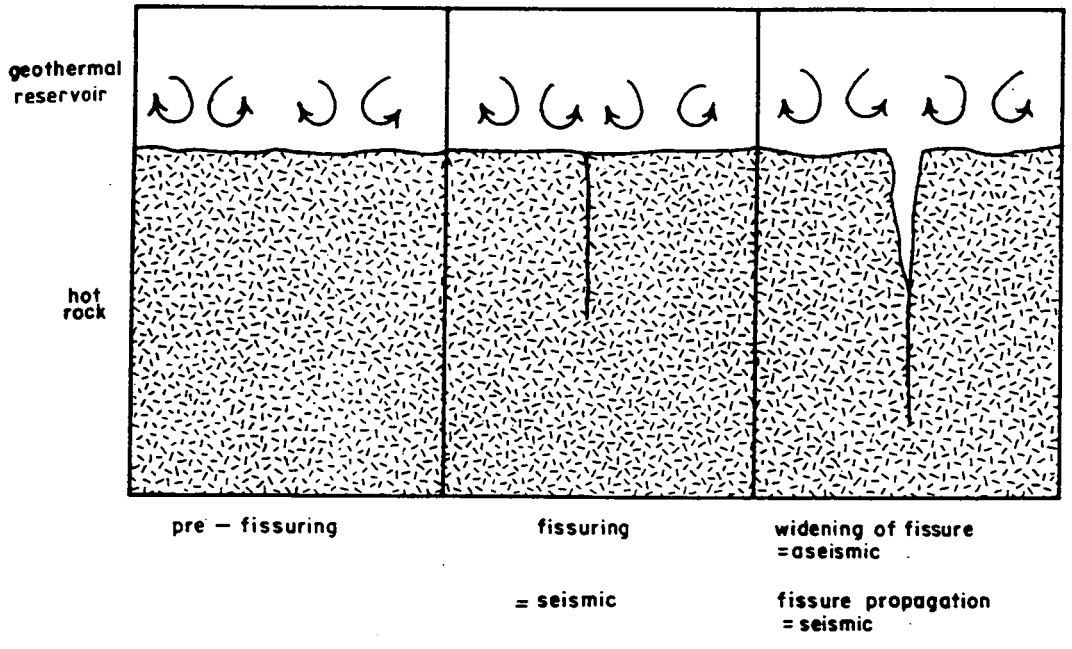

Figure 2.6: Model of tensile cracking by thermal stresses caused by convective cooling of rocks at the heat source of a geothermal system (from *Foulger*, 1988b).

Orthogonal nodal planes are consistent with the *P*-wave polarities for all these earthquakes, although for some events DC mechanisms require the assumption that large unsampled areas of the focal sphere are dilatational. Rapid technological developments in ocean-bottom geophysical instrumentation may soon provide data to resolve the question of whether small non-DC earthquakes occur on the MOR.

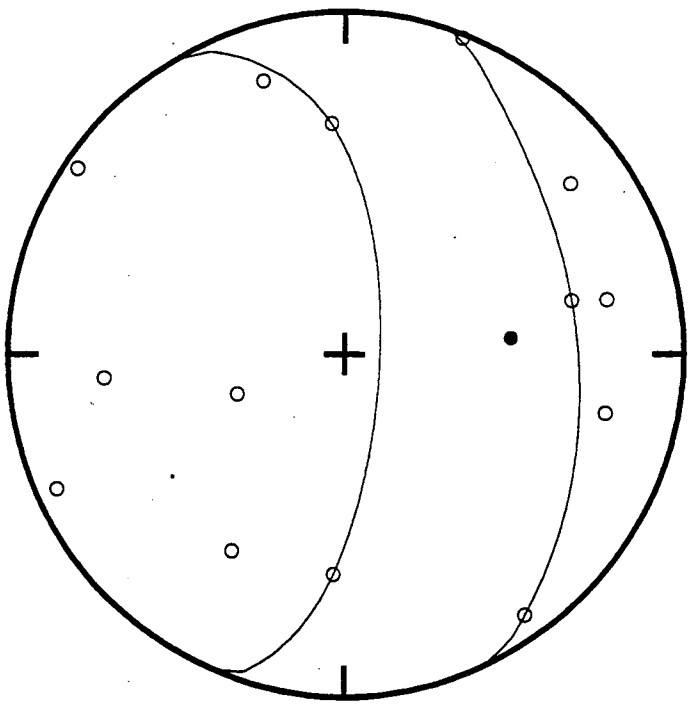

Figure 2.7: Observed *P*-wave polarities for a non-DC earthquake on 6 August 1985 at the Krafla volcano, northeast Iceland, after *Arnott and Foulger* (1994b). Open circles: dilatational polarities; solid circles: compressions. Nodal surfaces shown are for most explosive mechanism consistent with observations, which is still strongly implosive. Upper focal hemisphere is shown in equal-area projection.

2.4.6 The Geysers geothermal area, northern California

For more than a decade, large-scale steam mining has induced thousands of small earthquakes per month at The Geysers geothermal area in northern California. *P*-wave polarities for these earthquakes obtained from the permanent seismometer network of the U. S. Geological Survey (USGS) in the area usually allow DC interpretations (*Eberhart-Phillips and Oppenheimer*, 1984; *Oppenheimer*, 1986), although in some cases the polarities are all the same and polarity fields devoid of data must be assumed. In other cases a few polarity violations must be tolerated.

measured for 24 earthquakes in April 1991, using records from a dense local seismometer network (*Ross et al.*, 1996; Figure 2.8). The focal-sphere positions of the observations are computed by ray tracing in the three-dimensional wave-speed model of *Julian et al.* (1996b), and the observations were inverted using linear-programming methods (*Julian and Foulger*, 1996; Chapter 6) to determine moment tensors. Most of the studied earthquakes have moment tensors that can be interpreted as DCs, but 5 (21%) of the earthquakes studied were non-DC, with explosive volumetric components of 20-33% of the total moment. Three of the earthquakes can be explained by a shear and tensile fault model (*e.g.*, *Shimizu et al.*, 1987). The other two earthquakes have moment tensors equivalent to a tensile crack combined with a CLVD, and may be caused by opening cracks accompanied by fluid flow into the crack (*Julian*, 1983). Both mechanisms may be expected in volumes which experience major changes of pore pressure due to steam extraction and fluid injection, such as the Geysers.

2.4.7 Miyakejima, Izu islands, Japan

Many non-DC earthquakes with *P*-wave polarities that were either all dilatational or all compressional accompanied the 1983 eruption of Miyakejima volcano, in the Izu islands south of Honshu, Japan (Figure 2.9a). The earthquakes were recorded by 16 local short-period instruments (*Shimizu et al.*, 1987; *Ueki et al.*, 1984). One area, close to the eruptive fissures, produced many earthquakes with only dilatational *P* waves. The *P* waves from earthquakes in a second area, along the caldera rim, were all compressional. The earthquakes radiated significant *S* waves, however, so their mechanisms were not purely isotropic.

The observed *P*-wave polarities and *P*- and *SV*-wave amplitudes are compatible with sources involving combined tensile and shear faulting (Section 2.3.5). A kinematic model with tensile faults striking approximately 40°N, parallel to the eruptive fissures, fits data from both the implosive and explosive earthquakes. This interpretation is supported by the observation that many open cracks formed along the fissures prior to the eruption. An intrusion at the caldera rim could have caused these cracks to open and the explosive earthquakes. Closing of cracks during and after the eruption, as the magma pressure decreased, is the most probable explanation for the dilatational earthquakes.

2.4.8 The Unzen volcanic region, western Kyushu, Japan

A magnitude 3.2 earthquake on 13 May 1987, 10 km beneath the Unzen volcanic region in western Kyushu, Japan, had compressional *P*-wave polarities at 23 out of 24 local seismic stations, which were well distributed on the focal sphere (Figure 2.9b)

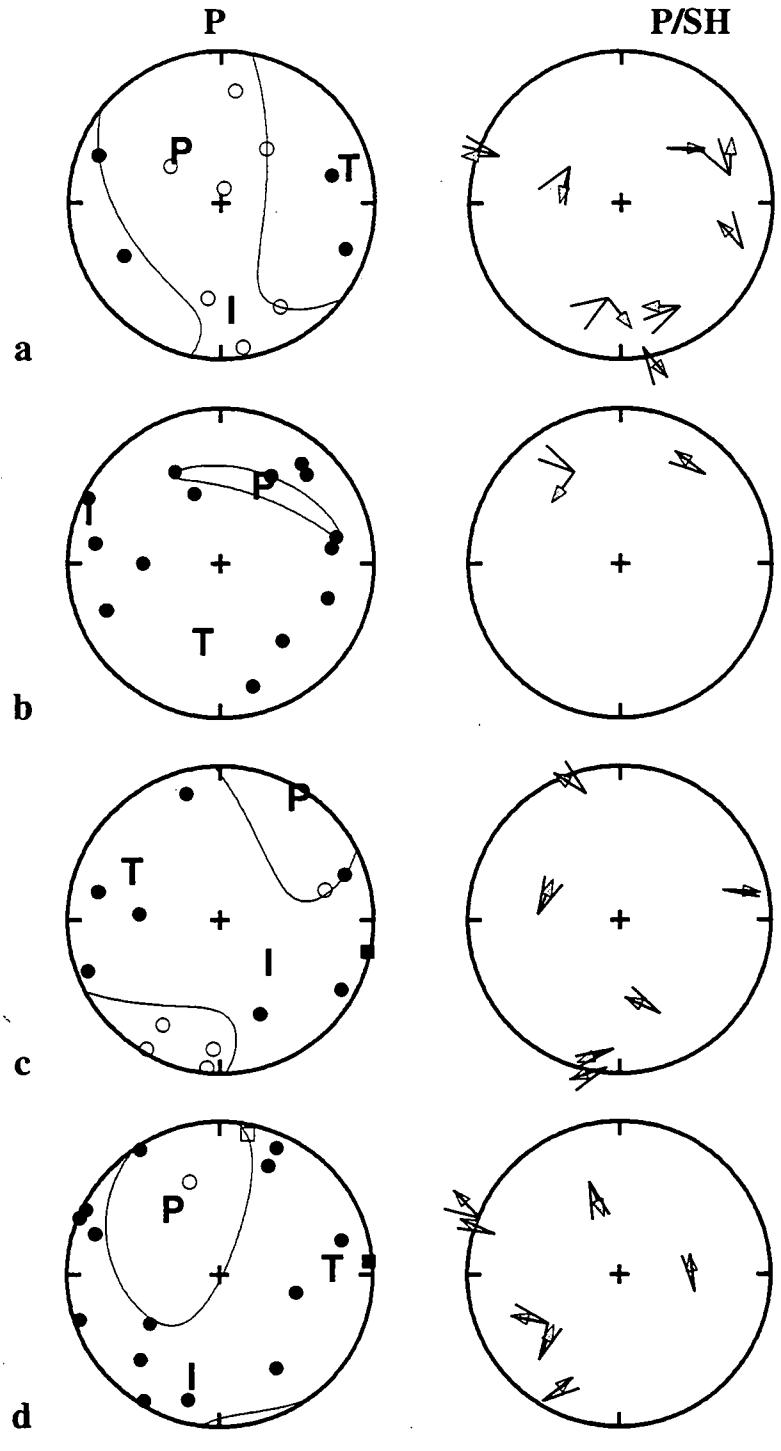

Figure 2.8: Focal mechanisms of (a) one earthquake interpreted as a DC and (b-d) three non-DC earthquakes at The Geysers geothermal area, northern California. Left column: P-wave polarities; Compressional motion is shown as solid symbols, and dilatational as open symbols. Squares are down-going arrivals that are projected onto the upper focal hemisphere. Right column, P:SH-wave amplitude ratios. Amplitude ratios are represented using scheme of *Julian and Foulger* (1996), with directions of small arrows giving theoretical ratios, and line segments indicating ranges compatible with observations (see Section 6.4.4). Upper focal hemispheres are shown in equal-area projection. From *Ross et al.* (1996).

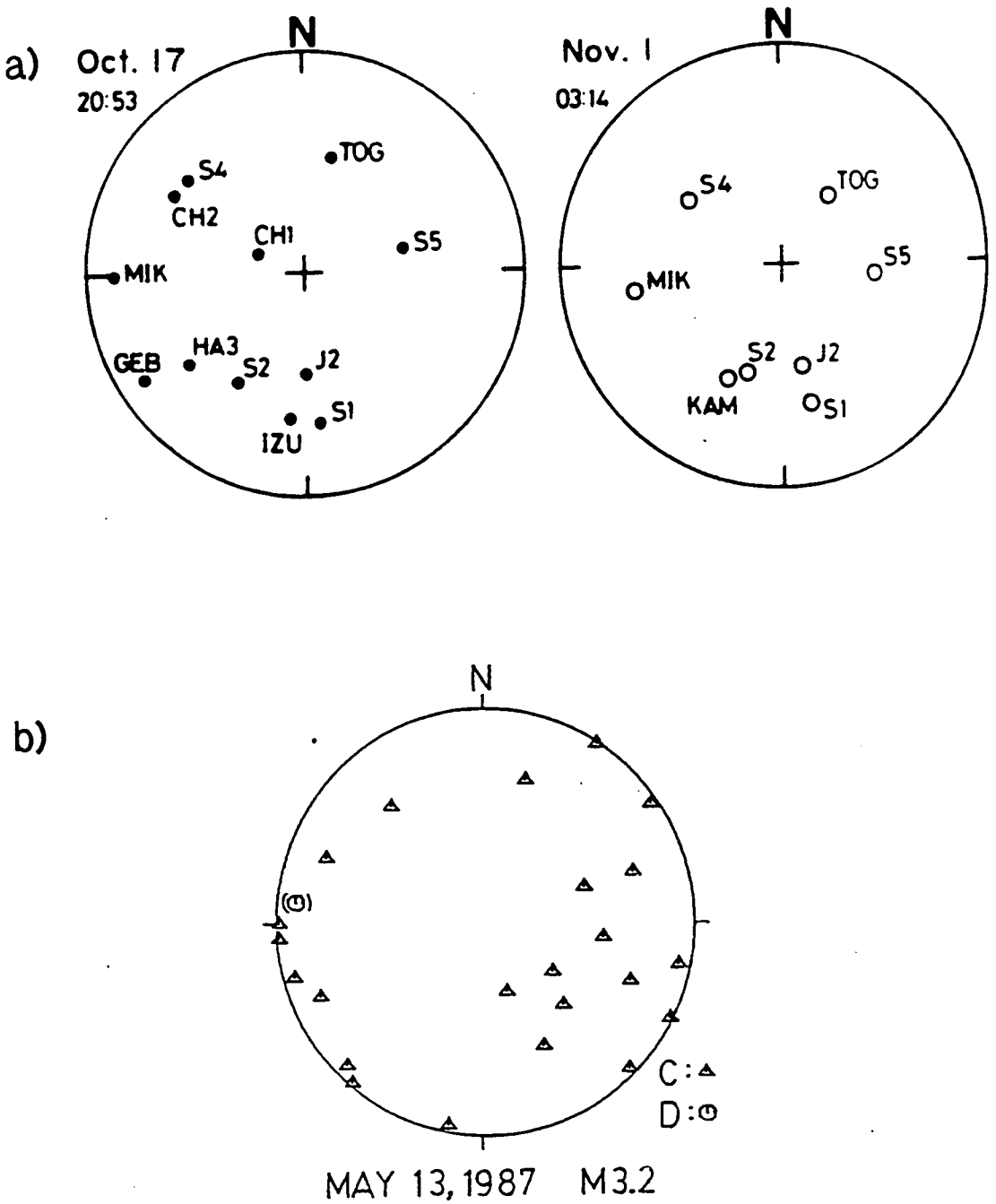

Figure 2.9: *P*-wave polarities for three non-DC earthquakes at volcanic regions in Japan. (a) earthquakes at Miyakejima Island in 1983. Solid circles: compressions; open circles: dilatations. Upper focal hemispheres are shown in equal-area projection. (From *Shimizu et al.*, 1987). (b) Earthquake of 13 May 1987 in the Unzen volcanic region. Upper hemisphere is shown in equal-area projection. Triangles: compressions; circles: dilatations. (From *Shimizu, unpublished manuscript,* 1987).

(*Shimizu et al.*, 1988; *Shimizu*, personal communication, 1988). The kinematic tensile-shear fault model proposed for the Miyakejima earthquakes (Sections 2.3.5 and 2.4.7) can fit the observed polarities and *P*:*SV* amplitude ratios, with opening on an near-vertical, east-striking tensile fault accompanied by minor slip on a vertical shear fault. The orientation of the tensile fault is compatible with the stress orientation implied by N-S spreading in the Unzen graben.

2.4.9 Sakurajima Volcano, southern Kyushu, Japan

The andesitic Sakurajima volcano has been active continuously since 1955, with frequent eruptions and earthquakes of various empirically recognised types (*Iguchi*, 1994). The volcano is monitored by a high-quality local network with eight seismographs, six of which have three components, as well as tiltmeters, extensometers, acoustic sensors, and video cameras. "A-type" earthquakes occur mainly outside the main magma conduit, excite both *P* and *S* waves, and have polarity and amplitude distributions consistent with DC mechanisms. They are probably caused by shear faulting. All the other types of earthquakes occur 2 to 3 km beneath the eruptive crater, and have identical polarities at all stations, inconsistent with DC mechanisms. "BL-type" earthquakes occur in swarms when the volcano is active. "BH-type" events are deeper, excite higher-frequency waves, and tend to occur when the volcano has been dormant for a few months. "Explosion" earthquakes accompany crater eruptions that radiate spectacular visible shock waves into the atmosphere (*Ishihara*, 1985). BH and explosion earthquakes have entirely compressional *P*-wave polarities, whereas BL earthquakes have either entirely compressional or entirely dilatational polarities. *S* waves from BH, BL, and explosion earthquakes are vertically polarised.

There have been two recent determinations of focal mechanisms for Sakurajima earthquakes, but the results are inconsistent. *Uhira and Takeo* (1994) inverted waveforms from two explosion earthquakes, using three-component seismograms from three local stations evenly spaced around the crater at distances from 3 to 10 km. The derived moment-tensor time functions for one earthquake are consistent with deflation of a north-striking vertical crack. The result for the other earthquake is similar except that the M_{xx} and M_{yy} components are about equal, indicating a source with azimuthal symmetry (two or more cracks with different strikes?). Rapid deflation of vertical cracks might rapidly expel gas and excite the observed atmospheric shock waves that accompany explosion earthquakes. Vertical forces accompanying the earthquakes, which would be expected consequences of eruption (Section 4.1.2 of *Julian et al.*, 1996a) are consistent with the observations, but cannot be resolved well. *Iguchi* (1994) inverted *P*-wave amplitudes recorded at 8 stations within 5 km of the crater to obtain "moment acceleration" ($\ddot{\mathbf{M}}$) tensors for five explosion earthquakes, seven BL earthquakes, seven BH earthquakes, and two A earthquakes. The observed amplitudes

were corrected for site effects using empirical factors determined from observations of teleseisms. The results for BH, BL, and explosion earthquakes are dominated by the vertical dipole components, as might be expected for inflation of horizontal cracks. Thus the two separate moment tensor determinations are interpreted as expansion of tensile cracks of different orientations for the same type of earthquakes. If the reasons for the differences between the results of these two studies can be determined, the results are likely to greatly clarify our understanding of processes within Sakurajima.

2.4.10 Long Valley Caldera, California

Four earthquakes with $M_L > 6$, at least two of which had non-DC mechanisms, occurred near Long Valley caldera, eastern California, on 25 and 27 May 1980 (Figure 2.10). Open surface rupture on cracks striking NNW-SSE, and parallel normal faulting with downthrow to the ENE, accompanied these earthquakes. The region had been dormant for decades until the M_L 5.7 "Wheeler Crest" earthquake of 4 October 1978, which was followed during the next two years by increasing numbers of small-magnitude earthquakes (Figure 2.10). Geodetic measurements made in the summer of 1980 showed that the caldera floor had been uplifted by as much as 20 cm, in a pattern consistent with inflation of a magma chamber under the caldera (*Rundle and Hill*, 1988). Earthquakes and deformation have continued to the present, at gradually diminishing rates.

Unusually numerous and diverse seismic data are available for the large 1980 earthquakes, and they have been analysed independently by a variety of methods. These data include polarities of short- and long-period *P* waves (*Cramer and Toppozada*, 1980; *Ryall and Ryall*, 1981; *Given et al.*, 1982; *Julian*, 1983; *Julian and Sipkin*, 1985), long-period *P* waveforms (*Barker and Langston*, 1983; *Julian and Sipkin*, 1985) and surface-wave amplitudes and initial phases (*Given et al.*, 1982; *Ekström and Dziewonski*, 1983; 1985). The results of the analyses are consistent in requiring similar, approximately deviatoric, non-DC mechanisms with large CLVD components for events 1 and 3 (Figure 2.10). The 1978 Wheeler Crest earthquake, which began the episode of unrest, is smaller, and its mechanism is harder to resolve, but it also appears to have a similar mechanism with a large CLVD component (*Ekström and Dziewonski*, 1983; 1985). The non-DC earthquakes occurred at widely separated locations, surrounding the DC event 2, suggesting that their mechanisms are not artefacts of wave-propagation or receiver effects.

At three stations to the northeast, near a nodal surface, short-period instruments show compressional first motions for the largest event and long-period instruments show dilatations (*Wallace et al.*, 1982). Similar observations are not uncommon in seismology, and are expected consequences of spatial or temporal source complexity. For the Long Valley earthquakes, the significance of frequency-dependent first motions

is unclear. They might be caused by complex shear faulting (*Wallace et al.*, 1982) or by propagating magma-filled cracks, with the initial compressional motions excited by tensile cracking, and later dilatations caused by pressure decreases in the cracks (*Aki*, 1984).

The source processes of these unusual earthquakes remains uncertain (*Wallace*, 1985). Any isotropic (volumetric) components in the mechanisms are unresolvably small, and thus the events could, in theory, result from complex shear faulting (Section 2.3.3). The decomposition of a deviatoric moment tensor into two DCs is non-unique, so many combinations of shear fault geometries and relative moments are theoretically

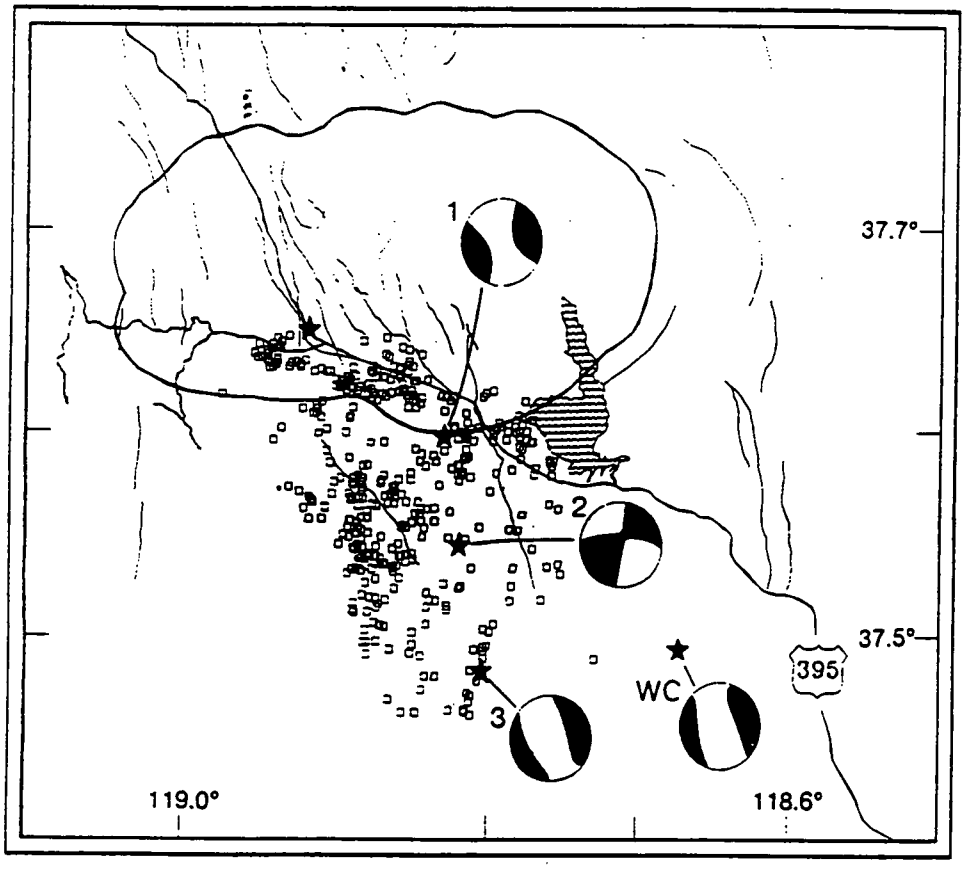

Figure 2.10: Map of Long Valley Caldera, California, and vicinity, showing best-located earthquakes in 1980 with coda-duration magnitude > 3 and mechanisms for largest earthquakes of 1978 and 1980. WC: M_S 5.3 "Wheeler Crest" earthquake of 4 October 1978; 1: M_S 6.1 earthquake of 16:34 on 25 May 1980; 2: M_S 6.0 earthquake of 19:45 on 25 May 1980; 3: M_S 6.0 earthquake of 14:51 on 27 May 1980. Unlabelled star: $M_S \geq 6$ earthquake of 16:49 on 25 May 1980, whose mechanism cannot be determined well. The Wheeler Crest earthquake and earthquakes 1 and 3 have mechanisms with large non-DC components. Heavy line: caldera boundary. Lower hemisphere equal-area projections, with fields of compressional P-wave polarity shaded. (From *Julian and Sipkin*, 1985). Mechanism of Wheeler Crest earthquake from *Ekström and Dziewonski* (1983).

possible, and indeed many mutually incompatible suggestions have been made (*Barker and Langston*, 1983; *Wallace et al.*, 1982; *Lide and Ryall*, 1984). The complex shear-faulting hypothesis is contradicted by the finding of *Julian and Sipkin* (1985) that the largest event can be resolved into three sub-events, but that these all have similar, non-DC mechanisms. This finding contrasts with results from most complex earthquakes, which have DC sub-events (*e.g.*, *Sipkin*, 1986; *Kikuchi et al.*, 1993).

Alternatively, the non-DC Long Valley earthquakes may have been caused by tensile faulting at high fluid pressure (*Julian*, 1983; *Julian and Sipkin*, 1985). In this case, the volumetric component expected for a tensile fault (Section 2.3.4) must be compensated by fluid (CO_2, other gases, or magma) flowing into the opening crack. The rather tentative available models of seismic-wave radiation in such processes do not seem to support this possibility quantitatively (*Chouet and Julian*, 1985).

2.4.11 Tori Shima, Izu-Bonin arc

An anomalous shallow earthquake of M_S 5.6 occurred on 13 June 1984 near Tori Shima island, located in the Izu-Bonin arc south of Honshu, Japan (*Kanamori et al.*, 1993). This earthquake generated much larger tsunamis than would be expected from its magnitude (*Satake and Kanamori*, 1991) and produced anomalous seismic radiation that is deficient in horizontally polarised shear (SH) waves and has little azimuthal variation in the waves excited (Figure 2.11). Love-wave amplitudes were negligible compared with those of the Rayleigh waves, which had similar amplitudes and initial phases in all azimuths. All recorded *P*-wave first motions were compressional (Figure 2.11). These observations imply that the source was approximately symmetrical about a vertical axis, a situation that simplifies analysis, and rules out DC mechanisms.

Kanamori et al. (1993) inverted both long-period surface waves and teleseismic long-period body waves and obtained moment tensors with ε values between 0.3 and 0.4. Because the earthquake was shallow, the full moment tensor cannot be determined well (Section 3.4.3 of *Julian et al.*, 1996a), so in most inversions moment tensors were constrained to be deviatoric. The result of one unconstrained inversion (Figure 2.11b) indicates that the earthquake may have had a substantial volumetric component, and that the deviatoric component was close to a CLVD with its symmetry axis vertical.

Sudden horizontal intrusion of magma into ocean-floor sediments is kinematically consistent with the observations for this earthquake, and the resulting uplift of the ocean floor might explain the anomalously large tsunami. The seismic moment and source duration require the intrusion of approximately 0.02 km^3 of fluid within 10 to 40 seconds. Such a rate of intrusion may be possible for a mixture of magma and super-critical water (*Kanamori et al.*, 1993).

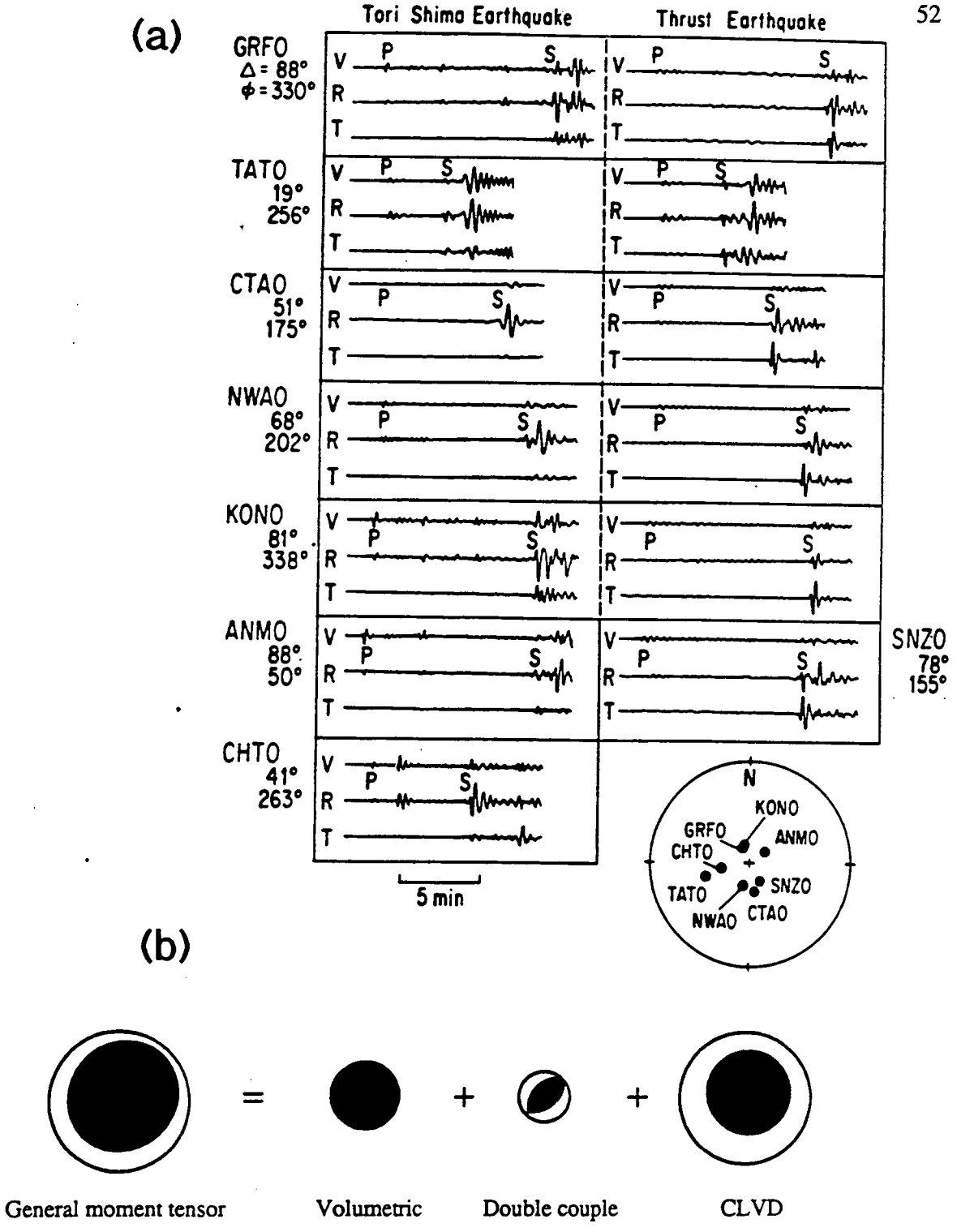

Figure 2.11: (a) Body waves from the 13 June 1984 Tori Shima earthquake and, for comparison, a nearby thrust-faulting earthquake in November 1983. Vertical (V), radial horizontal (R) and transverse horizontal (T) seismograms are shown for stations plotted on the lower focal hemisphere (equal-area projection) at the lower right. *P* and *S* phases are marked. The tangential records show a clear difference in *P*:*SH* amplitude ratios between the two events. All recorded *P* waves for the Tori Shima earthquake had compressional first motions. Δ : epicentral distance; ϕ : epicentre-to-station azimuth. (From *Kanamori et al.*, 1993). (b) Decomposition of strongly non-DC focal mechanism of *Kanamori et al.* (1993). The area of the focal-sphere plots is proportional to the scalar moments of the components.

An alternative possibility is shear slip on a ring fault, which has a deviatoric, non-DC equivalent force system whose CLVD component increases with the arc spanned by faulting and decreases with fault dip (*Ekström*, 1994; Section 2.3.3). For a fault dipping at 75°, the observed ε value of about 0.35 requires that the fault's strike vary by 180° or more. The required angle of fault rupture decreases for more shallow fault dips. Thus slip on a curved fault that has a dip <75°, such as a cone-sheet, would not require such a large fault rupture azimuth.

2.4.12 Bárðarbunga volcano, southeast Iceland

Ekström (1994) searched the Harvard CMT catalogue for earthquakes in volcanic areas with nearly vertical CLVD-like mechanisms that might be caused by ring faulting, and found ten earthquakes world-wide, six of which occurred between 1977 and 1993 at the Bárðarbunga volcano, beneath the Vatnajökull icecap in southeast Iceland. These earthquakes, of M_w 5.2 – 5.6 ($M_0 = 8-30\times10^{16}$ Nm), have ε values between 0.36 and 0.48 (Figure 2.12).

Seismic observations impose constraints on the size and geometry of the hypothetical ring fault, because ε depends on the dip of the fault and the azimuthal range over which faulting occurs (i.e. the range of fault strikes). For a dip of 75°, the observed ε values require that the strike must span a range of 180° to 250°. The epicentral locations indicate that the ring has a radius of at least 10 km (Figure 2.12), which implies a fault length of 30-45 km and a scalar moment of at least 8×10^{17} Nm (using empirical moment-source dimension relations from *Kanamori and Anderson*, (1975) and accounting for cancellation of moment release from different portions of the curved fault). This scalar moment is larger than those observed. Alternatively, if the fault dips at less than 60°, the predicted seismic moments would be consistent with those observed. Ring faults exposed in ancient calderas are usually vertical or dip steeply outwards (*e.g.*, *Clough et al.*, 1909), which makes them inefficient generators of non-DC earthquakes. Cone sheets, which dip inward at shallow angles, are more likely to cause non-DC earthquakes.

2.4.13 "Long-period" volcanic earthquakes

Many small earthquakes in volcanic regions have spectra dominated by frequencies roughly ten times lower than ordinary shear-faulting earthquakes of comparable magnitudes. These "long-period" earthquakes are attributed to the underground movement of magmatic fluids, and are expected to have mechanisms involving net forces (Section 2.3.2).

Few analyses of long-period earthquakes have allowed for the possibility of net forces, however. A notable exception is the study by *Ukawa and Ohtake* (1987) of a long-period earthquake at Izu-Ooshima volcano, Japan. This volcano, located on a

small island east of the Izu Peninsula in south-central Honshu, began a major eruption on 15 November 1986. Fifteen months earlier, on 27 August 1985, an unusual earthquake occurred about 30 km beneath the volcano. Several analogue and 18 digital three-component local stations recorded the earthquake, producing a data set of unusually high quality. At all stations a monochromatic S-wave train with a dominant frequency of 1 Hz lasted for more than one minute. The observed *P*:*S* amplitude ratios are small, and inconsistent with sources involving tensile cracks or oscillations of magma chambers. The *S*-wave polarisation directions agree much better with those predicted for a force oriented north-south than with those from a DC (Figure 2.13). These observations confirming the predicted net-force component of the mechanism support the attribution of long-period earthquakes to unsteady fluid flow.

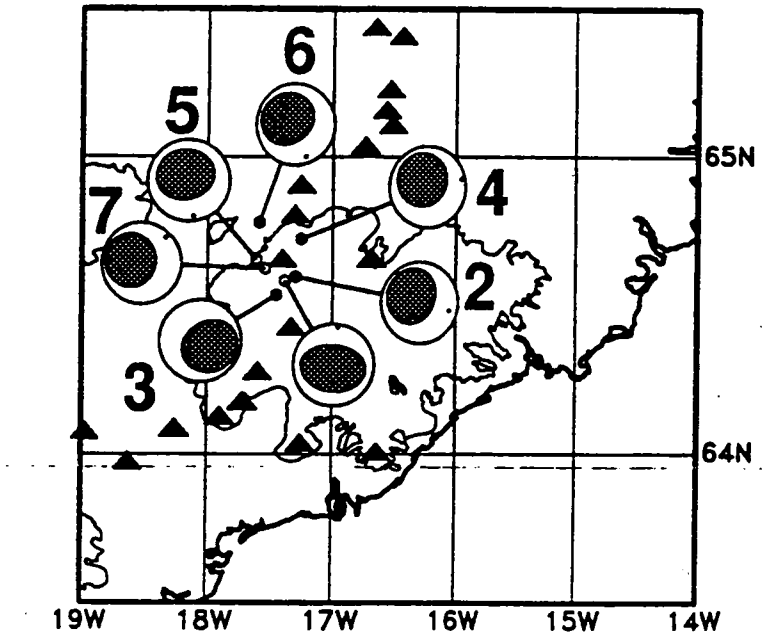

Figure 2.12: Map showing Harvard CMT focal mechanisms of earthquakes at Bárðarbunga volcano, southeast Iceland, from Ekström (1994). Also shown are the southeast coast of Iceland and the outline of the Vatnajökull icecap. Lower hemisphere is shown in equal-area projection.

2.4.14 Evidence for fault-normal motion

Unlike the planar idealisations used in mathematical analysis, real fault surfaces are rough, so "shear" slip is expected to involve some amount of motion normal to faults. Furthermore, motion occurs normal to even planar faults in laboratory experiments on stick-slip sliding in foam rubber (Section 2.3.6). Kinematically, fault-normal motion is equivalent to tensile faulting. There is some evidence that such motion occurs in many earthquakes.

Haskell (1964) found that *P*:*S* amplitude ratios at high frequencies are usually larger than those expected for shear faulting, and suggested that this indicates fault-normal motion caused by the roughness of natural fault surfaces. High *P*:*S* ratios might also be caused by anelastic attenuation (which affects shear waves more than compressional waves) or *S*-to-*P* mode conversion, but the observed effect is too large to be explained entirely by propagation effects. The theoretical *P*:*S* energy ratio for fault-normal motion is about ten times greater than for shear faulting, so only a small amount of fault-normal motion is needed to explain the observed ratios.

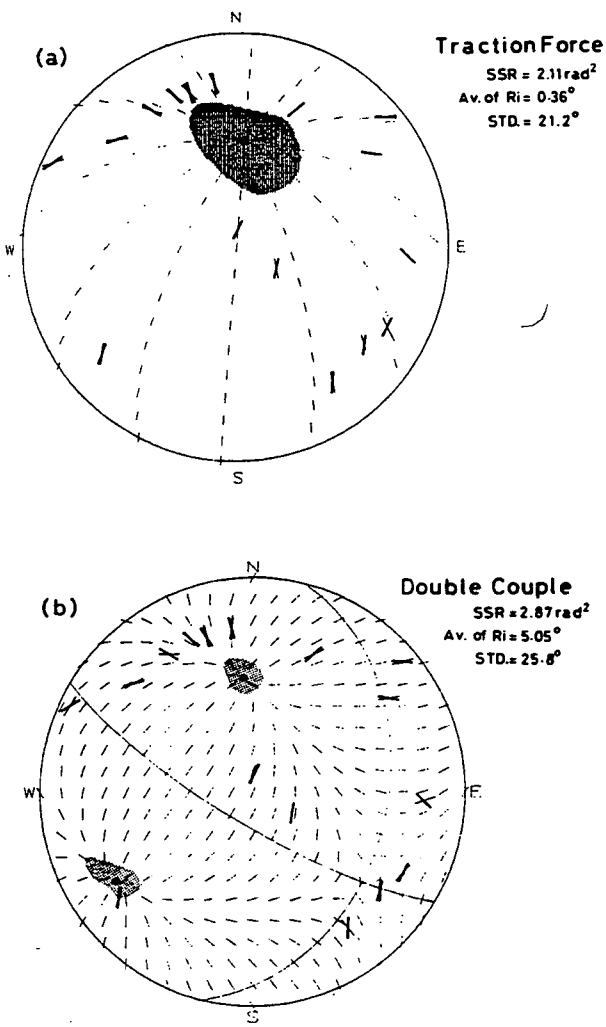

Figure 2.13: Polarisation directions of *S* waves from the long-period earthquake of 27 August 1985 beneath Izu-Ooshima volcano, Japan. (a) best-fit model, a single force oriented to the north; (b) best-fit double couple. The sums of squared residuals ("SSR"), mean residuals ("Av. of Ri") and standard deviations ("STD") of the fits to polarisation directions are shown for each solution. Shading shows the range of axis positions for SSR < 30 rad^2. Lower hemisphere equal-area projections (from *Ukawa and Ohtake*, 1987).

High *P*:*S* amplitude ratios at frequencies above 10 Hz were measured for local earthquakes at the Guerrero accelerometer array, Mexico (*Castro et al.*, 1991). The ratio varies greatly for different source-station pairs but on average is far higher than expected for a DC source. *Castro et al.* (1991) show that the ratio varies even for events at similar distances from a single station. These observations cannot be explained by attenuation effects alone, and must be at least partly due to a source effect.

2.5 Discussion

The term "non-double-couple" is uninformative and negative, expressing merely what these earthquakes are not, and implying that they deviate from some standard. The observations now available make it clear that the term actually encompasses several physical phenomena, although our understanding of them is still highly incomplete. Furthermore, theoretical considerations and recent laboratory experiments hint that such processes may be intrinsic in the nucleation and continuation of predominately-shear earthquakes also. Attention to non-DC processes is likely to become increasingly important as the quality of seismic data, the power of analytical methods, and the sophistication of our understanding of earthquake processes continue to increase.

Even "common" shear-faulting earthquakes have small non-DC components, because of departures from ideal geometry such as fault curvature and roughness, and variations in slip direction. Furthermore, the formation of shear faults is thought to involve tensile micro-cracking, though this has not yet been detected by seismological methods.

A disproportionate fraction of non-DC earthquakes occur in volcanic and geothermal areas. Some, such as the Tori Shima earthquake (Section 2.4.11), the Bárðarbunga earthquakes (Section 2.4.12), and the Long Valley caldera earthquakes (Section 2.4.10), appear to have mechanisms close to pure CLVDs and may be caused by rapid intrusions, probably of gas-rich magma, although ring faulting or simultaneous slip on multiple shear faults cannot be ruled out, in theory. Other earthquakes in volcanic and geothermal areas have mechanisms with isotropic components, involving volume increases or (more rarely) decreases, which are consistent with mixed-mode failure, involving simultaneous shear and tensile faulting. In geothermal areas, high temperature/pressure geothermal fluids may provide mobile material to fill cavities and enable tensile cracks to form and remain open at depths of several km. Data from MORs are not yet adequate to determine whether small, non-DC earthquakes occur there also, although the resemblance of geologic processes and structures on MORs to those in Iceland makes this likely. Some volcanic earthquake mechanisms include net forces, indicating that these events involve the advection of magmatic fluids. Future analyses of volcanic earthquake mechanisms must allow for possible net force components if the source processes are to be fully understood.

2.6 Summary

Observations of non-DC earthquakes have become increasingly common in recent years. There are several possible non-DC earthquake mechanisms that could occur in volcanic and geothermal areas. These include single-force sources such as volcanic eruptions and advective processes, shear slip on multiple faults of different orientations, and sources that involve tensile faulting. Only restricted geometries of shear slip on multiple faults can produce a non-DC equivalent force system, and this mechanism cannot have a volumetric component. Some well-constrained large earthquakes appear to have negligible volumetric components and may be caused by simultaneous shear faulting on multiple faults, or by rapid intrusions. Many non-DC earthquakes in geothermal and volcanic areas, especially in Iceland, have volumetric components (predominantly explosive) and may be due to some form of tensile cracking accompanied by shear faulting. These processes may be facilitated by high-pressure geothermal fluids.

Chapter 3

The 1991 field experiment and primary data processing

3.1 The field experiment

3.1.1 Experiment objectives and design

The primary aim of the 1991 field experiment was to record high-quality earthquake data from the Hengill volcanic complex, in order to study the focal mechanisms of the non-DC earthquakes known to occur there in as great a detail as possible. Thirty digital, three-component instruments were installed in a regular array covering an area of 25×25 km. The network was designed to give good focal sphere coverage for earthquakes in the most seismically active volumes. The network operated for 64 days, from 29 July to 30 September 1991. The field experiment was a collaboration between the Department of Geological Sciences, University of Durham, and the United States Geological Survey (USGS).

3.1.2 Locations of stations

The seismometer network (Figure 3.1; Table 3.1) was designed using information from a previous local earthquake monitoring experiment in 1981, which identified regions of intense, continuous seismicity in the Hengill area (*Foulger*, 1988a; Section 1.3.4.3). Stations were located to give uniform, dense coverage of the upper focal hemisphere for earthquakes beneath the centre of the network. Heterogeneous crustal structure can severely affect raypaths, and thus the position of stations on the focal sphere. To achieve uniform focal-sphere coverage, rays were traced through a three-dimensional V_P model determined by simultaneous inversion of the 1981 data (*Toomey and Foulger*, 1989; Section 1.3.4.3.3). For a point at 64°02.5'N, 21°14.0'W and 4 km deep (the centre of the most seismically active volume), the 30 stations deployed were located in concentric rings at take-off angles of approximately 100°, 110°, 130° and 150° (measured from the nadir), and at regularly spaced azimuths (Figure 3.2). The Hengill area has rugged topography and poor road access, and the network design meant that many stations were not easily accessible. Twelve stations were accessible by vehicle, 8 were within 300 m of a road, and the remaining 10 stations required walks of up to 75 minutes.

Additional data were available from the South Iceland Lowland (SIL) regional seismic network, which has two stations, Bjarnastaðir (bja) and Heiðarbær (hei) near Hengill (Figure 3.1). The SIL network is operated by the Geophysical Division of the Iceland Meteorological Office.

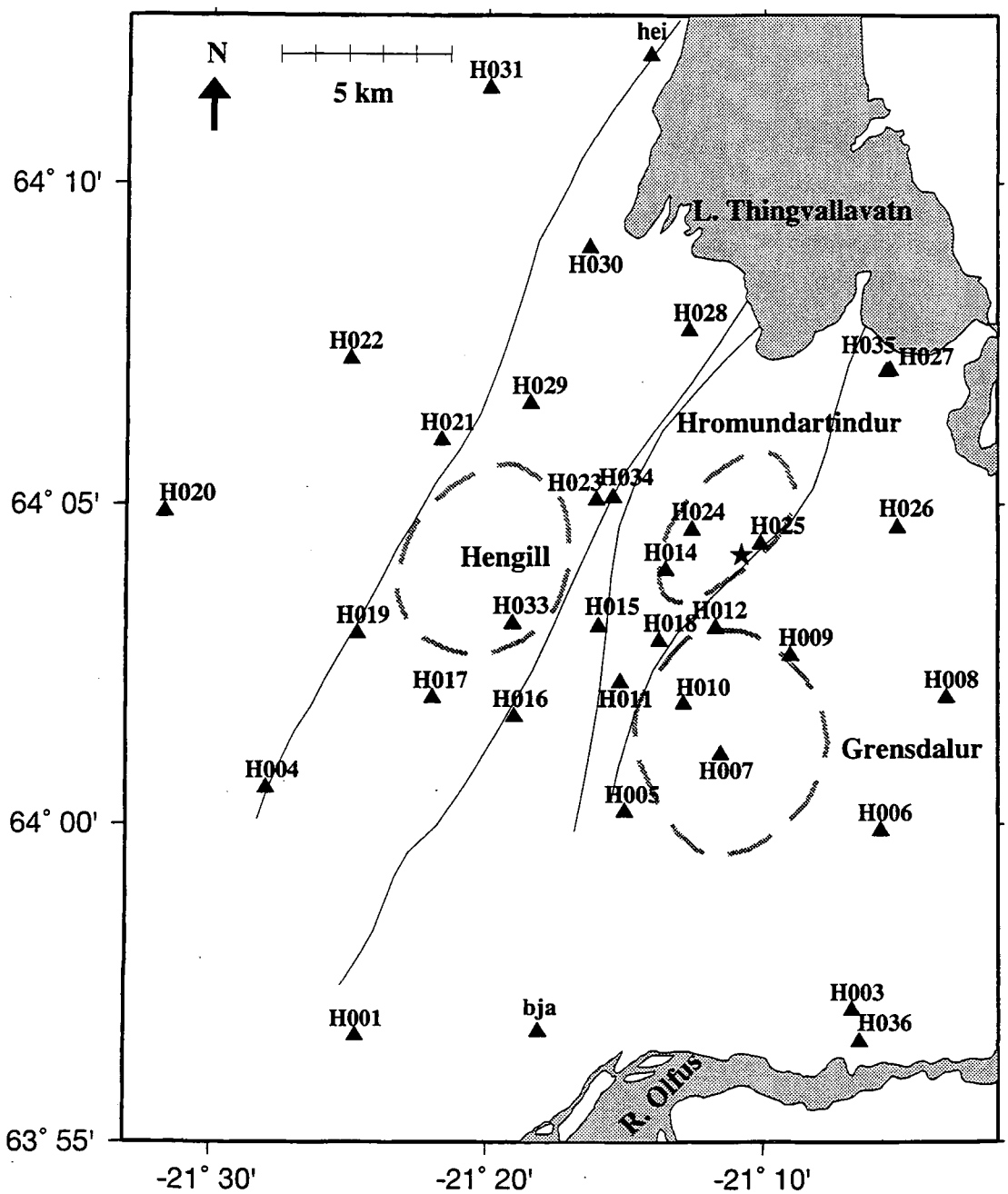

Figure 3.1: Map showing station locations. Solid triangles: stations; dashed lines: outlines of the Hromundartindur, Grensdalur, and Hengill volcanic centres; solid lines: outlines of the Hengill and Hromundartindur fissure swarms; star, explosion.

Table 3.1: Station locations with reference to the WGS84 ellipsoid. GPS point: station surveyed as part of a differential GPS geodetic survey (*Hodgkinson and Foulger*, 1996); 15 mins: GPS receiver deployed at site for about 15 minutes (in differential mode) to get approximate location; Photo: location determined from aerial photograph. *P*-wave picked column shows the percentage of the 448 located earthquakes for which a *P*-wave was picked at that station.

Station code	Station name	Latitude (°N)	Longitude (°E)	Altitude (m)	Azimuth of "North" component	Location method	*P* waves picked (%)
Temporary stations:							
H001	Krossfjöll	63:56:40.4	-21:24:45.0	268	337°N	GPS point	44.8
H003	Bræðraból	63:57:05.0	-21:06:48.9	93	339°N	GPS point	13.8
H036	Bræðraból2	63:56:33.7	-21:06:29.7	77	339°N	Photo	13.1
H004	Lambafell	64:00:33.9	-21:28:02.6	353	339°N	15 mins	64.4
H005	Núpafjall	64:00:11.1	-21:15:03.9	388	338°N	15 mins	77.7
H006	Æðagil	63:09:54.4	-21:05:45.7	186	339°N	GPS point	52.1
H007	Tindar	64:01:05.8	-21:11:33.4	155	340°N	GPS point	81.5
H008	Stórahálsfjall	64:01:60.0	-21:03:23.4	57	334°N	15 mins	59.7
H009	Álútur	64:02:39.8	-21:09:03.8	510	334°N	15 mins	69.3
H010	Rjúpnabrekkur	64:01:53.6	-21:12:54.6	309	339°N	15 mins	87.1
H011	Smjörþýfi	64:02:14.0	-21:15:13.7	435	339°N	15 mins	72.8
H012	Grensdalur	64:03:05.0	-21:11:44.9	333	334°N	15 mins	84.4
H014	Laki	64:03:59.5	-21:13:34.6	470	340°N	15 mins	71.5
H015	Fremstidalur	64:03:06.5	-21:16:00.6	467	334°N	15 mins	74.4
H016	Hellisheiði	64:01:41.4	-21:19:02.5	419	340°N	15 mins	72.4
H017	Gígir	64:01:59.0	-21:21:59.7	453	338°N	GPS point	76.6
H018	Klambragil	64:02:52.7	-21:13:49.2	404	339°N	GPS point	87.3
H019	Draugatjörn	64:03:00.3	-21:24:43.8	319	339°N	GPS point	92.4
H020	Lyklafell	64:04:52.9	-21:31:38.9	270	339°N	GPS point	82.6
H021	Marardalur	64:06:00.7	-21:21:40.2	361	341°N	GPS point	70.4
H022	Eiturhóll	64:07:16.5	-21:24:58.4	391	337°N	GPS point	51.0
H023	Hengill	64:05:04.5	-21:16:05.6	425	339°N	15 mins	16.9
H034	Hengill2	64:05:06.6	-21:15:29.4	369	339°N	GPS point	42.1
H024	Hrómundartindur	64:04:37.3	-21:12:36.4	390	339°N	15 mins	78.6
H025	Katlatjörn	64:04:23.9	-21:10:07.6	418	335°N	15 mins	54.6
H026	Selflatir	64:04:38.8	-21:05:09.8	258	339°N	GPS point	55.0
H027	Villingavatn	64:07:07.0	-21:05:24.3	182	339°N	15 mins	11.6
H035	Villingavatn2	64:07:05.7	-21:05:31.9	192	339°N	GPS point	41.6
H028	Nesjahraun	64:07:43.3	-21:12:42.6	202	338°N	15 mins	43.0
H029	Dyradalur	64:06:35.0	-21:18:27.4	407	336°N	15 mins	72.4
H030	Jórugil	64:09:00.7	-21:16:20.8	302	339°N	GPS point	45.0
H031	Þrívörður	64:11:28.6	-21:19:56.9	324	339°N	GPS point	39.2
H033	Skarðsmýrarfjall	64:06:35.0	-21:18:27.4	407	341°N	15 mins	86.8
Permanent stations (SIL):							
bja	Bjarnastaðir	63:56:44.4	-21:18:08.7	118	0°N	GPS point	28.5
hei	Heiðarbær	64:11:59.0	-21:14:09.4	222	0°N	GPS point	17.1

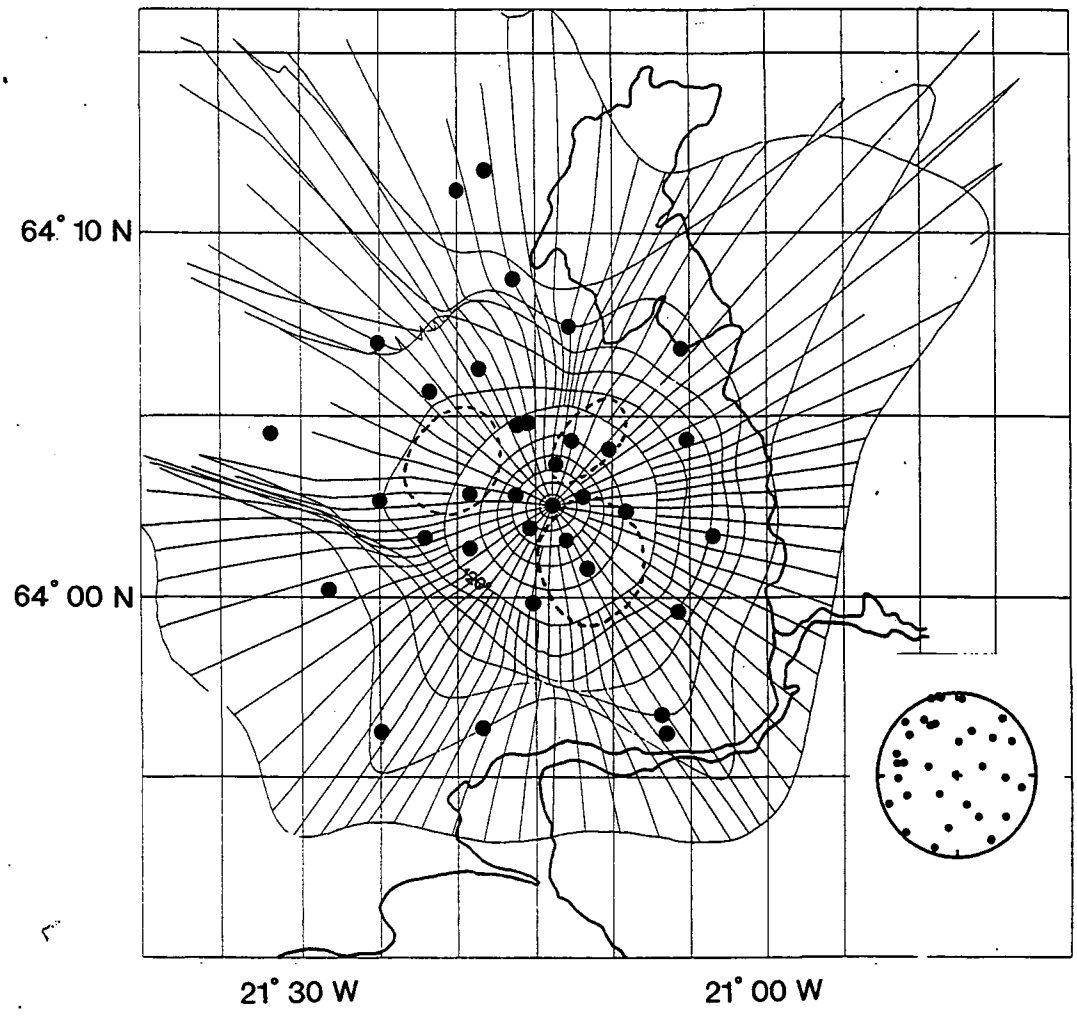

Figure 3.2: Map view of rays traced through the three-dimensional wave-speed model derived from the 1981 data for an event at 4 km depth beneath the centre of the network. Azimuth and takeoff angle (toa) are spaced at 5° intervals for 90° < toa < 120°, and at 10° intervals for 120° < toa < 180°. Dots: stations deployed in 1991, dashed lines: volcanic centres. Upper-hemisphere, equal-area focal sphere plot is shown at the lower right.

3.1.3 Station Installation

3.1.3.1 Equipment used

The equipment used was lent by the IRIS-PASSCAL and NERC geophysical instrument pools. The following equipment was installed at each station (Figure 3.3):

- REFTEK 72A-02 Data Acquisition System (DAS)
- Mark Products 2.0 Hz L-22D three-component geophone (Figure 3.4).
- 190 or 660 Mbyte storage disk
- 85 or 125 amp-hr lead-acid battery
- solar panels (remote sites only)
- antenna for receiving Omega timing signal

Figure 3.3: Photograph of the Tirdar station (H007), showing typical station setup.

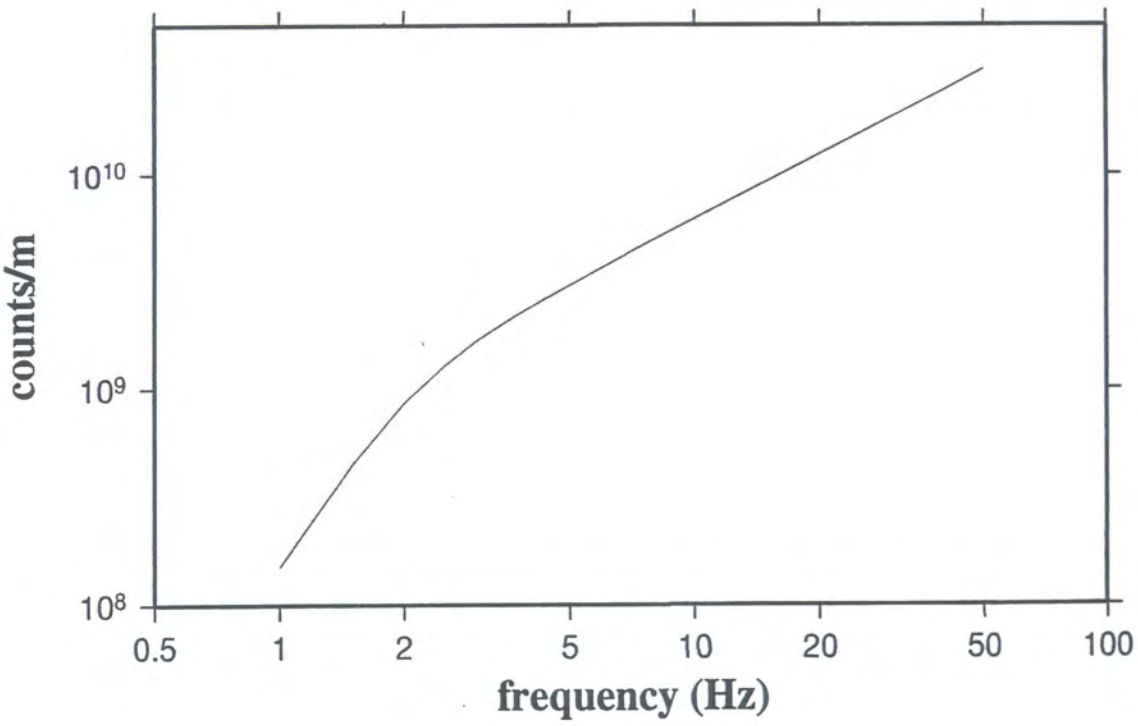

Figure 3.4: Nominal response of the L22-D sensor to ground displacement.

Each DAS recorded two data streams, (1) data from three channels sampled continuously at 100 samples per second, and (2) triggered data, *i.e.*, 10 seconds of vertical-component data only when the DAS software recognised an event. The trigger times from all the stations were used after the field experiment to construct an event list, which was used to extract events from the continuous data stream. The two SIL network stations (bja and hei) have three-component, Lennartz model LE-30, 1-Hz digital seismometers and record in triggered mode at 100 samples per second.

3.1.3.2 Station installation procedure

Instrument installation started on 6 July 1991, and involved five field workers with three vehicles. Sensors were plastered to solid bedrock at depths of about 50 cm, covered with plastic wash bowls, and buried. The "north"-component sensor was aligned with magnetic north using a handheld Brunton compass, and the orientation was rechecked at the end of the experiment (Table 3.1). The DAS, disk and battery were sited a few metres away from the sensor and covered by a tarpaulin. All cables were buried to protect them from sheep.

The larger, 32 kg batteries were difficult to carry to remote sites, so 25 kg, 85 amp-hr batteries were deployed there with solar panels, which extended the battery lifetime from about 6 to 12 days. All instruments were set to start recording at 0000 hrs, 29 July 1991 (day 210).

3.1.3.3 Station location determination

The Global Positioning System (GPS) enables points on the Earth's surface to be accurately located by receiving timed signals from orbiting satellites. Most station locations were determined using differential GPS. Many of the seismometer sites were surveyed as part of a first-epoch geodetic survey of the region (Table 3.1) (*Hodgkinson and Foulger*, 1996). For these sites the GPS receiver was operated on site for 8 hours, giving location accuracies of less than 1 cm relative to a master site of known location (Figure 3.5). At other sites the GPS receiver was operated for about 15 minutes, giving a relative location accuracy of a few dm. One station, H036, was not surveyed using GPS, and its location was estimated from a map and an aerial photograph.

3.1.4 Station maintenance and data collection

Stations were serviced every three to six days to check that they were operational, and to change disks and batteries. Battery voltage was measured at every visit, and if the voltage was projected to fall below 12 V before the next visit the battery was replaced. The 660 Mbyte disks were installed at the most remote stations, as they had the capacity for 12 days of data. The failure of five 660 Mbyte disks to arrive in Iceland prior to the start of the experiment increased the workload greatly, as smaller disks,

requiring more frequent site visits, had to be used at some remote stations. Once network installation was complete, station servicing was carried out by three field workers.

The field headquarters were in a rented farmhouse near station Bræðraból (H003/H036). Two SUN workstations were used there to download data from field disks and to copy them to Exabyte tapes. The data from each field disk were converted to SEGY format and examined to check that the station was operating correctly. Both the raw disk-dump data and the SEGY-format data were copied to tape.

Three stations, at Bræðraból (H003), Hengill (H023) and Villingavatn (H027), were located at sites that turned out to have high noise levels due to nearby traffic, geothermal activity or poor bedrock quality. These stations were relocated to quieter sites nearby during the experiment (Table 3.1). The station at Bræðraból was often used to test suspect equipment and parts were sometimes removed from here to keep other stations operational, with the result that this station was out of operation for most of the experiment.

To check the station polarities a timed explosion was detonated in Lake Katlatjörn Nyðri at 64°04.228'N, 21°10.815'W at 18:59:59.096 September 16 1991 (day 259) (Figure 3.1). The polarities of first motions from the explosion showed that the DASs

Figure 3.5: Photograph showing typical GPS measurement setup.

supplied by NERC had been reverse wired compared with the IRIS-PASSCAL DASs. The NERC DASs were later returned to the supplier to correct this fault. This illustrates the importance of thorough polarity testing of networks, for the primary goal of this experiment would have been jeopardised if the polarity reversals had not been discovered.

3.1.5 The final data set collected

Approximately 100 Gbytes of data were collected, representing about 39,000 hours of continuous, three-component, 100 sps data. The station down-time was about 10% of the total recording period. Instrument malfunctions caused most of the data loss (*Foulger and Julian*, 1991). Examples of some of the seismograms recorded are shown in Appendix 1.

3.2 Data processing

3.2.1 Event identification and extraction

Events were identified using the triggered data recorded on stream 2 at each station. Times of interest were identified when at least three stations triggered within 5 s, and event segments at least 30 s long were then extracted from the continuous data. The event windows were extended if further trigger coincidences occurred during this time segment, so that some segments contained more than one event. Over 3800 segments were extracted in this way. The two SIL stations record a triggered stream only and thus did not record all these events. Throughout this thesis, earthquakes are identified by a 10 digit number, in the format *aaa.bbbbbb.c*, where *aaa* is the day-of-year, *bbbbbb* is the time of the start of the event segment, and *c* is the number of the earthquake within the segment.

3.2.2 Automatic phase identification

The arrival times of *P* waves were measured for all the earthquakes using an automatic process. *P* waves are relatively easy to identify automatically, as the seismogram before the *P* wave is usually uncontaminated by previous arrivals, and *P* waves normally have a high signal-to-noise ratio on the vertical component at local stations. The program *autopick* was used, which is based on a program developed by R. Crosson that was modified by M. O'Neill, B. R. Julian and author of this thesis. It measures *P*-wave arrival times, polarities and qualities from AH-format ("adhoc") digital seismograms. Each seismogram is processed in two stages. The first stage identifies the approximate arrival time, and the second stage refines it. Both stages use the same algorithm to calculate an "fbcurve", the ratio of two sliding, triangularly-weighted sums of the seismogram amplitude. When the signal:noise ratio is high the

fbcurve has a maximum at a phase arrival, because the seismogram amplitude after the phase arrival is higher than before the arrival.

The *autopick* program picked an average of 7 *P*-wave arrival times per earthquake, with a range from 0 to more than 20 picks. For seismograms with low noise levels, the *P*-wave pick was usually accurate to the nearest sample. The number of picks for each earthquake was used to identify good-quality, widely recorded earthquakes for further processing.

3.2.3 Phase picking

Seismograms were processed interactively using the program *epick* (B. R. Julian, *pers. comm.*) which is an extensively modified version of an earlier program *sunpick* (R. Ryan and R. Davis, *pers. comm.*). The *epick* program runs in the X-windows environment, and enables the user to examine the seismograms for one earthquake at a time, measure or modify time picks on any traces, and to locate earthquakes. A "pick" consists of a time, measurable to the nearest millisecond, a phase identification label, and optional quality, arrival type, polarity, amplitude and frequency measurements.

All earthquakes for which *autopick* picked more than 8 *P*-wave arrivals were processed using *epick*. Earthquakes that were located outside the network, or had low signal-to-noise ratios at most stations were discarded. *P*-wave arrivals were picked only from vertical components, and *S*-waves from the horizontal component where they were most clearly recorded. All *P*-wave picks made by *autopick* were checked, and adjusted if necessary. Only clear, impulsive arrivals with large signal-to-noise ratios were selected. If both horizontal components showed clear *S*-wave arrivals, the earliest arrival was chosen.

Earthquakes with fewer than 10 high-quality *P*-wave picks, or that lay outside of the network were discarded. The final set of processed earthquakes consists of 448 earthquakes and one explosion, with 9130 *P*-wave arrival times and 6448 *S*-wave arrival times.

3.2.4 Clock corrections

Each DAS has an internal, temperature-compensated, crystal oscillator to keep time. This oscillator drifts by a few tens of ms per day, so to maintain accurate time the clock must be frequently calibrated with an external time signal. The DASs received time signals from the Omega radio navigation system, which broadcasts second marks every 10 seconds from a global network of eight ~20 Hz radio transmitters. The nearest Omega transmitter to Iceland is in Norway, and the oceanic travel path gives good reception.

If the Omega signal is received clearly and continuously then the clock is said to be "locked", *i.e.*, the oscillator is phase-locked to the time signal. In this case timing errors of less than 1 ms are achieved at all times. If the Omega signal quality is poor and lock is lost, the oscillator runs freely until the signal quality improves and lock can again be

achieved. If the internal clock has drifted by more than 10 ms or less than -5 ms when lock is reachieved a "time jerk" is applied. All time jerks are recorded in a log file. For smaller amounts of drift, the oscillator rate is slewed until the clock is brought back into phase with the time signal. The log files were used to calculate clock correction functions for every station (Figure 3.6). While the clock was unlocked, a constant drift rate was assumed. Clock corrections were applied to every pick time before an earthquake was located.

Data from the two SIL stations were supplied with clock corrections already applied. The SIL stations were set to record Omega signals from the Norway transmitter only, and when the transmitter was out of operation for routine maintenance from 19 to 26 August 1991 the timing of the SIL stations was unreliable. Station bja also had timing problems from 19 September 1991 until the end of the experiment.

3.3 Earthquake locations

3.3.1 The location procedure

The earthquake location procedure involves finding a hypocentral location and origin time that minimises some function of the travel-time residuals. Travel times are non-linear with respect to hypocentral parameters and thus the best-fit location is usually obtained by iteratively improving a trial solution. The program *qloc* (B. R. Julian, *pers. comm.*) was used, which carries out an iterative, damped inversion of *P* and *S* travel times to minimise the sum of squared travel-time residuals. For each earthquake, *P* and *S* arrival times were weighted according to the pick quality. *S*-wave picks are normally of lower quality because they arrive within the *P*-wave coda. An initial location at 3 km beneath the station with the earliest arrival time was used.

The operation of *qloc* is controlled by a UNIX Bourne-shell script, *eloc*, that reads an *epick*-format pick file. The output of *eloc* is an ASCII list, giving the hypocentre location and information about every pick.

3.3.2 The one-dimensional wave-speed model

The earthquakes were located using a layered, one-dimensional crustal model that was the lateral average of a three-dimensional V_P model of the Hengill area (*Toomey and Foulger*, 1989; Section 1.3.4.3.3). That model consists of V_P values at nodes spaced 2-3 km horizontally and 1 km vertically, with V_P interpolated linearly between nodes. The one-dimensional V_P model was derived by calculating a mean V_P for each horizontal layer (Figure 3.7).

The one-dimensional V_S model was derived from the V_P model, assuming a constant value of V_P / V_S throughout the model volume. This V_P / V_S value was calculated using Wadati diagrams (Figure 3.8). A Wadati diagram is a plot of *S–P* times against *P*-wave

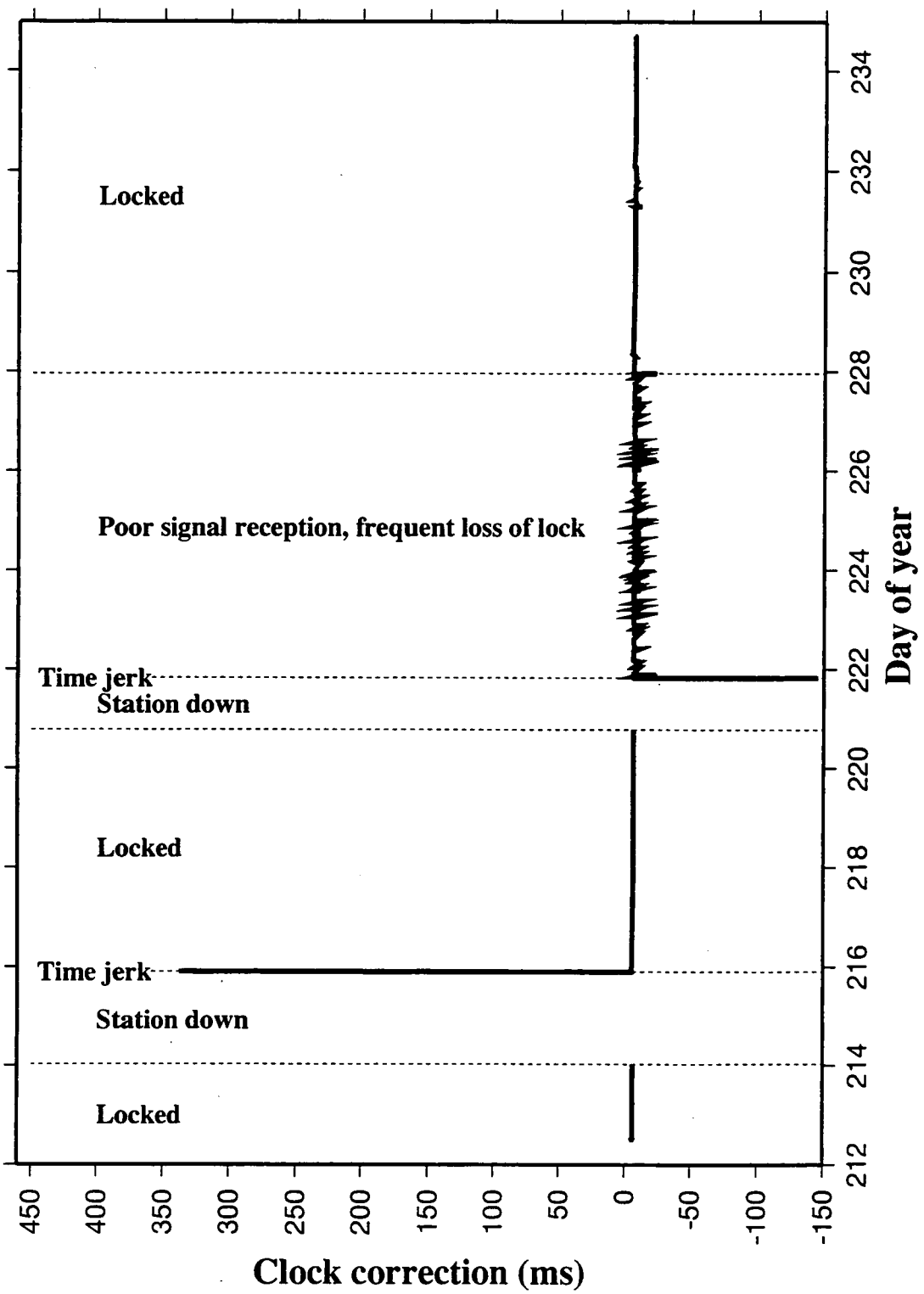

Figure 3.6: Example of a clock-correction function. Variation in value of the clock correction for station H001, for days 212 to 235. The station was down for several hours on two occasions, and "time jerks" were made when the station was restarted at the end of these periods. Between days 222 and 228, the Omega signal reception was poor, leading to numerous short-term losses of lock and minor amounts of clock drift.

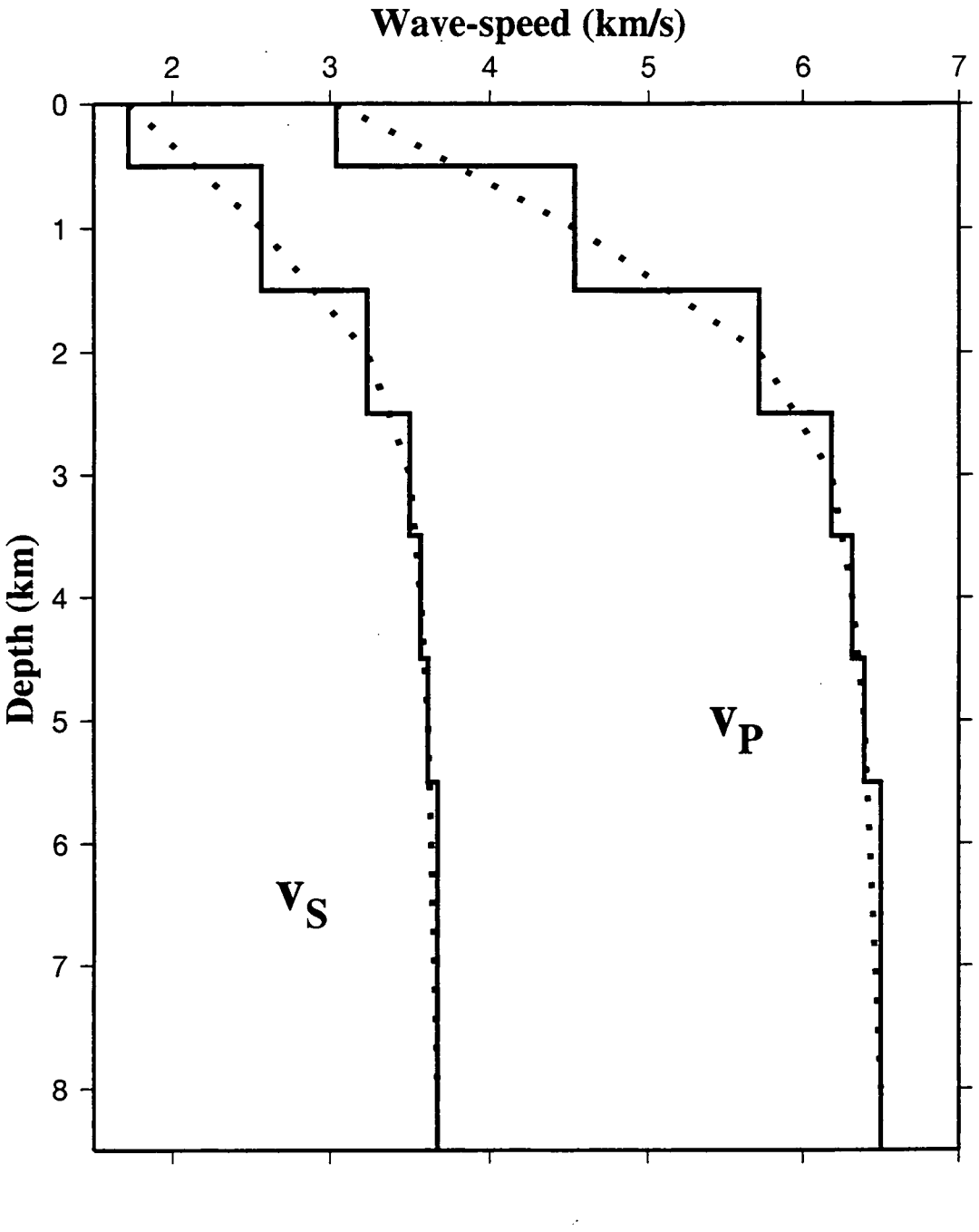

Figure 3.7: The one-dimensional wave-speed model used to locate the earthquakes. Dotted lines indicate the one-dimensional model calculated from the three-dimensional tomographic model of *Toomey and Foulger* (1989). The one-dimensional V_P model is a horizontal average of the three-dimensional V_P model. The one-dimensional v_S model is calculated from the one-dimensional V_P model by assuming $V_P / V_S = 1.77$. Solid lines show the one-dimensional layered model used to locate the earthquakes. The upper layer extends above 0 km to the altitude of the station.

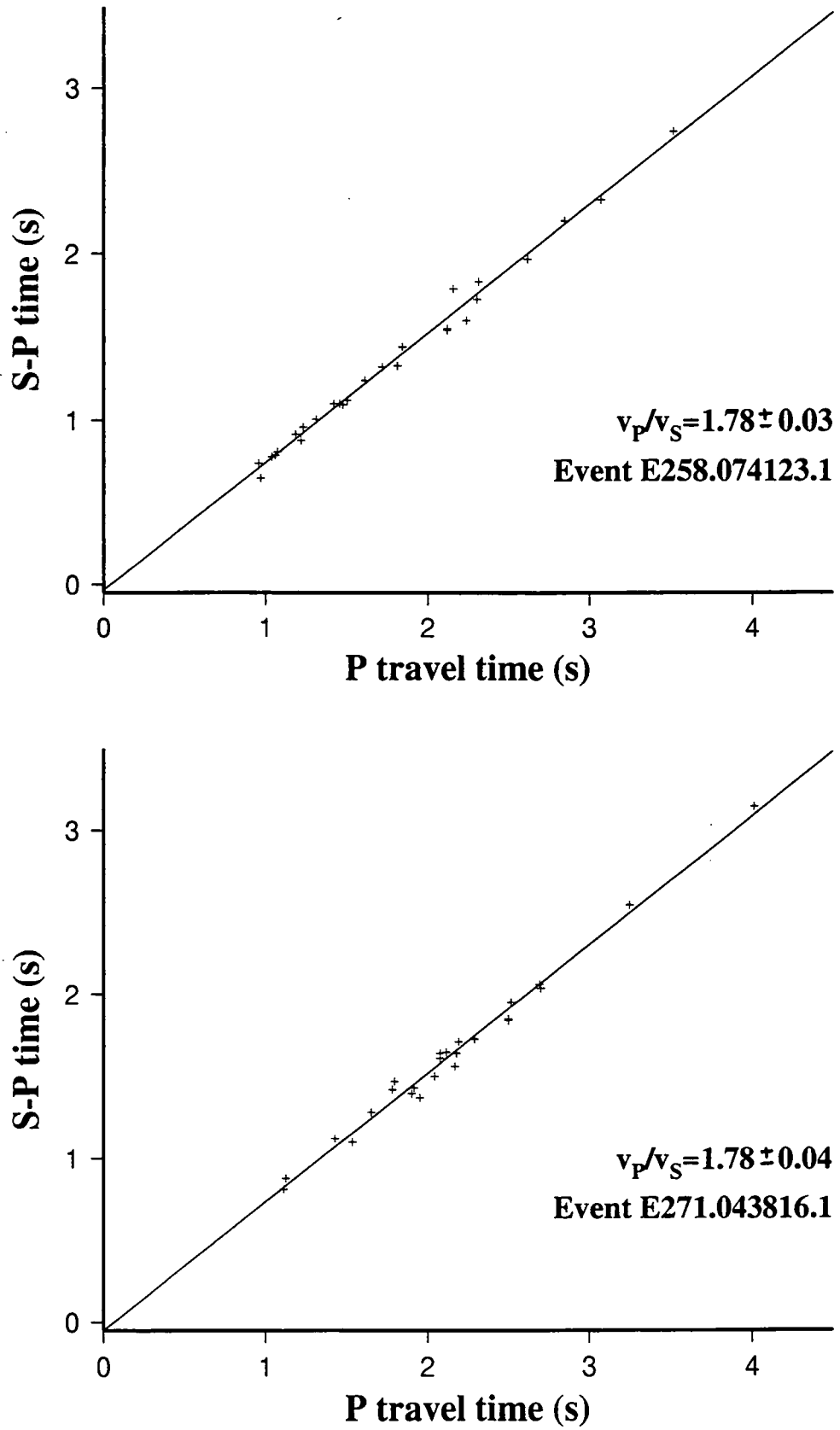

Figure 3.8: Examples of Wadati diagrams used to calculate V_P / V_S for the two best recorded events, with least-squares, best-fit lines. Event 258.074123.1 occurred in the geothermal field. Event 271.043816.1 occurred in the Dyradalur cluster (Figure 3.9).

arrival times at several stations for the same earthquake (*Wadati*, 1933). If Poisson's ratio, and therefore V_P/V_S, is constant throughout the volume, the points on a Wadati diagram lie on a straight line with a slope of $(V_P/V_S - 1)$. *P* and *S–P* times are independent of the earthquake location, so the calculated V_P/V_S value does not depend on an assumed wave-speed model. All earthquakes with more than 15 *P* and *S–P* times were used to calculate the average V_P/V_S value of 1.77±0.02 (Figure 3.8). This value was used to calculate the one-dimensional V_S model (Figure 3.7).

3.3.3 The hypocentral distribution

Earthquakes were distributed throughout the area covered by the network. Much of the seismicity was concentrated in the southeast of the geothermal area (Figure 3.9). Within the geothermal area, a cluster of 63 earthquakes occurred beneath the Grensdalur area. No earthquakes were located north of 64°08N, or in the area around the Skálafell shield volcano (Figure 3.9), despite adequate station coverage in these areas. In the Ölfus lowlands, in the south of the area, earthquakes are concentrated in linear zone along a westward extension of the SISZ (Section 1.3.1.4). Very few earthquakes occurred within the Hengill fissure swarm, and most of those that did were concentrated within the Gigir cluster and south of the Nesjavellir geothermal field. In the northwest of the area, the activity was concentrated in two clusters at Marardalur and Dyradalur.

The seismicity extended down to 7.8 km depth, but most earthquakes occurred between 2 and 6 km, with only a few in the east shallower than 1 km (Figure 3.10). A 3-km wide east-west aseismic zone about 64°N marks the boundary between the geothermal and spreading regime to the north, and the western end of the SISZ to the south. The seismicity generally extends deeper in the south and north, away from the geothermal field. Three dense clusters of earthquakes occurred at Gigir, Marardalur and Dyradalur (Figures 3.9 and 3.10).

3.3.4 Temporal distribution of the earthquakes

The seismic rate varied during the recording period, with more earthquakes per day in August than in September (Figure 3.11). This variation cannot be explained by changes in the network geometry, as the distribution of stations remained nearly constant during the recording period. The peaks in activity on days 217, 226 and 271 are associated with the Gigir, Marardalur and Dyradalur clusters respectively. Many of the earthquakes on day 253 were in a cluster located east of the network.

Earthquakes in the eastern section of the geothermal area occurred throughout the recording period, and this volume was active on almost a daily basis. This contrasts with the Gigir, Marardalur and Dyradalur clusters, where most of the earthquakes occurred within intervals of a few days (Figure 3.12).

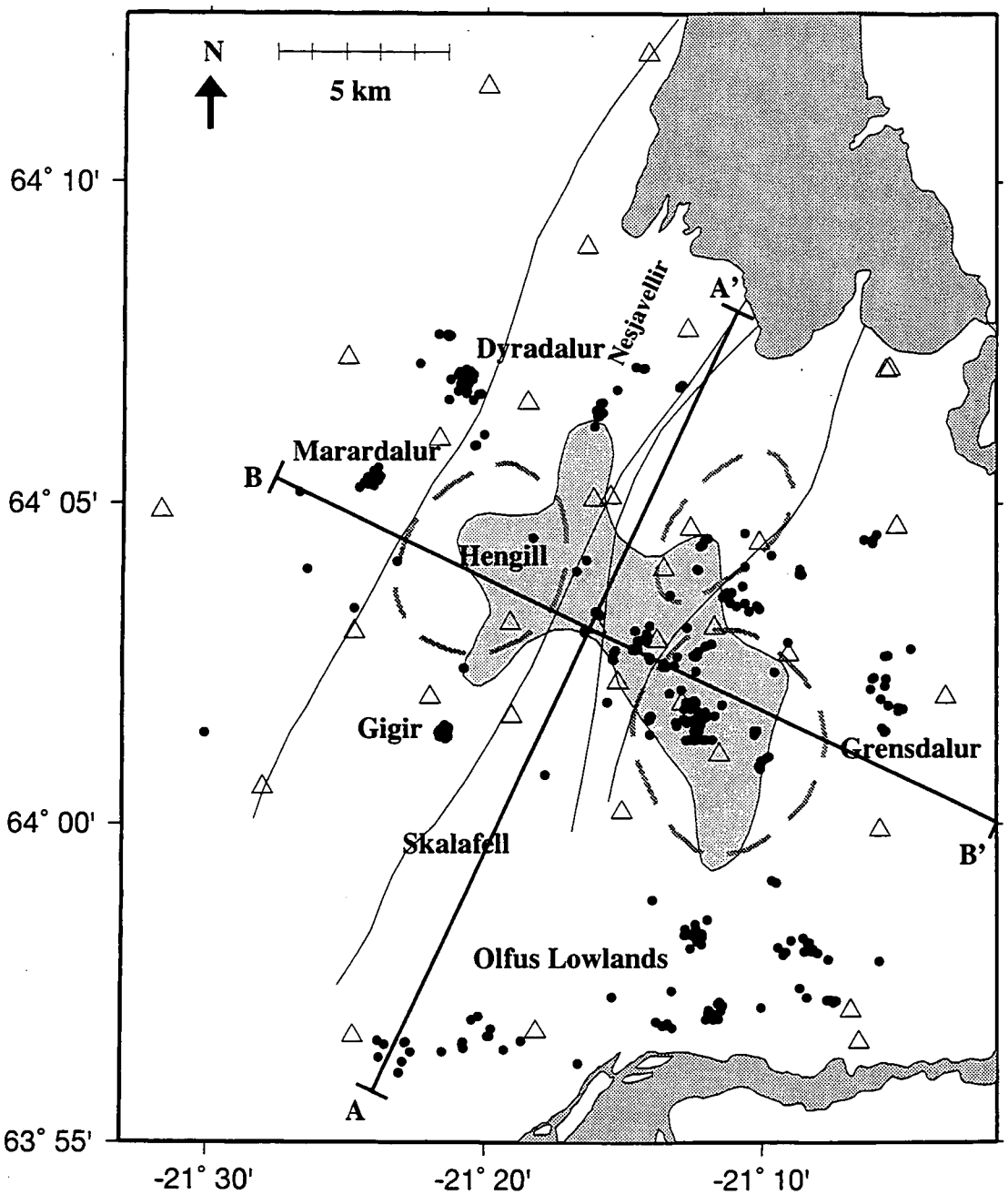

Figure 3.9: Map of hypocentre locations (solid dots). Dashed lines: outlines of volcanic centres; solid lines, outlines of fissure swarms; light grey shading: geothermal field; open triangles: stations. Lines A-A' and B-B': positions of depth sections shown in Figure 3.10.

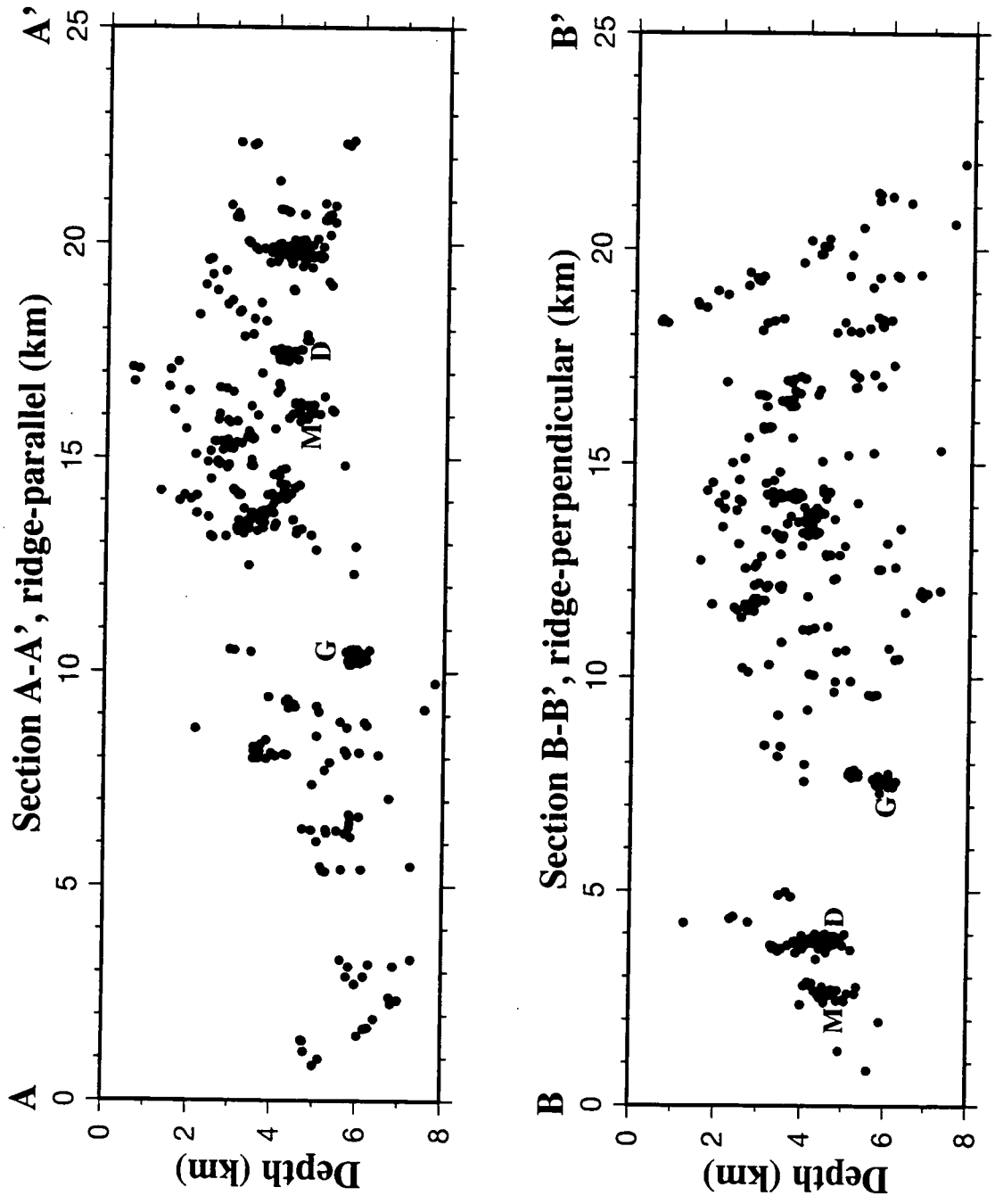

Figure 3.10: Depth sections of hypocentres illustrated in Figure 3.9, projected into the section plane. G, M and D label the Gigir, Marardalur and Dyradalur clusters.

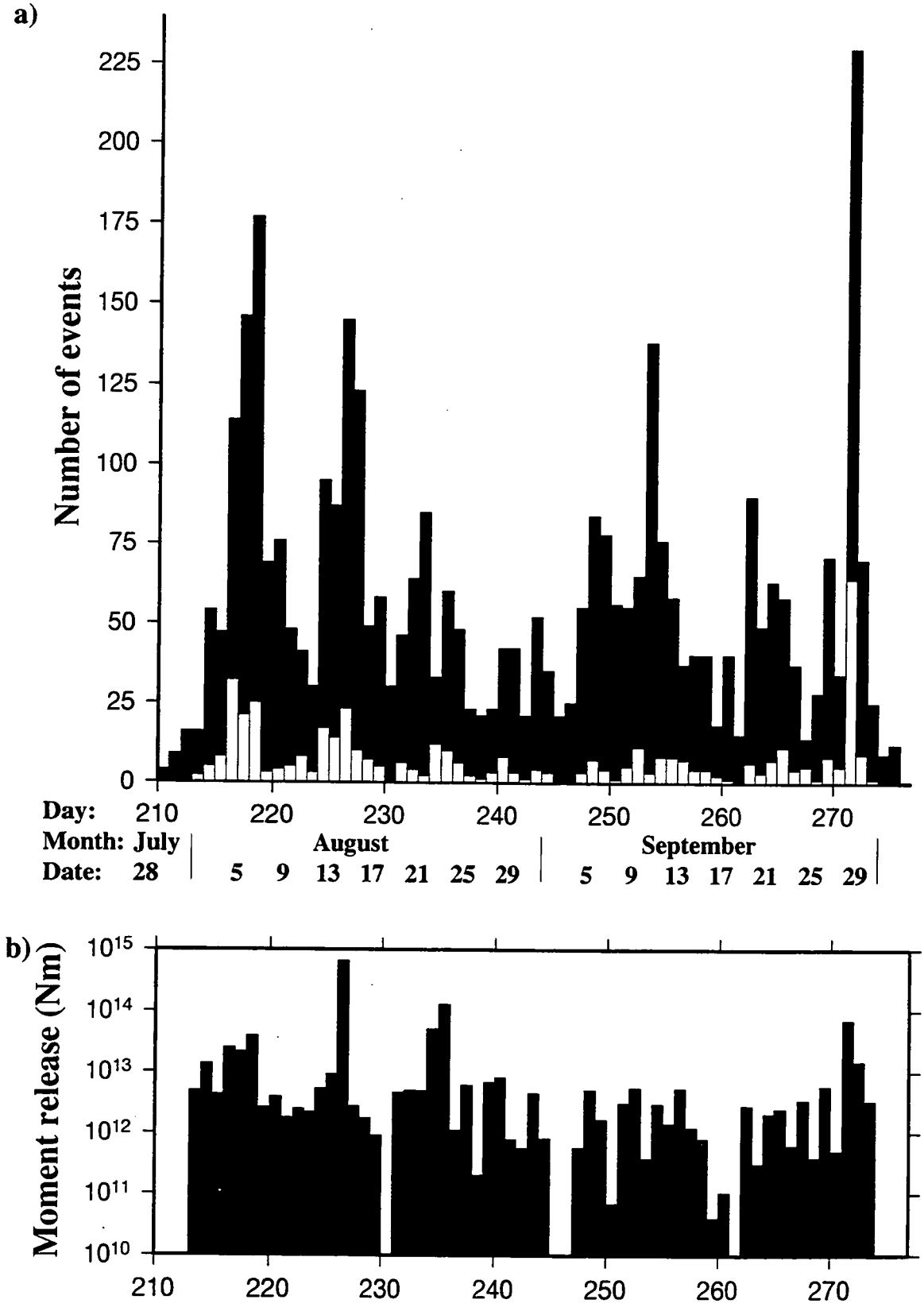

Figure 3.11: Temporal distribution of the earthquakes and seismic moment release. (a) Histograms of the number of event segments (solid bars) and number of located earthquakes (open bars) per day during the recording period. (b) Total daily moment release for all the located events.

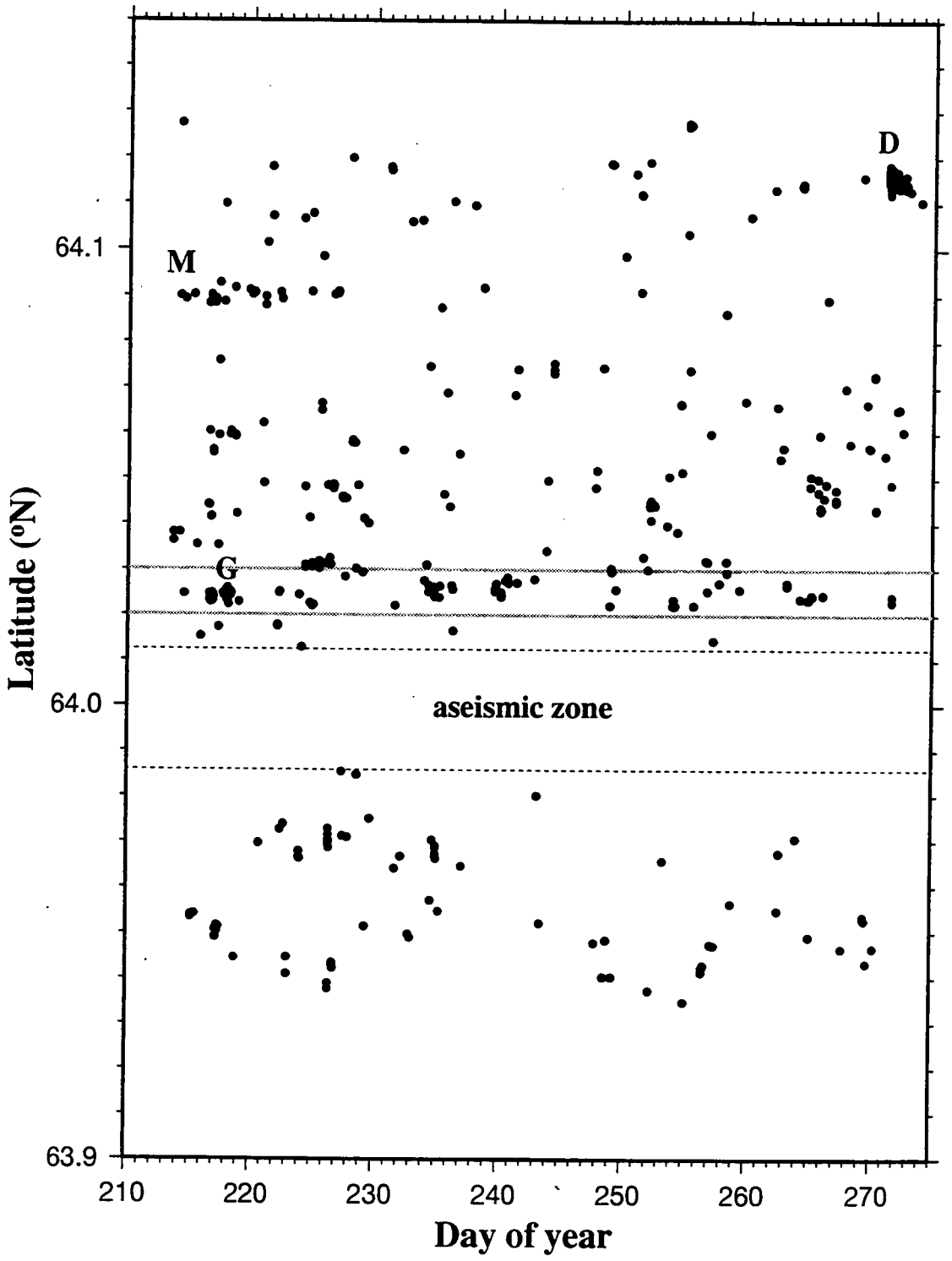

Figure 3.12: Plot of earthquake latitudes vs. time. Most of the events between the grey lines (except for the Gigir (G) earthquakes) are in the Grensdalur volcanic centre, which was active throughout the recording period. In contrast, most events in the Gigir (G), Marardalur (M) and Dyradalur (D) clusters occurred within intervals of a few days. Dashed lines show the boundaries of the aseismic zone around 64°N, where no events were located.

3.3.5 Comparison with the 1981 seismicity

The seismicity detected by the 1981 temporary network was similar to that recorded in 1991 (Figure 3.13). In both years the geothermal field was the most seismically active area, there were few earthquakes within the Hengill volcanic centre, and most earthquakes within the Hengill fissure swarm occurred to the south of Nesjavellir. The aperture of the 1981 network was smaller, so well constrained earthquakes in the western part of the Ölfus lowlands were rare in the 1981 dataset. The L-shaped zone of seismicity in the Gigir / Skálafell area detected in 1981 was not observed in 1991, despite better station coverage in this area.

The seismicity located using the 1981 network is more diffuse, with less obvious clustering of earthquakes. This could result from the larger number of earthquakes in the 1981 dataset, and poorer quality locations due to the lack of *S*-wave travel times. The depth distribution is similar in the two datasets, with the exception of the few shallow earthquakes near Stórahálsfjall in 1991 (Figure 3.13).

3.4 Earthquake magnitudes

3.4.1 Method of magnitude determination

The best measure of the size of an earthquake is the scalar moment, M_0, which is derived from the earthquake moment tensor using the relation:

$$M_0 = \sqrt{\tfrac{1}{2}\sum_i |m_i|^2}, \qquad 3.1$$

where m_i are the principal moments (*Silver and Jordan*, 1982).

It is convenient to express scalar moments using the moment-magnitude scale (*Hanks and Kanamori*, 1979), where

$$M = \tfrac{2}{3}\log M_0 - 6.0, \qquad 3.2$$

with M_0 in Nm.

Moment tensors for the Hengill earthquakes were calculated from the polarities and amplitudes of *P* and *S* first motions, using the method described in Section 6.3.5. The moment tensors of 98 selected earthquakes were calculated using the polarities and amplitudes of *P*, *SH* and *SV* waves at all suitable stations (Chapter 7). For the remaining located earthquakes, moment tensors were calculated using the amplitudes of *P* and *SH* waves at up to 4 close stations combined with all the available *P*-wave polarities.

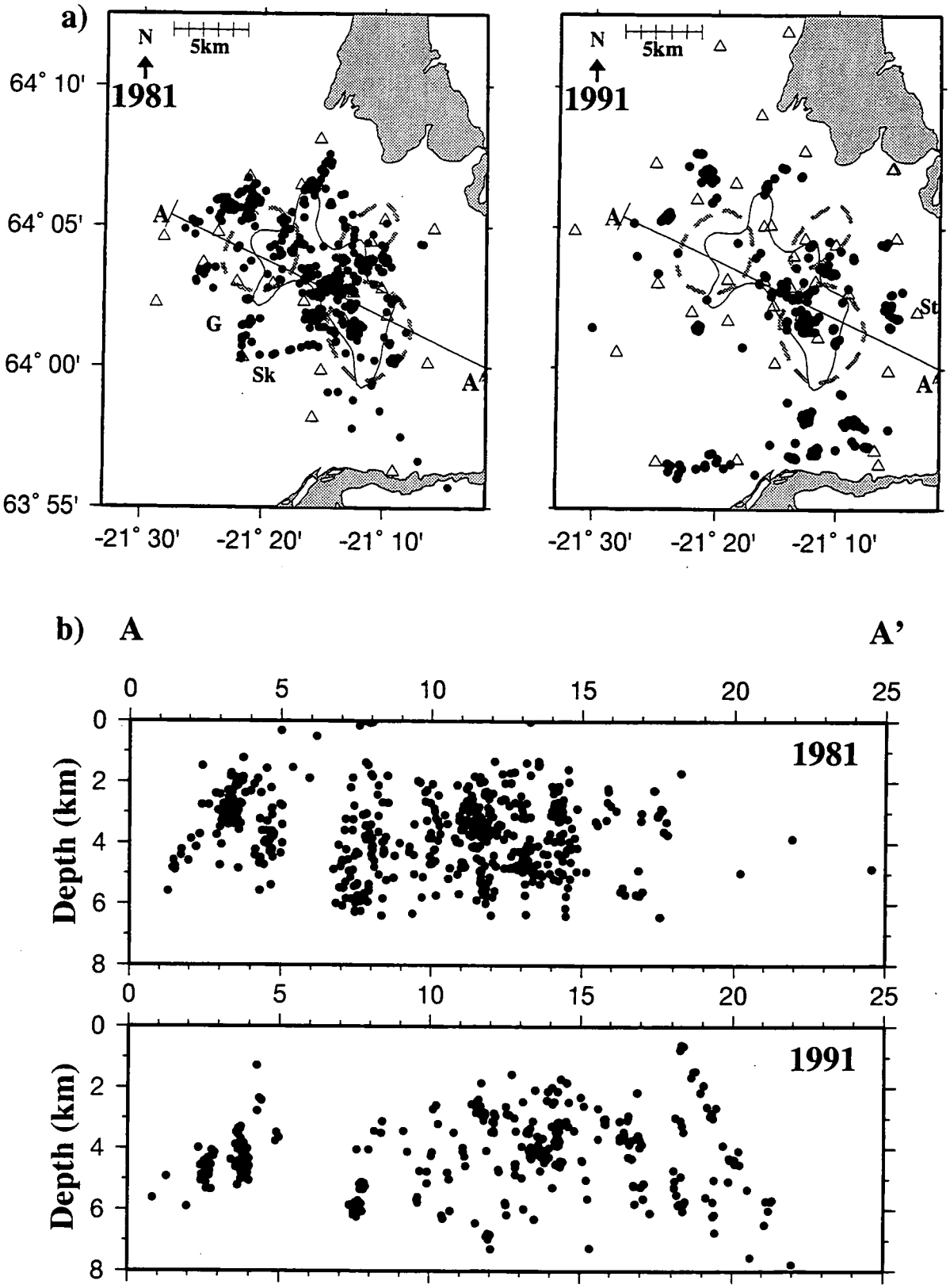

Figure 3.13: Comparison between the seismicity distributions determined from the 1981 and 1991 data. (a) Epicentral distribution of the 625 best-constrained earthquakes located using data from the 1981 network (left) and all 448 earthquakes located using data from the 1991 network (right). Triangles: stations; dashed lines: outlines of volcanic centres; solid line: outline of the geothermal field; G: Gigir; Sk: Skálafell; St: Stórahálsfjall. (b) Depth sections along line A-A' for the 1981 earthquakes (top) and 1991 earthquakes (bottom).

Amplitudes were measured from low-pass filtered traces with a corner frequency of 5 Hz (Section 6.5.2.1). The measured amplitudes were converted from counts to metres using the sensor response to displacement (Figure 3.4) for a frequency of 5 Hz, and the amplitudes were corrected for geometrical spreading and attenuation.

For earthquakes, the empirical magnitude-frequency relationship is often approximated well by

$$\log n = a - bM \qquad 3.3$$

(*Gutenberg and Richter*, 1954), where n is the number of earthquakes with magnitude greater than or equal to M and a and b are constants. The constant b, commonly called the "b-value", is a measure of the relative numbers of large and small earthquakes.

3.4.2 Results

The largest earthquake recorded during the experiment was earthquake 226.091934.2 which had a moment of 4.2×10^{14} Nm (M 3.8) and was located in the SISZ. Five of the largest eight earthquakes in the dataset occurred on day 226. The b-value for the whole data set, calculated using the method of maximum likelihood (*Page*, 1968) is 1.00±0.12 (Figure 3.14). This is slightly higher than the value of 0.76±0.05 calculated by *Foulger* (1984) for M_{IL} in the same area.

Although only 17% (77) of the 449 located earthquakes are south of 64°N, they released 70% of the measured moment (Figure 3.15). In contrast, the 145 earthquakes within the Gigir, Marardalur and Dyradalur clusters account for 32% of the earthquakes but only 6% of the total moment release.

Local magnitudes are routinely calculated for all earthquakes located using the SIL network, using an empirical formula designed to replicate the Icelandic local magnitude scale originally calculated for the permanent station at Reykjavik (*Tryggvason*, 1973). For some earthquakes, moment magnitudes are also calculated. There are large discrepancies between the moment magnitudes calculated for the same earthquakes using data from the 1991 temporary network and the local and moment magnitudes calculated from SIL network data (Figure 3.16). The SIL local and moment magnitudes are comparable, but the temporary network moment magnitudes are approximately 1 magnitude unit higher.

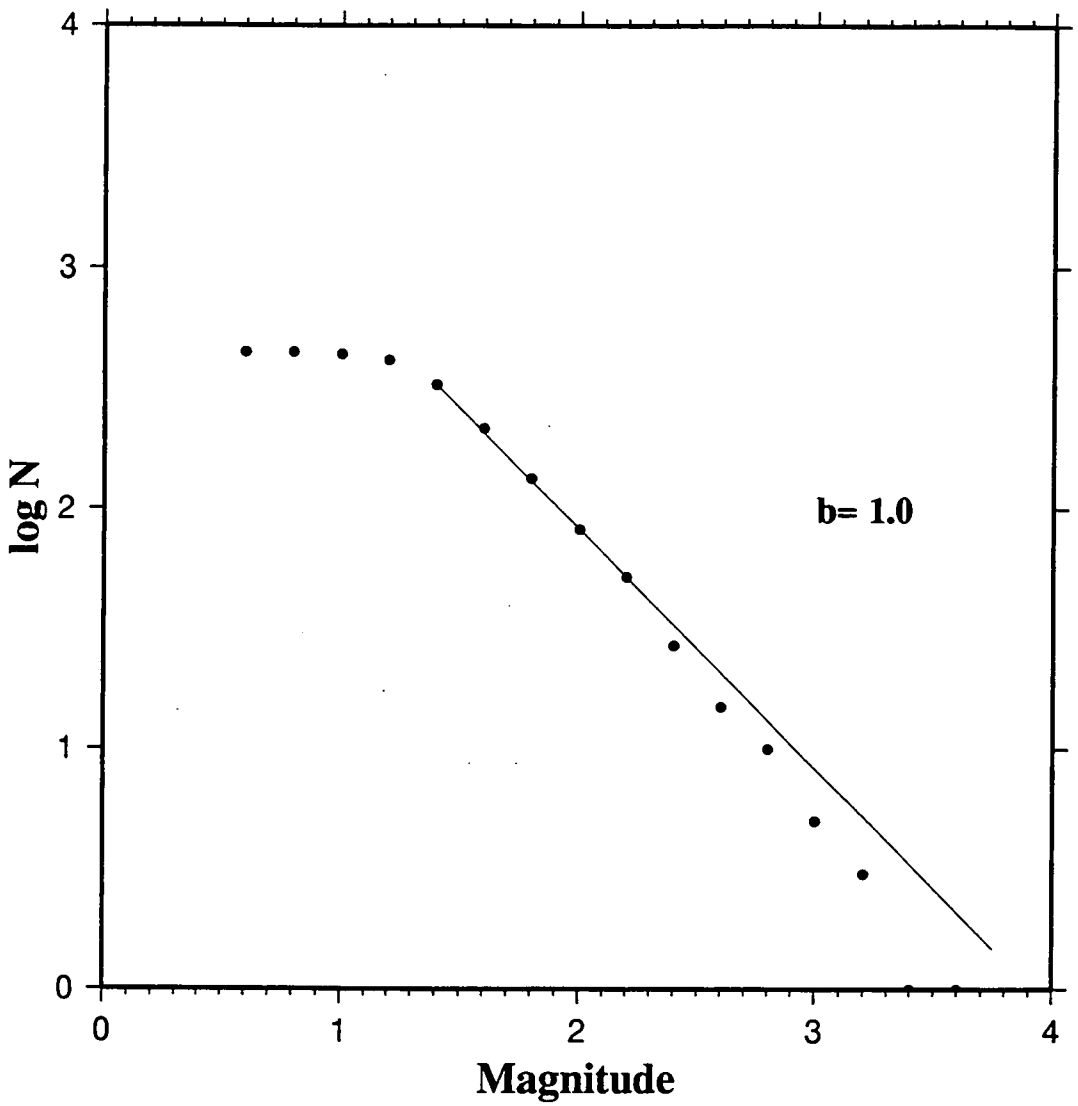

Figure 3.14: Frequency-magnitude distribution for all the located earthquakes from 1991, and best-fit line using the method of maximum likelihood.

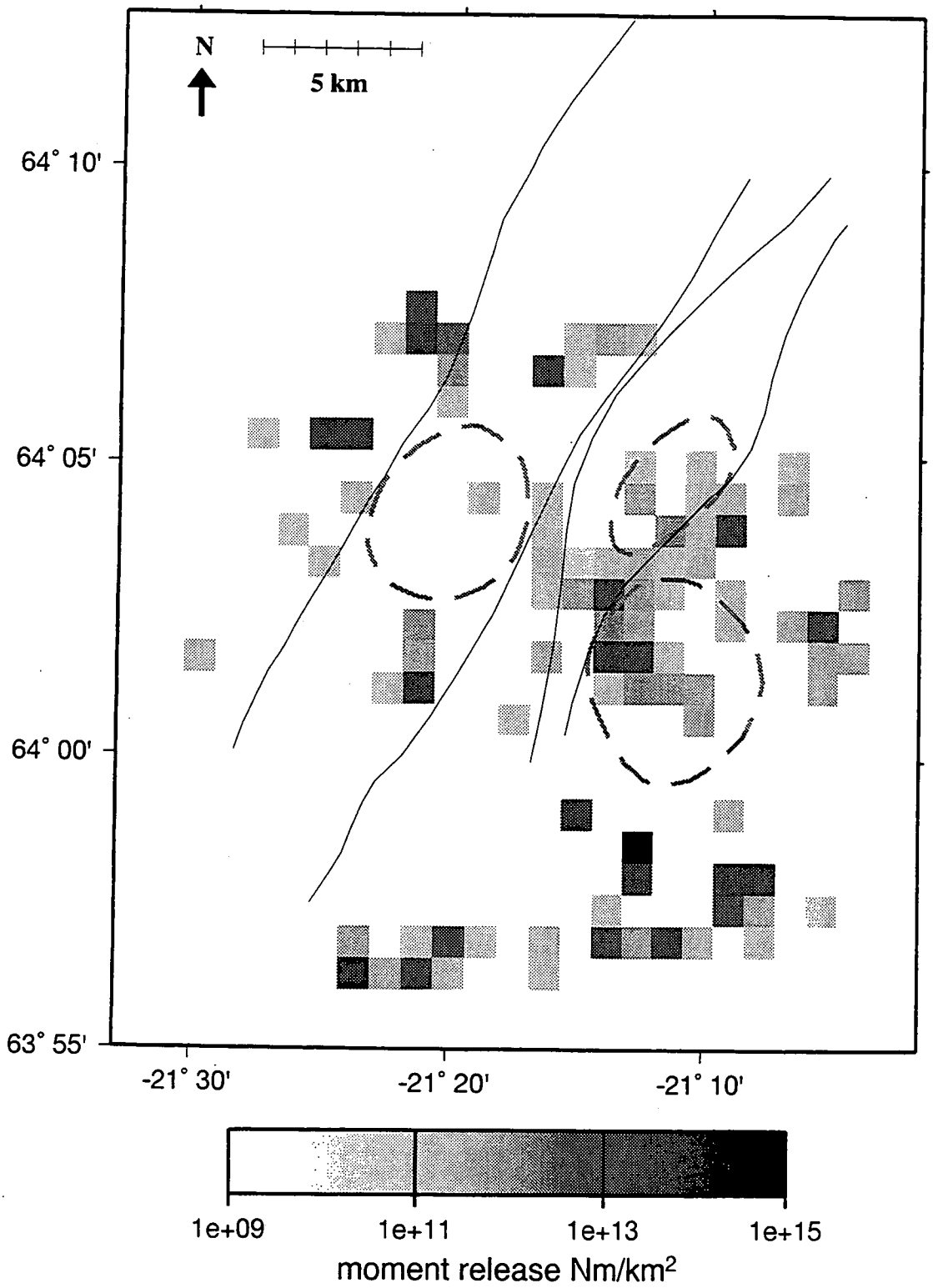

Figure 3.15: The spatial distribution of moment release. Total moment release in 1 km^2 blocks for all located earthquakes from 1991.

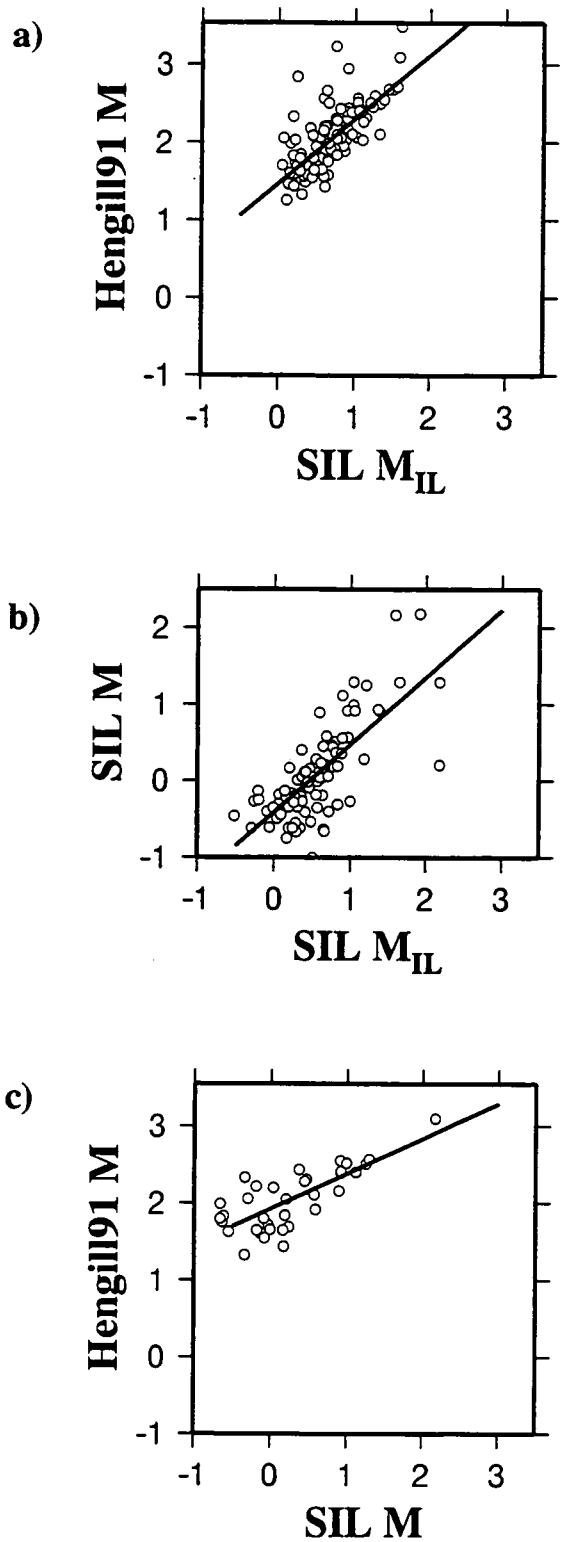

Figure 3.16: Comparison between moment magnitudes calculated from the temporary network data and magnitudes calculated from SIL network data for the same events. (a) temporary network moment magnitudes against SIL local magnitudes, L2-norm best-fit line is y=0.83x+1.47. (b) SIL moment magnitudes against SIL local magnitudes. L2-norm best-fit line is y=0.88x-0.41. (c) temporary network moment magnitudes against SIL moment magnitudes. L2-norm best-fit line is y=0.45x+1.92.

3.5 Earthquake clusters

Over 30% of the earthquakes lie within three discrete clusters, at Gigir, Marardalur and Dyradalur (Figures 3.9 and 3.10). Most of the cluster earthquakes occurred within the space of a few days, during the days 216 to 219 (Gigir), 214 to 226 (Marardalur) and 271 (Dyradalur).

A master-event relocation technique was used to calculate accurate relative locations for the earthquakes in each cluster. This technique assumes that most of the travel-time residuals of an earthquake are due to differences between the true wave-speed structure and the model used to locate the earthquake, and that nearby earthquakes have similar raypaths and thus similar travel-time residuals. Small differences in measured arrival times between earthquakes are then due to differences in their relative locations.

For each cluster, the best recorded earthquake (the one with the most measured arrival times) was designated the "master" earthquake. The residuals calculated for this earthquake, using the one-dimensional wave-speed model, were then subtracted from the arrival times measured for other earthquakes in the cluster, and these earthquakes were located using the adjusted travel times.

In the Gigir and Marardalur clusters (Figures 3.17 and 3.18), the earthquakes were located in steeply-dipping, linear, northeast trending zones approximately 400 m in vertical extent. In both clusters, there is some evidence of migration with time towards the northeast. At Gigir, the three largest earthquakes, with magnitudes of 2.7-2.8, occurred during a four-hour interval and were spatially close. In the Marardalur cluster the largest earthquakes were well spaced with time.

In the Dyradalur cluster, most of the earthquakes occurred in an east-west oriented zone 700 m by 400 m and 1 km high (Figure 3.19). The eight earthquakes that occurred before day 271 were located above this volume. Within the cluster, activity migrated from the centre to both top and bottom during day 271, but the final 7 earthquakes are spread throughout the volume. Most of the larger earthquakes ($M>1$) occurred in the deeper half of the cluster, and two of the largest earthquakes were located at its base.

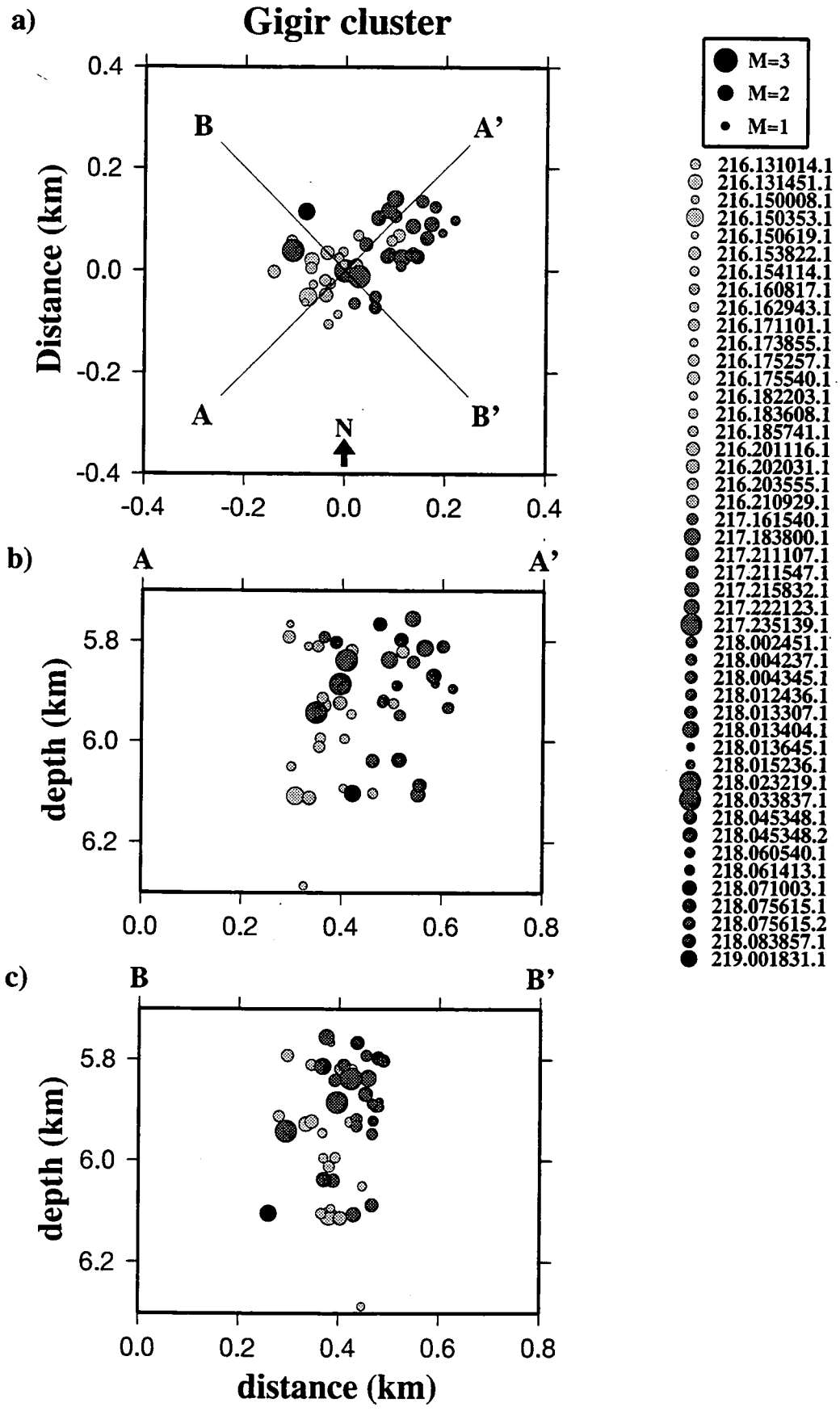

Figure 3.17: Map and depth sections of earthquakes in the Gigir cluster. (a) Map view, (b) and (c) depth sections A-A' and B-B'. A list of all earthquakes in chronological order is shown on right. Dots are hypocentres calculated using relative relocations based on master event 218.023219.1.

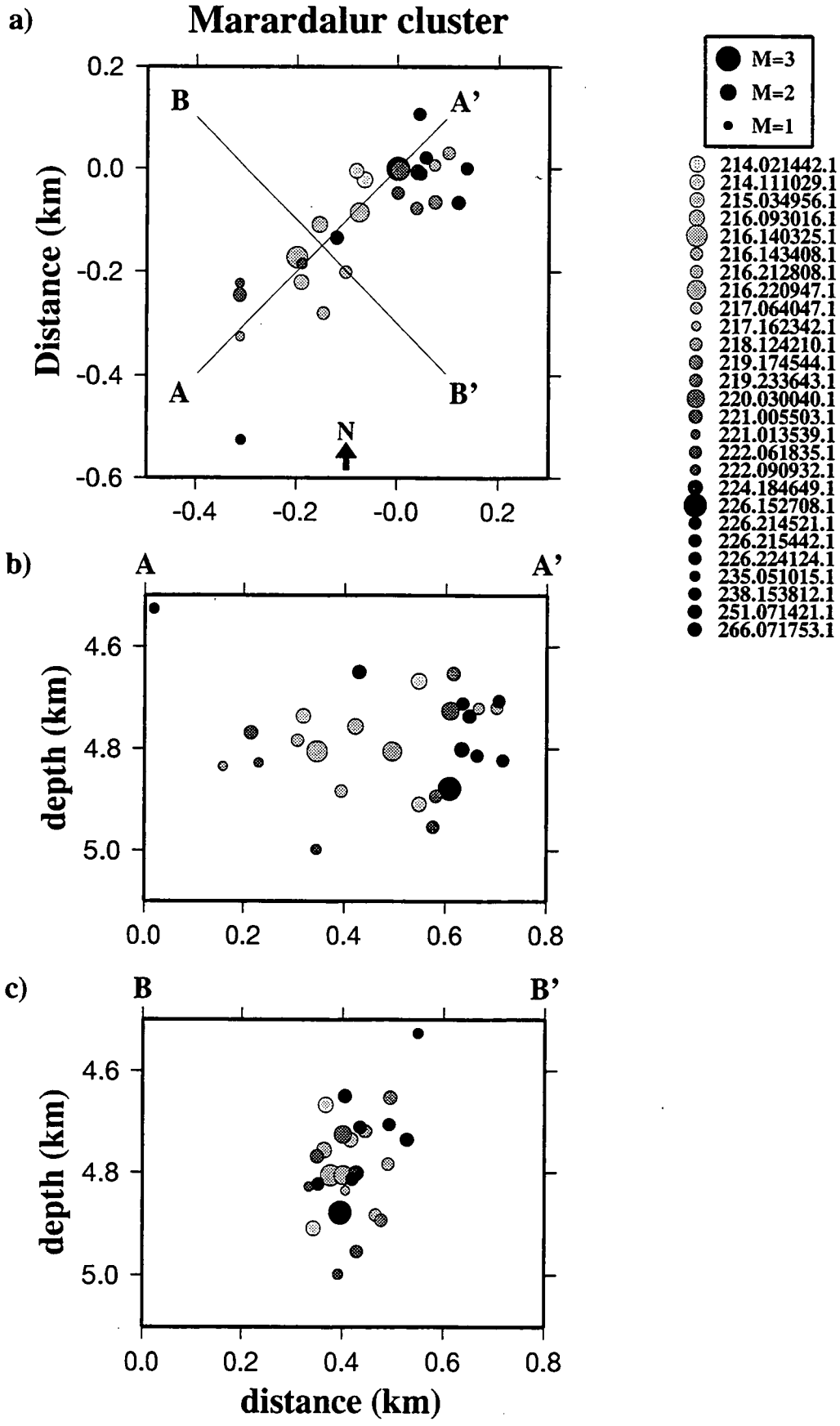

Figure 3.18: Same as Figure 3.17 for earthquakes in the Marardalur cluster. The master event is 226.152708.1.

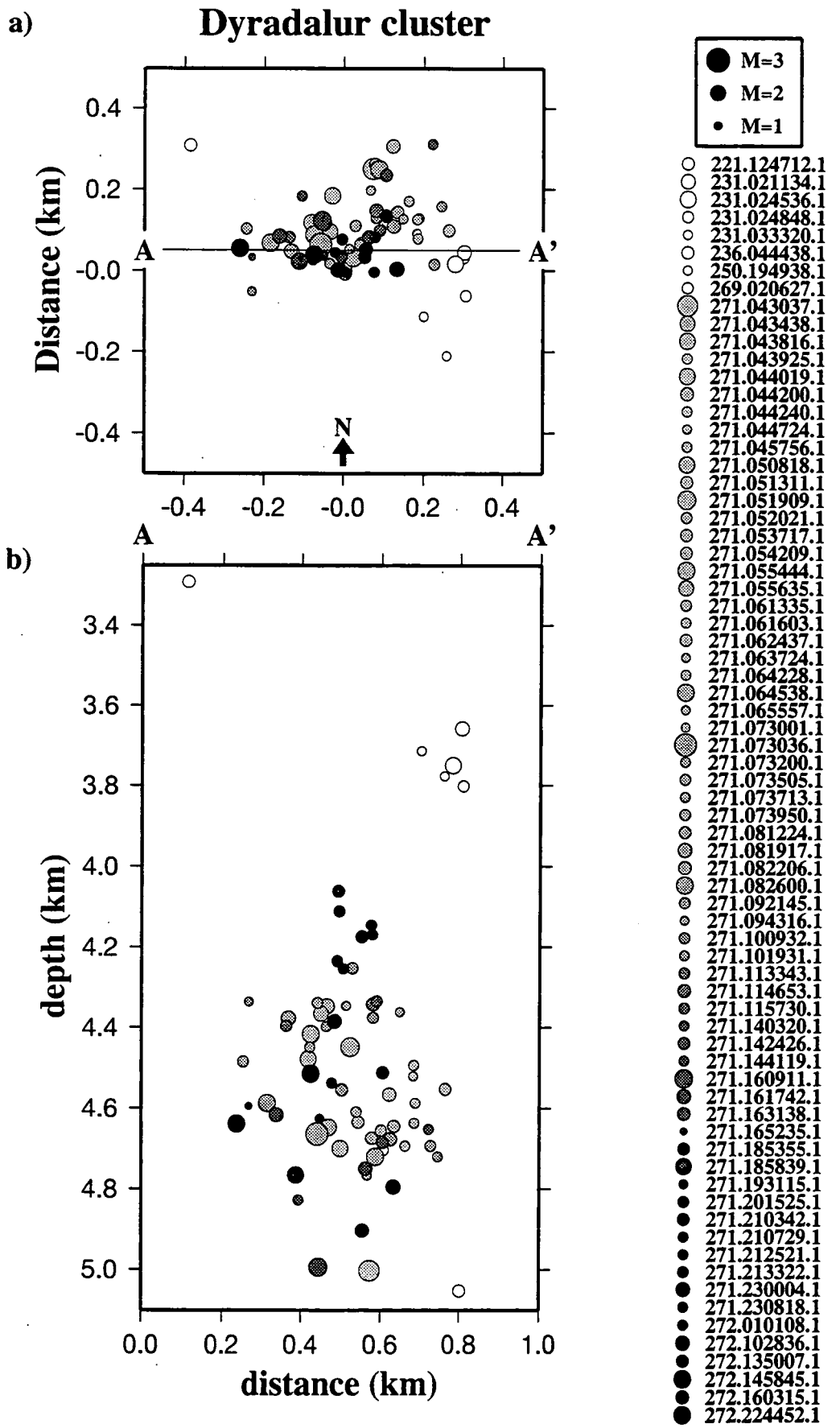

Figure 3.19: Map and depth section of earthquakes in the Dyradalur cluster. (a) Map view, (b) depth section A-A'. A list of all earthquakes in chronological order is shown on right. Dots are hypocentres calculated using relative relocations based on master event 271.043816.1.

3.6 Summary

The 1991 field experiment involved 30 three-component instruments deployed in a regular array in the Hengill area, and operated for two months. The network was designed to give excellent focal sphere coverage of small-magnitude earthquakes occurring beneath the centre of the geothermal area to enable study of non-DC earthquake mechanisms. Each station recorded continuous three-component data at 100 sps, and a separate stream of triggered data that was used to identify events. Most station locations were determined using differential GPS surveying. Over 3800 events were extracted from the 100 Gbytes of continuous data collected. The best-recorded earthquakes were identified using an automatic phase picker. *P* and *S* arrival times were interactively picked for 448 high-quality earthquakes that were located within the network. Earthquake locations were estimated using a one-dimensional layered wave-speed model. Most earthquakes occurred within the geothermal field, or within the western part of the SISZ. The Hengill volcanic centre and fissure swarm had low levels of seismicity. Hypocentral depths range down to 8 km, with most earthquakes between 2 and 6 km depth. Beneath the south-eastern section of the geothermal area, earthquakes occurred on an almost daily basis. The seismicity pattern was similar to that recorded by a temporary network in 1981. Moment magnitudes ranged up to 3.8, with most of the large earthquakes occurring in the SISZ. Dense clusters of earthquakes occurred at Gigir, Marardalur and Dyradalur, mostly within periods of 1 to 3 days. Within each cluster, earthquakes were located within a few hundred metres of each other, in narrow, vertical zones, and there is some indication that activity migrated with time.

Chapter 4

Local earthquake tomography: theory and method

4.1 Development of local earthquake tomography (LET)

In the last 20 years, arrival time data from local earthquakes in many regions have been inverted to determine three-dimensional variations in the seismic wave-speed of the crust. The method has proved particularly useful in volcanic and geothermal areas, where strong variations in wave speed are expected, and the level of local seismicity is often high (*e.g.*, *Foulger and Toomey*, 1988; *Arnott and Foulger*, 1994a). The use of local earthquake data offers advantages over controlled-source tomography. The sources are distributed within the imaged volume, rather than concentrated at the surface, and earthquakes generate *S*-wave energy, so variations in *S*-wave speed can be detected. However the hypocentres and origin times of the local earthquakes are unknown, and there is explicit coupling between the hypocentral parameters and the wave-speed model. This coupling makes the problem non-linear, so it is usually solved by an iterative procedure.

The most rigorous approach is to invert simultaneously for both hypocentral parameters and wave-speed model changes. If the earthquake hypocentres are held fixed while inverting for model changes, the resulting wave-speed model may be biased (*Thurber*, 1992). Schemes that carry out simultaneous inversion for the wave-speed model and hypocentral parameters differ in two major respects: the method of representing continuous variation of wave speeds within the study volume, and the computational method used to carry out the inversion (*Thurber*, 1993).

Several different parameterisations have been used to represent wave-speed structure. The spatial scale that can be imaged by local earthquake tomography (LET) depends on the ray density and distribution within the study volume. In reality the Earth's crust is usually heterogeneous on a small scale, particularly in the areas of most interest, so no parameterisation can represent the wave-speed structure completely. The earliest LET programs used constant wave-speed layers or blocks, but these are limited because they cannot adequately represent wave-speed gradients or sudden changes across inclined planes. This approach has been generalised to involve many, perhaps thousands, of blocks (*e.g.*, *Walck and Clayton*, 1987). A more general parameterisation involves defining the wave-speed at the nodes of a three-dimensional grid, with interpolation used to calculate the wave-speed between nodes (*e.g.*, *Thurber*, 1983). Another alternative is to represent the structure by a small number of analytical functions (*e.g.*, *Novotny*, 1981).

For most LET problems, the size of the matrix to be inverted means that direct inversion, for example using a singular value decomposition technique, is

computationally impossible. Instead, most simultaneous inversion methods use parameter separation (*Spencer and Gubbins*, 1980; *Palvis and Booker*, 1983) to separate calculation of changes to model parameters from changes to hypocentral parameters, while still maintaining the coupling between the two parts. Changes to the model parameters are calculated, then the earthquakes are relocated in the new wave-speed model. Usually, model changes are calculated using a damped least-squares approach, where a combination of model complexity and the squared data misfit is minimised. Alternative simultaneous inversion methods include applying algebraic reconstruction techniques (*e.g.*, *Kissling*, 1988).

To date, most LET has concentrated on calculating variations in V_P in the upper crust, as *P*-wave arrival times from vertical component seismometer networks are most commonly available. Networks with three-component seismometers from which reliable *S*-wave arrival times can be measured are rare. Even when horizontal components exist, *S*-wave arrivals tend to be sparser and less accurately timed than *P*-wave arrivals, because the *P*-wave coda makes seismograms noisy before the *S*-wave arrival, and *S*-to-*P* conversions can disguise the true *S*-wave arrival.

S-wave arrival times can be inverted to determine variations in *S*-wave speed. However, the resulting *S*-wave speed models are of lower quality than the equivalent *P*-wave speed models, making interpretation of variations in V_P/V_S more difficult. An alternative is to invert *S*–*P* times to determine variations in V_P/V_S. In volumes where *S*-wave coverage is sparse, the best estimate of the *S*-wave structure comes from the best available V_P model and a uniform V_P/V_S, rather than from a one-dimensional V_S model (*Evans et al.*, 1994).

4.2 The damped least-squares inversion method

4.2.1 Theory

The theory underlying damped least-squares inversion has been extensively described (*e.g.*, *Thurber,* 1983; 1993) and thus is only briefly reviewed in this section. Theoretical *P*-wave travel times are:

$$T_{ij} = \int_{source}^{receiver} 1/V_P \, ds \qquad 4.1$$

where ds is an element of path length, and theoretical *S*-*P* times are:

$$T_{ij} = \int_{source}^{receiver} \left((V_P/V_S - 1)/V_P \right) ds \qquad 4.2$$

Each travel time residual, r_{ij} is assumed to be a linear function of hypocentral and model parameter changes:

$$r_{ij} = \Delta t_{oi} + \frac{\partial T_{ij}}{\partial x}\Delta x + \frac{\partial T_{ij}}{\partial y}\Delta y + \frac{\partial T_{ij}}{\partial z}\Delta z + \sum_{j=1}^{M}\frac{\partial T_{ij}}{\partial V_j}\Delta V_j \qquad 4.3$$

where t_{oi} is the origin time of event i with location x_i, y_i, z_i, T_{ij} is the *P*-wave travel time or *S-P* time between event i and station j, M is the number of model parameters and V_j is the value of the j^{th} model parameter.

Equation 4.3 can be expressed in matrix form:

$$\mathbf{r}_i = H_i\Delta\mathbf{h}_i + M_i\Delta\mathbf{m} \qquad 4.4$$

where $\mathbf{r}_i$ is a vector of residuals of event i, H_i is a matrix of hypocentral partial derivatives, $\Delta\mathbf{h}_i$ is a vector of hypocentral changes, M_i is a matrix of model partial derivatives and $\Delta\mathbf{m}$ is a vector of model changes. Parameter separation simplifies the problem by solving Equation 4.4 only for $\Delta\mathbf{m}$. A QR decomposition of H_i is used to find a matrix Q_0^T such that

$$Q_0^T H_i = 0. \qquad 4.5$$

Thus

$$Q_0^T\mathbf{r}_i = Q_0^T M_i\Delta\mathbf{m} \qquad 4.6$$

or

$$\mathbf{r}_i' = M_i'\Delta\mathbf{m} \qquad 4.7$$

and a system of linear equations is obtained for each event. A system of "normal equations" can then be accumulated as each event is processed:

$$(M'^T M')\Delta\mathbf{m} = M'^T\mathbf{r}_i'. \qquad 4.8$$

This system of equations is solved by least-squares, with

$$\Delta\mathbf{m} = (M'^T M' + \lambda^2 I)^{-1} M'^T\mathbf{r}_i' \qquad 4.9$$

where λ is the damping parameter. In practice different damping values are added to the different sections of the diagonal of the $M'^{T}M'$ matrix, corresponding to different damping parameters for the V_P and V_P/V_S models.

This equation is solved by carrying out an LU (or "Cholosky") decomposition of G, where $G=(M'^{T}M'+\lambda^2 I)$, and the model changes, $\Delta\mathbf{m}$, are calculated. These changes are then applied to the model, and the events are relocated in the new model. Iterations of this model change and hypocentral relocation loop are carried out until the model changes are deemed insignificant.

4.2.2 Determining model resolution using a spread function

The resolution matrix R is defined as

$$R=G^{-1}G \qquad 4.10$$

and provides information about the distribution of ray paths within the model and the amount and direction of smoothing of model parameters. Each row of R describes the smoothing pattern of a single model parameter, which can be summarised by determining the resolving width of the model parameter. This is done by calculating a spread function S_{ij} for each row of the resolution matrix, where

$$S_{ij}=\left[\|R_j\|^{-2}\sum_k D_{jk}^2 R_{jk}^2\right]^{1/2}. \qquad 4.11$$

$\|R_j\|$ is the Euclidean (L2) norm of the j^{th} row of R and D_{jk} is the distance between the j^{th} and k^{th} nodes.

4.3 The *simulps12* program

4.3.1 Introduction

The *simulps12* program carries out an iterative, damped least-squares inversion of *P*-wave travel times and *S–P* times from local earthquakes and surface explosions to determine three-dimensional variations in V_P and V_P/V_S models. *simulps12* is a derivation of the program *simul3* (*Thurber*, 1981; 1983). Improvements on the original *simul3* program include the introduction of a "pseudo-bending" three-dimensional ray-tracer (*Um and Thurber*, 1987) and the ability to invert *S–P* times to calculate a V_P/V_S model (*Eberhart-Phillips, pers. comm.*, 1993; *Evans et al.*, 1994). This project is the first time that the current version of *simulps12* has been used on SUN workstations. In conjunction with John Evans, I made several changes to the code, and devised a test case that is now used to test new implementations of the program.

The V_P and V_P/V_S models used by *simulps12* are continuous. The models are defined at nodes and linear interpolation between nodes is used to calculate the model values at other positions within the model. Nodes are located at the junctions of vertical and horizontal planes, which need not be evenly spaced. This means that volumes within the model that are well-sampled by rays can have denser nodal spacings than peripheral areas (Figure 4.1). The model value at any node can be fixed, so that this node is not included in the inversion.

The input data to *simulps12* are *P*-wave travel times and *S–P* times from local earthquakes. The initial locations and *P*-wave travel times must be determined by some independent method. Data from timed explosions and blasts (with known locations but unknown origin times) can also be included. At the start of the inversion, the earthquakes are relocated by *simulps12* using the input wave-speed model. A series of iterations are then carried out, to calculate wave-speed model changes, apply these changes to the model and relocate the earthquakes in the new model.

The program terminates when any one of four conditions is satisfied:

- The maximum number of iterations specified by the user is reached
- The RMS travel-time residual falls below a threshold specified by the user
- The decrease in travel-time residual is not significant, as judged by an F-test
- The model solution norm falls below a threshold specified by the user.

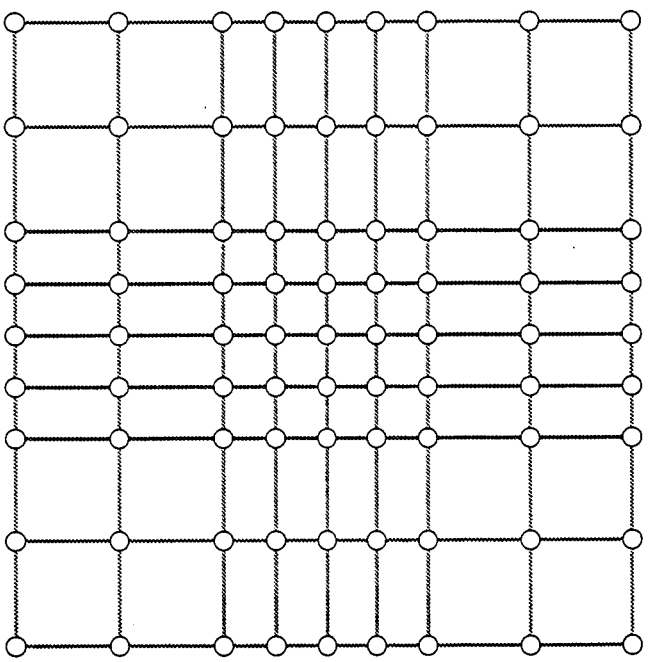

Figure 4.1: Example of a layer of nodes, which are defined at intersections of vertical planes. This means that defining a densely sampled region requires closely spaced planes that extend across the model, and may produce elongated cells at the periphery.

4.3.2 Input parameters

The operation of *simulps12* is controlled by parameters that are input via the control file (fort.1). Most of these parameters can be set at standard values, but a few are data-set dependent, and are best chosen after experimenting with different values. Appendix 2 contains a description of each input parameter, and suggestions for typical values.

4.3.3 Input and output files

Input to *simulps12* is given in up to 6 files:

fort.1	Control file
fort.2	Station data
fort.3	Node positions and starting wave-speed model
fort.4	Earthquake travel time data
fort.7	Shot travel time data
fort.8	Blast travel time data

There are up to 17 output files. The most useful of these are:

fort.16	"Printout" file with model changes and relocations at each iteration
fort.17	Resolution matrix
fort.20	Travel time residuals
fort.23	Final wave-speed models
fort.24	Recomputed travel time data
fort.36	Summary file

4.3.4 The derivative weight sum

The derivative weight sum (DWS) is a measure of ray density within the wave-speed model and can be used to identify well-sampled volumes. The DWS of the n^{th} model parameter is defined as:

$$\text{DWS}\ (n) = N \sum_i \sum_j \left(\int_{P_{ij}} w_n(\mathbf{x}) ds \right) \qquad 4.12$$

where i and j are the event and station indices, w is the weighting of the n^{th} model parameter used to interpolate the wave-speed at position $\mathbf{x}$, P_{ij} is the ray path between i and j and N is a normalisation factor that accounts for the volume influenced by the n^{th} model parameter. Values of DWS depend on the ray segment length ds, specified by the user (the "*scale1*" parameter). For a typical "*scale1*" value of 0.5 km, a DWS cut-off of 50 has been suggested to distinguish well-resolved from poorly-resolved nodes (*Arnott and Foulger*, 1994a).

4.3.5 Analysis and presentation of results

I wrote several UNIX Bourne-shell scripts to assist in the analysis and presentation of the output of *simulps12* (Appendix 3). General Mapping Tools (GMT) software (*Wessel and Smith*, 1991) was used to produce coloured and grey-scale images of the output wave-speed models.

4.4 Inversion procedure using *simulps12*

4.4.1 Data selection

An homogeneous set of ray paths that sample all of the target volume is required to produce a model of uniform quality. Unfortunately, the distribution of earthquakes is seldom uniform, and instead the seismic activity tends to be concentrated in certain volumes. Sometimes the network configuration is limited by constraints such as station accessibility, so that the station distribution is not uniform, further restricting the data set. Surface blasts and timed explosions can be included in the data set, and they provide valuable ray-paths through the upper layers that are usually poorly sampled.

The quality of the data used is important, as a small number of outliers, caused for example by phase misidentification or timing errors, can alter the resulting model. Trial inversions can reveal outliers which can then be checked before the final inversion.

4.4.2 The starting wave-speed model

The choice of starting model can have a large systematic effect on the final result. The starting model can be either one-dimensional or contain some *a priori* information about the three-dimensional structure based on geological knowledge or controlled source profiles. *Eberhart-Phillips* (1990) suggested that using an *a priori* three-dimensional starting model can result in bias and the inclusion of features in the final model that are not required by the data, and that using a simple, one-dimensional starting model produced a more dependable result.

A starting one-dimensional model is usually derived from wave-speed models determined from controlled-source studies, *e.g.*, seismic refraction experiments. Such layered models are generally used first to invert for a best-fit one-dimensional model, the so-called "minimum" one-dimensional model, using the same earthquake data that will be used for future three-dimensional inversions. This model is then used as the starting model for three-dimensional inversions. A one-dimensional starting model based only on *a priori* information can introduce significant bias in the final model (*Kissling et al.*, 1994).

Kissling et al. (1994) proposed a procedure for determining the "minimum" one-dimensional model of an area using local earthquake data and an inversion program such as *velest* (*Ellsworth*, 1977; *Roecker*, 1981; *Kradolfer*, 1989). The *velest* program inverts *P*-wave travel times from local earthquakes and explosions to calculate changes to a one-dimensional layered V_P model. Up to 200 events can be input, and *velest* iteratively calculates model changes and relocates the events in the new model. Damping can be applied separately to the model and each hypocentral parameter.

4.4.3 Grid configuration

In areas with strong wave-speed contrasts across structural boundaries, such as faults, it is advisable to align nodes parallel to the geological structure. Nodes can be placed close to a discontinuity on both sides to allow a high wave-speed gradient across the discontinuity. The minimum nodal spacing must be selected so that reasonable ray sampling occurs throughout the volume, and there are not too many nodes that have only a few rays passing close to them.

The ray tracer used by *simulps12* requires that planes of fixed nodes are placed at large distances from the model space in all directions (the "exterior" nodes), and that no rays travel more than 50% of the distance between these and the "interior" nodes. It is best to ensure that no rays travel outside the interior nodes, as this could result in unrealistic long, columnar wave-speed anomalies. Layers of interior nodes can be placed above the highest station and below the deepest earthquake in order to avoid this problem. The volumes adjacent to these node layers are likely to be poorly sampled, and thus the model values at these nodes should be held fixed (*Evans et al.*, 1994).

4.4.4 Selection of the damping parameters

Eberhart-Phillips (1986) suggested a scheme for empirically selecting damping parameters from "damping trade-off curves" of model variance plotted against data variance reduction (Figure 4.2). These curves can be constructed from the results of a series of single-iteration inversions using different damping parameters, and the same initial model, nodal configuration and event data that will be used in the full inversion.

These damping curves often exhibit a minimum, with very low damping values yielding relatively low data variance decrease and large model variance. The optimum damping value will yield a substantial data variance reduction with a minimally complex model.

When inverting for V_P and V_P / V_S models simultaneously, varying both the damping parameters together through n values each would involve n^2 trial inversions, each with a large number of model parameters. An alternative method is to first select the damping parameter for the V_P model while holding the V_P / V_S model fixed, then to calculate the V_P / V_S model damping parameter with the V_P / V_S model held fixed. Tests using the Hengill data set showed that the damping curves derived using this method varied little from those calculated by inverting for both models and varying both damping parameters simultaneously.

The shape of the damping trade-off curves is insensitive to variations, within reasonable limits, of the starting wave-speed model and the earthquake data used. However, significant differences in damping curves do occur between inversions with different nodal spacings and the same starting model and earthquake data. As a general rule, inversions with large horizontal nodal spacing require higher damping values than those with small nodal spacings.

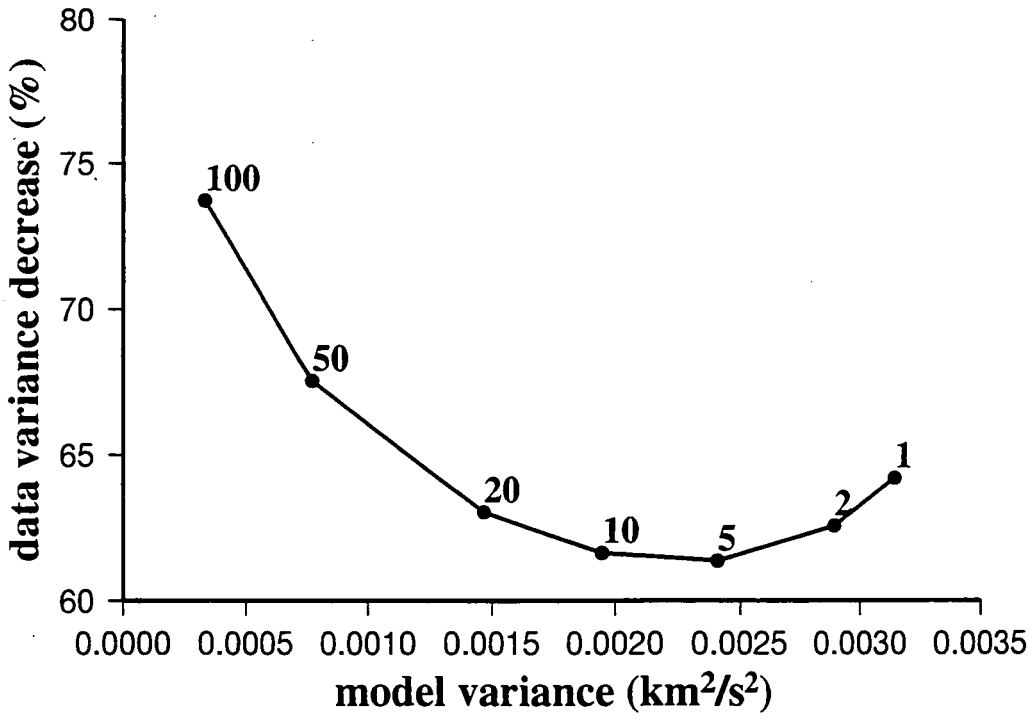

Figure 4.2: A typical damping parameter trade-off curve of data variance decrease against model variance, for different values of the damping parameter. Highly non-linear behaviour occurs for low damping values, typically of less than 5, as indicated by the upturn in the damping curve at right.

4.4.5 Inversion strategies

Graded inversion. A graded inversion involves a series of inversions with progressively finer nodal spacings. The output model (interpolated to the finer nodal spacing) and the output hypocentres of the coarser inversion are used as input for the finer inversion (*e.g.*, *Eberhart-Phillips*, 1993). This allows the one-dimensional model to be adjusted to a more realistic regional model at the early stages and ensures that points at the periphery of the grid, which are poorly sampled at dense spacings, have wave-speeds representative of the local structure rather than the regional average.

In carrying out a graded inversion, there are two alternatives: inverting for both V_P and V_P / V_S at every stage, or inverting first for a detailed V_P model, and then inverting for both V_P and V_P / V_S models at the minimum nodal spacing. In the latter strategy, the V_P / V_S model can be held fixed while inverting for the V_P model, so that *S–P* times are used to locate the earthquakes. The alternative, of not using *S–P* times at all in the initial inversions, could result in poorly located earthquakes and the introduction of bias into the V_P model.

In real cases the V_P / V_S model is constrained by fewer data, and varies less than the V_P / V_S model. For these reasons *Evans et al.* (1994) suggest inverting first for a detailed V_P model in a graded inversion. This strategy is also less computer intensive, as the initial inversions have half the number of model parameters.

One-step inversion. An alternative strategy is to invert in a single step for both V_P and V_P / V_S models at the minimum nodal spacing, using the one-dimensional wave-speed model as a starting model. This method is much faster than a graded inversion, and easier, as it does not require the interpolation of three-dimensional models on to grids with finer nodal spacing. It is a suitable method for trial inversions, for example to identify data outliers and test different nodal configurations.

4.4.6 Model resolution

Model resolution can be assessed using the spread function (Equation 4.11) to determine how much the wave-speed value of a node is affected by other parts of the model. Small spread values indicate nodes with only local wave-speed averaging. The spread value at a node gives no indication of the directional nature of volume averaging. This information can be obtained by making plots of individual rows of the resolution matrix (*Eberhart-Phillips*, 1993). Such plots can be used to determine an appropriate spread cut-off value for well-resolved nodes (*e.g.*, *Toomey and Foulger*, 1989).

4.5 Summary

LET uses local earthquake travel times to determine three-dimensional variations in crustal wave-speed and accurate hypocentral locations. The problem is non-linear and there is explicit coupling between the calculated changes to the wave-speed model and changes to the hypocentral locations. *S–P* times can be inverted to determine variations in V_P / V_S structure. LET problems can be solved using a damped least-squares, iterative approach, which is simplified by using parameter separation to calculate changes to the wave-speed model only, while still retaining the coupling between model changes and hypocentral location changes. The *simulps12* program carries out an iterative, damped-least-squares tomographic inversion of *P* and *S–P* times from local earthquakes to determine three-dimensional V_P and V_P / V_S models. The models are defined at nodes, and linear interpolation is used to create continuous wave-speed models. Starting models usually come from controlled-source studies, and these can be modified by inverting first for a one-dimensional model using the local earthquake data set. Damping parameters may be selected empirically by carrying out series of one-iteration inversions with different damping values. Different inversion strategies are possible, either inverting for a series of models with progressively finer nodal spacing or carrying out a one-step inversion directly from a one-dimensional starting model to the final nodal spacing.

Chapter 5

Local earthquake tomography: results

5.1 Inversion of the Hengill data set

5.1.1 Data selection

5.1.1.1 Events from 1981

P-wave arrival time data from 158 earthquakes and two timed explosions recorded by the 1981 temporary network were used in a previous tomographic inversion (*Toomey and Foulger,* 1989; Section 1.3.4.3.3; Figure 5.1a). The 1981 network consisted of vertical-component seismometers only, so only *P*-wave arrival times were available. Travel-time data from two stations, KST and BBL (Figure 5.1a) that fell outside the area of the model of *Toomey and Foulger* (1989) were added to the 1981 data set as part of the present study, giving a total of 2529 *P*-wave arrival times. Large residuals of 0.25 to 1 s were calculated for 24 of the arrival times in this data set. These data were discarded (15 of these outliers were included in the previous inversion by *Toomey and Foulger*, 1989). The 1981 data are of lower quality than the 1991 data, because the 1981 arrival times were read from paper records. The original weights given to the 1981 arrival-time picks were not easily available, so the 1981 travel times were all given a quality value of 1. This meant that the 1981 data had approximately half the weight of the 1991 data when the combined 1981 and 1991 data were inverted (75% of the 1991 *P*-wave arrival times were given a quality of 0).

5.1.1.2 Events from 1991

A total of 448 earthquakes and one explosion were located using data from the 1991 experiment (Section 3.2.3; Figure 3.9). Some of the earthquakes, particularly those located south of 64°N, were at the margins of the network, where station coverage was poor. Earthquakes were excluded if the maximum azimuthal gap between stations was greater than 200°. Many of the earthquakes occurred within clusters, and thus some volumes had very dense ray coverage. To make the ray distribution more uniform, only the best-recorded earthquakes were selected from each cluster. To do this, the imaged volume was divided into $40\times40\times20$ boxes, of dimension $550\times610\times400$ m. A total of 165 boxes contained at least one earthquake. A maximum of three earthquakes were selected from each box. Travel-time data were also available from a single timed explosion (Section 3.1.4; Figure 3.1), which was recorded at 27 stations.

Data from the stations hei and H031 (Figure 3.1) were not used, as these stations lay

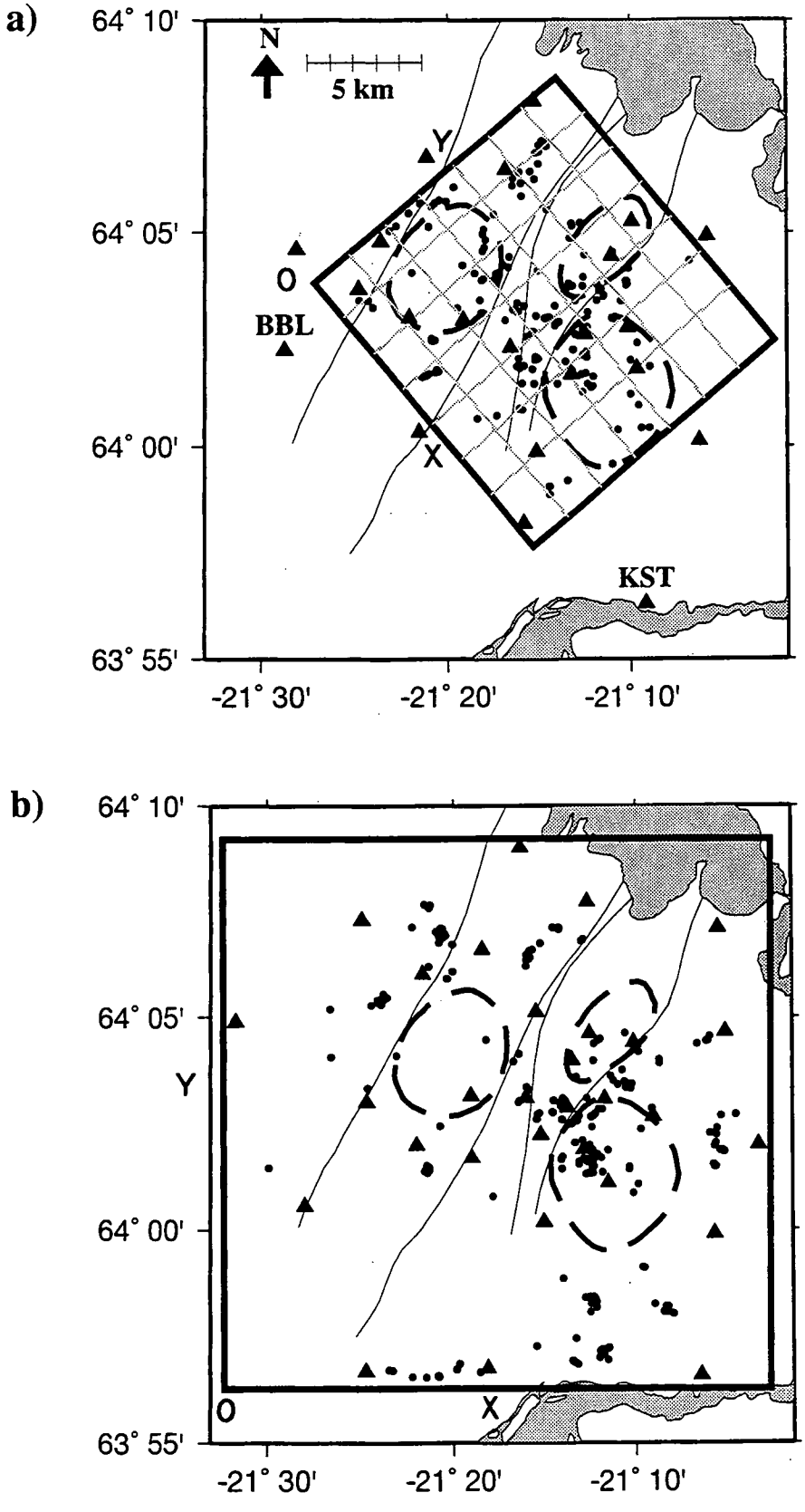

Figure 5.1: The areas studied in the two different LET inversions. (a) The study of *Toomey and Foulger* (1989). Triangles: 1981 stations; solid dots: epicentres of earthquakes used in the inversion; dashed lines: outlines of volcanic centres; thin lines: outlines of the volcanic systems; box: outline of the area studied; 0; origin of local coordinate system. Nodes were defined at the intersections of the grey lines. (b) Area studied in this project. Triangles: 1991 stations; dots: 1991 earthquakes used in the inversion. Other symbols as for (a).

well outside of the model area. Only *S–P* times were available from 30 event-station pairs where the absolute timing of the stations involved was uncertain, making accurate *P*-wave arrival times unobtainable. The final 1991 dataset used contains 228 earthquakes with 4748 *P*-wave arrival times and 3678 *S–P* times (Figure 5.1b).

5.1.2 The starting wave-speed model

Two potential starting V_P models were available: (1) the one-dimensional model used to locate the earthquakes, derived from the three-dimensional model of *Toomey and Foulger* (1989) (Section 3.3.2), and (2) a model based on a local refraction line (*Pálmason*, 1971; Figure 3 of *Toomey and Foulger*, 1989). An average of these two models was used to create a one-dimensional layered starting model for *velest* (Figure 5.2a). This layered model was designed so that the centres of the layers were at the depths of the intended node layers in *simulps12*, which simplified conversion of the layered model to the *simulps12* input model.

The 448 earthquakes from 1991, with some small-magnitude cluster earthquakes removed, were divided into two sets with 197 earthquakes in each. The *P*-wave arrival times from each set were processed separately to determine two layered V_P models. These were very similar, and the models were averaged to give an intermediate one-dimensional layered model (Figure 5.2b).

A final inversion was carried out of *P*-wave data from a carefully selected set of 191 earthquakes. These earthquakes all had a maximum azimuthal gap of less than 180°, and were optimally distributed throughout the area, with the best-recorded earthquakes selected in volumes of dense seismicity. The starting model for this inversion was the average model from the two previous inversions. The resulting model differed only slightly from the starting model, with an RMS travel-time residual decrease from 0.38 to 0.35 s (Figure 5.2c). This final one-dimensional layered V_P model was converted to a *simulps12*-format starting model with the wave-speed defined at nodes with 1 km vertical spacing between 0 and 6 km.

The starting V_P / V_S ratio used was 1.77, the same as the ratio used to locate the earthquakes (Section 3.3.2). A uniform V_P / V_S ratio was used for all depths.

5.1.3 Grid configuration

The volume imaged extends from 0 to 6 km beneath a 24 × 24 km area centred at the point 64°02.75N, 21°17.5W. This area contains 30 out of the 32 stations available in 1991, and all of the epicentres in the 1991 dataset (Figure 5.3). Additional planes of fixed nodes were placed at -50, -1, 8 and 50 km depth and at ±150 km horizontally.

Trial inversions with horizontal nodal spacings of 1 and 2 km were used to determine the minimum suitable nodal spacing. The 1-km spacing model had $21 \times 21 \times 7 = 3087$ nodes, over three times more than the 2-km spacing model, which had $12 \times 11 \times 7 = 924$ nodes (Figure 5.3). A one-iteration inversion of the 1-km spacing model was carried out

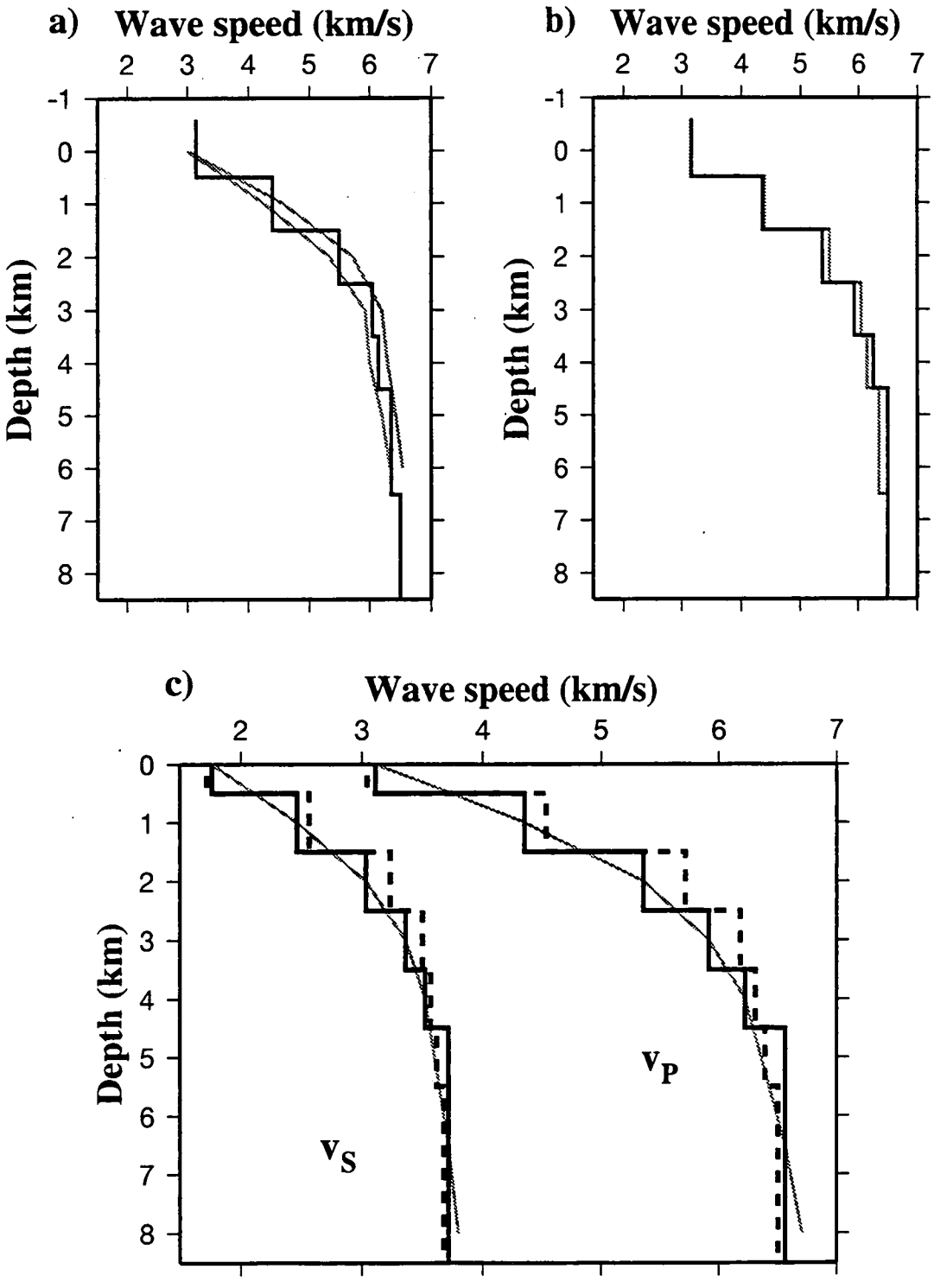

Figure 5.2: (a) Starting layered V_P model (solid line) derived from an average of the two one-dimensional models of *Toomey and Foulger* (1989) (grey lines). (b) Intermediate *velest* model (solid line), an average of the V_P models resulting from inversion of two subsets of the 1991 data set. Grey line: starting model shown in (a). (c) Final one-dimensional wave-speed model resulting from inversion using *velest*. The V_S model is calculated from the V_P model using a uniform V_P / V_S of 1.77. Solid line: one-dimensional layered model; grey line: continuous one-dimensional model used as input to *simulps12*; Dashed line: one-dimensional model described in Section 3.3.2.

to determine the ray distribution, as measured by the DWS (Section 4.3.4). The ray coverage was not sufficient to allow inversion for a model with 1 km spacing, as most of the model nodes had a DWS of less than 100 (Figure 5.3). At 2 km spacing, the north, south and west margins of the model had poor ray coverage due to the lack of earthquakes in these areas, so in the final model 4-km wide gaps were inserted at the north, south and west margins (Figure 5.3).

5.1.4 Inversion strategies

5.1.4.1 Graded inversion

The inversions were carried out in three stages, with 12-km, 4-km and the final (2/4-km) horizontal nodal spacings. The vertical nodal spacing was always 1 km. The final stage involved inverting for both V_P and V_P/V_S models, using a starting V_P model interpolated from the output of the 4 km spacing stage, and a uniform starting V_P/V_S.

The V_P damping parameter was selected from damping curves (Figure 5.4), and set at 20 s^2km^{-1} for all stages. A value of 5 s^2km^{-1} could have been used for the final stage (Figure 5.4) but this resulted in large V_P oscillations in the surface layer, so 20 s^2km^{-1} was used instead. The V_P/V_S damping used was 2 s.

5.1.4.2 One-step inversion

A 4-iteration inversion for both V_P and V_P/V_S models was carried out in one step at the final nodal configuration, starting from the one-dimensional model. The damping parameters were set at 5 s^2km^{-1} for V_P and 2 s for V_P/V_S (Figure 5.4).

5.1.5 Model resolution

A single-iteration inversion of the *P*-wave data only from the combined 1981 and 1991 data set was carried out to obtain the resolution matrix of the *P*-wave data. Individual rows of the resolution matrix were plotted for selected nodes, to determine the amount of wave-speed averaging at these nodes (Figure 5.5). From these plots, nodes with spread < 4 km^2 were deemed well-resolved, as they involved only local averaging of the model. Figure 5.5 also illustrates the directional nature of volume averaging for different nodes. For shallow nodes (depth < 3 km) the averaging volumes are elongated in the vertical direction, whereas the volumes are elongated horizontally for deeper nodes. This reflects the dominant ray directions at depth, with ray paths becoming steeper as they approach the surface.

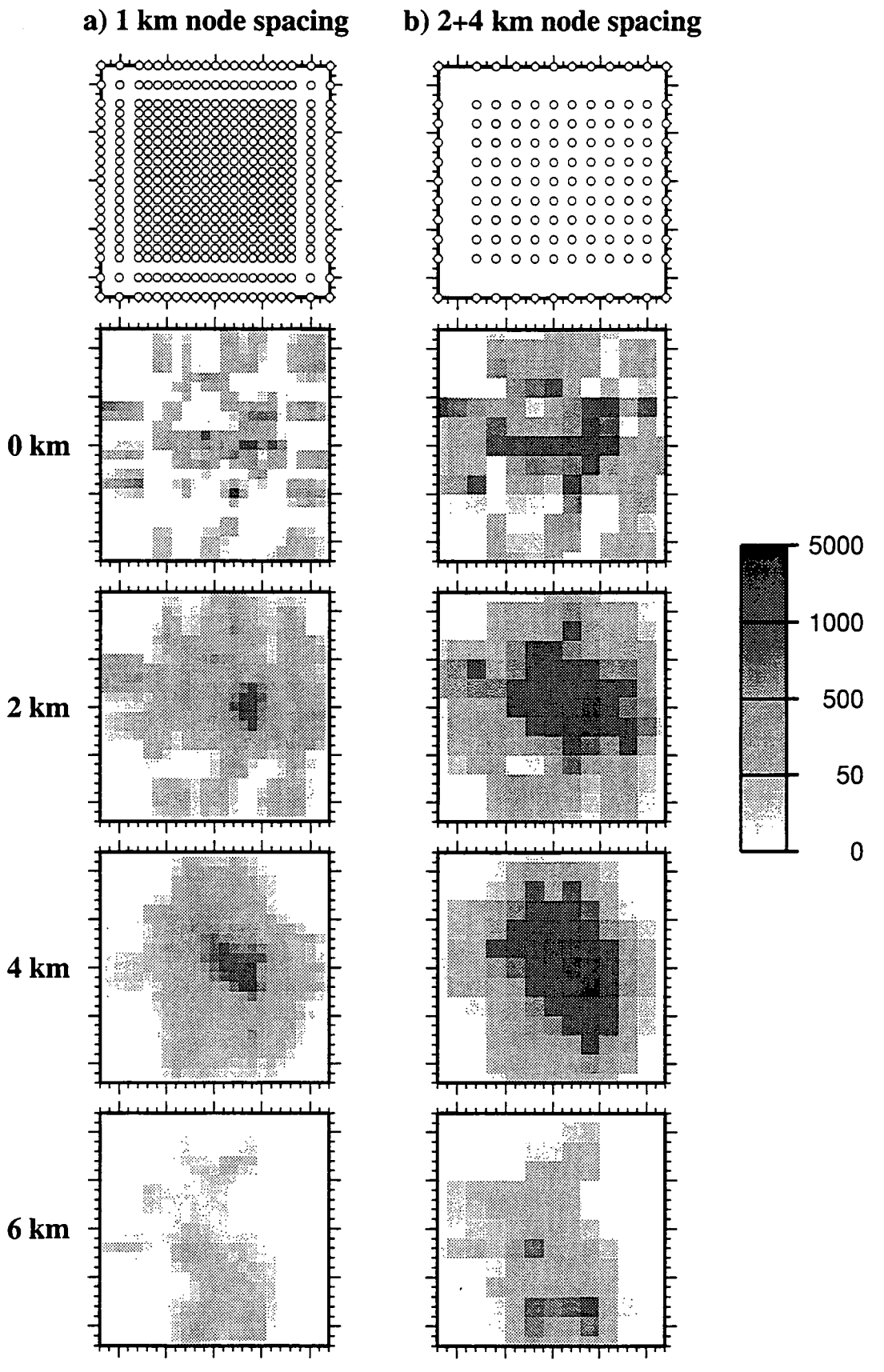

Figure 5.3: Results from trial inversions at (a) 1 km and (b) 2-4 km nodal spacings, with 1 km vertical spacing from 0 to 6 km depth. Top figures show nodal positions in each layer. The lower figures show values of the DWS at 0, 2, 4 and 6 km depth.

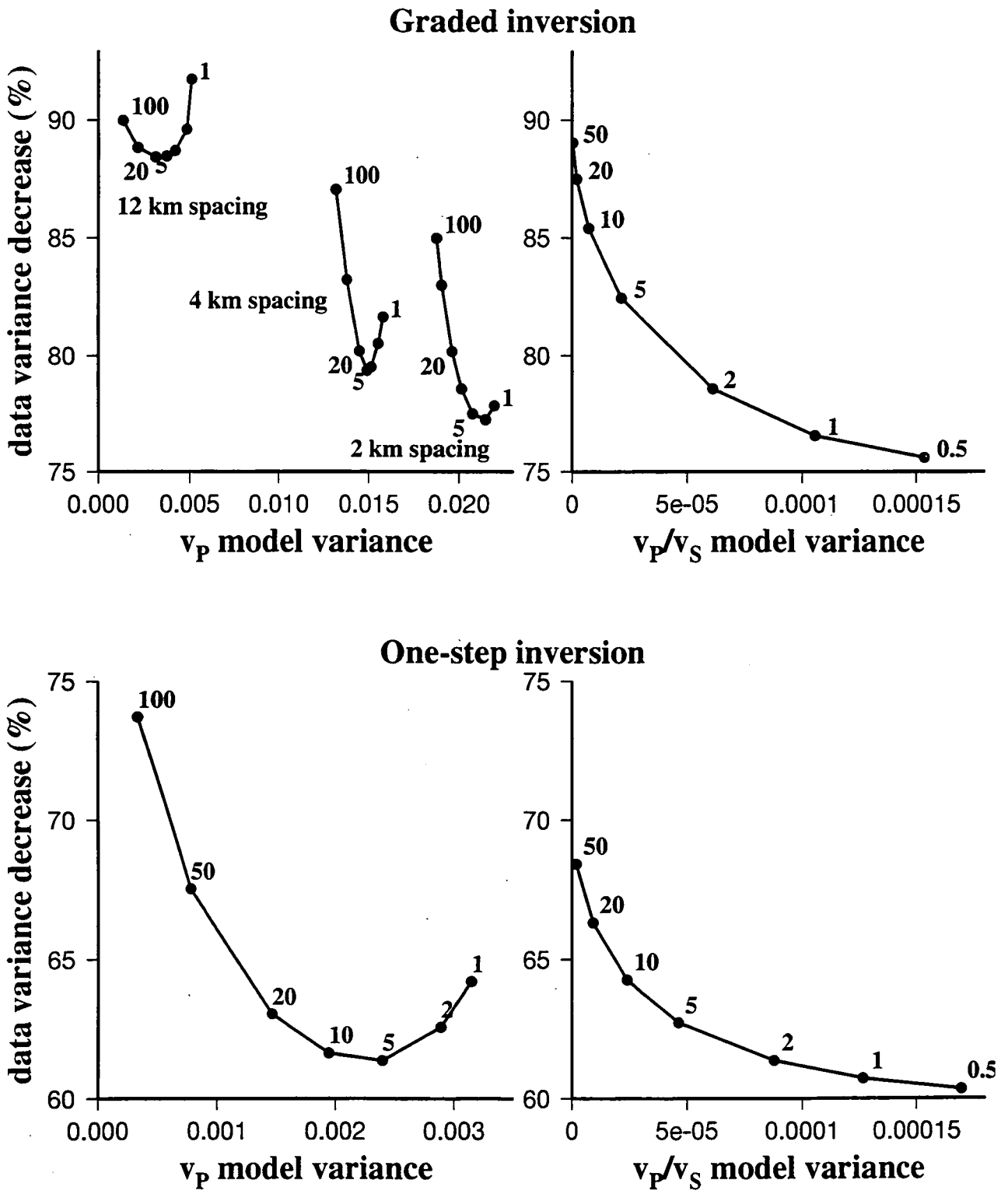

Figure 5.4: Damping curves for V_P and V_P / V_S for the graded inversion (top figures) and the one-step inversion (bottom figures) of the combined 1981 and 1991 dataset. For the graded inversion for V_P (top left), the curves for inversions at 12, 4 and 2 km nodal spacings are shown. The data variance decrease is measured from the start of each inversion, using the output wave-speed model from the previous step to locate the events.

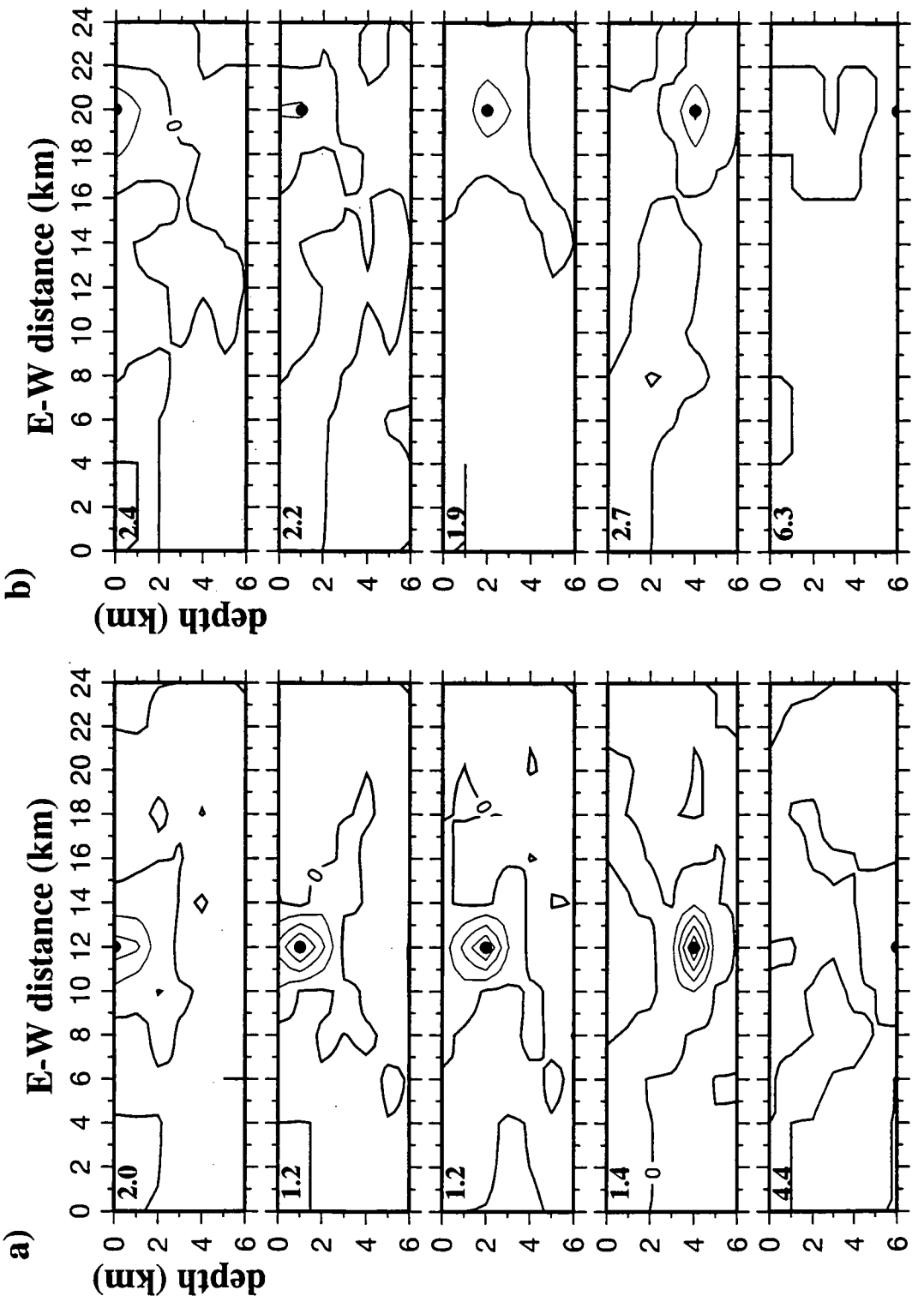

Figure 5.5: Depth sections with contoured values of individual rows of the resolution matrix obtained from the one-step inversion of the combined 1981 and 1991 dataset. The plots show an east-west section through the model, for nodes at 0, 1, 2, 4 and 6 km depths. Solid dot shows the position of the node associated with each row. The spread function values calculated for each node are shown at upper left. (a) for nodes at $x = 0, y = 0$. (b) for nodes at $x = 8, y = 0$.

5.1.6 Selection of the final three-dimensional wave-speed models

The data used. The V_P models resulting from one-step inversion of the 1991 data only and the combined 1981 and 1991 data are very similar (Figure 5.6; Table 5.1). The major difference is the improvement in resolution of the upper layers when the 1981 data are also used. This improvement in resolution is due to the differences in station locations between the 1981 and 1991 arrays (Figure 5.1), so the inclusion of the 1981 data adds raypaths in parts of the upper section of the model that are not sampled by the 1991 data. This leads to small differences between the V_P models at these depths. The combined 1981 and 1991 data were used to invert for the final three-dimensional models.

Inversion strategy. The V_P models resulting from the graded inversion and one-step inversion of the combined 1981 and 1991 data show some differences, particularly in shallow layers (Figure 5.7). In general, the wave-speed anomalies resulting from the graded inversion fill a larger volume and have larger maximum amplitudes. High-amplitude V_P variations of up to 22% are imaged in the 0-km layer during the final stage of the graded inversion, despite the use of high damping (Section 5.1.4.1). Both strategies give similar reductions in RMS travel-time residuals (Table 5.1). The V_P and V_P / V_S models resulting from the one-step inversion are simpler than the graded-inversion models, and this strategy requires much less processing time and operator interaction. There is no evidence that a graded inversion is necessary for this data set, perhaps because the lateral variations in wave-speed are relatively small.

Table 5.1: Inversion details.

Inversion	Eqs + shots	No. of stns	No. of *P* times	No. of *S-P* times	Number of nodes	*P* RMS residual (s) 1d → 3d	*P* & *S* RMS residual (s) 1d → 3d
1981 data (Model of *Toomey and Foulger*, 1989)	158+2	20	2409	0	8×8×7=448	0.055 → 0.044	
1981 data (outliers removed, using *simul3*)	158+2	20	2394	0	8×8×7=448	0.038 → 0.022	
1981 data (outliers removed, using *simulps12*)	158+2	20	2394	0	8×8×7=448	0.038 → 0.022	
1991 data, one-step inversion	228+1	33	4748	3678	12×11×7=924	0.037 → 0.020	0.054 → 0.038
1981 & 1991 data, one-step inversion (Final model)	386+3	55	7253	3678	12×11×7=924	0.037 → 0.023	0.054 → 0.037
1981 & 1991 data, graded inversion	386+3	55	7253	3678	12×11×7=924	0.037 → 0.023	0.054 → 0.036
1991 data, one-step inversion with anisotropy correction	228+1	33	4748	3678	12×11×7=924	0.037 → 0.020	0.054 → 0.037

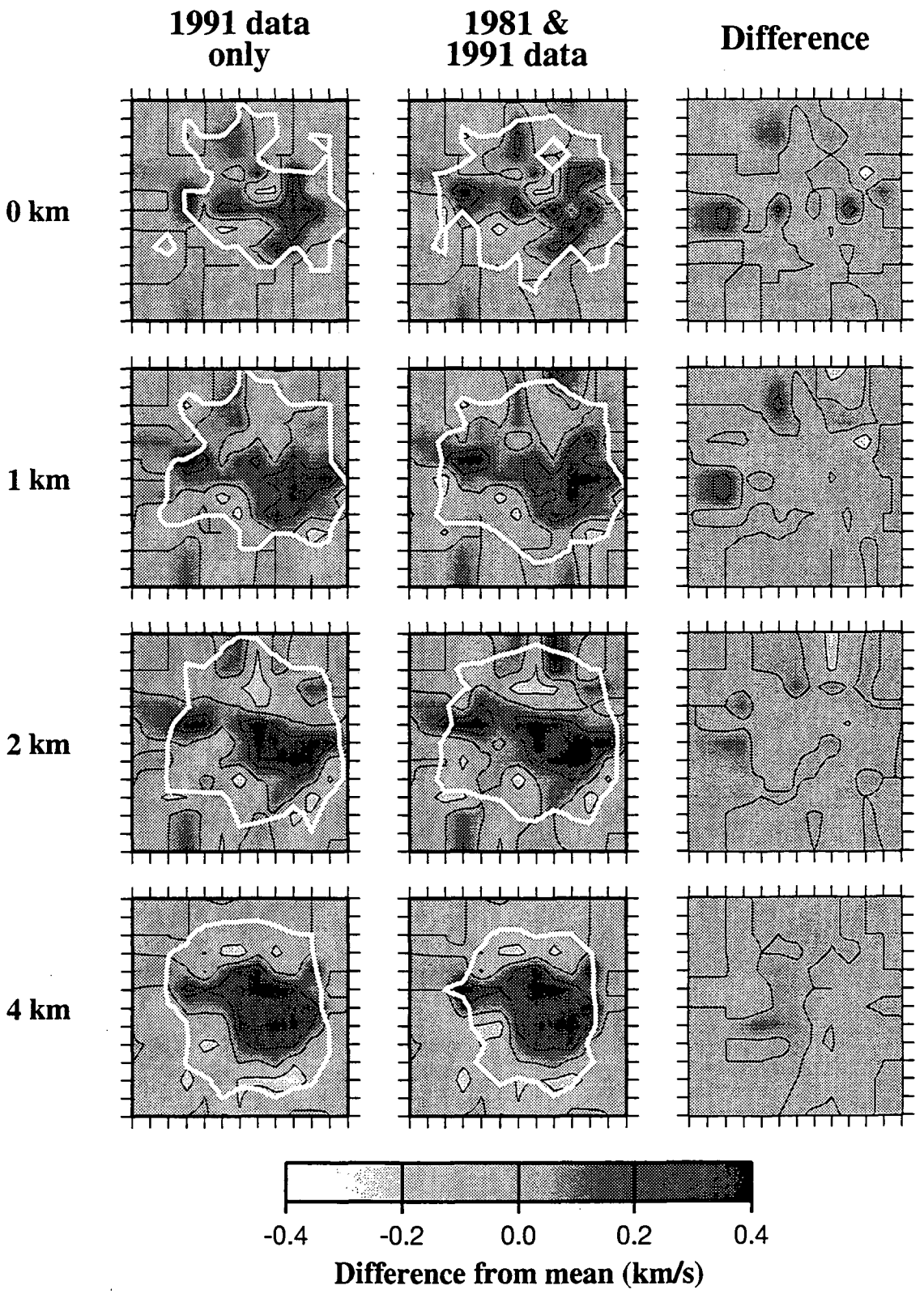

Figure 5.6: Map views at 0, 1, 2 and 4 km depths of the V_P models resulting from one-step inversion of the 1991 data only, the combined 1981 and 1991 data, and the difference between the models. The difference from the mean wave speed in each layer is plotted. White lines are the spread=4 km contour for each model.

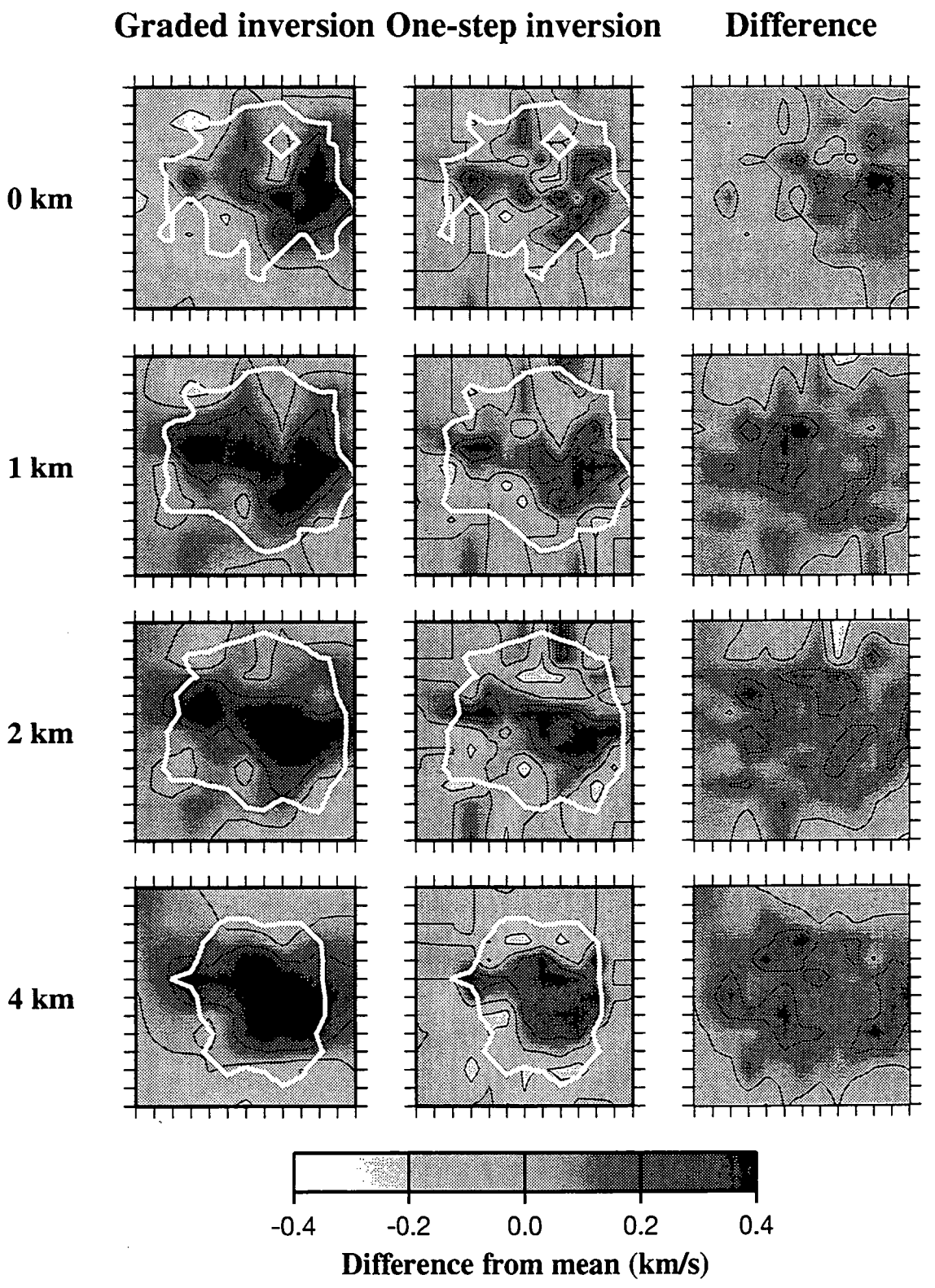

Figure 5.7: Map views at 0, 1, 2 and 4 km depths of the V_P models resulting from graded and one-step inversion of the combined 1981 and 1991 data, and the difference between the models. The difference from the mean wave-speed in each layer is plotted. White lines are the spread=4 km contour for each model.

5.2 The final wave-speed models

5.2.1 Introduction

The final V_P and V_P/V_S models result from a one-step inversion of the combined 1981 and 1991 data (Appendix 4). These models give a data variance reduction of 53% from the *velest*-derived one-dimensional model. The RMS travel-time residual for the earthquakes used in the inversion reduced from 0.054 to 0.037 s (Table 5.1). For the 448 located earthquakes in the 1991 data set, the RMS travel-time residual reduces from 0.076 to 0.059 s.

5.2.2 The V_P model

V_P varies laterally from -0.34 to +0.40 km/s from the starting one-dimensional model (Figure 5.8). There are three major high-V_P structures in the model, with a V_P difference of >0.3 km/s from the starting model. These are (1) near the Grensdalur volcano from 0 and 4 km depth, (2) beneath the Húsmúli shield volcano from 0 to about 4 km depth and (3) from 2 to 5 km depth under the southern part of the Hromundartindur system at Ölkelduhals (see Figure 1.10 for locations). Beneath 3 km the Grensdalur and Ölkelduhals bodies merge to form a single large body. At lower V_P contrasts (+0.1 km/s) there is a single zone oriented parallel to the spreading direction and traversing all three volcanic systems. No major low-V_P bodies were imaged.

5.2.3 The V_P/V_S model

The V_P/V_S model varies by ±4%, from 1.70 to 1.84, throughout the area (Figure 5.9), with a mean value of 1.77 in every layer. The most coherent anomaly is low V_P/V_S between 0 and 3 km depth. This anomaly narrows in the NW-SE direction with depth, but is still present down to 4 km. At the surface, the V_P/V_S anomaly corresponds closely to the areas of hot springs and fumaroles. The low-V_P/V_S anomaly occupies part of high-V_P anomaly volume between 2 and 4 km depth (Figures 5.10 and 5.11).

5.2.4 The final hypocentre locations

All the earthquakes in the 1991 data set were relocated using the final three-dimensional model and the program *qloc3d* (B. Julian, *pers. comm.*), which is similar to *qloc* (Section 3.3.1) but uses the "bending" method (*Julian and Gubbins*, 1977) to trace rays exactly in a three-dimensional wave-speed model. The hypocentral locations, magnitudes and RMS travel-time residuals for all earthquakes are listed in Appendix 5. The mean relocation of hypocentres between the original one-dimensional model (Section 3.3.2) and the final three-dimensional model is 0.23 km horizontally and 0.30 km vertically (Figures 5.12 and 5.13), with maximum relocations of 1.5 km horizontally and 2.6 km vertically. In general the hypocentres move outward from the centre of the model and clusters of hypocentres become more compact. There is a systematic

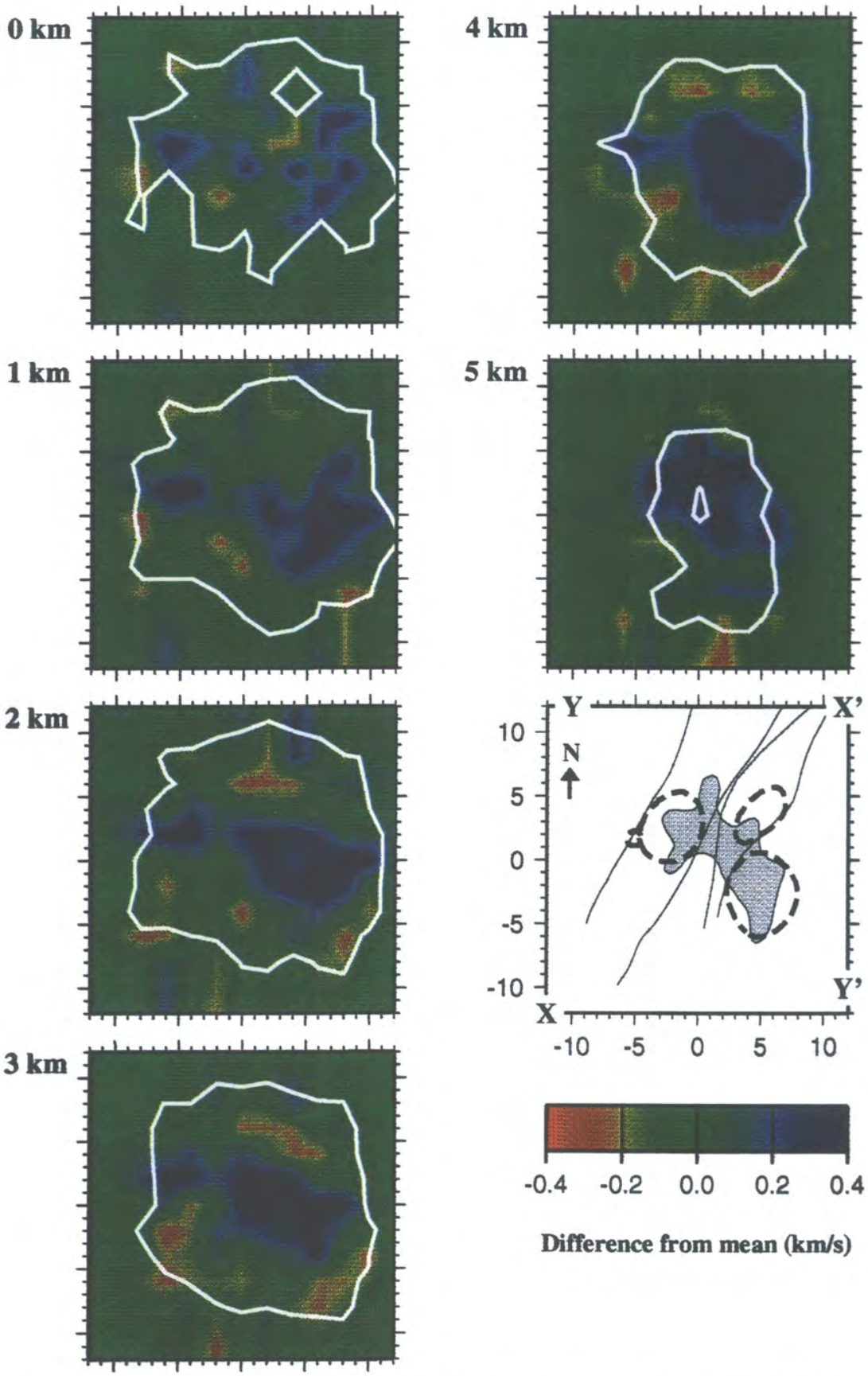

Figure 5.8: Map views of the final V_P model, from 0 to 5 km depth. The difference from the mean wave-speed in each layer is plotted. White lines are the spread = 4 km^2 contour. Map at lower right shows the positions of the volcanic centres (dashed lines), volcanic systems (thin lines) and the geothermal field (shaded). X-X' and Y-Y' show positions of sections in Figures 5.10 and 5.11.

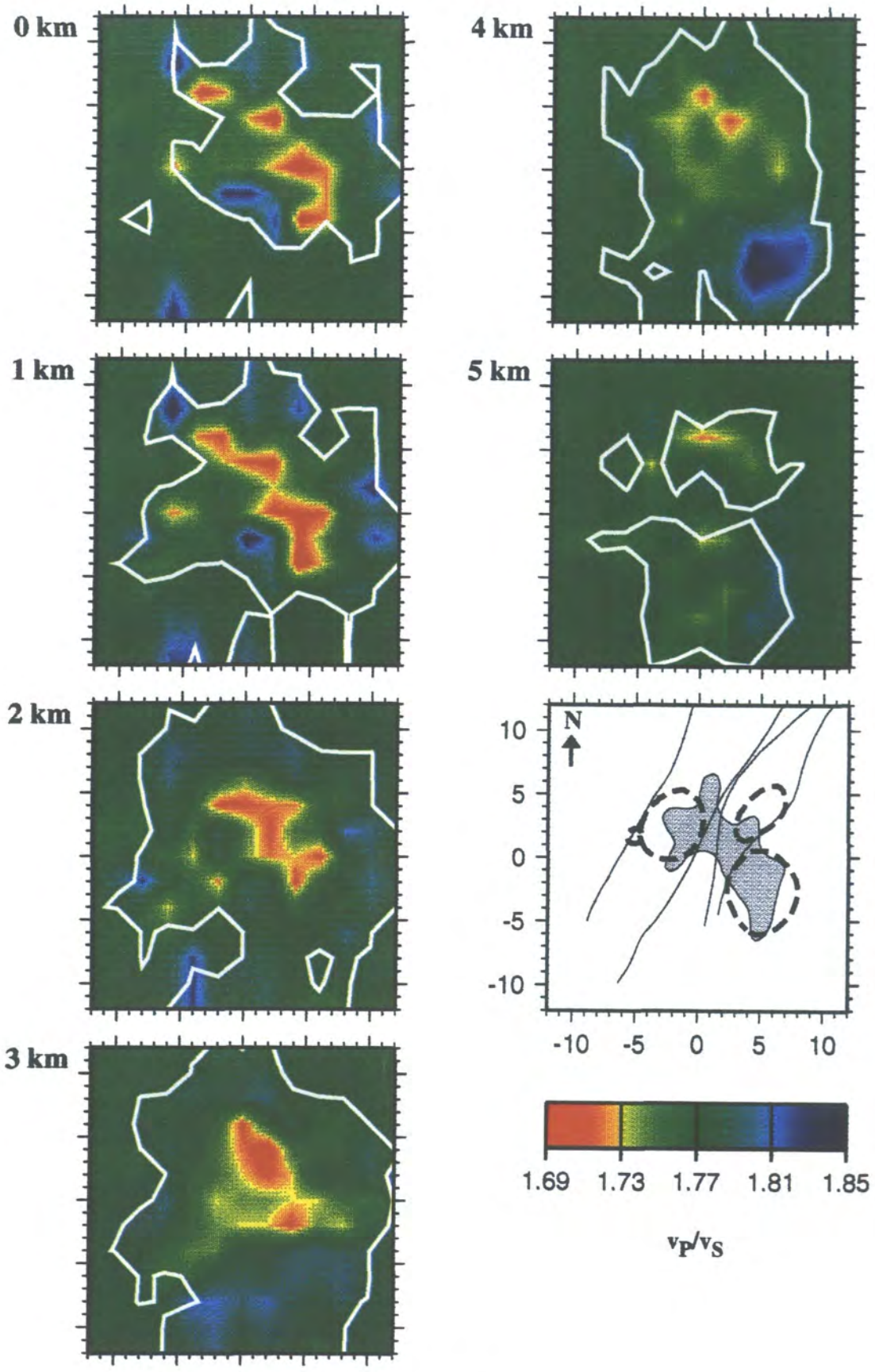

Figure 5.9: Same as Figure 5.8, except for V_P / V_S.

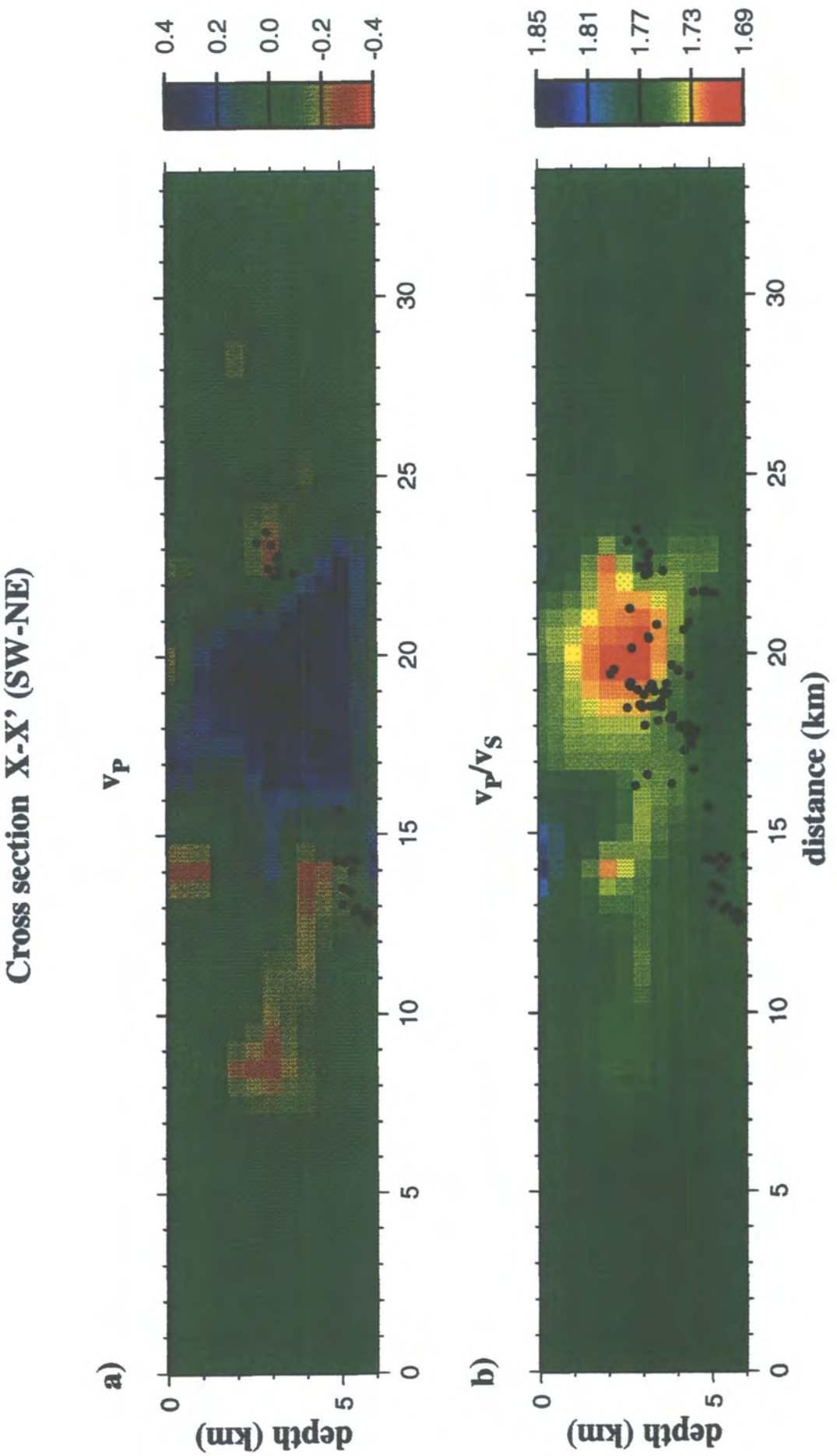

Figure 5.10: SW-NE sections through the final three-dimensional models (a) V_P and (b) V_P / V_S. Dots are hypocentres that lie within ±2 km of the plane of section. The position of the section is shown in Figure 5.8.

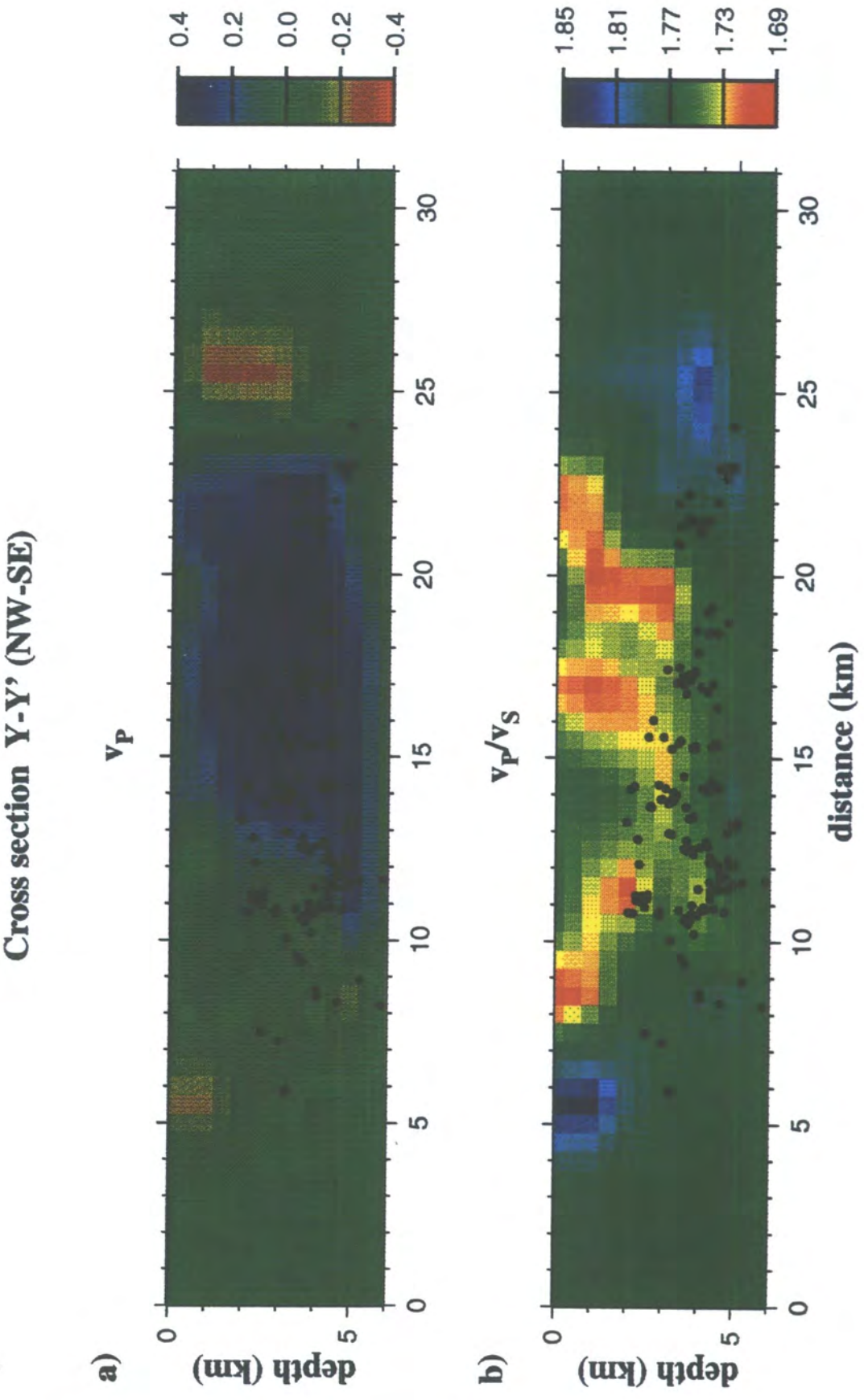

Figure 5.11: Same as Figure 5.10, except for a NW-SE section.

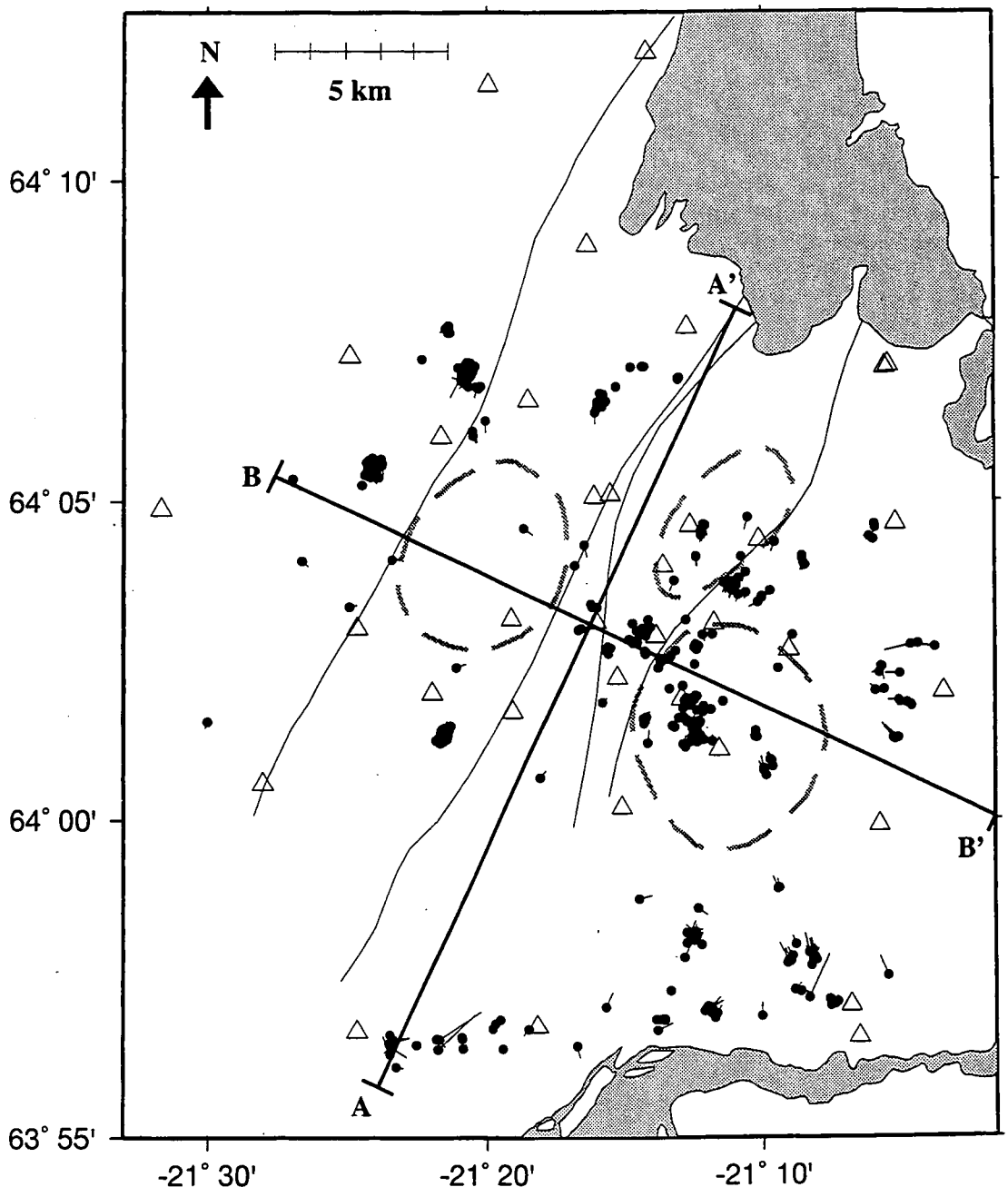

Figure 5.12: Map of hypocentre locations (solid dots) calculated using the final three-dimensional models, and changes (lines) from the one-dimensional model locations of Figure 3.9. Lines A-A' and B-B' mark the positions of depth sections shown in Figure 5.13.

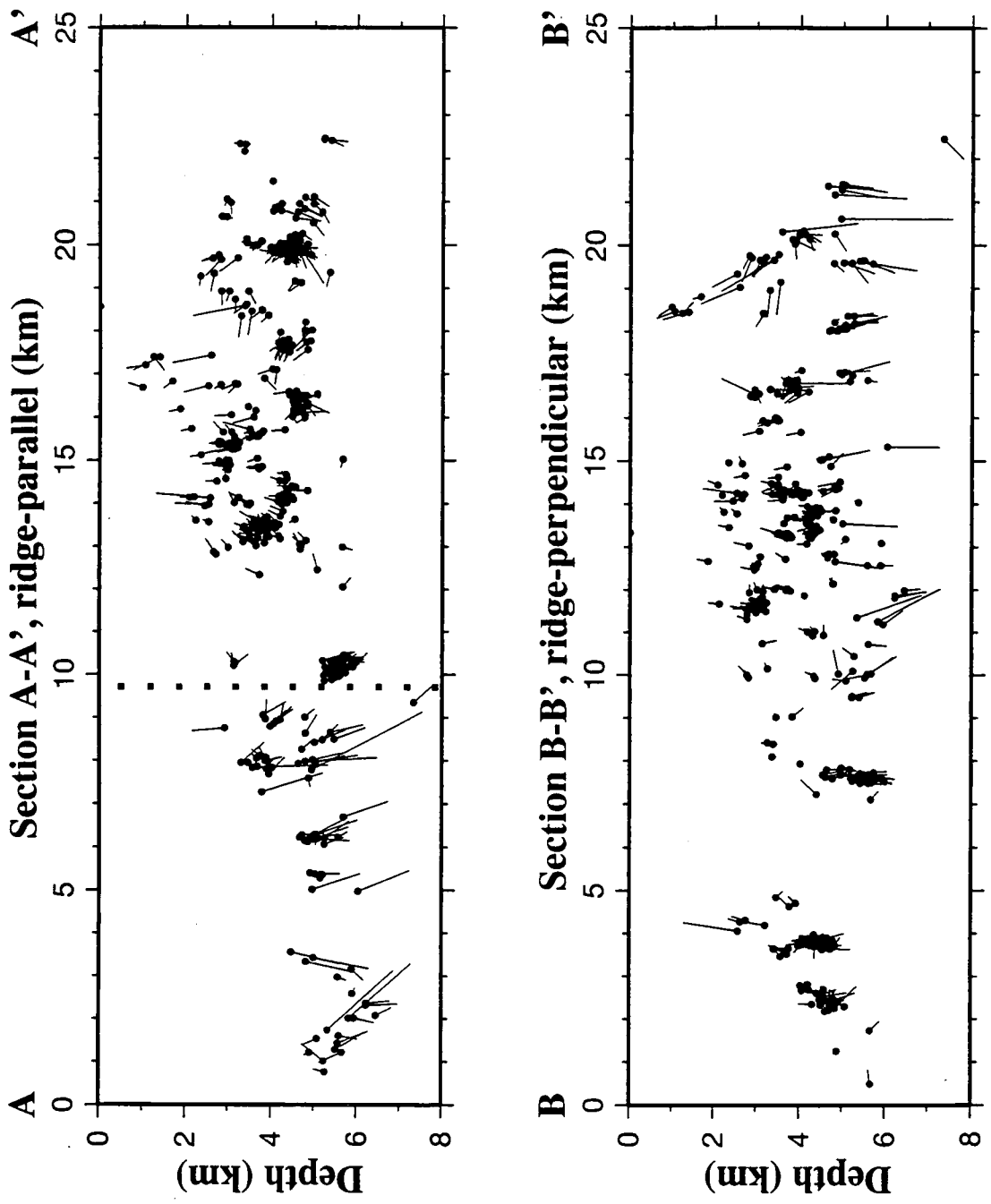

Figure 5.13: Depth sections showing hypocentres (solid dots) of Figure 5.12, and changes (lines) from the one-dimensional model locations of Figure 3.10. Lines of sections are shown in Figure 5.12. The dashed line in section A-A' shows the boundary between the northern and southern hypocentres that exhibit different behaviour (Section 5.2.4).

difference between the relocations of hypocentres north and south of the 64°N aseismic zone (Section 3.3.3). In general the southern hypocentres shallow significantly between the one-dimensional and three-dimensional models, whereas the northern earthquakes become slightly deeper (Figure 5.13).

In depth section, it can be seen that the hypocentres are concentrated near volumes that have large wave-speed anomalies, but the volumes with the largest wave-speed anomalies tend to be aseismic (Figures 5.10 and 5.11). A cluster of earthquakes occurred within a small low-V_P volume beneath Hromundartindur (Figure 5.10).

5.3 Comparison with the early model from the 1981 data only

5.3.1 The 1981 data set and inversion

Toomey and Foulger (1989) and *Foulger and Toomey* (1989) inverted the 1981 data for a V_P model and hypocentral parameters using the program *simul3* (*Thurber*, 1981; 1983). They imaged a 14×15×6 km volume with nodes spaced at 2 to 4 km horizontally and 1 km vertically (Figure 5.1). The starting model came from preliminary test inversions. Damping was set at 2 s^2km^{-1} after experimenting with different values. Hereafter, this model is called the TF81 model.

The inversion of the 1981 data was repeated as part of the current project, with the 15 outliers with large residuals removed (Section 5.1.1.1), using both *simul3* and *simulps12* and the same starting model and damping parameters as the early inversion (Figure 5.14; Table 5.1). The repeat inversion using *simul3*, but without the data outliers, results in a very similar model, with an RMS wave-speed difference of 0.07 km/s. The model resulting from an outlier-free inversion using *simulps12* has slightly smaller wave-speed anomalies and an RMS wave-speed difference of 0.13 km/s from the TF81 model.

5.3.2 Comparison of the V_P models

The TF81 model is compared with the final V_P model obtained using the 1981 and 1991 data in a single-step inversion (hereafter called the 81+91 model). The two models have different nodal configurations and the TF81 model covers a smaller area (Figure 5.1). To compare the models the 81+91 model was interpolated to the TF81 model nodes, so that the values of wave speed at exactly the same points could be compared.

The relative differences in wave speed within each layer are compared rather than absolute wave-speed, as the absolute wave-speeds in three-dimensional models are known to be slightly dependent on starting models, whereas the relative wave speeds within each layer are less dependent (*Toomey and Foulger*, 1989). For each model, the relative wave speeds were calculated as the difference from the starting model. The

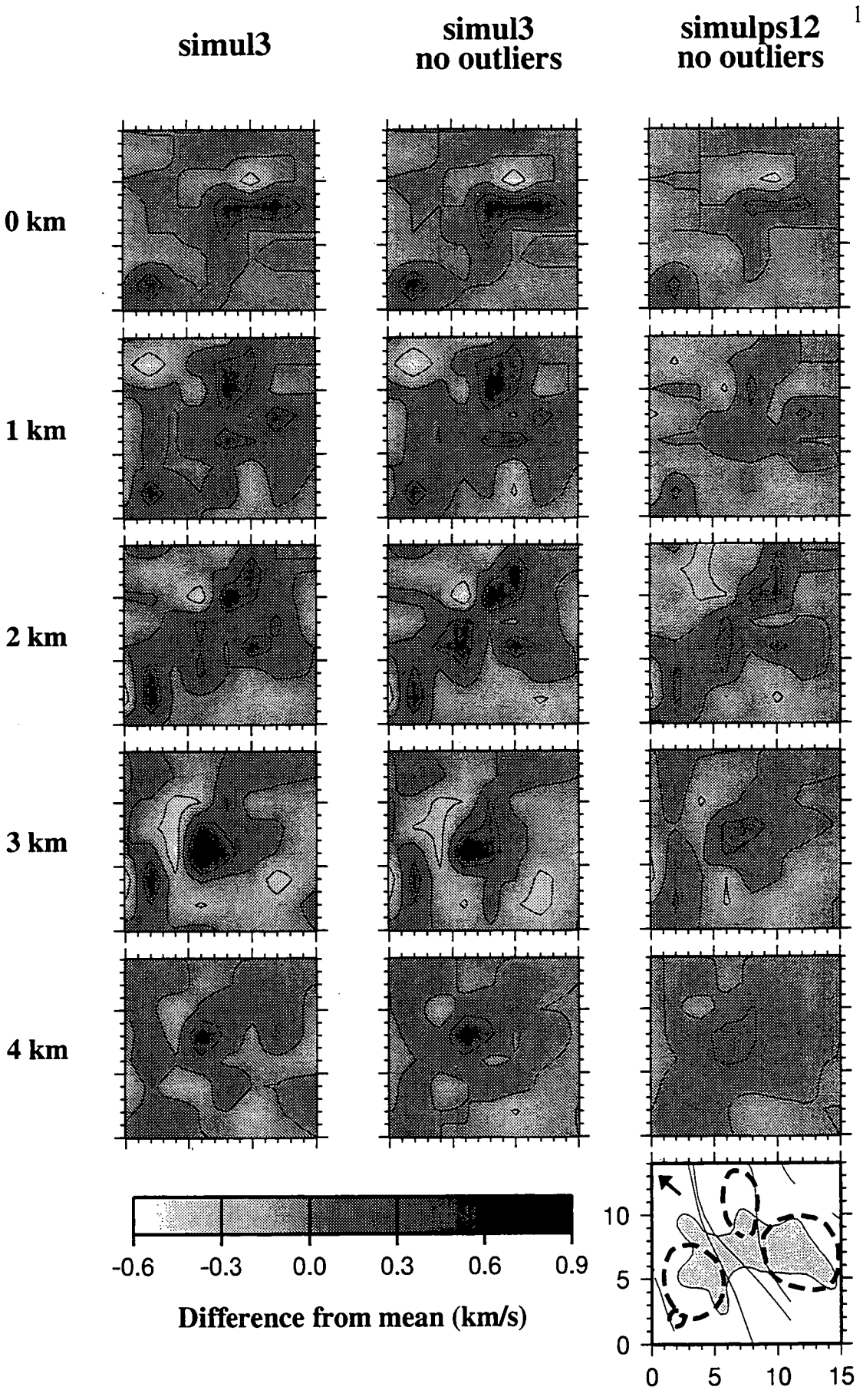

Figure 5.14: Comparison between models resulting from different inversions of the 1981 data. Left: model from *Toomey and Foulger* (1989). Centre: repeat of *Toomey and Foulger* (1989) inversion, using *simul3*, with 15 data outliers removed. Right: inversion of the outlier-free dataset using *simulps12*.

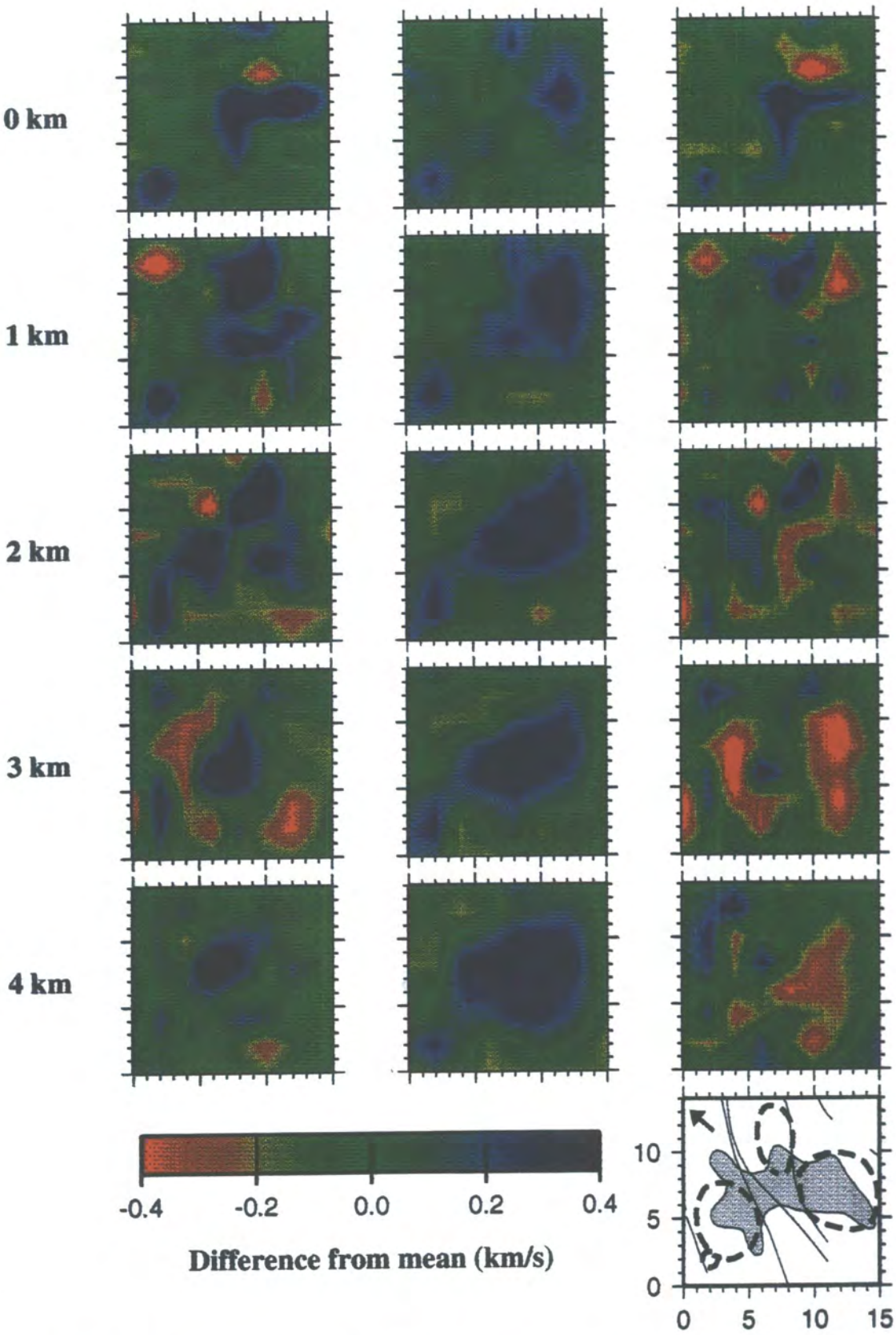

Figure 5.15: Comparison between the V_P model of *Toomey and Foulger* (1989) (the TF81 model) and the final V_P model (81+91 model), interpolated to the nodal positions of the TF81 model. Both models are plotted as the difference from the mean wave-speed of each layer. Rightmost column shows difference (in the same units) between the two models.

difference between the two models at each node was then found by subtracting the relative-difference value of the 81+91 model from that of the TF81 model (Figure 5.15).

Three main high-V_P bodies were identified in the TF81 model. These were (1) beneath Grensdalur from 0 to 4 km depth, (2) beneath Húsmúli from 0 to 4 km depth and (3) from 2 to 5 km depth beneath Ölkelduhals (Figure 1.16; *Foulger and Toomey*, 1989). These three bodies correspond to the main high-V_P anomalies in the 81+91 model (Section 5.2.2; Figure 5.15). The anomalies in the TF81 model were defined using a percentage wave-speed contrast of +7% (*Foulger and Toomey*, 1989). If a 0.3 km/s contrast is used to define the high-V_P bodies then they extend to greater depths, because 0.3 km/s is a smaller percentage of the wave-speed at depth. There are slight differences in the shape of the bodies between the TF81 and 81+91 models, and the bodies are larger in the 81+91 model, with the Ölkelduhals and Grensdalur bodies merging beneath 2 km depth.

The amplitudes of the anomalies in the 81+91 model tend to be smaller than those of the TF81 model, probably due to the larger errors in the 1981 data set, and because the TF81 model was obtained using a slightly lower damping (2 s^2km^{-1} versus 5 s^2km^{-1}). If the absolute wave-speed values at each node are compared, there is an RMS difference between the models of 0.25 km/s (Table 5.2). This RMS value is slightly lower, 0.19 km/s, if the V_P variations from the mean value of each layer are compared instead of the absolute values. The absolute wave-speed values between the two models have a mean difference of 0.04 km/s; *i.e.*, the TF81 model has a slightly higher V_P on average.

Table 5.2: Difference in wave speed between the TF81 and 81+91 models.

Depth (km)	Mean of 1981 model (km/s)	Mean of 1991 model (km/s)	Mean difference between models (km/s)	RMS difference between models (km/s)
Absolute wave speed				
0	3.035	3.219	-0.18	0.24
1	4.541	4.422	0.12	0.21
2	5.723	5.432	0.29	0.34
3	6.182	5.974	0.21	0.33
4	6.317	6.280	0.04	0.20
5	6.386	6.516	-0.13	0.23
6	6.486	6.535	-0.05	0.08
All layers			0.04	0.25
Difference from starting model				
0	-0.078	-0.010	-0.07	0.17
1	-0.024	0.000	-0.02	0.17
2	-0.029	0.003	-0.03	0.19
3	0.010	0.000	0.01	0.25
4	-0.052	-0.013	-0.04	0.20
5	0.070	-0.035	0.10	0.21
6	-0.014	-0.058	0.04	0.08
All layers			-0.00	0.19

The TF81 model contains a small volume of relatively low V_P (-8%) at 3 km depth ($x = 4, y = 7$; see Figure 5.1 for coordinate system), which was interpreted as a possible volume of partial melt by *Foulger and Toomey* (1989). In the 81+91 model, this volume at 3 km depth has a V_P value of +4% (Figure 5.15). There is thus no evidence of this low-V_P volume in the 81+91 model.

5.4 Empirical correction for anisotropy

The travel time residuals of *S* waves in the Hengill region show a clear variation with azimuth when the earthquakes are located in a one-dimensional model (Figure 5.16). This variation is probably due to anisotropy. A systematic variation in travel-time residuals could lead to bias in three-dimensional tomographic models. To quantify the effect that this variation could have on the final V_P / V_S model, an empirical anisotropy correction was made to all the measured *S-P* times used in the inversion.

The starting one-dimensional model was used to calculate the travel-time residuals of all the *S* waves used in the inversion. If a constant amount of anisotropy along all ray paths is assumed, then the size of the residual due to unmodelled anisotropy should be proportional to the ray length. To find an empirical correction for unmodelled anisotropy, the residual of each *S* wave as a percentage of total travel time was plotted against ray azimuth, and a best fit (L1-norm) sinusoidal function was found:

$$y = 1.4684 \times \sin 2x + 2.0466 \times \cos 2x - 1.4605, \qquad 5.1$$

where x is ray azimuth and y is the percentage residual / travel time (Figure 5.16). The negative offset of this function indicates that the mean of *S*-wave residuals in the one-dimensional model is slightly negative, suggesting that the V_S model is marginally slow, by about 1.5%.

For each ray, the value of this function was converted to time and subtracted from the measured *S–P* time, and the one-step inversion of the 1991 data was repeated. The resulting V_P / V_S model is very similar to the model resulting from inversion of the uncorrected 1991 data (Figure 5.17). The RMS difference between the values of the two models at each node is 0.01. This empirical correction of the *S–P* times suggests that the observed azimuthal variation does not cause any major artefacts in the final V_P / V_S model.

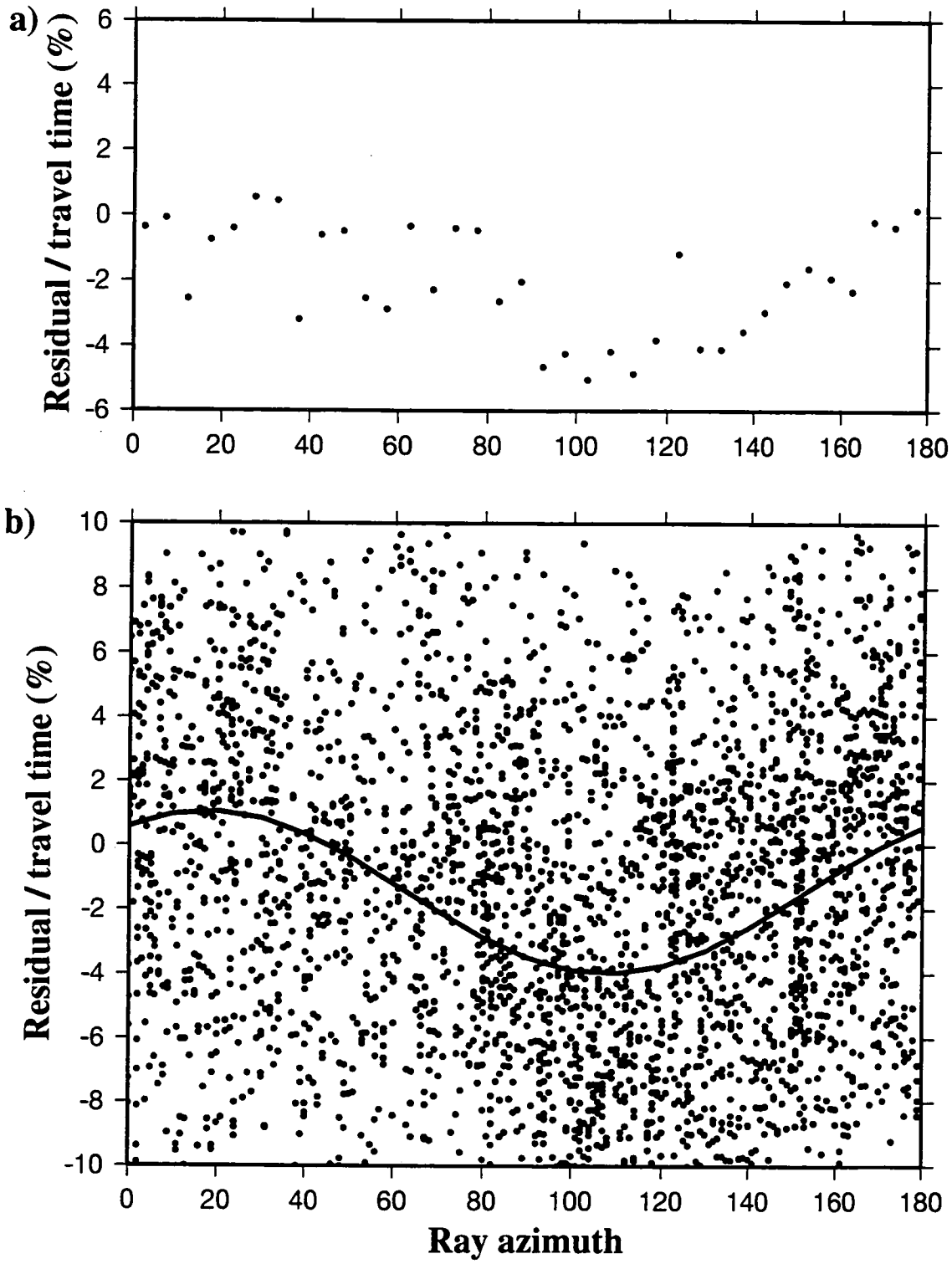

Figure 5.16: Plots of variation of *S*-wave travel time residuals with ray azimuth. (a) Mean residual in 5° azimuthal bins. (b) Residuals for all *S* waves in the 1991 data set. Solid line is best-fit (L1 norm) line through all the points.

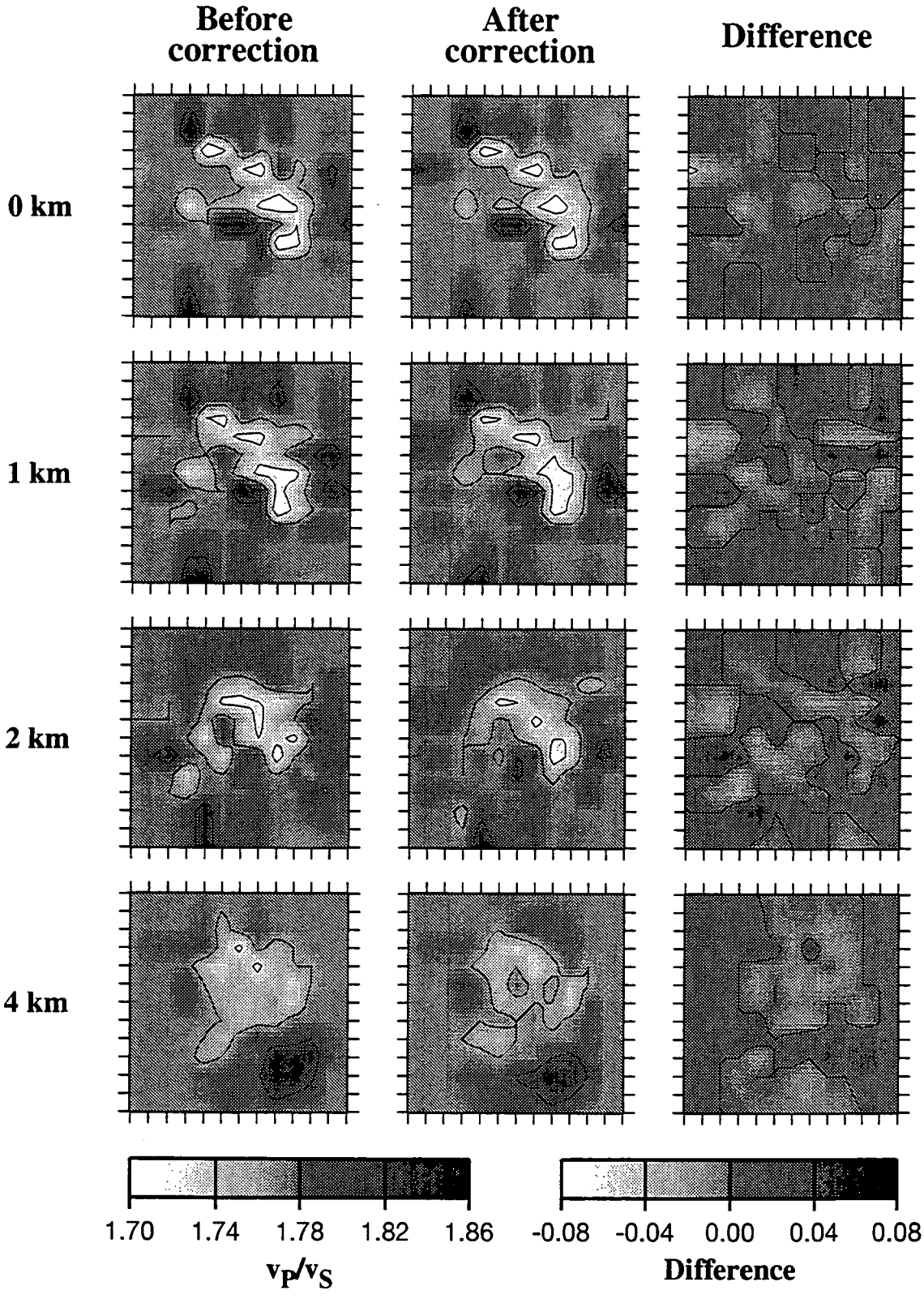

Figure 5.17: The V_P / V_S models resulting from one-step inversion of the 1991 data set, before and after the *S–P* times were corrected for anisotropy. Right column shows the difference between the two models.

5.5 Summary

The *simulps12* program was used to determine V_P and V_P / V_S models for a 24×24×6 km volume, using data collected in 1981 and 1991. The starting one-dimensional V_P model was obtained from an inversion of 1991 data using the *velest* program, and a uniform starting V_P / V_S of 1.77 was used. After experimenting with different minimum nodal spacings, a model with 2-4 km horizontal spacing was chosen. Two different inversion strategies were tested: a three-stage graded inversion, where the horizontal nodal density was increased at each stage and the output three-dimensional model of the previous stage was used to create a three-dimensional input model; and a one-step inversion. Both strategies gave similar results. Inversions of the 1991 data only, and the combined 1981 and 1991 data gave similar V_P models. The final model comes from a one-step inversion of the combined data, and contains high-V_P bodies underlying the main volcanic centres, and a low V_P / V_S anomaly from 0 to 2 km beneath the geothermal area. There is no evidence of substantial low-V_P anomalies. The final V_P model is similar to an independently-derived V_P model resulting from inversion of the 1981 data, although the models differ in detail. An empirical correction for *S*-wave anisotropy shows that anisotropy has very little influence on the V_P / V_S structure for this data set.

Chapter 6

Determination of moment tensors

6.1 Introduction

A six-component moment tensor provides an almost complete description of the seismic source, although certain classes of seismic source, with mechanisms involving single forces, cannot be described by a moment tensor (Section 2.3.2). There have been few determinations of moment tensors for local earthquakes, and these have mostly used polarities (*e.g.*, *McGarr*, 1992) or amplitudes (*e.g.*, *Feignier and Young*, 1992). Most local earthquake mechanisms are determined using *P*-wave polarities alone, which give poor constraint, and DC mechanisms are often assumed.

This chapter describes a new approach to determining the moment tensors of local earthquakes by inverting the polarities and amplitude ratios of the first arrivals of *P* and *S* waves. The use of amplitude ratios reduces some of the uncertainties caused by scattering and attenuation of body waves (*Julian and Foulger*, 1996). Moment tensors are calculated using linear programming methods, which allow inversion of constraints involving inequalities.

6.2 Inversion of polarities, amplitudes and amplitude ratios to determine moment tensors

6.2.1 Linear programming

The term "linear programming" refers to a class of problems involving systems of inequalities and linear operators. Such a problem involves maximising a linear "objective" function

$$z \stackrel{def}{=} a_{01}x_1 + a_{02}x_2 + \cdots + a_{0N}x_N \qquad 6.1$$

of N independent, non-negative variables $x_1, \cdots, x_N$, subject to constraints of the form

$$\begin{aligned} a_{i1}x_1 + a_{i2}x_2 + \cdots + a_{iN}x_N &\leq b_i \\ a_{j1}x_1 + a_{j2}x_2 + \cdots + a_{jN}x_N &\geq b_j \\ a_{k1}x_1 + a_{k2}x_2 + \cdots + a_{kN}x_N &= b_k \end{aligned} \qquad 6.2$$

(*e.g.*, *Dantzig*, 1963).

A set of $x_1, \cdots, x_N$ non-negative variables that satisfies equation 6.2 is called a "feasible vector". A feasible vector that maximises equation 6.1 is an "optimal feasible

vector". Geometrically, inequalities of the form of equations 6.2 define hyperplanes in N-dimensional space that bound the set of all feasible vectors. The vertices of this solution space are called the "basic vectors", and one or more of them are the optimal feasible vectors. This situation can be visualised easily in two dimensions (Figure 6.1).

The "simplex method" (*Dantzig*, 1963) is the simplest and most widely used way of solving linear-programming problems. The method involves (1) finding a feasible basic vector and then (2) traversing a sequence of other feasible basic vectors, seeking to increase the value of the objective function at each step until an optimal feasible vector is found.

6.2.2 The application of linear programming to moment tensor determination

Linear programming methods can be used to invert polarities, amplitudes and amplitude ratios of seismic waves from local earthquakes to determine moment tensors (*Julian*, 1986; *Julian and Foulger*, 1996). A seismic wave amplitude, u, is linearly related to the six independent moment-tensor components by

$$u = \mathbf{g}^T \mathbf{m}, \tag{6.3}$$

where $\mathbf{g}$ is a column vector of Green's functions and $\mathbf{m} = \left[M_{xx}\ M_{xy}\ M_{yy}\ M_{xz}\ M_{yz}\ M_{zz} \right]^T$ is a column vector of the moment-tensor components. Green's functions for any particular wave type and source and station locations can be calculated from equations 4.91 of *Aki and Richards* (1980), assuming an infinite homogeneous, elastic and isotropic medium.

A polarity observation is expressed as

$$\mathbf{g}^T \mathbf{m} \le 0$$

or (6.4)

$$\mathbf{g}^T \mathbf{m} \ge 0.$$

An amplitude observation is expressed as a pair of inequalities, bounded by the estimated maximum and minimum values of the amplitude, u_{max} and u_{min}:

$$\mathbf{g}^T \mathbf{m} \le u_{max}$$

and (6.5)

$$\mathbf{g}^T \mathbf{m} \ge u_{min}$$

For the amplitudes $A^{(1)}$ and $A^{(2)}$ of two seismic waves the value of the ratio $r = A^{(1)}/A^{(2)}$ can similarly be expressed as two inequalities involving bounds r_{max} and r_{min}:

$$u^{(1)} \le r_{\max} u^{(2)}$$

and

$$u^{(1)} \ge r_{\min} u^{(2)},$$

or

$$\mathbf{g}^{(1)T}\mathbf{m} \le r_{\max}\mathbf{g}^{(2)T}\mathbf{m} \qquad 6.6$$

and

$$\mathbf{g}^{(1)T}\mathbf{m} \ge r_{\min}\mathbf{g}^{(2)T}\mathbf{m}.$$

These are equivalent to

$$\left(\mathbf{g}^{(1)T} - r_{\max}\mathbf{g}^{(2)T}\right)\mathbf{m} \le 0$$

and

$$\left(\mathbf{g}^{(1)T} - r_{\min}\mathbf{g}^{(2)T}\right)\mathbf{m} \ge 0, \qquad 6.7$$

which are in the same form as equations 6.4 with modified Green's functions.

By reversing the sign of $\mathbf{g}$ (or its equivalent expression in equation 6.7) as appropriate, equations 6.4, 6.5 and 6.7 can all be expressed in the form

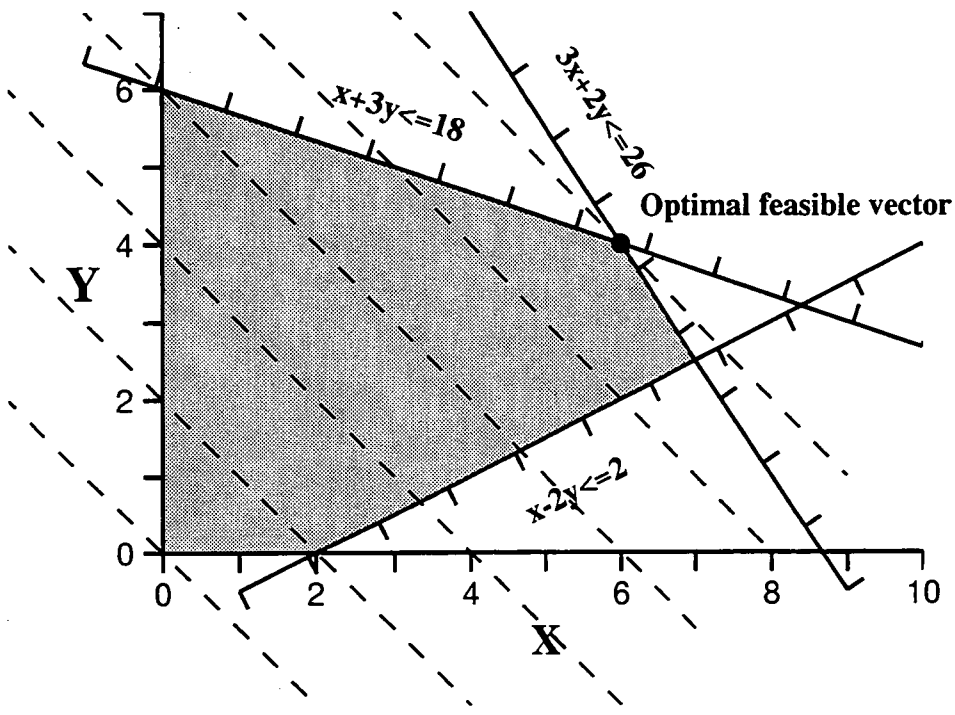

Figure 6.1: Example of a linear programming problem in two dimensions. The feasible region (grey shading) is bounded by the constraint equations containing inequalities in the form of equations 6.2 and 6.3. Feasible basic vectors lie at the vertices of the feasible region. The objective function Z=X+Y is maximised at a vertex of the feasible region, at the optimal feasible vector (dot). Dashed lines are contours of Z.

$$\mathbf{g}^T\mathbf{m} \le a. \tag{6.8}$$

The moment tensor components can be either positive or negative. In linear programming problems such an unconstrained variable is expressed as the difference between two non-negative variables:

$$\mathbf{m} = \mathbf{m}^+ - \mathbf{m}^-. \tag{6.9}$$

with the requirement that one of these variables equals zero. Each inequality is converted into an equality by introducing non-negative slack variables, *s* and *e*:

$$\mathbf{g}^T\left(\mathbf{m}^+ - \mathbf{m}^-\right) + s - e = a. \tag{6.10}$$

In matrix form, the system of constraint equations is then

$$\left[\ \mathbf{g}^T \ \middle|\ -\mathbf{g}^T \ \middle|\ \mathrm{I} \ \middle|\ -\mathrm{I}\ \right]\begin{bmatrix}\mathbf{m}^+\\ \mathbf{m}^-\\ \mathbf{s}\\ \mathbf{e}\end{bmatrix} = \mathbf{b} \tag{6.11}$$

or more briefly,

$$\mathrm{A}\mathbf{x} = \mathbf{b}.$$

All the inequalities of the form of equation 6.8 are satisfied if and only if $\mathbf{e} = \mathbf{0}$ in equations 6.11. Equations involving linear combinations of components of $\mathbf{m}$ can be added to this system of equations. For example, to constrain the moment tensor to be deviatoric, we add the constraint equation

$$M_{xx} + M_{yy} + M_{zz} = 0. \tag{6.12}$$

The simplex algorithm maximises the function

$$z \stackrel{def}{=} \mathbf{c}^T\mathbf{x} \tag{6.13}$$

subject to the constraints of equations 6.11. Seeking a feasible solution corresponds to the choice

$$\mathbf{c} = \left[\mathbf{0} \mid \mathbf{0} \mid \mathbf{0} \mid -\mathbf{1}\right]^T \tag{6.14}$$

If a feasible solution exists (for which $\mathbf{c}^T\mathbf{x} = 0$), then all components of $\mathbf{e}$ are zero in equations 6.11, and all the observations are satisfied. If no feasible solution exists, then $\mathbf{x}$ is the non-feasible solution that minimises the mean absolute deviation (the L1 norm) of the residuals of the observations that are not satisfied. This is equivalent to minimising the function

$$E = \sum_{i \in P} |u_i| + \sum_{i \in Q} |u_i - a_i| + \sum_{i \in R} |u_i^{(1)} - r_i u_i^{(2)}| \qquad 6.15$$

where P is the set of polarity constraints that are not satisfied, Q is the set of amplitude constraints that are not satisfied and R is the set of amplitude-ratio constraints that are not satisfied.

If a feasible solution exists then other objective functions can be used to maximise physically motivated linear combinations of the components of $\mathbf{m}$. For example, the objective function

$$\mathbf{c} = [1 \;\; 0 \;\; 1 \;\; 0 \;\; 0 \;\; 1 \,|\, -1 \;\; 0 \;\; -1 \;\; 0 \;\; 0 \;\; -1 \,|\, \mathbf{0} \,|\, \mathbf{0}]^T \qquad 6.16$$

maximises the isotropic (explosive) component of the moment tensor, $M_{xx} + M_{yy} + M_{zz}$. *Julian* (1986) presents other examples.

6.3 Inversion procedure

6.3.1 Measurement of polarities and amplitudes

6.3.1.1 Phases used

The motion of an *S* wave is partitioned into two components, which have orthogonal particle motions. The two components propagate independently but at the same speed. *SH* waves have horizontal particle motion, and the particle motion of *SV* waves is in vertical planes containing the propagation direction. Both SH and SV particle motions are perpendicular to the propagation direction, and so *SV* motion is only vertical if the ray is horizontal. Polarities and amplitudes were measured for *P*, *SH* and *SV* waves.

6.3.1.2 Seismogram rotation and filtering

SH and *SV* polarities and amplitudes were measured from horizontal-component seismograms that were rotated from the field orientations. *SH* measurements were made from transverse components, oriented perpendicular to the station-to-epicentre azimuth, and *SV* measurements are made from radial components, oriented parallel to the station-to-epicentre azimuth.

Scattering and attenuation of seismic waves are frequency dependent, and have more effect on the high-frequency components of a seismic signal. Thus the low-frequency

components suffer less from propagation effects, and it is easier to extract source-mechanism information from them.

6.3.1.3 The use of *S*-wave data from close stations

The directions of the radial and transverse components are undefined at the epicentre, and are very sensitive to epicentral errors for close observations. However, geographically oriented horizontal components for stations close to the epicentre are insensitive to minor epicentral mislocations, so it is better to use amplitudes from the north and east horizontal components for close stations.

6.3.2 Wave-propagation corrections to amplitude ratios

6.3.2.1 Attenuation

The attenuation of seismic waves is quantified by the "figure of merit", $Q(f)$, where

$$A(f) = A_0(f)R^{-1}\exp-[\pi ft/Q(f)]. \qquad 6.17$$

f is frequency, $A_0(f)$ is the radiation pattern at the source, $A(f)$ is the radiation pattern at the observation point, R is the geometrical-spreading coefficient and t is the wave travel time.

The ratio of P and S radiation patterns at the source is

$$\frac{A_{P_0}}{A_{S_0}} = \frac{A_P}{A_S}\frac{R_P}{R_S}\exp[\pi f\left(t_P/Q_P - t_S/Q_S\right)] \qquad 6.18$$

or

$$\frac{A_{P_0}}{A_{S_0}} = \frac{A_P}{A_S}\frac{R_P}{R_S}\exp[\pi f\, t_P/Q_P\left(1-\left(Q_P/Q_S\right)\left(V_P/V_S\right)\right)], \qquad 6.19$$

where A_P and A_S are the observed P-wave and S-wave amplitudes, respectively.

If variations in V_P/V_S are small, then it can be assumed that $R_P \cong R_S$. Calculation of the P:S amplitude ratio at the source then requires t_P and t_S (or t_P and V_P/V_S) and estimates of Q_P and Q_S along the ray path.

6.3.2.2 Free surface effects

Seismic waves are reflected at the free surface and the motion of the sensor is the sum of the motions of the incident and reflected waves. An incoming *SH* wave is reflected only as an SH wave of the same amplitude, and thus the sensor motion is double that of the incoming wave. *P* and *SV* waves are each reflected as both *P* and *SV* waves. Thus the total motion of a *P* wave is the sum of the incident and reflected *P* waves and the reflected *SV* wave. The amplification factor of the incident *P*- and *SV*-wave amplitudes is a complicated function of the angle of incidence and the wave

speeds, and can be calculated using the *rtcoef* program (B. R. Julian, *pers. comm.*), which uses the method of *Frasier* (1970). SV waves with incidence angles greater than about 35° undergo severe amplitude distortions at the free surface because of complicated conversion effects, rendering them practically unusable for focal mechanism studies.

6.3.3 Estimation of amplitude and amplitude-ratio error bounds

There are three main sources of amplitude uncertainty: unknown instrument gains, seismogram noise, and unmodelled seismic-wave propagation effects. The use of amplitude ratios decreases the latter uncertainty, if the effects are similar for the types of wave used. The use of amplitude ratios also eliminates the need to know the absolute sensitivities of individual stations.

For amplitudes, the estimated error bounds due to noise and propagation effects, expressed as a fraction of the measured amplitude, are used to calculate the total fractional error bound on the amplitude, σ_{total}:

$$\sigma_{total} = \sigma_n + \sigma_p \qquad 6.22$$

where σ_n is the estimated fractional error bound due to noise and σ_p is the estimated fractional error bound due to unmodelled propagation effects. The estimated fractional error bound for an amplitude ratio are:

$$\sigma_{total} = \sigma_a + \sigma_b + \sigma_p \qquad 6.23$$

where σ_a and σ_b are the estimated fractional error bounds in the two respective amplitudes due to noise.

The additional fractional error bounds for amplitudes and amplitude ratios due to unmodelled propagation effects were estimated statistically. This was done by calculating the goodness-of-fit for a range of additional fractional error bounds. The chi-square statistic, χ^2 is

$$\chi^2 = \sum_{i=1}^{N} \left(\frac{y_{i(o)} - y_{i(c)}}{\sigma_i} \right)^2 \qquad 6.24$$

where $y_{i(o)}$ and $y_{i(c)}$ are the i^{th} observed and calculated data, respectively, and σ_i is the estimated fractional error bound in the i^{th} datum. The probability that χ^2 should exceed a particular value by chance is the function $Q(\chi^2|\nu)$, where ν is the number of degrees of freedom (the number of observations minus the number of independent moment tensor components). $Q(\chi^2|\nu)$ can be calculated using the function *gammq* (*Press et al.*, 1992, p 218). Very low $Q(\chi^2|\nu)$ values, *e.g.*, <0.001, indicate that the uncertainties are under-estimated. An appropriate level of additional uncertainty to account for unmodelled propagation effects was determined by inverting data with a range of

additional uncertainty estimates, and calculating χ^2 and $Q(\chi^2|\nu)$. An appropriate σ_p value will have $0.001 < Q(\chi^2|\nu) << 1$.

6.3.4 Wave-speed models

Using a three-dimensional wave-speed model to locate earthquakes and trace rays can significantly affect the computed positions of stations on the focal sphere (Section 1.3.4.3.4). For the 1981 data from the Hengill area the use of a one-dimensional wave-speed model causes stations to be mislocated by up to 40° on the focal sphere compared with the results obtained using a three-dimensional model (*Foulger and Julian*, 1993). It is thus important to use the most accurate wave-speed model available for focal mechanism studies, both to locate events and to determine ray paths.

6.3.5 Inverting amplitudes to determine scalar moments

Observations of polarities and amplitude ratios give no information about scalar moments. If no absolute amplitudes are used, computed moment tensor components must be arbitrarily normalised. To calculate scalar moments, amplitude observations are required from at least one station.

Amplitude values must be corrected for propagation effects (equation 6.17), which requires knowledge of geometrical spreading and attenuation. In the geometrical-optics approximation, energy is assumed to propagate along rays, with the total power within a "pencil" of rays remaining constant. The power per unit area of wavefront E at the surface is related to the power per unit solid angle I at the source by

$$\frac{E}{I} = \frac{d\Omega}{dA \cos i_1}, \qquad 6.25$$

where a tube of rays subtending a solid angle $d\Omega$ at the source spreads out to cover an area dA at the surface, and i_1 is the ray incidence angle at the surface (*Julian and Gubbins*, 1977).

$$d\Omega = di_0 dj_0 \sin i_0$$

and

$$dA = dN dE, \qquad 6.26$$

so

$$\frac{E}{I} = \frac{\sin i_0}{\cos i_1} \frac{\partial(i_0, j_0)}{\partial(N, E)} = \frac{\sin i_0}{\cos i_1} \begin{vmatrix} \frac{\partial i_0}{\partial N} & \frac{\partial j_0}{\partial N} \\ \frac{\partial i_0}{\partial E} & \frac{\partial j_0}{\partial E} \end{vmatrix}. \qquad 6.27$$

where i_0 and j_0 are the ray take-off angle (measured from the nadir) and azimuth, respectively, at the source. The geometrical spreading coefficient is:

$$R^2 = \frac{I}{E} \qquad 6.28$$

(*Aki and Richards*, 1980, p 99) and so, from equation 6.17,

$$A(f) \propto \sqrt{\frac{E}{I}} A_0(f). \qquad 6.29$$

6.3.6 Measurement of goodness-of-fit

Two measures of the quality of the data fit are available. These are (1) the number of polarity misfits and (2) some measure of the absolute misfit of amplitudes and amplitude ratios. In local-earthquake focal mechanism studies that use *P*-wave polarities only, it is often considered acceptable to have one or two polarity misfits, especially if the stations concerned are close to the nodal planes of the solution. These misfits are usually explained as the result of using inadequate wave-speed models to locate the earthquakes, or as station polarity reversals. In this project, a three-dimensional wave-speed model was used to locate the earthquakes, and exact ray tracing was used to map stations onto the focal sphere. The station polarities were confirmed by setting off an explosion. However *SH* and *SV* polarities are much less dependable than *P* polarities, and even when only high-quality arrivals are picked, outliers may occur and so a small number of *S* polarity misfits is to be expected.

The mean absolute relative deviation (MARD) is the mean of the absolute misfits of all data, where each misfit is normalised by the measured value (*Julian and Foulger*, 1996). For an amplitude observation, the MARD is defined as

$$E \stackrel{def}{=} \frac{1}{N} \sum_{i=1}^{N} \left| \frac{u_i - a_i}{a_i} \right| \qquad 6.30$$

and for amplitude ratios as

$$E \stackrel{def}{=} \frac{1}{N} \sum_{i=1}^{N} \left| \frac{a_i^{(2)} u_i^{(1)} - a_i^{(1)} u_i^{(2)}}{a_i^{(1)} u_i^{(1)} + a_i^{(2)} u_i^{(2)}} \right| \qquad 6.31$$

where a_i, $a_i^{(1)}$ and $a_i^{(2)}$ are the observed amplitudes and u_i, $u_i^{(1)}$ and $u_i^{(2)}$ are the corresponding theoretical amplitudes.

The MARD can be used to compare the fit of moment tensors obtained from inversion of amplitudes and amplitude ratios from the same earthquake. It has been used

to show that inversion of amplitude ratios gives a better fit to the data, which supports the assumption that amplitudes are affected more by propagation effects than are amplitude ratios (*Julian and Foulger*, 1996).

The MARD can give misleading results for amplitude ratios when one of the phases is of the incorrect polarity. For example if $a_i^{(1)}$ and $u_i^{(1)}$ are of opposite sign and $a_i^{(2)}$ and $u_i^{(2)}$ are of the same sign then the denominator in equation 6.31 can approach zero, giving a high MARD value.

An alternative measure of the data fit is the mean absolute deviation, which is the mean of the absolute misfits of all the polarity, amplitude and amplitude ratio data. For an amplitude ratio, the mean absolute deviation is measured as:

$$|a^{(1)} - ra^{(2)}| \qquad 6.32$$

where the predicted ratio $r = u^{(1)}/u^{(2)}$.

When a moment tensor is calculated by inverting only polarities and/or amplitude ratios (*i.e.*, no absolute amplitude values are used) the moment tensor is arbitrarily scaled. This means that the calculated amplitudes, and thus the mean absolute deviation, are in arbitrary units. To compare the mean absolute deviations of different mechanisms the moment tensor components need to be normalised.

6.3.7 Display of moment tensors

Several complicated diagrams have been proposed that display the principal moments and the directions of the principal axes (*e.g.*, *Riedesel and Jordan*, 1989; *Sipkin*, 1993). An alternative approach is to "decompose" the moment tensor and display the relative magnitudes of the three principal moments, which provide a description of the source type that is independent of the source orientation (Section 2.2). This information can be parameterised in many different ways, including using ε values or the magnitudes of volumetric, DC and CLVD components (Section 2.2).

Hudson et al. (1989) introduced the "source-type plot" which uses two parameters:

$$T \stackrel{def}{=} -2\varepsilon = \frac{2m_1'}{|m_3'|} \qquad 6.33$$

and

$$k \stackrel{def}{=} \frac{m^{(V)}}{|m^{(V)}| + |m_1'|}. \qquad 6.34$$

The parameter ε is defined by equation 2.3, m_1', m_2' and m_3' are the principal moments of the deviatoric moment tensor arranged so that $|m_1'| \le |m_2'| \le |m_3'|$, and the volumetric component of the moment tensor $m^{(V)}$ is defined by equation 2.1. The parameter k is a measure of the relative volumetric change of the source, with $-1 \le k \le 1$. For deviatoric

mechanisms, including DCs, $k = 0$. The source-type plot is scaled so that the probability density of all source types is uniform throughout the plot, assuming that the principal moments have a uniform distribution (*Hudson et al.*, 1989).

In this thesis, I adopt a similar but simpler diagram, with k plotted against ε (The "ε-k diagram", Figure 6.2). The requirement of equal probability density of all source types leads to a complicated plot which is difficult to comprehend, and is unnecessary for the interpretation of the results presented here. In addition, ε is a more widely used parameter than T.

On an ε-k diagram, any combination of a DC and an opening tensile crack (TC) plots within a three-sided region defined by curved lines (the "TC-DC region": figure 6.2). Within this region, any DC and TC combination of a fixed geometry plots along a curved line connecting the DC point to the TC point (*e.g.*, the solid squares in Figure 6.2). If the T axis of the TC lies in the plane of the T and P axes of the DC then the mechanisms are restricted to one line, the "TC-DC line", that forms the rightmost edge of the TC-DC region. The largest departures from the TC-DC line occur when the TC is orthogonal to both DC nodal planes. The addition of other components to a DC and

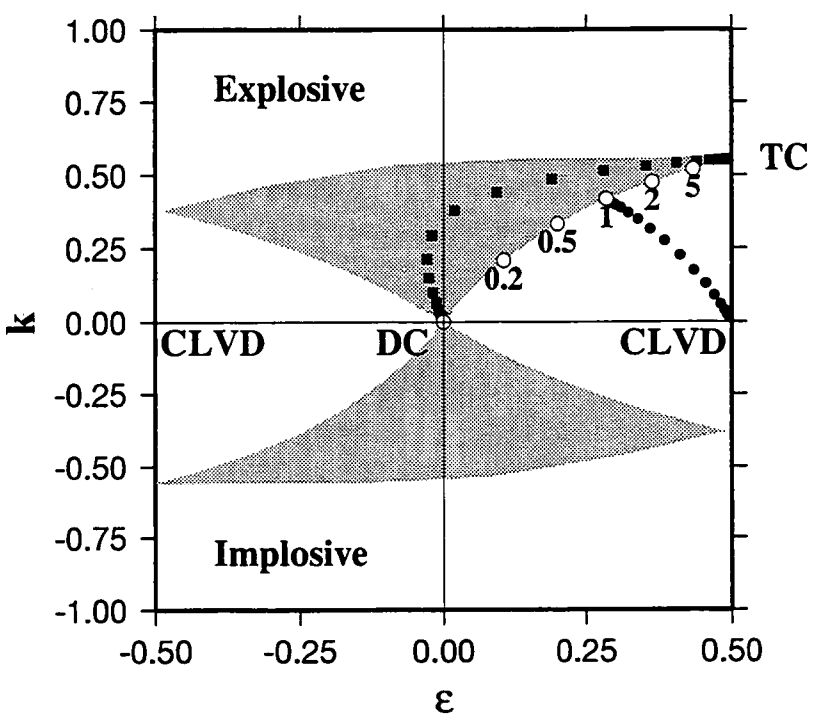

Figure 6.2: An ε-k diagram showing positions of various source types. DC: double couple; CLVD: Compensated linear vector dipole; TC: tensile crack. Grey areas are positions of combined shear-tensile faulting mechanisms, for opening ($k > 0$) and closing ($k < 0$) tensile faults (the "TC-DC regions"); Open circles: combined tensile-shear faulting under restricted conditions (the "TC-DC line": see text), for different values of $m^{(tf)}/m^{(sf)}$. Solid squares: mechanisms with the tensile fault T axis is inclined at 45° to the T-P plane of the shear fault. Solid circles: mechanisms with a CLVD component added to a tensile-shear mechanism.

TC combination can move the mechanism out of the TC-DC region. For example, the addition of a CLVD component to a point on the TC-DC line moves the point along a curved line towards the CLVD point as the magnitude of the CLVD component is increased (figure 6.2). For a closing TC, there is a mirror-image TC-DC line and TC-DC region for negative k.

6.4 Data processing scheme

6.4.1 Seismogram rotation and filtering

The hypocentre locations obtained using the final three-dimensional wave-speed model were used to calculate station-to-epicentre azimuths. The *ahrotate* program (B. R. Julian, *pers. comm.*) reads sets of three-component AH-format seismograms and carries out a numerical rotation of the horizontal components to the radial and transverse directions (Figure 6.3). The *ahrotate* program follows the convention that the positive radial component direction is away from the source, and the positive transverse component is to the left (anti-clockwise) as viewed from the source. The built-in frequency-dependent filter within the *epick* program (Section 3.2.3) was used to perform low-pass frequency filtering by applying a three-pole Butterworth filter to seismograms.

6.4.2 The *focmec* program

The *focmec* program (B. R. Julian, *pers. comm.*) uses the simplex method (Section 6.2.1) to seek moment tensors that are consistent with *P*, *SH* and *SV* polarity, amplitude and amplitude ratio observations. Any combination of polarity, amplitude or amplitude ratio data may be used. The moment tensor can be constrained to be deviatoric (equation 6.12). The program first seeks a feasible solution, and if successful can then apply user-specified objective functions to maximise linear combinations of the moment tensor components. If no feasible solution exists, then the moment tensor that minimises the mean absolute deviation of the data misfit is calculated.

Amplitude values input to *focmec* need to be normalised to a unit distance from the source and multiplied by the factor $4\pi\rho v^3$, where ρ is density and v is *P*- or *S*-wave speed, as appropriate, at the source. Amplitude ratios need only be normalised by the ratio of the wave speeds of the two phases involved. Positive *P*-wave motion is upwards, positive *SH* motion is to the right (clockwise) as viewed from the source, and positive *SV* motion is upwards (towards the source).

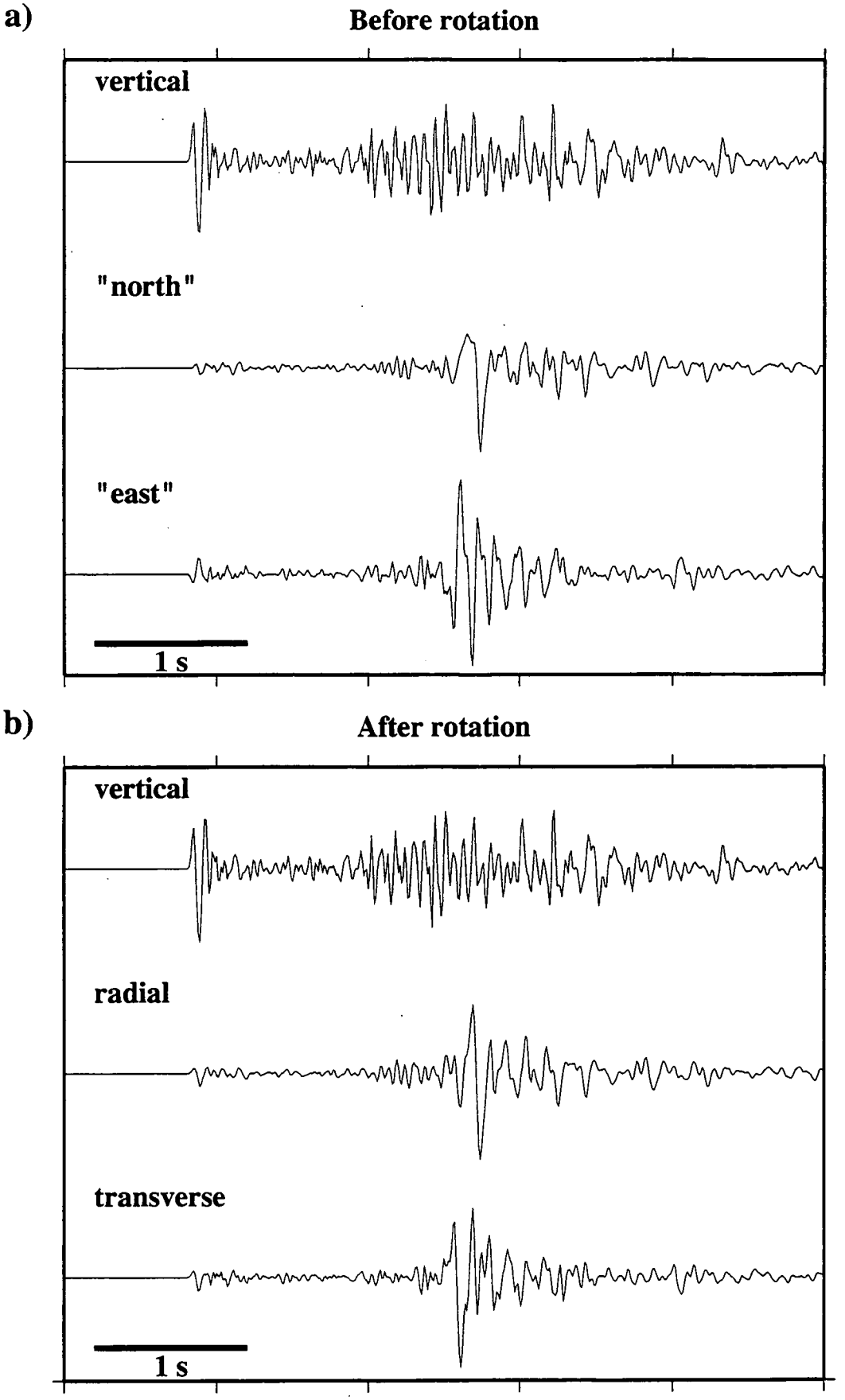

Figure 6.3: An example of seismogram rotation, for station H020 and event 218.023219.1. (a) The seismograms before rotation. The "north" component is aligned to magnetic north (339°N), and the "east" component to 069°N. (b) The seismograms after rotation to radial and transverse directions. The station-to-epicentre azimuth is 136°N, so the radial component is aligned to 316°N (close to the "north" component) and the transverse component to 226°N (close to the "east" component, but of opposite polarity). The window width is 5 s.

6.4.3 Preparation of data for *focmec*

Two UNIX Bourne-shell scripts, *el2fm.rat* and *el2fm.amp*, were used to prepare polarity and amplitude data (Appendix 6). Both scripts process output from the q*loc3d* program (Section 5.2.4). The *el2fm.rat* script prepares polarity and amplitude-ratio data, multiplying amplitudes by v^3 and correcting for the free surface effect. *P*:*S* amplitude ratios are optionally corrected for differential attenuation between *P* and *S* waves. Amplitude-ratio uncertainties are calculated from equation 6.23, using noise uncertainties, if these are available, and an optional additional uncertainty specified by the user. The amplitude ratios *P*:*SH* and *SH*:*SV* are output for each station if these phases are available. At stations where there are *P* and *SV* picks, but no *SH* pick is available, *P*:*SV* ratios are used instead. For close stations picks made on the north and east horizontal components are output as the ratios *P*:*SN* and *P*:*SE*.

The *el2fm.amp* script prepares polarity and amplitude data, multiplying amplitudes by $4\pi\rho v^3$ and correcting for the free surface effect and optionally attenuation. The uncertainties are estimated in the same way as *el2fm.rat*. Geometrical spreading may either be calculated by the script *get.gs* (Appendix 6), or can be approximated by assuming straight-line rays. The program *bendray* (B. R. Julian, *pers. comm.*) is called by *get.gs* to calculate geometrical spreading. The program traces rays in a three-dimensional wave-speed model using the "bending" method, and calculates $\partial i_0/\partial N$, $\partial j_0/\partial N$, $\partial i_0/\partial E$ and $\partial j_0/\partial E$.

The program *noisepick*, written by the author of this thesis, measures seismogram noise levels. The program reads AH-format seismograms and *epick*-format pick files, and measures the RMS value of the seismogram immediately before each pick. The window lengths used for averaging are user-defined, with defaults of 1 s for *P* waves and 50% of the *S*–*P* time for *S* waves.

6.4.4 Presentation of the results

Plots of polarity data in this thesis follow the convention of *focmec*, with positive polarities (solid dots) for *P*, *SH* and *SV* waves indicating upwards, clockwise and towards-source motion respectively (Section 6.4.2). Amplitude ratios are represented by arrows of unit length plotted on the focal sphere. For a ratio $A:B$, the arrow is oriented so that its slope equals A/B (*Julian and Foulger*, 1996; Figure 6.4). This means that information on the size of the ratio and the polarities of both phases is contained in the plot, because the quadrant in which the arrow plots depends on the signs of the phases. Also, such a plot is not disproportionately sensitive to relative amplitudes that tend to zero. The ratio uncertainty bounds are shown by pairs of lines forming an acute angle. Thus if the arrow falls within the acute angle, the amplitude observation is consistent with the moment tensor result (Figure 6.4).

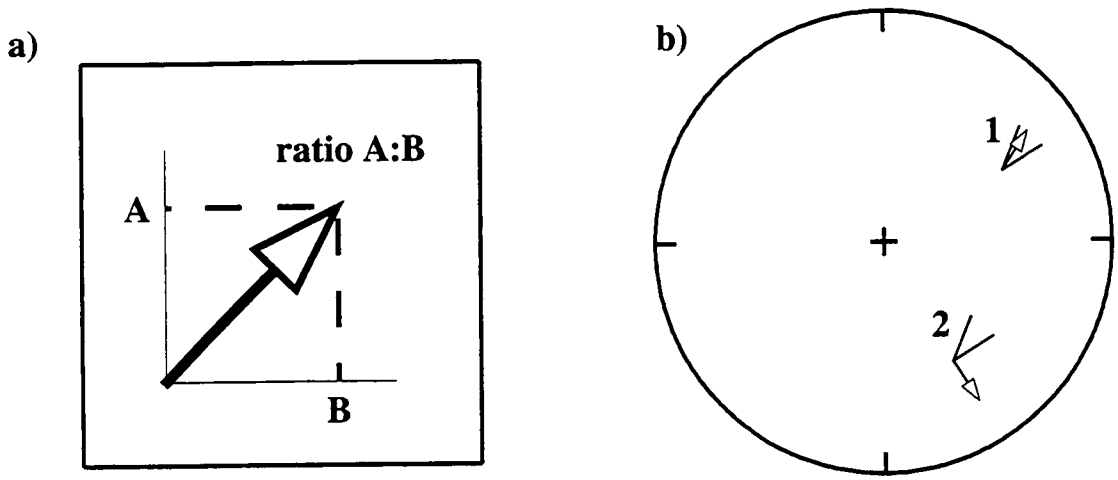

Figure 6.4: The method of representing amplitude ratios on focal mechanism plots. (a) The ratio A:B is shown as an arrow of unit length and slope A/B. The orientation of the arrow depends on the ratio A:B and the signs of A and B. (b) Arrows show calculated A:B ratios, and the lines forming an acute angle show the estimated error bounds. An observation is consistent with the calculated ratio if the arrow lies within the acute angle (*e.g.*, 1) and is inconsistent otherwise (*e.g.*, 2).

6.5 Inversion of data from the Hengill area

6.5.1 Earthquake selection

The seismograms from all earthquakes with at least 20 measured *P*-wave arrivals were rotated and examined using *epick*. Events were discarded if the rotated and filtered seismograms had low signal-to-noise ratio, or if the pickable stations did not give adequate focal sphere coverage. Earthquakes in the periphery of the network, for example in the Ölfus lowlands, did not have good focal sphere coverage and focal mechanisms could only be reliably determined for well-recorded earthquakes (Figure 6.5). Polarity and amplitude measurements were made for 98 earthquakes, which are divided into 9 geographical groups (Figure 6.6).

The selected earthquakes lie mainly in the geothermal field, between 1.9 and 6.0 km depth. Earthquakes in the Gigir cluster (Section 3.5) had good coverage, and the 13 best-recorded earthquakes from there were processed. Only a few earthquakes in the north, including the Marardalur and Dyradalur clusters (Section 3.5) were suitably well-recorded. An average of 22 *P*-wave and 17 *S*-wave amplitude determinations were made per earthquake.

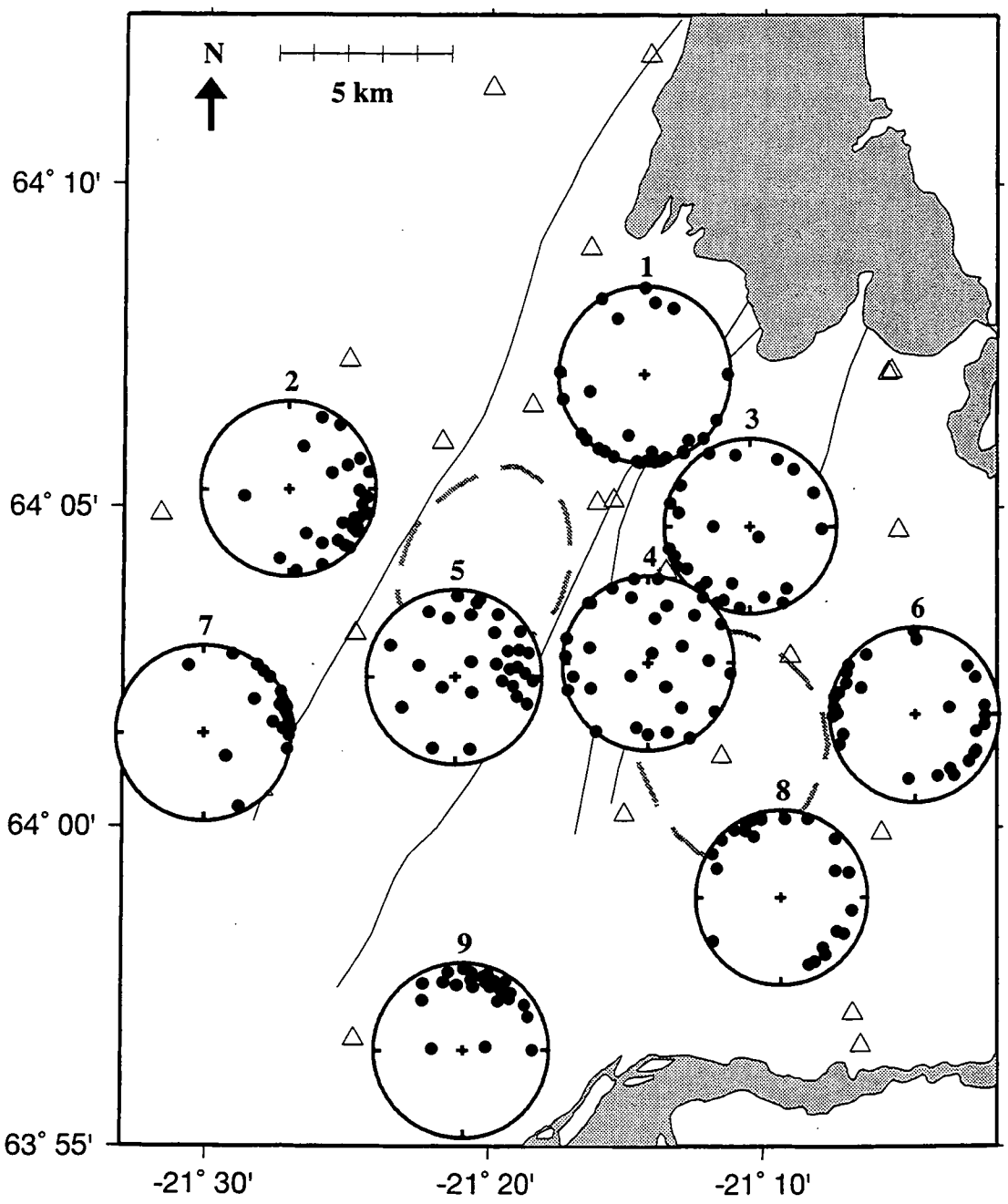

Figure 6.5: Map showing variations in focal sphere coverage in the Hengill area, with upper focal-hemisphere projections of the station positions (solid dots) for earthquakes located at the centre of each plot. Earthquakes 3, 4 and 5 had sufficient focal sphere coverage to allow high-quality focal mechanism determinations. Triangles: stations; dashed lines: outlines of volcanic centres; thin lines: outlines of the volcanic systems.

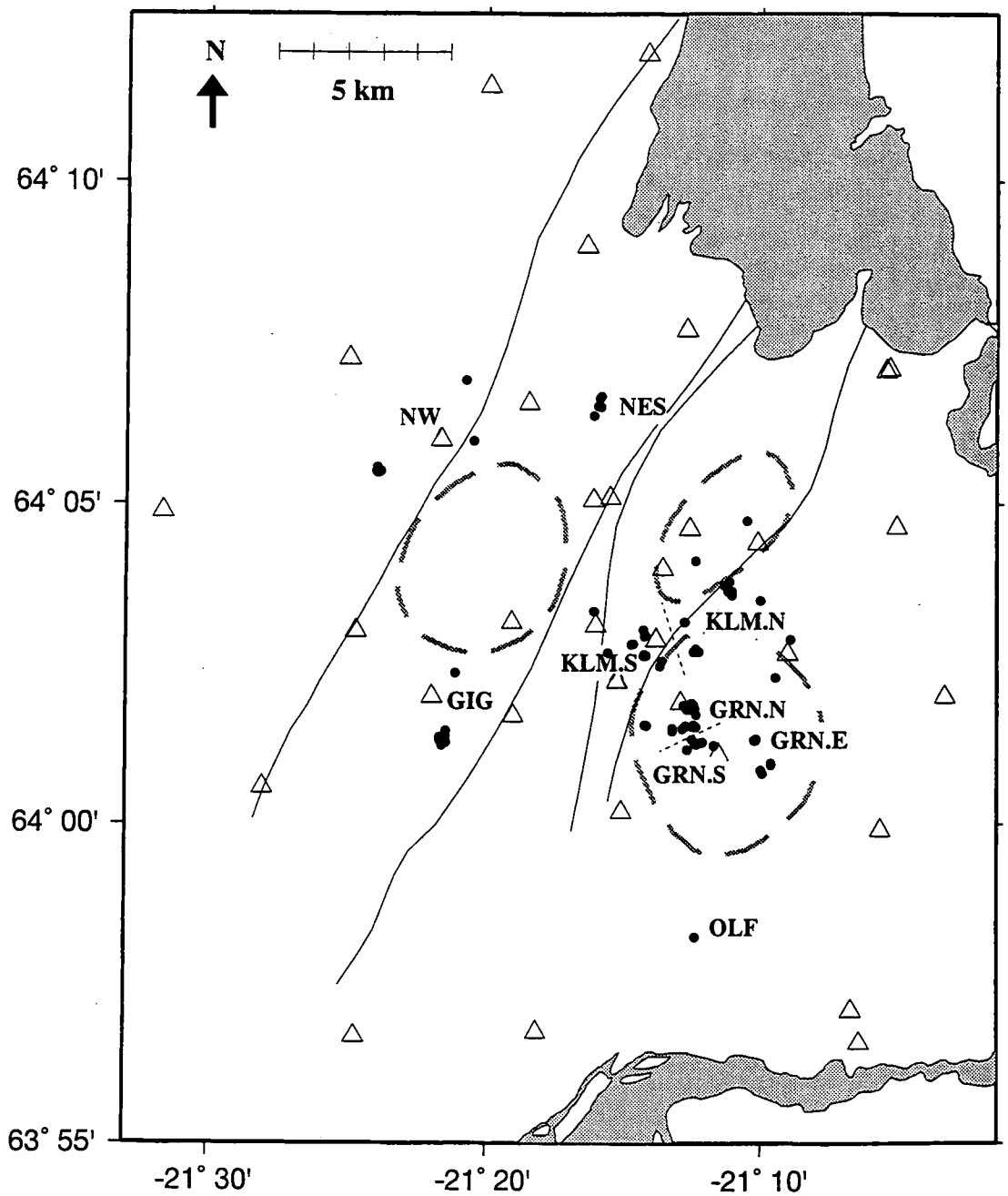

Figure 6.6: Map showing the locations of the earthquakes (solid dots) for which moment tensors were calculated, and the names and positions of the 9 groups. Group names are NW = northwest; NES = Nesjavellir; GIG = Gigir; KLM = Klambragil; GRN = Grensdalur; OLF = Ölfus, and E, N, S mean east, north and south respectively. Other symbols as for Figure 6.4.

6.5.2 Amplitude measurement

6.5.2.1 Choice of high-frequency cut-off for low-pass filtering

To determine an appropriate corner frequency for low-pass filtering, the seismograms from a well-recorded event (258.074123.1) were filtered with different corner frequencies (Figure 6.7), and the amplitudes of *P*, *SH* and *SV* waves were measured from the filtered traces. For each corner frequency, amplitude ratios were inverted using *focmec* to determine the best-fit moment tensor. Amplitude-ratio uncertainties were estimated from the noise levels on the filtered traces.

The resulting moment tensors are similar, with the goodness of fit improving with lower corner frequencies (Figure 6.8), At all stations, the measured polarities of each phase are the same for the suite of corner frequencies tested. Seismograms filtered with a 5-Hz filter tend to have clear arrivals and high signal-to-noise ratios, yielded more amplitude data than ones filtered with other frequencies and had the best data fit. Thus 5 Hz was chosen as the low-pass corner frequency for the Hengill data set.

6.5.2.2 Phase selection

Amplitude measurements were made only for phases with similar rise-times and similar waveform shapes. In rare cases only polarity measurements were made, for example where the waveform shape was non-uniform or the frequency response of the sensor seemed different from that of the other components. The SIL stations bja and hei had sensors with a different frequency response from the temporary stations, so only polarities were measured for these stations. *SV* arrivals with incidence angles greater than 25° were discarded.

6.5.3 Use of a three-dimensional wave-speed model

Between the one-dimensional and three-dimensional wave-speed models (Section 5.2) hypocentre locations differed by up to 1.5 km horizontally and 2.6 km vertically. The differences in the locations of well-constrained earthquakes suitable for focal mechanism determination are smaller, and thus result in relatively minor changes in station position on the focal sphere (Figure 6.9). For all the selected earthquakes the mean change in station positions is 6°, with a maximum change of 27°. Errors of this magnitude in station positions have only minor effects on derived moment tensors. However, to improve the accuracy of moment tensors as much as possible, all the earthquakes were located using the three-dimensional wave-speed models presented in Section 5.2, and ray take-off directions were determined by tracing rays through these models.

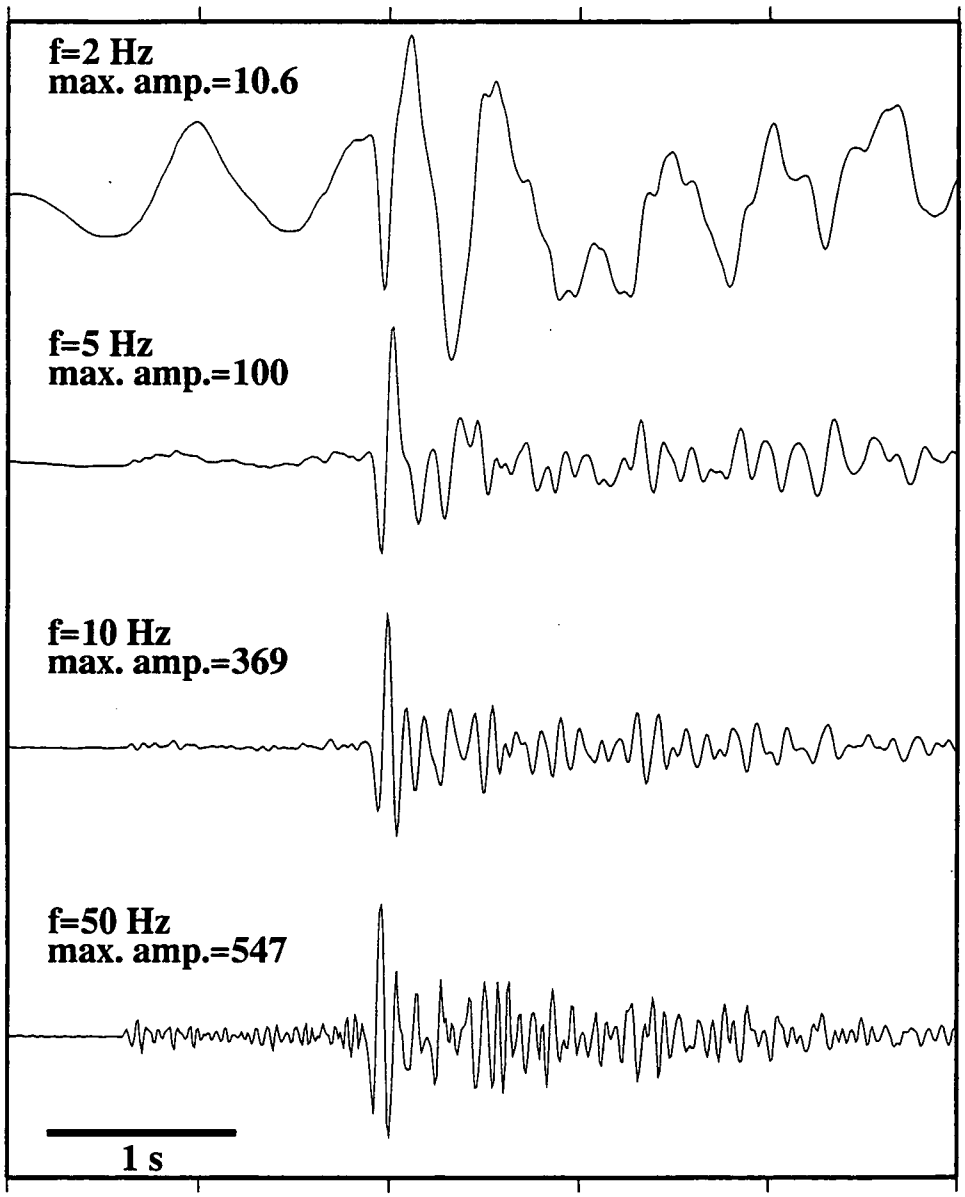

Figure 6.7: The effect of low-pass filtering on a seismogram. The transverse horizontal component from station H017 for event 258.074123.1 is shown, after low-pass filtering with corner frequencies of 2, 5, 10 and 50 Hz. The *SH* arrival is clear at all frequencies, but is more impulsive and has a higher signal-to-noise ratio for a corner frequency of 5 Hz. Note that, as this is a horizontal seismogram, the *P*-wave arrival is not clear for the lower corner frequencies. Seismograms are scaled according to their maximum amplitude. The window width is 5 s.

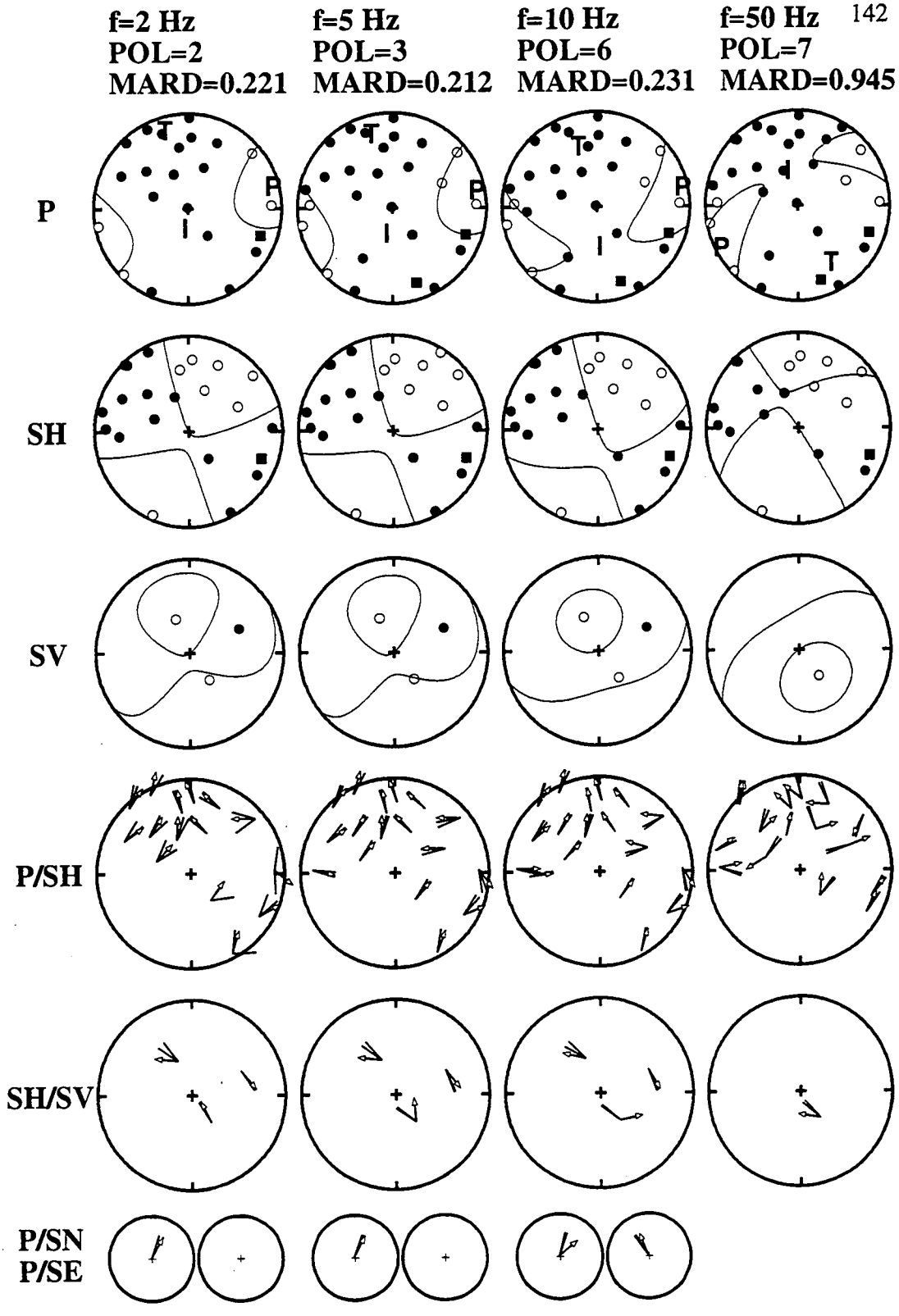

Figure 6.8: The effect of low-pass filtering of seismograms on the derived moment tensor. The moment tensors result from inversion of polarity and amplitude-ratio data from seismograms of event 258.074123.1 that have been low-pass filtered with corner frequencies of 2, 5, 10 and 50 Hz. POL: number of polarity misfits; MARD: mean absolute relative deviation. First three rows: measured *P*, *SH* and *SV* polarities (solid dots, positive; open dots, negative polarity); Thin lines: nodal lines; P, T and I: the positions of the principal axes of the moment tensors. Last three rows: *P/SH*, *SH/SV*, *P:SN* (bottom left) and *P:SE* (bottom right) amplitude ratios (*c.f.* Figure 6.4). The greatest number of picks was possible when the seismograms were filtered with a corner frequency of 5 Hz (2nd column).

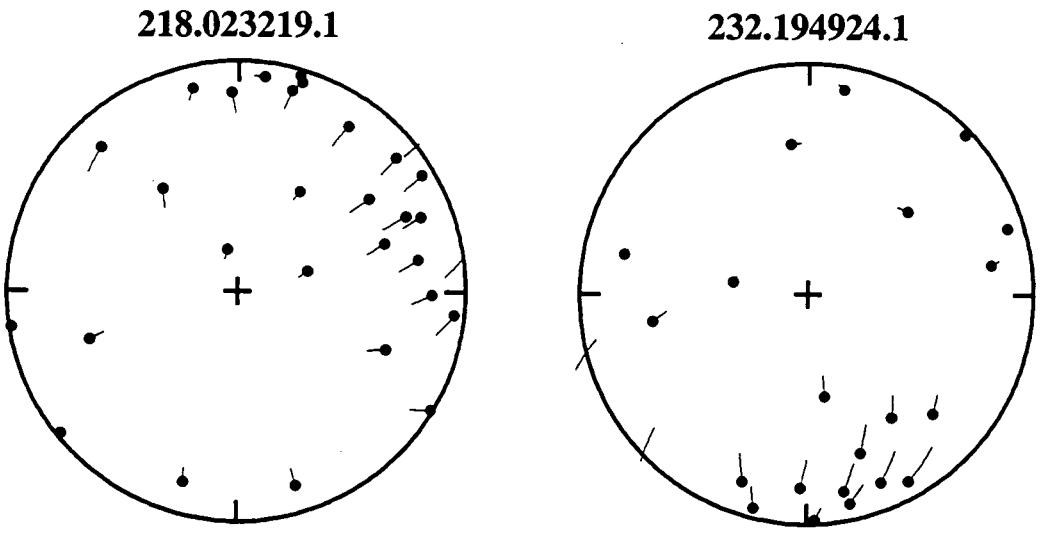

Figure 6.9: Differences in station focal-hemisphere distribution between one-dimensional and three-dimensional models. The changes in station positions on the focal sphere between one-dimensional (symbol tail) and three-dimensional (symbol head) wave-speed models are shown for events 218.023219.1 and 232.194924.1. Note that for event 232.194924.1, two of the rays were down-going (and projected to the other side of the focal sphere) in the one-dimensional model.

6.5.4 Accounting for attenuation

Menke et al. (1995) measured the attenuation of P and S waves in south Iceland and estimated $Q_P \cong 60$ and $Q_S \cong 95$ for the upper 4 km with the Hengill region (Section 1.3.1.4), giving $Q_P/Q_S = 0.63$. This ratio differs significantly from the commonly assumed value of 9/4, which corresponds to attenuation occurring only in shear (*Aki and Richards*, 1980, p192). *Foulger and Julian* (1994) estimated $t^* = T_P/Q_P = 0.03$ from a single P waveform recorded in 1991, giving $Q_P = 47$.

For the Q_P and Q_S values of *Menke et al.* (1995) attenuation has little effect on P:S amplitude ratios. From equation 6.17, with $f = 5\text{Hz}$, $T_P/Q_P = 0.03$ and $v_P/v_S = 1.77$,

$$\frac{A_{P_0}}{A_{S_0}} = 0.95\frac{A_P}{A_S} \qquad 6.35$$

In contrast, if $Q_P/Q_S \cong 9/4$,

$$\frac{A_{P_0}}{A_{S_0}} = 0.25\frac{A_P}{A_S}. \qquad 6.36$$

These two different estimates of attenuation were used to correct the observed amplitude ratios of event 258.074123.1. The attenuation estimated by *Menke et al.*

(1995) gives a much better fit to the data than the classical attenuation estimate does, and gives a slightly better fit than if attenuation effects are ignored (Figure 6.10).

An independent estimate of $1/Q_P$ and $1/Q_S$ may be obtained from the fits to *P* and *S* amplitudes corrected for different estimates of attenuation. This was done by inverting *P*, *SH* and *SV* amplitudes corrected for a range of $1/Q_P$ and $1/Q_S$ values from 0.005 to 0.035 for six earthquakes (Figure 6.11). The mechanisms with the best fit for each earthquake cover a broad range of attenuation values, showing that uncertainty in attenuation does not strongly affect the goodness of fit of the resulting moment tensors. In most cases, the best-fit mechanisms occur for $1/Q_P > 1/Q_S$, which is consistent with the estimates of *Menke et al.* (1995). Values of $Q_P \cong 60$, $Q_S \cong 95$ were used to correct amplitudes and amplitude ratios for all earthquakes.

6.5.5 Modelling of amplitude and amplitude-ratio error bounds

An appropriate additional fractional error bound to compensate for unmodelled propagation effects was chosen by calculating χ^2 and $Q(\chi^2|\nu)$ for a range in fractional error bounds (Section 6.3.3). To determine a value of σ_p, that could be used for all earthquakes, two earthquakes were processed using a range in σ_p from 0 to 0.7, for both amplitudes (Table 6.1) and amplitude ratios (Table 6.2), and χ^2 and $Q(\chi^2|\nu)$ values were calculated. Event 222.034641.1 is moderately well constrained earthquake, typical of the data set as a whole, with 41 amplitude measurements and 17 ratios. Event 258.074123.1 is one of the best-constrained earthquakes in the data set, with 50 amplitude measurements and 22 ratios.

Table 6.1: Goodness of fit and probability values for different amounts of additional fractional error bound for amplitudes

Additional fractional error bound	chi-square	DOF	Q
Event 222.034641.1			
0.0	2772.442	34	0.000000
0.1	508.123	35	0.000000
0.2	223.355	35	0.000000
0.3	123.416	35	0.000000
0.4	26.000	35	0.865026
0.5	24.984	35	0.894978
0.6	16.617	35	0.996417
0.7	12.706	35	0.999803
Event 258.074123.1			
0.0	5278.557	44	0.000000
0.1	881.937	44	0.000000
0.2	315.267	44	0.000000
0.3	155.591	44	0.000000
0.4	88.010	44	0.000091
0.5	51.544	44	0.202552
0.6	32.940	44	0.889269
0.7	24.605	44	0.992061

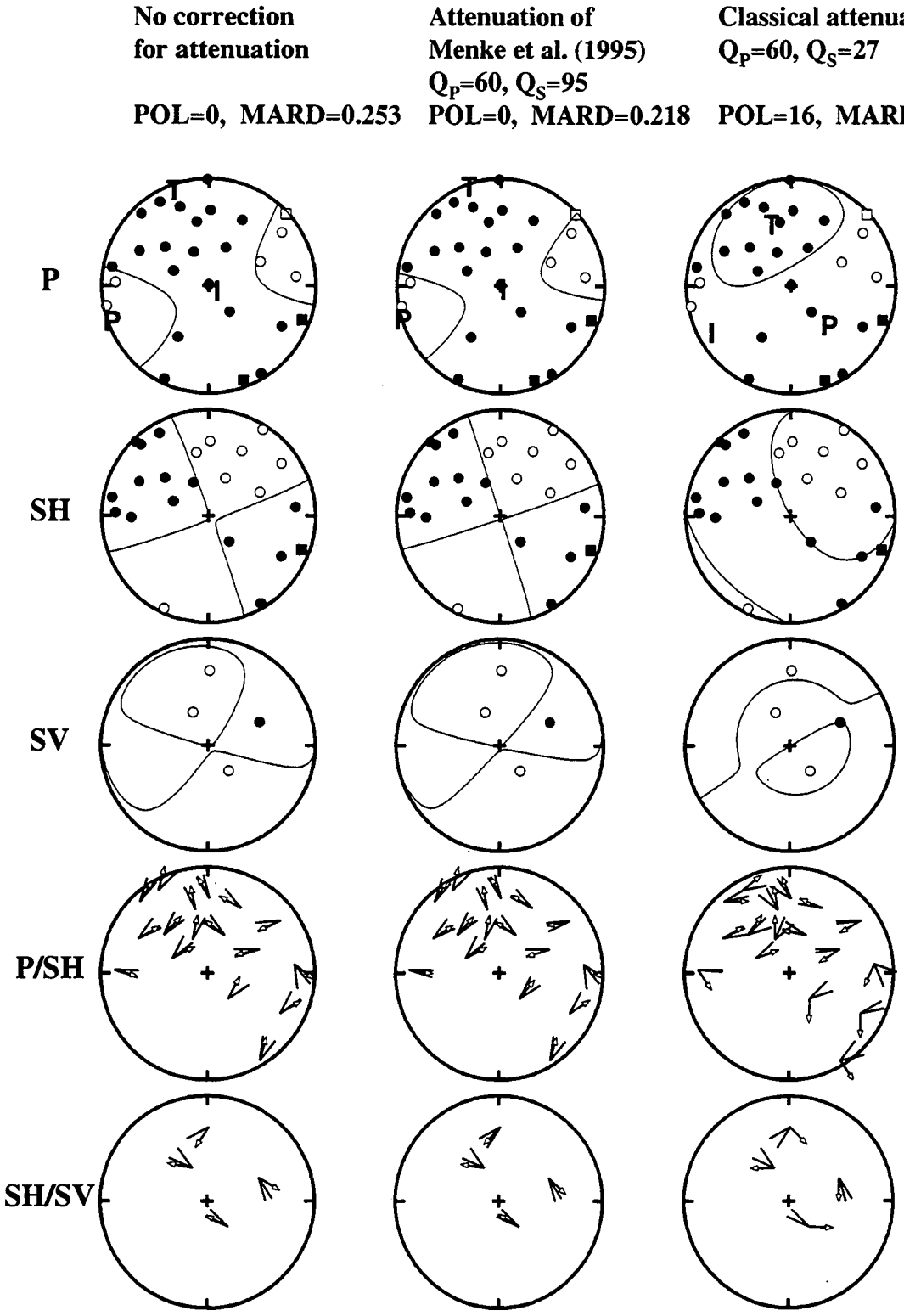

Figure 6.10: The effect of attenuation on the derived moment tensor. The moment tensors result from inversion of polarity and amplitude-ratio data from seismograms of event 258.074123.1, corrected for different assumptions about attenuation. Layout of figure is the same as that of Figure 6.8.

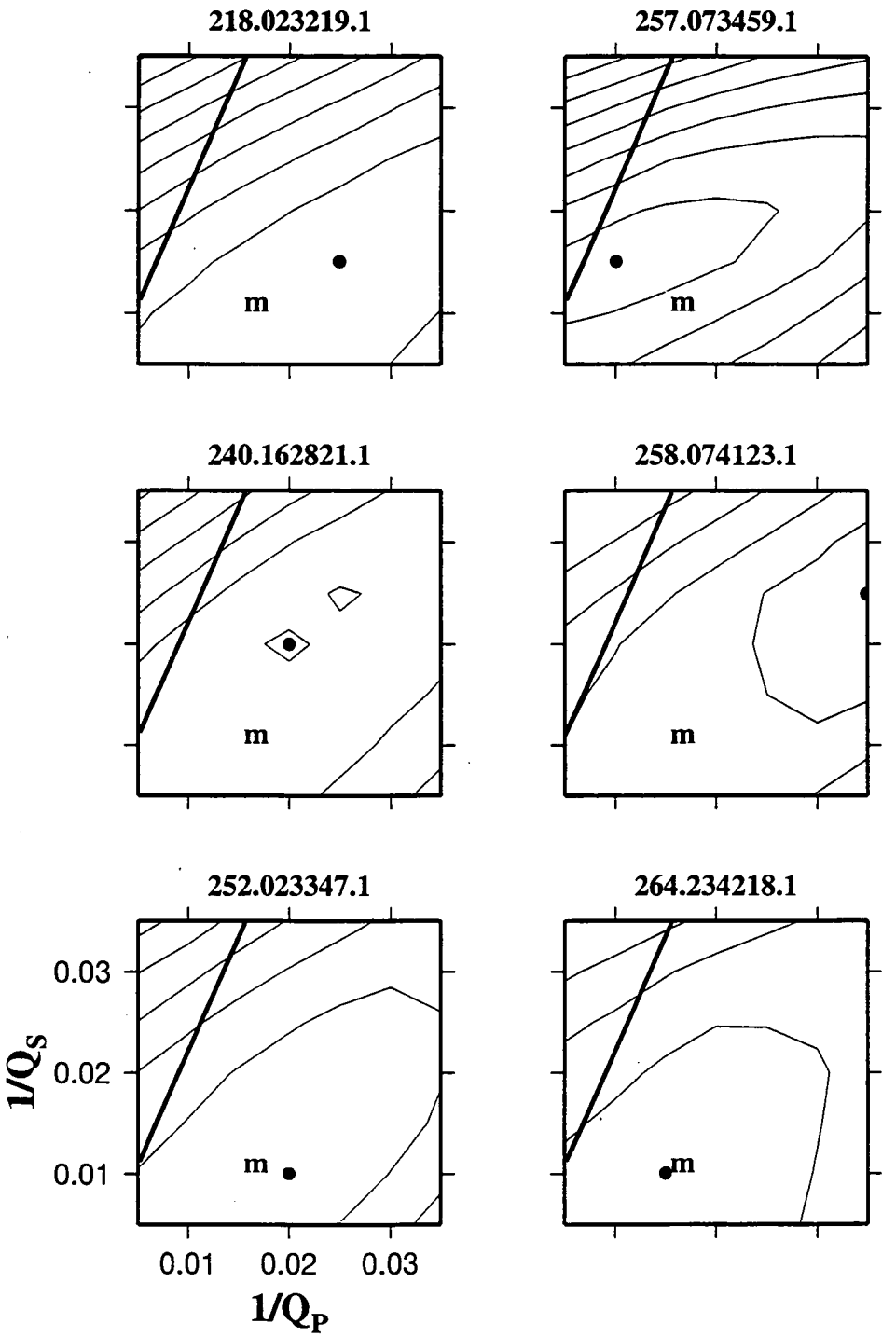

Figure 6.11: The effect of attenuation on the goodness-of-fit for six earthquakes. The mean absolute deviation is contoured for the moment tensors that result from the inversion of amplitude data corrected for different amounts of *P* and *S* attenuation. **m** shows the attenuation values of *Menke et al.*, (1995), and the solid line represents the range of values compatible with classical attenuation. Solid dots are the minimum mean absolute deviation values achieved for each earthquake.

For event 222.034641.1 values of $\sigma_p = 0.4$ gave values of $Q(\chi^2|\nu)$ that were within the acceptable range $(0.001 < Q(\chi^2|\nu) << 1)$ for both amplitudes and amplitude ratios. For the less-typical event 258.074123.1 $\sigma_p = 0.4$ is a slight over-estimate of the additional error bound for amplitude ratios and a slight under-estimate for amplitudes. A value of $\sigma_p = 0.4$ was selected for both amplitudes and amplitude ratios.

Table 6.2: Goodness-of-fit and probability values for different amounts of additional fractional error bound for amplitude ratios.

Additional fractional error bound	chi-square	DOF	Q
Event 222.034641.1			
0.0	421.354	12	0.000000
0.1	183.642	11	0.000000
0.2	66.048	12	0.000000
0.3	34.328	12	0.000599
0.4	27.221	12	0.007181
0.5	17.474	12	0.132630
0.6	9.715	11	0.556206
07	8.917	10	0.540044
Event 258.074123.1			
0.	534.545	17	0.000000
0.1	73.535	17	0.000000
0.2	45.992	17	0.000173
0.3	19.227	17	0.315647
0.4	14.077	17	0.661622
0.5	10.162	17	0.896680
0.6	9.725	17	0.914747
0.7	7.570	16	0.960659

6.5.6 Calculation of scalar moments from amplitude inversion

Scalar moments of all the earthquakes were calculated by inverting polarities and amplitudes. The measured amplitudes were converted from counts to metres using the nominal instrument gain for a frequency of 5 Hz (Figure 3.4). Amplitudes were corrected for attenuation using values of $Q_P \cong 60$ and $Q_S \cong 95$, and for geometrical spreading calculated from the final three-dimensional *P*- and *S*-wave speed models. Error bounds for the amplitudes were obtained from the RMS seismogram noise before each pick, with an additional fractional error bound of 0.4 to account for unmodelled propagation effects.

6.6 Summary

Linear programming methods can be used to solve systems of equations that contain inequalities. They can be used to invert polarities, amplitudes and amplitude ratios from local earthquakes to determine moment tensors. Each polarity observation is expressed as an inequality. Amplitude and amplitude ratio observations are expressed as pairs of

inequalities, bounded by estimated error bounds. Linear programming methods were used to seek moment tensors that are compatible with all observations, or failing that, the solution which minimises the sum of the absolute deviations (the L1 norm). *P*, *SH* and *SV* polarities and amplitude ratios are used. The amplitude ratios are corrected for attenuation and free-surface effects. Error bounds are estimated from seismogram noise levels and from an additional term added to account for unmodelled propagation effects. For the Hengill area, moment tensors were calculated for 98 earthquakes. The seismograms were low-pass filtered with a cutoff of 5 Hz, to remove the complicating effects of propagation that affect higher frequencies more. Rays were traced in the three-dimensional wave-speed models. Trial runs, where corrections were made for different amounts of attenuation, showed that the method is fairly insensitive to variations in attenuation. Appropriate additional error bounds to account for unmodelled propagation was determined by modelling the observed goodness-of-fit for different error bound values. The scalar moments of the earthquakes were calculated by inverting amplitudes instead of amplitude ratios. The amplitudes were corrected for geometrical spreading in the three-dimensional models.

Chapter 7

Earthquake mechanisms: results and source modelling

7.1 Introduction

Moment tensors were calculated for 98 earthquakes using the method described in Chapter 6 (Appendix 7). For almost all the processed earthquakes the moment tensors give a good fit to data, with few polarity and amplitude-ratio misfits. The fit of each moment tensor to the polarity and amplitude-ratio data is shown in Appendix 8.

The best-recorded earthquakes from each geographic group (Section 6.5.1) were selected as representative earthquakes (Figure 7.1). The earthquakes in each group were relocated with respect to a master event, using the technique described in Section 3.5 to determine accurate relative locations. The distribution of earthquakes within each group is shown in Appendix 9. Most of the earthquakes occur in clusters and the moment tensors are generally similar within each cluster.

The calculated moment tensors provide a general description of the earthquake source. Most of the moment tensors are non-DC with explosive volumetric components. In this chapter two potential source mechanisms are considered that can explain the non-DC moment tensors: (1) the combined tensile-shear fault model (the T+S model), and (2) the opening-shear fault model (the OS model). For any moment tensor, both of these mechanisms give an exactly equal fit to the data, and so it is impossible to choose between them on the basis of the moment tensors alone.

7.2 Decomposition of the moment tensors

7.2.1 Source orientations

7.2.1.1 Introduction

If a moment tensor is expressed in its principal-axis coordinate system, three values are needed to specify the orientations of the axes and the three principal moments give the strengths of the orthogonal dipoles that describe the earthquake source. The principal axes are conventionally labelled T, I and P and are associated with the principal moments m_T, m_I and m_P respectively, where $m_T > m_I > m_P$.

The majority of the earthquakes studied have near-horizontal T axes that trend northwest-southeast and P-axis orientations that vary from horizontal to vertical (Figure 7.2). For all earthquakes the mean T-axis azimuth is 127±33° and the mean plunge is -6±26° (where the error estimates are one standard deviation of the mean).

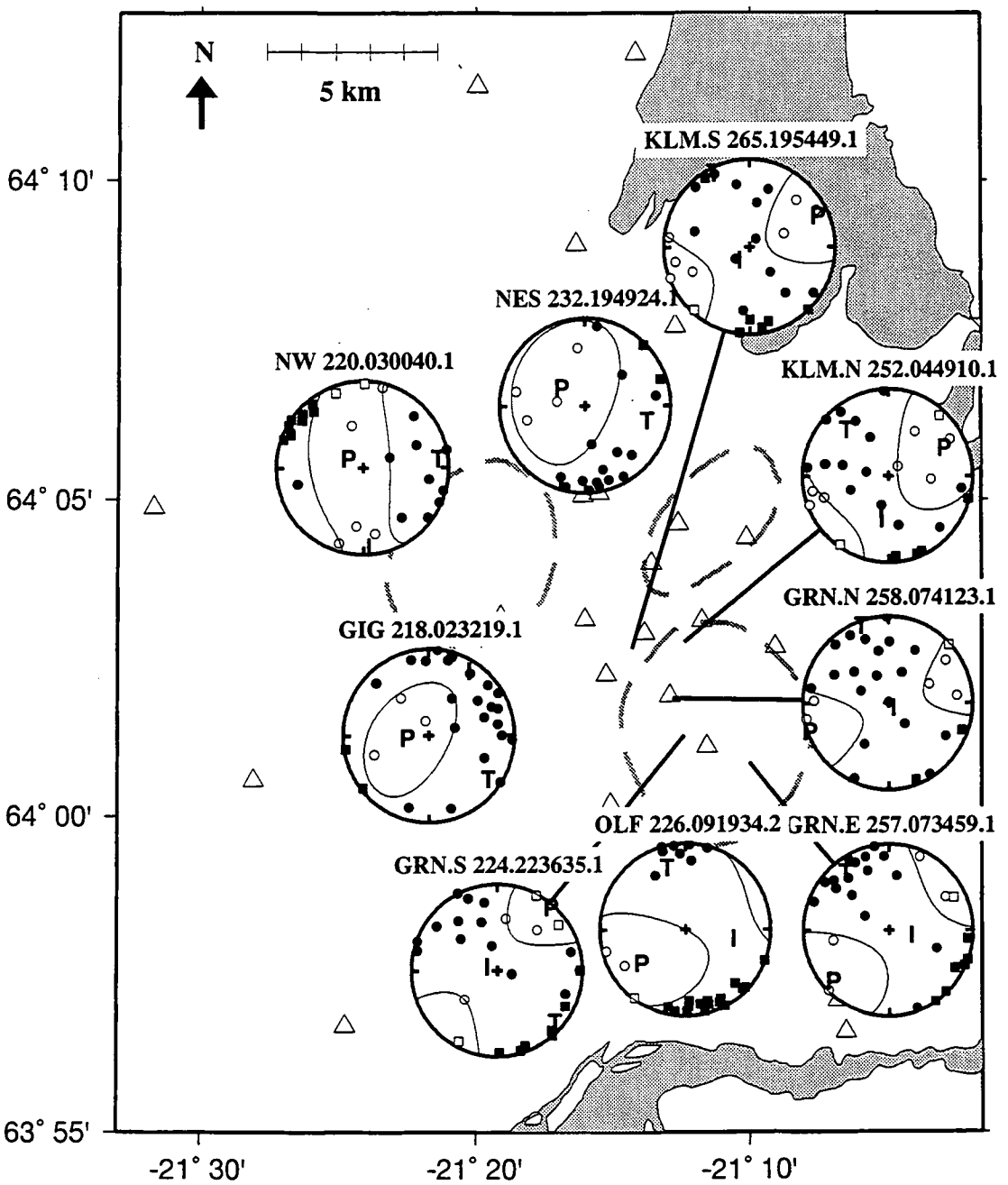

Figure 7.1: Map showing the locations and focal mechanisms of representative earthquakes, shown in equal-area upper focal-hemisphere projections. *P*-wave polarities (solid symbols: compressions; open symbols: dilatations) and *P*-wave nodal lines are shown. Squares indicate down-going rays that are projected onto the upper hemisphere. *T*, *I* and *P* show the positions of the principal axes. Lines connect mechanisms to their epicentral positions. Where no line is shown, the mechanisms are centred on the epicentre. Triangles: stations; dashed lines: outlines of the Hromundartindur, Grensdalur, and Hengill volcanic centres.

P-axis orientations show more scatter and generally trend northeast-southwest. A total of 35 of the earthquakes have *P*-axis plunges greater than 45° (Figure 7.2). The mean *P*-axis azimuth is 65±40° and the mean plunge is 10±41°. This pattern is similar to that of DC earthquakes measured in the Hengill area in 1981 (*Foulger*, 1988b; Figure 1.17).

7.2.1.2 Variations across the area

Within each group the principal axis orientations tend to be consistent (Figure 7.3). In particular the 14 earthquakes in group GIG have almost identical mechanisms. There is more scatter in the orientations of the axes in the north (groups NW, NES, KLM.N and KLM.S) than elsewhere (Figure 7.3). There is a noticeable variation in mean *T*-axis orientation between groups. Earthquakes in the northwest (groups NW and NES) have *T*-axes that are aligned mostly east-west (Figure 7.3). The single well-constrained earthquake south of 64°N (OLF) has a *T*-axis oriented almost due north.

7.2.1.3 Variations with hypocentral depth

The plunges of the *P* axes increase with focal depth (Figure 7.4). The average plunge is 17° between 2 and 4 km depth, and 47° between 4 and 6 km. The earthquakes in group GIG, all of which occurred at a depth of about 5.5 km, have *P*-axis plunges in

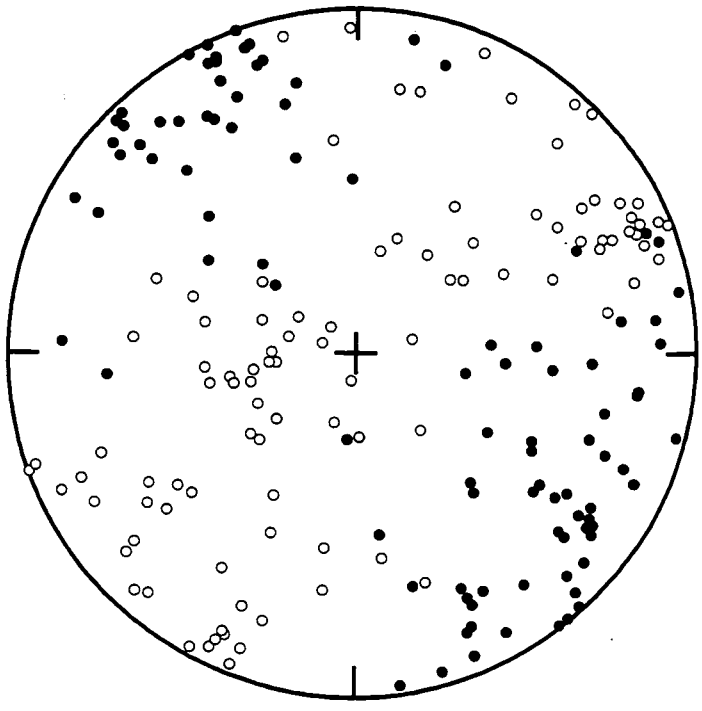

Figure 7.2: Equal-area upper hemisphere projection showing the orientations of *P* (open dots) and *T* (solid dots) axes for all earthquakes for which moment tensors were obtained.

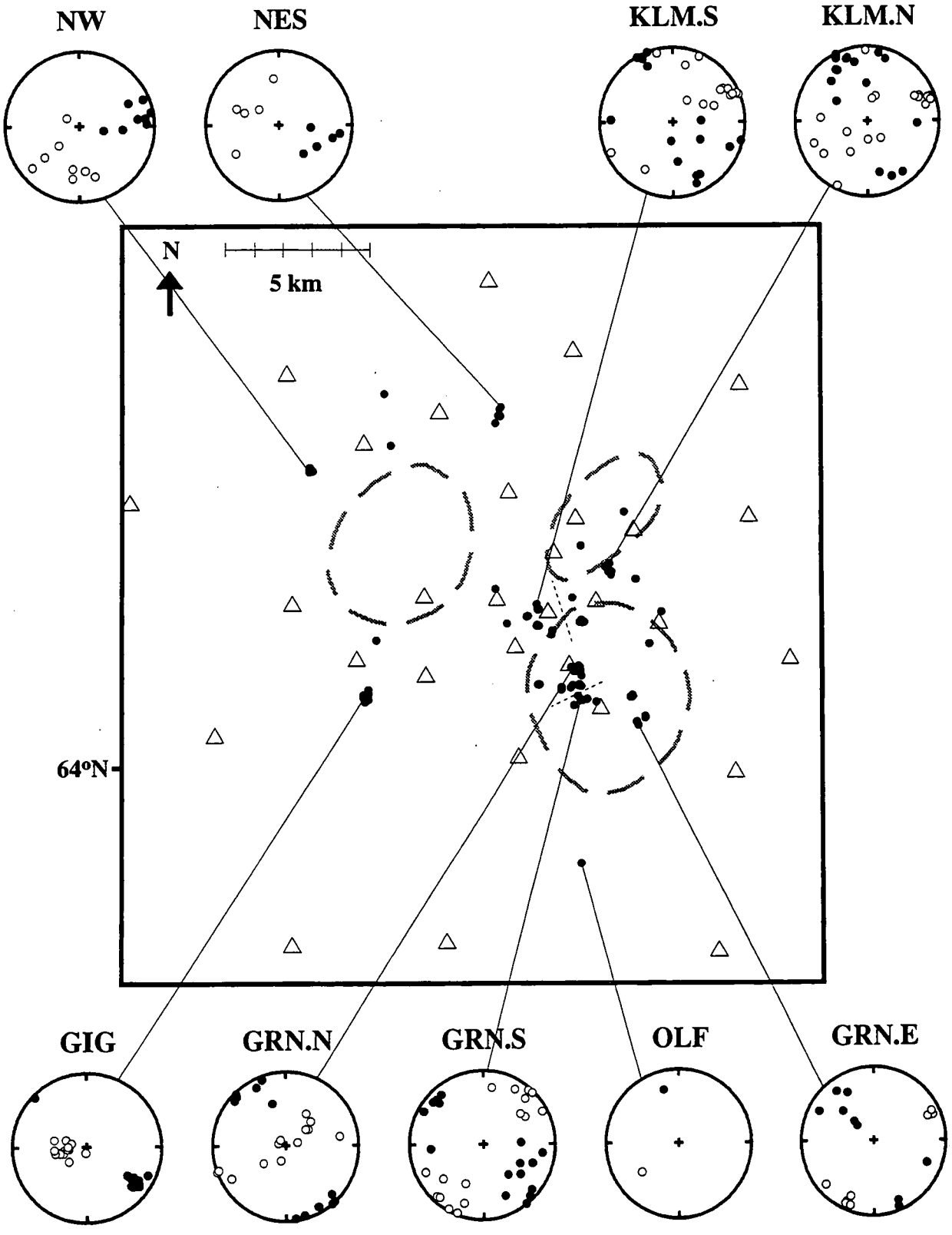

Figure 7.3: Equal-area upper hemisphere projections of *P* (open dots) and *T* (solid dots) axes for the processed earthquakes in each group. The lines connect each projection to the location of the corresponding group. Other symbols as for Figure 7.1.

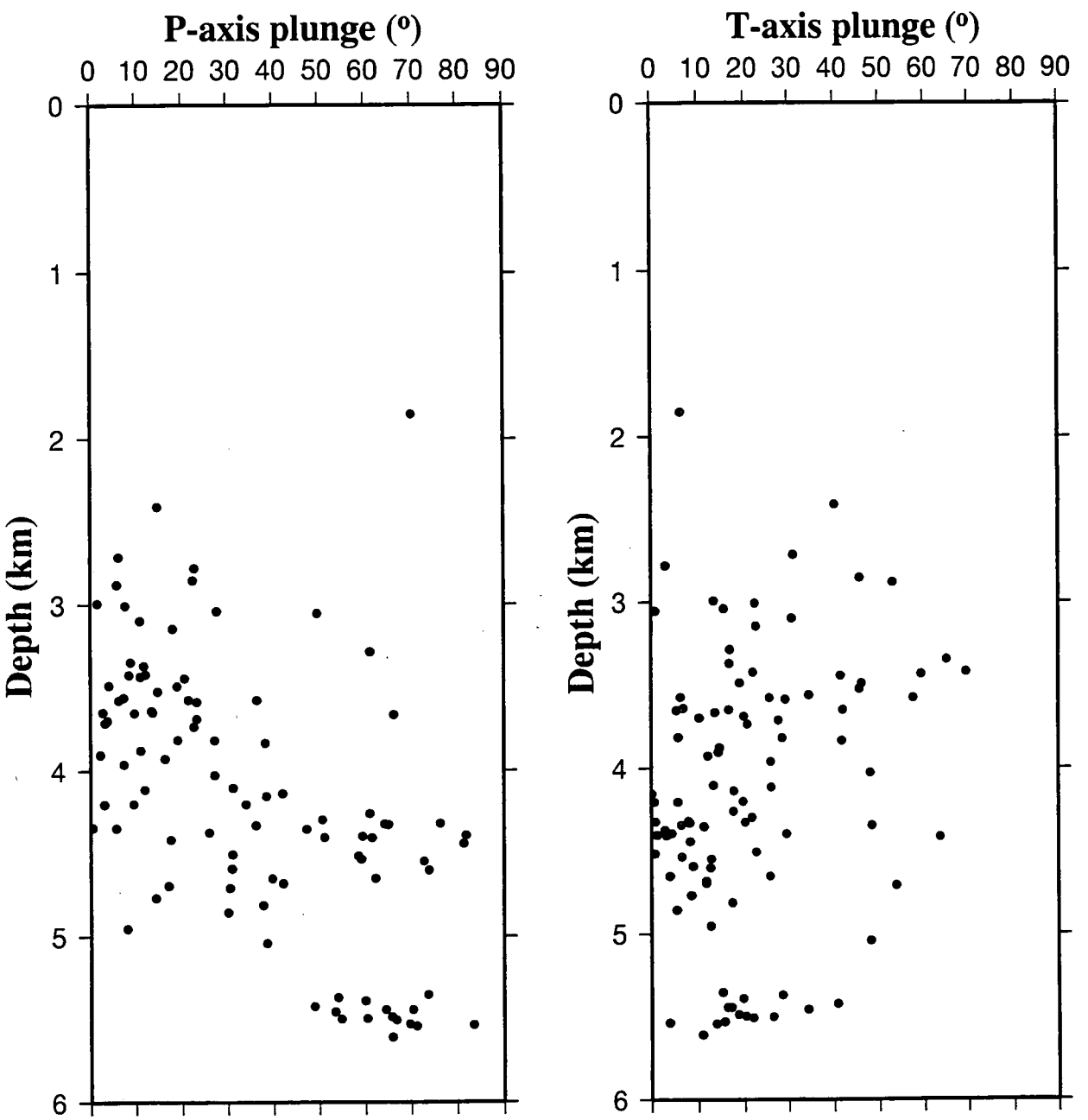

Figure 7.4: The plunge of *P*- and *T*-axes against earthquake depth for all earthquakes for which moment tensors were obtained.

the range 53° to 84°. This pattern is caused by mechanisms changing from "strike-slip" type to "normal" type with increasing depth. There is no clear variation in *T*-axis plunge with depth (Figure 7.4).

7.2.2 Distribution of the principal moments

Figure 7.5 shows the positions of all the calculated moment tensors on an ε-*k* diagram. Most of the earthquakes have substantial explosive volumetric components, with a mean *k* value of 0.20 and a maximum of 0.42. Only five earthquakes have implosive volumetric components, with *k* ranging from -0.19 to -0.01. About 50% of the earthquakes lie within the TC-DC region.

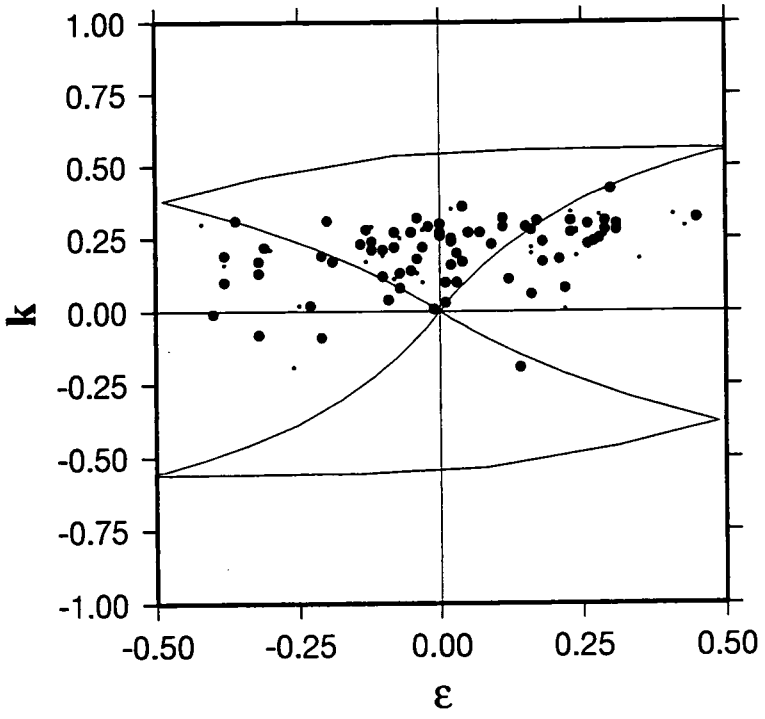

Figure 7.5: An ε-*k* diagram showing positions of the calculated moment tensors. The positions of the poorly-constrained earthquakes (Appendix 7) are shown by small dots.

The stability of the moment tensors of all the earthquakes was tested by inverting subsets of the data. For each earthquake ten inversions were carried out, with data from 10% of the stations discarded at random each time. The stability of the moment tensors varies greatly from earthquake to earthquake (Figure 7.6). For the best-constrained earthquakes, *e.g.*, 258.074123.1, ε varies by less than 0.1 and *k* by less than 0.2. From the ε-*k* diagrams 70 of the earthquakes are classified as well constrained, as they have stable mechanisms with only small changes in ε and *k* values when subsets of the data are removed.

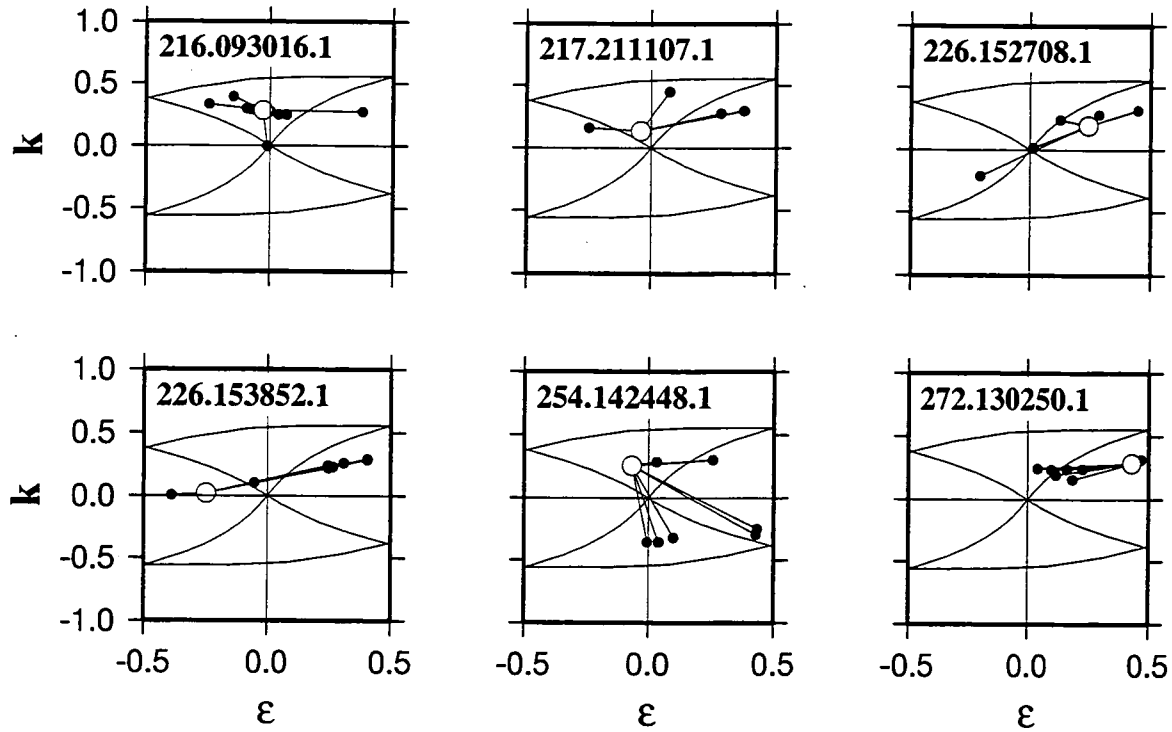

Well-constrained earthquakes

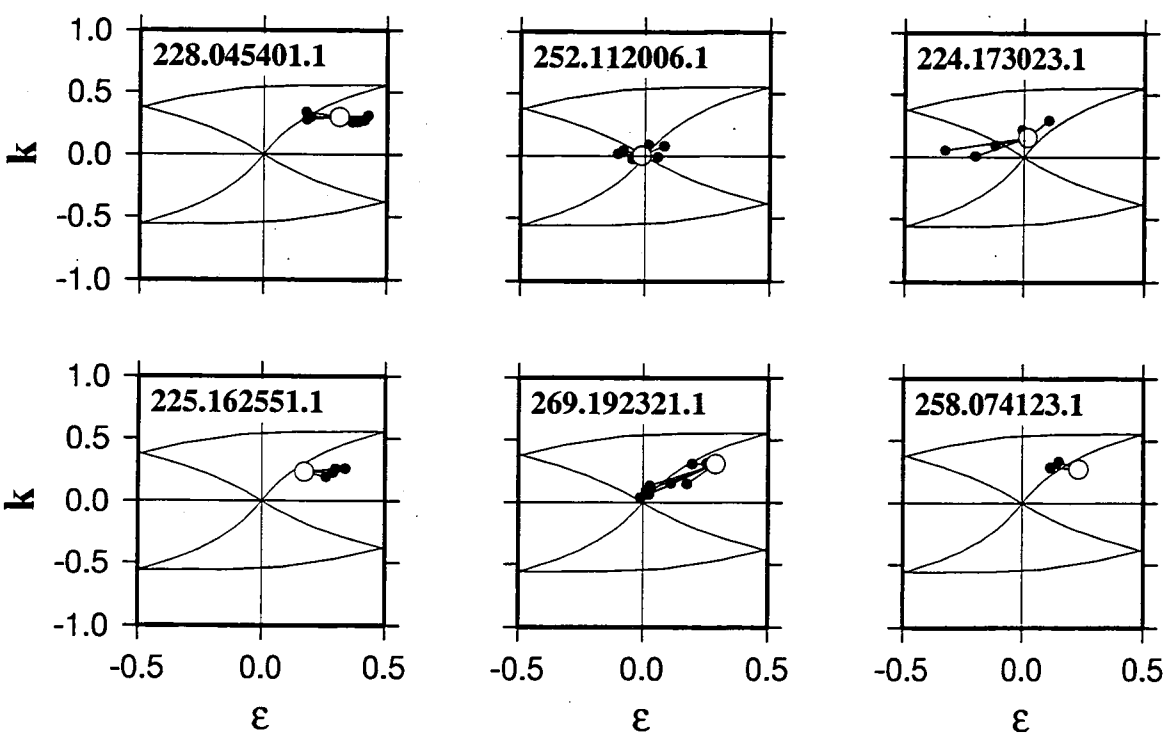

Figure 7.6: Examples of variations in moment tensors obtained by inverting different subsets of data. Open dots show positions of the moment tensors obtained by inverting the full data set for each earthquake, and solid dots are positions of the moment tensors obtained when 10% of the data are removed at random. Ten such inversions were carried out for each earthquake, but all attempts are not visible on each plot, as sometimes the resulting moment tensor was exactly the same as that obtained from inverting all the data. Top figures: examples of poorly constrained earthquakes; bottom figures: examples of well-constrained earthquakes.

7.3 Source models

7.3.1 Theory and modelling strategy

7.3.1.1 Shear faulting

The DC mechanism that best fits a set of polarity and amplitude or amplitude-ratio data can only be found by searching the three-parameter space of all possible DCs. It is not possible to linearly invert the data to determine the best-fit DC moment tensor, because this restriction imposes a non-linear constraint on the moment tensor. An *ad-hoc* approximation to the best-fit DC source is the DC component of the best-fit deviatoric moment tensor. The best-fit deviatoric moment tensor can be found by applying the linear constraint that the trace of the moment tensor is zero (equation 6.12).

7.3.1.2 Tensile and shear faulting

A combination of an opening tensile fault and a shear fault has a moment tensor with an explosive volumetric component (Figures 2.4 and 7.7). Any tensile-shear fault combination lies within one of the TC-DC regions on an ε-k diagram. The sign of k depends on whether the tensile fault component opens or closes.

For arbitrarily scaled moment tensors (Section 6.3.5) the absolute sizes of the tensile and shear fault components are unknown. The parameter R_{TF} expresses the relative sizes of the two components:

$$R_{TF} \stackrel{def}{=} \frac{m^{(TF)}}{\left(\left|m^{(SF)}\right| + \left|m^{(TF)}\right|\right)}. \qquad 7.1$$

where $m^{(SF)}$ and $m^{(TF)}$ are the scalar moments of the shear-fault and tensile-fault components respectively.

A model with tensile and shear fault components requires 7 parameters for a full description:

- The scalar moment of the shear fault
- The scalar moment of the tensile fault
- The orientation of the shear-fault (2 parameters)
- The slip direction (rake) of the shear fault (1 parameter)
- The orientation of the tensile fault (2 parameters)

This is too many parameters to determine from a general moment tensor, which has only six parameters, unless some restrictions are imposed. One possibility is to restrict the T axis of the tensile fault to lie in the plane that contains the T and P axes of the shear fault, thus reducing the number of parameters by one. Any mechanism of this

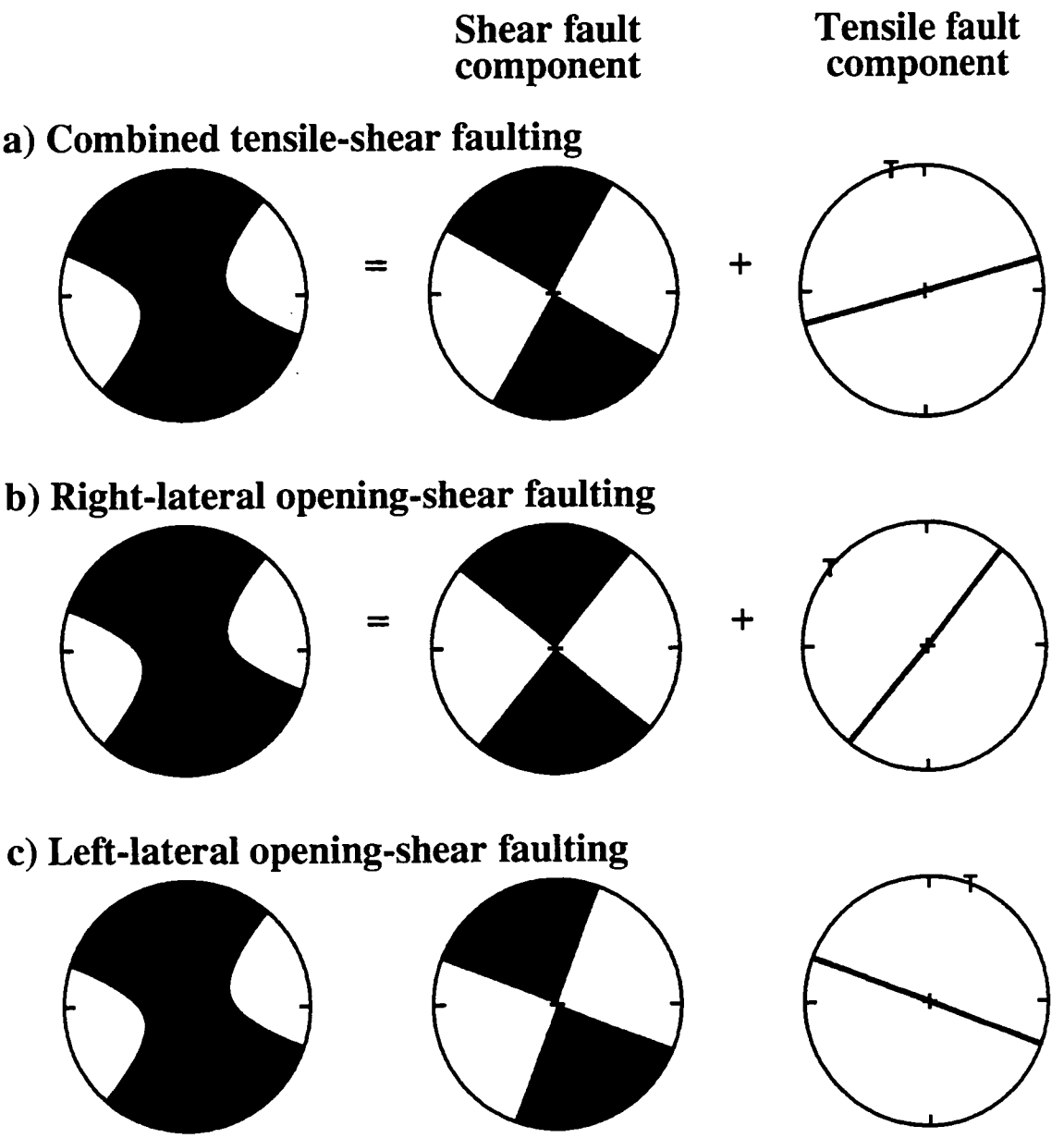

Figure 7.7: Three different tensile-shear faulting models that have the same resultant moment tensor. All models have a vertical tensile fault and a strike-slip shear fault. (a) the combined tensile-shear fault model (Figure 2.4), which has the tensile fault oriented at 45° to both of the nodal planes of the shear fault mechanism. (b) and (c) the opening-shear model, with the tensile fault coplanar with one of the nodal planes of the DC. The right-hand plots show the orientation of the tensile fault and *T* axis.

restricted geometry will plot along the TC-DC line of an ε-k diagram. The angle between the two T axes is difficult to determine, as changes to this angle have only a small effect on the resulting moment tensor (*Julian et al.*, 1996).

If the angle between the two T axes is set at 0° (*i.e.*, an angle 45° between the two fault planes), then the two components have the same principal axes (Figure 2.4). It makes sense for the two components to have parallel principal axes, and this constraint greatly simplifies the problem as the orientation of the best-fit model does not need to be calculated, because it has the same axes as the general moment tensor. Hereafter, this model is called the T+S model.

The problem of finding the T+S model from a general moment tensor then involves two unknowns, the scalar moments of the two components, and three data, the three principal moments of the general moment tensor:

$$\begin{pmatrix} m_1 \\ m_2 \\ m_3 \end{pmatrix} = m^{(SF)} \begin{pmatrix} 1 \\ 0 \\ -1 \end{pmatrix} + m^{(TF)} \begin{pmatrix} 3 \\ 1 \\ 1 \end{pmatrix}, \qquad 7.2$$

where $m_1 \geq m_2 \geq m_3$. When $m^{(SF)} \leq m^{(TF)}$ the principal moments are all non-negative, and the P-wave radiation is compressive in all directions. Equation 7.2 can be solved by least-squares to calculate the best-fit T+S model.

The orientations of the two fault planes can be deduced from a T+S model moment tensor, although there is ambiguity about which of the nodal planes of the DC component represents the shear fault plane. The tensile fault plane is oriented perpendicular to the T axis (*i.e.*, at 45° to the DC-component nodal planes).

An alternative shear and tensile fault combination is to make the two faults coplanar (with an angle of 45° between their T-axes), which is equivalent to the opening-shear faulting proposed by *Haskell* (1964) (Section 2.3.5). Hereafter this model is called the OS model.

An OS model has five unknowns:

- The scalar moment of the DC component
- The scalar moment of the tensile-fault component
- The orientation of the fault plane (2 parameters)
- The slip direction (rake) of the shear motion (1 parameter)

Finding the orientation and the scalar moments of the components of the OS model that fits a given moment tensor involves solving 6 equations for 5 unknowns. This system of equations is complicated, and cannot be simplified or solved easily (Appendix 10). However the moment tensor of the best-fit OS model is exactly the same as the best-fit T+S model. This is because both mechanisms have the same restricted geometry (the T axis of the tensile fault lies in the T-P plane of the shear fault) so that they plot along

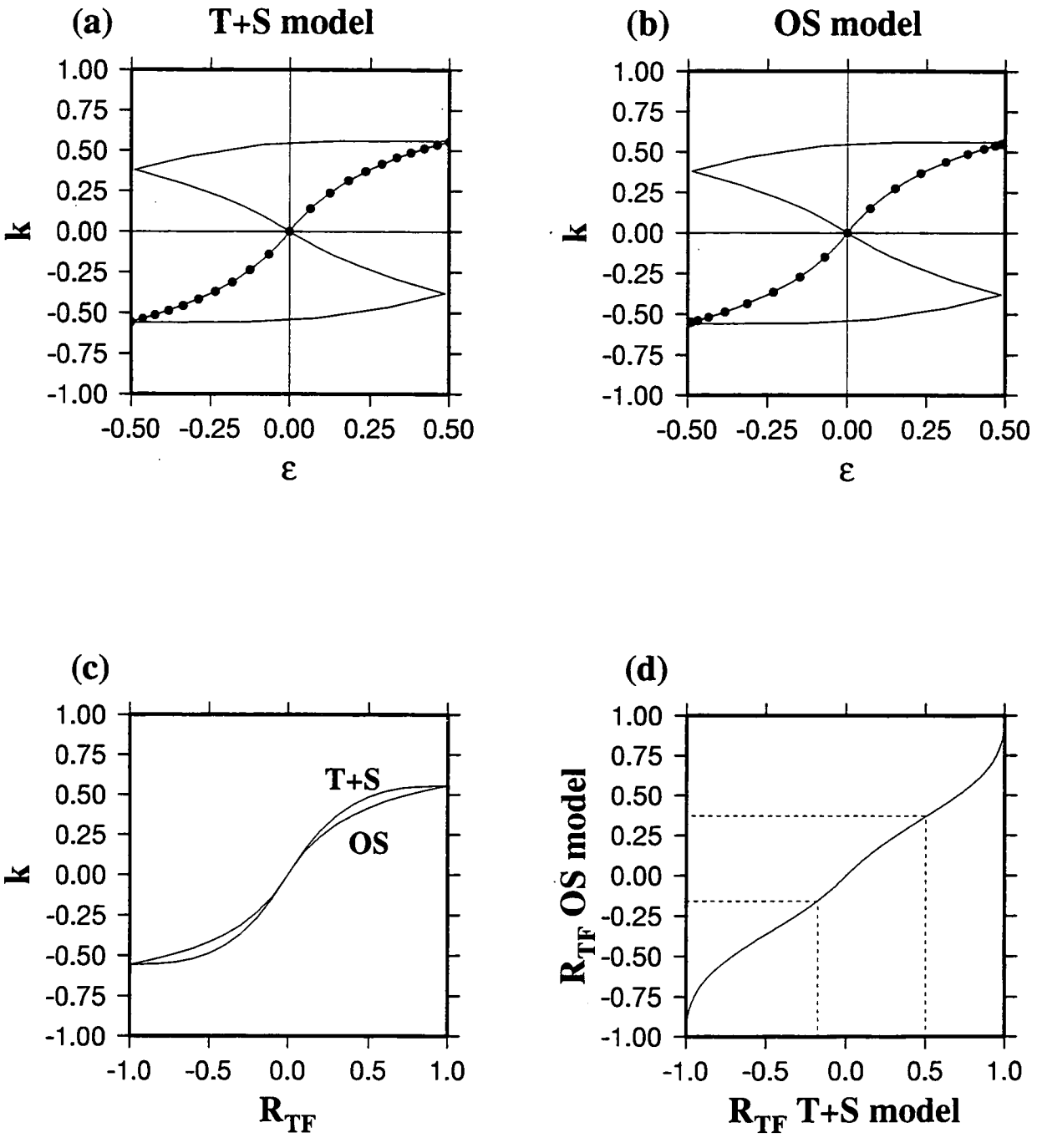

Figure 7.8: Positions of tensile-shear mechanisms on ε-k diagrams for (a) the combined tensile-shear (T+S) model, and (b) the opening-shear (OS) model. For any earthquake, the moment tensors of the T+S and OS models are the same, although they have different R_{TF} values, as shown in (c) and (d). Dashed lines in (d) show the range in values calculated for the earthquakes studied here.

the TC-DC line on an ε-k diagram (Figure 7.8a, b). Any general moment tensor will have a best-fit mechanism at the same place on the TC-DC line for both models. However, for a given general moment tensor, the best-fit T+S and OS models have different R_{TF} values (Figure 7.8c, d). There is no need to solve independently for the best-fit OS model, and instead the best-fit T+S model moment tensor can be used, and all that is required is to find the appropriate R_{TF} value. This can be done using Figures 7.8c or d.

There are two possible interpretations of an OS model, for there are two potential fault planes which give the same resultant moment tensor (Figure 7.7). If $R_{TF} = 0$ then these fault planes are orthogonal and are represented by the nodal planes of the DC mechanism. For other values of R_{TF} the two possible fault planes are non-orthogonal. Thus the interpretation of an OS model has the same ambiguity as the interpretation of a DC mechanism, and it is not possible to distinguish between the two potential fault planes from the moment tensor.

7.3.2 Assessment of data fit

7.3.2.1 DC models

Some of the earthquakes studied have moment tensors that are close to DCs. The most rigorous approach to determining whether these earthquakes are caused solely by shear faulting would be to test whether the general moment tensor, with 6 parameters, gives a statistically significant improvement in the fit to data when compared with the DC model, which has 4 parameters. Additional degrees of freedom in the model will always give a better data fit, but this improvement may not be significant. This statistical analysis should be the subject of future work, and an empirical approximation only is used here.

For each earthquake with $|k| < 0.2$, the fit to data of the general moment tensor was compared with the fit of the DC component of the best-fit deviatoric moment tensor (Section 7.3.2.2). On the basis of the number of polarity misfits and the mean absolute deviation, 17 of these earthquakes were classified as shear-fault earthquakes (Table 7.1). All the earthquakes had few polarity misfits (mostly less than four) for stations close to nodal lines, and had only a small increase (mostly less than a factor of 2) in the mean absolute deviation when compared with the fit of the general moment tensor (Figures 7.9 and 7.10). All of these earthquakes had $|k| < 0.13$ for the T+S model.

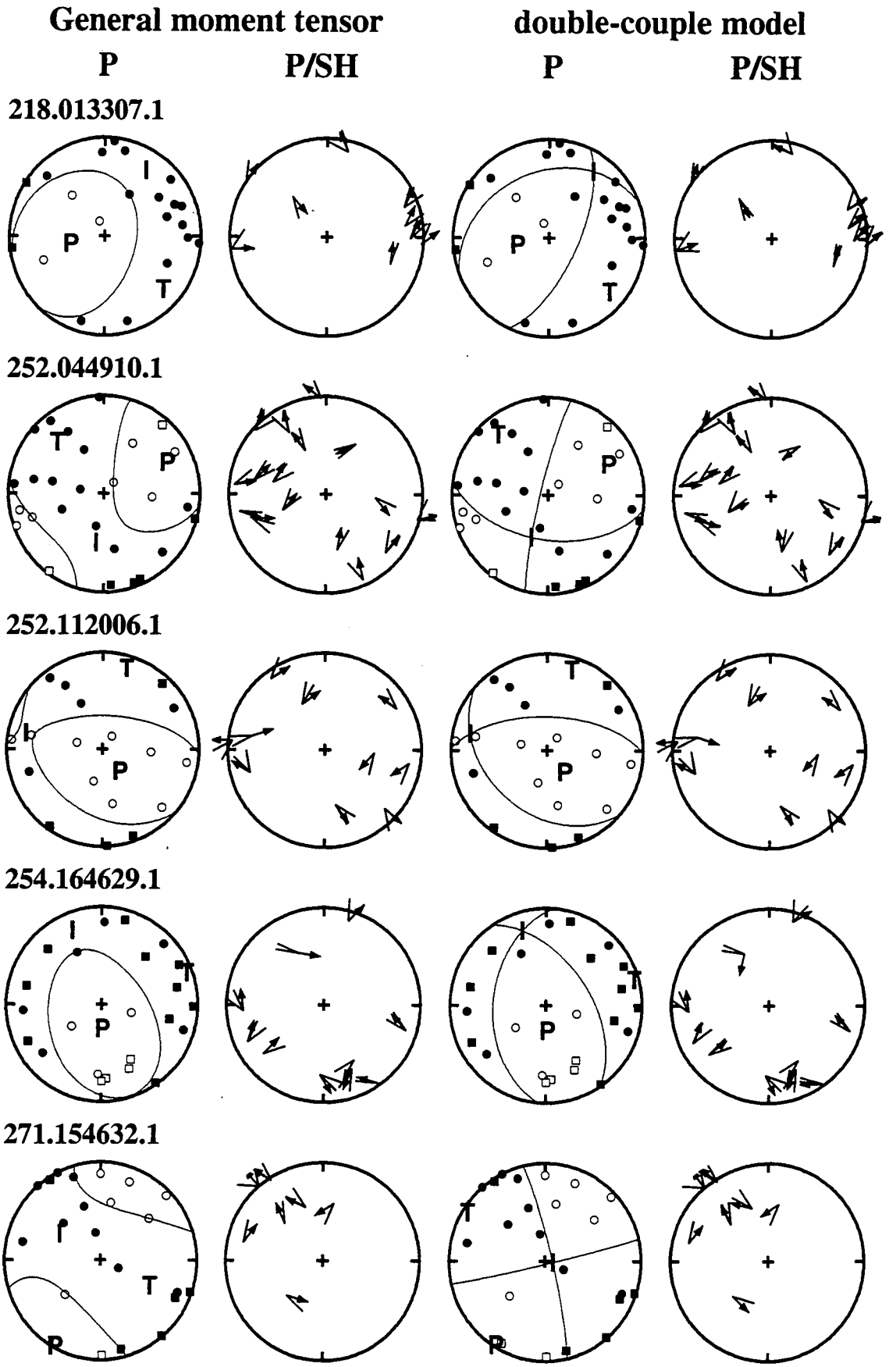

Figure 7.9: Examples of earthquakes interpreted as shear faulting. *P*-wave polarities and *P:SH* amplitude ratio fit for the general moment tensors (left two columns) and for the shear fault mechanisms (right two columns). Symbol conventions are the same as Figure 6.8.

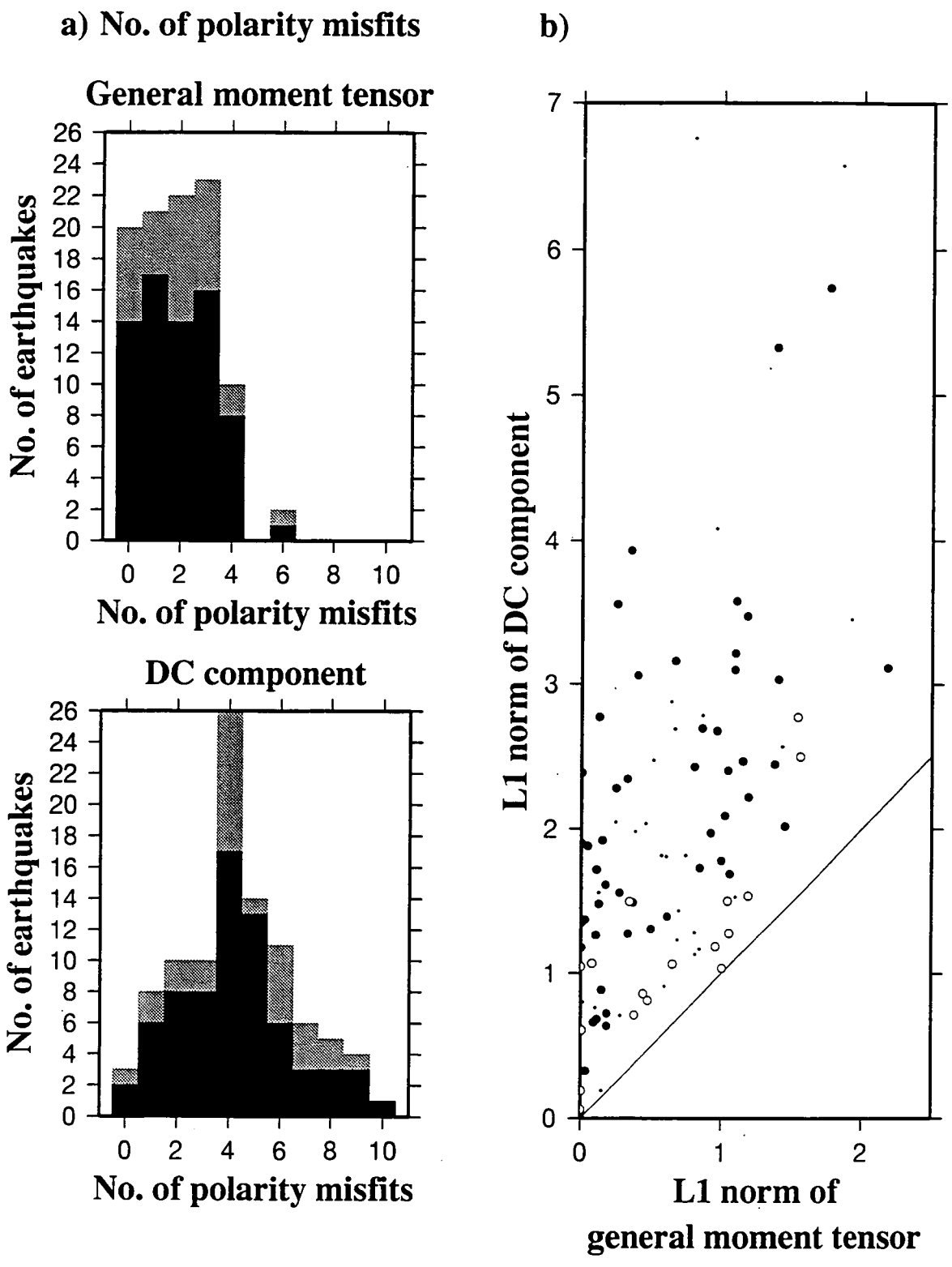

Figure 7.10: Comparison of the fit to the data of the general moment tensor and the DC component of the deviatoric moment tensor, for all earthquakes. (a) Histograms of the number of polarity misfits. Grey parts of bars represent the poorly constrained earthquakes. (b) Graph of the mean absolute deviation (L1 norm: in arbitrary units) for the general moment tensor and the DC mechanism. Small dots: poorly constrained earthquakes; open circles: earthquakes that are classified here as shear-faulting.

Table 7.1: Shear-faulting earthquakes, for which a DC model gives a good fit to the data.

Event	General moment tensor		DC model		ε	*k*	Group
	No. of polarity misfits	Mean absolute deviation	No. of polarity misfits	Mean absolute deviation			
217.183800.1	3	0.649	4	1.066	-0.07	0.08	GIG
217.235139.1	4	1.534	7	2.771	-0.23	0.02	GIG
218.013307.1	1	0.008	2	0.610	-0.32	-0.08	GIG
220.030040.1	2	1.187	5	1.539	0.22	0.08	NW
224.184649.1	4	0.374	3	0.713	0.12	0.11	NW
226.091934.2	1	0.004	0	0.192	-0.07	0.13	OLF
226.214521.1	4	0.470	4	0.815	0.16	0.06	NW
227.092526.1	1	1.045	6	1.504	-0.40	-0.01	KLM.S
231.161335.1	0	0.439	1	0.860	0.03	0.10	GRN.S
232.194924.1	3	0.077	5	1.071	-0.21	-0.09	NES
240.163545.1	2	0.000	1	0.062	0.01	0.03	GRN.S
252.044910.1	2	1.552	4	2.499	-0.10	0.12	KLM.N
252.112006.1	3	1.002	1	1.037	-0.01	0.01	KLM.N
254.164629.1	2	0.956	2	1.188	-0.09	0.04	KLM.N
264.193202.1	2	0.336	3	1.501	-0.32	0.13	GRN.E
265.040149.1	0	0.000	2	1.049	-0.38	0.10	GRN.E
265.201436.1	2	1.056	1	1.281	0.01	0.10	KLM.S

7.3.2.2 Tensile-shear models

As the moment tensors of the best-fit T+S model and OS model are the same for a given earthquake, the models both provide the same fit to data. The two models have fewer degrees of freedom than a general source, and so they will always give a poorer fit to the data than the general moment tensor does. For most of the earthquakes, the models give a good fit to the data, with 41 out of 53 having at most three polarity misfits, and 31 having a mean absolute deviation of less than twice that of the general moment tensor (Figures 7.11 and 7.12; Table 7.2). The fits of the mechanisms of the representative earthquakes to the *P*-wave polarity data are shown in Figure 7.13.

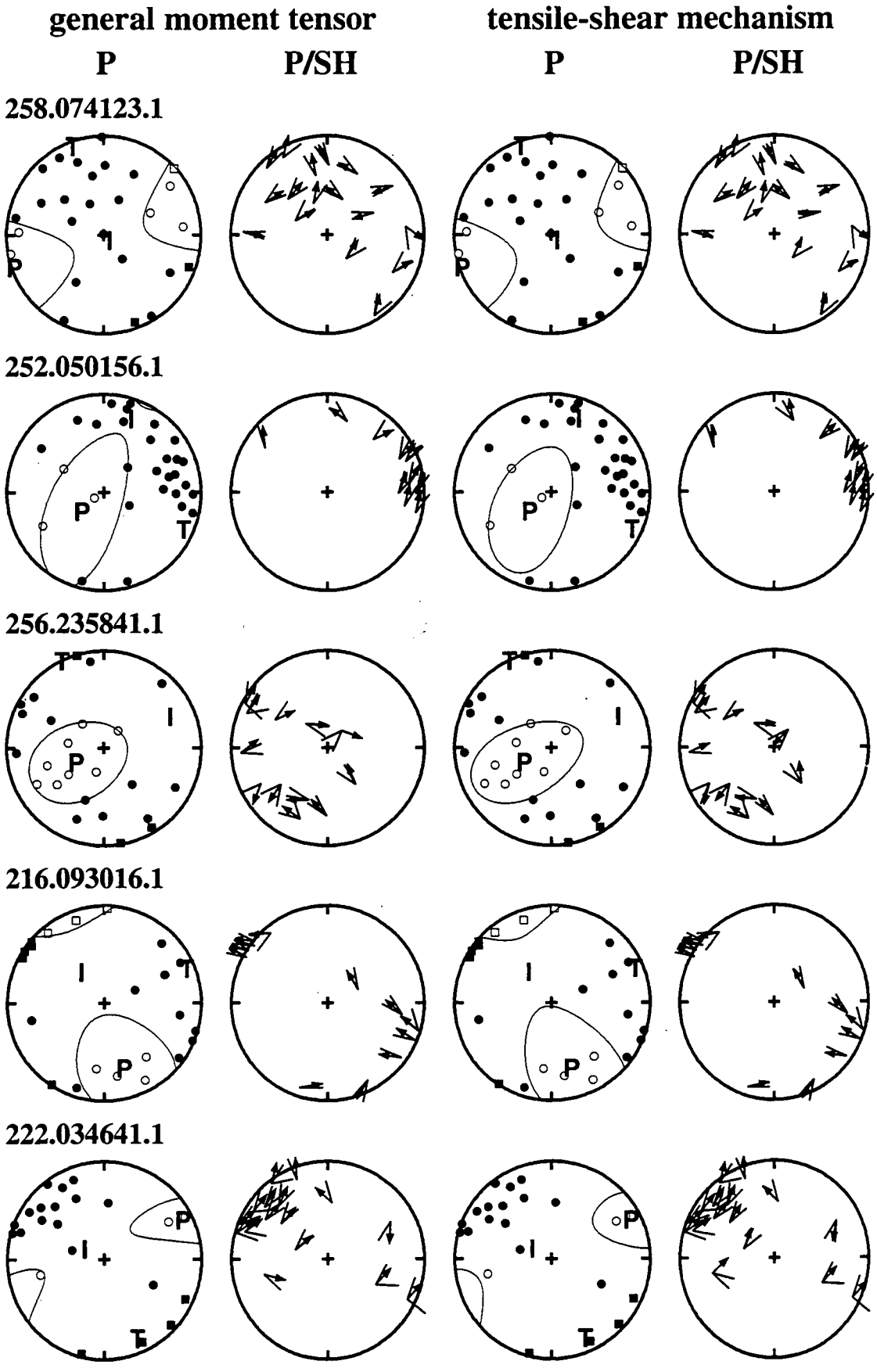

Figure 7.11: Examples of earthquakes interpreted as tensile-shear faulting. *P*-wave polarities and *P:SH* amplitude ratio fit for the general moment tensors (left two columns) and for the tensile-shear mechanisms (right two columns). Symbol conventions are the same as Figure 6.8.

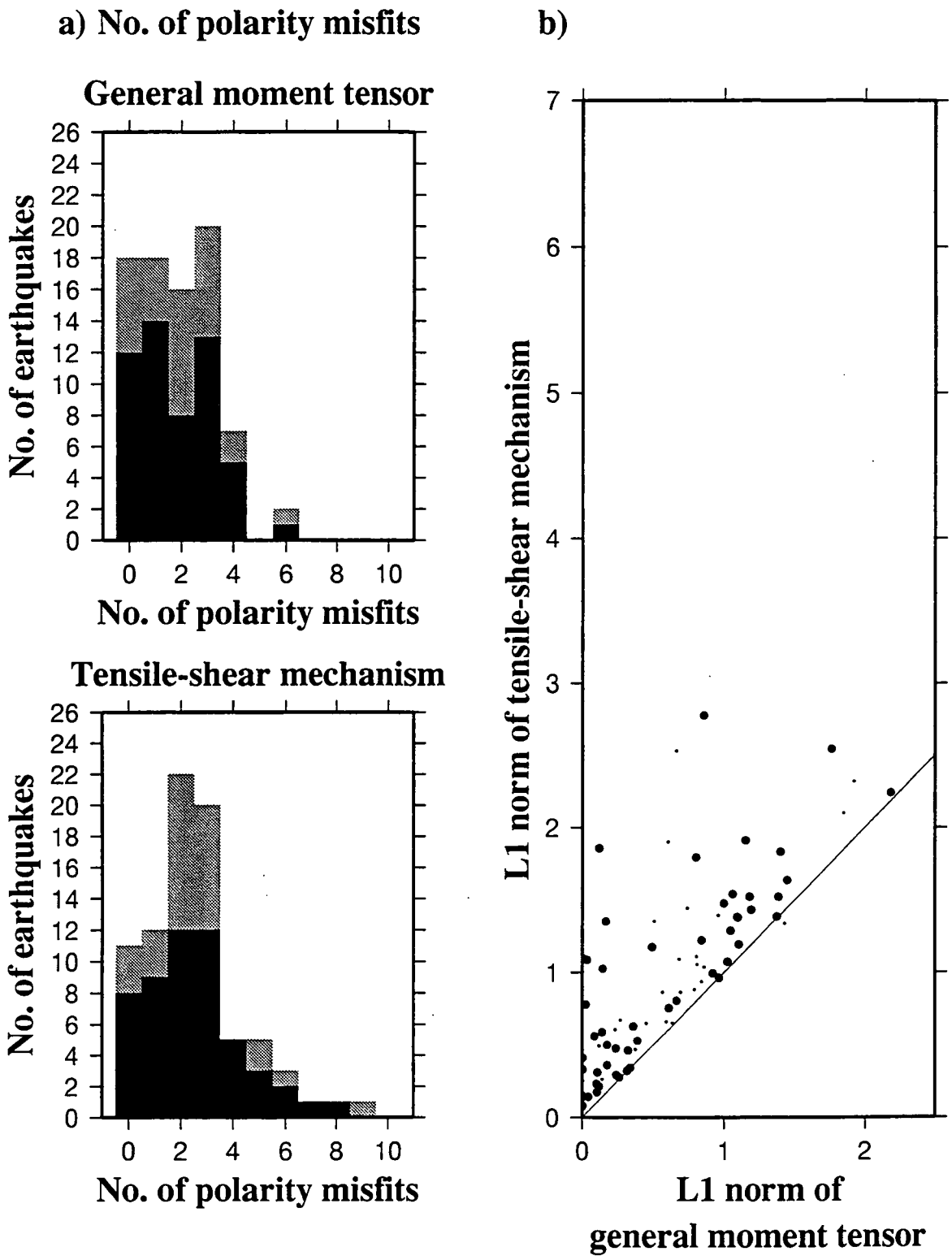

Figure 7.12: Comparison of the fit to data of the general moment tensor and the best-fit tensile-shear mechanism derived from the general moment tensor, for all non-shear earthquakes. (a) Histograms of the number of polarity misfits. Grey parts of bars represent the poorly constrained earthquakes. (b) Graph of the mean absolute deviation (L1 norm: in arbitrary units) for the general moment tensor and the tensile-shear mechanism. Poorly constrained earthquakes are shown by small dots.

Table 7.2: Tensile-shear fault earthquakes. POL: number of polarity misfits; MAD: mean absolute deviation

Event	Gen. moment tensor		Tensile-shear model		ε	*k*	Group
	POL	MAD	POL	MAD			
216.131451.1	1	0.176	3	0.361	-0.030	0.222	GIG
216.150353.1	2	0.998	4	1.472	0.025	0.254	GIG
217.064554.1	2	0.002	1	0.143	0.005	0.257	KLM.N
217.164959.1	3	0.841	5	1.220	-0.125	0.240	NES
218.023219.1	1	0.608	1	0.756	0.027	0.195	GIG
218.045348.1	2	0.088	3	0.565	-0.053	0.273	GIG
218.061609.1	0	0.121	3	1.856	-0.378	0.188	KLM.N
219.001831.1	2	0.107	3	0.311	-0.017	0.286	GIG
220.235442.1	1	0.178	2	0.504	-0.078	0.219	KLM.S
222.034524.1	0	0.320	0	0.323	0.160	0.275	GRN.E
224.023135.1	1	0.001	0	0.074	0.035	0.171	NES
224.173023.1	1	1.021	2	1.074	0.016	0.161	KLM.S
224.184254.1	3	0.802	3	1.791	-0.205	0.309	GRN.S
224.223635.1	3	1.369	2	1.381	0.153	0.292	GRN.S
224.224403.1	3	1.045	3	1.284	0.276	0.253	GRN.N
225.010319.1	1	0.118	2	0.216	0.075	0.274	GRN.S
225.083219.1	3	1.396	2	1.832	0.267	0.244	GRN.N
225.122104.1	3	1.101	2	1.191	0.228	0.314	GRN.N
225.122759.1	3	1.188	3	1.427	-0.041	0.178	GRN.N
225.122941.1	1	0.963	1	0.962	0.166	0.305	GRN.N
225.123131.1	2	0.921	2	0.993	0.107	0.291	GRN.N
225.123340.1	0	0.042	0	0.144	0.043	0.357	GRN.N
225.162551.1	3	0.325	3	0.464	0.175	0.235	NW
226.020942.1	4	1.095	3	1.375	0.291	0.284	GRN.N
226.151111.1	2	1.759	4	2.545	-0.081	0.271	KLM.S
227.092421.1	1	0.002	6	1.098	-0.358	0.307	KLM.S
228.040122.1	0	0.002	3	0.413	-0.120	0.207	KLM.N
228.045401.1	3	1.382	3	1.517	0.307	0.304	KLM.N
228.083300.1	0	0.002	2	0.334	-0.144	0.233	KLM.N
229.033558.1	1	0.363	4	0.631	-0.003	0.301	KLM.S
234.000219.1	1	0.341	1	0.344	0.303	0.416	GRN.S
236.052400.1	0	0.000	0	0.152	0.213	0.175	GRN.S
236.065252.1	0	0.003	1	0.084	0.053	0.265	GRN.S
237.212559.1	3	0.146	2	1.026	0.143	-0.188	NES
239.160308.1	3	0.166	6	1.348	-0.126	0.281	GRN.S
241.105349.1	0	0.105	0	0.175	0.106	0.322	GRN.S
252.023347.1	3	2.180	2	2.240	-0.052	0.143	KLM.N
252.050156.1	4	1.058	2	1.536	0.260	0.233	GIG
253.125604.1	0	0.025	1	0.784	-0.316	0.170	KLM.N
255.021714.1	1	0.240	2	0.477	-0.004	0.265	NES
255.173510.1	1	0.494	1	1.173	-0.306	0.217	GRN.S
256.235841.1	2	0.391	0	0.533	-0.038	0.324	KLM.N
257.073459.1	0	0.141	0	0.592	-0.099	0.208	GRN.E
258.074123.1	0	0.241	0	0.294	0.230	0.275	GRN.N
264.053355.1	4	1.147	4	1.910	-0.194	0.166	GRN.E
264.234218.1	4	1.092	5	1.380	0.019	0.244	KLM.S
265.191813.1	6	1.177	7	1.519	0.313	0.282	KLM.S
265.195449.1	2	0.266	3	0.276	0.089	0.229	KLM.S
265.201436.2	3	1.442	4	1.633	0.185	0.166	KLM.S
267.001816.1	1	0.663	1	0.807	0.259	0.301	KLM.N
269.192321.1	0	0.100	1	0.232	0.289	0.312	KLM.N
271.043816.1	4	0.856	8	2.778	0.451	0.317	NW
271.154632.1	1	0.034	5	1.088	-0.212	0.193	GRN.S

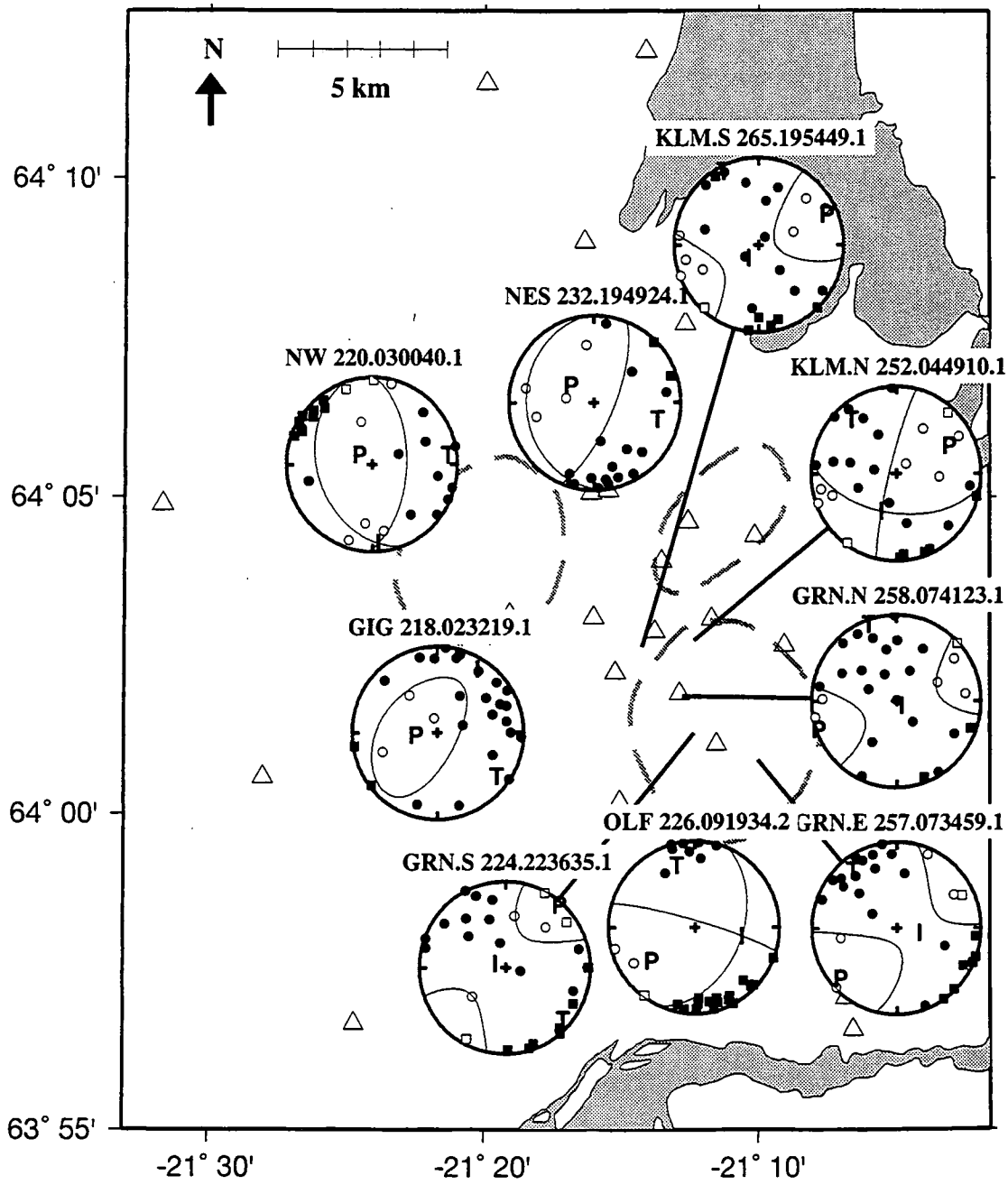

Figure 7.13: As Figure 7.1, except that the fit to the source models are shown. Events 220.030040.1, 232.194924.1, 252.044910.1 and 226.091934.2 are interpreted as shear faults, and the other earthquakes are interpreted as tensile-shear faults.

7.3.2.3 Other source models

Six of the earthquakes studied have a poor data fit, with more than five polarity misfits to the DC or tensile-shear models (Table 7.3). The two of these earthquakes that are interpreted as DC mechanisms do not have a substantially better fit with a tensile-shear model. These earthquakes plot in diverse positions on the ε-*k* diagram (Figure 7.14). Most polarity misfits are for stations that are close to nodal lines (Figure 7.15).

Table 7.3: Earthquakes with a poor fit to the DC and tensile-shear models.

Event	General moment tensor		DC model		ε	*k*	Group
	No. of polarity misfits	Mean absolute deviation	No. of polarity misfits	Mean absolute deviation			
217.235139.1	4	1.534	7	2.771	-0.23	0.02	GIG
227.092526.1	1	1.045	6	1.504	-0.40	-0.01	KLM.S
Event	**General moment tensor**		**Tensile-shear model**		**ε**	***k***	**Group**
227.092421.1	1	0.002	6	1.098	-0.358	0.307	KLM.S
239.160308.1	3	0.166	6	1.348	-0.126	0.281	GRN.S
265.191813.1	6	1.177	7	1.519	0.313	0.282	KLM.S
271.043816.1	4	0.856	8	2.778	0.451	0.317	NW

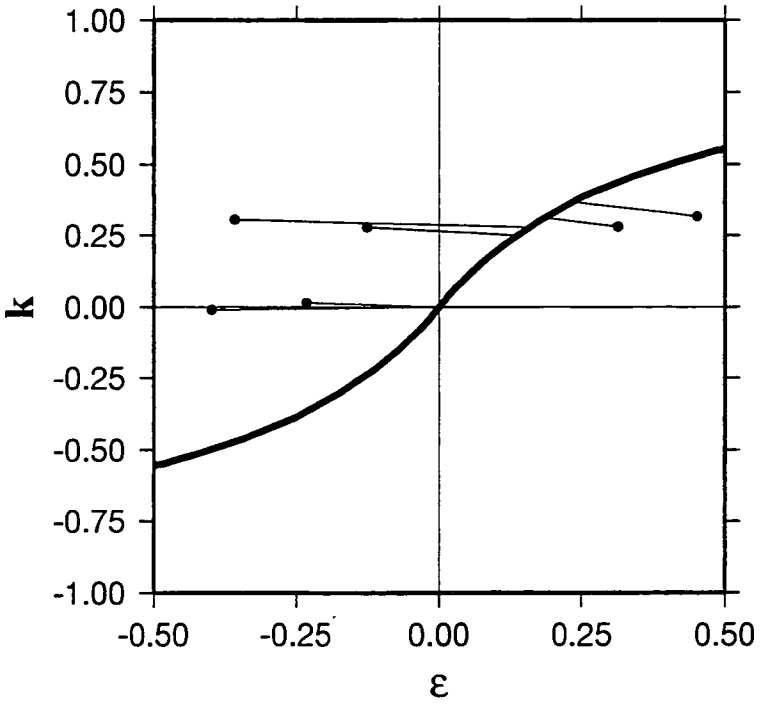

Figure 7.14: The positions of the six earthquakes that give a poor data fit on the ε-*k* diagram. Lines connect the mechanisms to the positions of the best-fit models that are shown in Figure 7.15.

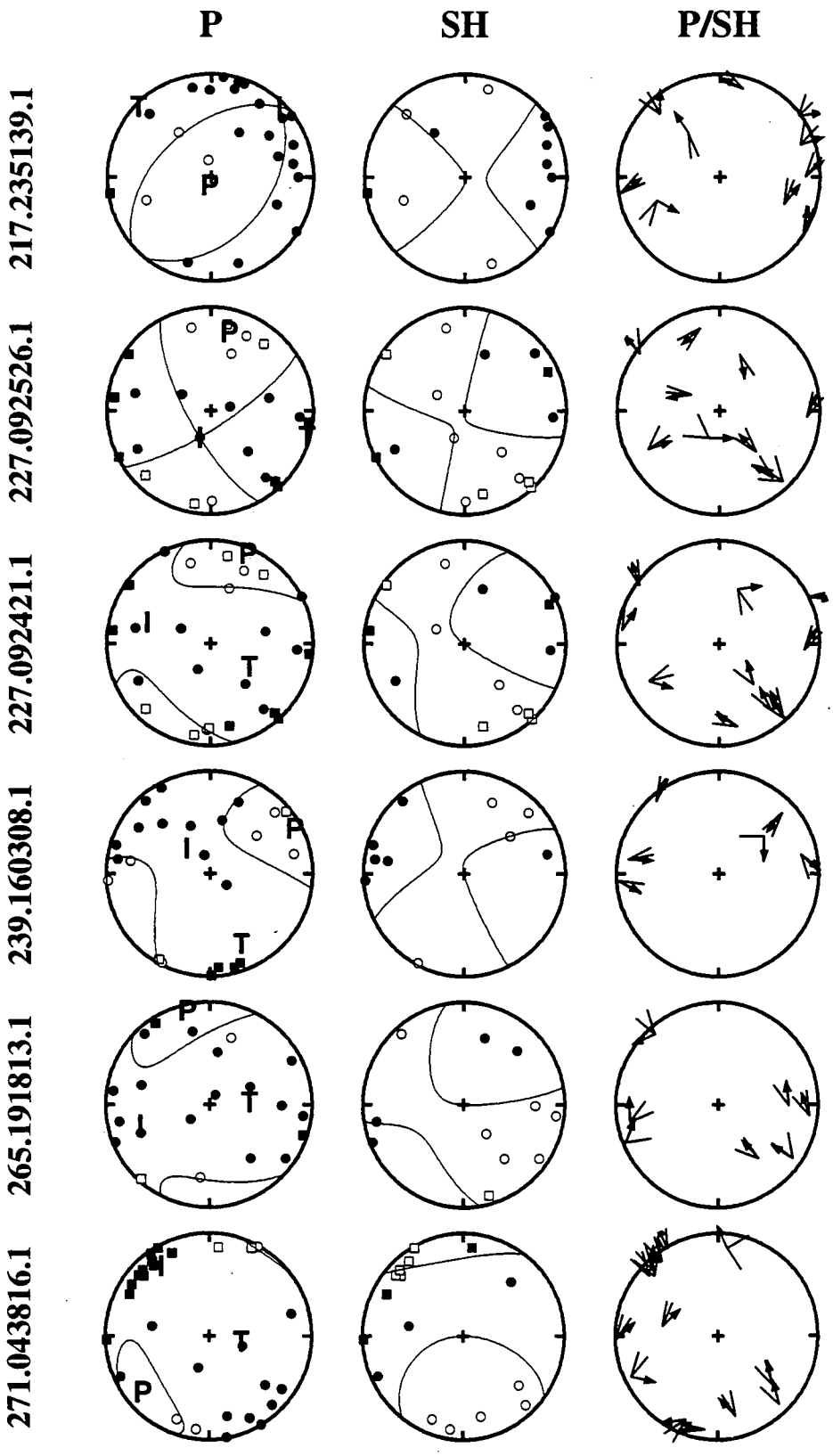

Figure 7.15: The six earthquakes that give a poor data fit. All of the earthquakes have more than 5 polarity misfits to the DC or tensile-shear models, although these are often for stations close to the nodal lines. Events 217.235139.1 and 227.092526.1 are interpreted as shear-fault earthquakes. Symbol conventions are as Figure 6.8.

7.3.3 Modelling the results

7.3.3.1 The size of the shear and tensile fault components

For all the processed earthquakes the value of R_{TF} varied from -0.18 to 0.50 for the T+S model and -0.16 to 0.37 for the OS model (Figure 7.8d). This means that for all the earthquakes the scalar moments of the shear-fault components are as large or larger than those of the tensile-fault component in both models.

The value of R_{TF} varies across the region (Figure 7.16). On average it is higher in the centre of the area (groups KLM.N, KLM.S, GRN.N and GRN.S) than in the north and west. In the GIG group, the first 13 earthquakes were part of the Gigir cluster (Section 3.5) and show a variation of R_{TF} with time, with the size of the tensile component decreasing to zero and then increasing again (Figure 7.16). There is no clear variation in R_{TF} with either earthquake depth or magnitude, although there is a very slight tendency for R_{TF} to decrease with magnitude (Figure 7.17).

The shear-fault earthquakes are distributed throughout the area (Figure 7.18), but there are proportionately more in the north and west (groups GIG, NW and NES; Table 7.4). There were no shear-fault earthquakes in the GRN.N group, which also has the highest average R_{TF} value.

Table 7.4: Distribution of the shear-fault earthquakes.

Group	No. of shear-fault earthquakes	No. of well-constrained earthquakes	% of earthquakes that are shear-fault
GIG	3	9	33
GRN.E	2	5	40
GRN.N	0	9	0
GRN.S	2	12	17
KLM.N	3	13	23
KLM.S	2	11	18
NW	3	5	60
NES	1	5	20
OLF	1	1	100
All groups	17	70	24

7.3.3.2 Fault orientations

Shear-fault earthquakes. The shear-fault earthquakes in the north and west (groups GIG, NW and NES) all have normal-fault mechanisms, whereas the other shear-fault earthquakes are predominantly strike-slip, although the earthquakes in the KLM.N group have a range of mechanisms (Figure 7.18). This pattern is similar to that of the general moment tensors. The shear-fault earthquakes are not distinguished from the other earthquakes by their fault orientation, location (Figure 7.18) or magnitude (Figure 7.17).

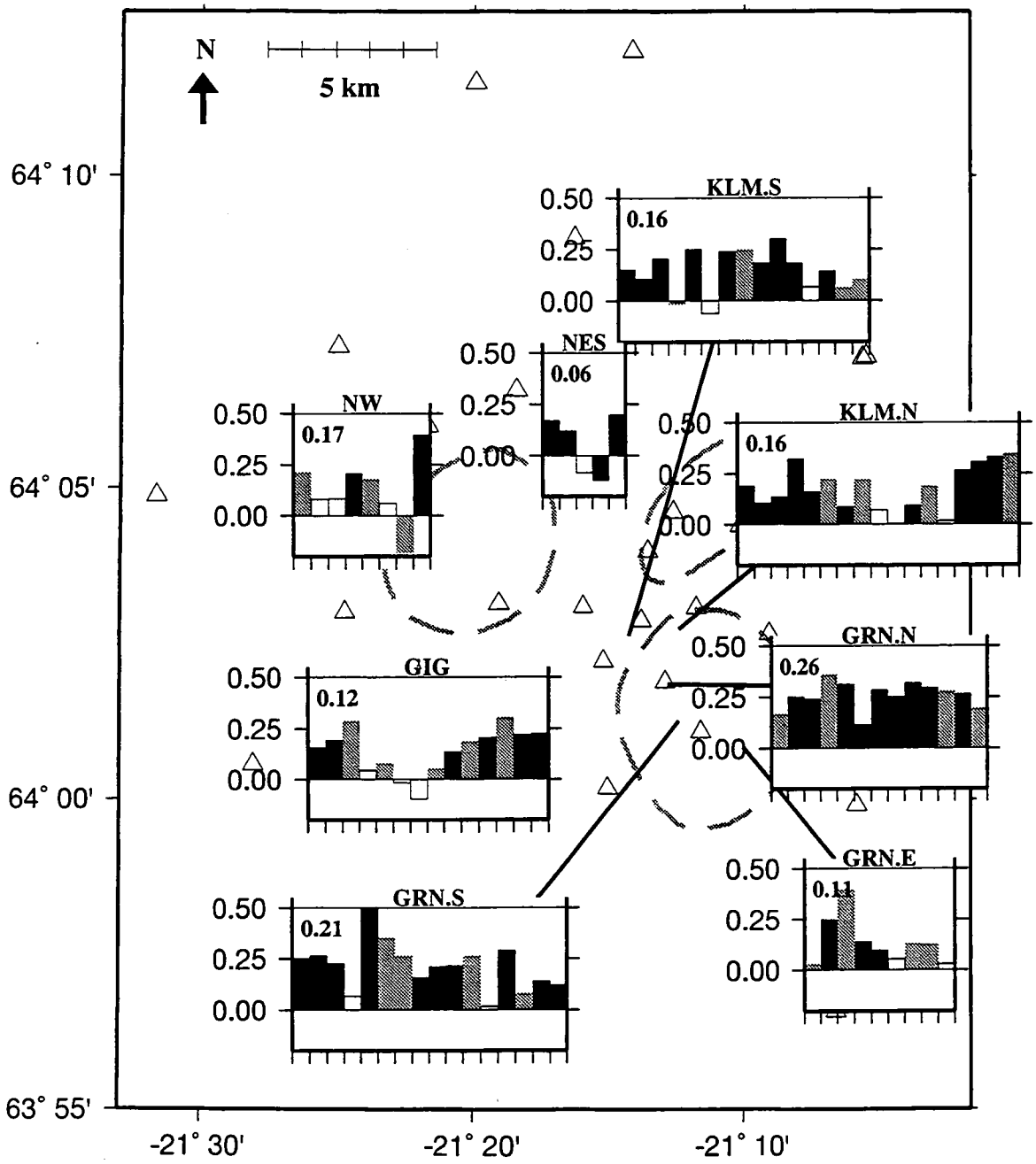

Figure 7.16: The distribution of R_{TF} for the combined tensile-shear fault model. Within each group the earthquakes are arranged in chronological order. Bars show the value of R_{TF} for earthquakes interpreted as shear-fault mechanisms (white) and tensile-shear mechanisms (black), and for poorly-constrained (grey) earthquakes. The average value of the well-constrained earthquakes in each group is shown at the top left of each graph. Other symbols are the same as for Figure 7.1.

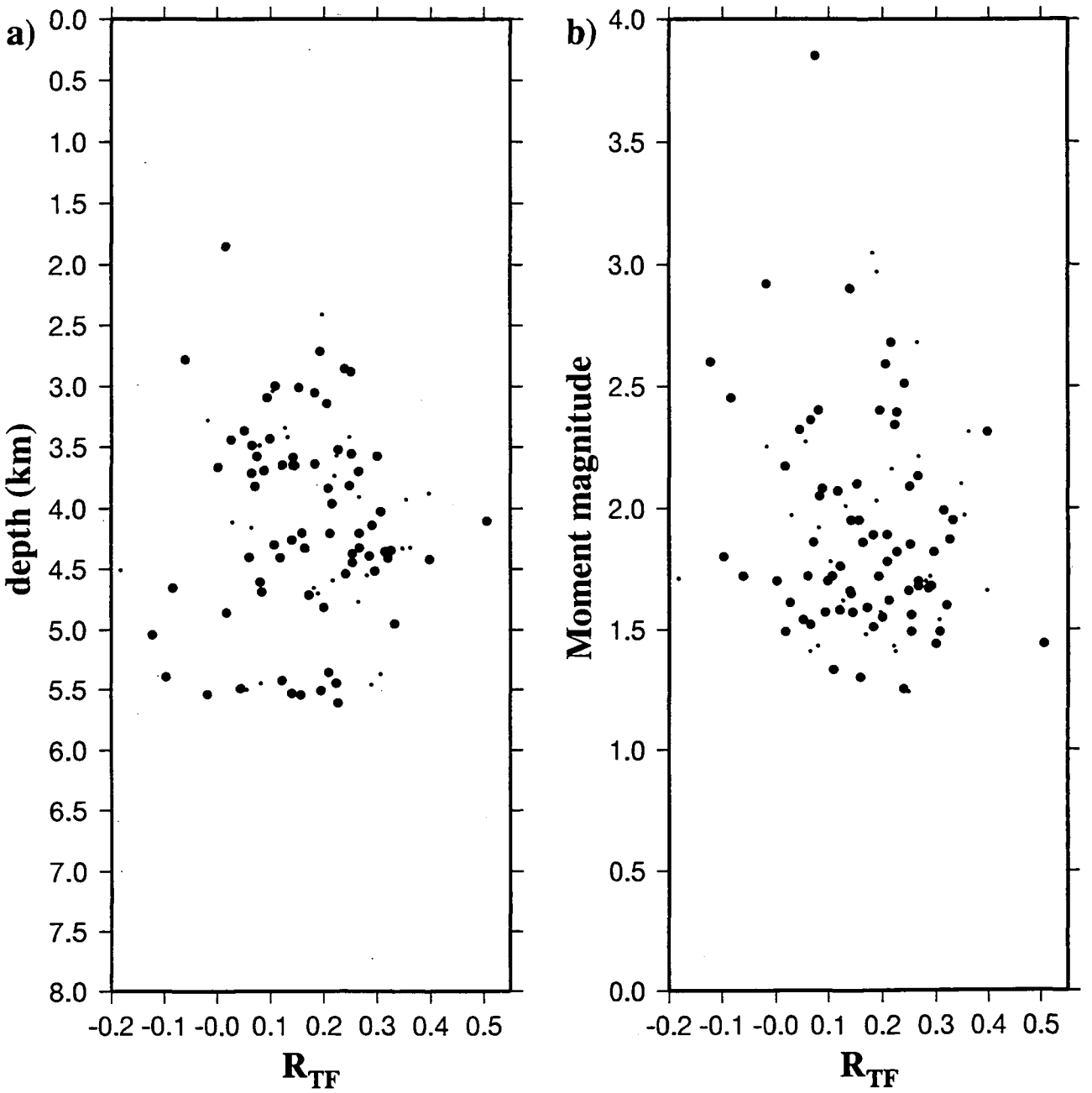

Figure 7.17: Graphs of R_{TF} for the combined tensile-shear model against (a) earthquake depth and (b) magnitude for well-constrained (large dots) and poorly-constrained (small dots) earthquakes.

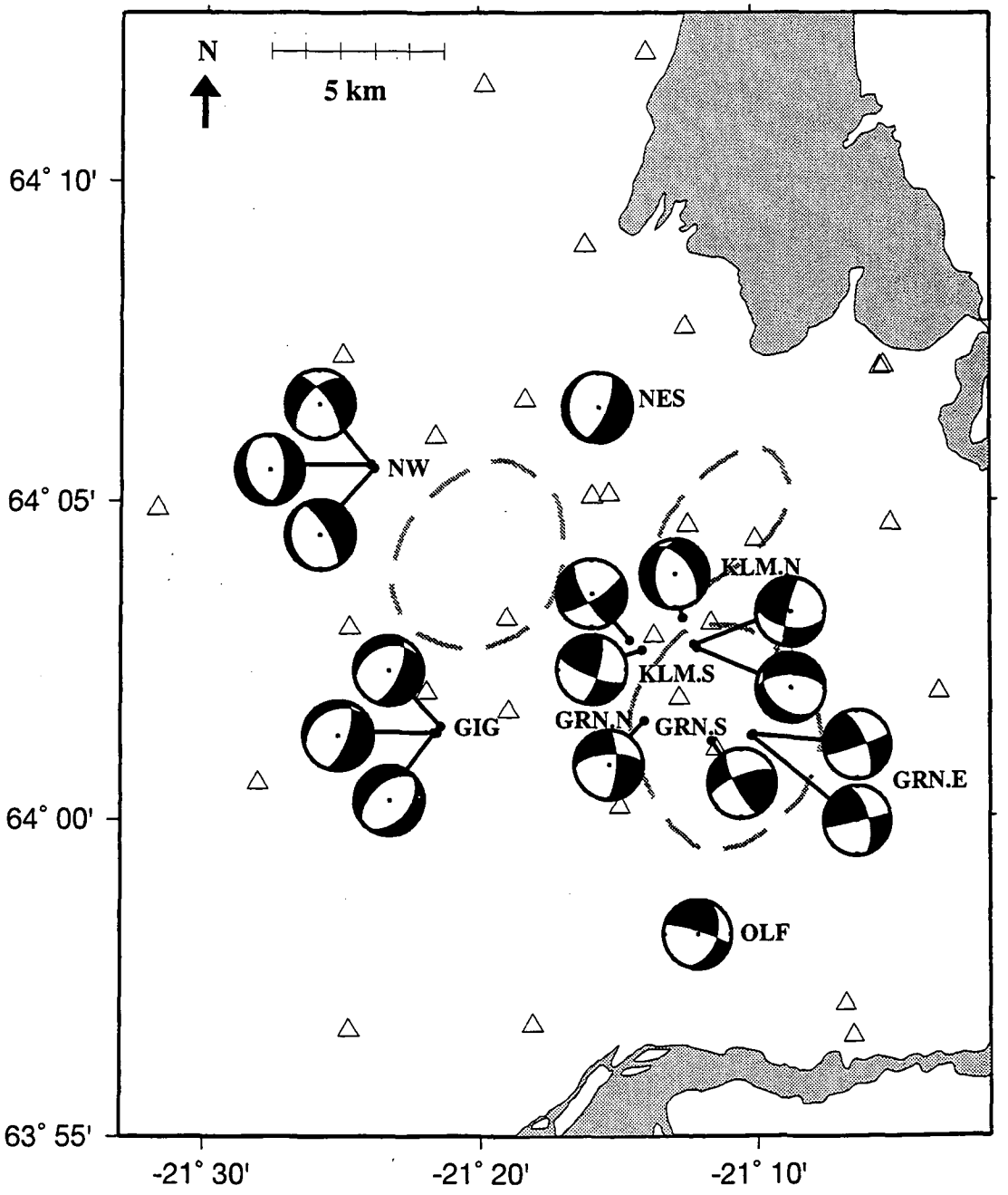

Figure 7.18: Map showing locations and focal mechanisms of the shear-faulting earthquakes. Focal mechanisms are shown in equal-area upper focal-sphere projections. Lines connect mechanisms to their epicentral positions. Where no line is shown, the mechanisms are centred on the positions of their respective epicentres. Other symbols are the same as for Figure 7.1.

The T+S model. The earthquakes lie in a range between two end-member model types, which have near-vertical tensile faults and either (1) strike-slip shear faulting or (2) normal shear faulting. Earthquakes in the north and west (groups GIG, NW and NES) tend to have normal-faulting shear-fault components, which is a pattern similar to that for the shear-fault earthquakes described above (Appendix 11). Within some groups (*e.g.*, GIG and GRN.S) there is remarkable consistency in the shear-fault components, while in other groups (*e.g.*, GRN.N and KLM.N) there are much greater variations (Appendix 11).

The tensile fault component is always orthogonal to the *T* axis of the moment tensor, and so in general the tensile faults are near-vertical and oriented northeast to southwest (Figure 7.19). There is some variation in this general trend across the area. In the northern groups (NW and NES) the strike varies from NNW to NNE. The strike is northeast to ENE in the other groups, with only a few earthquakes falling outside this trend. There is a wide variation in the orientations of the nodal planes of the DC components (Figure 7.19).

The OS model. The best-fit OS models can generally be interpreted as either (1) opening-shear, right-lateral faulting on north- to northeast-striking, near-vertical faults or (2) opening-shear, left-lateral faulting on east- to southeast-striking, near-vertical faults. Similar patterns are observed as described above for the T+S model, with some groups having very similar mechanisms and other groups showing more variation (Appendix 11). However for either interpretation of the OS model, the fault orientations show slightly less variation than for the T+S model (Figure 7.20; Appendix 11). The fault strikes are generally consistent within groups even where there is a range from strike-slip to normal faulting mechanisms (*e.g.*, the KLM.S group).

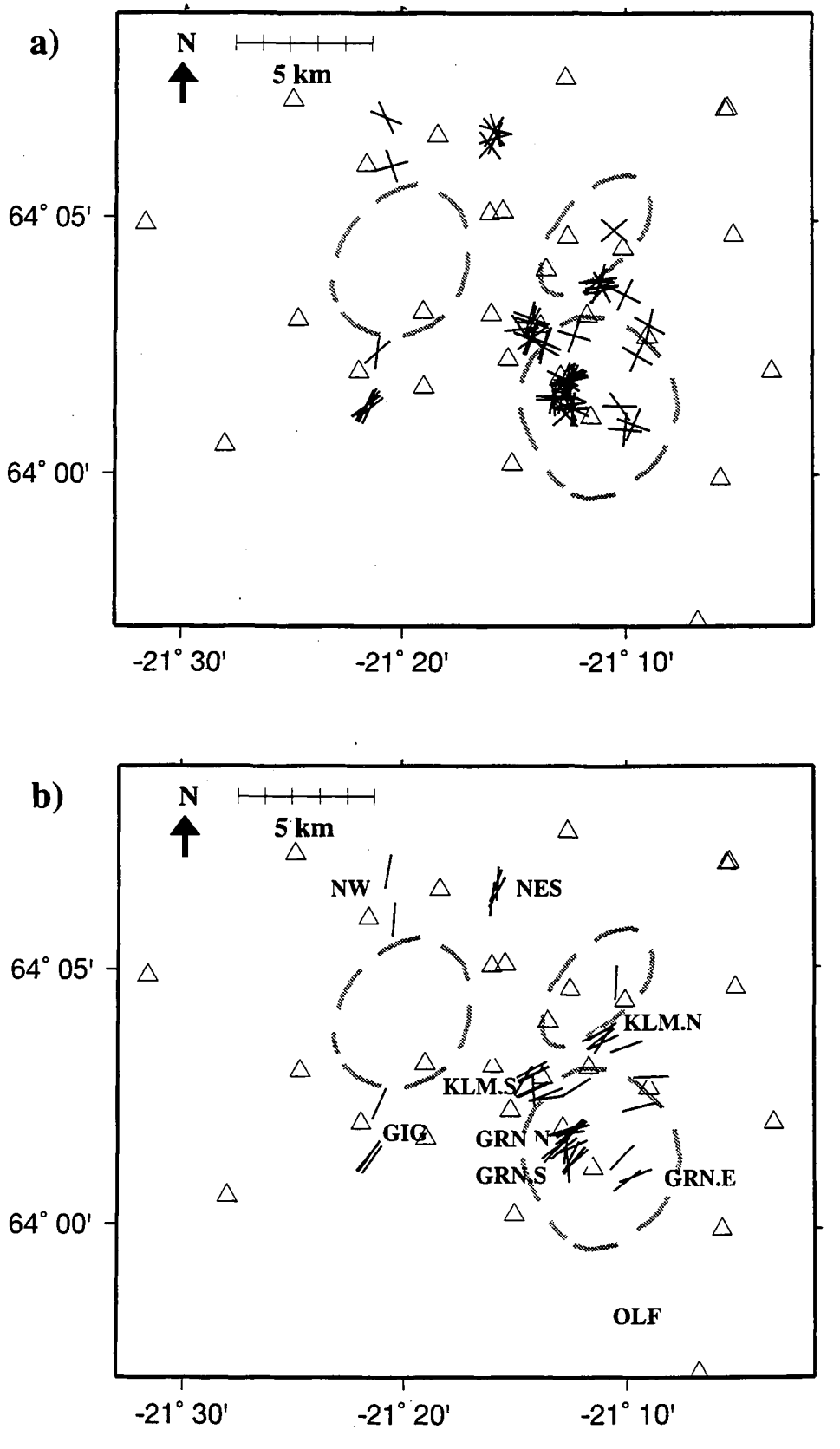

Figure 7.19: Maps showing the strike directions of the fault planes of combined tensile-shear fault models of the well-constrained tensile-shear earthquakes. (a) Orientations of both nodal planes of the shear-fault components. (b) Orientations of the tensile fault planes. Other symbols are the same as for Figure 7.1.

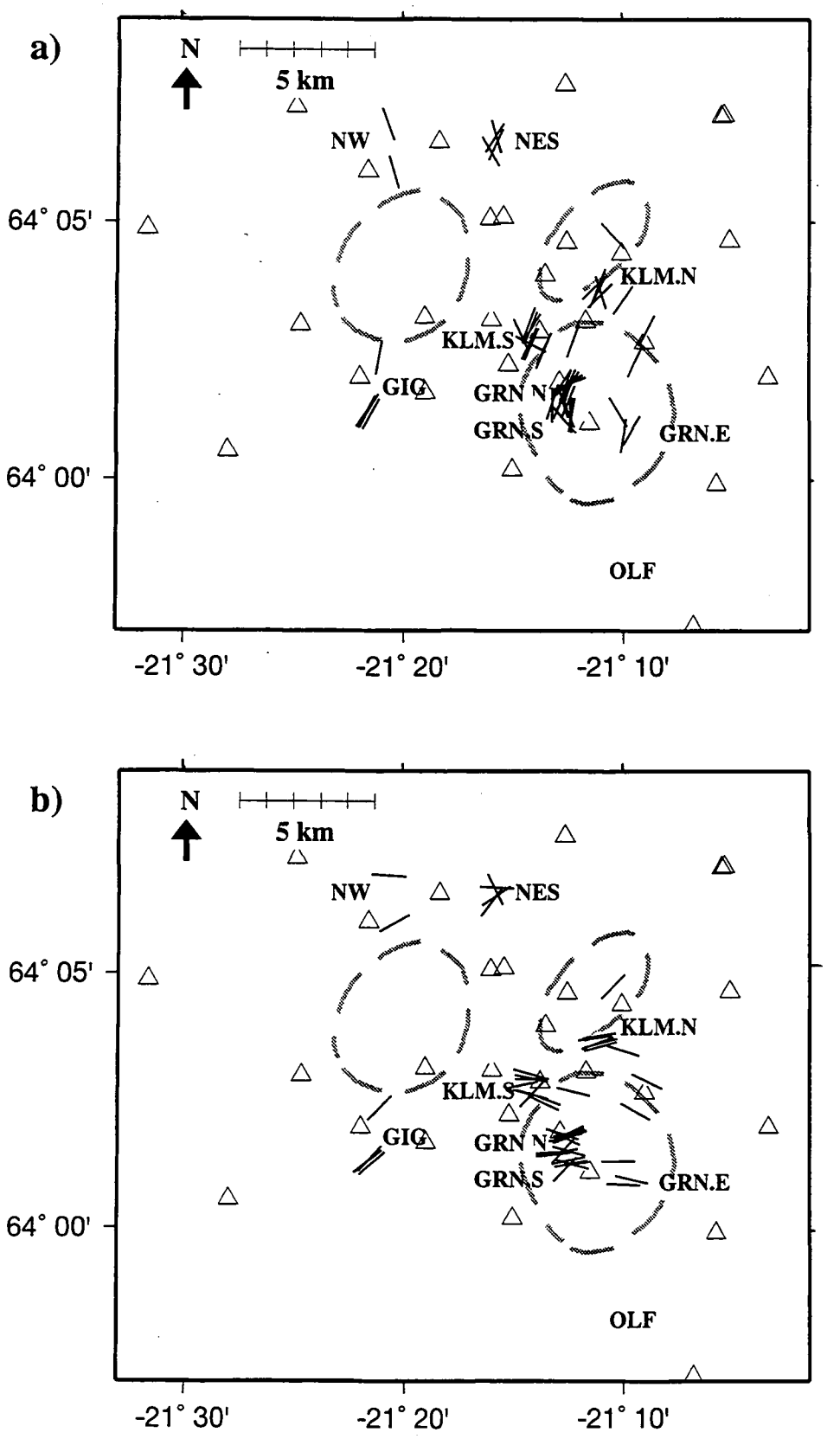

Figure 7.20: Maps showing the strike directions of the fault planes of the opening-shear fault models of the well-constrained tensile-shear earthquakes. (a) Orientations of right-lateral opening-shear fault planes. (b) Orientations of the left-lateral opening-shear fault planes. Other symbols are the same as for Figure 7.1

7.4 Summary

Moment tensors were obtained for 98 of the best-recorded earthquakes. The *T* axes are mostly aligned northwest-southeast with low angles of plunge. The *P*-axis plunges are more varied, and increase with depth. Variations in source mechanisms can be displayed on ε-*k* diagrams. Most of the earthquakes are non-DC with substantial explosive volumetric components. The stability of the moment tensors was tested by inverting subsets of data obtained by removing random selections of stations from the full data sets. Well-constrained earthquakes were identified from the amount of variation this technique produced on an ε-*k* diagram. For 17 of the earthquakes, a DC model gave a good fit to the data with a small number of polarity misfits. As a model for the non-DC earthquakes, two possible mechanisms with combinations of tensile and shear faults were considered — the "combined tensile-shear fault" model, which has two separate, inclined faults and the "opening-shear fault" model where the tensile and shear faults are coplanar. The general moment tensors were fitted to these models by least-squares fitting of the principal moments. Both mechanisms have the same best-fit moment tensor for a given earthquake, and thus give the same fit to data. The best-fit T+S model generally has steeply dipping tensile fault components striking east or northeast, accompanied by either strike-slip or normal shear fault components. There are two different possible interpretations of a best-fit opening-shear mechanism, with either right- or left-lateral faulting. Most of the opening-shear fault planes are vertical. The right-lateral faults mostly strike north to northeast, and the left-lateral faults strike easterly.

Chapter 8

Discussion and Conclusions

8.1 The station locations and design of the network

The temporary network installed in 1991 was designed to give good focal-hemisphere coverage of local earthquakes, and the resulting dataset is of excellent quality, with hundreds of earthquakes recorded by more than 10 stations. Unfortunately, the station coverage in the south of the network was sparse (Figure 3.1). The SIL station bja was a crucial component of the network, but it recorded triggered data only, unlike the temporary stations that recorded continuously. This meant that only 29% of the located earthquakes had *P*-wave arrival times from this station (Table 3.1). During two periods totalling 19 days (30% of the recording period) the timing of bja was unreliable (Section 3.2.4).

The stations installed at Bræðraból (H003 and H036) were the least reliable in the network, with *P*-wave arrival times from a combined total of only 27% of the located earthquakes (Table 3.1). These stations were located close to the field headquarters and, because of a shortage of spares, parts of them were often removed to keep other stations operational. During the period 8 August to 7 September 1991 (48% of the recording period) no station was operated at Bræðraból.

The unreliability of two out of three of the stations in the south of the network meant that analysis of the earthquakes there was restricted. This part of the area is seismically active, with a different style of activity than is found further north (Section 3.3.3; *Foulger*, 1988a). Moment tensors could not be determined for most of the southern earthquakes, despite their being well-recorded by most stations, because of poor focal-sphere coverage.

In future projects of this type, data from independent sources should be used as an addition to, rather than a crucial component of, the dataset. It makes sense that functioning equipment should be removed occasionally from an easily accessible station to allow crucial and less-accessible stations to remain operational. However, the station chosen should not be in a location that will cause a substantial gap in the network if it is out of operation for a long period.

8.2 Earthquake distribution and magnitudes

8.2.1 Distribution of hypocentres

Most of the earthquakes are located beneath the eastern part of the geothermal area and there are very few earthquakes within the Hengill fissure swarm and north of

64°08'N (Figure 3.9). This pattern is similar to that observed in 1981, suggesting that it is a persistent feature of the seismicity of the area.

Three tectonic zones are identified that have different levels of seismicity, and characteristic earthquake mechanisms and source orientations (Figure 8.1). These zones are hereafter called the northwest, geothermal, and Ölfus zones. The northwest zone includes the Hengill fissure swarm and exhibits sparse seismicity, comprising normal-faulting DC earthquakes that occur predominantly in clusters (Figures 5.12 and 7.18).

The geothermal zone covers most of the centre of the area, including the Hromundartindur and Grensdalur volcanic systems. It is intensely seismically active, with mostly non-DC earthquake mechanisms that range from strike-slip to normal faulting (Figures 7.13 and 7.16). The continuous, daily seismicity in the geothermal zone is thought to be a result of thermal contraction accompanying the cooling of heat sources beneath the geothermal area (*Foulger*, 1988b). The lack of geothermal seismicity beneath the Hengill volcanic centre, and the nature of the seismic activity in the northwest zone suggest that there is no rapidly cooling heat source there. The low-level geothermal activity at Nesjavellir is accompanied by only a small number of earthquakes (Figure 5.12).

In the Ölfus zone the seismicity is generally deeper, and separated from the seismic activity in the north by a three-km wide aseismic zone (Figures 5.12 and 5.13). The earthquakes in the Ölfus zone lie mostly in an east-west line, and are larger in magnitude than the earthquakes in the north (Figure 3.15). Only one focal mechanism could be determined, which was interpreted as a strike-slip shear fault (Figure 7.13). This zone probably reflects a different tectonic regime, dominated by the SISZ (Section 1.3.1.4).

8.2.2 Earthquake clusters

The three clusters for which accurate relative locations were obtained show linear arrangements of hypocentres, especially the Gigir and Marardalur clusters, that suggest the earthquakes in each cluster occurred on the same fault plane (Section 3.5). At Gigir and Marardalur, the fault planes are near-vertical and strike northeast.

The Marardalur and Dyradalur clusters to the northwest are not in the same locations as similar clusters observed in 1981 (Figure 3.13). The differences in location are larger than the errors in the 1981 locations, suggesting that these clusters represent activity on different faults. The seismicity in the northwest is dominated by cluster activity that lasts for a few days only. These clusters mostly consist of earthquakes with similar magnitudes, and there are no clear mainshocks (Figures 3.18 and 3.19).

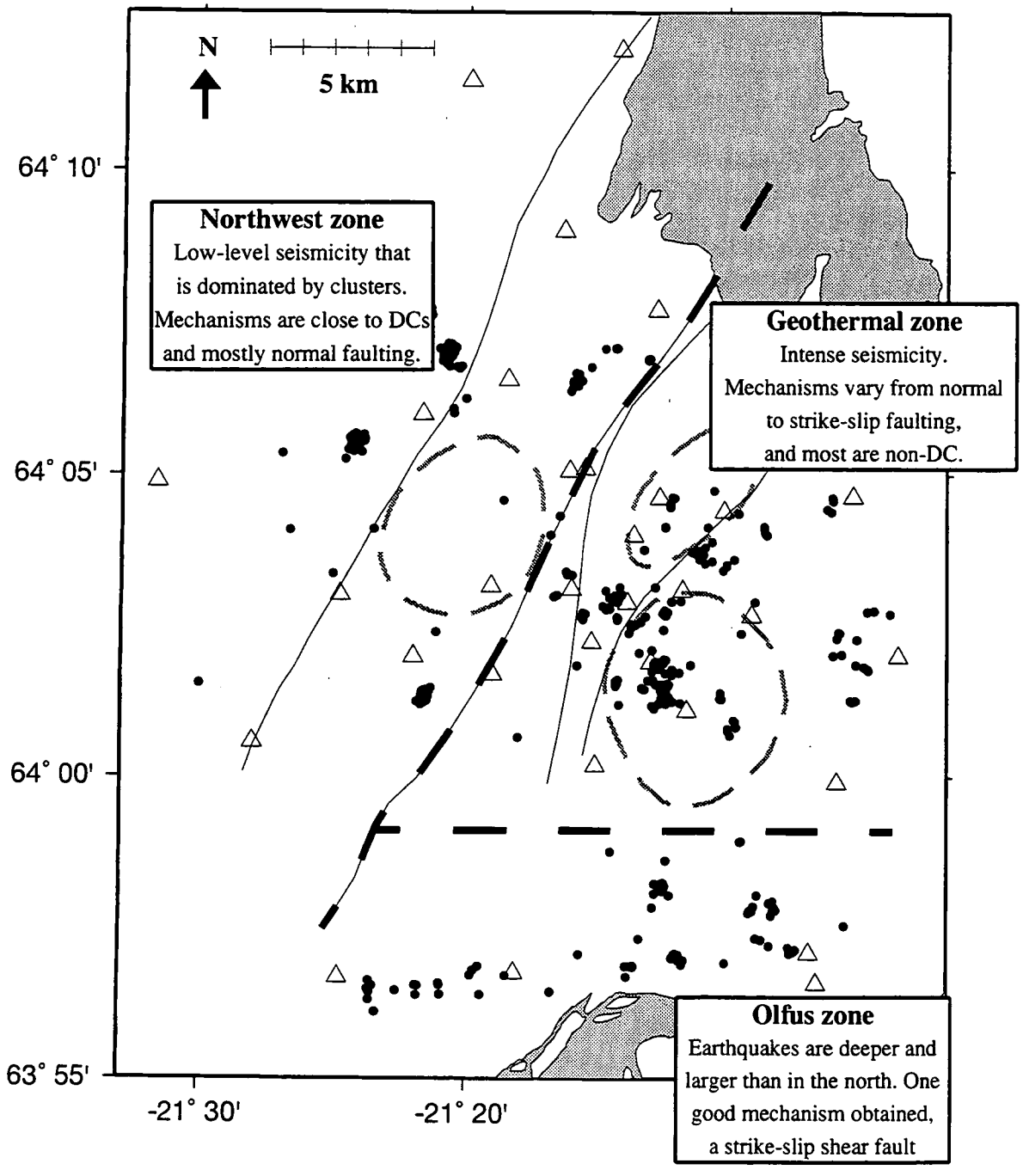

Figure 8.1: Map showing the three zones that exhibit different characteristic earthquake activity. Black dashed lines: zone boundaries; grey dashed lines: outlines of volcanic centres; thin lines: outlines of the volcanic systems; triangles: seismic stations; solid dots: earthquakes of the 1991 dataset.

8.2.3 Earthquake magnitudes

The magnitudes calculated for earthquakes in the 1991 dataset are generally over-estimated compared with the M_{IL} and M values calculated from the SIL network data (Figure 3.16). The systematic offset from the straight-line magnitude-frequency relationship for high magnitudes (Figure 3.14) suggest that the method used to calculate scalar moment (Section 6.5.6) may under-estimate high magnitudes or over-estimate low magnitudes. The latter is supported by comparison with the moment magnitudes calculated from the SIL network (Figure 3.14c).

A more sophisticated method of calculating scalar moments from the amplitudes of first motions is required. For small earthquakes, a step-function release of moment can be assumed, and then the ground displacement will approximate a delta function whose area is proportional to the moment release. To obtain the true ground displacement, the responses of the instrument and the low-pass filter must be removed from the seismogram. For the purposed of this study, the calculated scalar moments give an adequate approximation to the relative sizes of the studied earthquakes.

8.3 The local earthquake tomographic method

8.3.1 The use of *velest* to determine the starting one-dimensional model

Several attempts were made to improve the one-dimensional wave-speed model input to *simulps12* (Section 5.1.2). In retrospect, this effort was unnecessary. The "minimum" one-dimensional model used for the final inversion differed only slightly from the most obvious starting model, which was based on the previous three-dimensional model obtained by *Toomey and Foulger* (1989). The starting model can have a small effect on the absolute values of the final models, but the main interpretable features of the final models are variations in wave speed, and these are affected only slightly by different starting models.

8.3.2 Inversion strategies

After extensive testing, the simplest inversion strategy was followed which is inverting for both the V_P and V_P/V_S models at the minimum nodal spacing in one step, using a one-dimensional starting model (Section 5.1.6). This method was chosen because it resulted in smooth models with low-amplitude anomalies that gave a good reduction in data variance. In other areas, graded inversions, where the models evolve through several stages of decreasing nodal spacing and increasing complexity, have been found to give better results (*e.g.*, *Julian*, 1996b).

8.3.3 Repeatability of local earthquake tomography

This study is the first time to the author's knowledge that the results of two separate LET studies of the same area have been compared in detail (Section 5.3). The two

inversions used different model parameterisations and slightly different inversion programs. There was some overlap in the earthquake datasets used, as earthquakes from 1981 were used in both inversions.

The TF81 model has a "checkerboard" pattern in some parts, where the wave speed oscillates between adjacent nodes (Figure 5.15). In contrast, the 81+91 model is much smoother with few sharp changes in wave speed. The anomalies tend to fill larger volumes but have smaller maximum amplitudes in the 81+91 model (Figure 8.2). This is mainly a result of the TF81 model being obtained using slightly lower damping, and also because the residuals of the 1981 dataset are larger and more scattered, leading to a more complex model. Some of the extreme values in the TF81 model are reduced when the inversion of the 1981 data is repeated using *simulps12* and with outliers in the dataset removed (Figure 5.14). This suggests that some of the differences between the TF81 and 81+91 models are due to the changes between the *simul3* and *simulps12* programs. These improvements include the use of more exact three-dimensional ray tracing. Also, the inclusion of a small number of outliers in the initial 1981 dataset have a relatively large effect, especially in the inversion statistics (Table 5.1) but also in the final model (Figure 5.14). This emphasises the importance of checking datasets for mispicks.

When the absolute values of the two models are compared, the RMS difference is high (0.25 km/s) and approaching the size of the anomalies in the 81+91 model. The LET method does not constrain absolute values well, as there is a trade-off between absolute values and earthquake depth, and the final absolute wave speed depends on the initial model. The use of *S*-waves improves this situation as the depth of the earthquakes is better constrained. In comparing and interpreting models the wave-speed variations in each layer are thus the most significant features. The lack of repeatability of fine details emphasises that only the major features of LET models can be interpreted with confidence.

There are only small differences between the hypocentral locations of the 1981 earthquakes located in the TF81 and 81+91 models. Most of the earthquakes have relocations of less than 200 m both vertically and horizontally (Figure 8.3). However a few earthquakes experience major changes in depth, of over 1 km in four cases. Earthquakes that show such large instabilities when located in different models should not be included in LET datasets.

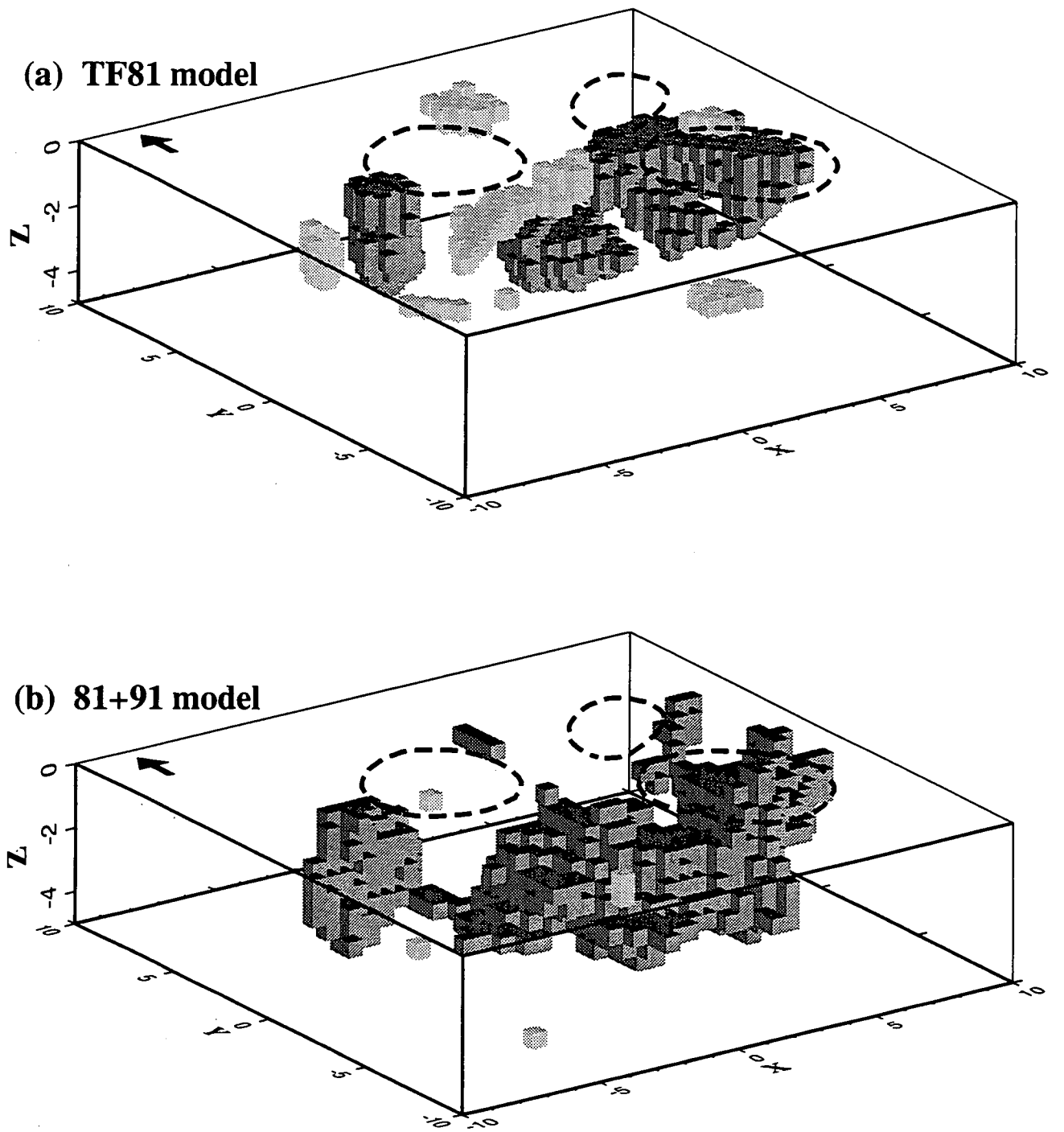

Figure 8.2: Three dimensional views from the southwest of (a) the model of *Toomey and Foulger* (1989) (the TF81 model) and (b) the final V_P model determined in this study (the 81+91 model). Wave speed is represented as constant-value blocks of side 0.5 km, although the models actually vary continuously. Only blocks with differences of larger than ±0.3 km/s from the starting wave-speed are shown. Light grey: low V_P; dark grey: high V_P; dashed lines: outlines of volcanic centres. Black arrows point north. The local co-ordinate system used is that of the 81+91 model (Figure 5.1b).

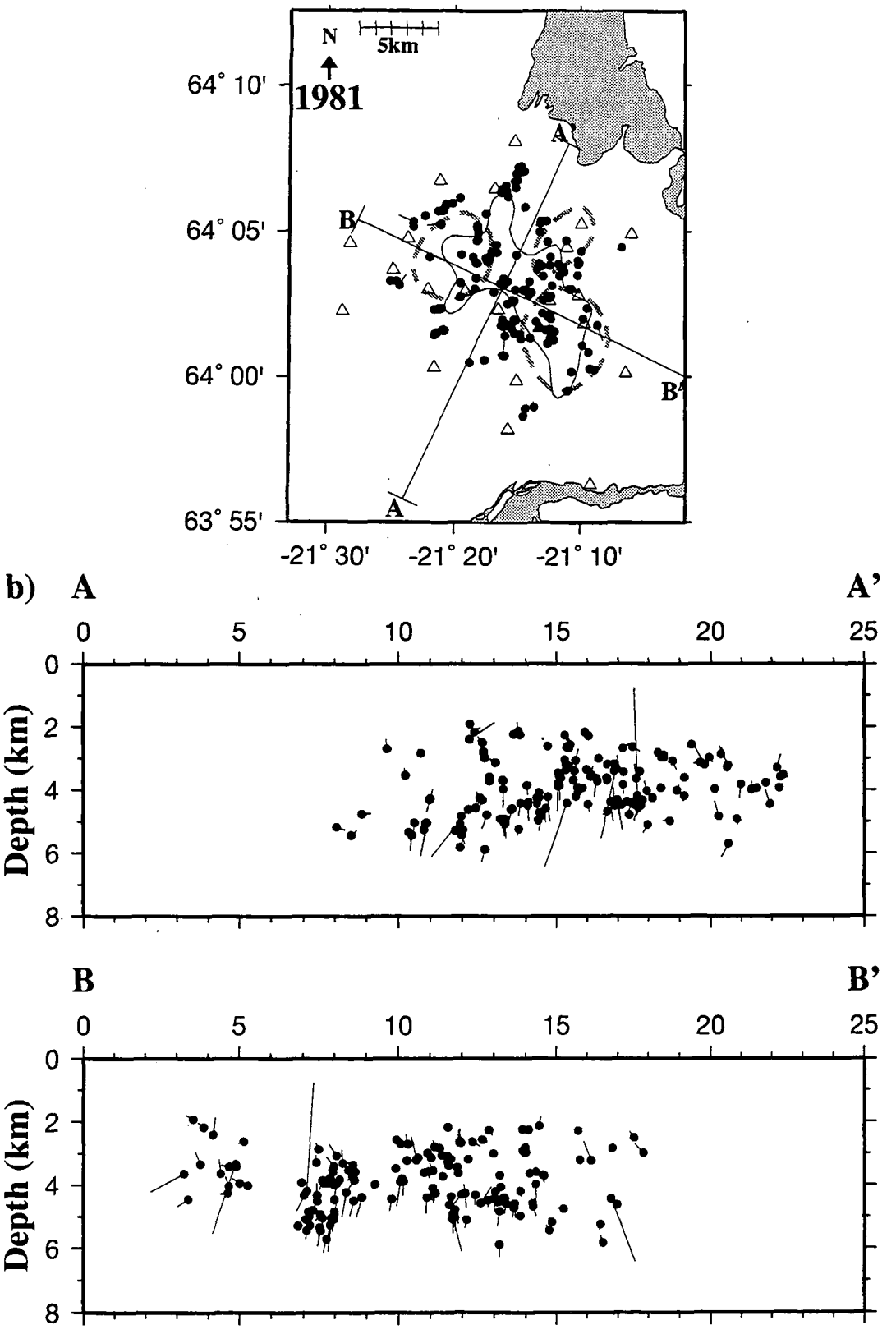

Figure 8.3: (a) Map and (b) depth sections of hypocentre locations (solid dots) in the final three-dimensional model, and changes in locations (lines) from the three-dimensional model of *Toomey and Foulger* (1989). In (a) the lines A-A' and B-B' mark the positions of the depth sections shown in (b). Dashed lines: outlines of volcanic centres; triangles: stations installed in 1981.

8.4 Interpretation of the seismic structure

8.4.1 The V_P model

The main features of the V_P model obtained in this study are similar to those of the TF81 model (Figures 5.15 and 8.2). The 81+91 model covers a larger area than the TF81 model, but no additional significant anomalies were detected. The major differences between the models are in the amplitudes of the calculated wave-speed anomalies, and the lack of significant volumes of low relative wave-speed in the 81+91 model. In the 81+91 model the anomalies tend to be broader but of a lower maximum amplitude. However the same three high-V_P bodies can be identified in both models (Section 5.2.2; Figure 8.2). These bodies are probably solidified, high-density magma intrusions (*Foulger and Toomey*, 1989).

The body beneath Húsmúli is a narrow, cylindrical conduit that extends to 4 km depth. In the TF81 model this body curves slightly towards the Hengill volcano at depth, but this second-order feature is not visible in the 81+91 model (Figure 8.4). The Grensdalur body lies at 0-2 km beneath the northern section of the mapped Grensdalur volcano, and extends slightly to the east. This body is interpreted as the exhumed centre of an extinct and eroded volcano (*Foulger and Toomey*, 1989). The third body lies beneath Ölkelduhals between 2-4 km depth and continues to 5 km depth, where it is displaced slightly northwest (Figure 8.4) In the 81+91 model, the Grensdalur and Ölkelduhals bodies are joined together below 2 km. The Ölkelduhals body is relatively aseismic from 4 to 5 km, and is associated with a temperature maximum in the geothermal area (Figure 1.11). It is thought to be the solidified magma chamber that supplied magma to the Hromundartindur system to the northeast (*Foulger and Toomey*, 1989).

The 81+91 model has no significant volumes of low V_P. This may be due partly to the generally lower starting model used (Figure 5.2). However there is no evidence of relatively low V_P in the 81+91 model that corresponds with the volume of low-V_P in the TF81 model (Section 5.3.2). The low V_P body in the TF81 model may be a spurious artefact caused by low damping that lead to unrealistic oscillations between adjacent nodes (a "checkerboard" pattern). A low-V_P volume is not required to explain the residuals in the higher-quality 1991 data set. The 81+91 model is smoothly varying, and almost certainly under-estimates the geological complexity of the region. However it is constrained by a high-quality data set and gives a good final data variance value, so it is probably an improvement on the TF81 model.

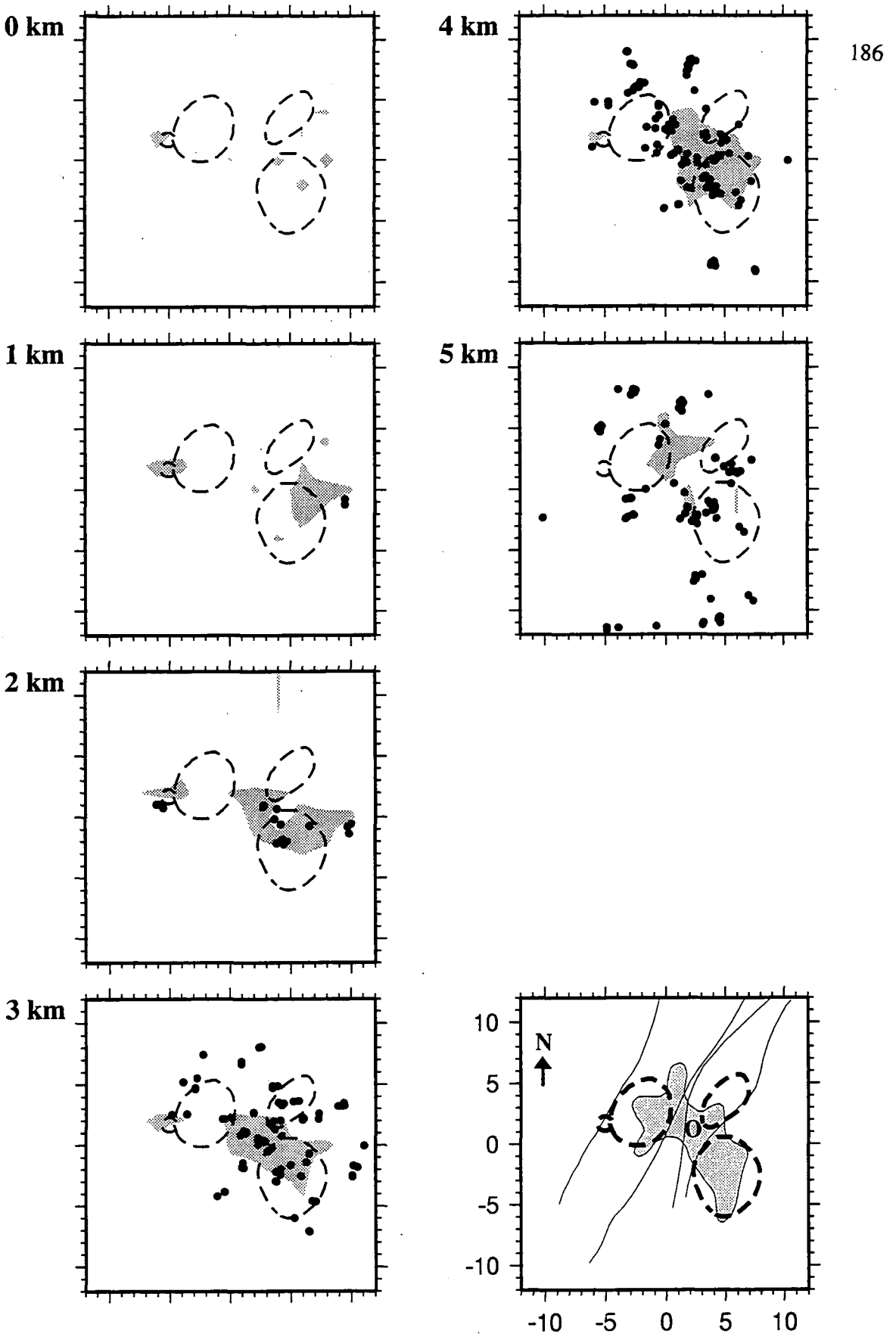

Figure 8.4: Map views from 0 to 5 km depth of the high-V_P bodies (grey), defined as V_P greater than 0.3 km/s difference from the starting value. Solid dots are hypocentres between ±0.5 km of each depth. Map at lower right shows the positions of the volcanic centres (dashed lines), volcanic systems (thin lines) and the geothermal field (shaded). O: Ölkelduhals.

8.4.2 The V_P/V_S model

8.4.2.1 Factors affecting V_P/V_S

The main factors that affect V_P/V_S are depth, porosity, saturation, lithology, pore fluid content, the presence of partial melt and temperature. Clearly, when so many inter-related factors can explain changes in V_P/V_S, it is impossible to uniquely determine the cause of a V_P/V_S anomaly unless detailed information about the rock type, pore fluids and amount of saturation is available.

Depth: The value of V_P/V_S decreases with confining pressure and thus with depth. This has been illustrated by borehole measurements in various geographical regions, which show that V_P/V_S varies from 2-4 in the upper 2 km and then decreases to a constant value at deeper levels (*e.g.*, Figure 11 of *Nicholson and Simpson*, 1985). Decreasing V_P/V_S with depth is also detected by graphical analysis of local earthquake arrival times (*e.g.*, *Nicholson and Simpson*, 1985) and inversion of *P* and *S*-wave travel times (*Walck*, 1988; *Thurber and Atre*, 1993). In laboratory experiments with saturated Casco granite, *Nur and Simmons* (1969) measured a decrease in V_P/V_S from 2.19 to 1.76 as confining pressure increased from 0 to 2×10^8 Pa (equivalent to depths of approximately 0 to 7 km).

Calculations of V_P/V_S using LET tend to yield smaller-magnitude decreases in V_P/V_S that are not just restricted to the upper 2 km. In the Coso region, California, *Walck* (1988) found a change in V_P/V_S from about 1.9 to 1.5 in the upper 10 km, although this pattern was complicated by low V_P/V_S associated with surface geothermal areas. At Loma Prieta, California, a systematic decrease was detected in V_P/V_S, from >1.8 at the surface to 1.57 at 16 km depth, although part of this decrease may be due to a change in lithology at about 10 km depth (*Thurber and Atre*, 1993).

LET methods are not suitable for detecting shallow variations in V_P/V_S. All the raypaths used in the inversion pass through the whole of the layer above the shallowest earthquake, and vertical V_P/V_S variations along the sections of raypaths within this layer cannot be detected. Although surface explosions have raypaths through the upper crust, they generate poor *S* waves and thus cannot be used to detect V_P/V_S variations. This may explain why LET models do not show high V_P/V_S values (>2) at the surface.

The decrease of V_P/V_S with depth has been attributed to the closing of cracks with increasing confining pressure. For saturated cracks, theoretical studies show that V_P/V_S decreases with increasing pressure, as V_S increases at a higher rate than V_P (*O'Connell and Budiansky*, 1974).

Lithology: The variation of V_P/V_S between different igneous rocks has not been extensively studied, but it is known that the chemical composition of sedimentary rocks has a smaller affect on V_P/V_S than other factors, such as porosity (*e.g.*, *Tatham*, 1982). For most rock types, the V_P/V_S value is similar if all other factors are equal. One

exception is quartz-rich rocks, which have low V_P / V_S values because quartz has a low Poisson's ratio. Pure quartz has a V_P / V_S value of 1.48 (*Simmons and Wang*, 1971).

Temperature and the presence of partial melt: In dry rocks, there is negligible change in V_P / V_S with increasing temperature for a range of lithologies, although both V_P and V_S decrease (*Kern and Richter*, 1981). Theoretical calculations of wave speed in rocks with small melt fractions show that V_P / V_S should increase in the presence of partial melt (*Mavko*, 1980). Both V_P and V_S decrease but V_S decreases at a higher rate. The amount of change of V_P / V_S depends on the size of the melt fraction and the geometry of the melt. For a 5% melt fraction with tube geometry, olivine at 2×10^9 Pa is predicted to have a 5% decrease in V_P and a 10% decrease in V_S, giving a V_P / V_S increase of about 6%.

Porosity and saturation: The behaviour of V_P / V_S with changes in porosity is closely related to changes with depth, as porosity decreases with depth if the lithology remains the same. The value of V_P / V_S is sensitive to saturation in the shallow crust. Dry laboratory samples at surface pressures have much lower V_P / V_S values than saturated samples, but this difference decreases with increasing pressure. When samples are saturated at lithostatic pressures they have constant, high V_P / V_S values that are not pressure-dependent. Dry samples, or those saturated at hydrostatic pressures have lower V_P / V_S (*Nur and Simmons*, 1969).

To determine the behaviour of V_P / V_S under different pore-fluid conditions *Ito et al.* (1979) measured wave speeds in water-filled Berea sandstone under a range of pore pressures and at three different temperatures. Under P and T conditions that spanned the liquid-vapour transformation boundary, it was found that V_P / V_S decreased as the rock became vapour-saturated, because V_P decreased at a higher rate than V_S (Figure 8.5). A similar response of V_P / V_S to lowered pressure and an increase in vapour phase component was inferred by *Julian et al.* (1996b) for The Geysers geothermal area, California.

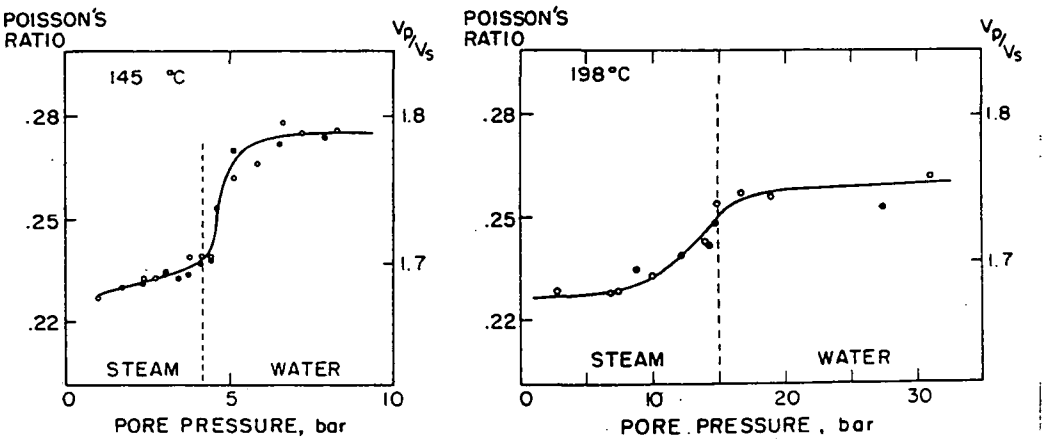

Figure 8.5: Graphs of Poisson's ratio and V_P / V_S against pore pressure for temperatures of 145°C (left) and 198°C (right) in water-filled Berea sandstone samples. Lines are hand-fitted curves through the points (from *Ito et al.*, 1979).

8.4.2.2 Measurements of V_P / V_S in other geothermal areas

There have been only a few V_P / V_S determinations in other geothermal areas. In the Yellowstone caldera, Wyoming, a low, caldera-wide V_P / V_S value of 1.65 (compared with a mean of 1.78 outside the caldera) was attributed to the effect of high-temperature geothermal reservoirs that contained hot water close to the water-vapour transition (*Chaterjee et al.*, 1985). Even lower V_P / V_S anomalies (of about -4% from the caldera average) were associated with surface geothermal areas within the caldera. *Walck* (1988), in a regional three-dimensional tomographic study at Coso, California, detected abnormally low V_P / V_S (-10% to -15%) in the upper 3 km at surface geothermal areas. At The Geysers geothermal area, California, a three-dimensional tomographic inversion for V_P and V_P / V_S structure detected a low V_P / V_S anomaly (-9%) that corresponds closely to the most intensively exploited part of the geothermal reservoir (*Julian et al.*, 1996b). This anomaly is attributed to low pore pressure and relative dryness due to steam extraction (*Julian et al.*, 1996b).

8.4.2.3 V_P / V_S in the Hengill area

The mean V_P / V_S value of 1.77 at depth of 0 to 6 km in the Hengill area is similar to determinations of shallow crustal V_P / V_S in other regions (*e.g.*, *Chaterjee et al.*, 1985; *Walk*, 1988; *Thurber and Atre*, 1993; *Julian et al.*, 1996b). There is no evidence of a decrease in V_P / V_S with depth although, as mentioned above, the LET method is not able to detect vertical variations in V_P / V_S above the shallowest earthquakes used, *i.e.*, above about 2 km over most of the area and above 4 km in the south. Given the presence of numerous open fissures at the surface, it seems likely that V_P / V_S at the surface is significantly higher than the mean value of 1.77.

The negative V_P / V_S anomaly that correlates with the surface expression of the geothermal field (Figure 8.6) is consistent with the findings of previous studies of V_P / V_S in geothermal areas. The shape of the anomaly in depth section (Figure 5.11) suggests that it has a source within a discrete volume at a depth of 3-4 km beneath Ölkelduhals, corresponding to one of the high-V_P bodies, and one of the geothermal maxima.

The amplitude of the Hengill V_P / V_S anomaly (-4%) is substantially smaller than those of anomalies detected elsewhere. This suggest that the heterogeneity that causes the low V_P / V_S at Hengill is not as extreme as is found in other areas. No high V_P / V_S anomalies were detected, which supports the theory that there are no major volumes of partial melt in the upper 6 km.

It is difficult to identify the cause of the V_P / V_S anomaly without more detailed information about the state of pore fluids and cracks at depth within the geothermal area. Unfortunately, boreholes in the Hengill area are located to the north and south of the main geothermal area, so no borehole information is available from the areas where the V_P / V_S anomaly is most intense.

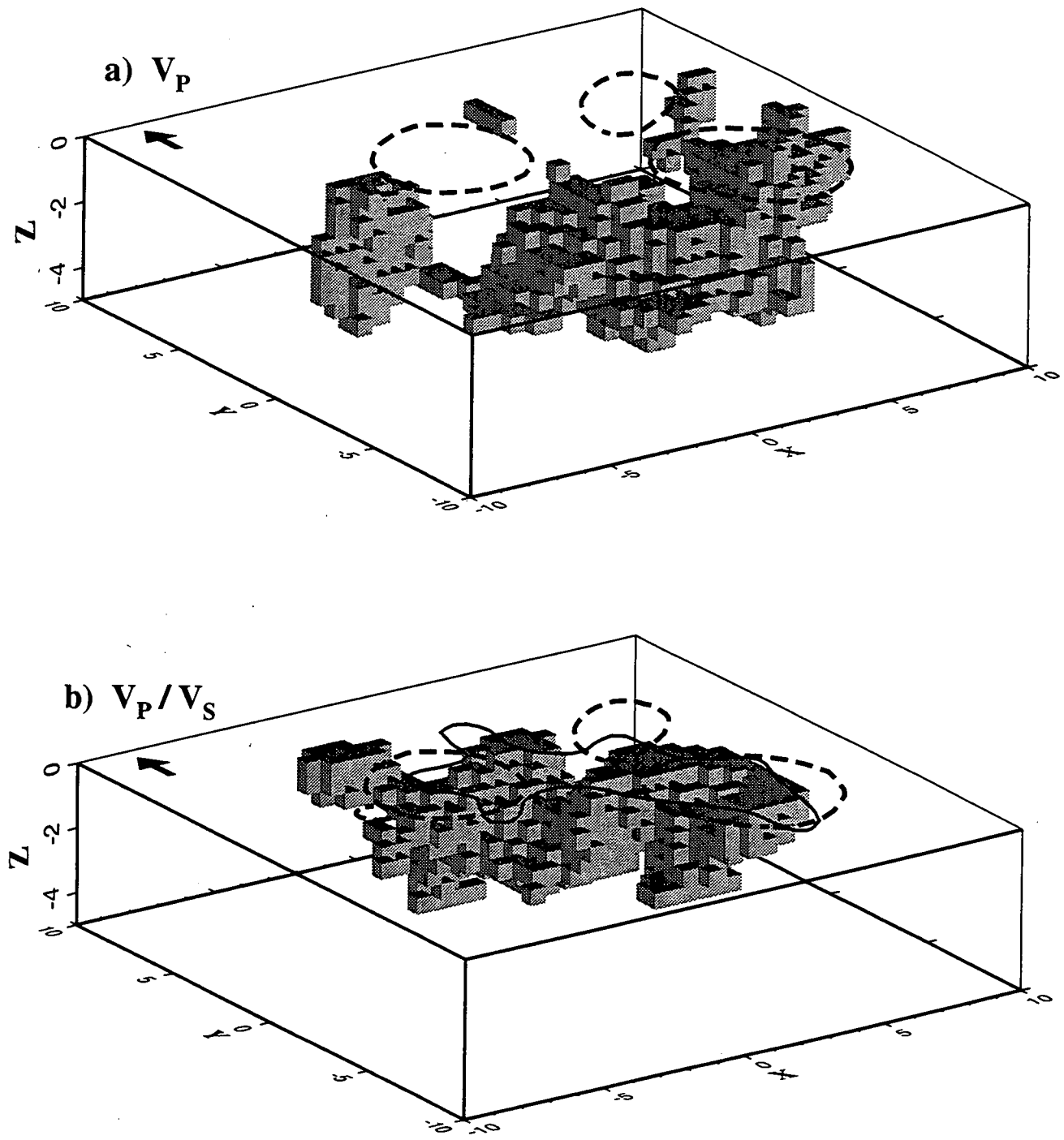

Figure 8.6: Three-dimensional views from the southwest of the final (a) V_P and (b) V_P / V_S models in this study. The values of V_P and V_P / V_S are represented as constant-value blocks of side 0.5 km, although the models actually vary continuously. Only the significant anomalies are shown, of (a) V_P greater than 0.3 km/s difference from the starting model and (b) $V_P / V_S < 1.71$. Dashed lines: outlines of volcanic centres; black line on (b) is the outline of the geothermal field. Black arrows point north. The local co-ordinate system used is shown in Figure 5.1c

A small decrease in pore fluid pressure (or equivalently a small increase in the steam content) could easily cause a 4% decrease in V_P/V_S if all other factors were equal (Figure 8.5). Such a change would be associated with a decrease in V_P, which is not observed, and in fact the volumes with low V_P/V_S are generally associated with volumes of above-average V_P (Figure 8.6). The changes in lithology associated with the high-V_P bodies (Section 8.4.1) may cancel out the V_P decrease caused by a decrease in the pore fluid pressure. Alternatively, the Hengill V_P/V_S anomaly could be due to a systematic difference in the rock matrix between the area of maximum geothermal activity and the surrounding area. This difference may be due to the presence of silicic geothermal alteration products, which would lower V_P/V_S. It is probable that the V_P/V_S anomaly is due to a combination of factors that cannot be accurately quantified using the data currently available.

8.6 Inversion of polarities and amplitude ratios to determine moment tensors

8.6.1 The data used

The *focmec* program can invert any combination of *P*, *SH* and *SV* polarities, amplitudes or amplitude ratios to determine the range of mechanisms that are compatible with the data, or the best-fit mechanism if no compatible mechanisms exist (Section 6.4.2). Where the amplitudes of two phases are available (*e.g.*, *P* and *SH* amplitudes) then it is best to invert amplitude ratios rather than amplitudes, as this eliminates differences in the response of different instruments and reduces the effects of scattering and attenuation. Differential attenuation of *P* and *S* waves still has to be accounted for, and can make a significant difference to the values of *P*:*S* ratios (Section 6.5.4).

The best constraint on earthquake mechanisms comes from *P*-wave polarities and *P*:*SH* amplitude ratios. For a range of mechanisms with varying explosive components, the polarities and amplitudes of *SH* and *SV* waves vary little (Figure 8.7), and so place little constraint on mechanisms, and especially their volumetric components.

8.6.2 Inversion of fewer data: applicability to other areas

All of the earthquakes for which well-constrained moment tensors were calculated had at least 14 *P* and 9 *S* polarity measurements and 4 amplitude ratios. The best-recorded earthquake had 27 *P* and 28 *S* polarities and 22 amplitude ratios. In local earthquake studies this number of high-quality records is rarely available. To test the reliability of the method for a smaller number of stations, inversions using data from a selection of stations only were carried out for a trial earthquake (Figure 8.8). Only *P* and *SH* polarities and *P*:*SH* amplitude ratios were used, as these are the data that best constrain the moment tensor, and are also the easiest to measure.

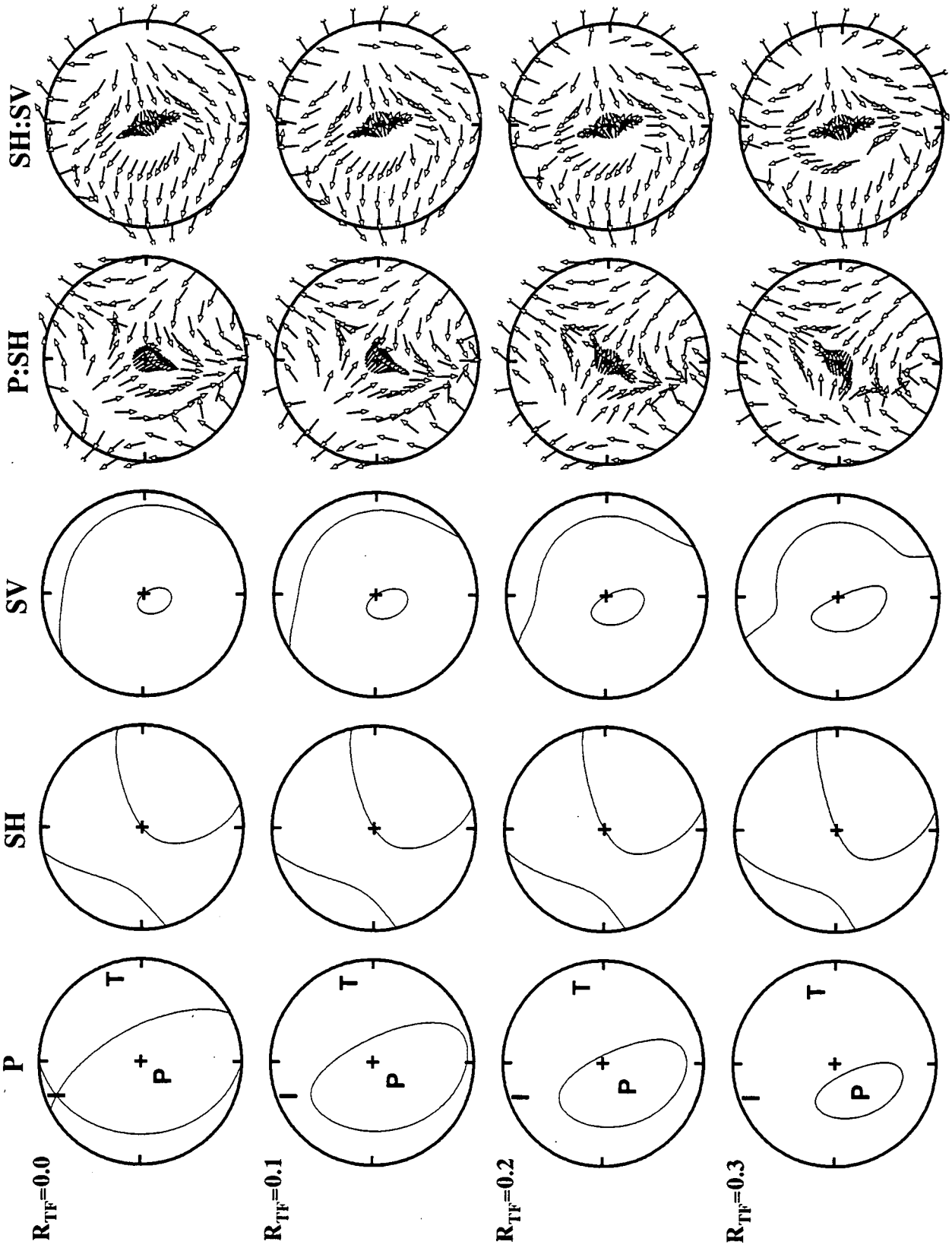

Figure 8.7: *P*, *SH* and *SV* polarity fields and the distribution of *P*:*SH* and *SH*:*SV* amplitude ratios for an opening-shear fault with different amounts of tensile opening. Plots are equal-area, upper focal-hemisphere projections. On the polarity plots at left, the black lines are the nodal lines for the *P*, *SH* and *SV* radiation patterns. *T*, *I* and *P* show the positions of the principal axes. The arrows represent the amplitude ratios, and follow the convention of Figure 6.4.

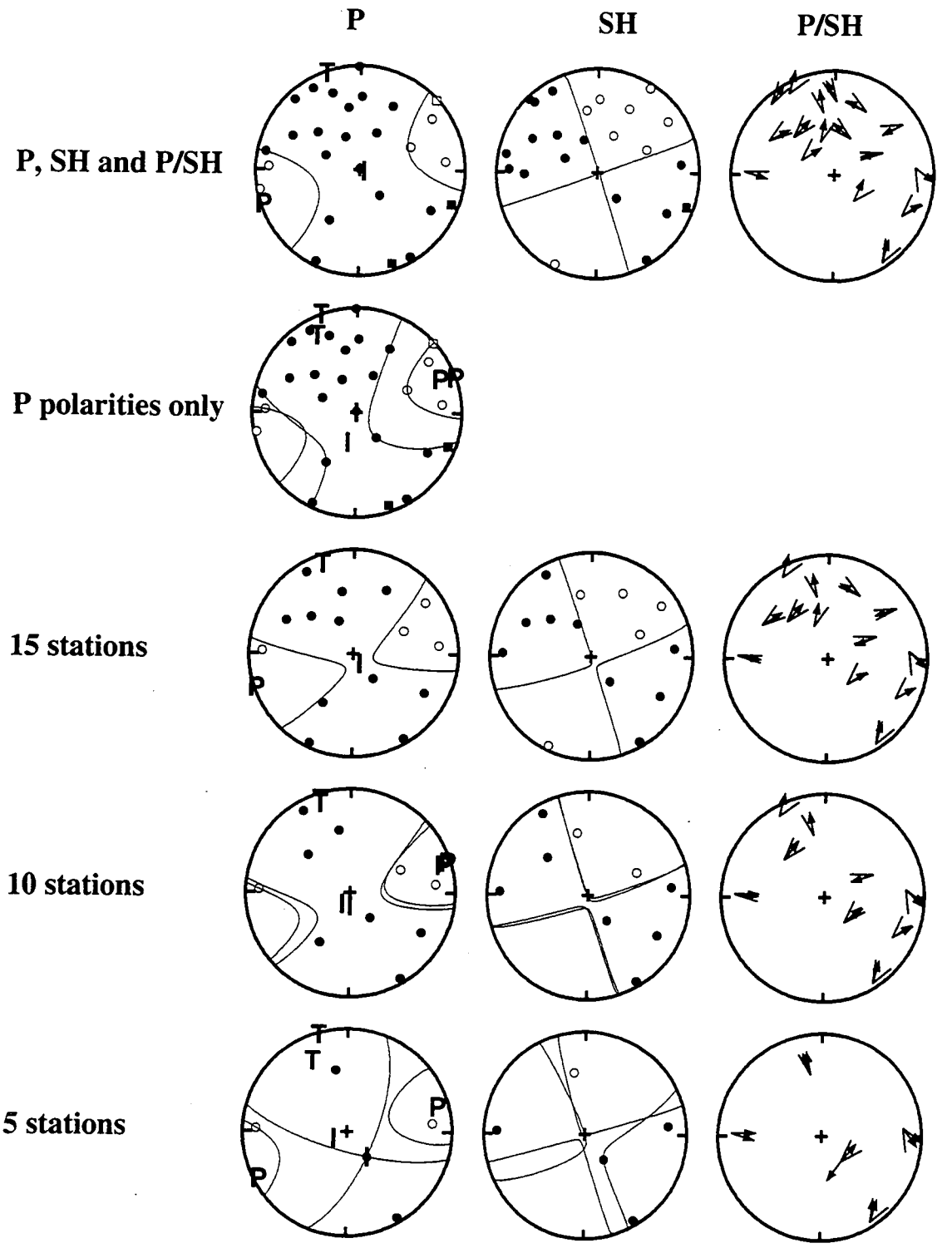

Figure 8.8: Inversions of different combinations of *P* and *P:SH* data from event 258.074123.1. *P*-wave, *SH*-wave polarities and *P:SH* amplitude ratios are shown. *T*, *I* and *P* show positions of the principal axes. Where data from only a selection of stations are used, the stations were selected to give the best possible focal sphere coverage. Where two sets of nodal lines are shown, they are for the most-explosive and most-implosive mechanisms that are compatible with the data. Symbol conventions are as for Figure 6.8.

With 10 well-spaced stations a reasonable solution is found that is very similar to the solution obtained using the full 27-station dataset. The solution with 10 stations is clearly non-DC, and constrained to a narrow range of mechanisms by the *P*:*SH* amplitude ratios. A much wider range in solutions is possible with five stations, but the orientations of the principal axes are successfully recovered. When the *P*-wave polarities only from all the stations are inverted, a fairly wide range of mechanisms are permitted, and the most-implosive mechanism is close to a DC. Thus 10 stations with *P* and *SH* data provide better constraint than 27 stations with *P* polarities only. These results show that constraint on the non-DC nature of local earthquakes could be obtained with 10 three-component stations, if they gave good focal sphere coverage.

8.7 Earthquake mechanisms

8.7.1 General trends

The earthquakes in the Hengill area predominantly have *T* axes that are aligned with the local extensional stress regime and are perpendicular to the tectonic fabric (Figure 7.2). The type of faulting varies from strike-slip to normal-faulting earthquakes with increasing depth, corresponding to a rotation of *P* axes from horizontal to vertical. This rotation of *P*-axis orientations has also been observed in the Reykjanes peninsula (*Klein et al.*, 1977), and is due to the vertical compressive stress increasing lithostatically with depth until it exceeds the horizontal compressive stress.

The majority of the earthquakes studied have explosive mechanisms (Figure 7.5), and 76% of the measured *P*-wave arrivals are compressional. Only three out of 98 earthquakes have more dilatational than compressional arrivals. This clear evidence of explosive volumetric components rules out non-DC mechanisms that involve the combination of DC sources, for these can never have a volumetric component (Section 2.3.3). Mechanisms which involve tensile faulting provide the most likely explanation for the explosive nature of most of the studied earthquakes, and the two mechanisms of tensile-shear faulting considered here can adequately explain most of the observations (Section 7.3.2). However, no mechanism can ever be uniquely constrained by seismic data alone, and it remains possible that these earthquakes are caused by some other process.

In the northwest zone, most of the earthquakes are normal faulting and are interpreted as shear faulting. The value of R_{TF} is highest for earthquakes in the geothermal zone, and the proportion of shear-faulting earthquakes is lowest there. This suggests that the non-DC earthquake mechanisms are related to geothermal activity.

8.7.2 Mechanisms with tensile-fault components

8.7.2.1 Interpretation of the T+S and OS models

Two possible models that combine tensile and shear faults have been proposed in this thesis; the T+S and OS models (Section 7.3.1.2). Both of these models have the same best-fit moment tensors to any data set, and so the observed polarities and amplitudes cannot be used to distinguish between them.

The T+S model has two fault planes of a fixed geometry, with an angle of 45° between the fault normals, and the constraint that the *T* axis of the tensile fault lies in the plane of the *T* and *P* axes of the shear fault. This geometry is geologically reasonable and simplifies the model, but a wide range of other geometries are possible that might give a slightly better fit to the data (Section 7.3.1.2). The fault plane geometries described in Section 7.3.3.2 must be interpreted with this in mind.

In volumes of unfaulted homogeneous rock, the orientations of fresh fractures would be controlled by the local stress field, and the geometrical relationship between tensile and shear faults would be similar to that of the T+S model. However if there are pre-existing fractures, movement will preferentially occur on these fractures even if they are not optimally oriented with respect to the ambient stress system (*McKenzie*, 1969). There is also no need for the two fault planes to be physically connected as shown in Figure 2.4, although it is perhaps unlikely that the two faults would rupture simultaneously if they were not connected.

The only restriction on the respective positions of the two fault planes is that they are spatially close and that faulting occurs on them simultaneously, so that far-field observations cannot discriminate two separate sources. If, however, the rupture of one fault plane triggers the rupture of the other, the fault planes must be close together, or two *P* arrivals would be observed. If the fault planes are separated by 100 m then a *P* wave from the first rupture would take about 0.02 s to reach the second fault. The second *P* arrival in this case would probably be obvious as a sharp inflection in the first *P*-wave pulse. Ruptures on separate faults that are hundreds of metres apart would certainly produce two clear *P* arrivals.

In the OS model the tensile and shear components are coplanar. For any moment tensor there is only one best-fit OS model, although this model can be interpreted as opening-shear failure on one of two possible fault planes (Section 7.3.1.2). The opening-shear model of *Haskell* (1964) proposes that faults open during rupture and then close as the rupture terminates. In this case the overall force system would not have a volumetric component. However, for large earthquakes with a source duration that is longer than the rise time of the *P* and *S* waves (the time from the first arrival to the first peak or trough), then the first motions would contain information about the first part of the rupture only. Thus large opening-shear earthquakes would have larger

amplitude *P*-waves than if the motion was purely shear, and moment tensors calculated from first motions would have explosive components.

Some simple calculations suggest that the rupture durations of the small-magnitude earthquakes studied at Hengill are comparable to the rise times, which are typically about 0.05 s. For an earthquake with $M_0 = 2.5 \times 10^{13}$ Nm ($M = 2.7$), the source radius is in the order of 140 m (Figure 4.10 of *Scholz*, 1990). The source duration D is related to the source radius r by

$$D = \frac{r}{0.8V_S} \qquad 8.1$$

For $V_S = 3.4$ km/s, the source duration is 0.05 s. This is only an approximate estimate, as M_0 values for the studied earthquakes vary by two orders of magnitude, and a wide range of source radius estimates are possible. However, this calculation suggests that, at least for the smaller earthquakes studied, opening-shear faulting with fault closure as rupture terminates would result in DC moment tensors. It is possible that conditions in the Hengill area are acting to keep tensile faults open, perhaps high pore-fluid pressures in the geothermal reservoir, so that the sides of shear faults remain open after rupture has terminated.

8.7.2.2 Mechanisms with closing tensile faults

There are four well-constrained earthquakes with negative k values and implosive moment tensors (Figure 7.5). The k values are close to zero for three of these earthquakes and they interpreted as shear faulting. Thus there is only one well-constrained earthquake, event 237.212559.1 in the NES group, with a substantial, well-constrained implosive volumetric component. Clearly, earthquake mechanisms with closing tensile faults are rare in the Hengill area in the magnitude range studied (M 1.2-3.8).

Closing tensile fault mechanisms may be able to help differentiate between the T+S and OS models. This is because a closing tensile fault in the T+S model requires that the direction of shearing is reversed in order that the direction of movement is compatible on the two faults (Figure 8.9). Thus, for a fixed faulting geometry, an opening episode and a closing episode would be expected to have exactly inverse moment tensors, reversed first-motion directions at all stations, and reversed positions of the T and P axes. For the OS model, the direction of shearing can remain the same during opening and closing episodes, the moment tensors would differ only in the sign of the volumetric component, and the principal axes and most first-motion directions would be the same (Figure 8.9).

Event 237.212559.1 is one of a sequence of earthquakes at Nesjavellir. The hypocentres of this cluster are aligned along a NNE-striking plane (Appendix 9). The

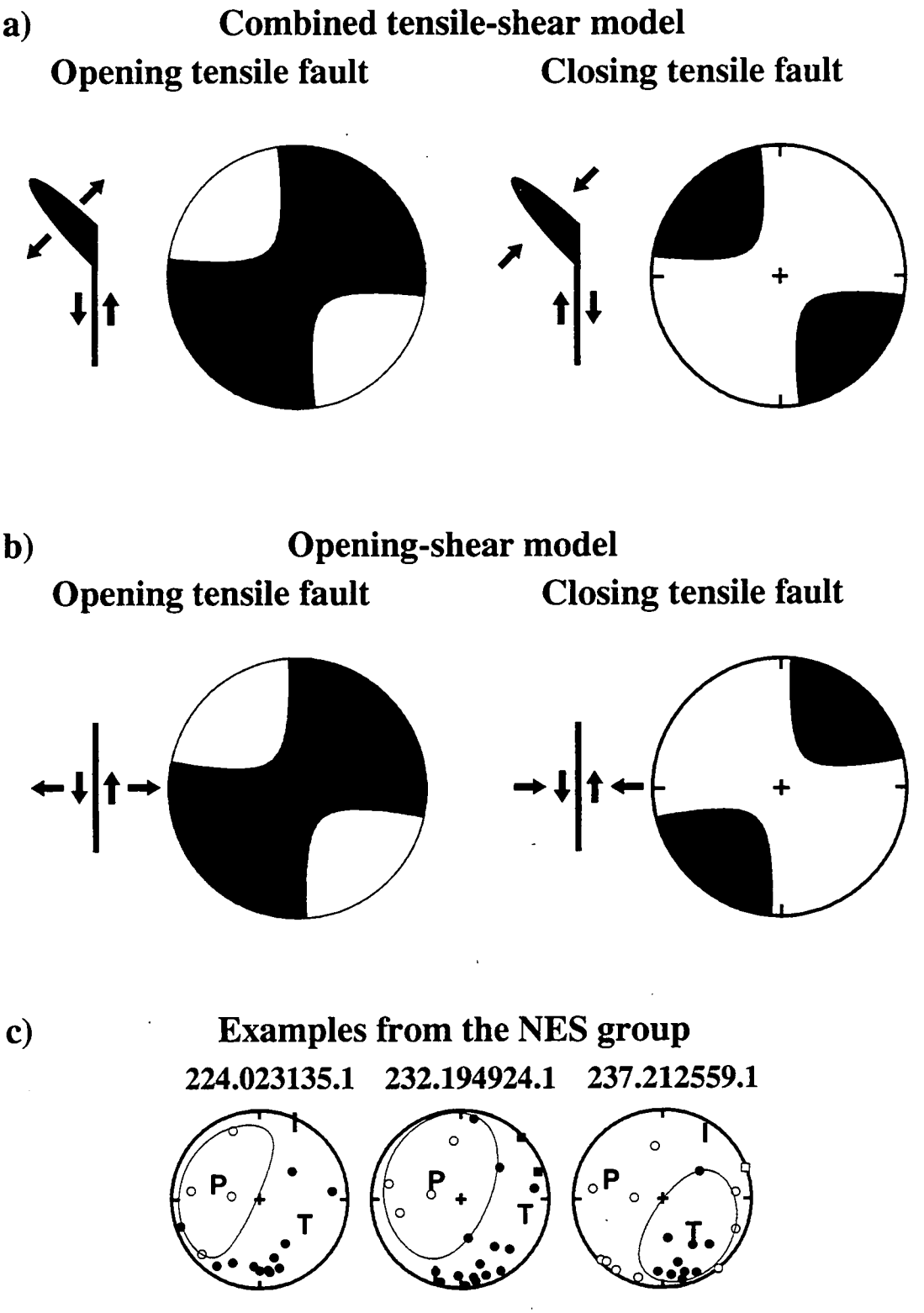

Figure 8.9: Comparison between mechanisms with opening and closing tensile-fault components for (a) the combined tensile-shear model and (b) the opening-shear fault model. (c) *P* polarities and nodal curves for three earthquakes from the NES group that have similar mechanisms. Variations in the *P* polarities and *P*:*SH* amplitude ratios result in moment tensors with a range of volumetric components but similar orientations. Event 237.212559.1 is the only well-constrained implosive earthquake.

first-motion directions of the five earthquakes in this cluster for which moment tensors were determined show that the mechanism of event 237.212559.1 is very similar to those of two other earthquakes in the series (Figure 8.9c). These earthquakes have similar principal axes, and similar polarity and amplitude-ratio distributions, with the constraint on the size of the volumetric component coming from a small number of measurements. This pattern is more consistent with OS faulting than T+S faulting.

8.7.2.3 Fault orientations

Some information on the orientations of possible fault planes comes from accurate relative locations of earthquakes in clusters (Section 3.5). The Gigir and Marardalur clusters are interpreted as occurring on northeast-striking vertical faults (Section 8.2.2), and they contain earthquakes with similar mechanisms (Appendix 11).

In the Gigir cluster, there are 9 earthquakes for which well-constrained moment tensors were determined. Three of these are consistent with a DC interpretation of normal faulting on a near-vertical, northeast-striking plane (Figure 7.18). The T+S model interpretations have near-vertical tensile faults that strike at about 37° accompanied by normal faulting on northeast-striking planes that dip at either 30° to the southeast or 60° to the northwest (Appendix 11). The OS model interpretations are either right-lateral faulting on planes with a strike of 30° and dip of 70°, or left-lateral faulting on planes with a strike of 50° and dip of 35° (Appendix 11). Either the tensile fault of the T+S model or the right-lateral OS model are consistent with the fault plane orientation inferred from the hypocentre distributions.

In the Marardalur cluster, only three out of the five earthquakes have well-constrained moment tensors, and these are all interpreted as shear-fault earthquakes. Only one has a mechanism consistent with shear faulting on a vertical northeast-striking fault. The other two earthquakes have steeply dipping nodal planes that strike north and northwest (Figure 7.18).

The abundant surface fissures in the Hengill area are oriented 30°N (Section 1.3.2.1), a direction that is approximately perpendicular to the regional extensional strain field (*Sigmundsson et al.*, 1995) and the mean *T*-axis direction of the calculated moment tensors (Section 7.2.1.1). It is probable that fault planes at depth would follow this orientation, with the type of shear-faulting changing from strike slip to normal with increasing depth. Vertical, 30°N-striking fault planes are compatible with the tensile components of the T+S model for earthquakes in the northwest zone, but in the geothermal zone the tensile fault orientation is more easterly (Figure 7.19). Alternatively, in the case of the OS model, most of the right-lateral faults strike north to northeast (Figure 7.20). For the earthquakes in the northwest zone, either the right-lateral or left-lateral OS models give similar fault strikes, because the earthquakes have normal-faulting components. The single earthquake in the Ölfus zone has a shear-fault

mechanism, compatible with right-lateral faulting on a near-vertical, north-striking plane (Figure 7.18).

It is possible that the geothermal and Ölfus zones are influenced by the left-lateral regional shear regime of the adjoining SISZ, which causes right-lateral strike-slip faulting on north-striking vertical planes there (Section 1.3.1.4). Thus these zones may be extensions of the SISZ, with predominantly right-lateral strike-slip faulting on vertical planes that strike north to northeast. Alignments of hypocentres in the Ölfus zone are consistent with north-striking faults (Section 1.3.4.3.2). Shallow earthquakes in the Reykjanes peninsula had strike-slip mechanisms consistent with right-lateral faulting on NNE-striking faults, a fault orientation that was supported by some alignments of hypocentres (*Klein et al.*, 1977). Also, the *S*-wave anisotropy detected using data from the 1991 dataset is consistent with near-vertical, NNE-trending fissures in the geothermal and Ölfus zones (*Evans et al.*, 1996; Figure 1.19).

Perhaps the interaction of the SISZ stress regime with the geothermal area has resulted in right-lateral, OS faulting in the Ölfus and geothermal zones. This gives tentative support to the OS model, but it must be emphasised that the source mechanisms of the Hengill earthquakes remain ambiguous. The two simple models considered here can both explain the non-DC nature of the earthquakes, but the data cannot distinguish between these competing models, nor indeed other, more complex models.

8.7.2.4 Other possible source models

On an ε-k diagram, the earthquakes are scattered and in some cases lie far away from the TC-DC line (Figure 7.5). Some of these earthquakes could be interpreted as (1) involving some other geometrical combination of tensile and shear faults (which would plot within the TC-DC triangle on an ε-k diagram), (2) the result of an additional component being added to the models considered, or (3) some other type of earthquake that does not involve tensile faulting. *Ross et al.* (1996) suggest that some non-DC earthquakes in The Geysers area, California, may result from the combination of a tensile fault, a shear fault and CLVD source. This additional CLVD source could be caused by the movement of pore fluids in response to the opening of a tensile fault.

Almost all the processed earthquakes have only a few data misfits with the T+S and OS models. More complex source models are needed to explain the moment tensors of the small number of earthquakes that give a poor data fit to the simple models considered here (Section 7.3.2.3).

8.7.3 Implications for other areas

Non-DC earthquakes have been recorded in many areas and in different environments (Chapter 2). The question remains as to whether these are unusual earthquakes, or whether departures from shear faulting are common but so far have been observed only rarely. The temporary network at Hengill in 1991 was designed

specifically to record high-quality data from non-DC earthquakes to enable detailed focal mechanisms to be calculated. It has been shown that the majority of Hengill earthquakes are non-DC and most of these can be explained by some combination of shear and tensile faulting. It is likely that these results are not unique to the Hengill area, but instead apply to many other geothermal fields that are seismically active. Perhaps earthquakes with non-shear components are common, but that these components are simply small and difficult to observe for most "tectonic" earthquakes.

8.8 Suggestions for further work

The Hengill dataset has a rich potential for further work. Some possibilities are:

- Location of more earthquakes to examine the distribution of seismicity in more detail. There are hundreds more earthquakes for which locations could be obtained. Of particular interest would be to determine more accurate relative locations by cross-correlating waveforms from cluster earthquakes (*e.g.*, *Thorbjarnardóttir and Pechmann*, 1987). There are many other clusters that could be analysed to determine potential fault plane orientations, which could then be related to focal mechanisms.
- More accurate determination of scalar moments (Section 8.2.3).
- Attenuation tomography. Three-dimensional variations in attenuation could be determined by inverting variations in pulse width (*e.g.*, *Ponko and Sanders*, 1994). This would give more constraint on the conditions within the geothermal field, and would also be useful in improving the attenuation correction applied to the amplitudes in moment tensor determination.
- Further study of focal mechanisms. There is potential to constrain focal mechanisms better by comparing the polarity and amplitude ratios of earthquakes within clusters. Subtle differences between mechanisms could perhaps shed light on the source processes.
- Quantification of moment tensor uncertainties. There are many sources of error in the moment tensor calculations, ranging from uncertainty in the positions of stations on the focal sphere to the effect of propagation on amplitudes. Some method of formally quantifying these errors is required.

8.9 Conclusions

The main conclusions of this thesis are:

The distribution of earthquakes in the Hengill area in 1991 was similar to that observed in 1981, suggesting that this pattern is persistent. Three zones of seismic activity are identified: (1) the northwest zone, where the seismicity is sparse and earthquakes occur mainly in clusters that are active over a period of a few days, (2) the geothermal zone, where most of the earthquakes occur, and seismicity is caused by

geothermal activity, and (3) the Ölfus zone, where the earthquakes are generally deeper and of larger magnitude.

A local earthquake tomographic inversion was carried out to determine the three-dimensional V_P and V_P / V_S structure of a 24×24 km area from 0-6 km depth, using *P*-wave travel times and *S-P* times from local earthquakes recorded in 1981 and 1991. The best method was to invert for both models simultaneously in a single step, starting from a one-dimensional wave-speed model. The resulting models are smoothly varying and give a good data variance reduction.

The V_P model is similar to that of a previous tomographic inversion in the area that used data collected in 1981, although the models differ in detail, with the later model having broader but smaller-amplitude anomalies. The main high-V_P features of these models are interpreted as solidified intrusions. A low-V_P body in the earlier model is probably an inversion artefact. A low V_P / V_S body (-4%) is detected from 0-3 km depth underlying the surface expression of the geothermal field. This anomaly could be caused by a combination of effects, including a slightly lower pore fluid pressure and higher steam content, or rock matrix alteration within the geothermal field.

Well-constrained moment tensors were determined for 70 local earthquakes by inverting the polarities and amplitude ratios of *P* and *S* arrivals. This method gives good constraint of the moment tensors and is relatively insensitive to wave-speed model and attenuation variations in this area. Most of the earthquakes are non-DC with explosive volumetric components. Only 17 (28%) of the earthquakes are consistent with a DC model.

The remaining earthquakes are modelled as combinations of an opening tensile cracks and shear faults. Two geometries are considered: (1) rupture on two separate fault planes aligned at 45°, and (2) opening-shear rupture on a single fault plane, which is equivalent to coplanar tensile and shear faults. Both models have the same moment tensors, and the data cannot distinguish between them. They give a good fit to the data, with few polarity misfits for most of the earthquakes.

Data from one well-constrained implosive earthquake, and the orientations of the model faults, give tentative support to the opening-shear model although this is far from conclusive. Right-lateral, opening-shear, strike-slip faulting on near-vertical planes is consistent with the regional seismicity of the South Iceland Seismic Zone. The non-DC earthquakes may be caused by the geothermal field interacting with the regional stress regime.

References

Agenheister, G., H. Gebrande, H. Miller, P. Goldflam, W. Weigel, W. R. Jacoby, G. Pálmason, S. Björnsson, P. Einarsson, N. I. Pavlenkova, S. M. Zverev, I. V. Litvinenko, B. Loncarevic and S. C. Solomon, Reykjanes Ridge Iceland seismic experiment, *J. Geophys.*, 47, 228-238, 1980.

Aki, K., Evidence for magma intrusion during the Mammoth Lakes earthquakes of May 1980, and implications of the absence of volcanic (harmonic) tremor, *J. Geophys. Res.*, 89, 7689-7696, 1984.

Aki, K. and P. G. Richards, *Quantitative Seismology, vol 1*, Freeman, New York, 557 pp., 1980.

Arnason, K., G. I. Haraldsson, G. V. Johnsen, G. Thorbergsson, G. P. Hersir, K. Sæmundsson, L. S. Georgsson and S. P. Snorrason, Nesjavellir: Jardfraedi- og jardedlisfraedileg könnun 1985 (Nesjavellir: Geological and geophysical overview 1985) *Rep OS-86014/JHD-02*, 125 pp., Natl. Energy Auth., Reykjavik, Iceland, 1986.

Arnott, S. K., A seismic study of the Krafla volcanic system, Ph.D. thesis, Univ. Durham, U.K., 283 pp., 1990.

Arnott, S. K. and G. R. Foulger, The Krafla spreading segment, Iceland: 1. Three-dimensional crustal structure and the spatial and temporal distribution of local earthquakes, *J. Geophys. Res.*, 99, 23801-23825, 1994a.

Arnott, S. K. and G. R. Foulger, The Krafla spreading segment, Iceland: 2. The accretionary stress cycle and non-shear earthquake focal mechanisms, *J. Geophys. Res.*, 99, 23827-23842, 1994b.

Barker, J. S. and C. A. Langston, A teleseismic body wave analysis of the May, 1980 Mammoth Lakes, California earthquakes, *Bull. Seismol. Soc. Am.*, 73, 419-434, 1983.

Bjarnason, I. T., W. Menke, O. G. Flóvenz and D. Caress, Tomographic image of the mid-Atlantic plate boundary in southwestern Iceland, *J. Geophys. Res.*, 98, 6607-6622, 1993a.

Bjarnason, I. T., P. Cowie, M. H. Anders, L. Seeber and C. H. Sholz, The 1912 Iceland earthquake rupture: growth and development of a nascent transform system, *Bull. Seismol. Soc. Am.*, 83, 416-435, 1993b.

Bjarnason, I. T., W. Menke and O. G. Flóvenz, Reply, *J. Geophys. Res.*, 99, 17915-17917, 1994.

Björnsson, A., Dynamics of crustal rifting in NE Iceland, *J. Geophys. Res.*, 90, 10151-10162, 1985.

Björnsson, H., S. Björnsson and T. Sigurgeirsson, Penetration of water into hot rock boundaries of magma at Grímsvötn, *Nature*, 295, 580-581, 1982.

Böðvarsson, G., Report on the geothermal research in Hengill, Hveragerði and surroundings, 1947-1949, *J. Eng. Soc. Iceland*, pp. 1-48, 1951.

Böðvarsson, G. S., S. Björnsson, A. Gunnarsson, E. Gunnlaugsson, O. Sigurdsson, V. Stefánsson, and B. Steingrimsson, The Nesjavellir geothermal field, Iceland: Part 1. Field characteristics and the development of the three-dimensional numerical model, *Geotherm. Sci. Tech.*, 2, 189-228, 1990.

Bott, M. H. P., Plate tectonic evolution of the Icelandic transverse ridge and adjacent regions, *J. Geophys. Res.*, 90, 9953-9960, 1985.

Brune, J. N., S. Brown and P. A. Johnson, Rupture mechanism and interface separation in foam rubber models of earthquakes: A possible solution to the heat flow paradox and the paradox of large overthrusts. *Tectonophysics*, 218, 59-67, 1993.

Castro, R. R., J. G. Anderson and J. N. Brune, Origin of high P/S spectral ratios from the Guerrero Accelerograph array, *Bull. Seismol. Soc. Am.*, 81, 2268-2288, 1991.

Chaterjee, S. N., A. M. Pitt and H. M. Iyer, V_P / V_S ratios in the Yellowstone National Park region, Wyoming, *J. Volcanol. Geotherm. Res.*, 26, 213-230, 1985.

Chouet, B., Dynamics of a fluid-driven crack in three dimensions by the finite difference method, *J. Geophys. Res.*, 91, 13967-13992, 1986.

Chouet, B. and B. R. Julian, Dynamics of an expanding fluid-filled crack, *J. Geophys. Res.*, 90, 11187-11198, 1985.

Clough, C. T., H. B. Maufe and E. B. Bailey, The cauldron-subsidence of Glen Coe, and the associated igneous phenomena., *Q. J. Geol. Soc. London*, 65, 611-678, 1909.

Cramer, C. H. and T. R. Toppozada, A seismological study of the May 1980, and earlier earthquake activity near Mammoth Lakes, California, *California Division of Mines Geological Special Report*, 150, 91-130, 1980.

Dantzig, G. B., *Linear programming and extensions*, Princeton University Press, Princeton, 627 pp., 1963.

DeMets, C., R. G. Gordon, D. F. Argus and S. Stein, Current plate motions, *Geophys. J. Int.*, 101, 425-478, 1990.

Eberhart-Phillips, D., Three-dimensional velocity structure in the northern California coast ranges from inversion of local earthquake arrival times, *Bull. Seismol. Soc. Am.*, 76, 1025-1052, 1986.

Eberhart-Phillips, D., Three-dimensional *P*- and *S*- velocity structure in the Coalinga region, California, *J. Geophys. Res.*, 95, 15343-15363, 1990.

Eberhart-Phillips, D., Local earthquake tomography: earthquake source regions, in H. M. Iyer and K. Hirahara (eds.) *Seismic tomography: Theory and practice*, Chapman & Hall, London, 613-643, 1993.

Eberhart-Phillips, D., and D. H. Oppenheimer, Induced seismicity in the Geysers geothermal area, California, *J. Geophys. Res.*, 89, 1191-1207, 1984.

Einarsson, P., S-wave shadows in the Krafla caldera in NE-Iceland, evidence for a magma chamber in the crust, *Bull. Volcanol.*, 41, 1-9, 1978.

Einarsson, P., Hversu hratt lengist eystra gosbeltð, *Symp. Volcanic Activity in Iceland*, Icelandic Geoscience Soc., Reykjavik, 1988.

Einarsson, P., Earthquakes and present-day tectonism in Iceland, *Tectonophysics*, 189, 261-279, 1991.

Einarsson, P., S. Björnsson, G. Foulger, R. Stefánsson and T. Skaftadóttir, Seismicity pattern in the South Iceland Seismic Zone, in Simpson, D. W. and P. G. Richards (eds.), *Earthquake prediction: an international review, Maurice Ewing Ser. 4*, AGU, Washington, D.C., 141-151, 1981.

Einarsson, P. and K. Sæmundsson, Earthquake epicenters 1982-1985 and volcanic systems in Iceland, in: Th. Sigfússon (ed.) *Íhlutarins eðli: Festschrift for Þorbjörn Sigurgeirsson, Menningarsjóður*, Reykjavik (map), 1987.

Ekström, G., Anomalous earthquakes on volcano ring-fault structures, *Earth Planet. Sci. Lett.*, 128, 707-712, 1994.

Ekström, G. and A. M. Dziewonski, Moment tensor solutions of Mammoth Lakes earthquakes, *EOS Trans. AGU*, 64, 262 (abstract), 1983.

Ekström, G. and A. M. Dziewonski, Centroid-moment Tensor solutions for 35 earthquakes in Western North America (1977 to 1983), *Bull. Seismol. Soc. Am.*, 75, 23-39, 1985.

Ellsworth, W. L., Three-Dimensional Structure of the Island of Hawaii: Ph.D. Thesis, Massachusetts Institute of Technology, Cambridge, MA, 327 pp., 1977.

Evans, J. R., D. Eberhart-Phillips and C. H. Thurber, User's manual for SIMULPS12 for imaging V_P and V_P/V_S, a derivative of the Thurber tomographic inversion SIMUL3 for local earthquakes and explosions, *U.S. Geol. Surv. Open File Rep.*, 94-431, 142 pp., 1994.

Evans, J. R., G. R. Foulger, B. R. Julian and A. D. Miller, Crustal shear-wave splitting from local earthquakes in the Hengill triple junction, southwest Iceland, *Geophys. Res. Lett.*, submitted, 1996.

Feignier, B. and R. P. Young, Moment tensor inversion of induced microseismic events: evidence of non-shear failures in the $-4 < M < -2$ moment magnitude range, *Geophys. Res. Lett.*, 19, 1503-1506, 1992.

Field, P., Crustal structure of the spreading plate boundary in Iceland and the north Atlantic from gravity data, Ph.D. thesis, Univ. Durham, U.K., 225 pp., 1994.

Flóvenz, O. G., Seismic structure of the Icelandic crust above layer three and the relation between body wave velocity and the alteration of the basaltic crust, *J. Geophys.*, 47, 211-220, 1980.

Flóvenz, O. G., Gerð jarðskorpu og efri möttuls undir Íslandi samkvæmt jarðeðlisfræðilegum mælingum, Eðlisfræði á Íslandi VI, Eðlisfræðifélag Íslands, 89-104, 1992.

Foulger, G. R., Seismological studies at the Hengill geothermal area, SW Iceland, Ph.D. thesis, Univ. Durham, U.K., 313 pp., 1984.

Foulger, G. R., Hengill Triple Junction, SW Iceland. 1. Tectonic structure and the spatial and temporal distribution of local earthquakes, *J. Geophys. Res.*, 93, 13493-13506, 1988a.

Foulger, G. R., Hengill Triple Junction, SW Iceland. 2. Anomalous earthquake focal mechanisms and implications for processes within the geothermal reservoir at accretionary plate boundaries, *J. Geophys. Res.*, 93, 13507-13523, 1988b.

Foulger, G. R., The Hengill geothermal area, Iceland- Variation of temperature-gradients deduced from the maximum depth of seismogenesis, *J. Volcanol. Geotherm. Res.*, 65, 119-133, 1995.

Foulger, G. R. and P. Einarsson, Recent earthquakes in the Hengill-Hellisheidi area in SW-Iceland, *J. Geophys.*, 47, 171-175, 1980.

Foulger, G. R. and R. E. Long, Anomalous focal mechanisms: Tensile crack formation on an accreting plate boundary, *Nature*, 310, 43-45, 1984.

Foulger, G. R. and D. R. Toomey, Structure and evolution of the Hengill-Grensdalur Volcanic Complex, Iceland: Geology, geophysics, and seismic tomography, *J. Geophys. Res.*, 94, 17511-17522, 1989.

Foulger, G. R., R. E. Long, P. Einarsson and A. Björnsson, Implosive earthquakes at the active accretionary plate boundary in Iceland, *Nature*, 337, 640-642, 1989.

Foulger, G. R. and B. R. Julian, *Joint report to NERC geophysical equipment pool and IRIS-PASSCAL on REF TEK and associated equipment malfunctions, Hengill earthquake project, July-Oct. 1991*, 12 pp., 1991.

Foulger, G. R. and R. E. Long, Non-double couple earthquake focal mechanisms and the accretionary tectonic cycle, in: Gasparini, P., Scarpa, R. and Aki, K. (Eds) *Volcanic Seismology*, IAVCEI Proceedings in Volcanology 3, Springer-Verlag, pp. 223-234, 1992.

Foulger, G. R. and B. R. Julian, Non-double-couple earthquakes at the Hengill-Grensdalur Volcanic Complex, Iceland: Are they the artefacts of crustal heterogeneity?, *Bull. Seismol. Soc. Am.*, 83, 38-52, 1993.

Foulger, G. R., G. Beutler, R. Bilham, P. Einarsson, S. Fankhauser, W. Gurtner, U. Hugentobler, W. J. Morgan, M. Rothacher, G. Thorbergsson and U. Wild, The Iceland 1986 GPS geodetic survey: tectonic goals and data processing results, *B. Geod.*, 67, 148-172, 1993.

Foulger, G. R. and B. R. Julian, Study of the source mechanisms of non-double-couple earthquakes, *Final report to NERC on Grant GR9/134*, 22 pp., 1994.

Frasier, C. W., Discrete time solution of plane *P-SV* waves in a plane layered medium, *Geophysics*, 35, 197-219, 1970.

Frohlich, C., Note concerning non-double couple source components from slip along surfaces of revolution, *J. Geophys. Res.*, 95, 6861-6866, 1990.

Frohlich, C., M. A. Riedesel and K. D. Apperson, Note concerning possible mechanisms for non-double-couple earthquake sources, *Geophys. Res. Lett.*, 16, 523-526, 1989.

Gebrande, H., H. Miller and P. Einarsson, Seismic structure of Iceland along RRISP-profile I, *J. Geophys.*, 47, 239-249, 1980.

Gilbert, G. K., A theory of the earthquakes of the Great Basin, with a practical application, *Am. J. Sci., XXVII*, 49-54, 1884.

Given, J. W., T. C. Wallace and H. Kanamori, Teleseismic analysis of the 1980 Mammoth Lakes earthquake sequence, *Bull. Seismol. Soc. Am.*, 72, 1093-1109, 1982.

Gudmundsson, A., Tectonics of the Thingvellir fissure swarm, SW Iceland, *J. Struct. Geol.*, 9, 61-69, 1987.

Gutenburg, B. and C. F. Richter, *Seismicity of the Earth and related phenomena*, (2nd ed.), Princeton University Press, Princeton, 1954.

Hanks, T. C. and H. Kanamori, A moment magnitude scale, *J. Geophys. Res.*, 84, 2348-2350, 1979.

Haskell, N. A., Total energy and energy spectral density of elastic wave radiation from propagating faults, *Bull. Seismol. Soc. Am.*, 54, 1811-1841, 1964.

Hersir, G. P., Electric and electromagnetic measurements across the mid-Atlantic ridge in southwest-Iceland, with special reference to the high temperature area of Hengill, M.Sc. thesis, Univ, Aarhus, Denmark, 165 pp., 1980.

Hersir, G. P., A. Björnsson, and L. B. Pedersen, Magnetotelluric survey across the active spreading zone in southwest Iceland, *J. Volcan. Geoth. Res.*, 20, 253-265, 1984.

Hodgkinson, K. and G. R. Foulger, First epoch GPS survey of the Hengill triple junction, S Iceland, and the effect of ocean loading, *Jökull*, in press, 1996.

Hudson, J. A., R. G. Pearce and R. M. Rogers, Source type plot for inversion of the moment tensor, *J. Geophys. Res.*, 94, 765-774, 1989.

Hyndman, R. D., L. L. Vanyan, G. Marquis and L. K. Law, The origin of electrically conductive lower continental crust: Saline water or graphite?, *Phys. Earth. Planet. Inter.*, 81, 325-344, 1993.

Iguchi, M., A vertical expansion source model for mechanisms of earthquakes originating in the magma conduit of an andesitic volcano, Japan, *Bull. Volcanol. Soc. Japan*, 39, 49-67, 1994.

Isacks B., J. Oliver and L. R. Sykes, Seismology and the new global tectonics, *J. Geophys. Res.*, 73, 5855-5899, 1968.

Ishihara, K., Dynamical analysis of volcanic explosion, *J. Geodynamics*, 3, 327-349, 1985.

Ito, H., J. De Vilbiss, and A. Nur, Compressional and shear waves in saturated rock during water-steam transition, *J. Geophys. Res.*, 84, 4731-4735, 1979.

Julian, B. R., Evidence for dyke intrusion earthquake mechanisms near Long Valley Caldera, California, *Nature*, 303, 323-325, 1983.

Julian, B. R., Analysing seismic-source mechanisms by linear-programming methods, *Geophys. J. R. astr. Soc.*, 84, 431-443, 1986.

Julian, B. R., Volcanic tremor: nonlinear excitation by fluid flow, *J. Geophys. Res.*, 99, 11859-11877, 1994.

Julian, B. R. and D. Gubbins, Three-dimensional seismic ray tracing, *J. Geophys.*, 43, 95-113, 1977.

Julian, B. R. and S. A. Sipkin, Earthquake processes in the Long Valley Caldera Area, California, *J. Geophys. Res.*, 90, 11155-11169, 1985.

Julian, B. R. and G. R. Foulger, Moment tensors from linear inversion of body-wave amplitude ratios: powerful constraints on earthquake mechanisms, *Bull. Seismol. Soc. Am.*, submitted, 1996.

Julian, B. R., A. D. Miller and G. R. Foulger, Non-double-couple earthquakes I. Theory, *Rev. Geophys.* (submitted), 1996a.

Julian, B. R., A. Ross, G. R. Foulger, and J. R. Evans, Three-dimensional seismic image of a geothermal reservoir: The Geysers, California, *Geophys. Res. Lett.* (submitted), 1996b.

Kanamori, H and D. L. Anderson, Theoretical basis for some empirical relations in seismology, *Bull. Seismol. Soc. Am.*, 65, 1073-1092, 1975.

Kanamori, H., G. Ekström, A. Dziewonski, J. S. Barker and S. A. Sipkin, Seismic radiation by magma injection - An anomalous seismic event near Tori Shima, Japan, *J. Geophys. Res.*, 98, 6511-6522, 1993.

Kern, H. and A. Richter, Temperature derivatives of compressional and shear wave velocities in crustal and mantle rocks at 6 kbar confining pressure, *J. Geophys. Res.*, 49, 47-56, 1981.

Kikuchi, M., H. Kanamori and K. Satake, Source complexity of the 1988 Armenian Earthquake: Evidence for a slow after-slip event, *J. Geophys. Res.*, *98*, 15797-15808, 1993.

Kissling, E., Geotomography with local earthquake data, *Rev. Geophys.*, 26, 659-698, 1988.

Kissling, E., W. L. Ellsworth, D. Eberhart-Phillips and U. Kradolfer, Initial reference models in local earthquake tomography, *J. Geophys. Res.*, 99, 19635-19646, 1994.

Klein, F. W., P. Einarsson and M. Wyss, The Reykjanes Peninsula, Iceland, earthquake swarm of September 1972 and its tectonic significance, *J. Geophys. Res.*, 82, 865-887, 1977.

Knopoff, L., Q, *Rev. Geophys.*, 2, 625-660, 1964.

Knopoff, L. and M. J. Randall, The compensated linear vector dipole: a possible mechanism for deep earthquakes, *J. Geophys. Res.*, 75, 4957-4963, 1970.

Kradolfer, U., Seismische Tomographie in der Schweiz Mittels Lokaler Erdbeben: Ph.D. Thesis, Eidgenossischen Technischen Hochschule Zurich, Switzerland, 109 pp., 1989.

Lawson, A. C., The California Earthquake of April 18, 1906. *Report of the State Earthquake Investigation Commission, Volume I*, Carnegie Institution, Washington D. C., 451 pp., 1908.

Lawver, L. A. and R. D. Müller, Iceland hotspot track, *Geology*, 22, 311-314, 1994.

Lide, C. S. and A. S. Ryall, Relationship between aftershock locations and mechanisms of the May, 1980 Mammoth Lakes earthquakes, In: Active Tectonic and Magmatic Processes Beneath Long Valley Caldera, Eastern California, *U. S. Geol. Surv. Open File Report*, 84-939, 440-452, 1984.

Mavko, G. M., Velocity and attenuation in partially molten rocks, *J. Geophys. Res.*, 85, 5173-5189, 1980.

McGarr, A., Moment tensors of ten Witwatersrand mine tremors, *Pageoph.*, 139, 781-800, 1992.

McKenzie, D. P., Earthquakes and the directions of the principal stresses, *Bull. Seismol. Soc. Am.*, 59, 591-601, 1969.

Menke, W., B. Bransdóttir, S. Jakobsdóttir and R. Stefánsson, Seismic anisotropy in the crust at the mid-Atlantic plate boundary in south-west Iceland, *Geophys. J. Int.*, 119, 783-790, 1994.

Menke, W., V. Levin and R. Sethi, Seismic attenuation in the crust at the mid-Atlantic plate boundary in south-west Iceland, *Geophys. J. Int.*, 122, 175-182, 1995.

Menke W., B. Brandsdóttir, P. Einarsson, I. T. Bjarnason, Reinterpretation of the RRISP-77 Iceland shear wave profiles, *Geophys. J. Int.*, submitted, 1996.

Miller, A. D., G. R. Foulger and B. R. Julian, Non-double-couple earthquakes II. Observations, *Rev. Geophys.* (submitted), 1996.

Morgan, J. P. and M. C. Kleinrock, Transform zone migration: implications of bookshelf faulting at oceanic and Iceland propagating ridges, *Tectonics*, 10, 950-935, 1991.

Nicholson, C. and D. W. Simpson, Changes in V_P / V_S with depth: implications for appropriate velocity models, improved earthquake locations, and material properties of the upper crust, *Bull. Seismol. Soc. Am.*, 75, 1105-1123, 1985.

Novotny, M., Two methods of solving the linearized two-dimensional inverse seismic kinematic problem, *J. Geophys*, 50, 7-15, 1981.

Nur, A. and G. Simmons, The effect of saturation on velocity in low porosity rocks, *Earth Planet. Sci. Lett.*, 7, 183-193, 1969.

O'Connell, R. J. and B. Budiansky, Seismic velocities in dry and saturated cracked solids, *J. Geophys. Res.*, 79, 5412-5426, 1974.

Oppenheimer, D. H., Extensional tectonics at the Geysers geothermal area California, *J. Geophys. Res.*, 91, 11463-11476, 1986.

Page, R., Aftershocks and microaftershocks of the great Alaska earthquake of 1964, *Bull. Seismol. Soc. Am.*, 58, 1131-1168, 1968.

Pálmason, G., Crustal structure of Iceland from explosion seismology, *Greinar Vísindafélag Ísl.*, 40, 187 pp., 1971.

Pálmason, G., A continuum model of crustal generation in Iceland; kinematic aspects, *J. Geophys.*, 47, 7-18, 1980.

Palvis, G. L. and J. R. Booker, A study of the importance of non-linearity in the inversion of earthquake arrival time data for velocity structure, *J. Geophys. Res.*, 88, 5047-5055, 1983.

Ponko, S. C. and C. O. Sanders, Inversion for *P* and *S* wave attenuation structure, Long Valley caldera, California, *J. Geophys. Res.*, 99, 2619-2635, 1994.

Press, W. H., S. A. Teukolsky, W. T. Vetterling and B. P. Flannery, *Numerical Recipes in C*, 2nd edition, Cambridge University Press, 994 pp., 1992.

Price, N. J., *Fault and Joint Development in Brittle and Semi-brittle rock*, Pergammon, New York, 176 pp., 1966.

Reid, H. F., The California Earthquake of April 18, 1906. *Report of the State Earthquake Investigation Commission, Volume II: The Mechanics of the Earthquake*, Carnegie Institution, Washington D. C., 192 pp., 1910.

Riedesel, M. A. and T. H. Jordan, Display and assessment of seismic moment tensors, *Bull. Seismol. Soc. Am.*, 79, 85-100, 1989.

Richter, C. F., *Elementary Seismology*, Freeman, San Francisco, 768 pp., 1958.

Roecker, S. W., Seismicity and Tectonics of the Pamir-Hindu Kush Region of Central Asia: Ph.D. Thesis, Massachusetts Institute of Technology, Cambridge, MA, 294 pp., 1981.

Rögnvaldsson, S. T. and R. Slunga, Single and joint fault plane solutions for microearthquakes in South Iceland, *Tectonophysics*, 237, 73-80, 1994.

Ross, A., G. R. Foulger and B. R. Julian, Non-double-couple earthquake mechanisms at the Geysers geothermal area, California, *Geophys. Res. Lett.*, submitted, 1996.

Rundle, J. B. and D. P. Hill, The geophysics of a restless caldera- Long Valley, California, *Ann. Rev. Earth Planet. Sci.*, 16, 251-71, 1988.

Ryall, A. and F. Ryall, Spatial temporal variations in seismicity preceding the May 1980, Mammoth Lakes, California, earthquakes, *Bull. Seismol. Soc. Am.*, 71, 747-760, 1981.

Sammis, C. G. and B. R. Julian, Fracture instabilities accompanying dike intrusion, *J. Geophys. Res.*, 92, 2597-2605, 1987.

Sæmundsson, K., Fissure swarms and central volcanoes of the neovolcanic zones of Iceland, *Geol. J. Spec. Iss.*, 10, 415-432, 1978.

Sæmundsson, K., Outline of the geology of Iceland, *Jökull*, 29, 7-28, 1979.

Sæmundsson, K., Geology of the Thingvallavatn area, *Oikos*, 64, 40-68, 1992.

Satake, K. and H. Kanamori, Abnormal tsunamis caused by the June 13 1984 Tori Shima, Japan, earthquake, *J. Geophys. Res.*, 96, 19933-19939, 1991.

Scholz, C. H., *The mechanics of earthquakes and faulting*, Cambridge University Press, Cambridge, 1990.

Shimizu, H., S. Ueki and J. Koyama, A tensile-shear crack model for the mechanism of volcanic earthquakes, *Tectonophysics*, 144, 287-300, 1987.

Shimizu, H., N. Matsuwo and S. Ohmi, A non double-couple seismic source: Tensile-shear crack formation in the Unzen Volcanic Region, *Seismol. Res. Lett.*, 59, 5, 1988.

Sigmundsson, F., P. Einarsson, R. Bilham and E. Sturkell, Rift-transform kinematics in south Iceland: deformation from Global Positioning System measurements, 1986 to 1992, *J. Geophys. Res.*, 100, 6235-6248, 1995.

Silver, P. G. and T. H. Jordan, Optimal estimation of scalar seismic moment, *Geophys. J. R. astr. Soc.*, 70, 755-787, 1982.

Simmons, G. and H. Wang, *Single crystal constants and calculated aggregated properties: a handbook*, M.I.T. press, Cambridge, Mass., 2nd ed., 370 pp., 1971.

Sipkin, S. A., Estimation of earthquake source parameters by the inversion of waveform data: Global seismicity 1981-1985, *Bull. Seismol. Soc. Am.*, 76, 1515-1541, 1986.

Sipkin, S. A., Display and assessment of earthquake focal mechanisms by vector representation, *Bull. Seismol. Soc. Am.*, 83, 1871-1880, 1993.

Spencer, C. and D. Gubbins, Travel-time inversion for simultaneous earthquake location and velocity structure determination in lateral varying media, *Geophys. J. R. astr. Soc.*, 63, 95-116, 1980.

Stefánsson, R., R. Böðvarsson, R. Slunga, P. Einarsson, S. Jakobsdóttir, H. Bungum, S. Gregersen, J. Havskov, J. Hjemle and H. Korhonen, Earthquake prediction research in the South Iceland Seismic Zone and the SIL project, *Bull. Seismol. Soc. Am.*, 83, 696-716, 1993.

Takei, Y. and M. Kumazawa, Why have the single force and torque been excluded from seismic source models?, *Geophys. J. Int.*, 118, 20-30, 1994.

Talwani, M. and O. Eldholm, Evolution of the Norwegian-Greenland Sea, *Bull. Geol. Soc. Am.*, 88, 969-999, 1977.

Tatham, R. H., V_P / V_S and lithology, *Geophysics*, 47, 336-344, 1982.

Thorbergsson, G., I. T. Magnusson, A. Gunarsson, G. V. Johnsen and A. Björnsson, Landmælingar og thyngdarmælingar a Hengilsvædi 1982 og 1983 (Surveying and gravity measurements in the Hengill area 1982 and 1983), Nat. Energy Auth., Reykjavik, report OS-84003/VOD-03B, 1984.

Thorbjarnardóttir, B. S. and J. C. Pechmann, Constraints on relative earthquake locations from cross-correlation of waveforms, *Bull. Seismol. Soc. Am.*, 77, 1626-1634, 1987.

Thurber, C. H., Earth structure and earthquake locations in the Coyote Lake area, central California, Ph.D. thesis, Massachusetts Institute of Technology, Cambridge, MA, 332 pp., 1981.

Thurber, C. H., Earthquake locations and three-dimensional crustal structure in the Coyote Lake area, central California, *J. Geophys. Res.*, 88, 8226-8236, 1983.

Thurber, C. H., Hypocenter-velocity coupling in local earthquake tomography, *Phys. Earth. Planet. Inter.*, 75, 55-62, 1992.

Thurber, C. H., Local earthquake tomography: velocities and V_P / V_S-theory, in H. M. Iyer and K. Hirahara (eds.) *Seismic tomography: Theory and practice*, Chapman & Hall, London, 563-583, 1993.

Thurber, C. H. and S. R. Atre, Three-dimensional V_P / V_S variations along the Loma Prieta rupture zone, *Bull. Seismol. Soc. Am.*, 83, 717-736, 1993.

Toomey, D. R., S. C. Solomon, G. M. Purdy and M. H. Murray, Microearthquakes Beneath the median valley of the Mid-Atlantic Ridge near 23N: Hypocenters and focal mechanisms, *J. Geophys. Res.*, 90, 5443-5458, 1985.

Toomey, D. R., S. C. Solomon and G. M. Purdy, Microearthquakes Beneath the median valley of the Mid-Atlantic Ridge near 23N: Tomography and tectonics, *J. Geophys. Res.*, 93, 9093-9112, 1988.

Toomey, D. R. and G. R. Foulger, Inversion of local earthquake data from the Hengill-Grensdalur Central Volcanic complex, Iceland, *J. Geophys. Res.*, 94, 17497-17510, 1989.

Torfason, H., G. P. Hersir, K. Sæmundsson, G. V. Johnsen and E. Gunnlaugsson, Vestur-Hengill: Yfirbordsrannsokn jardhitasvaedisins (West Hengill: Surface research of the geothermal area), *Rep OS-83119/JHD-22*, 133 pp., Natl. Energy Auth., Reykjavik, Iceland, 1983.

Tryggvason, E., Seismicity, earthquake swarms and plate boundaries in the Iceland region, *Bull. Seismol. Soc. Am.*, 63, 1327-1348, 1973.

Tryggvason, E., Höggun Almannagjá (Displacement of the Almannagjá fault), *Rep. 9001 Nord. Volcanol. Inst.*, Reykjavik, Iceland, 1990.

Ueki, S., H. Shimizu, J. Comm and A. Takagi, Seismic activity following the 1983 eruption of Miyakejima, in: The 1983 eruption of Miyakejima, *Bull. Volcanol. Soc. Japan, Series II*, 29, S81-S100, 1984.

Uhira, K. and M. Takeo, The source of explosive eruptions of Sakurajima volcano, Japan, *J. Geophys. Res.*, 99, 17775-17789, 1994.

Ukawa, M. and M. Ohtake, A monochromatic earthquake suggesting deep-seated magmatic activity beneath the Izu-Ooshima volcano, Japan, *J. Geophys. Res.*, 92, 12649-12663, 1987.

Um, J. and C. H. Thurber, A fast algorithm for two-point seismic ray tracing, *Bull. Seismol. Soc. Am.*, 77, 972-986, 1987.

Vink, G. E., A hotspot model for Iceland and the Vøring Plateau, *J. Geophys. Res.*, 89, 9949-9959, 1984.

Wadati, K., On travel time of earthquake waves, part II. *Geophys. Mag.*, 7, 101-111, 1933.

Walck, M. C. Three-dimensional v_P / v_S variations for the Coso region, California, *J. Geophys. Res.*, 93, 2047-2052, 1988.

Walck, M. C. and R. W. Clayton, P-wave velocity variations in the Coso region, California, derived from local earthquake travel times, *J. Geophys. Res.*, 92, 393-405, 1987.

Walker, C. L., The volcanic history and geochemical evolution of the Hveragerði region, S.W. Iceland, Ph.D. Thesis, Univ Durham, U.K., 356 pp., 1992.

Walker, G. P. L, The structure of eastern Iceland, in L. Kristjansson (ed.), *Geodynamics of Iceland and the North Atlantic area*, D. Reidel, Hingham, Mass., 177-188, 1974.

Wallace, T., A Re-examination of the moment tensor solutions of the 1980 Mammoth Lakes earthquakes, *J. Geophys. Res.*, 90, 11171-11176, 1985.

Wallace, T., J. Given and H. Kanamori, A discrepancy between long and short period mechanisms of earthquakes near the Long Valley Caldera, *Geophys. Res. Lett.*, 9, 1131-1134, 1982.

Wessel, P. and W. H. F. Smith, Free software helps map and display data, *EOS Trans. AGU*, 72, 441, 445-446, 1991.

Appendix 1: Example seismograms

This appendix contains some representative seismograms recorded at a range of stations for two well-recorded earthquakes. For each earthquake, the vertical scaling is the same at all stations.

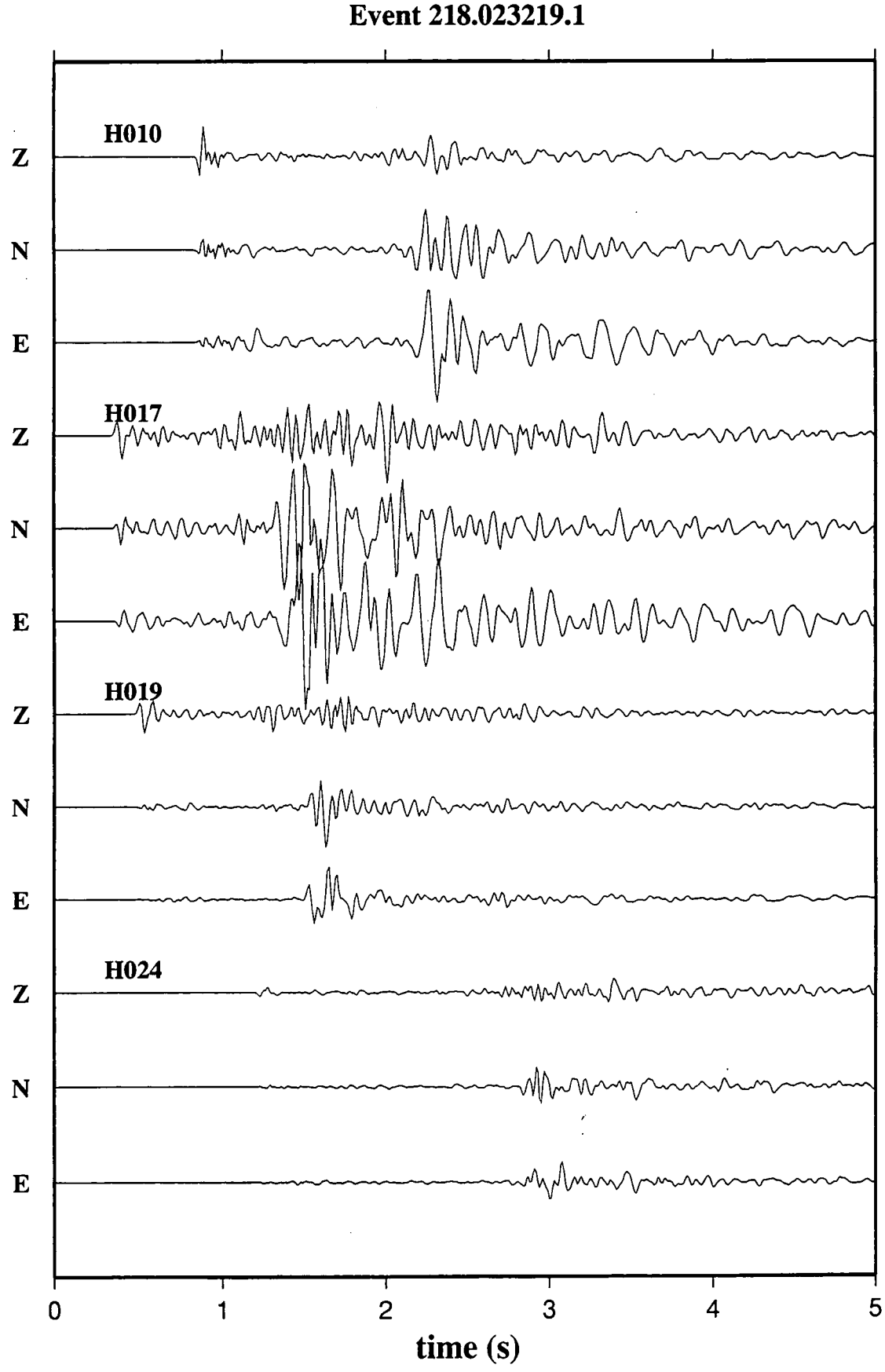

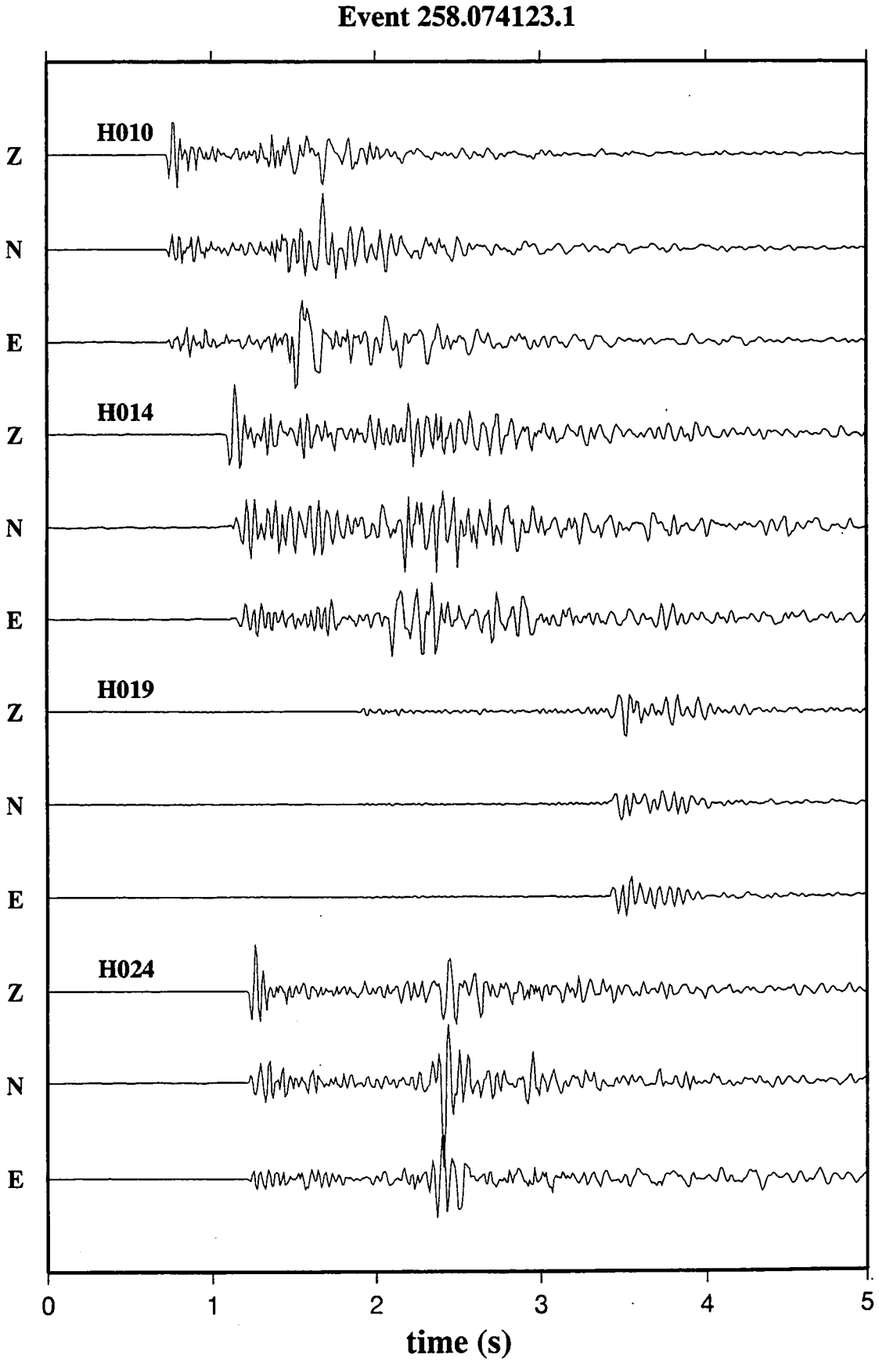
Event 258.074123.1
H010
Z
N
E
H014
Z
N
E
H019
Z
N
E
H024
Z
N
E
0
1
2
3
4
5
time (s)

Appendix 2: *simulps12* example control file

A2.1 Control file used in the final inversion

386 3 0 1.0 4 1 0	neqs, nshot, nblast, wtsht, kout, kout2, kout3
10 1.0 0.02 0.01 0.0 0.50 0.01 0.0	nitloc, wtsp, eigtol, rmscut, zmin, dxmax, rderr, ercof
1 0.1 0.03 1 5.0 2.0 99.0 0.50	hitct, dvpmax, dvpvsmax, idmp, vpdmp, vpvsdmp, stadmp, stepl
1 2 4 0.005 1 0.01 0	ires, i3d, nitmax, snrmct, ihomo, rmstop, ifixl
20.0 35.0 0.10 0.25 0.30	delt1, delt2, res1, res2, res3
9 2 0.5 0.5	ndip, iskip, scale1, scale2
1.2 0.001 15 15	xfax, tlim, nitpb1, nitpb2
1 1 0	iusep, iuses, invdel

A2.2 Description of parameters

Parameter	value	Description
neqs	386	Number of earthquakes
nshot	3	Number of shots
nblast	0	Number of blasts
wtsht	1.0	Weight given to shots (relative to earthquakes)
kout	4	Output control parameter
kout2	1	Output control parameter
kout3	0	Output control parameter
nitloc	10	Maximum number of iterations of event location routine
wtsp	1.0	Weight given to *S-P* times (relative to *P* times)
eigtol	0.020	SVD cut-off in hypocental adjustments
rmscut	0.01	RMS residual cutoff to terminate location iterations
zmin	0.0	Minimum earthquake depth
dxmax	0.50	Maximum horizontal hypocentral relocation per iteration
rderr	0.01	Estimated reading uncertainty
ercof	0.00	Used for hypocentral error calculations
hitct	1	DWS cutoff to remove node from inversion
dvpmax	0.10	Maximum V_P adjustment
dvpvsmax	0.03	Maximum V_P/V_S adjustment
idmp	1	Damping control parameter
vpdmp	5.0	V_P damping parameter
vpvsdmp	2.0	V_P/V_S damping parameter
stadmp	99.00	Station delay damping parameter
stepl	0.50	raypath step length used in partial derivative calculations
ires	1	Resolution output control parameter
i3d	2	three-dimensional ray tracing control parameter
nitmax	4	Maximum number of iterations of the hypocentral relocation model adjustment loop
snrmct	0.005	Solution norm cutoff to terminate inversion
ihomo	1	Number of iterations to use ray-tracing in vertical planes
rmstop	0.01	RMS residual (for all events) to terminate inversion
ifixl	0	Number of iterations to fix hypocentres for
delt1	20.0	Raylength cut-off used to weight residuals
delt2	35.0	Raylength cut-off used to weight residuals
res1	0.10	Residual cut-off used for weighting
res2	0.25	Residual cut-off used for weighting
res3	0.30	Residual cut-off used for weighting
ndip	9	Number of planes searched during approximate ray tracing (ART)
iskip	2	Number of planes near horizontal to skip during ART
scale1	0.5	Ray segment length
scale2	0.5	Controls number of paths tried during ray-tracing
xfax	1.2	Pseudo-bending control parameter
tlim	0.001	Travel-time difference cut-off to terminate pseudo-bending iterations
nitpb1	15	Maximum number of iterations during pseudo-bending
nitpb2	15	Maximum number of iterations during pseudo-bending
iusep	1	Flag to use *P* travel times (0=No; 1=Yes)
iuses	1	Flag to use *S-P* times (0=No; 1=Yes)
invdel	0	Flag to invert for station delays (0=No; 1=Yes)

Appendix 3: Bourne shell scripts for processing output of *simulps12*

A3.1 *s12spread*

s12spread calculates values of the spread function (equation 4.11). It reads information from two *simulps12* output files; the "printout" file (fort.16) and the resolution matrix file (fort.17). Output is an ascii-format *x, y, z, spread* list, where *spread* is the spread function value at the node with co-ordinates *x, y, z*.

```
#! /bin/sh
# s12spread: ADM Apr 1994
# Calculates spread function for rows of resolution matrix.  Assumes zi=1,
# zi=nz layers are fixed nodes. Also assumes that only one model has been
# inverted for, either vp or vpvs, not both.

usage="Usage: $0 print_file resolution_file"

case $# in
   0|1) echo $usage 1>&2; exit 1 ;;
esac

fpr=$1; shift
fres=$1; shift

while test "$1" != ""
do
   case "$1" in
      *) echo $usage 1>&2; exit 1;;
   esac
done

head -58 $fpr > print$$
nawk '
   $0 ~ /velocity grid size/ || $0 ~ /VELOCITY GRID SIZE/ {
      while ($1!="bld") getline
      nx=$(NF-6)-2; ny=$(NF-3)-2; nz=$NF-2;
      getline; getline; getline
      # Note: +ve x is west, when y is north.
      # For ease of plotting, next line reverses this.
      for (xi=1; xi<=nx; xi++) xa[xi]=-$(xi+1)
      getline; getline; getline
      for (yi=1; yi<=ny; yi++) ya[yi]=$(yi+1)
      getline; getline; getline
      for (zi=1; zi <= nz; zi++) za[zi]=0+$(zi+1)
      partot=nx*ny*(nz-2)
      row=1

      x1=1; y1=1; z1=2
   }
   /row= / {
      while (row != substr($0, 6, 4)+0) {
         spread[row]=-1
         row++
         x1++
      }
      if (x1 > nx) {
         y1+=int(x1/nx); x1-=nx*int(x1/nx)
         if (y1 > ny) {y1=1; z1++}
```

```
    }
    sum2=0
    sj2=0
    getline; getline
    m=0
    for (z2=2; z2<nz; z2++) {
    for (y2=1; y2<=ny; y2++) {
    for (x2=1; x2<=nx; x2++) {
            if (m >= 18) { getline; m=0 }
            res=substr($0, m*7+1, 7)+0
            d2=(za[z1]-za[z2])**2+(ya[y1]-ya[y2])**2+(xa[x1]-xa[x2])**2
            sum2+=d2*res**2
            sj2+=res**2
            m++
    }
    }
    }
    if (sj2==0) spread[row]=-1
    else spread[row]=sqrt(sum2/sj2)
    row++
    x1++
}
END {
    n=1
    for (zi=2; zi < nz; zi++) {
        for (yi=1; yi <= ny; yi++) {
            for (xi=1; xi <= nx; xi++) {
                if (spread[n]==0) spread[n]=-1
                print xa[xi], ya[yi], za[zi], spread[n]
                n++
            }
        }
    }
}
```

```
' print$$ $fres

rm print$$
```

A3.2 *plotmod*

plotmod produces coloured or grey-scale map-view plots of a three-dimensional wave-speed model output by *simulps12*. It calls GMT programs to produce a *postscript*-format output file. The input file contains a list of *x, y, z, v* values, where *x, y, z* are the local co-ordinates of a point with wave-speed or V_P / V_S value *v*. This list should have *x* and *y* spacing throughout the model that is equal to the nodal spacing defined by the -I option (default 0.25 km). The colours or shading of the plot are determined from the "colourscale" file specified in the command line, which can be created using the GMT program *makecpt*.

```
#! /bin/sh
# plotmod: ADM Apr 1994
# Draw shaded images of layers of simul12 output P-, vpvs-model

usage="Usage: $0 [-vpl-vpvs] [-Inode_spacing] [-title string] -shade
colourscale_file xyzv_file"

case $# in
    0|1) echo $usage 1>&2; exit 1;;
```

```
esac

# Set defaults
I=-I0.25
model=vp
# The "depths" and "R" variables are model dependent and are defined here.
depths="0 1 2 3 4 5 6"; R=-R-12/12/-12/12

# Process command-line options
while test "$1" != ""
do
    case "$1" in
        -I*) I=$1; shift ;;
        -s*) cs=$2; shift 2 ;;
        -t*) title=$2; shift 2 ;;
        -vp) shift ;;
        -vpvs) model=vpvs; shift ;;
        -*) echo $usage 1>&2 ; exit 1 ;;
        *) break ;;
    esac
done

fxyzv=$1; shift
psbasemap -Jx1 -R0/9/0/12 -X0 -Y0 -P -K

# Plot labels
echo $depths |
nawk '
    BEGIN {
        x=2.5; y=10.5
        printf " 6.5  1.0 16 0.0 5  6 '$title'\n"
    }
    {
        for (i=1; i<=NF; i++) {
            if (i==5) { x=5.5; y=y+9 }
            printf "%f %f 14 0.0 5 10 %s km\n", x-0.3, y, $i
            y=y-2.25
        }
    }
' |
pslabel -Jx -R -O -K

if test "$model" = "vp"
then
    echo 3.5 0.8 12 0.0 5 6 % difference from mean v@-@#P@-@# |
    pslabel -Jx -R -O -K
else
    echo 3.5 0.8 12 0.0 5 6 v@-@#P@-@#/v@-@#S@-@# |
    pslabel -Jx -R -O -K
fi

# Plot colour scale
psscale -C$cs -D3.5/1.55/2/0.3h -O -K -V
sx=2.5; sy=8.5

# Plot model layers
for ldepth in `echo $depths`
do
    nl=`echo $nl | awk '{print $1+1}'`
    echo layer $nl 1>&2
    if test "$nl" = 5
    then
        sx=3; sy=6.75
    fi
    nawk ' $3 == '$ldepth' { print $1, $2, $4 }' $fxyzv > xyv.in$$

    psbasemap -JX2 $R -B1a5swen -X$sx -Y$sy -O -K
    xyz2grd xyv.in$$ -Ggrd$$ $I -R
```

```
    grdimage grd$$ -JX2 -R -C$cs -X0 -Y0 -O -K -V

    sx=0; sy=-2.25
done

# Commands to plot a location map can be added here

psbasemap -JX -R -O
rm xyv.in$$ grd$$
```

A3.3 *plotcs*

plotcs is similar to *plotmod* but produces a plot of depth sections of V_P and V_P/V_S models. The input files need not be interpolated to the final desired node spacing, as this is done internally by calling the shell script *csinterpolate*. The *x, y* endpoints of the sections and the depth range are defined on the command line. A file of (*x, y, z*) hypocentral co-ordinates can be specified so that hypocentres within *u* km of the section line are projected onto the sections.

```
#! /bin/sh
# plotcs: ADM Apr 1995
# Draw vertical color plots of simul vp and vpvs models

usage="Usage: $0 x1 y1 x2 y2 z-top z-bottom -Inode_spacing -shade cscale_vp
cscale_vpvs [-hypos hypo-file] [-Wu/-u] [-title string] xyzv.vp_file xyzv.vpvs_file"

case $# in
    0|1|2|3|4|5|6|7|8|9|10|11) echo $usage 1>&2; exit 1 ;;
esac

# Set defaults
title=""; fhypo=/dev/null
# Process command-line options
x1=$1; y1=$2; x2=$3; y2=$4; shift 4
z1=$1; z2=$2; shift 2
while test "$1" != ""
do
    case "$1" in
        -I*) node=`echo $1 | sed 's,-I,,'`; shift ;;
        -s*) csvp=$2; csvpvs=$3; shift 3 ;;
        -h*) fhypo=$2; shift 2 ;;
        -W*) W=$1; shift ;;
        -t*) title=$2; shift 2 ;;
        -*) echo $usage 1>&2 ; exit 1 ;;
        *) break ;;
    esac
done
fvp=$1; fvpvs=$2; shift 2

# Get depth positions
project -C$z1/0 -E$z2/0 -G$node |
nawk 'int($3/'$node')==($3/'$node') {print $1}' | uniq > dep$$

# Get x,y positions of cross-section points
project -C$x1/$y1 -E$x2/$y2 -G$node |
nawk 'int($3/'$node')==($3/'$node')' | uniq > xy$$
len=`tail -1 xy$$ | nawk '{print $3}'`

# Calculate size of plots (default length = 8 inches)
scale=`echo $depth $len | nawk '{ z=8*$1/$2; print 8 "/" z }'`
```

```
# Project hypocentres into plane of cross-section
project $fhypo -C$x1/$y1 -E$x2/$y2 -Fpz -V $W > hypos$$

# Create target-node file: "x, y, z, a", where a is length along cross-section
for depth in `cat dep$$`
do
    nawk '{ print $1, $2, '$depth', $3}' xy$$
done > targ$$

# Plot labels and title
nawk ' BEGIN {
    print "5.2 7.5 24 0.0 5 6 '$title'"
    print "5.2 7.0 24 0.0 5 6 v@-P@-"
    print "5.2 3.8 24 0.0 5 6 v@-P@-/v@-S@-"
}' /dev/null |
pslabel -Jx1 -R0/12/0/9 -X0 -Y0 -K

# Plot vp model
psbasemap -JX$scale -R0/$len/$z1/$z2 -Ba5f1::/:depth:SWen -X1.2 -Y4.5 -O -K
sort +2 -n +1 -n +0 -n $fvp | csinterpolate -t targ$$ |
xyz2grd -Ggrd$$ -I$node -R
grdimage grd$$ -JX -R -C$csvp -X0 -Y0 -V -O -K

# Plot hypocenters
psxy hypos$$ -JX -R -Sc0.05 -G0 -X0 -Y0 -O -K

# Plot vpvs model
psbasemap -JX -R -Ba5f1:"distance (km)":/:depth:SWen -X0 -Y-3.2 -O -K
sort +2 -n +1 -n +0 -n $fvpvs | csinterpolate -t targ$$ |
xyz2grd -Ggrd$$ -I$node -R
grdimage grd$$ -JX -R -C$csvpvs -X0 -Y0 -V -O -K

# Plot hypocenters
psxy hypos$$ -JX -R -Sc0.05 -G0 -X0 -Y0 -O -K

# Add colourscales
psscale -C$csvp -D8.5/4.2/2/0.3 -O -K -V
psscale -C$csvpvs -D8.5/1/2/0.3 -O -K -V

psbasemap -Jx -R -O
rm grd$$ xy$$ dep$$ hypos$$ targ$$
```

A3.4 csinterpolate

csinterpolate is called by *plotcs* to interpolate the input *x, y, z, v* list to the desired spacing.

```
#! /bin/sh
# csinterpolate: ADM Apr 1995
# Interpolates x,y,z,v input to a, z, v output, where a is distance along cross-section.
# target-node file format: x y z a (i.e. x,y,z position of node at a)

usage="Usage: $0 -t target-node_file [xyzv_file]"
case $# in
    0|1) echo $usage 1>&2; exit 1 ;;
esac

# Process command-line options
while test "$1" != ""
do
    case "$1" in
        -t*) ftar=$2; shift 2 ;;
        -*) echo $usage 1>&2 ; exit 1 ;;
        *) break ;;
```

```
    esac
done
cat $* > xyzv$$

nawk '
    function interpolate(xt, yt, zt) {
        for (xi=1; xi<=nx; xi++) if (xt<xa[xi]) break
        for (yi=1; yi<=ny; yi++) if (yt<ya[yi]) break
        for (zi=1; zi<=nz; zi++) if (zt<za[zi]) break
        x1=xi-1; x2=xi; y1=yi-1; y2=yi; z1=zi-1; z2=zi
        # interpolate at z=z1
        t=(xt-xa[x1])/(xa[x2]-xa[x1])
        u=(yt-ya[y1])/(ya[y2]-ya[y1])
        v1=(1-t)*(1-u)*v[x1,y1,z1]+t*(1-u)*v[x2,y1,z1]+t*u*v[x2,y2,z1]+(1-
t)*u*v[x1,y2,z1]
        # interpolate at z=z2 if neccessary
        v2=v1
        if              (zt!=za[z1])            v2=(1-t)*(1-u)*v[x1,y1,z2]+t*(1-
u)*v[x2,y1,z2]+t*u*v[x2,y2,z2]+(1-t)*u*v[x1,y2,z2]
        return v1+(v2-v1)*(zt-za[z1])/(za[z2]-za[z1])
    }
    BEGIN {
        # Load v[x,y,z] array
        lastza=0.55; lastya=0.55
        while (getline <"'xyzv$$'" > 0) {
            if ($3!=lastza) {
                zi++; yi=0
                za[zi]=$3; lastza=$3
            }
            if ($2!=lastya) {
                yi++; xi=0
                ya[yi]=$2; lastya=$2
            }
            xi++
            xa[xi]=$1
            v[xi,yi,zi]=$4
        }
        nx=xi; ny=yi; nz=zi
    }
    {
        # read xt, yt, zt, a; get velocity at xt, yt, zt
        xt=$1; yt=$2; zt=$3; a=$4
        vel=interpolate(xt, yt, zt)
        print a, zt, vel
    }
' $ftar

rm xyzv$$
```

Appendix 4: The final V_P and V_P/V_S models

This appendix lists the V_P and V_P/V_S values at all the model nodes, including edge nodes. The first 5 lines contain information about the node positions, and are followed by the V_P model then the V_P/V_S model for all nodes. For each depth slice, x increases across the page and y increases down the page.

```
 1.0 14 13 11          number of x, y, z nodes
-245.0 -12.0 -10.0  -8.0  -6.0  -4.0  -2.0   0.0   2.0   4.0   6.0   8.0  12.0 245.0   x nodes
-245.0 -12.0  -8.0  -6.0  -4.0  -2.0   0.0   2.0   4.0   6.0   8.0  12.0 245.0        y nodes
-150.0  -1.0   0.0   1.0   2.0   3.0   4.0   5.0   6.0   8.0 150.0                    z nodes
 0 0 0
1.00 1.00 1.00 1.00 1.00 1.00 1.00 1.00 1.00 1.00 1.00 1.00 1.00 1.00
1.00 1.00 1.00 1.00 1.00 1.00 1.00 1.00 1.00 1.00 1.00 1.00 1.00 1.00
1.00 1.00 1.00 1.00 1.00 1.00 1.00 1.00 1.00 1.00 1.00 1.00 1.00 1.00
1.00 1.00 1.00 1.00 1.00 1.00 1.00 1.00 1.00 1.00 1.00 1.00 1.00 1.00
1.00 1.00 1.00 1.00 1.00 1.00 1.00 1.00 1.00 1.00 1.00 1.00 1.00 1.00
1.00 1.00 1.00 1.00 1.00 1.00 1.00 1.00 1.00 1.00 1.00 1.00 1.00 1.00
1.00 1.00 1.00 1.00 1.00 1.00 1.00 1.00 1.00 1.00 1.00 1.00 1.00 1.00
1.00 1.00 1.00 1.00 1.00 1.00 1.00 1.00 1.00 1.00 1.00 1.00 1.00 1.00
1.00 1.00 1.00 1.00 1.00 1.00 1.00 1.00 1.00 1.00 1.00 1.00 1.00 1.00
1.00 1.00 1.00 1.00 1.00 1.00 1.00 1.00 1.00 1.00 1.00 1.00 1.00 1.00
1.00 1.00 1.00 1.00 1.00 1.00 1.00 1.00 1.00 1.00 1.00 1.00 1.00 1.00
1.00 1.00 1.00 1.00 1.00 1.00 1.00 1.00 1.00 1.00 1.00 1.00 1.00 1.00
1.00 1.00 1.00 1.00 1.00 1.00 1.00 1.00 1.00 1.00 1.00 1.00 1.00 1.00
2.10 2.10 2.10 2.10 2.10 2.10 2.10 2.10 2.10 2.10 2.10 2.10 2.10 2.10
2.10 2.10 2.10 2.10 2.10 2.10 2.10 2.10 2.10 2.10 2.10 2.10 2.10 2.10
2.10 2.10 2.10 2.10 2.10 2.10 2.10 2.10 2.10 2.10 2.10 2.10 2.10 2.10
2.10 2.10 2.10 2.10 2.10 2.10 2.10 2.10 2.10 2.10 2.10 2.10 2.10 2.10
2.10 2.10 2.10 2.10 2.10 2.10 2.10 2.10 2.10 2.10 2.10 2.10 2.10 2.10
2.10 2.10 2.10 2.10 2.10 2.10 2.10 2.10 2.10 2.10 2.10 2.10 2.10 2.10
2.10 2.10 2.10 2.10 2.10 2.10 2.10 2.10 2.10 2.10 2.10 2.10 2.10 2.10
2.10 2.10 2.10 2.10 2.10 2.10 2.10 2.10 2.10 2.10 2.10 2.10 2.10 2.10
2.10 2.10 2.10 2.10 2.10 2.10 2.10 2.10 2.10 2.10 2.10 2.10 2.10 2.10
2.10 2.10 2.10 2.10 2.10 2.10 2.10 2.10 2.10 2.10 2.10 2.10 2.10 2.10
2.10 2.10 2.10 2.10 2.10 2.10 2.10 2.10 2.10 2.10 2.10 2.10 2.10 2.10
2.10 2.10 2.10 2.10 2.10 2.10 2.10 2.10 2.10 2.10 2.10 2.10 2.10 2.10
2.10 2.10 2.10 2.10 2.10 2.10 2.10 2.10 2.10 2.10 2.10 2.10 2.10 2.10
2.10 2.10 2.10 2.10 2.10 2.10 2.10 2.10 2.10 2.10 2.10 2.10 2.10 2.10
3.17 3.17 3.17 3.17 3.17 3.17 3.17 3.17 3.17 3.17 3.17 3.17 3.17 3.17
3.17 3.17 3.13 3.10 3.25 3.17 3.17 3.14 3.14 3.16 3.33 3.17 3.17 3.17
3.17 3.17 3.16 3.11 3.17 3.17 3.19 3.17 3.16 3.17 3.21 3.17 3.17 3.17
3.17 3.17 3.04 3.10 3.17 3.18 3.10 3.16 3.17 3.17 3.17 3.11 3.17 3.17
3.17 3.17 3.16 3.18 3.31 3.44 3.25 3.13 3.13 3.13 3.17 3.14 3.17 3.17
3.17 3.18 3.20 3.29 3.56 3.17 3.05 3.09 2.88 3.11 3.17 2.96 3.11 3.17
3.17 3.23 3.22 3.57 3.15 3.57 3.24 3.49 3.19 3.27 3.38 2.92 3.11 3.17
3.17 3.17 3.06 3.18 3.49 2.95 2.92 3.34 3.30 3.39 3.57 3.22 3.16 3.17
3.17 3.17 3.32 3.50 3.44 2.97 3.39 3.08 3.17 3.16 3.15 3.24 3.26 3.17
3.17 3.17 3.18 3.17 3.21 3.17 3.17 3.39 3.25 3.16 3.17 3.17 3.17 3.17
3.17 3.17 3.24 3.18 3.17 3.01 3.13 3.42 3.09 3.02 2.94 3.17 3.17 3.17
3.17 3.17 3.17 3.17 3.31 3.26 3.08 3.16 3.17 3.17 3.15 3.17 3.17 3.17
3.17 3.17 3.17 3.17 3.17 3.17 3.17 3.17 3.17 3.17 3.17 3.17 3.17 3.17
4.35 4.35 4.35 4.35 4.35 4.35 4.35 4.35 4.35 4.35 4.35 4.35 4.35 4.35
4.35 4.35 4.35 4.14 4.52 4.35 4.36 4.34 4.22 4.31 4.55 4.35 4.35 4.35
4.35 4.35 4.35 4.15 4.37 4.35 4.37 4.35 4.30 4.35 4.45 4.35 4.35 4.35
4.35 4.35 4.15 4.08 4.35 4.37 4.20 4.31 4.34 4.35 4.32 4.12 4.35 4.35
4.35 4.34 4.44 4.46 4.56 4.68 4.49 4.07 4.28 4.35 4.31 4.28 4.36 4.35
4.35 4.21 4.41 4.58 4.75 4.51 4.55 4.28 4.07 4.34 4.27 4.15 4.35 4.35
4.35 4.45 4.68 4.74 4.70 4.60 4.67 4.49 4.49 4.41 4.51 4.05 4.35 4.35
4.35 4.35 4.42 4.48 4.67 4.35 4.59 4.53 4.38 4.74 4.75 4.54 4.32 4.35
4.35 4.35 4.27 4.70 4.52 4.22 4.40 4.18 4.41 4.44 4.33 4.44 4.46 4.35
4.35 4.35 4.42 4.41 4.26 4.28 4.33 4.48 4.33 4.44 4.30 4.35 4.35 4.35
4.35 4.35 4.42 4.31 4.38 4.17 4.21 4.52 4.17 4.20 4.12 4.35 4.35 4.35
4.35 4.35 4.35 4.35 4.54 4.70 4.15 4.43 4.35 4.35 4.34 4.35 4.35 4.35
4.35 4.35 4.35 4.35 4.35 4.35 4.35 4.35 4.35 4.35 4.35 4.35 4.35 4.35
5.36 5.36 5.36 5.36 5.36 5.36 5.36 5.36 5.36 5.36 5.36 5.36 5.36 5.36
5.36 5.36 5.37 5.31 5.36 5.38 5.42 5.40 5.13 5.30 5.58 5.36 5.36 5.36
5.36 5.36 5.35 5.17 5.18 5.36 5.36 5.31 5.21 5.39 5.49 5.35 5.36 5.36
5.36 5.36 5.28 5.06 5.39 5.53 5.29 5.28 5.32 5.35 5.12 5.08 5.36 5.36
5.36 5.32 5.13 5.42 5.59 5.44 5.37 5.02 5.38 5.40 5.22 5.29 5.37 5.36
5.36 5.30 5.29 5.72 5.76 5.72 5.62 5.45 5.42 5.30 5.11 5.38 5.36 5.36
5.36 5.35 5.73 5.76 5.72 5.59 5.76 5.47 5.32 5.42 5.26 5.20 5.35 5.36
```

5.36 5.37 5.44 5.41 5.61 5.70 5.76 5.68 5.47 5.75 5.74 5.63 5.28 5.36
5.36 5.36 5.26 5.37 5.29 5.29 5.30 5.43 5.48 5.59 5.25 5.47 5.43 5.36
5.36 5.36 5.48 5.49 5.33 5.10 5.11 5.05 5.28 5.40 5.29 5.32 5.35 5.36
5.36 5.36 5.39 5.17 5.42 5.66 5.15 5.39 5.43 5.18 5.25 5.36 5.36 5.36
5.36 5.36 5.36 5.36 5.41 5.69 5.24 5.52 5.37 5.36 5.36 5.36 5.36 5.36
5.36 5.36 5.36 5.36 5.36 5.36 5.36 5.36 5.36 5.36 5.36 5.36 5.36 5.36
5.92 5.92 5.92 5.92 5.92 5.92 5.92 5.92 5.92 5.92 5.92 5.92 5.92 5.92
5.92 5.92 5.92 6.00 5.88 5.90 6.03 5.91 5.59 5.96 6.06 5.92 5.92 5.92
5.92 5.92 5.90 5.77 5.67 5.76 6.01 5.83 5.81 6.04 5.90 5.87 5.92 5.92
5.92 5.92 5.77 5.69 5.71 5.96 5.84 5.72 5.77 5.72 5.64 5.79 5.92 5.92
5.92 5.92 5.64 5.82 6.25 6.03 6.02 5.78 6.02 5.75 5.73 5.93 5.92 5.92
5.92 5.91 5.89 5.96 6.32 6.28 6.17 6.12 6.12 5.73 5.59 5.92 5.93 5.92
5.92 5.94 6.01 6.30 6.28 6.28 6.31 6.27 5.86 5.67 6.08 5.82 5.87 5.92
5.92 5.96 5.78 5.87 5.91 6.32 6.32 6.26 6.12 6.23 6.32 6.13 5.85 5.92
5.92 5.93 5.91 5.95 5.66 5.66 5.90 6.15 5.91 6.15 5.99 6.01 5.95 5.92
5.92 5.92 5.96 6.05 5.94 5.70 5.68 5.66 6.00 5.81 5.85 5.87 5.92 5.92
5.92 5.92 5.92 5.86 5.89 6.14 5.82 5.84 6.03 5.76 5.89 5.92 5.92 5.92
5.92 5.92 5.92 5.92 5.92 5.94 5.96 5.99 5.97 5.92 5.92 5.92 5.92 5.92
5.92 5.92 5.92 5.92 5.92 5.92 5.92 5.92 5.92 5.92 5.92 5.92 5.92 5.92
6.22 6.22 6.22 6.22 6.22 6.22 6.22 6.22 6.22 6.22 6.22 6.22 6.22 6.22
6.22 6.22 6.22 6.25 6.29 6.09 6.18 6.04 6.01 6.28 6.23 6.22 6.22 6.22
6.22 6.22 6.19 6.08 5.94 5.99 6.03 5.99 6.15 6.17 5.91 6.21 6.22 6.22
6.22 6.22 6.07 6.14 6.15 6.32 6.23 6.21 6.08 6.09 6.07 6.19 6.22 6.22
6.22 6.22 6.13 6.14 6.55 6.44 6.52 6.32 6.09 6.01 6.18 6.20 6.23 6.22
6.22 6.21 6.15 6.45 6.60 6.58 6.56 6.49 5.92 6.00 6.03 6.06 6.22 6.22
6.22 6.22 6.24 6.54 6.57 6.50 6.54 6.48 6.27 6.30 6.42 6.03 6.19 6.22
6.22 6.22 6.21 6.29 6.52 6.62 6.62 6.50 6.43 6.49 6.57 6.22 6.22 6.22
6.22 6.22 6.22 6.50 6.15 6.29 6.60 6.49 6.26 5.99 6.30 6.27 6.24 6.22
6.22 6.22 6.22 6.24 6.07 5.98 6.12 5.95 6.00 6.23 6.20 6.21 6.22 6.22
6.22 6.22 6.22 6.22 6.18 6.07 6.15 6.10 6.07 6.07 6.25 6.22 6.22 6.22
6.22 6.22 6.22 6.22 6.22 6.22 6.22 6.20 6.25 6.22 6.22 6.22 6.22 6.22
6.22 6.22 6.22 6.22 6.22 6.22 6.22 6.22 6.22 6.22 6.22 6.22 6.22 6.22
6.44 6.44 6.44 6.44 6.44 6.44 6.44 6.44 6.44 6.44 6.44 6.44 6.44 6.44
6.44 6.44 6.44 6.44 6.41 6.36 6.15 6.24 6.40 6.58 6.37 6.44 6.44 6.44
6.44 6.44 6.44 6.37 6.23 6.38 6.22 6.42 6.47 6.47 6.18 6.43 6.44 6.44
6.44 6.44 6.44 6.39 6.62 6.64 6.64 6.55 6.57 6.48 6.40 6.41 6.44 6.44
6.44 6.44 6.44 6.48 6.51 6.36 6.48 6.46 6.29 6.42 6.31 6.34 6.44 6.44
6.44 6.44 6.43 6.52 6.75 6.65 6.79 6.58 6.26 6.23 6.32 6.31 6.43 6.44

6.44 6.44 6.43 6.47 6.75 6.59 6.75 6.72 6.64 6.65 6.44 6.51 6.45 6.44
6.44 6.44 6.44 6.42 6.54 6.63 6.69 6.78 6.73 6.74 6.49 6.44 6.44 6.44
6.44 6.44 6.44 6.46 6.39 6.77 6.83 6.74 6.71 6.70 6.46 6.46 6.44 6.44
6.44 6.44 6.44 6.44 6.39 6.36 6.25 6.83 6.56 6.26 6.41 6.44 6.44 6.44
6.44 6.44 6.44 6.44 6.42 6.40 6.26 6.25 6.52 6.37 6.45 6.44 6.44 6.44
6.44 6.44 6.44 6.44 6.44 6.44 6.44 6.44 6.44 6.44 6.44 6.44 6.44 6.44
6.44 6.44 6.44 6.44 6.44 6.44 6.44 6.44 6.44 6.44 6.44 6.44 6.44 6.44
6.50 6.50 6.50 6.50 6.50 6.50 6.50 6.50 6.50 6.50 6.50 6.50 6.50 6.50
6.50 6.50 6.50 6.50 6.50 6.52 6.38 6.37 6.51 6.42 6.50 6.50 6.50 6.50
6.50 6.50 6.50 6.49 6.59 6.57 6.61 6.69 6.75 6.28 6.48 6.50 6.50 6.50
6.50 6.50 6.50 6.49 6.58 6.60 6.70 6.66 6.62 6.37 6.47 6.50 6.50 6.50
6.50 6.50 6.50 6.49 6.53 6.52 6.62 6.53 6.37 6.50 6.47 6.49 6.50 6.50
6.50 6.50 6.50 6.51 6.51 6.49 6.65 6.80 6.75 6.41 6.50 6.54 6.51 6.50
6.50 6.50 6.50 6.51 6.52 6.51 6.53 6.47 6.46 6.49 6.50 6.52 6.50 6.50
6.50 6.50 6.50 6.50 6.52 6.52 6.49 6.48 6.51 6.54 6.56 6.48 6.50 6.50
6.50 6.50 6.50 6.50 6.50 6.53 6.55 6.54 6.58 6.60 6.61 6.49 6.50 6.50
6.50 6.50 6.50 6.50 6.50 6.55 6.58 6.58 6.56 6.48 6.48 6.50 6.50 6.50
6.50 6.50 6.50 6.50 6.50 6.50 6.52 6.52 6.53 6.50 6.50 6.50 6.50 6.50
6.50 6.50 6.50 6.50 6.50 6.50 6.50 6.50 6.50 6.50 6.50 6.50 6.50 6.50
6.50 6.50 6.50 6.50 6.50 6.50 6.50 6.50 6.50 6.50 6.50 6.50 6.50 6.50
6.60 6.60 6.60 6.60 6.60 6.60 6.60 6.60 6.60 6.60 6.60 6.60 6.60 6.60
6.60 6.60 6.60 6.60 6.60 6.60 6.60 6.60 6.60 6.60 6.60 6.60 6.60 6.60
6.60 6.60 6.60 6.60 6.60 6.60 6.60 6.60 6.60 6.60 6.60 6.60 6.60 6.60
6.60 6.60 6.60 6.60 6.60 6.60 6.60 6.60 6.60 6.60 6.60 6.60 6.60 6.60
6.60 6.60 6.60 6.60 6.60 6.60 6.60 6.60 6.60 6.60 6.60 6.60 6.60 6.60
6.60 6.60 6.60 6.60 6.60 6.60 6.60 6.60 6.60 6.60 6.60 6.60 6.60 6.60
6.60 6.60 6.60 6.60 6.60 6.60 6.60 6.60 6.60 6.60 6.60 6.60 6.60 6.60
6.60 6.60 6.60 6.60 6.60 6.60 6.60 6.60 6.60 6.60 6.60 6.60 6.60 6.60
6.60 6.60 6.60 6.60 6.60 6.60 6.60 6.60 6.60 6.60 6.60 6.60 6.60 6.60
6.60 6.60 6.60 6.60 6.60 6.60 6.60 6.60 6.60 6.60 6.60 6.60 6.60 6.60
6.60 6.60 6.60 6.60 6.60 6.60 6.60 6.60 6.60 6.60 6.60 6.60 6.60 6.60
6.60 6.60 6.60 6.60 6.60 6.60 6.60 6.60 6.60 6.60 6.60 6.60 6.60 6.60
6.60 6.60 6.60 6.60 6.60 6.60 6.60 6.60 6.60 6.60 6.60 6.60 6.60 6.60
8.00 8.00 8.00 8.00 8.00 8.00 8.00 8.00 8.00 8.00 8.00 8.00 8.00 8.00
8.00 8.00 8.00 8.00 8.00 8.00 8.00 8.00 8.00 8.00 8.00 8.00 8.00 8.00
8.00 8.00 8.00 8.00 8.00 8.00 8.00 8.00 8.00 8.00 8.00 8.00 8.00 8.00
8.00 8.00 8.00 8.00 8.00 8.00 8.00 8.00 8.00 8.00 8.00 8.00 8.00 8.00
8.00 8.00 8.00 8.00 8.00 8.00 8.00 8.00 8.00 8.00 8.00 8.00 8.00 8.00

```
8.00 8.00 8.00 8.00 8.00 8.00 8.00 8.00 8.00 8.00 8.00 8.00 8.00 8.00
8.00 8.00 8.00 8.00 8.00 8.00 8.00 8.00 8.00 8.00 8.00 8.00 8.00 8.00
8.00 8.00 8.00 8.00 8.00 8.00 8.00 8.00 8.00 8.00 8.00 8.00 8.00 8.00
8.00 8.00 8.00 8.00 8.00 8.00 8.00 8.00 8.00 8.00 8.00 8.00 8.00 8.00
8.00 8.00 8.00 8.00 8.00 8.00 8.00 8.00 8.00 8.00 8.00 8.00 8.00 8.00
8.00 8.00 8.00 8.00 8.00 8.00 8.00 8.00 8.00 8.00 8.00 8.00 8.00 8.00
8.00 8.00 8.00 8.00 8.00 8.00 8.00 8.00 8.00 8.00 8.00 8.00 8.00 8.00
8.00 8.00 8.00 8.00 8.00 8.00 8.00 8.00 8.00 8.00 8.00 8.00 8.00 8.00
1.77 1.77 1.77 1.77 1.77 1.77 1.77 1.77 1.77 1.77 1.77 1.77 1.77 1.77
1.77 1.77 1.77 1.77 1.77 1.77 1.77 1.77 1.77 1.77 1.77 1.77 1.77 1.77
1.77 1.77 1.77 1.77 1.77 1.77 1.77 1.77 1.77 1.77 1.77 1.77 1.77 1.77
1.77 1.77 1.77 1.77 1.77 1.77 1.77 1.77 1.77 1.77 1.77 1.77 1.77 1.77
1.77 1.77 1.77 1.77 1.77 1.77 1.77 1.77 1.77 1.77 1.77 1.77 1.77 1.77
1.77 1.77 1.77 1.77 1.77 1.77 1.77 1.77 1.77 1.77 1.77 1.77 1.77 1.77
1.77 1.77 1.77 1.77 1.77 1.77 1.77 1.77 1.77 1.77 1.77 1.77 1.77 1.77
1.77 1.77 1.77 1.77 1.77 1.77 1.77 1.77 1.77 1.77 1.77 1.77 1.77 1.77
1.77 1.77 1.77 1.77 1.77 1.77 1.77 1.77 1.77 1.77 1.77 1.77 1.77 1.77
1.77 1.77 1.77 1.77 1.77 1.77 1.77 1.77 1.77 1.77 1.77 1.77 1.77 1.77
1.77 1.77 1.77 1.77 1.77 1.77 1.77 1.77 1.77 1.77 1.77 1.77 1.77 1.77
1.77 1.77 1.77 1.77 1.77 1.77 1.77 1.77 1.77 1.77 1.77 1.77 1.77 1.77
1.77 1.77 1.77 1.77 1.77 1.77 1.77 1.77 1.77 1.77 1.77 1.77 1.77 1.77
1.77 1.77 1.77 1.77 1.77 1.77 1.77 1.77 1.77 1.77 1.77 1.77 1.77 1.77
1.77 1.77 1.77 1.77 1.77 1.77 1.77 1.77 1.77 1.77 1.77 1.77 1.77 1.77
1.77 1.77 1.77 1.77 1.77 1.77 1.77 1.77 1.77 1.77 1.77 1.77 1.77 1.77
1.77 1.77 1.77 1.77 1.77 1.77 1.77 1.77 1.77 1.77 1.77 1.77 1.77 1.77
1.77 1.77 1.77 1.77 1.77 1.77 1.77 1.77 1.77 1.77 1.77 1.77 1.77 1.77
1.77 1.77 1.77 1.77 1.77 1.77 1.77 1.77 1.77 1.77 1.77 1.77 1.77 1.77
1.77 1.77 1.77 1.77 1.77 1.77 1.77 1.77 1.77 1.77 1.77 1.77 1.77 1.77
1.77 1.77 1.77 1.77 1.77 1.77 1.77 1.77 1.77 1.77 1.77 1.77 1.77 1.77
1.77 1.77 1.77 1.77 1.77 1.77 1.77 1.77 1.77 1.77 1.77 1.77 1.77 1.77
1.77 1.77 1.77 1.77 1.77 1.77 1.77 1.77 1.77 1.77 1.77 1.77 1.77 1.77
1.77 1.77 1.77 1.77 1.77 1.77 1.77 1.77 1.77 1.77 1.77 1.77 1.77 1.77
1.77 1.77 1.77 1.77 1.77 1.77 1.77 1.77 1.77 1.77 1.77 1.77 1.77 1.77
1.77 1.77 1.77 1.77 1.77 1.77 1.77 1.77 1.77 1.77 1.77 1.77 1.77 1.77
1.77 1.77 1.77 1.77 1.77 1.77 1.77 1.77 1.77 1.77 1.77 1.77 1.77 1.77
1.77 1.77 1.77 1.77 1.77 1.77 1.77 1.79 1.77 1.78 1.84 1.77 1.77 1.77
1.77 1.77 1.77 1.77 1.77 1.77 1.77 1.78 1.77 1.77 1.79 1.77 1.77 1.77
1.77 1.77 1.78 1.78 1.77 1.77 1.80 1.77 1.77 1.77 1.77 1.77 1.77 1.77
```

```
1.77 1.77 1.77 1.77 1.72 1.70 1.82 1.77 1.77 1.77 1.77 1.76 1.77 1.77
1.77 1.81 1.79 1.78 1.72 1.77 1.79 1.83 1.83 1.76 1.77 1.78 1.77 1.77
1.77 1.78 1.78 1.76 1.72 1.70 1.72 1.75 1.75 1.76 1.72 1.77 1.77 1.77
1.77 1.77 1.80 1.77 1.76 1.73 1.75 1.76 1.77 1.77 1.75 1.77 1.77 1.77
1.77 1.77 1.82 1.77 1.76 1.80 1.70 1.72 1.77 1.77 1.77 1.77 1.76 1.77
1.77 1.77 1.77 1.77 1.77 1.77 1.76 1.79 1.72 1.70 1.77 1.77 1.77 1.77
1.77 1.77 1.78 1.77 1.77 1.81 1.77 1.80 1.79 1.77 1.84 1.77 1.77 1.77
1.77 1.77 1.77 1.77 1.77 1.78 1.79 1.79 1.77 1.77 1.78 1.77 1.77 1.77
1.77 1.77 1.77 1.77 1.77 1.77 1.77 1.77 1.77 1.77 1.77 1.77 1.77 1.77
1.77 1.77 1.77 1.77 1.77 1.77 1.77 1.77 1.77 1.77 1.77 1.77 1.77 1.77
1.77 1.77 1.77 1.76 1.77 1.77 1.78 1.80 1.77 1.82 1.82 1.77 1.77 1.77
1.77 1.77 1.77 1.77 1.77 1.77 1.77 1.79 1.77 1.79 1.79 1.77 1.77 1.77
1.77 1.77 1.79 1.79 1.77 1.78 1.79 1.77 1.77 1.77 1.77 1.76 1.77 1.77
1.77 1.77 1.77 1.76 1.73 1.70 1.80 1.78 1.77 1.77 1.75 1.76 1.77 1.77
1.77 1.80 1.82 1.78 1.74 1.71 1.80 1.84 1.76 1.76 1.77 1.81 1.77 1.77
1.77 1.78 1.79 1.77 1.71 1.71 1.71 1.74 1.78 1.74 1.72 1.77 1.77 1.77
1.77 1.77 1.83 1.80 1.78 1.75 1.73 1.76 1.79 1.76 1.77 1.77 1.76 1.77
1.77 1.77 1.79 1.77 1.75 1.76 1.71 1.71 1.73 1.76 1.77 1.76 1.76 1.77
1.77 1.77 1.78 1.77 1.77 1.77 1.76 1.78 1.71 1.72 1.79 1.77 1.77 1.77
1.77 1.77 1.78 1.77 1.77 1.82 1.78 1.80 1.78 1.78 1.84 1.77 1.77 1.77
1.77 1.77 1.77 1.77 1.77 1.78 1.78 1.80 1.77 1.77 1.77 1.77 1.77 1.77
1.77 1.77 1.77 1.77 1.77 1.77 1.77 1.77 1.77 1.77 1.77 1.77 1.77 1.77
1.77 1.77 1.77 1.77 1.77 1.77 1.77 1.77 1.77 1.77 1.77 1.77 1.77 1.77
1.77 1.77 1.77 1.76 1.76 1.77 1.79 1.78 1.78 1.82 1.78 1.77 1.77 1.77
1.77 1.77 1.78 1.78 1.77 1.77 1.79 1.79 1.77 1.82 1.78 1.77 1.77 1.77
1.77 1.77 1.78 1.80 1.77 1.77 1.78 1.77 1.77 1.77 1.75 1.76 1.77 1.77
1.77 1.77 1.79 1.76 1.78 1.76 1.78 1.79 1.76 1.77 1.73 1.77 1.77 1.77
1.77 1.78 1.80 1.78 1.76 1.71 1.79 1.79 1.72 1.76 1.78 1.82 1.77 1.77
1.77 1.77 1.79 1.77 1.71 1.73 1.72 1.74 1.79 1.73 1.76 1.77 1.77 1.77
1.77 1.77 1.80 1.81 1.76 1.75 1.71 1.75 1.79 1.75 1.78 1.76 1.76 1.77
1.77 1.77 1.78 1.76 1.76 1.72 1.72 1.71 1.71 1.76 1.78 1.76 1.77 1.77
1.77 1.77 1.79 1.76 1.77 1.79 1.76 1.74 1.76 1.77 1.80 1.77 1.77 1.77
1.77 1.77 1.77 1.77 1.77 1.80 1.79 1.79 1.78 1.79 1.80 1.77 1.77 1.77
1.77 1.77 1.77 1.77 1.77 1.77 1.78 1.79 1.77 1.77 1.77 1.77 1.77 1.77
1.77 1.77 1.77 1.77 1.77 1.77 1.77 1.77 1.77 1.77 1.77 1.77 1.77 1.77
1.77 1.77 1.77 1.77 1.77 1.77 1.77 1.77 1.77 1.77 1.77 1.77 1.77 1.77
1.77 1.77 1.77 1.77 1.76 1.78 1.78 1.77 1.80 1.78 1.77 1.77 1.77 1.77
1.77 1.77 1.78 1.79 1.78 1.79 1.81 1.80 1.81 1.81 1.78 1.77 1.77 1.77
```

1.77	1.77	1.78	1.80	1.79	1.80	1.78	1.79	1.78	1.75	1.75	1.77	1.77	1.77
1.77	1.77	1.79	1.79	1.80	1.79	1.78	1.78	1.74	1.74	1.76	1.77	1.77	1.77
1.77	1.77	1.76	1.73	1.74	1.71	1.73	1.73	1.74	1.76	1.79	1.79	1.77	1.77
1.77	1.77	1.75	1.75	1.73	1.73	1.74	1.74	1.73	1.76	1.80	1.78	1.77	1.77
1.77	1.77	1.79	1.77	1.78	1.73	1.71	1.73	1.75	1.76	1.78	1.76	1.77	1.77
1.77	1.77	1.79	1.76	1.76	1.75	1.70	1.72	1.75	1.78	1.79	1.76	1.77	1.77
1.77	1.77	1.77	1.76	1.76	1.79	1.76	1.71	1.76	1.77	1.78	1.78	1.77	1.77
1.77	1.77	1.77	1.77	1.77	1.77	1.80	1.79	1.78	1.79	1.78	1.77	1.77	1.77
1.77	1.77	1.77	1.77	1.77	1.77	1.77	1.78	1.78	1.77	1.77	1.77	1.77	1.77
1.77	1.77	1.77	1.77	1.77	1.77	1.77	1.77	1.77	1.77	1.77	1.77	1.77	1.77
1.77	1.77	1.77	1.77	1.77	1.77	1.77	1.77	1.77	1.77	1.77	1.77	1.77	1.77
1.77	1.77	1.77	1.77	1.77	1.78	1.77	1.78	1.78	1.77	1.77	1.77	1.77	1.77
1.77	1.77	1.77	1.81	1.83	1.84	1.79	1.79	1.78	1.78	1.77	1.77	1.77	1.77
1.77	1.77	1.78	1.82	1.82	1.83	1.77	1.78	1.77	1.75	1.77	1.77	1.77	1.77
1.77	1.77	1.78	1.80	1.79	1.78	1.79	1.77	1.74	1.76	1.77	1.77	1.77	1.77
1.77	1.77	1.77	1.78	1.77	1.75	1.75	1.74	1.76	1.77	1.77	1.77	1.77	1.77
1.77	1.77	1.77	1.77	1.73	1.76	1.75	1.74	1.74	1.77	1.79	1.78	1.77	1.77
1.77	1.77	1.77	1.76	1.74	1.75	1.74	1.76	1.74	1.76	1.80	1.77	1.77	1.77
1.77	1.77	1.77	1.76	1.76	1.74	1.71	1.75	1.73	1.74	1.77	1.77	1.77	1.77
1.77	1.77	1.77	1.77	1.76	1.75	1.77	1.71	1.75	1.79	1.78	1.78	1.77	1.77
1.77	1.77	1.77	1.77	1.77	1.77	1.79	1.77	1.75	1.78	1.77	1.77	1.77	1.77
1.77	1.77	1.77	1.77	1.77	1.77	1.77	1.77	1.78	1.77	1.77	1.77	1.77	1.77
1.77	1.77	1.77	1.77	1.77	1.77	1.77	1.77	1.77	1.77	1.77	1.77	1.77	1.77
1.77	1.77	1.77	1.77	1.77	1.77	1.77	1.77	1.77	1.77	1.77	1.77	1.77	1.77
1.77	1.77	1.77	1.77	1.77	1.77	1.77	1.77	1.76	1.76	1.77	1.77	1.77	1.77
1.77	1.77	1.77	1.79	1.79	1.80	1.75	1.74	1.75	1.78	1.77	1.77	1.77	1.77
1.77	1.77	1.77	1.78	1.80	1.76	1.74	1.77	1.76	1.77	1.77	1.77	1.77	1.77
1.77	1.77	1.77	1.78	1.80	1.78	1.78	1.77	1.75	1.77	1.76	1.77	1.77	1.77
1.77	1.77	1.77	1.78	1.78	1.77	1.74	1.73	1.79	1.76	1.75	1.75	1.77	1.77
1.77	1.77	1.77	1.78	1.79	1.78	1.76	1.76	1.77	1.76	1.77	1.78	1.77	1.77
1.77	1.77	1.77	1.77	1.76	1.76	1.78	1.79	1.77	1.76	1.78	1.77	1.77	1.77
1.77	1.77	1.77	1.77	1.76	1.74	1.76	1.79	1.77	1.73	1.76	1.77	1.77	1.77
1.77	1.77	1.77	1.77	1.77	1.75	1.73	1.72	1.74	1.79	1.77	1.77	1.77	1.77
1.77	1.77	1.77	1.77	1.77	1.77	1.77	1.76	1.76	1.79	1.77	1.77	1.77	1.77
1.77	1.77	1.77	1.77	1.77	1.77	1.77	1.77	1.77	1.77	1.77	1.77	1.77	1.77
1.77	1.77	1.77	1.77	1.77	1.77	1.77	1.77	1.77	1.77	1.77	1.77	1.77	1.77
1.77	1.77	1.77	1.77	1.77	1.77	1.77	1.77	1.77	1.77	1.77	1.77	1.77	1.77
1.77	1.77	1.77	1.77	1.77	1.76	1.76	1.77	1.78	1.76	1.77	1.77	1.77	1.77

1.77	1.77	1.77	1.77	1.77	1.76	1.73	1.79	1.80	1.75	1.77	1.77	1.77	1.77
1.77	1.77	1.77	1.77	1.78	1.77	1.76	1.79	1.76	1.77	1.77	1.77	1.77	1.77
1.77	1.77	1.77	1.77	1.77	1.77	1.77	1.77	1.76	1.77	1.77	1.77	1.77	1.77
1.77	1.77	1.77	1.77	1.77	1.77	1.77	1.76	1.76	1.78	1.77	1.76	1.77	1.77
1.77	1.77	1.77	1.77	1.77	1.77	1.77	1.76	1.76	1.77	1.77	1.77	1.77	1.77
1.77	1.77	1.77	1.77	1.77	1.77	1.77	1.77	1.77	1.77	1.76	1.77	1.77	1.77
1.77	1.77	1.77	1.77	1.77	1.77	1.77	1.77	1.77	1.77	1.76	1.76	1.77	1.77
1.77	1.77	1.77	1.77	1.77	1.77	1.77	1.77	1.77	1.77	1.77	1.77	1.77	1.77
1.77	1.77	1.77	1.77	1.77	1.77	1.77	1.77	1.77	1.77	1.77	1.77	1.77	1.77
1.77	1.77	1.77	1.77	1.77	1.77	1.77	1.77	1.77	1.77	1.77	1.77	1.77	1.77
1.77	1.77	1.77	1.77	1.77	1.77	1.77	1.77	1.77	1.77	1.77	1.77	1.77	1.77
1.77	1.77	1.77	1.77	1.77	1.77	1.77	1.77	1.77	1.77	1.77	1.77	1.77	1.77
1.77	1.77	1.77	1.77	1.77	1.77	1.77	1.77	1.77	1.77	1.77	1.77	1.77	1.77
1.77	1.77	1.77	1.77	1.77	1.77	1.77	1.77	1.77	1.77	1.77	1.77	1.77	1.77
1.77	1.77	1.77	1.77	1.77	1.77	1.77	1.77	1.77	1.77	1.77	1.77	1.77	1.77
1.77	1.77	1.77	1.77	1.77	1.77	1.77	1.77	1.77	1.77	1.77	1.77	1.77	1.77
1.77	1.77	1.77	1.77	1.77	1.77	1.77	1.77	1.77	1.77	1.77	1.77	1.77	1.77
1.77	1.77	1.77	1.77	1.77	1.77	1.77	1.77	1.77	1.77	1.77	1.77	1.77	1.77
1.77	1.77	1.77	1.77	1.77	1.77	1.77	1.77	1.77	1.77	1.77	1.77	1.77	1.77
1.77	1.77	1.77	1.77	1.77	1.77	1.77	1.77	1.77	1.77	1.77	1.77	1.77	1.77
1.77	1.77	1.77	1.77	1.77	1.77	1.77	1.77	1.77	1.77	1.77	1.77	1.77	1.77
1.77	1.77	1.77	1.77	1.77	1.77	1.77	1.77	1.77	1.77	1.77	1.77	1.77	1.77
1.77	1.77	1.77	1.77	1.77	1.77	1.77	1.77	1.77	1.77	1.77	1.77	1.77	1.77
1.77	1.77	1.77	1.77	1.77	1.77	1.77	1.77	1.77	1.77	1.77	1.77	1.77	1.77
1.77	1.77	1.77	1.77	1.77	1.77	1.77	1.77	1.77	1.77	1.77	1.77	1.77	1.77
1.77	1.77	1.77	1.77	1.77	1.77	1.77	1.77	1.77	1.77	1.77	1.77	1.77	1.77
1.77	1.77	1.77	1.77	1.77	1.77	1.77	1.77	1.77	1.77	1.77	1.77	1.77	1.77
1.77	1.77	1.77	1.77	1.77	1.77	1.77	1.77	1.77	1.77	1.77	1.77	1.77	1.77
1.77	1.77	1.77	1.77	1.77	1.77	1.77	1.77	1.77	1.77	1.77	1.77	1.77	1.77
1.77	1.77	1.77	1.77	1.77	1.77	1.77	1.77	1.77	1.77	1.77	1.77	1.77	1.77
1.77	1.77	1.77	1.77	1.77	1.77	1.77	1.77	1.77	1.77	1.77	1.77	1.77	1.77
1.77	1.77	1.77	1.77	1.77	1.77	1.77	1.77	1.77	1.77	1.77	1.77	1.77	1.77
1.77	1.77	1.77	1.77	1.77	1.77	1.77	1.77	1.77	1.77	1.77	1.77	1.77	1.77
1.77	1.77	1.77	1.77	1.77	1.77	1.77	1.77	1.77	1.77	1.77	1.77	1.77	1.77
1.77	1.77	1.77	1.77	1.77	1.77	1.77	1.77	1.77	1.77	1.77	1.77	1.77	1.77
1.77	1.77	1.77	1.77	1.77	1.77	1.77	1.77	1.77	1.77	1.77	1.77	1.77	1.77
1.77	1.77	1.77	1.77	1.77	1.77	1.77	1.77	1.77	1.77	1.77	1.77	1.77	1.77

Appendix 5

Final locations of all earthquakes in the 1991 dataset

These are the locations obtained using the final three-dimensional wave-speed models. Asterisks indicate earthquakes used in local earthquake tomography. RMS % change is the percentage change in RMS from the one-dimensional to the three-dimensional model.

Event ID	Date	Time	Latitude (°N)	Longitude (°E)	Depth (km)	Moment mag.	RMS 1d (s)	RMS 3d (s)	RMS % change	
213.135704.1	19910801	13:57:09.309	64.03993	-21.09321	1.520	2.75	0.039	0.029	74	
213.140005.1	19910801	14:00:10.168	64.04016	-21.09303	1.448	2.24	0.050	0.034	68	*
214.014420.1	19910802	01:44:25.505	64.03833	-21.08188	2.634	1.71	0.059	0.063	106	*
214.021238.1	19910802	02:12:42.025	64.12859	-21.35830	4.087	2.72	0.061	0.039	63	*
214.021442.1	19910802	02:14:46.256	64.09283	-21.40293	4.458	2.12	0.064	0.048	75	
214.111029.1	19910802	11:10:32.161	64.09312	-21.40544	4.844	2.49	0.068	0.034	50	
214.112821.1	19910802	11:28:28.436	64.02413	-21.20754	3.360	2.51	0.062	0.046	74	*
215.034956.1	19910803	03:50:00.052	64.09102	-21.40586	4.510	1.99	0.065	0.042	64	
215.035731.1	19910803	03:57:35.686	63.95174	-21.12351	4.637	1.68	0.048	0.024	50	
215.040337.1	19910803	04:03:41.334	63.95226	-21.12183	4.979	1.91	0.057	0.028	49	
215.043301.1	19910803	04:33:05.817	63.95194	-21.12300	5.049	2.06	0.072	0.025	34	
215.064534.1	19910803	06:45:39.724	63.95293	-21.12671	4.806	1.81	0.076	0.037	48	
215.105307.1	19910803	10:53:11.001	63.95135	-21.12614	4.955	1.85	0.075	0.043	57	
215.114014.1	19910803	11:40:22.535	64.03371	-21.09863	0.974	2.16	0.046	0.039	84	*
215.195922.1	19910803	19:59:26.546	64.01273	-21.16592	4.201	2.00	0.044	0.029	65	
216.093016.1	19910804	09:30:20.573	64.09084	-21.40166	4.501	2.16	0.073	0.028	38	*
216.094259.1	19910804	09:43:02.805	64.04653	-21.06954	3.563	2.28	0.055	0.030	54	*
216.113315.1	19910804	11:33:19.447	64.06219	-21.18313	4.386	1.47	0.058	0.038	65	
216.121920.1	19910804	12:19:24.551	64.04566	-21.07669	3.297	1.68	0.054	0.035	64	
216.131014.1	19910804	13:10:34.390	64.02115	-21.36179	5.534	1.47	0.046	0.032	69	
216.131451.1	19910804	13:14:55.486	64.02092	-21.36133	5.554	1.96	0.046	0.033	71	
216.140325.1	19910804	14:03:30.619	64.09109	-21.40433	4.718	2.90	0.071	0.037	52	*
216.143408.1	19910804	14:34:11.935	64.09207	-21.40594	4.721	1.68	0.054	0.036	66	*
216.150008.1	19910804	15:00:11.766	64.02068	-21.36291	5.430	1.23	0.048	0.037	77	
216.150353.1	19910804	15:03:59.247	64.02123	-21.36285	5.562	2.38	0.042	0.036	85	*
216.150619.1	19910804	15:06:51.519	64.02004	-21.36173	5.246	1.10	0.042	0.024	57	
216.152405.1	19910804	15:24:09.329	64.03973	-21.22944	2.939	1.16	0.034	0.037	108	
216.153822.1	19910804	15:39:03.569	64.02249	-21.35925	5.406	1.65	0.052	0.052	100	
216.154114.1	19910804	15:41:18.303	64.02125	-21.36115	5.389	1.33	0.043	0.036	83	
216.154538.1	19910804	15:45:42.281	64.04281	-21.22175	3.664	1.31	0.049	0.048	97	*
216.160817.1	19910804	16:08:41.732	64.02262	-21.35997	5.489	1.41	0.051	0.050	98	
216.162943.1	19910804	16:29:47.370	64.02153	-21.35920	5.402	1.30	0.039	0.040	102	
216.171101.1	19910804	17:11:09.993	64.02099	-21.36114	5.556	1.59	0.042	0.033	78	
216.173855.1	19910804	17:38:58.927	64.02357	-21.35693	5.649	1.21	0.057	0.067	117	
216.175257.1	19910804	17:53:01.472	64.02101	-21.36060	5.414	1.52	0.041	0.028	68	
216.175540.1	19910804	17:55:44.231	64.02185	-21.36042	5.560	1.70	0.045	0.043	95	
216.182203.1	19910804	18:22:07.562	64.02099	-21.36140	5.586	1.22	0.042	0.029	69	
216.183608.1	19910804	18:36:11.629	64.02086	-21.36388	5.421	1.33	0.033	0.023	69	
216.185741.1	19910804	18:57:45.671	64.02176	-21.35945	5.401	1.48	0.039	0.041	105	
216.192101.1	19910804	19:21:21.537	64.05695	-21.16959	4.838	1.58	0.047	0.047	100	*
216.192635.1	19910804	19:26:39.063	64.06013	-21.16223	4.934	1.32	0.053	0.032	60	*
216.201116.1	19910804	20:11:21.715	64.02181	-21.35973	5.328	1.84	0.056	0.065	116	
216.202031.1	19910804	20:20:39.156	64.02124	-21.36202	5.601	1.88	0.043	0.031	72	
216.203555.1	19910804	20:35:58.958	64.02128	-21.36068	5.279	1.51	0.039	0.038	97	
216.210929.1	19910804	21:09:33.618	64.02197	-21.36112	5.349	1.66	0.043	0.033	76	
216.212808.1	19910804	21:28:12.561	64.08976	-21.40438	4.477	1.63	0.060	0.022	36	
216.220947.1	19910804	22:09:55.284	64.08958	-21.39923	4.586	2.46	0.067	0.042	62	*
217.044722.1	19910805	04:47:26.642	63.95041	-21.20003	4.944	1.98	0.052	0.027	51	*
217.045827.1	19910805	04:58:30.697	63.95037	-21.19982	5.086	1.72	0.038	0.035	92	*
217.051802.1	19910805	05:18:13.353	63.95041	-21.19973	4.912	1.99	0.054	0.027	50	*

217.063548.1	19910805	06:35:52.556	64.06213	-21.18672	4.330	1.41	0.043	0.037	86	
217.064047.1	19910805	06:40:50.829	64.09432	-21.39803	4.572	1.66	0.051	0.036	70	
217.064554.1	19910805	06:46:03.403	64.07937	-21.17480	2.809	1.73	0.063	0.046	73	*
217.071058.1	19910805	07:11:04.626	64.03498	-21.21481	4.470	1.45	0.041	0.027	65	*
217.073430.1	19910805	07:34:34.504	64.01392	-21.16084	3.834	1.62	0.045	0.027	60	
217.074710.1	19910805	07:47:14.288	63.95079	-21.20039	4.686	1.34	0.062	0.036	58	*
217.082512.1	19910805	08:25:16.022	63.94941	-21.19749	4.798	1.66	0.068	0.054	79	
217.091851.1	19910805	09:18:55.476	63.95004	-21.20152	4.862	1.88	0.061	0.028	45	*
217.105912.1	19910805	10:59:16.069	63.95122	-21.19960	4.731	1.87	0.069	0.037	53	*
217.161540.1	19910805	16:15:44.133	64.02292	-21.36023	5.379	1.61	0.052	0.041	78	
217.162342.1	19910805	16:23:45.889	64.09019	-21.40754	4.767	1.39	0.061	0.041	67	
217.164959.1	19910805	16:50:03.794	64.11197	-21.26383	4.776	1.61	0.051	0.050	98	*
217.183800.1	19910805	18:38:29.895	64.02252	-21.35860	5.446	2.30	0.053	0.028	52	*
217.211107.1	19910805	21:11:18.543	64.02214	-21.35874	5.555	1.90	0.058	0.050	86	*
217.211547.1	19910805	21:16:05.242	64.02223	-21.35819	5.609	1.74	0.050	0.025	50	
217.215832.1	19910805	21:58:36.645	64.02260	-21.35904	5.910	1.94	0.051	0.046	90	
217.222123.1	19910805	22:21:29.635	64.02220	-21.35747	5.420	2.15	0.046	0.026	56	
217.235139.1	19910805	23:51:46.535	64.02269	-21.36174	5.675	2.92	0.058	0.053	91	
218.002451.1	19910806	00:24:54.798	64.02236	-21.36086	5.406	1.53	0.043	0.031	72	
218.004237.1	19910806	00:42:40.989	64.02352	-21.35685	5.407	1.52	0.042	0.036	85	
218.004345.1	19910806	00:44:18.484	64.02186	-21.36033	5.534	1.75	0.049	0.053	108	
218.012436.1	19910806	01:24:39.764	64.02335	-21.36118	5.680	1.62	0.053	0.035	66	
218.013307.1	19910806	01:33:11.076	64.02400	-21.35889	5.553	1.80	0.042	0.040	95	
218.013404.1	19910806	01:34:27.500	64.02265	-21.35878	5.561	2.27	0.053	0.038	71	*
218.013645.1	19910806	01:36:49.360	64.02384	-21.35799	5.208	1.20	0.058	0.051	87	
218.015236.1	19910806	01:52:40.180	64.02377	-21.35964	5.449	1.34	0.054	0.035	64	
218.023219.1	19910806	02:32:24.565	64.02177	-21.36104	5.465	2.89	0.055	0.039	70	*
218.033837.1	19910806	03:38:44.047	64.02043	-21.36016	5.493	2.99	0.048	0.040	83	*
218.045348.1	19910806	04:53:52.068	64.02309	-21.35996	5.619	1.91	0.061	0.042	68	*
218.045348.2	19910806	04:54:18.735	64.02464	-21.35560	5.688	2.05	0.047	0.036	76	
218.052654.1	19910806	05:27:02.500	64.06221	-21.18859	4.205	1.25	0.021	0.011	52	
218.060540.1	19910806	06:05:44.452	64.02370	-21.36105	5.597	1.55	0.049	0.041	83	
218.061413.1	19910806	06:14:17.027	64.02258	-21.36136	5.472	1.39	0.051	0.027	52	
218.061609.1	19910806	06:16:13.339	64.06376	-21.18073	4.211	1.73	0.055	0.046	83	
218.071003.1	19910806	07:10:10.209	64.02228	-21.35818	5.609	2.01	0.039	0.037	94	
218.075615.1	19910806	07:56:18.784	64.02260	-21.35934	5.254	1.82	0.046	0.030	65	
218.075615.2	19910806	07:56:28.970	64.02130	-21.36241	5.226	1.68	0.048	0.045	93	
218.083857.1	19910806	08:39:00.776	64.02256	-21.35953	5.472	1.78	0.048	0.037	77	
218.124210.1	19910806	12:42:13.880	64.09474	-21.40295	5.067	1.79	0.068	0.050	73	*
218.155338.1	19910806	15:53:42.963	64.06266	-21.18512	4.279	1.72	0.042	0.037	88	
218.155338.2	19910806	15:54:02.235	64.06175	-21.18681	4.376	1.52	0.044	0.059	134	
218.185421.1	19910806	18:54:24.754	63.94659	-21.32824	5.887	2.08	0.065	0.043	66	*
218.192914.1	19910806	19:29:18.563	64.04211	-21.22816	2.943	1.41	0.068	0.039	57	
219.001831.1	19910807	00:18:35.428	64.02097	-21.35827	5.712	2.35	0.056	0.043	76	*
219.174544.1	19910807	17:45:48.497	64.09355	-21.40666	4.618	1.83	0.059	0.042	71	
219.233643.1	19910807	23:37:08.048	64.09229	-21.40130	4.548	1.75	0.057	0.024	42	
220.030040.1	19910808	03:00:44.379	64.09364	-21.40026	4.761	2.44	0.054	0.043	79	*
220.180022.1	19910808	18:00:39.300	63.96732	-21.14717	4.783	1.80	0.081	0.030	37	*
220.220926.1	19910808	22:09:30.580	64.06519	-21.17663	4.822	1.74	0.065	0.048	73	*
220.235442.1	19910808	23:54:47.163	64.04853	-21.23925	3.138	2.10	0.089	0.067	75	
221.005503.1	19910809	00:55:07.141	64.09114	-21.40612	4.717	1.82	0.069	0.038	55	*
221.013539.1	19910809	01:35:42.756	64.09225	-21.40504	4.842	1.27	0.063	0.041	65	
221.044257.1	19910809	04:43:02.914	64.10436	-21.33454	3.465	1.94	0.074	0.059	79	*
221.124712.1	19910809	12:47:16.138	64.11852	-21.34443	4.521	1.63	0.061	0.030	49	*
221.143416.1	19910809	14:34:20.103	64.10961	-21.26182	4.645	1.95	0.068	0.037	54	*
222.034524.1	19910810	03:45:28.017	64.01559	-21.16236	3.749	1.66	0.061	0.048	78	*
222.034641.1	19910810	03:46:45.166	64.01544	-21.16157	3.943	1.71	0.061	0.040	65	
222.061835.1	19910810	06:18:39.547	64.09233	-21.39947	4.500	1.65	0.064	0.039	60	
222.065254.1	19910810	06:52:58.611	64.02441	-21.20787	3.544	1.56	0.041	0.034	82	
222.084928.1	19910810	08:49:32.699	64.02401	-21.20921	3.614	1.84	0.030	0.023	76	
222.090932.1	19910810	09:09:36.177	64.09165	-21.40165	4.538	1.50	0.051	0.035	68	*
222.112829.1	19910810	11:28:32.926	63.97038	-21.20726	3.664	1.43	0.045	0.027	60	
222.174659.1	19910810	17:47:02.993	63.96998	-21.21057	3.308	2.20	0.068	0.046	67	*
223.021151.1	19910811	02:12:24.041	63.93992	-21.32340	5.903	2.11	0.058	0.042	72	
223.023247.1	19910811	02:32:50.597	63.94509	-21.32972	5.568	2.05	0.054	0.035	64	*
223.212321.1	19910811	21:23:25.478	64.02523	-21.20460	4.545	1.97	0.045	0.046	102	*
224.001618.1	19910812	00:16:21.833	63.96313	-21.15166	5.198	1.90	0.068	0.040	58	

224.001618.2	19910812	00:16:46.137	63.96428	-21.14932	5.391	1.55	0.054	0.056	103	
224.002737.1	19910812	00:27:40.927	63.96293	-21.15030	5.480	1.76	0.053	0.035	66	
224.023135.1	19910812	02:31:39.373	64.10867	-21.26651	4.607	1.61	0.057	0.039	68	*
224.030922.1	19910812	03:09:38.455	64.01086	-21.30094	3.138	1.48	0.057	0.045	78	*
224.081139.1	19910812	08:11:43.477	64.04938	-21.24133	3.124	1.47	0.033	0.024	72	
224.090528.1	19910812	09:05:36.725	64.03184	-21.20768	4.386	2.12	0.050	0.048	95	
224.092054.1	19910812	09:20:58.547	64.03170	-21.21003	4.260	1.73	0.047	0.059	125	
224.173023.1	19910812	17:30:31.348	64.04196	-21.22505	3.028	1.34	0.065	0.046	70	*
224.184254.1	19910812	18:43:01.354	64.02097	-21.20566	3.498	1.89	0.042	0.033	78	*
224.184649.1	19910812	18:46:53.417	64.09371	-21.39997	4.815	2.07	0.060	0.032	53	*
224.195524.1	19910812	19:55:28.549	64.10933	-21.26618	4.755	1.58	0.061	0.048	78	*
224.214956.1	19910812	21:50:00.226	64.03056	-21.21141	4.197	1.39	0.044	0.049	111	
224.223635.1	19910812	22:36:39.790	64.02084	-21.20878	3.617	2.14	0.070	0.052	74	*
224.224238.1	19910812	22:42:46.076	64.03128	-21.21302	4.214	1.49	0.041	0.037	90	
224.224403.1	19910812	22:44:33.870	64.03078	-21.21104	4.188	1.58	0.049	0.039	79	
224.224524.1	19910812	22:45:41.005	64.03106	-21.21134	4.297	1.37	0.047	0.055	117	
225.010319.1	19910813	01:03:23.710	64.02224	-21.20637	3.453	1.82	0.042	0.034	80	*
225.080422.1	19910813	08:04:27.211	64.03103	-21.19029	2.726	1.51	0.051	0.041	80	*
225.083219.1	19910813	08:32:23.949	64.03033	-21.21001	4.423	2.50	0.050	0.045	90	*
225.090227.1	19910813	09:02:35.421	64.03162	-21.20898	4.374	2.32	0.054	0.047	87	
225.094416.1	19910813	09:44:47.081	64.03024	-21.21049	4.290	1.75	0.050	0.044	87	
225.100307.1	19910813	10:03:11.981	64.03140	-21.20773	4.259	1.53	0.045	0.057	126	
225.122104.1	19910813	12:21:08.928	64.03082	-21.20945	4.252	1.98	0.050	0.050	100	
225.122759.1	19910813	12:28:04.942	64.03033	-21.21068	4.281	2.07	0.053	0.049	92	
225.122941.1	19910813	12:29:45.971	64.03191	-21.20735	4.400	1.67	0.039	0.047	120	
225.123131.1	19910813	12:32:07.556	64.03234	-21.20589	4.380	1.50	0.053	0.058	109	
225.123340.1	19910813	12:33:44.517	64.03123	-21.20880	4.481	1.57	0.063	0.053	84	
225.155354.1	19910813	15:54:02.504	64.06859	-21.14306	2.340	1.37	0.048	0.057	118	*
225.155659.1	19910813	15:57:32.061	64.06918	-21.14303	2.655	1.78	0.051	0.048	94	*
225.162551.1	19910813	16:25:55.041	64.10013	-21.34190	3.910	1.78	0.050	0.050	100	*
226.020942.1	19910814	02:09:46.525	64.03147	-21.20739	4.346	1.85	0.050	0.047	94	*
226.050551.1	19910814	05:05:56.044	64.04979	-21.23943	3.003	1.22	0.042	0.030	71	
226.091801.1	19910814	09:18:06.728	64.03240	-21.20717	4.839	2.27	0.034	0.031	91	*
226.091934.2	19910814	09:19:38.757	63.96983	-21.20612	3.869	3.93	0.043	0.038	88	*
226.092238.1	19910814	09:22:41.956	63.97049	-21.20751	3.868	2.03	0.046	0.019	41	
226.092337.1	19910814	09:23:44.605	63.97075	-21.20741	3.772	3.05	0.048	0.031	64	*
226.092757.1	19910814	09:28:01.205	63.96856	-21.20795	3.684	2.87	0.071	0.049	69	*
226.094230.1	19910814	09:42:33.780	63.96947	-21.20671	3.901	2.66	0.067	0.051	76	
226.101820.1	19910814	10:18:38.714	63.94090	-21.39249	4.929	3.47	0.065	0.042	64	
226.102000.1	19910814	10:20:06.187	63.96731	-21.20359	4.028	1.79	0.054	0.026	48	*
226.102347.1	19910814	10:23:53.654	63.94039	-21.39227	5.667	2.57	0.072	0.057	79	
226.110713.1	19910814	11:07:17.870	64.03081	-21.20917	4.509	1.73	0.041	0.042	102	*
226.151111.1	19910814	15:11:15.395	64.04905	-21.23740	3.097	2.57	0.084	0.056	66	
226.152708.1	19910814	15:27:12.247	64.09378	-21.40067	4.757	3.05	0.070	0.041	58	*
226.153852.1	19910814	15:38:56.495	64.04960	-21.23765	3.231	2.26	0.053	0.044	83	
226.164235.1	19910814	16:42:42.590	64.05028	-21.23397	3.128	1.53	0.031	0.020	64	*
226.181726.1	19910814	18:17:28.574	63.94239	-21.39072	5.598	2.47	0.050	0.053	105	
226.181726.2	19910814	18:17:53.334	63.94135	-21.39330	5.551	3.28	0.059	0.058	98	
226.184429.2	19910814	18:45:20.908	63.93850	-21.39269	5.235	2.40	0.079	0.043	54	*
226.194833.1	19910814	19:48:37.354	63.94373	-21.39245	5.081	2.38	0.088	0.053	60	*
226.214521.1	19910814	21:45:33.623	64.09273	-21.39747	4.562	1.72	0.055	0.031	56	
226.215442.1	19910814	21:54:46.829	64.09281	-21.40022	4.548	1.74	0.060	0.035	58	*
226.224124.1	19910814	22:41:31.695	64.09371	-21.39955	4.605	1.77	0.072	0.035	48	
227.090438.1	19910815	09:04:42.861	64.04645	-21.24166	2.944	1.15	0.055	0.037	67	
227.092421.1	19910815	09:24:25.348	64.04638	-21.24446	2.847	2.10	0.064	0.040	62	*
227.092526.1	19910815	09:25:34.872	64.04652	-21.24423	2.795	1.74	0.063	0.037	58	*
227.101813.1	19910815	10:18:17.733	64.04677	-21.24310	2.999	0.99	0.066	0.054	81	
227.102909.1	19910815	10:29:13.405	63.98205	-21.15785	3.162	1.46	0.094	0.050	53	*
227.110113.1	19910815	11:01:21.310	64.04717	-21.24677	2.777	1.47	0.071	0.056	78	
227.124405.1	19910815	12:44:09.317	63.97030	-21.21032	3.861	1.95	0.075	0.056	74	*
227.153210.1	19910815	15:32:15.303	64.02875	-21.19784	2.080	1.27	0.055	0.044	79	*
227.160700.1	19910815	16:07:04.523	64.04632	-21.24431	2.806	1.01	0.057	0.040	70	
227.225348.1	19910815	22:53:52.311	63.97039	-21.21236	3.468	1.91	0.080	0.036	44	*
228.005221.1	19910816	00:52:25.021	64.12052	-21.37247	4.922	1.70	0.083	0.043	51	*
228.040122.1	19910816	04:01:26.157	64.06046	-21.18470	4.203	1.66	0.054	0.041	75	
228.045401.1	19910816	04:54:05.254	64.06140	-21.18233	4.155	1.89	0.057	0.047	82	*
228.083300.1	19910816	08:33:04.118	64.06011	-21.18498	4.273	1.85	0.051	0.045	88	

228.130907.1	19910816	13:09:11.833	64.02913	-21.21459	4.267	1.40	0.043	0.036	83	
228.161423.1	19910816	16:14:28.076	64.04833	-21.23679	3.092	1.51	0.057	0.038	66	
228.161559.1	19910816	16:16:03.222	63.98227	-21.15725	3.130	1.73	0.077	0.040	51	*
229.020112.1	19910817	02:01:17.089	64.02980	-21.20218	2.191	1.00	0.054	0.051	94	*
229.033558.1	19910817	03:36:04.510	64.04132	-21.22785	2.982	1.26	0.049	0.037	75	*
229.091643.1	19910817	09:16:46.308	63.94931	-21.19416	5.102	1.78	0.057	0.045	78	
229.114512.1	19910817	11:45:20.569	64.04060	-21.20741	2.342	1.63	0.056	0.043	76	*
229.164834.1	19910817	16:48:39.778	63.97689	-21.20568	2.920	1.86	0.057	0.050	87	
231.021134.1	19910819	02:11:38.572	64.11893	-21.34643	3.419	1.99	0.067	0.041	61	
231.024536.1	19910819	02:45:40.989	64.11810	-21.34713	3.426	2.18	0.062	0.048	77	
231.024848.1	19910819	02:48:52.728	64.11835	-21.34671	3.756	1.61	0.067	0.036	53	
231.033320.1	19910819	03:33:45.799	64.11823	-21.35096	3.553	1.35	0.087	0.061	70	*
231.161335.1	19910819	16:13:39.518	64.02049	-21.19692	3.690	2.40	0.068	0.051	74	*
231.175629.1	19910819	17:56:31.406	63.95913	-21.09095	7.340	1.58	0.063	0.040	63	
232.060242.1	19910820	06:02:45.804	63.96168	-21.13776	4.801	2.30	0.067	0.044	65	*
232.065422.1	19910820	06:54:27.045	64.05581	-21.41660	3.716	1.75	0.083	0.056	67	*
232.194924.1	19910820	19:49:28.428	64.10809	-21.26333	5.174	2.44	0.062	0.047	75	*
232.212153.1	19910820	21:21:57.265	63.94225	-21.36275	5.830	2.05	0.055	0.104	189	
233.000123.1	19910821	00:01:26.888	63.93974	-21.36319	5.329	2.57	0.062	0.065	104	
233.155423.1	19910821	15:54:27.423	64.10742	-21.26674	4.546	2.14	0.069	0.044	63	*
234.000219.1	19910822	00:02:22.974	64.02667	-21.21724	3.702	1.44	0.070	0.059	84	*
234.044134.1	19910822	04:41:38.856	64.03107	-21.08409	2.515	1.80	0.057	0.047	82	*
234.080105.1	19910822	08:01:09.772	64.07628	-21.31042	4.399	1.80	0.065	0.034	52	*
234.080802.1	19910822	08:08:09.386	64.02573	-21.20441	3.898	1.76	0.075	0.051	68	
234.080946.1	19910822	08:09:50.754	64.02469	-21.20668	3.931	1.98	0.070	0.049	70	*
234.145308.1	19910822	14:53:11.556	63.95549	-21.14769	3.891	1.87	0.074	0.044	59	
234.162014.1	19910822	16:20:18.060	64.02554	-21.20620	3.832	1.69	0.048	0.042	87	
234.175608.1	19910822	17:56:11.816	63.96530	-21.13915	3.864	3.24	0.065	0.030	46	
234.183633.1	19910822	18:36:37.209	64.02460	-21.20546	3.897	2.24	0.072	0.047	65	*
234.185418.1	19910822	18:54:22.822	64.02388	-21.20702	3.864	1.88	0.054	0.058	107	
234.200003.1	19910822	20:00:40.852	64.02356	-21.20594	3.977	1.70	0.047	0.056	119	
234.235406.1	19910822	23:54:09.318	63.96480	-21.13721	4.208	2.25	0.074	0.039	52	*
235.000145.1	19910823	00:01:48.545	63.96566	-21.13656	3.819	1.87	0.065	0.036	55	*
235.000252.1	19910823	00:02:55.327	63.96326	-21.13458	4.072	3.50	0.071	0.025	35	*
235.000406.1	19910823	00:04:10.053	63.96311	-21.13672	3.967	2.95	0.075	0.031	41	*
235.012515.1	19910823	01:25:18.674	63.96402	-21.13569	4.125	2.27	0.081	0.043	53	*
235.051015.1	19910823	05:10:20.871	64.08773	-21.40919	4.303	1.31	0.048	0.034	70	*
235.052620.1	19910823	05:26:24.341	64.02573	-21.50008	4.880	2.03	0.078	0.058	74	*
235.061603.1	19910823	06:16:07.469	64.02355	-21.20680	4.100	0.98	0.057	0.031	54	
235.072640.1	19910823	07:26:43.333	63.95503	-21.14420	3.573	2.51	0.077	0.055	71	
235.133432.1	19910823	13:34:36.346	64.04838	-21.20267	3.585	1.38	0.050	0.046	91	*
235.184657.1	19910823	18:47:01.170	64.07201	-21.27428	3.830	1.43	0.066	0.041	62	*
236.004548.1	19910824	00:45:52.201	64.04430	-21.21890	3.082	1.09	0.055	0.052	94	*
236.044438.1	19910824	04:44:42.214	64.11316	-21.34000	3.209	1.73	0.063	0.029	46	
236.052400.1	19910824	05:24:05.920	64.02418	-21.21949	3.864	1.34	0.062	0.068	109	*
236.065252.1	19910824	06:52:57.304	64.02456	-21.22075	4.163	1.62	0.063	0.055	87	*
236.084121.1	19910824	08:41:25.528	64.01330	-21.16596	3.936	1.45	0.052	0.049	94	
236.181427.1	19910824	18:14:33.811	64.05649	-21.27017	2.815	1.88	0.044	0.039	88	*
237.032913.1	19910825	03:29:16.909	63.95336	-21.13902	4.948	1.99	0.108	0.040	37	
237.212559.1	19910825	21:26:03.005	64.11134	-21.26241	4.972	2.60	0.077	0.053	68	*
238.153812.1	19910826	15:38:15.841	64.09326	-21.39729	4.418	1.64	0.047	0.045	95	
239.160308.1	19910827	16:03:12.147	64.02432	-21.20628	4.137	2.68	0.062	0.041	66	
239.160508.1	19910827	16:05:12.751	64.02220	-21.20431	3.898	1.52	0.042	0.034	80	
239.184436.1	19910827	18:44:40.240	64.02444	-21.20739	4.027	1.87	0.051	0.044	86	
240.023038.1	19910828	02:30:42.185	64.02216	-21.08256	3.136	1.96	0.063	0.068	107	*
240.035151.1	19910828	03:51:56.054	64.02118	-21.08450	3.492	1.62	0.070	0.052	74	*
240.040141.1	19910828	04:01:45.902	64.02121	-21.08746	3.065	1.84	0.071	0.047	66	*
240.123425.1	19910828	12:34:29.678	64.02571	-21.20870	3.603	1.66	0.054	0.049	90	*
240.162821.1	19910828	16:28:25.273	64.02576	-21.23729	4.694	2.68	0.051	0.045	88	*
240.163545.1	19910828	16:35:49.275	64.02677	-21.23626	4.794	1.53	0.046	0.033	71	*
240.164059.1	19910828	16:41:03.414	64.02640	-21.23829	4.652	1.65	0.046	0.046	100	
240.175808.1	19910828	17:58:12.597	64.02508	-21.23796	4.668	1.71	0.045	0.044	97	*
241.045841.1	19910829	04:58:45.367	64.06831	-21.39113	2.573	1.89	0.092	0.041	44	*
241.101356.1	19910829	10:14:00.801	64.07330	-21.09956	2.948	1.55	0.057	0.078	136	*
241.105349.1	19910829	10:53:54.012	64.02558	-21.21232	4.174	1.69	0.066	0.046	69	*
242.211758.1	19910830	21:18:02.397	64.02820	-21.20246	2.528	1.91	0.057	0.048	84	*
243.031423.1	19910831	03:14:27.059	63.97925	-21.24086	4.714	2.84	0.054	0.055	101	*

243.111448.1	19910831	11:15:01.345	63.94856	-21.16752	5.691	2.12	0.066	0.050	75	
243.200853.1	19910831	20:08:57.595	64.03428	-21.22252	4.203	2.46	0.053	0.038	71	*
243.220553.1	19910831	22:06:02.337	64.04998	-21.23880	2.833	1.59	0.065	0.055	84	
244.084134.1	19910901	08:42:05.008	64.07405	-21.10226	2.848	1.92	0.067	0.064	95	*
244.084320.1	19910901	08:43:24.479	64.07701	-21.09762	3.098	1.64	0.057	0.069	121	*
244.084320.2	19910901	08:43:59.504	64.07740	-21.09944	2.907	1.43	0.076	0.065	85	*
247.175137.1	19910904	17:51:41.845	64.04955	-21.24226	3.208	1.71	0.037	0.029	78	
247.194058.1	19910904	19:41:01.413	63.94770	-21.22742	5.208	2.67	0.073	0.037	50	
247.201129.1	19910904	20:11:33.988	64.05236	-21.23517	2.118	1.44	0.052	0.045	86	*
248.070102.1	19910905	07:01:06.153	64.07737	-21.20026	3.056	2.07	0.064	0.057	89	*
248.132711.1	19910905	13:27:17.788	63.94101	-21.37612	5.602	2.14	0.088	0.045	51	*
248.184238.1	19910905	18:42:41.594	63.94756	-21.23045	5.162	1.60	0.070	0.034	48	
248.201303.1	19910905	20:13:07.733	64.11849	-21.23769	3.248	1.61	0.066	0.049	74	*
248.213616.1	19910905	21:36:21.132	64.11872	-21.23929	3.616	2.25	0.067	0.058	86	*
248.221755.1	19910905	22:17:59.372	64.02101	-21.20197	3.500	1.48	0.038	0.045	118	
248.235930.1	19910905	23:59:47.546	64.03003	-21.07785	3.242	2.06	0.077	0.057	74	*
249.005716.1	19910906	00:57:24.909	64.03025	-21.07494	3.301	2.18	0.074	0.043	58	*
249.044603.1	19910906	04:46:14.137	63.94252	-21.36385	5.952	1.71	0.058	0.052	89	*
249.091021.1	19910906	09:10:25.686	64.02510	-21.20818	4.086	1.34	0.040	0.037	92	*
249.233356.1	19910906	23:34:00.312	64.10160	-21.34239	3.768	1.50	0.061	0.049	80	*
250.194938.1	19910907	19:49:42.804	64.11800	-21.34898	3.666	1.35	0.067	0.039	58	
251.062003.1	19910908	06:20:07.916	64.11331	-21.33721	2.758	2.09	0.069	0.052	75	*
251.065913.1	19910908	06:59:17.920	64.11282	-21.33867	2.628	2.36	0.074	0.049	66	
251.071421.1	19910908	07:14:24.612	64.09320	-21.39980	4.498	1.88	0.064	0.041	64	
251.142913.1	19910908	14:29:18.171	64.03385	-21.09297	1.671	1.75	0.059	0.052	88	*
251.222614.1	19910908	22:26:18.917	64.11830	-21.24550	3.355	1.65	0.060	0.059	98	*
252.000816.1	19910909	00:08:20.692	64.02960	-21.07604	2.816	1.57	0.068	0.062	91	*
252.022807.1	19910909	02:28:11.663	64.04528	-21.20777	3.693	1.45	0.061	0.049	80	*
252.023347.1	19910909	02:33:51.795	64.04502	-21.20732	3.651	2.11	0.055	0.035	63	*
252.023757.1	19910909	02:38:01.981	64.04511	-21.20650	3.579	1.31	0.059	0.049	83	*
252.023939.1	19910909	02:39:43.682	64.04475	-21.20611	3.690	1.47	0.061	0.052	85	
252.042758.1	19910909	04:28:02.801	64.04550	-21.20504	3.506	1.36	0.053	0.037	69	*
252.044910.1	19910909	04:49:14.415	64.04590	-21.20716	3.706	1.89	0.057	0.037	64	*
252.050156.1	19910909	05:01:59.799	64.03989	-21.35228	5.674	2.41	0.054	0.039	72	*
252.055539.1	19910909	05:55:42.166	63.94048	-21.27912	4.475	2.03	0.081	0.035	43	
252.112006.1	19910909	11:20:10.264	64.04516	-21.20577	3.725	1.70	0.061	0.039	63	
252.123416.1	19910909	12:34:22.718	64.04561	-21.20638	3.771	1.81	0.049	0.038	77	*
253.081710.1	19910910	08:17:14.269	63.96247	-21.15211	5.007	1.69	0.059	0.038	64	
253.125604.1	19910910	12:56:08.394	64.03958	-21.15751	3.058	1.61	0.068	0.035	51	*
253.154935.1	19910910	15:49:39.432	64.05143	-21.24460	2.779	1.16	0.049	0.032	65	*
254.002100.1	19910911	00:21:07.155	64.02035	-21.20610	3.336	1.46	0.041	0.052	126	
254.013017.1	19910911	01:30:21.723	64.01995	-21.23568	5.070	1.50	0.055	0.037	67	*
254.035422.1	19910911	03:54:26.713	64.01973	-21.21464	2.652	1.37	0.053	0.045	84	*
254.042635.1	19910911	04:26:39.539	64.01891	-21.21333	2.710	0.87	0.047	0.038	80	*
254.085520.1	19910911	08:55:24.726	64.03834	-21.09603	1.045	1.69	0.065	0.058	89	*
254.142300.1	19910911	14:23:08.138	64.06897	-21.20662	4.784	1.69	0.045	0.030	66	*
254.142448.1	19910911	14:24:52.555	64.06914	-21.20648	4.771	2.07	0.064	0.062	96	*
254.164629.1	19910911	16:46:34.310	64.05226	-21.21285	1.854	2.21	0.048	0.039	81	*
255.020844.1	19910912	02:08:48.389	63.93524	-21.38858	5.261	2.09	0.094	0.048	51	
255.021714.1	19910912	02:17:18.012	64.10647	-21.26760	4.959	1.56	0.072	0.047	65	*
255.022343.1	19910912	02:23:50.481	64.12830	-21.35658	4.132	1.66	0.072	0.050	69	*
255.022343.2	19910912	02:24:16.745	64.12726	-21.35605	4.207	1.47	0.061	0.047	77	*
255.022902.1	19910912	02:29:05.813	64.12908	-21.35681	4.221	1.42	0.074	0.056	75	
255.070414.1	19910912	07:04:45.595	64.12729	-21.35677	4.033	1.72	0.069	0.074	107	*
255.081047.1	19910912	08:10:51.173	64.07733	-21.20232	2.826	1.28	0.059	0.058	98	*
255.173510.1	19910912	17:35:15.075	64.02026	-21.21061	3.640	1.68	0.050	0.043	85	*
256.132153.1	19910913	13:21:56.698	63.94003	-21.34838	6.452	2.03	0.075	0.050	66	*
256.142900.1	19910913	14:29:03.772	63.94229	-21.34902	6.272	2.54	0.069	0.047	68	*
256.153512.1	19910913	15:35:17.090	64.03071	-21.26317	2.988	1.98	0.058	0.034	58	
256.153903.1	19910913	15:39:09.223	63.94303	-21.34909	6.225	1.62	0.074	0.050	67	*
256.193716.1	19910913	19:37:20.480	64.03190	-21.21257	4.189	1.32	0.052	0.043	82	
256.193838.1	19910913	19:38:42.740	64.02313	-21.20752	3.756	1.40	0.049	0.036	73	
256.235841.1	19910913	23:58:45.334	64.06209	-21.18964	4.276	1.73	0.069	0.066	95	*
257.053050.1	19910914	05:30:53.384	63.94746	-21.22588	5.038	1.80	0.091	0.044	48	*
257.073459.1	19910914	07:35:03.524	64.01161	-21.16479	3.826	1.95	0.050	0.046	91	*
257.115537.1	19910914	11:55:40.669	63.94768	-21.22574	4.922	1.78	0.073	0.045	61	*
257.181759.1	19910914	18:18:03.006	64.02579	-21.20460	4.213	1.31	0.057	0.065	114	*

258.045435.1	19910915	04:54:39.315	64.08897	-21.44971	5.605	1.67	0.072	0.050	69	*
258.074123.1	19910915	07:41:27.793	64.03103	-21.21364	4.151	1.69	0.052	0.037	71	*
258.090235.1	19910915	09:02:40.168	64.02852	-21.20648	2.440	1.58	0.069	0.056	81	*
258.194632.1	19910915	19:46:34.833	63.95517	-21.22188	5.569	1.80	0.075	0.050	66	*
259.092326.1	19910916	09:23:30.708	64.02496	-21.20831	4.038	1.15	0.051	0.038	74	*
259.185954.1	19910916	18:59:59.153	64.06902	-21.17960	0.000	0.00	0.051	0.045	88	
260.031627.1	19910917	03:16:31.646	64.10953	-21.26085	4.974	1.46	0.071	0.043	60	*
262.010718.1	19910919	01:07:22.257	64.11327	-21.25463	4.008	1.66	0.064	0.036	56	*
262.082558.1	19910919	08:26:03.563	64.06670	-21.28029	3.459	1.34	0.056	0.056	100	*
262.131325.1	19910919	13:13:28.625	63.95088	-21.26109	6.038	2.19	0.082	0.074	90	*
262.140501.1	19910919	14:05:05.668	64.05564	-21.26653	3.259	1.28	0.058	0.042	72	*
262.150950.1	19910919	15:09:53.610	63.96585	-21.21244	3.932	2.22	0.092	0.051	55	*
262.195845.1	19910919	19:58:49.606	64.05891	-21.18136	4.440	1.47	0.053	0.041	77	*
263.034255.1	19910920	03:42:59.620	64.02673	-21.21507	2.534	1.39	0.050	0.042	84	*
263.034901.1	19910920	03:49:06.130	64.02688	-21.21402	2.232	1.49	0.057	0.045	78	*
263.224542.1	19910920	22:45:45.846	63.96762	-21.21222	3.947	1.55	0.079	0.041	51	*
264.040805.1	19910921	04:08:09.303	64.11551	-21.21663	5.229	1.69	0.070	0.044	62	*
264.053355.1	19910921	05:33:59.059	64.02167	-21.17144	3.484	1.72	0.058	0.054	93	
264.061649.1	19910921	06:16:53.352	64.11535	-21.21730	5.207	1.39	0.071	0.068	95	*
264.062738.1	19910921	06:27:42.590	64.11508	-21.21749	5.385	1.70	0.051	0.049	96	*
264.193202.1	19910921	19:32:06.080	64.02145	-21.17028	3.426	1.51	0.054	0.037	68	
264.212351.1	19910921	21:23:55.162	64.02170	-21.17070	3.475	2.05	0.053	0.050	94	*
264.234218.1	19910921	23:42:22.386	64.04895	-21.23706	3.146	1.92	0.063	0.036	57	*
265.010522.1	19910922	01:05:26.563	64.04957	-21.27792	4.371	1.28	0.061	0.036	59	*
265.015821.1	19910922	01:58:25.065	63.94819	-21.19561	5.224	2.21	0.068	0.039	57	*
265.030152.1	19910922	03:01:56.876	64.02324	-21.17096	3.250	1.65	0.052	0.046	88	*
265.040149.1	19910922	04:01:53.358	64.02199	-21.17104	3.513	1.63	0.052	0.036	69	
265.144919.1	19910922	14:49:23.502	64.05023	-21.27618	4.338	1.16	0.050	0.026	52	*
265.152747.1	19910922	15:27:51.060	64.04855	-21.19682	3.628	1.47	0.042	0.031	73	*
265.175521.1	19910922	17:55:28.498	64.06265	-21.21973	4.108	0.72	0.056	0.046	82	*
265.191813.1	19910922	19:18:18.090	64.04385	-21.23726	3.694	1.44	0.055	0.037	67	
265.195449.1	19910922	19:54:53.647	64.04343	-21.23680	3.712	1.55	0.067	0.051	76	*
265.201436.1	19910922	20:14:41.032	64.04403	-21.23718	3.780	1.57	0.056	0.043	76	*
265.201436.2	19910922	20:14:58.135	64.04379	-21.23655	3.704	1.56	0.060	0.041	68	
266.010343.1	19910923	01:03:47.144	64.02208	-21.17091	3.128	1.13	0.053	0.052	98	
266.015723.1	19910923	01:57:28.576	64.04502	-21.06142	3.410	1.33	0.075	0.059	78	*
266.053912.1	19910923	05:39:16.378	64.04997	-21.23792	3.195	1.02	0.047	0.041	87	*
266.071753.1	19910923	07:17:57.840	64.09090	-21.40080	4.549	1.89	0.071	0.036	50	*
267.001816.1	19910924	00:18:20.804	64.04834	-21.14888	4.019	1.52	0.062	0.048	77	*
267.002034.1	19910924	00:20:38.400	64.04494	-21.25807	4.203	1.47	0.059	0.042	71	*
267.002150.1	19910924	00:21:54.418	64.04528	-21.25986	4.304	1.48	0.058	0.050	86	*
267.155158.1	19910924	15:52:10.495	63.94633	-21.32608	5.117	2.51	0.067	0.059	88	*
267.180852.1	19910924	18:08:56.181	64.07271	-21.15957	5.357	1.84	0.064	0.045	70	*
268.035239.1	19910925	03:52:43.798	64.05959	-21.17672	4.479	1.80	0.045	0.039	86	*
269.020627.1	19910926	02:06:31.445	64.11746	-21.34472	4.562	1.59	0.059	0.038	64	
269.104101.1	19910926	10:41:04.993	63.95092	-21.19811	5.017	2.55	0.066	0.047	71	*
269.105022.1	19910926	10:50:26.572	63.95017	-21.19745	5.266	1.89	0.069	0.042	60	*
269.122923.1	19910926	12:29:27.459	64.06791	-21.44431	5.648	1.47	0.077	0.037	48	*
269.130955.1	19910926	13:10:02.763	63.95088	-21.19749	5.060	1.72	0.069	0.037	53	
269.163734.1	19910926	16:37:38.456	64.05850	-21.16711	4.907	1.34	0.062	0.037	59	*
269.172924.1	19910926	17:29:27.735	63.94498	-21.30772	5.006	1.76	0.060	0.061	101	*
269.192321.1	19910926	19:23:25.748	64.05821	-21.16685	4.826	1.97	0.065	0.048	73	*
270.035436.1	19910927	03:54:40.881	64.07450	-21.20373	3.410	1.30	0.053	0.057	107	*
270.035546.1	19910927	03:55:50.032	64.07575	-21.20356	3.147	1.29	0.042	0.033	78	
270.070534.1	19910927	07:05:37.381	63.94481	-21.22980	4.972	1.83	0.081	0.045	55	*
270.073340.1	19910927	07:33:44.284	64.04343	-21.25948	4.355	1.30	0.053	0.048	90	*
270.073340.2	19910927	07:33:54.893	64.04416	-21.26083	4.565	1.20	0.054	0.056	103	*
271.012220.1	19910928	01:22:24.747	64.05583	-21.26952	2.772	1.18	0.043	0.030	69	
271.043037.1	19910928	04:30:41.116	64.11627	-21.34328	4.662	2.72	0.080	0.093	116	*
271.043438.1	19910928	04:35:08.820	64.11683	-21.34589	4.274	2.06	0.070	0.048	68	*
271.043816.1	19910928	04:38:24.868	64.11638	-21.34713	4.530	2.31	0.076	0.042	55	*
271.043925.1	19910928	04:39:29.862	64.11680	-21.34523	4.600	1.41	0.055	0.032	58	
271.044019.1	19910928	04:41:00.503	64.11600	-21.34565	4.348	2.20	0.073	0.044	60	
271.044200.1	19910928	04:42:04.459	64.11785	-21.34141	4.493	1.83	0.063	0.041	65	*
271.044240.1	19910928	04:42:44.463	64.11806	-21.34403	4.446	1.44	0.059	0.039	66	
271.044724.1	19910928	04:47:27.968	64.11821	-21.34539	4.407	1.30	0.062	0.044	70	
271.045756.1	19910928	04:58:00.433	64.11808	-21.34446	4.444	1.45	0.057	0.037	64	

271.050818.1	19910928	05:08:22.399	64.11564	-21.34345	4.540	2.31	0.076	0.051	67	*
271.051311.1	19910928	05:13:16.355	64.11709	-21.34233	4.391	1.67	0.057	0.029	50	
271.051909.1	19910928	05:19:13.214	64.11713	-21.34688	4.356	2.57	0.069	0.051	93	
271.052021.1	19910928	05:20:25.624	64.11767	-21.34434	4.491	1.63	0.066	0.065	98	
271.053717.1	19910928	05:37:22.418	64.11910	-21.34502	4.472	1.66	0.078	0.060	76	*
271.054209.1	19910928	05:42:13.140	64.11650	-21.34556	4.523	1.75	0.059	0.047	79	
271.055444.1	19910928	05:54:49.414	64.11615	-21.34580	4.379	2.40	0.073	0.054	73	
271.055635.1	19910928	05:56:39.448	64.11632	-21.34465	4.275	2.16	0.056	0.047	83	
271.061335.1	19910928	06:14:06.268	64.11590	-21.34406	4.217	1.57	0.074	0.033	44	
271.061603.1	19910928	06:16:07.153	64.11681	-21.34572	4.489	1.44	0.044	0.030	68	
271.062437.1	19910928	06:24:41.184	64.11835	-21.34469	4.565	1.72	0.072	0.023	31	
271.063724.1	19910928	06:37:27.931	64.11642	-21.34558	4.222	1.36	0.053	0.020	37	
271.064228.1	19910928	06:42:37.312	64.11805	-21.34472	4.598	1.39	0.066	0.045	68	
271.064538.1	19910928	06:45:42.206	64.11684	-21.34260	4.549	2.41	0.074	0.051	68	*
271.065557.1	19910928	06:56:01.383	64.11675	-21.34351	4.591	1.38	0.049	0.033	67	
271.073001.1	19910928	07:30:05.279	64.11740	-21.34423	4.251	1.29	0.058	0.032	55	
271.073036.1	19910928	07:30:40.382	64.11600	-21.34639	4.561	3.10	0.069	0.045	65	
271.073200.1	19910928	07:32:04.656	64.11645	-21.34637	4.391	1.47	0.056	0.036	64	
271.073505.1	19910928	07:35:09.261	64.11594	-21.34532	4.214	1.51	0.057	0.022	38	
271.073713.1	19910928	07:37:17.267	64.11586	-21.34570	4.091	1.39	0.048	0.014	29	
271.073950.1	19910928	07:40:21.282	64.11330	-21.34488	4.344	1.56	0.065	0.040	61	
271.074652.1	19910928	07:46:56.539	64.11505	-21.34637	4.520	1.49	0.070	0.036	51	
271.080711.1	19910928	08:07:14.930	64.11868	-21.34355	4.407	1.69	0.064	0.046	71	
271.081224.1	19910928	08:12:28.556	64.11615	-21.34730	4.416	1.64	0.058	0.027	46	
271.081917.1	19910928	08:19:39.735	64.11587	-21.34588	4.296	1.94	0.061	0.033	54	
271.082206.1	19910928	08:22:10.858	64.11724	-21.34385	4.569	1.78	0.063	0.037	58	
271.082600.1	19910928	08:26:07.646	64.11441	-21.34610	4.453	2.33	0.082	0.055	67	
271.092145.1	19910928	09:21:49.211	64.11855	-21.34594	4.501	1.53	0.049	0.019	38	
271.094316.1	19910928	09:43:35.679	64.11485	-21.34899	4.379	1.34	0.035	0.024	68	
271.100932.1	19910928	10:09:36.198	64.11733	-21.34404	4.371	1.55	0.047	0.019	40	
271.101931.1	19910928	10:19:35.123	64.11872	-21.34409	4.586	1.40	0.056	0.029	51	
271.113343.1	19910928	11:33:47.532	64.11579	-21.34570	4.458	1.52	0.064	0.035	54	
271.114653.1	19910928	11:47:01.906	64.11732	-21.34382	4.188	1.85	0.057	0.016	28	
271.115730.1	19910928	11:57:34.579	64.11755	-21.34525	4.310	1.59	0.055	0.032	58	
271.133228.1	19910928	13:32:32.214	64.04932	-21.23742	3.109	1.80	0.059	0.035	59	*
271.140320.1	19910928	14:03:25.618	64.11847	-21.34101	4.563	1.47	0.049	0.017	34	
271.142426.1	19910928	14:24:30.078	64.11784	-21.34187	4.595	1.65	0.047	0.025	53	
271.144119.1	19910928	14:41:27.517	64.11640	-21.34449	4.715	1.49	0.060	0.021	35	
271.154632.1	19910928	15:46:36.621	64.02172	-21.20860	3.682	1.80	0.058	0.034	58	*
271.160911.1	19910928	16:09:24.805	64.11765	-21.34605	4.842	2.52	0.065	0.031	47	*
271.161559.1	19910928	16:16:05.684	64.02316	-21.20853	3.472	1.50	0.032	0.034	106	
271.161742.1	19910928	16:17:47.508	64.11545	-21.34584	4.571	1.99	0.083	0.046	55	
271.163138.1	19910928	16:31:42.470	64.11830	-21.34586	4.658	1.80	7.599	7.595	99	
271.165235.1	19910928	16:52:38.891	64.11412	-21.34677	4.517	1.05	0.039	0.020	51	
271.185355.1	19910928	18:53:59.403	64.11579	-21.34669	4.032	1.66	0.049	0.036	73	
271.185839.1	19910928	18:58:43.540	64.11604	-21.34729	4.672	2.28	0.063	0.045	71	*
271.193115.1	19910928	19:31:22.906	64.11565	-21.34691	4.471	1.37	0.044	0.020	45	
271.201525.1	19910928	20:15:44.165	64.11631	-21.34668	4.062	1.53	0.049	0.026	53	
271.210342.1	19910928	21:03:51.088	64.11689	-21.34683	3.976	1.75	0.051	0.038	74	
271.210729.1	19910928	21:07:37.947	64.11668	-21.34567	4.093	1.41	0.037	0.025	67	
271.212521.1	19910928	21:25:25.801	64.11704	-21.34565	4.156	1.43	0.047	0.028	59	
271.213322.1	19910928	21:33:26.524	64.11676	-21.34584	4.142	1.53	0.064	0.026	40	
271.230004.1	19910928	23:00:07.986	64.11540	-21.34713	4.196	2.01	0.092	0.041	44	
271.230818.1	19910928	23:08:22.728	64.11546	-21.34536	4.301	1.43	0.054	0.017	31	
272.010108.1	19910929	01:01:12.349	64.11551	-21.34454	4.078	1.42	0.091	0.053	58	*
272.014034.1	19910929	01:40:38.549	64.06677	-21.14138	4.698	2.68	0.063	0.047	74	*
272.054735.1	19910929	05:47:39.189	64.06744	-21.14237	4.544	1.65	0.066	0.044	66	*
272.102836.1	19910929	10:28:40.963	64.11766	-21.34696	4.614	1.92	0.048	0.025	52	
272.130250.1	19910929	13:02:55.438	64.06221	-21.18718	4.343	2.11	0.051	0.067	131	
272.135007.1	19910929	13:50:11.133	64.11599	-21.34583	4.359	1.69	0.051	0.028	54	
272.145845.1	19910929	14:58:51.788	64.11639	-21.34621	4.382	2.39	0.065	0.054	83	
272.160315.1	19910929	16:03:19.553	64.11576	-21.34521	4.791	1.80	0.074	0.044	59	
272.224452.1	19910929	22:44:56.250	64.11555	-21.34600	4.639	2.41	0.078	0.027	34	
273.204056.1	19910930	20:41:00.118	64.11618	-21.34895	4.731	2.43	0.069	0.035	50	*

Appendix 6: Shell scripts used to prepare *focmec* input

A6.1 el2fm.rat

The shell script *el2fm.rat* prepares polarity and amplitude ratio data for a single earthquake for input to the *focmec* program. It is based on an original version by B. R. Julian, and was modified by the author of this thesis.

```
#! /bin/sh
# Convert eloc output to focmec input format
# Amplitude ratio bounds determined from noise picks & additional uncertainty.
# Attenuation correction :  APo/ASo = AP/AS * exp ((PI*f) * (1-(QP/QS)*(vP/vS)) *
tP/QP)

usage="Usage: $0 [-pairs] [-focus vp vs] [-surface vp vs] [-unc value] [-attenuation QP
QS] [-verbose] eloc_file"

# Set defaults
vpsurf=3.17; vssurf=1.78
vpfoc=6.26; vsfoc=3.52
unc=0.0; ac=0
pf=print_rat; v=FALSE

while test "$1" != ""
do
    case "$1" in
        -p*) pf=print_pair; shift ;;
        -f*) vpfoc=$2; vsfoc=$3; shift 3 ;;
        -s*) vpsurf=$2; vssurf=$3; shift 3 ;;
        -u*) unc=$2; shift 2 ;;
        -a*) ac=`echo $2 $3 | nawk '{ print 15.71*(1-($1/$2)*('$vpfoc'/'$vsfoc'))/$1 }' ` ;
            shift 3 ;;
        -v*) v=TRUE; shift ;;
        -*) echo $usage 1>&2; exit 1 ;;
        *) break ;;
    esac
done

# Process eloc file
depth=`nawk 'NR==2 { print $6 }' $*`
tail +6 $* | sort +7 -f |
nawk '
    function abs(x) { return x>0 ? x : -x }
    function asin(x) { return atan2(x, sqrt(1.0 - x*x)) }
    function sign(x) { return x>0 ? "+" : "-" }
    function hypot(x,y) {
        if (x==0 || y==0) return abs(x+y)
        else return (abs(x)>abs(y) ? x*sqrt(1+(y/x)*(y/x)) : y*sqrt(1+(x/y)*(x/y)))
    }
    function print_pol(k, c, p) {
        printf "%s\t%6.2f %3.0f %3.0f\t%s\t%s\n",
            c, dist[k], az[k], toa[k], p, k
    }
    function print_rat(k, c1, a1, e1, c2, a2, e2, sf) {
        ru = hypot(e1, e2) + '$unc'
        if (ru >= 1 && "'$v'" == "TRUE")
            printf "%4s %s,%s : Rel. uncertainty >= 1\n",
                k, c1, c2 | "cat >&2"
        rat=sf*a1/a2
```

```
    printf "%s,%s\t%6.2f %3.0f %3.0f %s%.3f\t%s\n",
        c1, c2, dist[k], az[k], toa[k],
        (a1>0 ? ">" : "<"), rat-(ru*rat), k
    printf "%s,%s\t%6.2f %3.0f %3.0f %s%.3f\t%s\n",
        c1, c2, dist[k], az[k], toa[k],
        (a1>0 ? "<" : ">"), rat+(ru*rat), k
}
function print_pair(k, c1, a1, e1, c2, a2, e2, sf) {
    ru = hypot(e1, e2) + '$unc'
    if (ru >= 1 && "'$v'" == "TRUE")
        printf "%4s %s,%s : Rel. uncertainty >= 1\n",
            k, c1, c2 | "cat >&2"
    printf "%s:%s\t%6.2f %3.0f %3.0f %.3e %.3e\t%4.2f\t%s\n",
        c1, c2, dist[k], az[k], toa[k], sf*a1, a2, ru, k
}
BEGIN {
    DEG = 57.29578; RAD = 1/DEG
}
$8 == "noise" {
    # Store noise in assoc. array, keyed on stn & component codes
    ns[$1,$2]=$15
}
NF>0 && $2=="D" {
    # Correct vertical picks on non-rotated traces
    $14 = -$14; $15 = -$15
}
NF>0 && $8=="S" {
    # Infer S-wave polarization from channel ID
    if   ($2=="r" || $2=="R" )    $8 = "SV"
    else if ($2=="t" || $2=="T" )$8 = "SH"
    else if ($2=="N" )            $8 = "SN"
    else if ($2=="E" )            $8 = "SE"
    else {
        printf "Channel %s not recognized\n", $2 | "cat >&2"
        next
    }

    # Correct for SH & SV-wave polarity conventions
    if ($8=="SV" || $8=="SH" ) { $14 = -$14; $15 = -$15 }
}
NF>0 && $14 != 0 {
    dist[$1] = $3; az[$1] = $4; toa[$1] = $5
    if ($8=="P") ttp[$1] = $9

    # Discard SV & SH waves for stations close to epicenter
    if (($8 == "SH" || $8 == "SV") && $3/'$depth' < 0.33) next

    if ($15 != 0) {
        # Amplitude datum
        # Calculate relative uncertainty due to noise
        runc = abs(ns[$1,$2]/$15)
        if (runc == 0 && "'$v'" == "TRUE")
            printf "%4s %4s : No noise pick\n",
                $1, $2 | "cat >&2"
        if (runc >= 1 && "'$v'" == "TRUE")
            printf "%4s %4s : Noise > picked amplitude\n",
                $1, $2 | "cat >&2"

        # Store relative uncertainty in assoc. arrays
        if     ($8 == "P" )  rep[$1]=runc
        else if ($8 == "SV") resv[$1]=runc
        else if ($8 == "SH") resh[$1]=runc
        else if ($8 == "SN") resn[$1]=runc
        else if ($8 == "SE") rese[$1]=runc

        if ($14/$15 <= 0 && "'$v'" == "TRUE")
            printf "%4s %4s : Polarity discordance\n",
                $1, $2 | "cat >&2"

        # Normalize for wave speed at focus
```

```
        vfoc  = ($8 == "P" ? '$vpfoc'  : '$vsfoc' )
        vsurf = ($8 == "P" ? '$vpsurf' : '$vssurf')
        $15 *= vfoc*vfoc*vfoc

        # Correct for free-surface effect
        if ($8=="SH" || $8=="SN" || $8=="SE")
            $15 /= 2.0
        else {
            # Check SV is within shear wave window
            if ($8=="SV" && $7<155) next

            if ($2=="v" || $2=="z" || $2=="V" || $2=="Z" || $2=="D") chn="z"
            else if ($2=="r" || $2=="t" || $2=="R" || $2=="T" || $2=="N" || $2=="E")
chn="x"
            else {
                printf "Channel %s not recognized\n", $2 | "cat >&2"
                next
            }

            code = sprintf("%.1s1%.1s",
                ($8=="P" || $8=="p" ? "p" : "s"), chn)

            cmd = sprintf("echo %f | rtcoef -mod '$vpsurf' '$vssurf' 1 0 0 0 -type %s",
180-$7, code)
            cmd | getline a
            close(cmd)
            split(a, b)
            $15 /= abs(b[2])
        }

        # Store amp. in assoc. arrays, keyed on station code
        if     ($8 == "P" )  ap[$1]=$15
        else if ($8 == "SV") asv[$1]=$15
        else if ($8 == "SH") ash[$1]=$15
        else if ($8 == "SN") asn[$1]=$15
        else if ($8 == "SE") ase[$1]=$15
    }
    # Store polarity in assoc. arrays, keyed on station code
    if     ($8 == "P" )  pp[$1]=$14
    else if ($8 == "SV") psv[$1]=$14
    else if ($8 == "SH") psh[$1]=$14
    else if ($8 == "SN") psn[$1]=$14
    else if ($8 == "SE") pse[$1]=$14
}
END {
    # Produce output
    for (k in dist) {
        # Polarities
        if (k in  pp) print_pol(k, "P", sign(pp[k]))
        if (k in psv) print_pol(k, "SV", sign(psv[k]))
        if (k in psh) print_pol(k, "SH", sign(psh[k]))
        if (k in psn) print_pol(k, "SN", sign(psn[k]))
        if (k in pse) print_pol(k, "SE", sign(pse[k]))

        # Amplitude ratios
        if (k in ash) {
            if (k in ap)
                '$pf'(k,  "P",  ap[k],  rep[k], "SH", ash[k], resh[k], exp('$ac'*ttp[k]))
            if (k in asv)
                '$pf'(k, "SH", ash[k], resh[k], "SV", asv[k], resv[k], 1)
        }
        else if (k in ap && k in asv)
                '$pf'(k,  "P",  ap[k],  rep[k], "SV", asv[k], resv[k], exp('$ac'*ttp[k]))
        if (k in asn && k in ap)
                '$pf'(k,  "P",  ap[k],  rep[k], "SN", asn[k], resn[k], exp('$ac'*ttp[k]))
        if (k in ase && k in ap)
                '$pf'(k,  "P",  ap[k],  rep[k], "SE", ase[k], rese[k], exp('$ac'*ttp[k]))
    }
}
```

A6.2 *el2fm.amp*

The shell script *el2fm.amp* prepares polarity and amplitude data for a single earthquake for input to the *focmec* program. It is based on the *el2fm.rat* shell script, and was written by the author of this thesis.

```
#! /bin/sh
# Convert eloc output to focmec input format
# Amplitude bounds determined from noise picks & additional uncertainty.

usage="Usage: $0 [-density value] [-focus vp vs] [-surface vp vs] [-unc value] [-verbose] [-geom] [-attenuation QP QS] eloc_file"

# Set defaults
counts2m=3.2E-10          # Convert digital counts to metres of displacement
denfoc=2800      # Density at focus
vpsurf=3.17; vssurf=1.78
vpfoc=6.26; vsfoc=3.52
unc=0.0
v=FALSE; geom=FALSE; att=FALSE
qp=0; qs=0        # Not used unless "att" flag is "TRUE"

while test "$1" != ""
do
    case "$1" in
        -d*) denfoc=$2; shift 2 ;;
        -f*) vpfoc=$2; vsfoc=$3; shift 3 ;;
        -s*) vpsurf=$2; vssurf=$3; shift 3 ;;
        -u*) unc=$2; shift 2 ;;
        -v*) v=TRUE; shift ;;
        -g*) geom=TRUE; shift ;;
        -a*) att=TRUE; qp=$2; qs=$3; shift 3 ;;
        -*) echo $usage 1>&2; exit 1 ;;
        *) break ;;
    esac
done

# Calculate geometrical spreading if required
if test "$geom" = "TRUE"
then
    get.gs -P $* > gsP$$
    get.gs -S $* > gsS$$
fi

# Process eloc file
depth=`nawk 'NR==2 { print $6 }' $*`
tail +6 $* | sort +7 -f |
nawk '
    function abs(x) { return x>0 ? x : -x }
    function asin(x) { return atan2(x, sqrt(1.0 - x*x)) }
    function sign(x) { return x>0 ? "+" : "-" }
    function print_pol(k, c, p) {
        printf "%s\t%6.2f %3.0f %3.0f\t%s\t%s\n",
            c, dist[k], az[k], toa[k], p, k
    }
    function print_amp(k, c, a, e) {
        ru = e + '$unc'
        if (ru >= 1 && "$v" == "TRUE")
            printf "%4s %s : Rel. uncertainty >= 1\n", k, c | "cat >&2"

        printf "%s\t%6.2f %3.0f %3.0f %s%.3e\t%s\n",
            c, dist[k], az[k], toa[k],
            (a>0 ? ">" : "<"), a-(ru*a), k
        printf "%s\t%6.2f %3.0f %3.0f %s%.3e\t%s\n",
            c, dist[k], az[k], toa[k],
            (a>0 ? "<" : ">"), a+(ru*a), k
    }
    BEGIN {
```

```
    DEG = 57.29578; RAD = 1/DEG; PI=3.1415927
    # Load geometrical spreading array
    while (getline <"'gsP$$'" > 0)
        gsp[$1]=abs($2)
    while (getline <"'gsS$$'" > 0)
        gss[$1]=abs($2)
}
$8 == "noise" {
        # Store noise in assoc. array, keyed on stn & component codes
    ns[$1,$2]=$15
    next
}
NF>0 && $2=="D" {
    # Correct vertical picks on non-rotated traces
    $14 = -$14; $15 = -$15
}
NF>0 && $8=="S" {
    # Infer S-wave polarization from channel ID
    if   ($2=="r" || $2=="R" ) $8 = "SV"
    else if ($2=="t" || $2=="T" ) $8 = "SH"
    else if ($2=="N" )          $8 = "SN"
    else if ($2=="E" )          $8 = "SE"
    else {
        printf "Channel %s not recognized\n", $2 | "cat >&2"
        next
    }

    # Correct for SH & SV-wave polarity conventions
    if ($8=="SV" || $8=="SH" ) { $14 = -$14; $15 = -$15 }
}
NF>0 && $14 != 0 {
    dist[$1] = sqrt($3*$3+'$depth'*'$depth') # Straight line dist.
    az[$1] = $4; toa[$1] = $5

    # Discard SV & SH waves for stations close to epicenter
if (($8 == "SH" || $8 == "SV") && $3/'$depth' < 0.33) next

if ($15 != 0) {
    # Amplitude datum
    # Calculate relative uncertainty due to noise
    runc = abs(ns[$1,$2]/$15)
    if (runc == 0 && "'$v'" == "TRUE")
        printf "%4s %4s : No noise pick\n",
            $1, $2 | "cat >&2"
    if (runc >= 1 && "'$v'" == "TRUE")
        printf "%4s %4s : Noise > picked amplitude\n",
            $1, $2 | "cat >&2"

        # Store relative uncertainty in assoc. arrays
    if     ($8 == "P" )  rep[$1]=runc
    else if ($8 == "SV")  resv[$1]=runc
    else if ($8 == "SH")  resh[$1]=runc
    else if ($8 == "SN")  resn[$1]=runc
    else if ($8 == "SE")  rese[$1]=runc

    if ($14/$15 <= 0 && "'$v'" == "TRUE")
        printf "%4s %4s : Polarity discordance\n",
            $1, $2 | "cat >&2"

    # Normalize amplitudes (everything in SI units)
    vfoc  = ($8 == "P" ? '$vpfoc' *1000 : '$vsfoc' *1000)
    vsurf = ($8 == "P" ? '$vpsurf'*1000 : '$vssurf'*1000)
    if ("'$geom'" == "TRUE") {
        # Use 4PI*density*v-cubed/sqrt(geom_spread)
        # geom spread in units of km^-2
        gs=($8=="P" ? gsp[$1] : gss[$1])
        if (gs == 0 && "'$v'" == "TRUE")
            printf "%4s %4s : No geom. spreading\n",
            $1, $2 | "cat >&2"
        if (gs == 0) gs=1000*dist[$1]
```

```
            else gs=1000/sqrt(gs)
            $15 *= 4*PI*'$denfoc'*vfoc*vfoc*vfoc*gs
        } else {
            # Use 4PI*density*v-cubed*dist
            $15 *= 4*PI*'$denfoc'*vfoc*vfoc*vfoc*dist[$1]*1000
        }
        # Convert from counts to meters
        $15 *= '$counts2m'

        # Correct for free-surface effect
        if ($8=="SH" || $8=="SN" || $8=="SE")
            $15 /= 2.0
        else {
            # Check SV is within shear wave window
            if ($8=="SV" && $7<155) next

            if ($2=="v" || $2=="z" || $2=="V" || $2=="Z" || $2=="D") chn="z"
            else if ($2=="r" || $2=="t" || $2=="R" || $2=="T" || $2=="N" || $2=="E")
chn="x"
            else {
                printf "Channel %s not recognized\n", $2 | "cat >&2"
                next
            }

            code = sprintf("%.1s1%.1s",
                ($8=="P" || $8=="p" ? "p" : "s"), chn)

            cmd = sprintf("echo %f | rtcoef -mod '$vpsurf' '$vssurf' 1 0 0 0 -type %s",
180-$7, code)
            cmd | getline a
            close(cmd)
            split(a, b)
            $15 /= abs(b[2])
        }

        # Correct for attenuation
        if ("'$att'" == "TRUE")
            $15=$15*exp(PI*5*$9/($8=="P" ? '$qp' : '$qs'))

        # Store amp. in assoc. arrays, keyed on station code
        if      ($8 == "P" )  ap[$1]=$15
        else if ($8 == "SV") asv[$1]=$15
        else if ($8 == "SH") ash[$1]=$15
        else if ($8 == "SN") asn[$1]=$15
        else if ($8 == "SE") ase[$1]=$15
    }
    # Store polarity in assoc. arrays, keyed on station code
    if      ($8 == "P" )  pp[$1]=$14
    else if ($8 == "SV") psv[$1]=$14
    else if ($8 == "SH") psh[$1]=$14
    else if ($8 == "SN") psn[$1]=$14
    else if ($8 == "SE") pse[$1]=$14
}
END {
    # Produce output
    for (k in dist) {
        # Polarities
        if (k in  pp) print_pol(k, "P", sign(pp[k]))
        if (k in psv) print_pol(k, "SV", sign(psv[k]))
        if (k in psh) print_pol(k, "SH", sign(psh[k]))
        if (k in psn) print_pol(k, "SN", sign(psn[k]))
        if (k in pse) print_pol(k, "SE", sign(pse[k]))

        # Amplitudes
        if (k in ap)  print_amp(k, "P",  ap[k],  rep[k])
        if (k in ash) print_amp(k, "SH", ash[k], resh[k])
        if (k in asv) print_amp(k, "SV", asv[k], resv[k])
        if (k in asn) print_amp(k, "SN", asn[k], resn[k])
        if (k in ase) print_amp(k, "SE", ase[k], rese[k])
    }
```

```
    }

rm -f gsP$$ gsS$$
```

A6.3 *get.gs*

The shell script *get.gs* was written by the author of this thesis and is called by *el2fm.amp* to calculate geometrical spreading from output of the *benday* program (B. R. Julian, *pers. comm.*).

```
#! /bin/sh
# geom.spread: ADM Apr 1995
# calculate geometrical spreading through P or S velocity model.  Output units are km^-
2
usage="Usage: $0 [-P | -S] [-stations file] [-model file] eloc_file"

case $# in
    0) echo $usage 1>&2; exit 1 ;;
esac

# Set defaults
ph="P"
fsta=/usr/local/seismic/hengill91/hengill.sta.d
fmod=""

while test "$1" != ""
do
    case "$1" in
        -P*) ph="P"; shift ;;
        -S*) ph="S"; shift ;;
        -s*) fsta=$2; shift 2 ;;
        -m*) fmod=$2; shift 2 ;;
        -*) echo $usage 1>&2; exit 1 ;;
        *) break ;;
    esac
done
if test "$fmod"=""
    then fmod=/home/alice/amiller/raytrace/v${ph}3d.b
fi

feloc=$1; shift

# Convert eloc file into bendray input format
nawk '
    BEGIN {
        # Read in station latitude, longitude
        while (getline<"'$fsta'">0) { lt[$1]=$2; ln[$1]=$3; el[$1]=$4 }
    }
    /Lat/ {
        # Hypocentre
        depth =  $6; elat = $2; elon = $4
    }
    $8 == "'$ph'" { print elat, elon, depth, lt[$1], ln[$1], -0.001*el[$1], $1 }
' $feloc |
uniq |
# calculate geometric spreading
bendray -mod $fmod -amp |
nawk '
    BEGIN { RAD=0.01745 }
    NR>1 { print $16, (sin($4*RAD)/cos($9*RAD))*($12*$15-$14*$13) }
'
```

Appendix 7: Moment tensors

Relative moment tensor components and ε and k values for all processed earthquakes. The x-axis points north, the y-axis points east and the z-axis points down. Asterisks indicate the well-constrained earthquakes.

Event	M_{xx}	M_{xy}	M_{yy}	M_{xz}	M_{yz}	M_{zz}	ε	k
215.195922.1	1.294e-01	-1.720e-01	-1.246e-01	-1.059e-01	9.502e-02	0.000e+00	0.22	0.01
216.093016.1	-3.979e-02	1.571e-01	3.317e-01	-1.424e-01	0.000e+00	4.948e-02	-0.03	0.28
*216.131451.1	1.596e-01	-1.099e-01	1.925e-01	2.369e-02	-1.211e-01	-1.385e-01	-0.03	0.22
*216.150353.1	1.544e-01	-8.877e-02	1.576e-01	7.991e-02	-1.363e-01	-7.789e-02	0.02	0.25
216.175540.1	9.596e-02	-9.513e-02	1.349e-01	9.557e-02	-1.701e-01	5.705e-02	0.29	0.28
*217.064554.1	-1.835e-01	-2.685e-03	3.098e-01	3.608e-02	-1.286e-01	1.721e-01	0.00	0.26
*217.164959.1	5.353e-02	-1.053e-01	2.810e-02	-6.365e-02	-2.052e-01	1.701e-01	-0.12	0.24
*217.183800.1	1.044e-01	-1.030e-01	1.430e-01	2.073e-02	-1.663e-01	-1.726e-01	-0.07	0.08
217.211107.1	1.203e-01	-1.177e-01	1.528e-01	1.050e-02	-1.593e-01	-1.518e-01	-0.04	0.13
*217.235139.1	1.734e-01	-9.439e-02	1.823e-01	-5.691e-02	1.462e-03	-3.388e-01	-0.23	0.02
*218.013307.1	1.210e-01	-7.441e-02	3.358e-02	-1.102e-02	-2.177e-01	-2.392e-01	-0.32	-0.08
218.013404.1	1.064e-01	-1.193e-01	1.181e-01	1.890e-02	-1.793e-01	-1.405e-01	-0.03	0.10
*218.023219.1	1.356e-01	-1.156e-01	1.793e-01	3.065e-02	-1.290e-01	-1.346e-01	0.03	0.20
218.033837.1	1.034e-01	-1.250e-01	1.478e-01	5.021e-02	-1.860e-01	-2.631e-02	0.16	0.22
*218.045348.1	1.704e-01	-9.037e-02	2.168e-01	4.771e-02	-1.105e-01	-1.155e-01	-0.05	0.27
218.060540.1	1.766e-01	-9.031e-02	1.613e-01	4.596e-02	-1.808e-01	2.794e-02	0.02	0.35
*218.061609.1	9.560e-02	-9.123e-02	1.469e-01	-1.821e-01	-8.023e-02	-5.045e-02	-0.38	0.19
*219.001831.1	1.729e-01	-9.987e-02	2.060e-01	3.770e-02	-1.250e-01	-9.588e-02	-0.02	0.29
*220.030040.1	-4.799e-02	5.147e-02	3.416e-01	1.718e-02	-1.337e-01	-2.056e-01	0.22	0.08
*220.235442.1	1.851e-01	-1.833e-01	-8.766e-02	5.154e-02	-6.941e-02	1.186e-01	-0.08	0.22
*222.034524.1	3.344e-01	-1.862e-01	-3.943e-02	5.814e-02	4.486e-02	4.768e-02	0.16	0.28
222.034641.1	3.374e-01	-1.608e-01	4.211e-02	9.571e-02	-3.048e-02	4.651e-02	0.41	0.33
*224.023135.1	7.720e-02	-3.674e-02	7.889e-02	1.161e-01	-2.571e-01	2.404e-02	0.04	0.17
*224.173023.1	2.450e-01	-1.918e-01	-1.464e-01	6.279e-02	-1.723e-02	6.494e-02	0.02	0.16
*224.184254.1	4.328e-02	-2.140e-01	9.912e-02	1.528e-02	-8.753e-02	2.240e-01	-0.20	0.31
*224.184649.1	-1.296e-01	-9.394e-03	3.370e-01	-1.217e-01	-8.837e-02	-9.450e-02	0.12	0.11
*224.223635.1	1.024e-01	-2.492e-01	1.595e-01	4.640e-02	-3.303e-02	8.080e-02	0.15	0.29
224.224238.1	3.382e-01	-1.971e-01	-1.251e-01	-4.049e-02	1.301e-02	3.538e-02	0.16	0.20
*224.224403.1	5.083e-01	-8.965e-02	-1.034e-01	3.587e-02	6.470e-02	-7.841e-03	0.28	0.25
*225.010319.1	1.102e-01	-1.329e-01	-3.038e-02	7.554e-02	-1.274e-01	1.878e-01	0.07	0.27
*225.083219.1	1.836e-01	-1.979e-01	1.758e-01	4.346e-03	7.865e-02	-7.873e-02	0.27	0.24
225.090227.1	2.039e-01	-1.685e-01	2.439e-01	-2.443e-02	6.096e-02	-4.447e-02	0.28	0.33
*225.122104.1	1.838e-01	-1.945e-01	1.993e-01	1.083e-01	-3.072e-03	-5.235e-03	0.23	0.31
*225.122759.1	1.378e-01	-1.586e-01	1.087e-01	8.759e-02	8.556e-02	-8.998e-02	-0.04	0.18
*225.122941.1	4.333e-01	-9.541e-02	1.109e-01	3.597e-02	-3.630e-02	-1.205e-01	0.17	0.31
*225.123131.1	2.994e-01	-1.188e-01	1.447e-01	5.891e-02	-4.119e-02	-1.170e-01	0.11	0.29
*225.123340.1	2.221e-01	-1.424e-01	2.029e-01	4.454e-02	7.880e-02	-4.344e-02	0.04	0.36
*225.162551.1	-1.032e-02	-7.354e-02	1.604e-01	-4.554e-02	-2.372e-01	1.168e-01	0.18	0.24
*226.020942.1	2.414e-01	-1.975e-01	1.578e-01	-2.957e-02	-4.479e-02	-5.723e-02	0.29	0.28
*226.091934.2	1.635e-01	-1.400e-01	-4.651e-02	-1.692e-01	-8.577e-02	0.000e+00	-0.07	0.13
226.110713.1	2.958e-01	-1.348e-01	1.090e-01	-1.055e-01	2.129e-02	-7.209e-02	0.24	0.28
*226.151111.1	1.914e-01	-1.816e-01	-2.868e-02	1.121e-01	3.624e-02	1.199e-01	-0.08	0.27
226.152708.1	-9.168e-02	9.476e-02	4.179e-01	-9.595e-02	-1.805e-02	-7.290e-02	0.24	0.19
226.153852.1	2.278e-02	-4.607e-02	1.845e-01	1.248e-01	1.310e-01	-1.891e-01	-0.25	0.02
*226.214521.1	-5.372e-03	7.072e-02	1.524e-01	-1.157e-01	-1.905e-01	-8.845e-02	0.16	0.06

Event	M_{xx}	M_{xy}	M_{yy}	M_{xz}	M_{yz}	M_{zz}	ε	k
226.215442.1	-2.649e-01	-2.274e-02	1.246e-01	-1.740e-01	-7.305e-02	-7.088e-02	-0.26	-0.19
*227.092421.1	-8.777e-02	-1.501e-01	1.899e-01	5.594e-02	-1.797e-02	2.743e-01	-0.36	0.31
*227.092526.1	-2.228e-01	-9.811e-02	1.590e-01	1.506e-01	3.245e-02	5.583e-02	-0.40	-0.01
*228.040122.1	1.590e-01	-1.109e-01	1.603e-01	1.679e-01	6.990e-03	-1.091e-01	-0.12	0.21
*228.045401.1	-3.447e-03	-1.034e-01	1.171e-01	-9.589e-02	1.332e-01	2.145e-01	0.31	0.30
*228.083300.1	2.148e-01	-8.020e-02	1.543e-01	1.783e-01	0.000e+00	-1.141e-01	-0.14	0.23
*229.033558.1	1.513e-01	-1.040e-01	-3.787e-02	1.569e-01	5.316e-02	1.827e-01	-0.00	0.30
*231.161335.1	-1.676e-01	-1.530e-01	1.761e-01	2.541e-02	-1.105e-01	7.851e-02	0.03	0.10
*232.194924.1	1.343e-02	6.537e-03	1.259e-01	1.135e-01	-1.965e-01	-2.283e-01	-0.21	-0.09
*234.000219.1	2.311e-01	-1.625e-01	1.576e-01	-2.847e-02	7.372e-02	8.181e-02	0.30	0.42
234.080946.1	1.329e-01	-2.124e-01	1.884e-01	-1.416e-02	7.461e-02	7.678e-02	0.23	0.34
234.183633.1	1.200e-01	-2.310e-01	1.315e-01	-5.271e-02	6.217e-02	5.682e-02	0.24	0.27
*236.052400.1	5.670e-02	-2.412e-01	9.637e-02	-9.995e-02	6.428e-02	3.611e-02	0.21	0.18
*236.065252.1	1.930e-01	-2.086e-01	8.001e-02	6.777e-02	8.329e-02	7.651e-03	0.05	0.27
*237.212559.1	-4.303e-02	-3.189e-02	-1.549e-01	1.598e-01	-2.063e-01	-5.957e-03	0.14	-0.19
*239.160308.1	2.083e-01	-1.854e-01	-6.549e-02	9.024e-02	1.200e-03	1.725e-01	-0.13	0.28
240.162821.1	2.477e-02	-2.436e-01	3.143e-01	-2.882e-03	7.417e-02	1.968e-02	0.29	0.26
*240.163545.1	7.301e-02	-2.510e-01	1.683e-02	-5.849e-02	-1.134e-01	-6.447e-02	0.01	0.03
*241.105349.1	8.654e-03	-8.539e-02	3.521e-01	-8.530e-02	-1.330e-01	3.290e-02	0.11	0.32
248.221755.1	-1.434e-01	-9.990e-02	1.511e-01	-1.095e-01	-6.904e-02	1.484e-01	-0.38	0.16
252.022807.1	2.550e-01	-1.802e-01	-3.234e-02	2.275e-02	1.028e-01	1.011e-01	-0.12	0.29
*252.023347.1	1.790e-01	-1.866e-01	-8.463e-02	-2.548e-02	1.386e-01	4.332e-02	-0.05	0.14
252.023939.1	2.797e-01	-1.160e-01	-7.352e-02	-1.179e-01	-5.220e-02	7.721e-02	0.07	0.27
*252.044910.1	1.177e-01	-1.904e-01	-4.972e-02	-1.520e-02	1.825e-01	5.625e-02	-0.10	0.12
*252.050156.1	6.904e-02	-1.540e-01	3.040e-01	-5.410e-03	-1.065e-01	-9.510e-02	0.26	0.23
*252.112006.1	2.123e-01	9.418e-02	8.448e-03	-1.386e-01	4.928e-02	-2.152e-01	-0.01	0.01
*253.125604.1	1.731e-01	-1.337e-01	-1.603e-01	6.754e-02	5.267e-02	1.588e-01	-0.32	0.17
254.142448.1	2.982e-01	-1.289e-01	-1.159e-01	-2.401e-02	9.255e-02	9.490e-02	-0.07	0.25
*254.164629.1	3.371e-02	8.427e-02	2.645e-01	-1.184e-01	-2.110e-02	-2.543e-01	-0.09	0.04
*255.021714.1	-7.154e-02	-1.502e-02	3.693e-01	1.543e-01	-9.857e-02	2.338e-02	-0.00	0.27
*255.173510.1	-1.382e-01	-4.131e-02	2.393e-01	1.357e-01	6.758e-02	1.332e-01	-0.31	0.22
*256.235841.1	2.999e-01	-1.086e-01	1.315e-01	-4.916e-02	-8.701e-02	-7.908e-02	-0.04	0.32
*257.073459.1	1.128e-01	-2.617e-01	1.458e-02	-1.025e-01	-1.714e-02	1.100e-01	-0.10	0.21
*258.074123.1	4.044e-01	-1.895e-01	-6.766e-02	-4.261e-02	4.555e-03	5.465e-02	0.23	0.27
258.090235.1	1.482e-01	-9.839e-02	-7.617e-02	-1.920e-01	3.863e-02	1.176e-01	0.35	0.18
262.140501.1	1.460e-01	-1.558e-01	-4.533e-02	5.328e-02	6.960e-02	2.513e-01	-0.42	0.30
*264.053355.1	-1.353e-01	-1.436e-01	7.825e-02	-1.094e-01	2.818e-02	2.242e-01	-0.19	0.17
*264.193202.1	-1.506e-01	-1.900e-01	1.476e-01	-8.658e-02	-7.815e-03	1.330e-01	-0.32	0.13
264.212351.1	-1.209e-01	-1.740e-01	1.763e-01	-3.420e-02	-5.967e-02	1.670e-01	-0.30	0.21
*264.234218.1	2.500e-01	-1.522e-01	5.926e-02	5.358e-02	1.074e-01	-6.433e-02	0.02	0.24
265.030152.1	-1.461e-01	-1.149e-01	7.569e-02	-9.576e-02	4.772e-02	2.615e-01	-0.10	0.19
*265.040149.1	-1.305e-01	-1.482e-01	1.067e-01	-1.440e-01	-2.745e-02	1.236e-01	-0.38	0.10
*265.191813.1	-8.536e-02	3.349e-02	1.399e-01	1.104e-03	-1.923e-01	3.212e-01	0.31	0.28
*265.195449.1	2.865e-01	-2.137e-01	-7.209e-02	-1.221e-02	6.782e-02	5.388e-02	0.09	0.23
*265.201436.1	1.847e-01	-1.869e-01	-1.471e-01	-6.808e-02	5.170e-02	5.480e-02	0.01	0.10
*265.201436.2	2.970e-01	-2.342e-01	-9.518e-02	-1.969e-02	4.885e-02	2.439e-03	0.18	0.17
*267.001816.1	1.669e-01	-5.421e-02	-2.153e-02	-2.056e-01	-3.981e-02	2.123e-01	0.26	0.30
267.002034.1	2.344e-01	-1.345e-01	-7.308e-02	4.972e-02	1.334e-01	-5.732e-02	-0.08	0.11
*269.192321.1	3.709e-01	-1.517e-01	-2.373e-02	-7.342e-02	4.442e-02	6.625e-02	0.29	0.31
*271.043816.1	-5.314e-03	-3.186e-02	8.191e-02	2.865e-02	-1.996e-01	3.924e-01	0.45	0.32
271.133228.1	-5.512e-02	-1.697e-01	1.780e-01	-8.512e-02	-1.104e-01	3.633e-02	-0.13	0.17
*271.154632.1	-1.163e-01	-1.805e-01	1.198e-01	2.128e-02	-8.060e-02	1.992e-01	-0.21	0.19
272.130250.1	5.245e-01	9.850e-02	-2.840e-02	-7.583e-02	-4.067e-02	-1.724e-02	0.43	0.29

Appendix 8: Focal mechanisms

This appendix shows the focal mechanisms for all the earthquakes studied, arranged in chronological order. All plots are upper focal-sphere equal-area projections. For each earthquake, the observed *P*, *SH* and *SV* polarities are plotted with the nodal lines of the best-fit general moment tensor. Positive *P*-wave motion is upwards, positive *SH* motion is to the right (clockwise) as viewed from the source, and positive *SV* motion is upwards (towards the zenith). Positive motion is shown as solid symbols, and negative as open symbols. Squares are down-going rays that are projected onto the upper focal hemisphere. *P*:*SH*, *SH*:*SV*, *P*:*SN* and *P*:*SE* ratios are displayed using the method of Figure 6.4. The event name, group name and the moment magnitude are shown at the top.

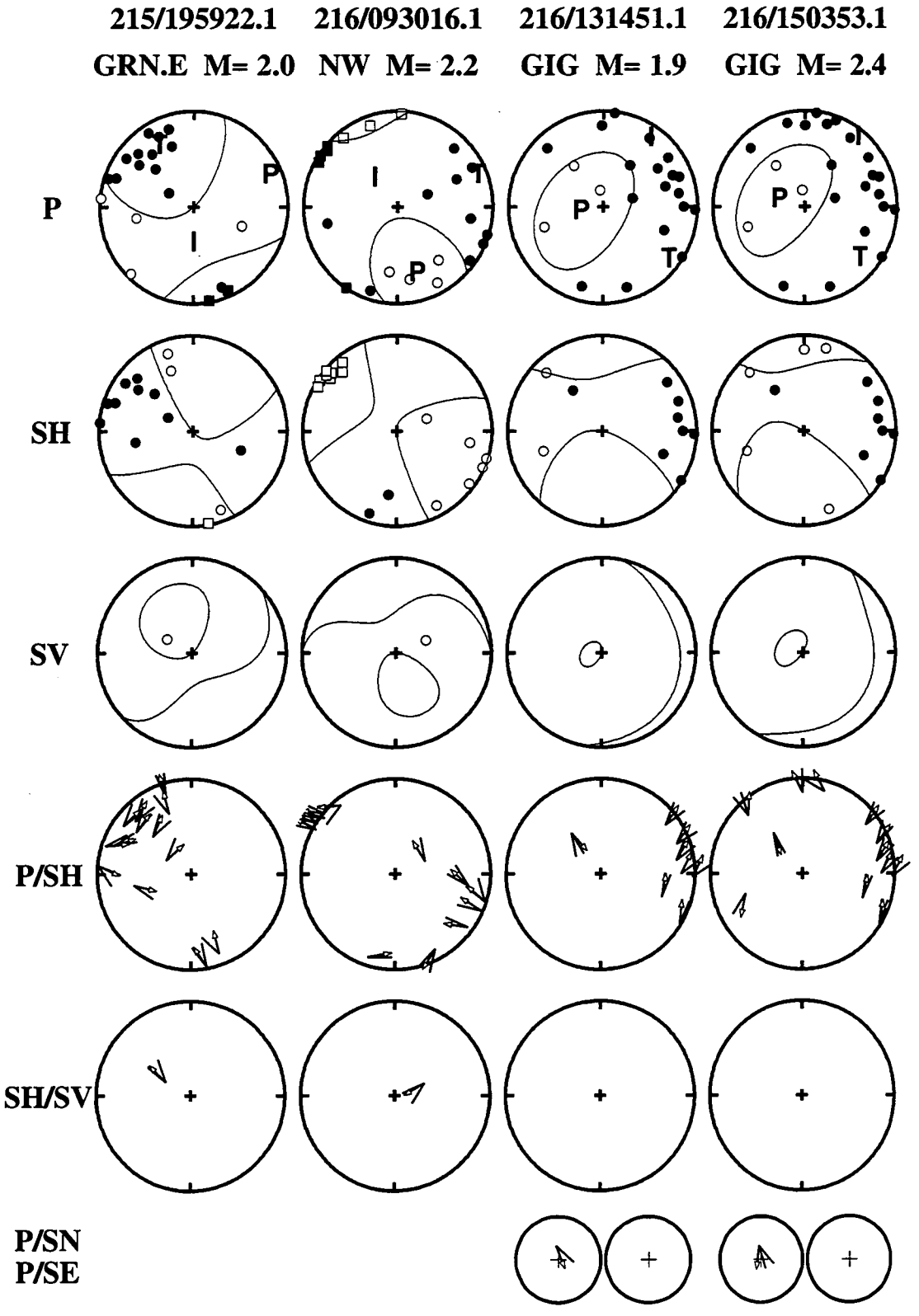
215/195922.1
GRN.E M= 2.0
216/093016.1
NW M= 2.2
216/131451.1
GIG M= 1.9
216/150353.1
GIG M= 2.4
P
SH
SV
P/SH
SH/SV
P/SN
P/SE
P
I
T

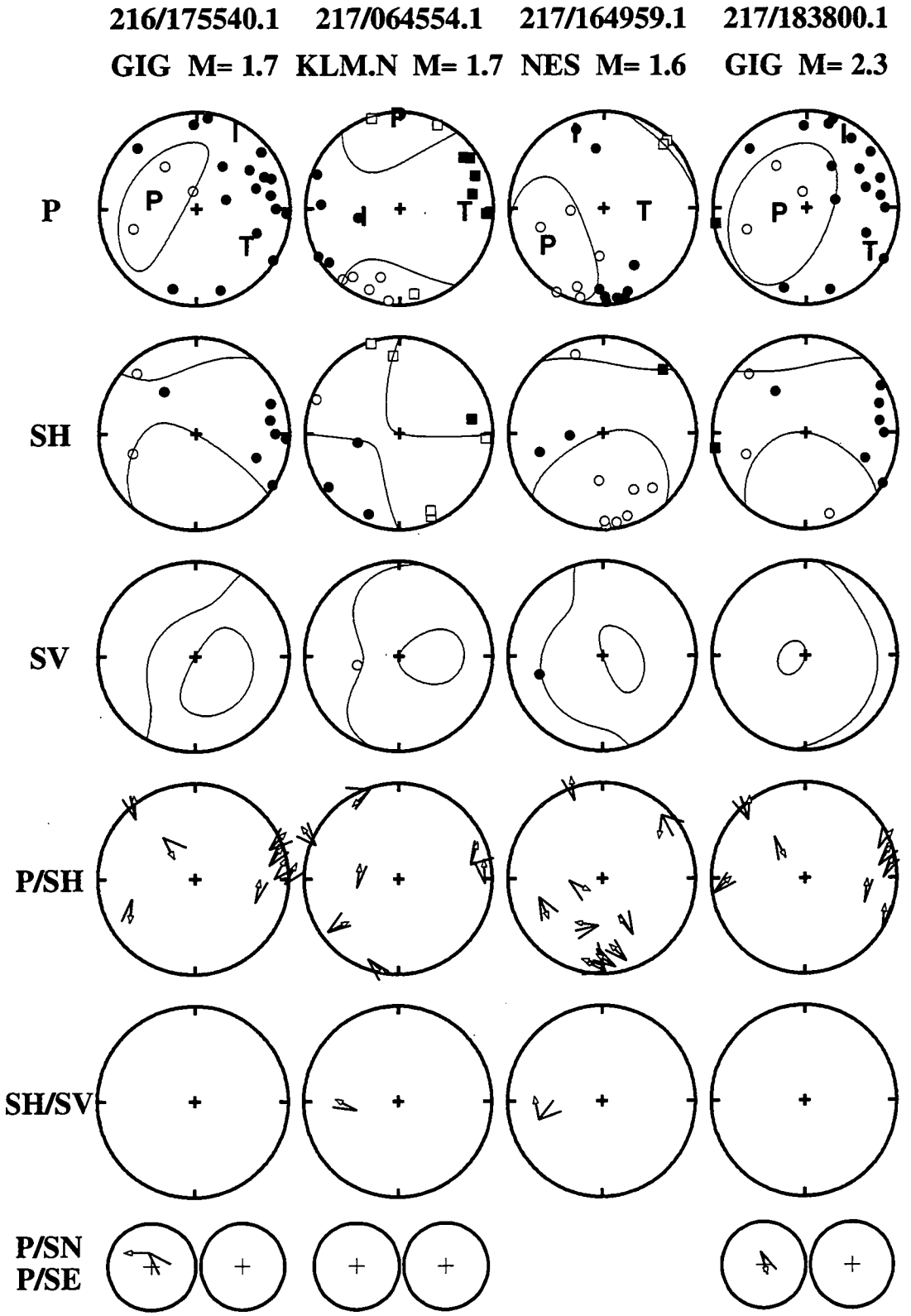
216/175540.1
GIG M= 1.7
217/064554.1
KLM.N M= 1.7
217/164959.1
NES M= 1.6
217/183800.1
GIG M= 2.3
P
SH
SV
P/SH
SH/SV
P/SN
P/SE
P
T

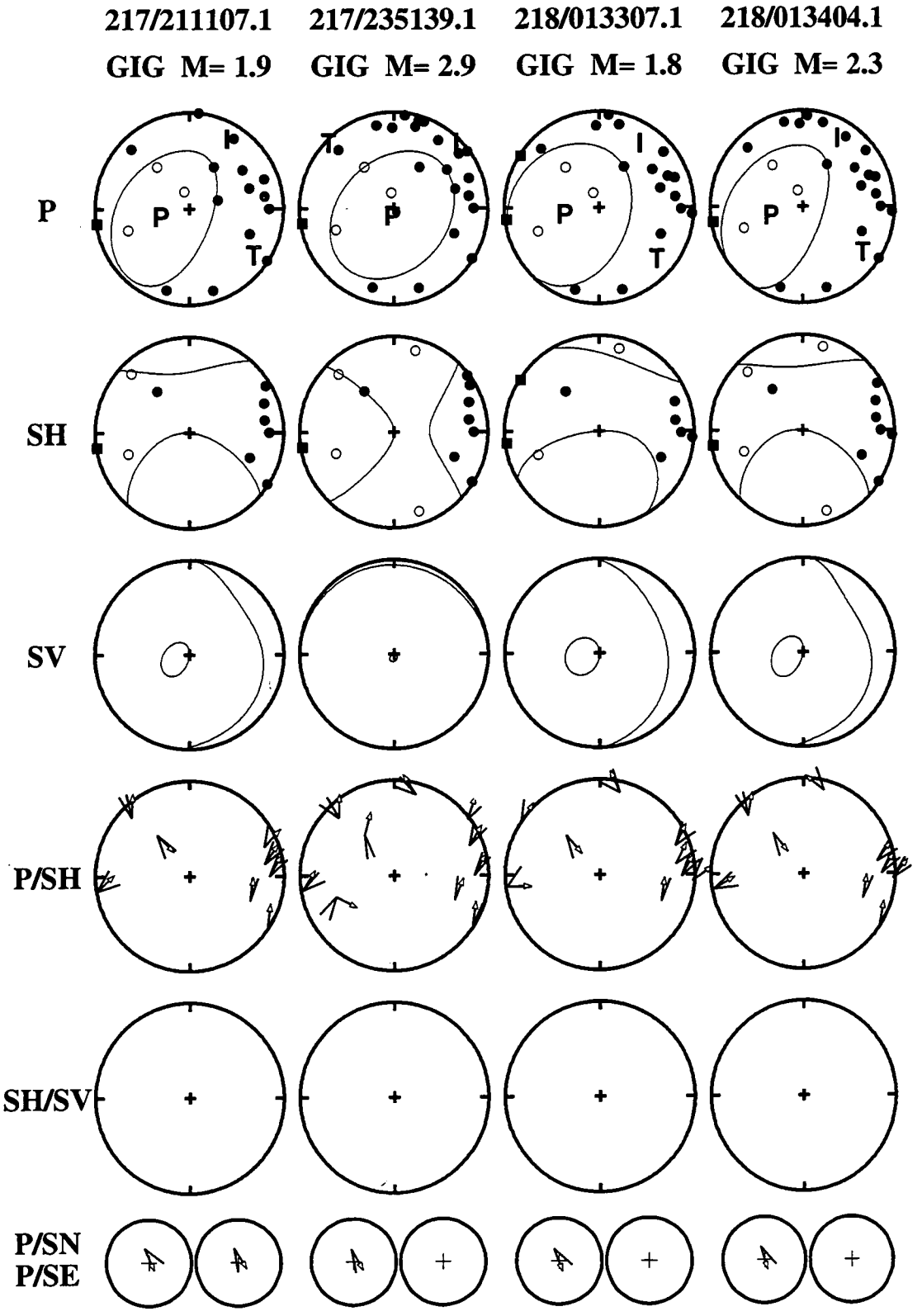
217/211107.1
GIG M= 1.9
217/235139.1
GIG M= 2.9
218/013307.1
GIG M= 1.8
218/013404.1
GIG M= 2.3
P
SH
SV
P/SH
SH/SV
P/SN
P/SE
P
T

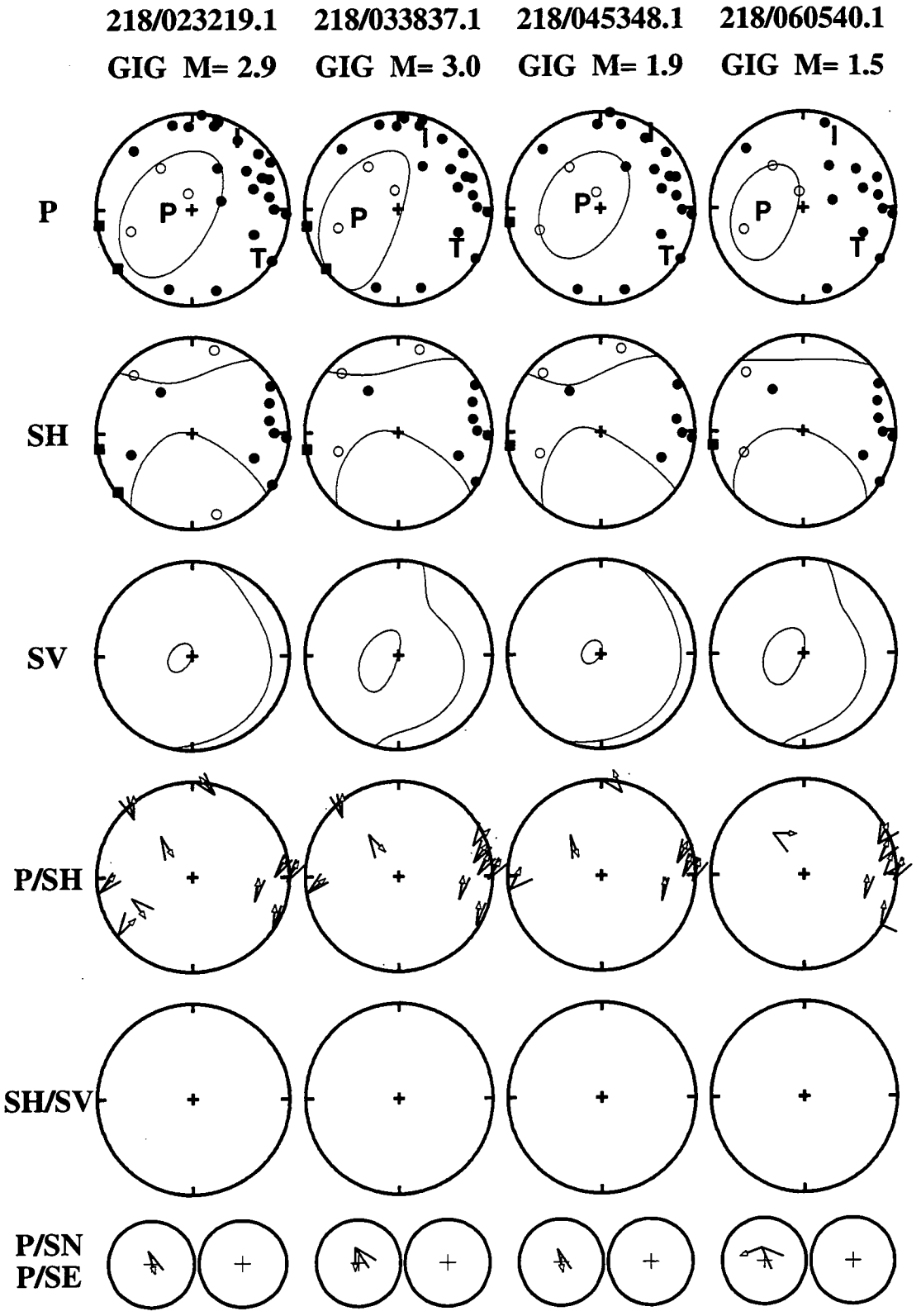
218/023219.1
GIG M= 2.9
218/033837.1
GIG M= 3.0
218/045348.1
GIG M= 1.9
218/060540.1
GIG M= 1.5
P
SH
SV
P/SH
SH/SV
P/SN
P/SE
P
T

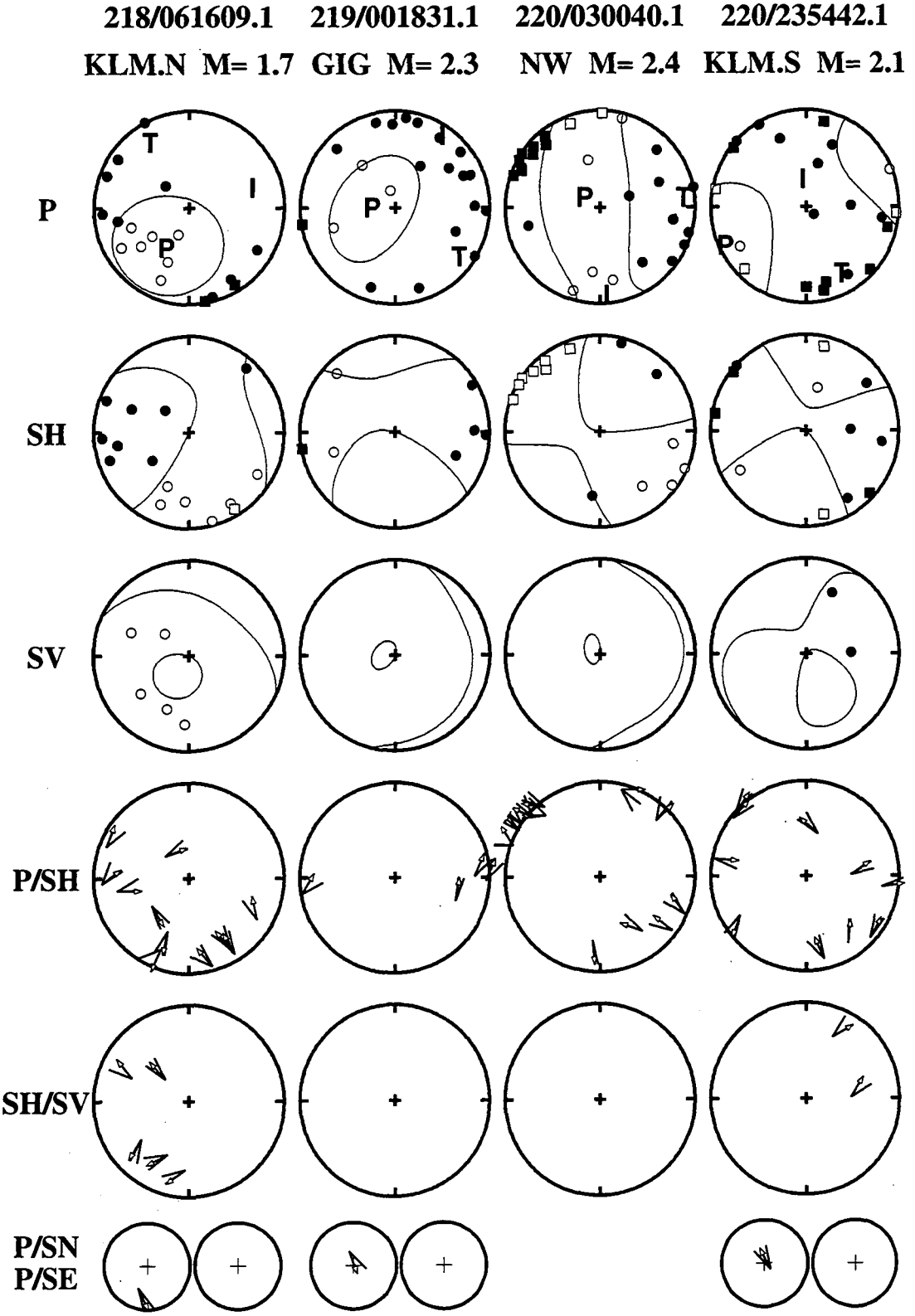
218/061609.1
KLM.N M= 1.7
219/001831.1
GIG M= 2.3
220/030040.1
NW M= 2.4
220/235442.1
KLM.S M= 2.1
P
SH
SV
P/SH
SH/SV
P/SN
P/SE

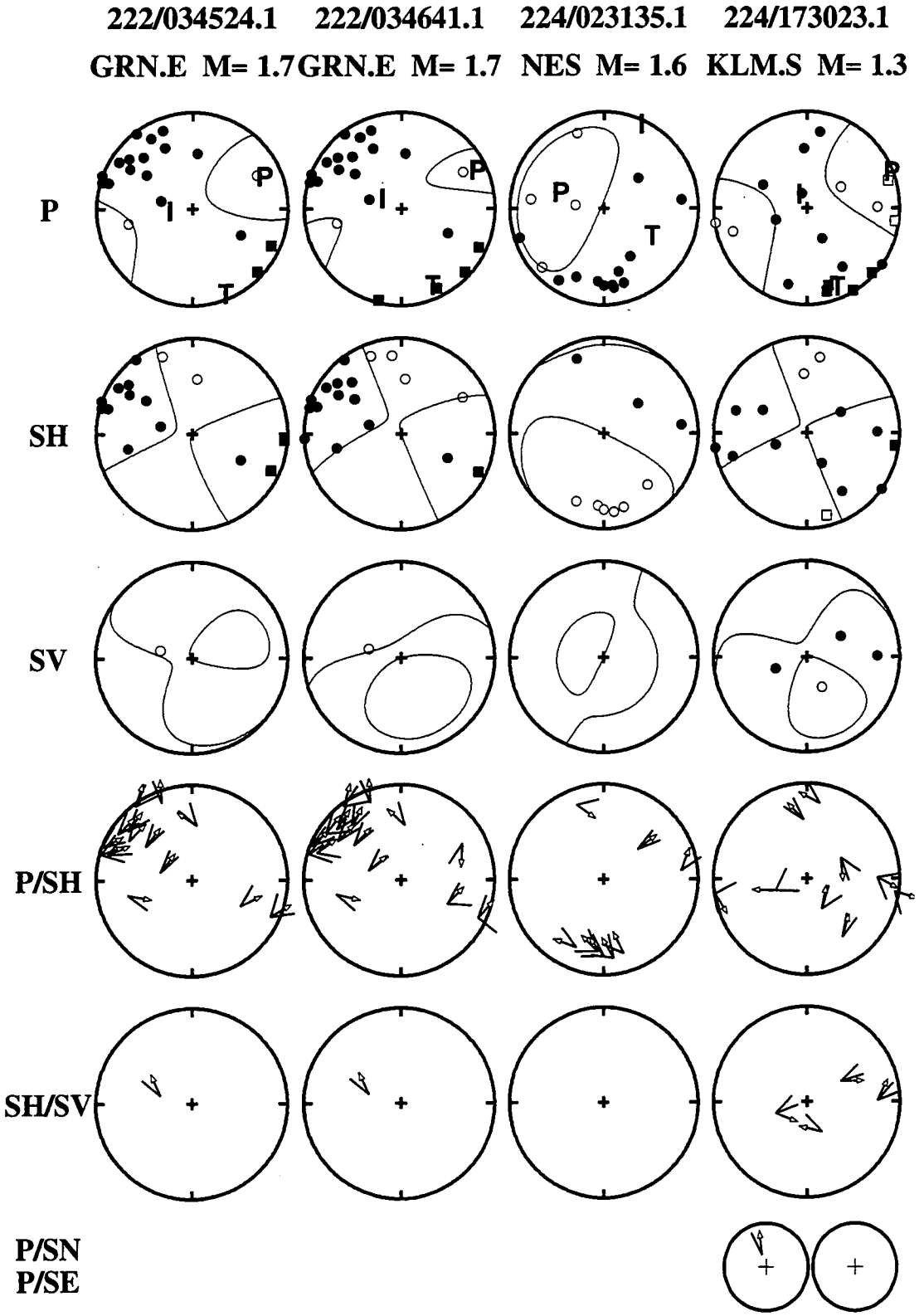
222/034524.1
GRN.E M= 1.7
222/034641.1
GRN.E M= 1.7
224/023135.1
NES M= 1.6
224/173023.1
KLM.S M= 1.3
P
SH
SV
P/SH
SH/SV
P/SN
P/SE

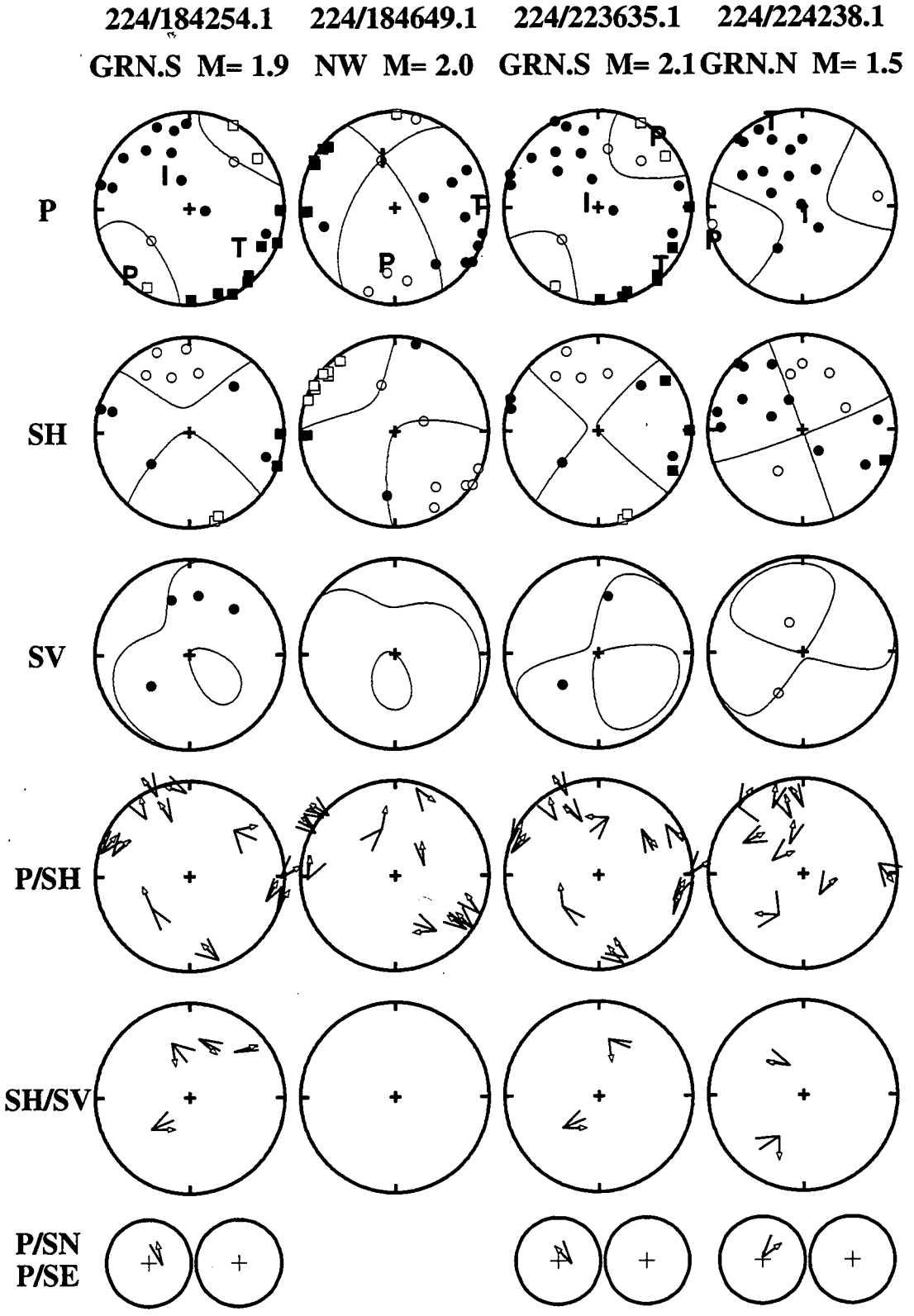
224/184254.1
GRN.S M= 1.9
224/184649.1
NW M= 2.0
224/223635.1
GRN.S M= 2.1
224/224238.1
GRN.N M= 1.5
P
SH
SV
P/SH
SH/SV
P/SN
P/SE

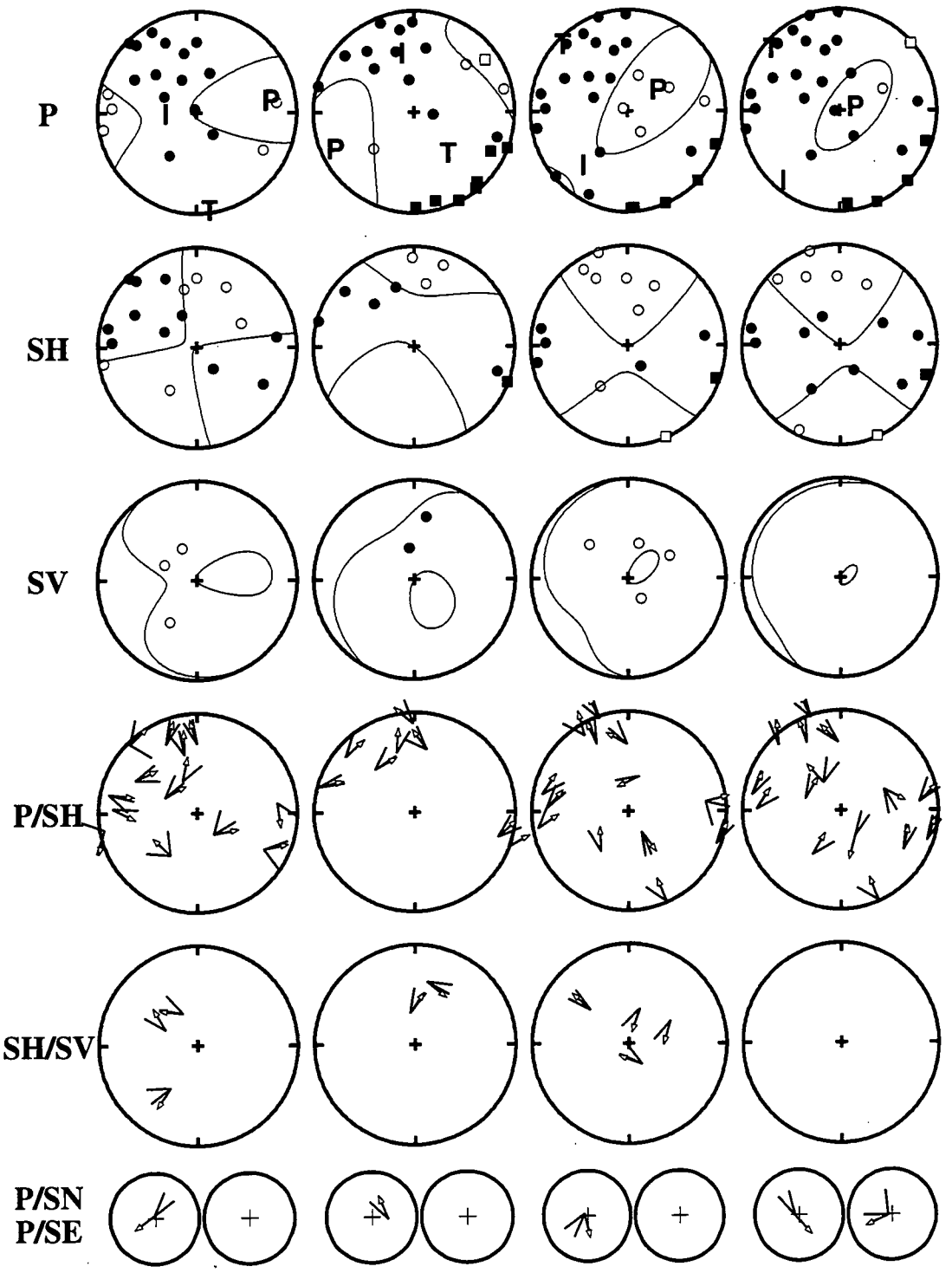
224/224403.1
GRN.N M= 1.6
225/010319.1
GRN.S M= 1.8
225/083219.1
GRN.N M= 2.5
225/090227.1
GRN.N M= 2.3
P
SH
SV
P/SH
SH/SV
P/SN
P/SE

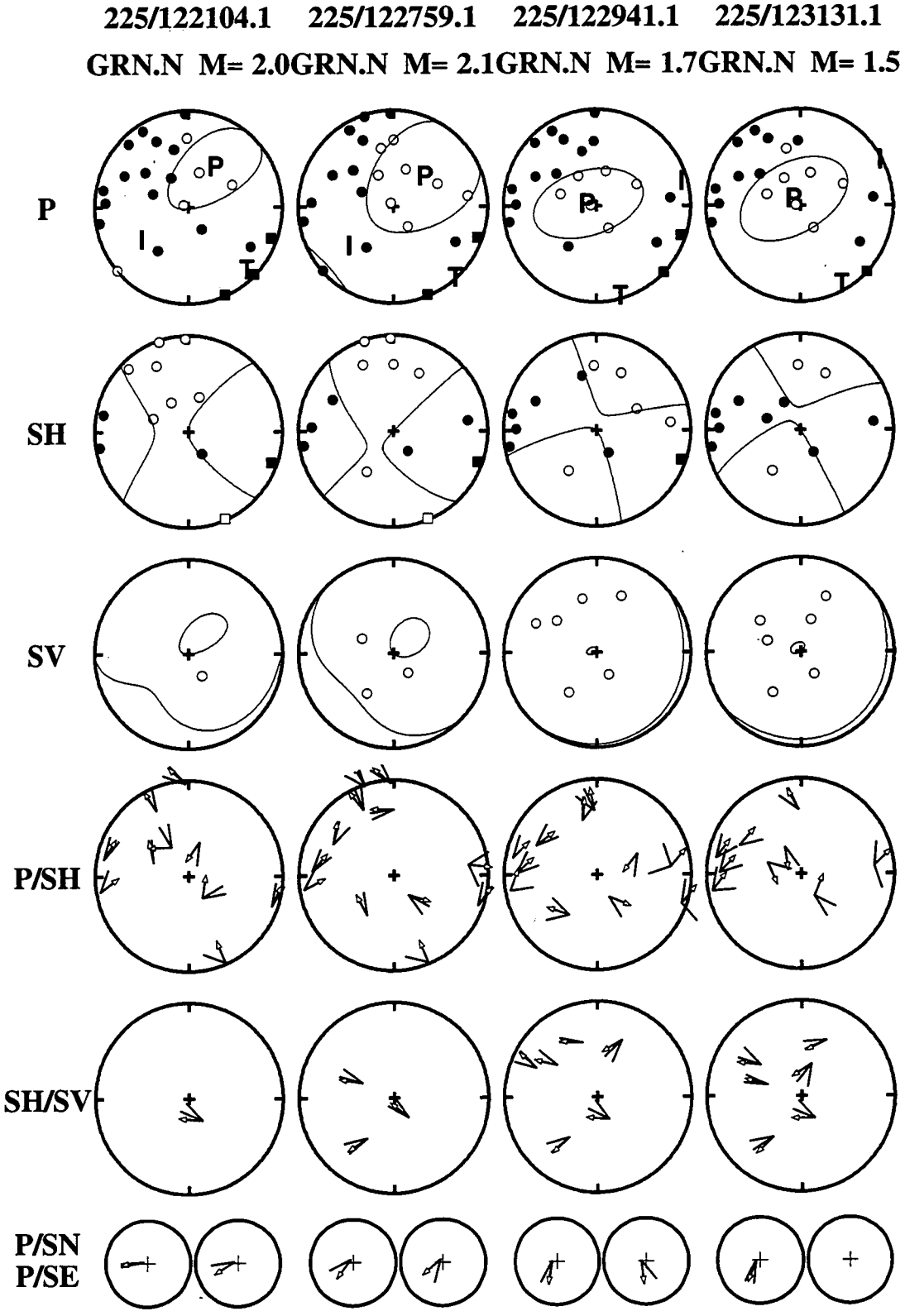
225/122104.1 225/122759.1 225/122941.1 225/123131.1
GRN.N M= 2.0GRN.N M= 2.1GRN.N M= 1.7GRN.N M= 1.5
P
SH
SV
P/SH
SH/SV
P/SN
P/SE

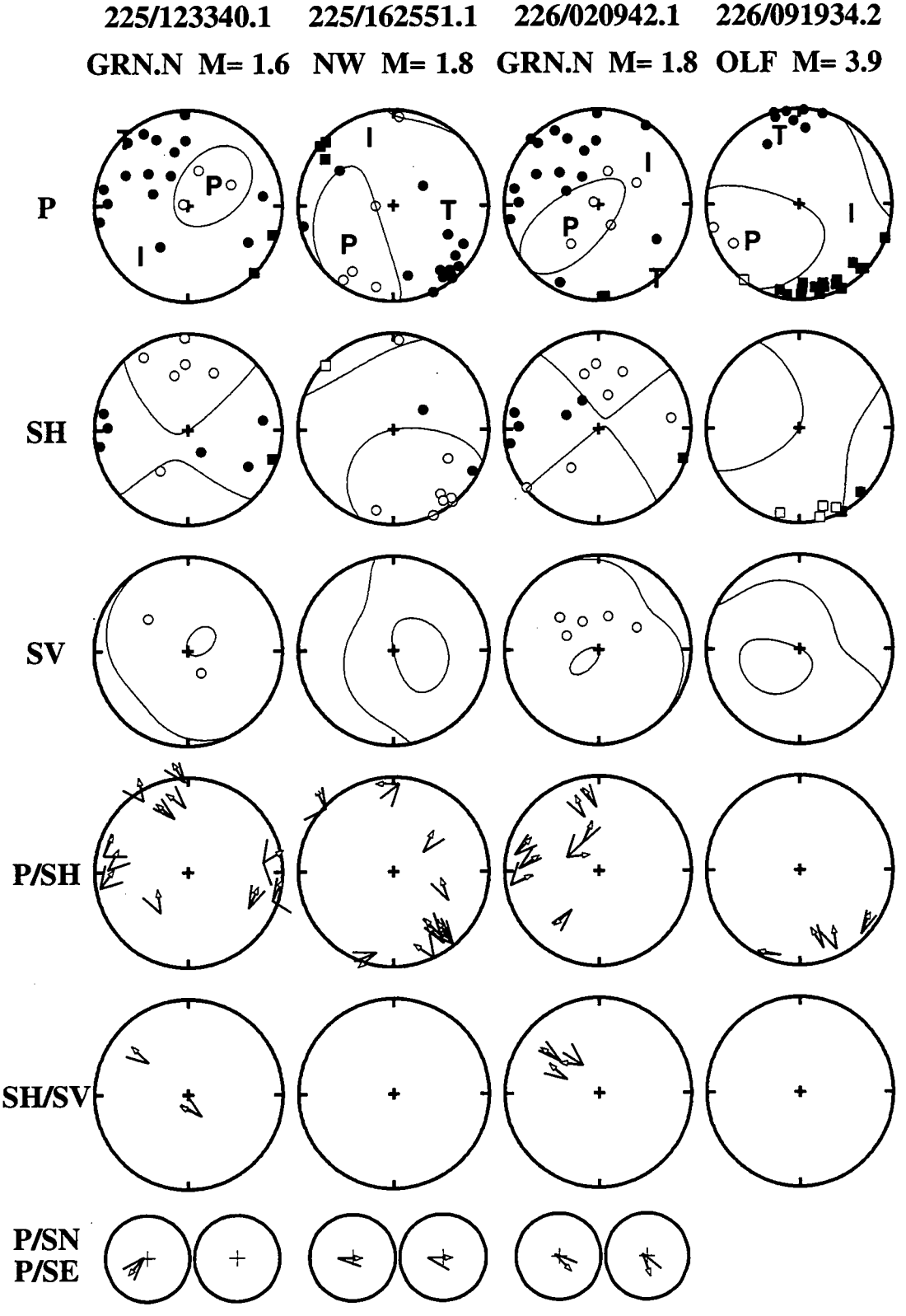
225/123340.1
GRN.N M= 1.6
225/162551.1
NW M= 1.8
226/020942.1
GRN.N M= 1.8
226/091934.2
OLF M= 3.9
P
SH
SV
P/SH
SH/SV
P/SN
P/SE
T
P
I

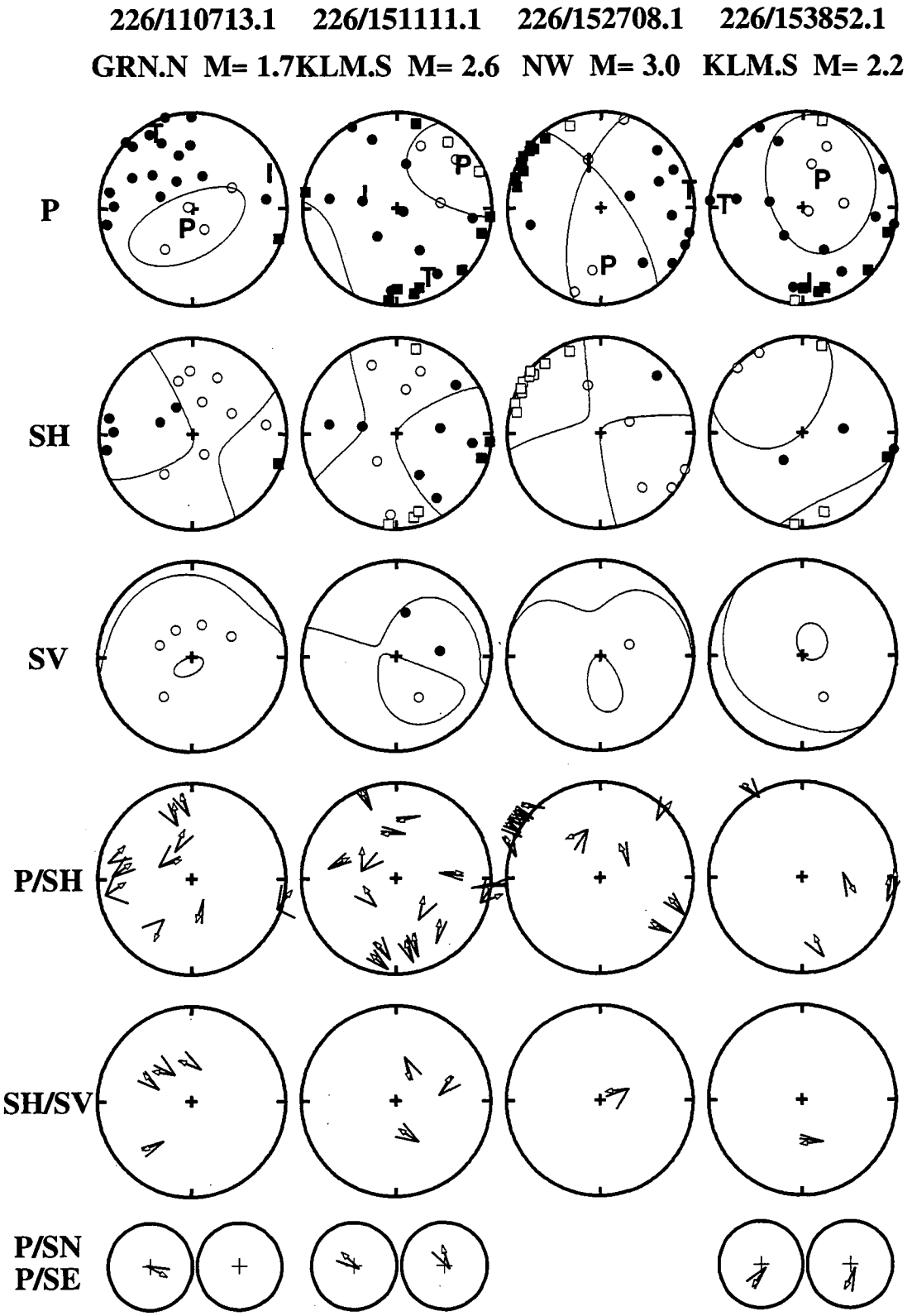
226/110713.1 226/151111.1 226/152708.1 226/153852.1
GRN.N M= 1.7 KLM.S M= 2.6 NW M= 3.0 KLM.S M= 2.2
P
SH
SV
P/SH
SH/SV
P/SN
P/SE

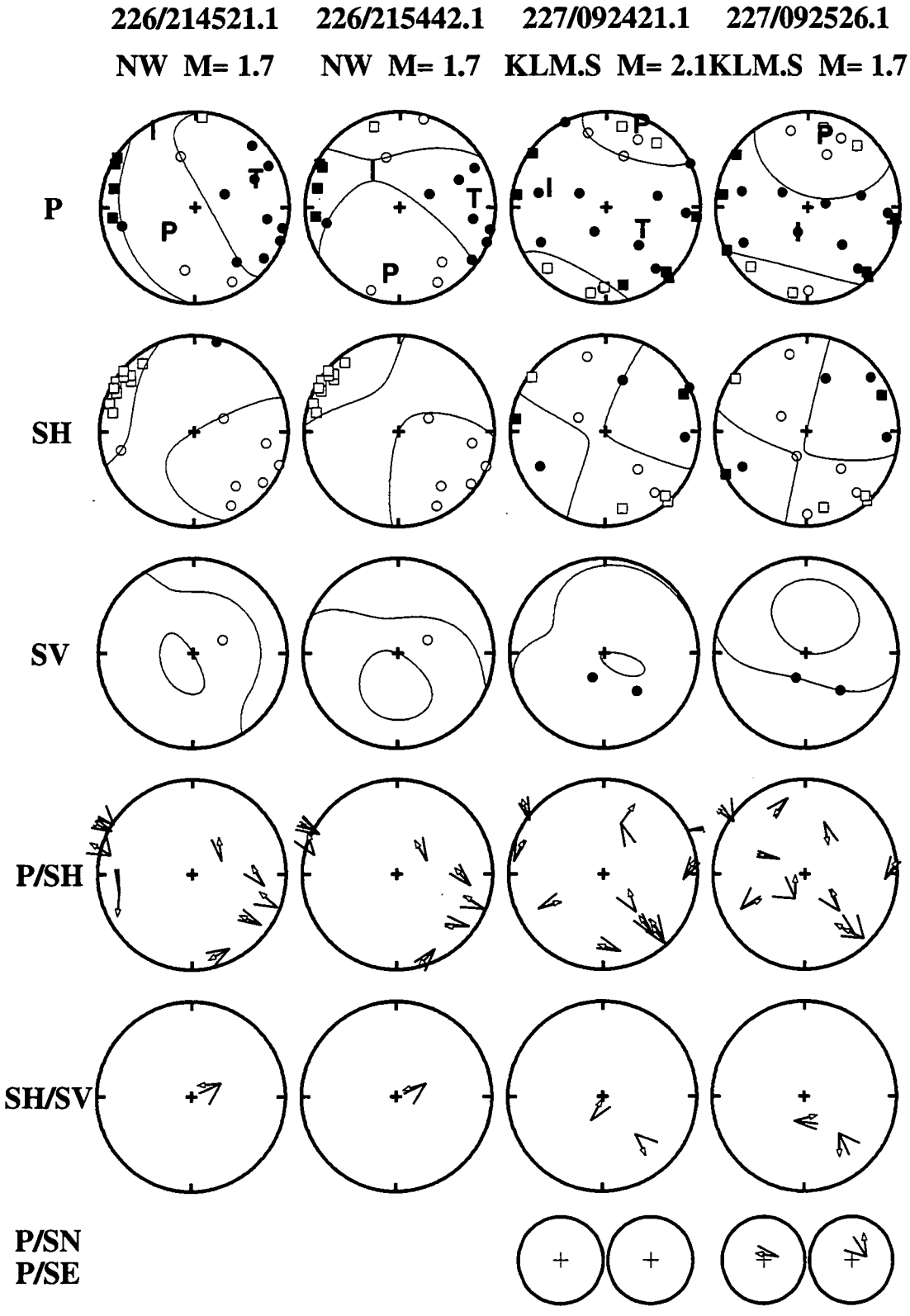
226/214521.1
NW M= 1.7
226/215442.1
NW M= 1.7
227/092421.1
KLM.S M= 2.1
227/092526.1
KLM.S M= 1.7
P
SH
SV
P/SH
SH/SV
P/SN
P/SE

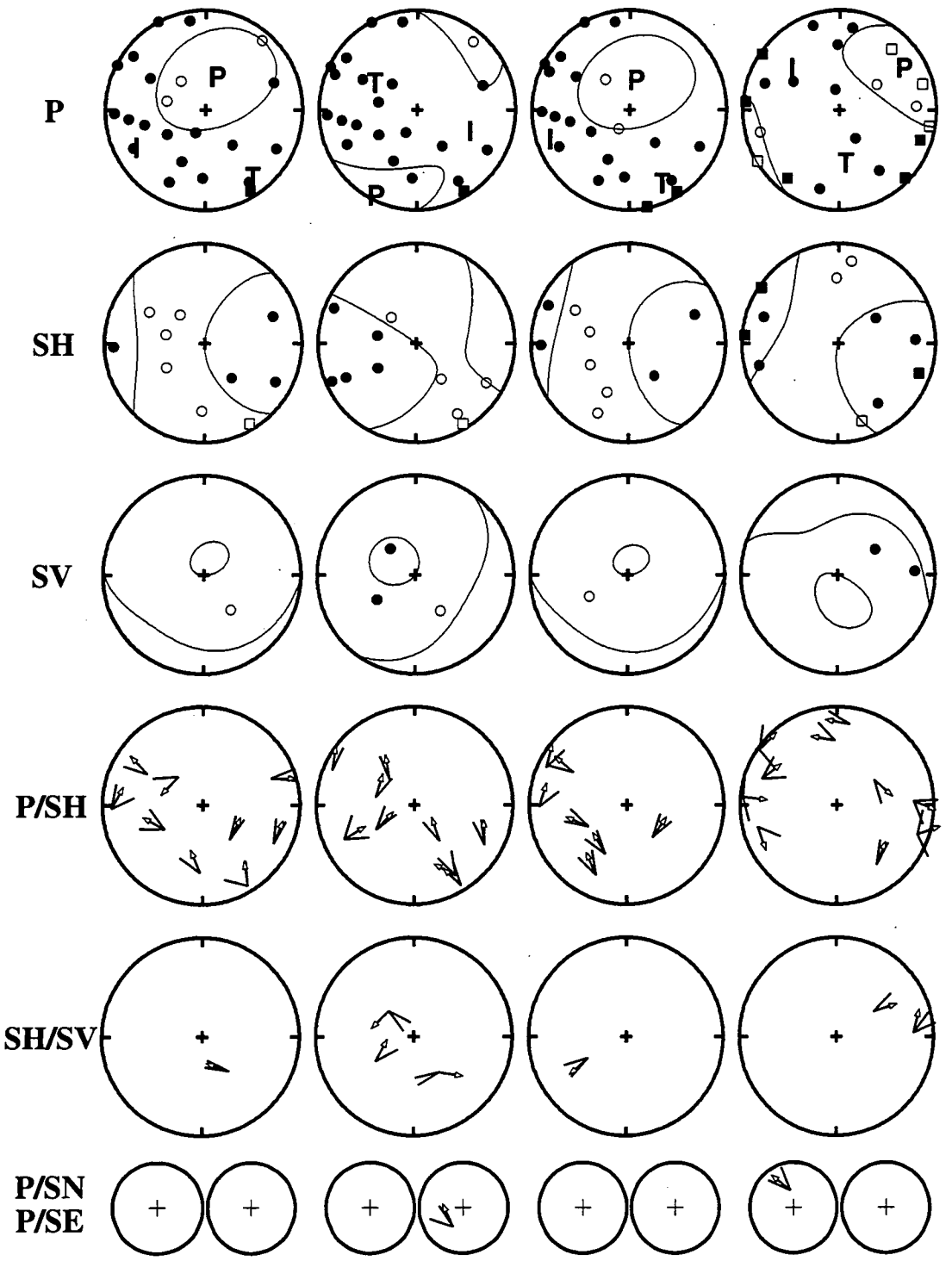
228/040122.1
KLM.N M= 1.7
228/045401.1
KLM.N M= 1.9
228/083300.1
KLM.N M= 1.9
229/033558.1
KLM.S M= 1.2
P
SH
SV
P/SH
SH/SV
P/SN
P/SE

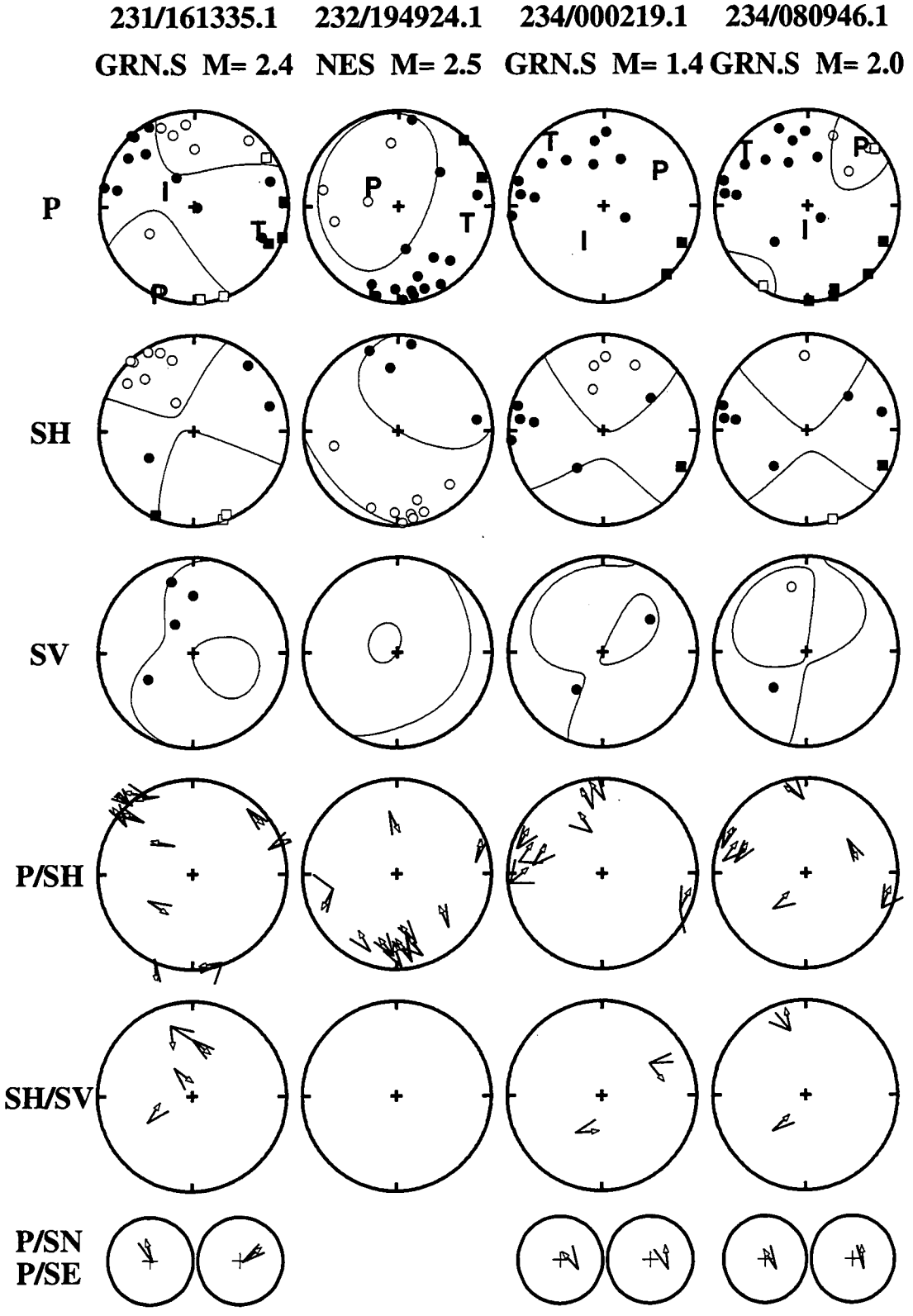
231/161335.1
GRN.S M= 2.4
232/194924.1
NES M= 2.5
234/000219.1
GRN.S M= 1.4
234/080946.1
GRN.S M= 2.0
P
SH
SV
P/SH
SH/SV
P/SN
P/SE

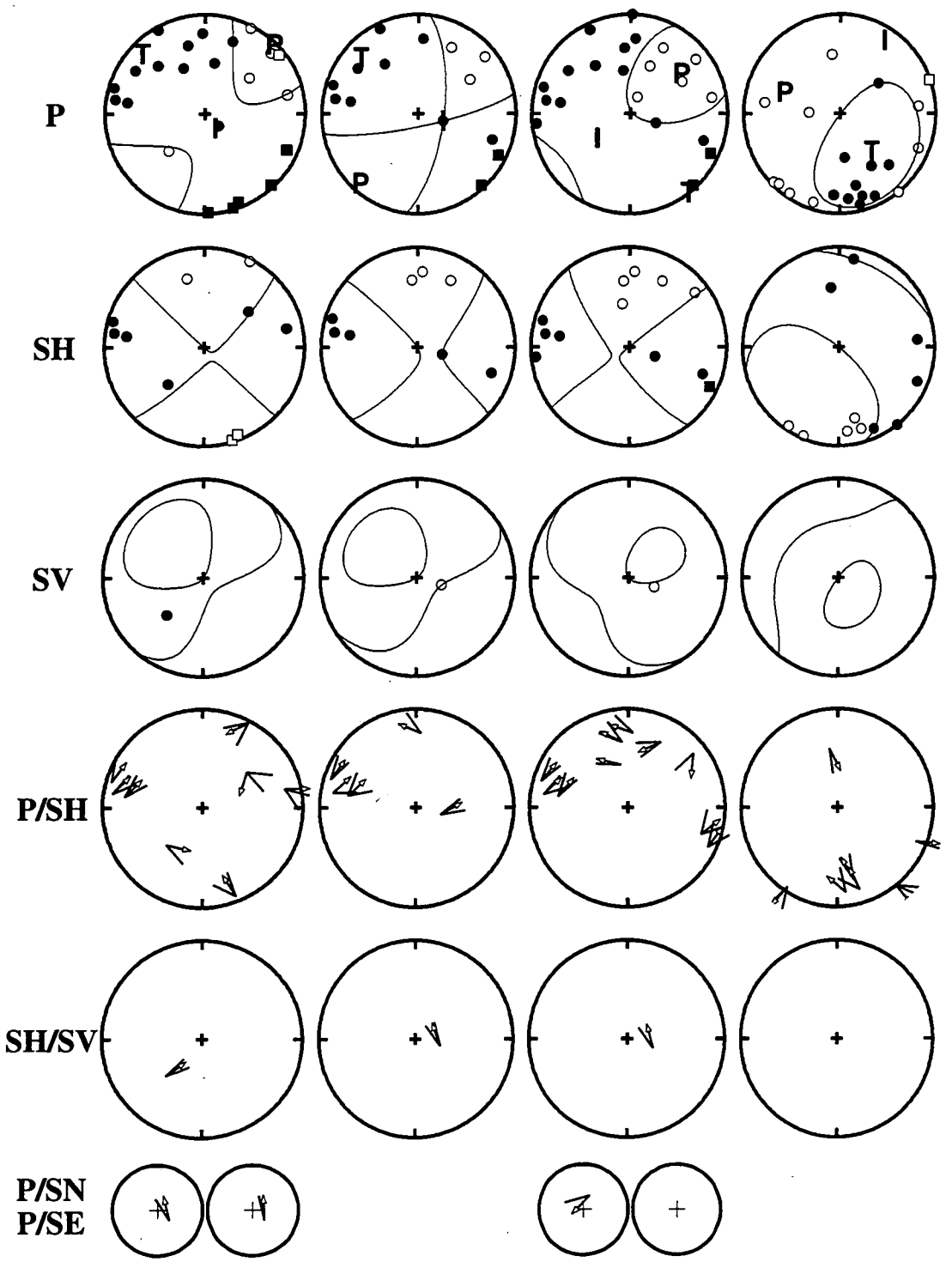
234/183633.1 GRN.S M= 2.2
236/052400.1 GRN.S M= 1.3
236/065252.1 GRN.S M= 1.6
237/212559.1 NES M= 2.6
P
SH
SV
P/SH
SH/SV
P/SN
P/SE

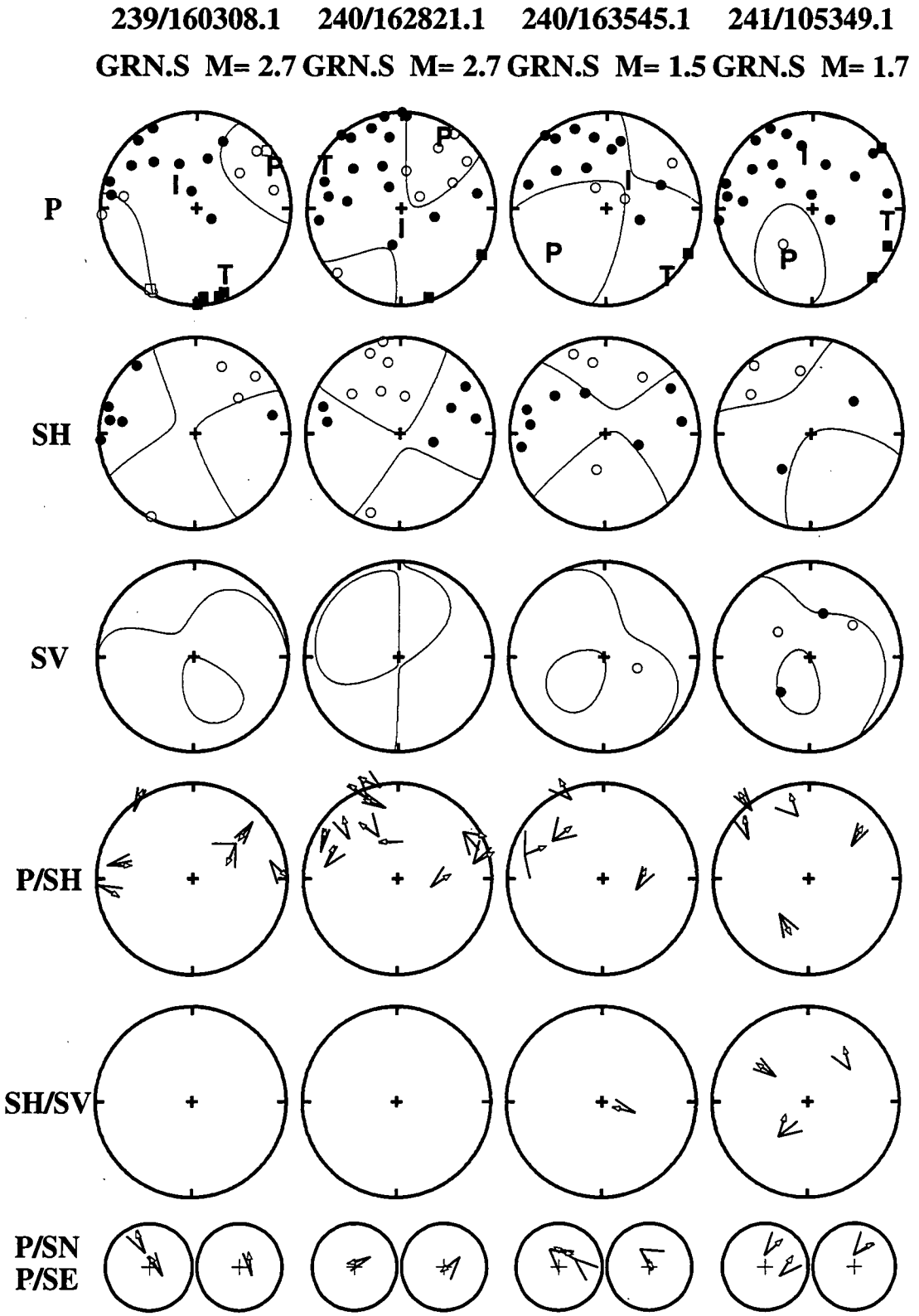
239/160308.1 GRN.S M= 2.7
240/162821.1 GRN.S M= 2.7
240/163545.1 GRN.S M= 1.5
241/105349.1 GRN.S M= 1.7
P
SH
SV
P/SH
SH/SV
P/SN
P/SE

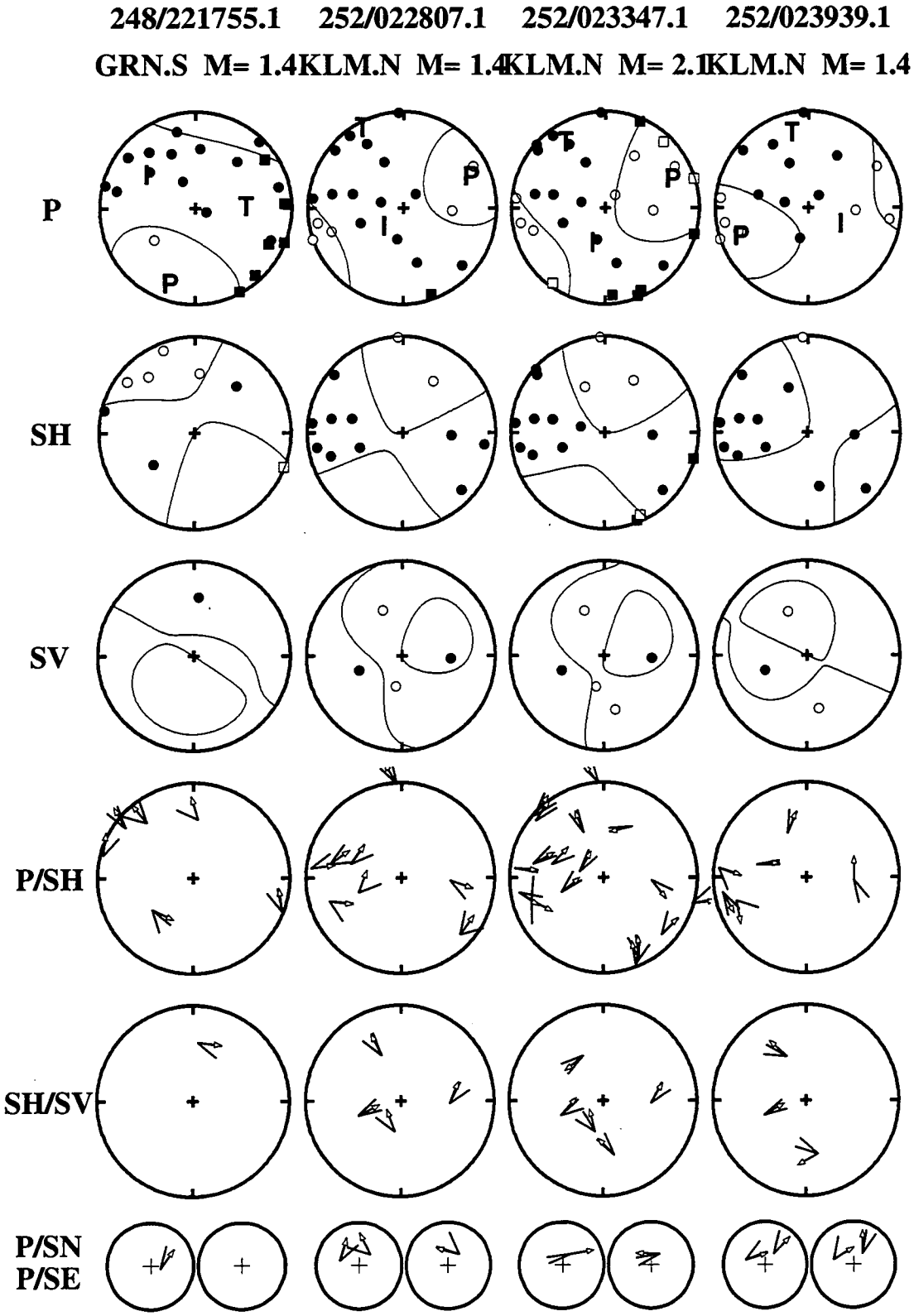
248/221755.1 252/022807.1 252/023347.1 252/023939.1
GRN.S M= 1.4KLM.N M= 1.4KLM.N M= 2.1KLM.N M= 1.4
P
SH
SV
P/SH
SH/SV
P/SN
P/SE
T
P
I

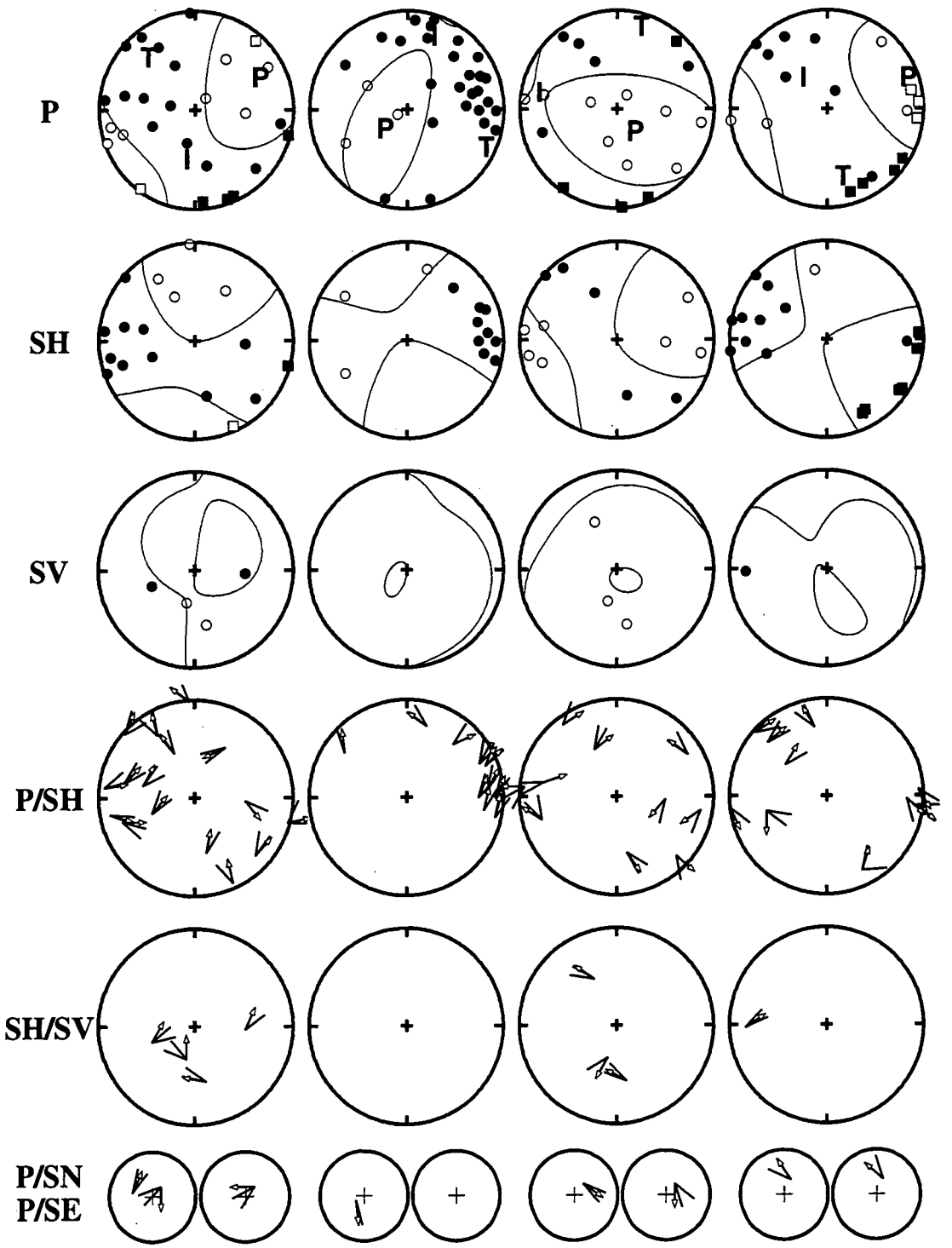
252/044910.1 KLM.N M= 1.9
252/050156.1 GIG M= 2.4
252/112006.1 KLM.N M= 1.7
253/125604.1 KLM.N M= 1.6
P
SH
SV
P/SH
SH/SV
P/SN
P/SE

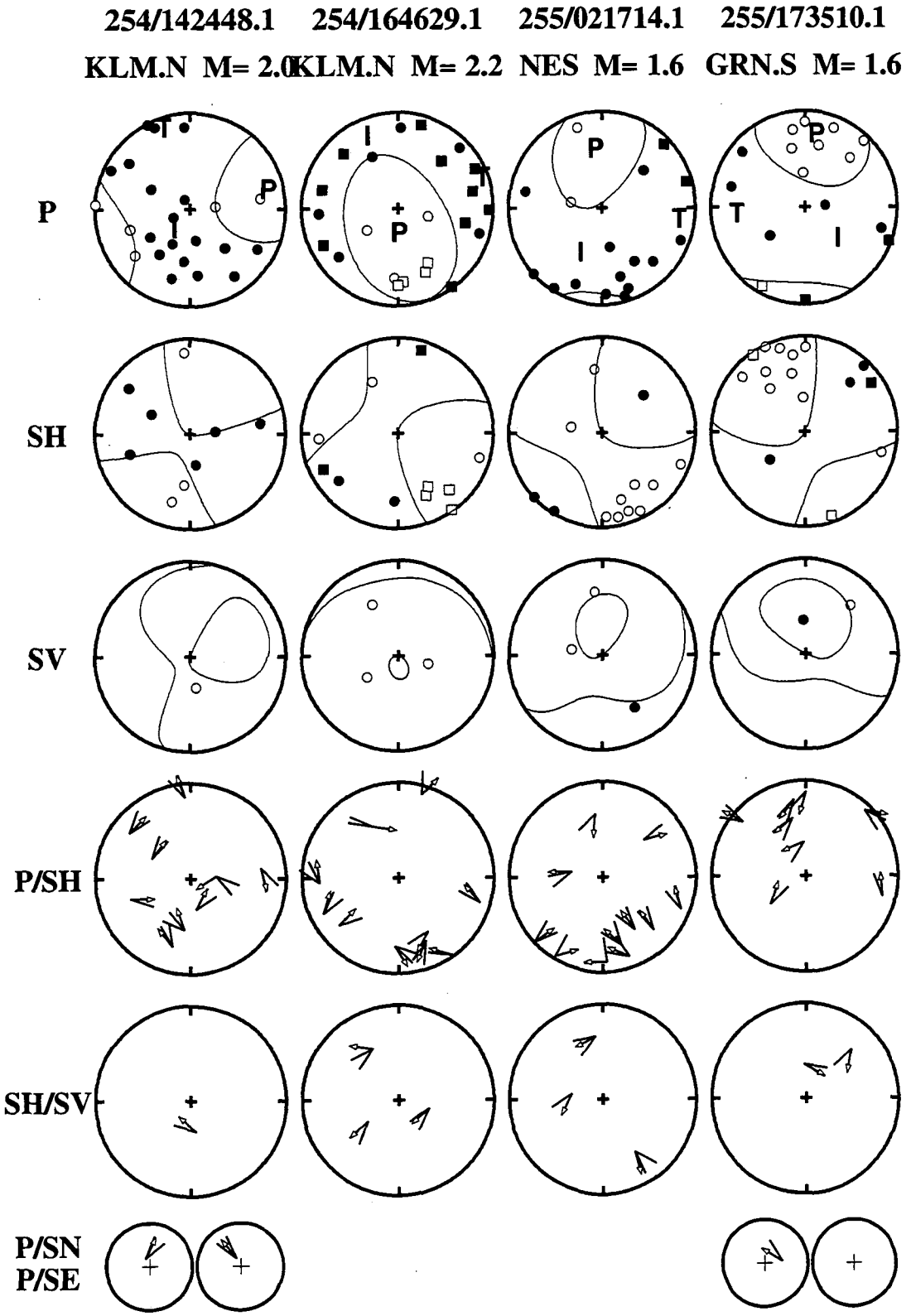
254/142448.1 KLM.N M= 2.0
254/164629.1 KLM.N M= 2.2
255/021714.1 NES M= 1.6
255/173510.1 GRN.S M= 1.6
P
SH
SV
P/SH
SH/SV
P/SN
P/SE

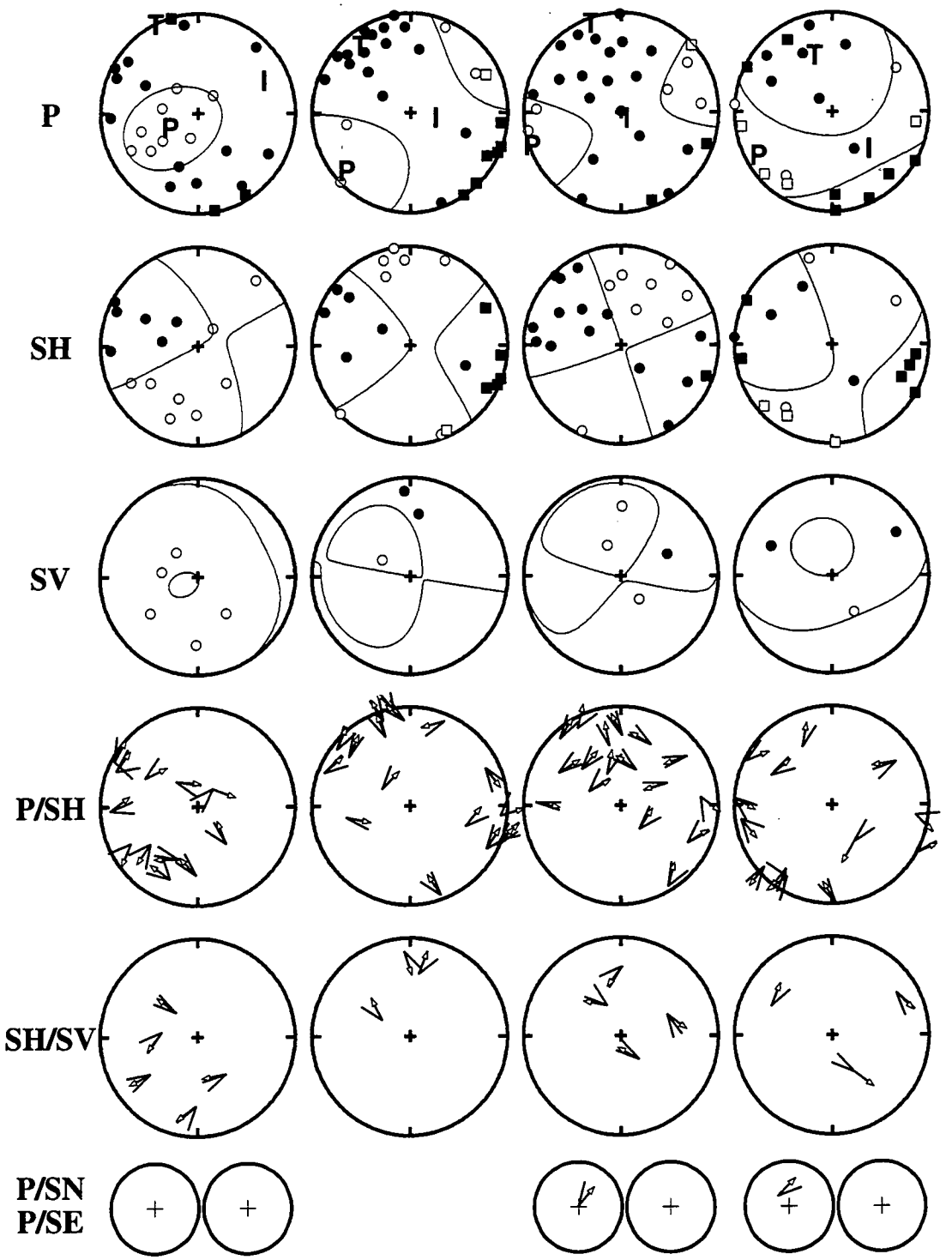
256/235841.1 KLM.N M= 1.7
257/073459.1 GRN.E M= 1.9
258/074123.1 GRN.N M= 1.7
258/090235.1 GRN.N M= 1.6
P
SH
SV
P/SH
SH/SV
P/SN
P/SE
T
P

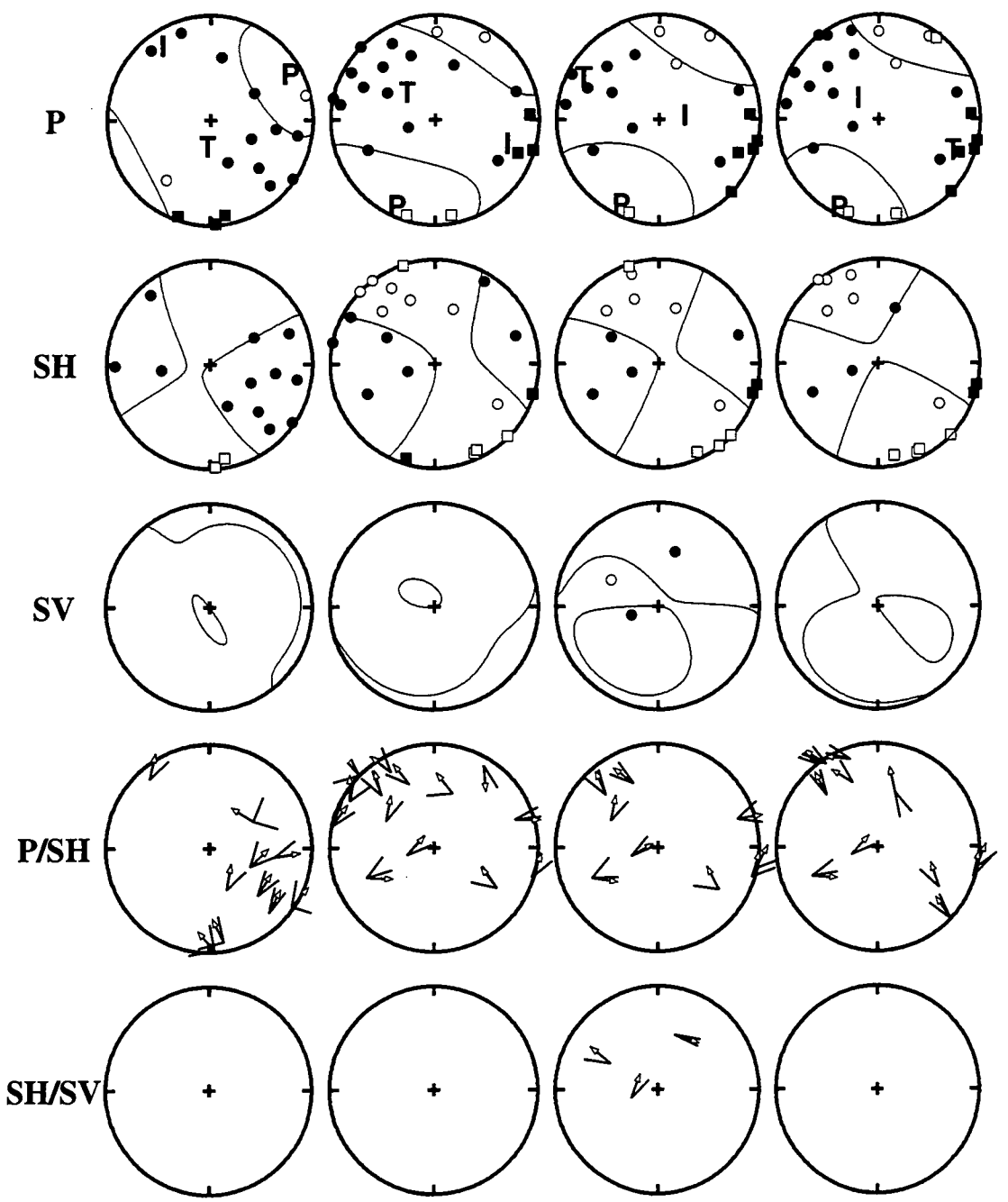
262/140501.1 264/053355.1 264/193202.1 264/212351.1
KLM.S M= 1.2GRN.E M= 1.7GRN.E M= 1.5GRN.E M= 2.0
P
SH
SV
P/SH
SH/SV
P/SN
P/SE

264/234218.1 KLM.S M= 1.9
265/030152.1 GRN.E M= 1.6
265/040149.1 GRN.E M= 1.6
265/191813.1 KLM.S M= 1.4

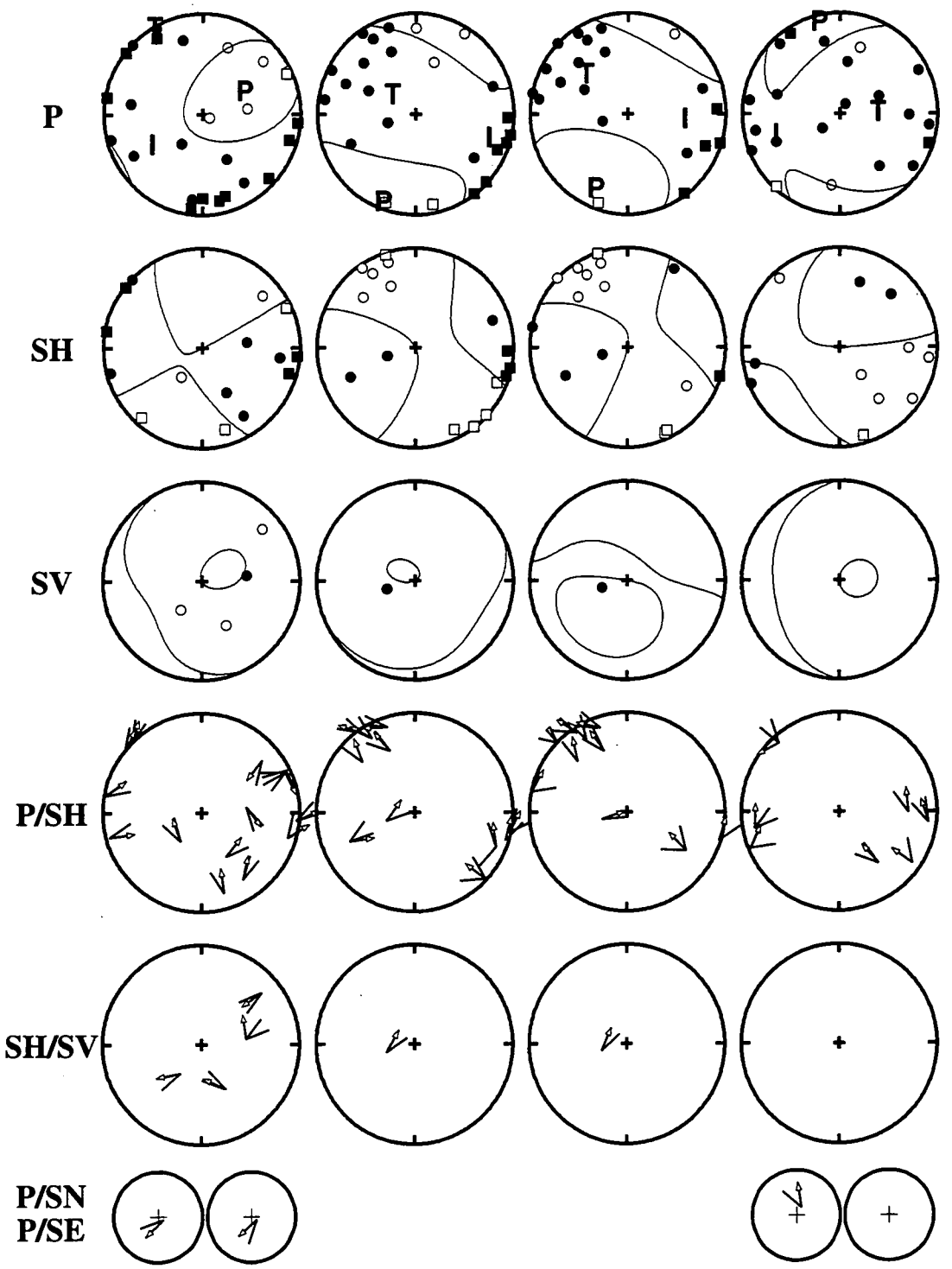

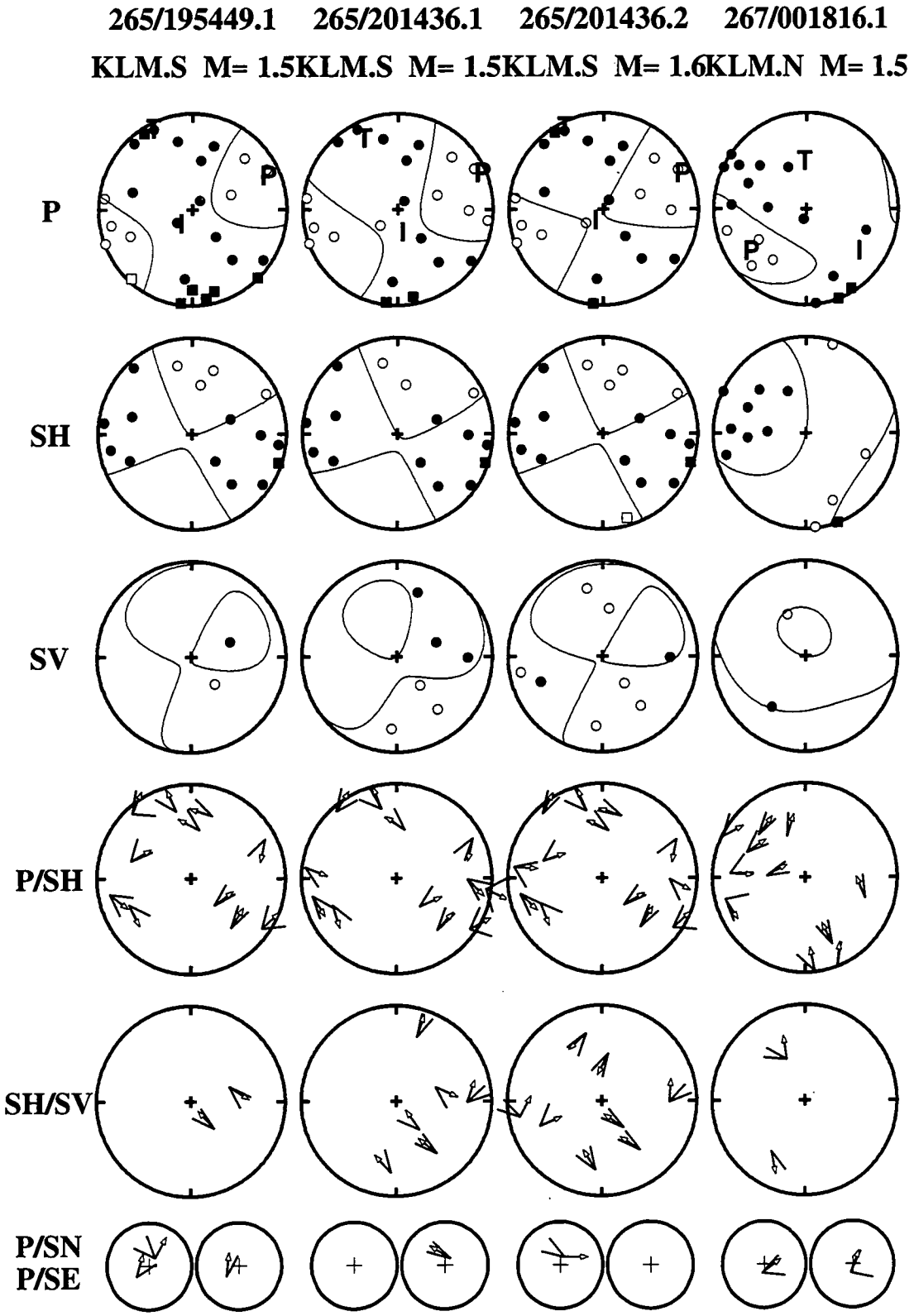
265/195449.1 265/201436.1 265/201436.2 267/001816.1
KLM.S M= 1.5KLM.S M= 1.5KLM.S M= 1.6KLM.N M= 1.5
P
SH
SV
P/SH
SH/SV
P/SN
P/SE
T
P
I

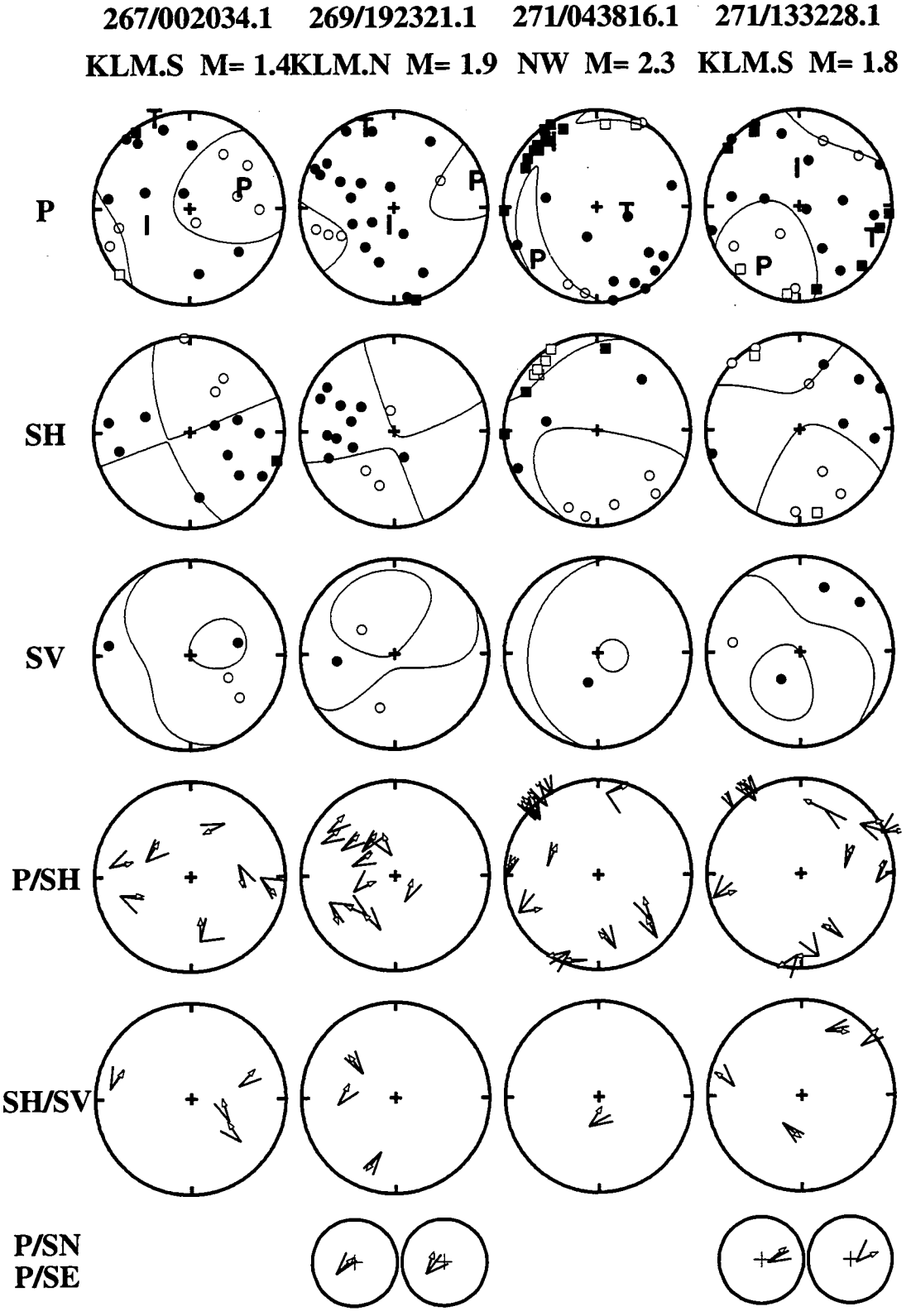
267/002034.1 KLM.S M= 1.4
269/192321.1 KLM.N M= 1.9
271/043816.1 NW M= 2.3
271/133228.1 KLM.S M= 1.8
P
SH
SV
P/SH
SH/SV
P/SN
P/SE

271/154632.1 272/130250.1

GRN.S M= 1.8KLM.N M= 2.1

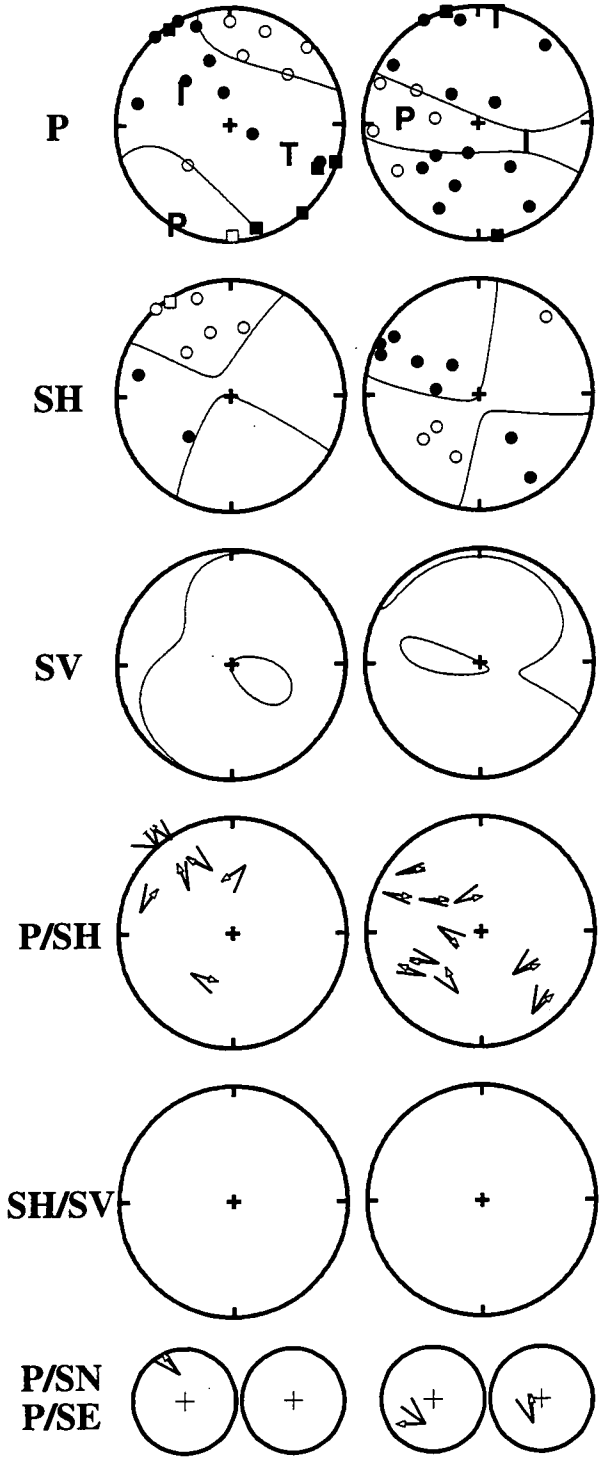

Appendix 9

Relative locations and focal mechanisms

The relative locations and *P*-wave radiation patterns of the earthquakes for which moment tensors were determined are shown here within the geographical groups. Lines connect the focal mechanisms to the epicentral positions. The positions of nearby stations are indicated on each map. For each earthquake, the *P*-wave nodal lines are shown on upper-hemisphere equal-area projections. *P*, *T* and *I* show axis positions.

Group GIG

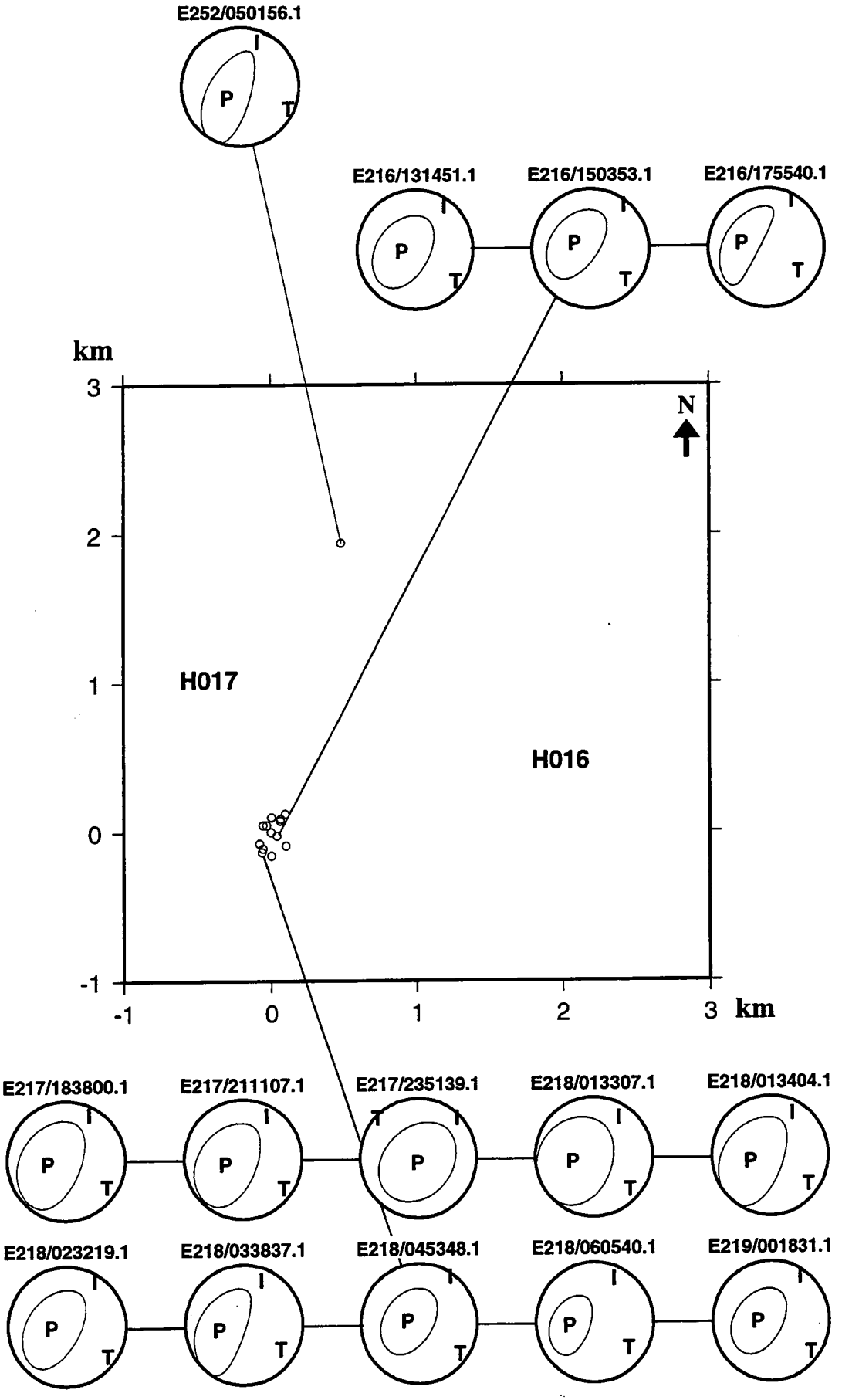
E252/050156.1
E216/131451.1
E216/150353.1
E216/175540.1
km
3
2
1
0
-1
N
H017
H016
-1
0
1
2
3 km
E217/183800.1
E217/211107.1
E217/235139.1
E218/013307.1
E218/013404.1
E218/023219.1
E218/033837.1
E218/045348.1
E218/060540.1
E219/001831.1
P
T

Group GRN.E

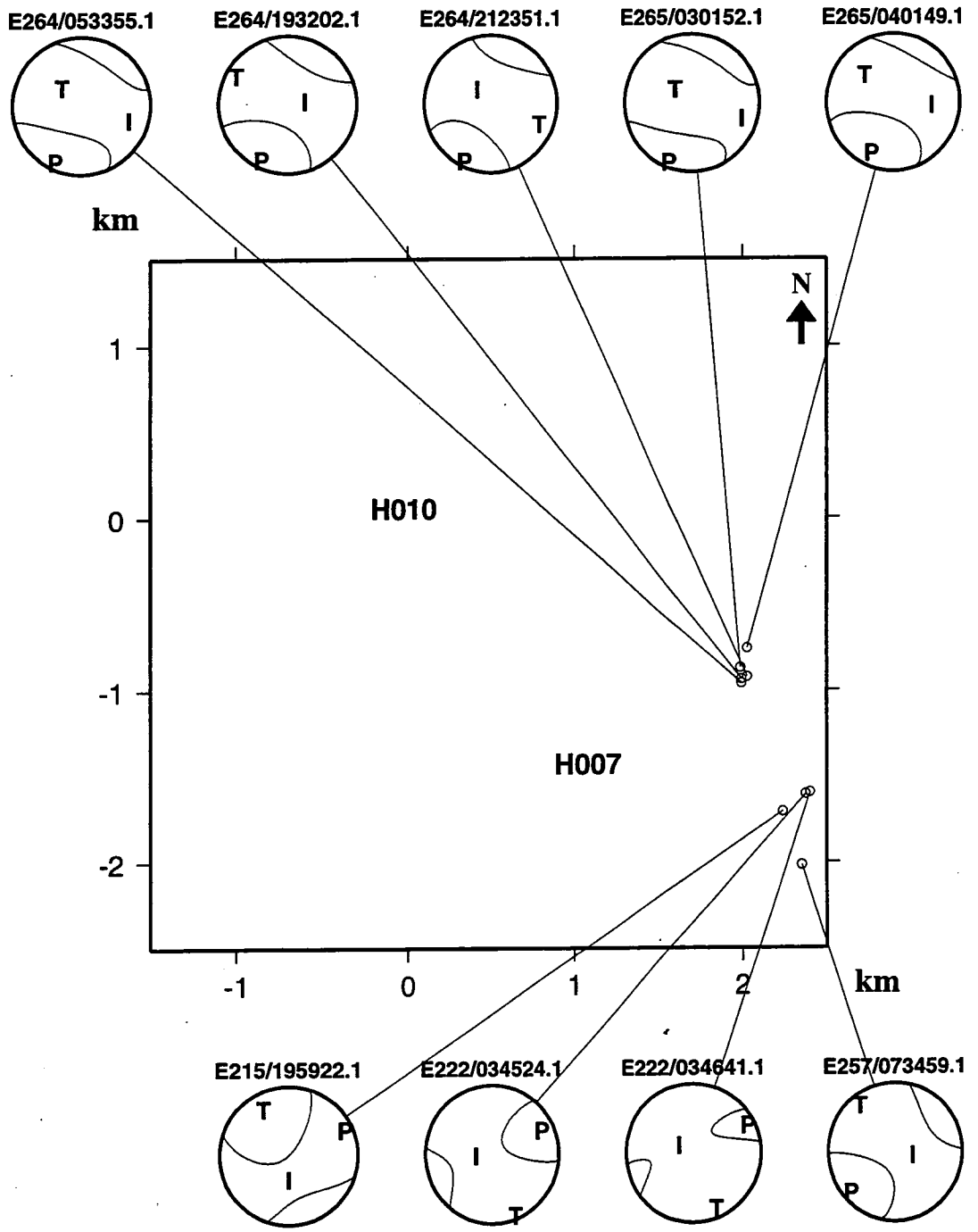
E264/053355.1
E264/193202.1
E264/212351.1
E265/030152.1
E265/040149.1
T
I
P
km
N
1
0
-1
-2
H010
H007
-1
0
1
2
km
E215/195922.1
E222/034524.1
E222/034641.1
E257/073459.1

Group GRN.N

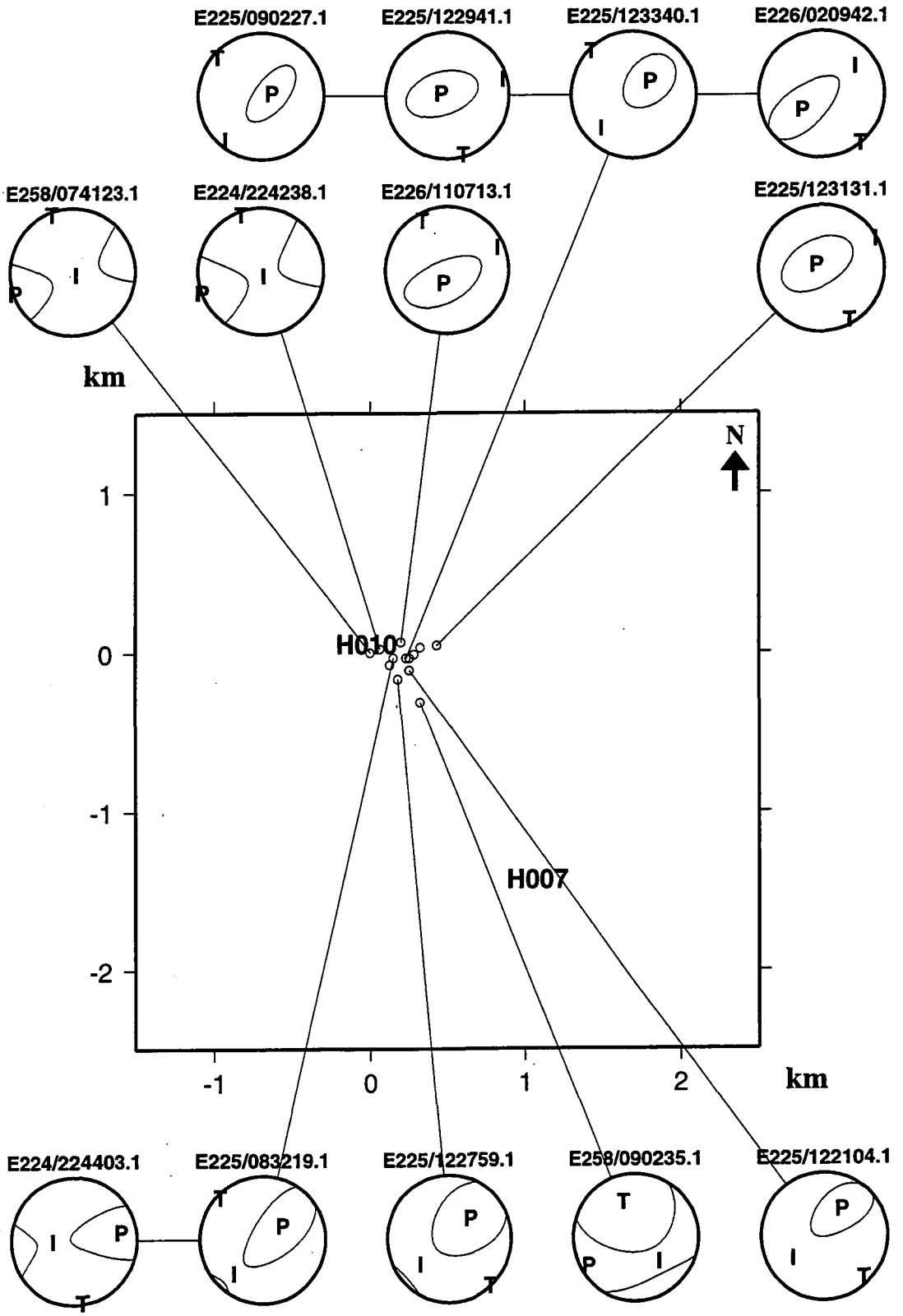
E225/090227.1
E225/122941.1
E225/123340.1
E226/020942.1
E258/074123.1
E224/224238.1
E226/110713.1
E225/123131.1
km
N
1
0
-1
-2
H010
H007
-1
0
1
2
km
E224/224403.1
E225/083219.1
E225/122759.1
E258/090235.1
E225/122104.1

Group GRN.S

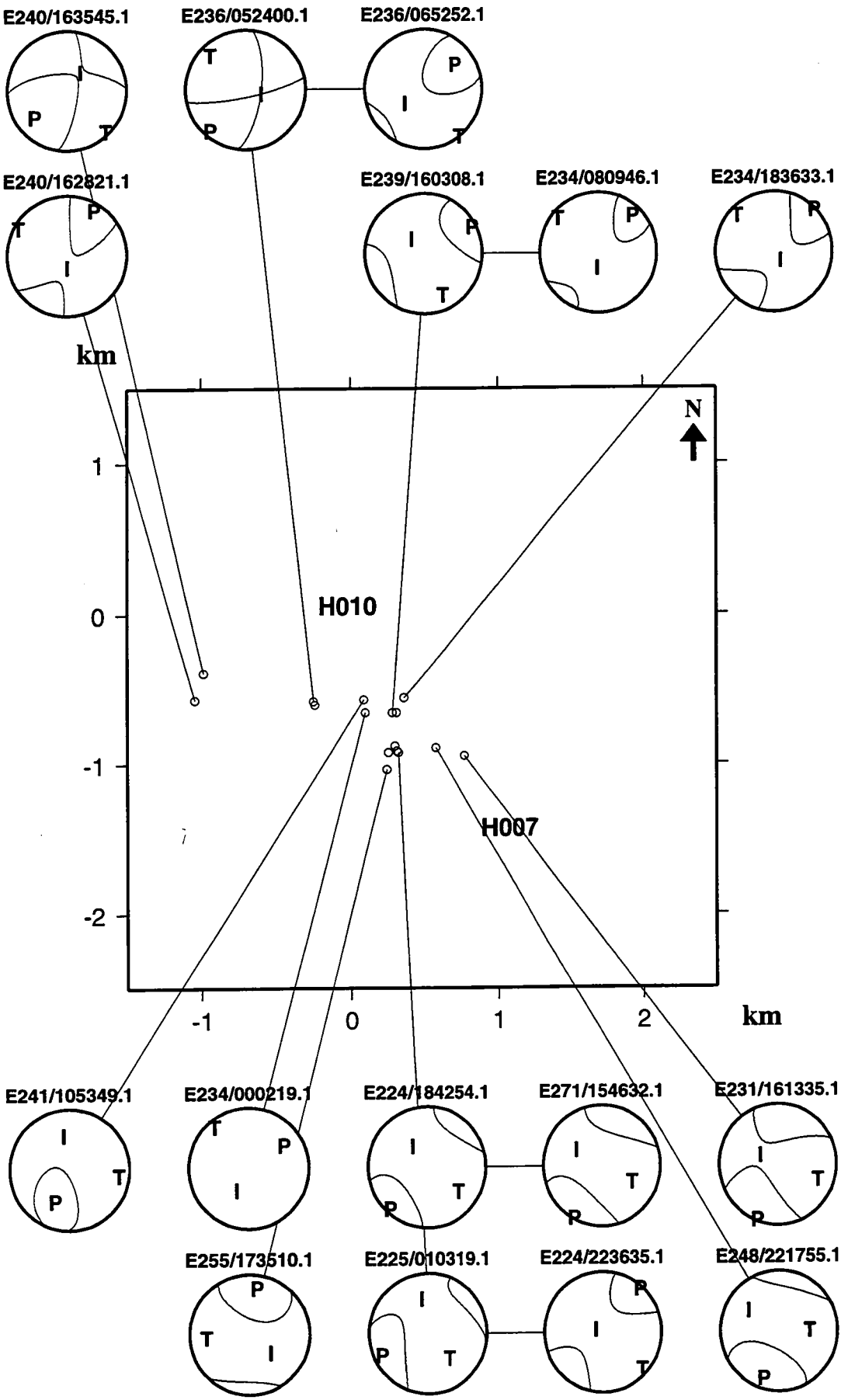
E240/163545.1
E236/052400.1
E236/065252.1
E240/162821.1
E239/160308.1
E234/080946.1
E234/183633.1
km
N
1
0
-1
-2
H010
H007
-1
0
1
2
km
E241/105349.1
E234/000219.1
E224/184254.1
E271/154632.1
E231/161335.1
E255/173510.1
E225/010319.1
E224/223635.1
E248/221755.1

Group KLM.N

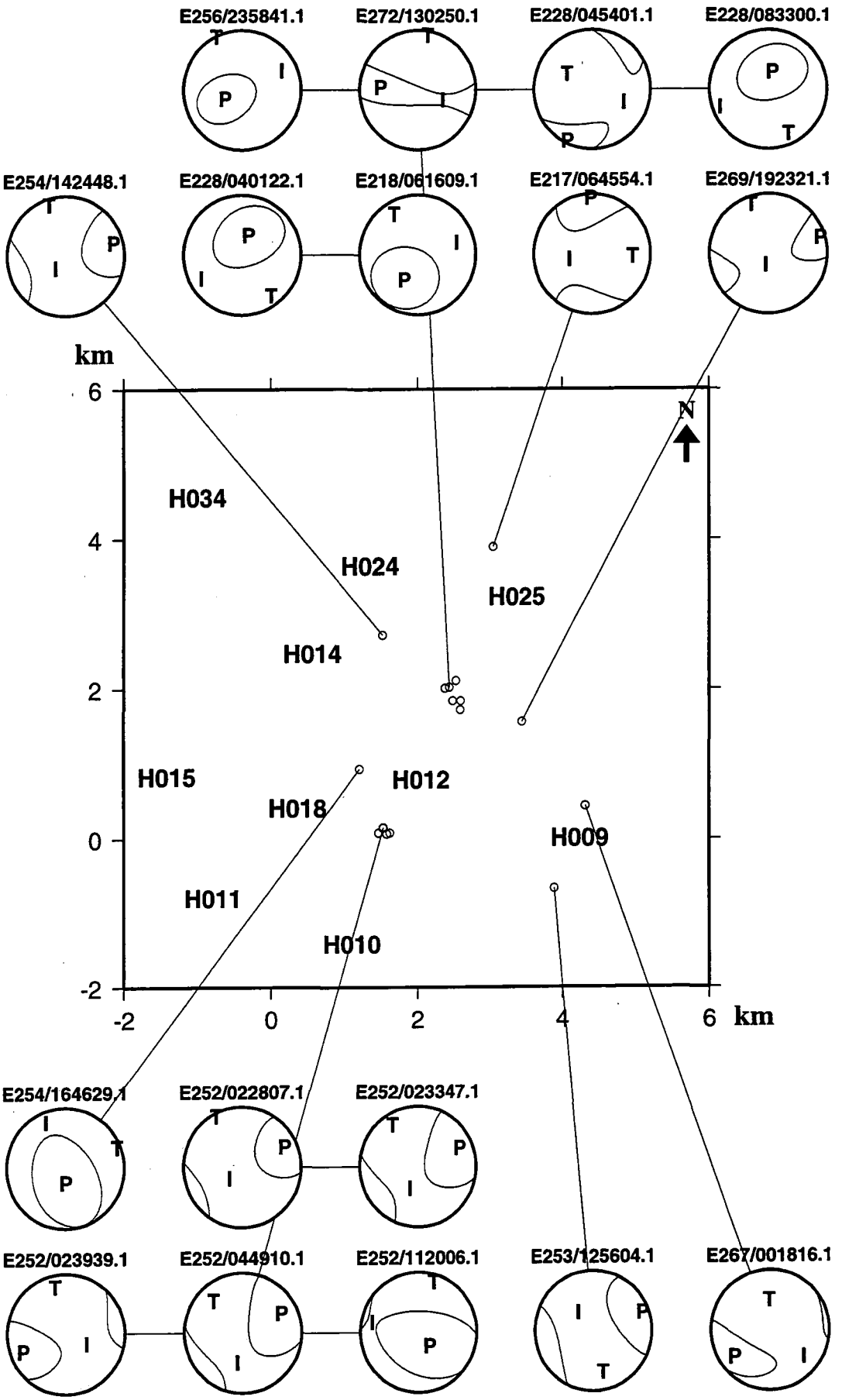
E256/235841.1
E272/130250.1
E228/045401.1
E228/083300.1
E254/142448.1
E228/040122.1
E218/061609.1
E217/064554.1
E269/192321.1
km
6
4
2
0
-2
-2
0
2
4
6 km
N
H034
H024
H025
H014
H015
H012
H018
H009
H011
H010
E254/164629.1
E252/022807.1
E252/023347.1
E252/023939.1
E252/044910.1
E252/112006.1
E253/125604.1
E267/001816.1

Group KLM.S

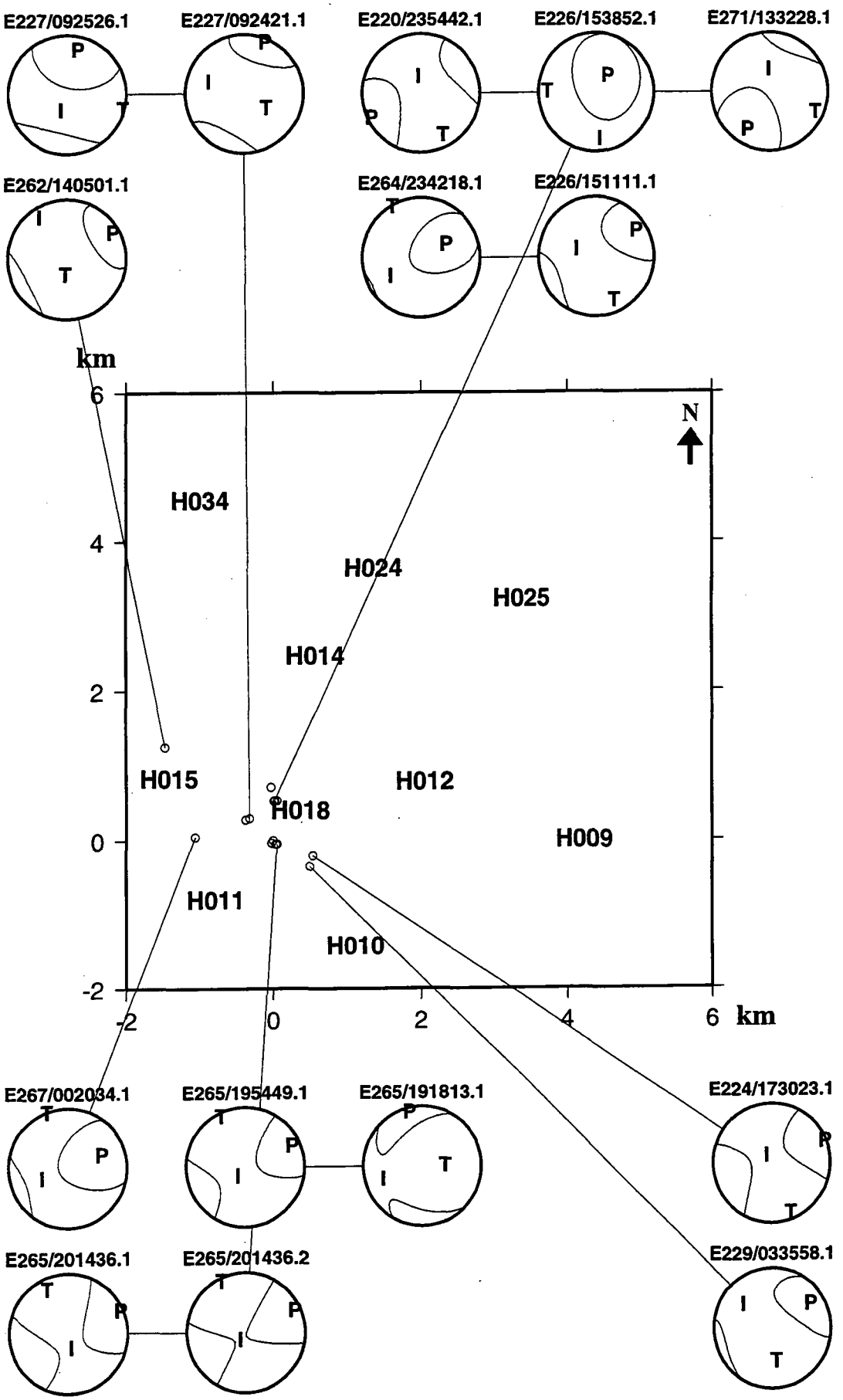
E227/092526.1
E227/092421.1
E220/235442.1
E226/153852.1
E271/133228.1
E262/140501.1
E264/234218.1
E226/151111.1
km
6
4
2
0
-2
-2
0
2
4
6 km
N
H034
H024
H025
H014
H015
H012
H018
H009
H011
H010
E267/002034.1
E265/195449.1
E265/191813.1
E224/173023.1
E265/201436.1
E265/201436.2
E229/033558.1

Groups NW and NES

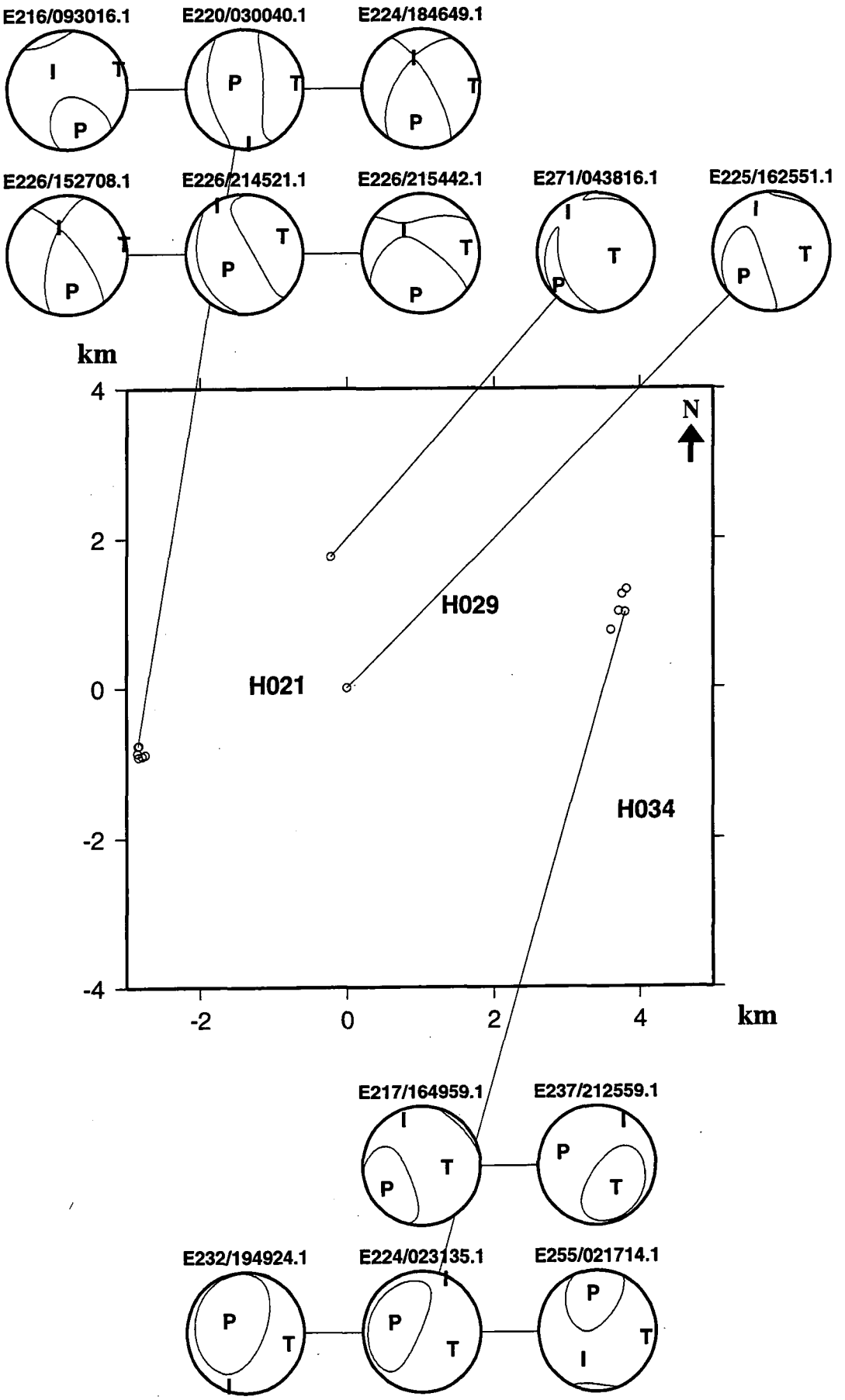

Appendix 10

Moment tensor components for an opening-shear fault

The moment tensor of an opening-shear fault can be calculated by adding together the moment tensors of a shear fault and a tensile fault that share the same fault plane. Following the conventions of *Aki and Richards* (1980, p. 114), fault strike (ϕ_s) is measured clockwise from north, fault dip (δ) is measured downwards from the horizontal, and fault rake (λ) is measured in the fault plane, upwards from the horizontal. The cartesian coordinate directions **x**, **y**, **z** are north, east and down repectively.

The moment tensor for the shear-fault component of an opening-tensile fault is (*Aki and Richards*, 1980, box 4.4):

$$
\begin{aligned}
M_{xx} &= -M_{SF}\left(\sin\delta\cos\lambda\sin 2\phi_s + \sin 2\delta\sin\lambda\sin^2\phi_s\right) \\
M_{xy} &= M_{SF}\left(\sin\delta\cos\lambda\cos 2\phi_s + \tfrac{1}{2}\sin 2\delta\sin\lambda\sin 2\phi_s\right) \\
M_{xz} &= -M_{SF}\left(\cos\delta\cos\lambda\cos\phi_s + \cos 2\delta\sin\lambda\sin\phi_s\right) \\
M_{yy} &= M_{SF}\left(\sin\delta\cos\lambda\sin 2\phi_s - \sin 2\delta\sin\lambda\cos^2\phi_s\right) \\
M_{yz} &= -M_{SF}\left(\cos\delta\cos\lambda\sin\phi_s - \cos 2\delta\sin\lambda\cos\phi_s\right) \\
M_{zz} &= M_{SF}\left(\sin 2\delta\sin\lambda\right)
\end{aligned}
\qquad \text{A10.1}
$$

For the tensile-fault component the moment tensor can be calculated by rotating a horizontal tensile fault moment tensor using equations 4-46 of *Goldstein* (1950) to calculate the rotation matrix A, with $\phi = 0$, $\theta = 180 - \delta$ and $\varphi = -\phi_s$. Then the moment tensor of the tensile fault is:

$$
M = A\begin{pmatrix} 1 & 0 & 0 \\ 0 & 1 & 0 \\ 0 & 0 & 3 \end{pmatrix}A^T \qquad \text{A10.2}
$$

and

$$
\begin{aligned}
M_{xx} &= M_{TF}\left(\cos^2\phi_s + \sin^2\phi_s\left(2\sin^2\delta + 1\right)\right) \\
M_{xy} &= -2M_{TF}\left(\sin^2\delta\cos\phi_s\sin\phi_s\right) \\
M_{xz} &= 2M_{TF}\left(\cos\delta\sin\delta\sin\phi_s\right) \\
M_{yy} &= M_{TF}\left(\sin^2\phi_s + \cos^2\phi_s\left(2\sin^2\delta + 1\right)\right) \\
M_{yz} &= -2M_{TF}\left(\cos\delta\sin\delta\cos\phi_s\right) \\
M_{zz} &= M_{TF}\left(2\cos^2\delta + 1\right)
\end{aligned}
\qquad \text{A10.3}
$$

Appendix 11

Combined tensile-shear and opening-shear mechanisms

The earthquakes are arranged in chronological order within the geographical groups. Mechanisms are shown as *P*-wave radiation patterns in upper focal-sphere, equal-area projection. Bars at the side of the tensile-shear and opening-shear mechanisms show the strike of the tensile fault component. Values of R_{TF} are shown to the left of each mechanism.

General moment tensors — Group GIG

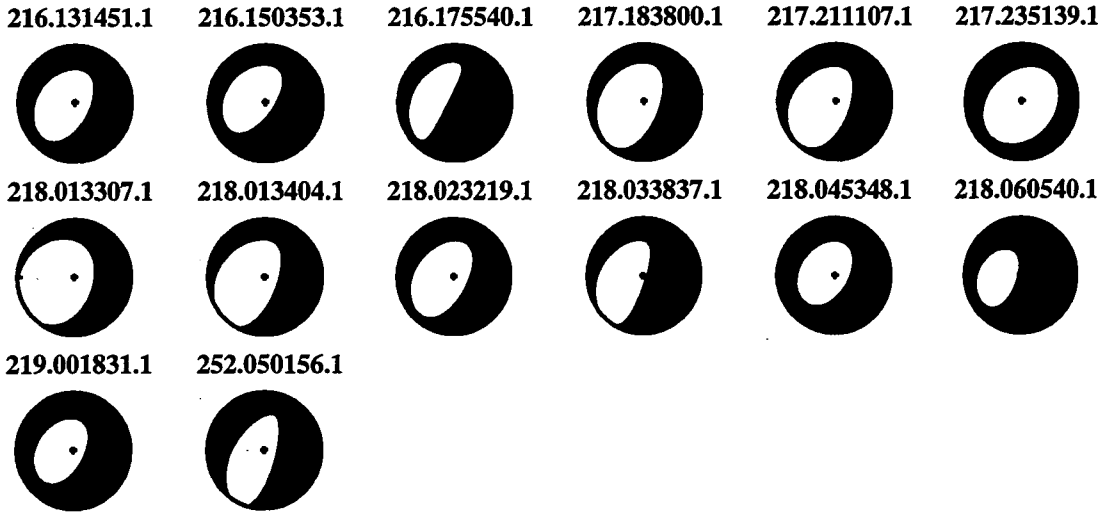

Combined tensile-shear mechanisms

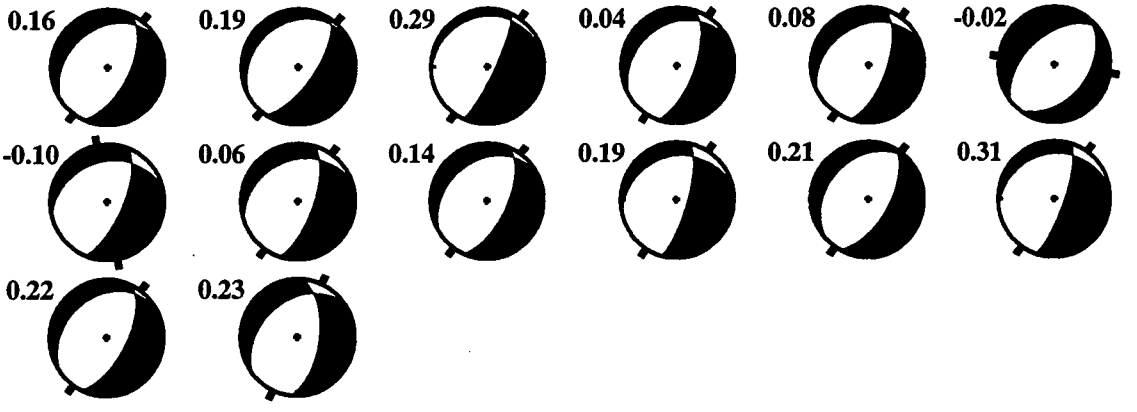

Right-lateral opening shear mechanisms

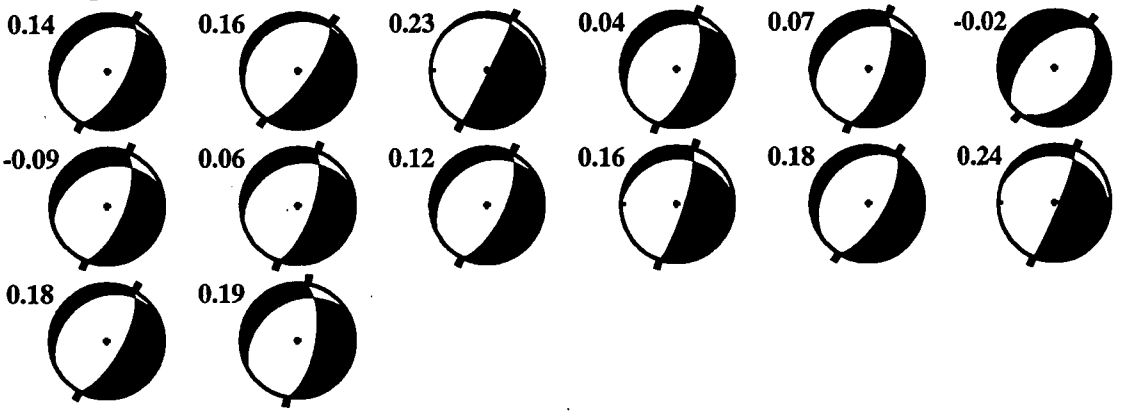

Left-lateral opening shear mechanisms

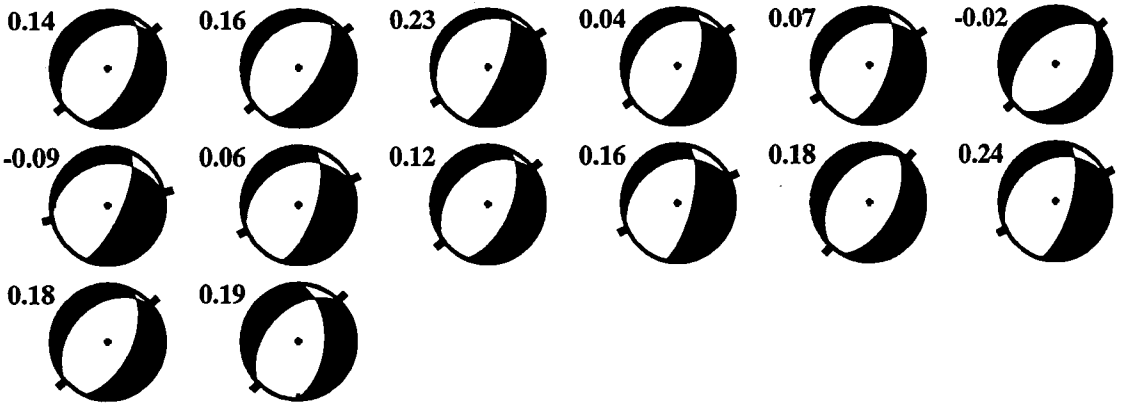

General moment tensors — Group GRN.E

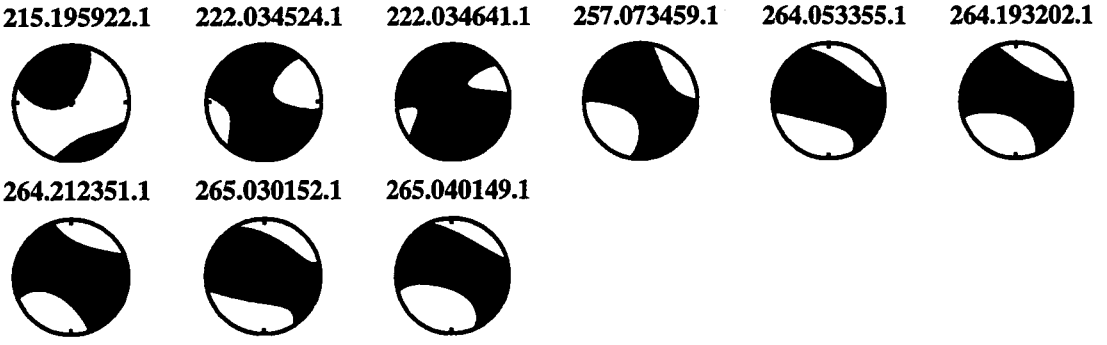

Combined tensile-shear mechanisms

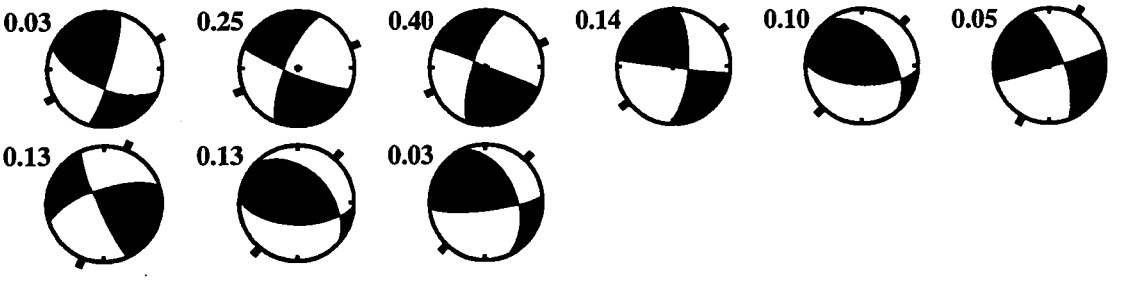

Right-lateral opening shear mechanisms

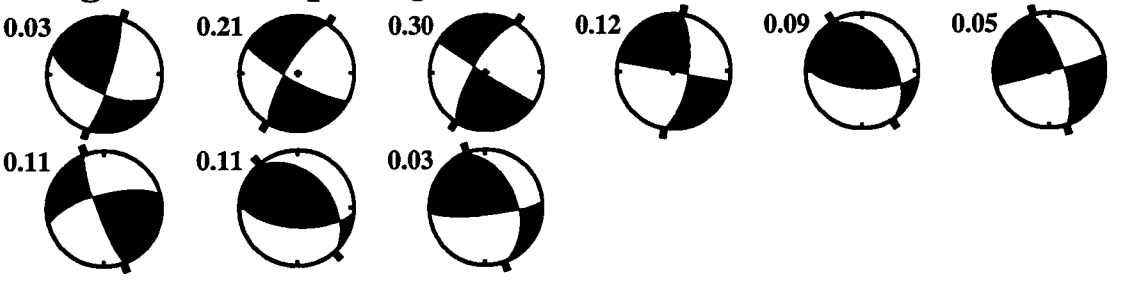

Left-lateral opening shear mechanisms

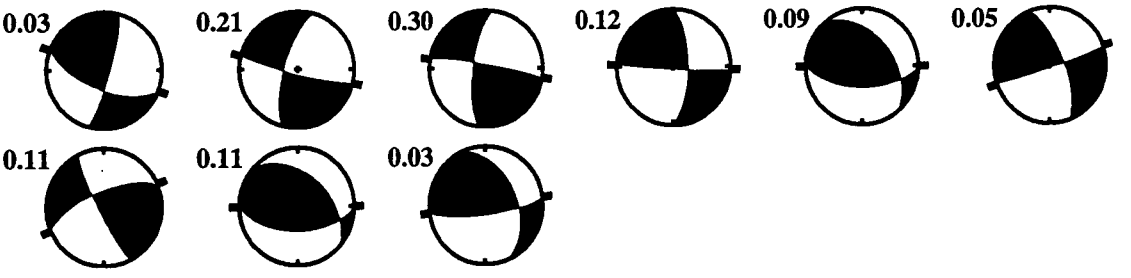

General moment tensors Group GRN.N

224.224238.1 224.224403.1 225.083219.1 225.090227.1 225.122104.1 225.122759.1

225.122941.1 225.123131.1 225.123340.1 226.020942.1 226.110713.1 258.074123.1

258.090235.1

Combined tensile-shear mechanisms

0.17 0.25 0.24 0.36 0.32 0.12

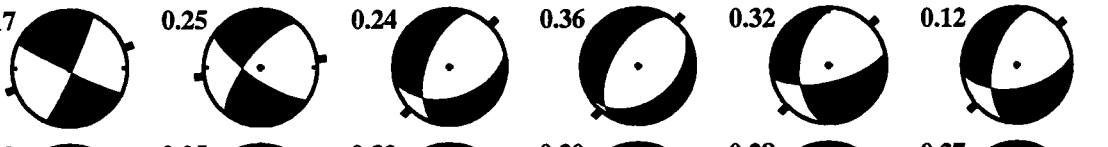

0.29 0.25 0.32 0.30 0.28 0.27

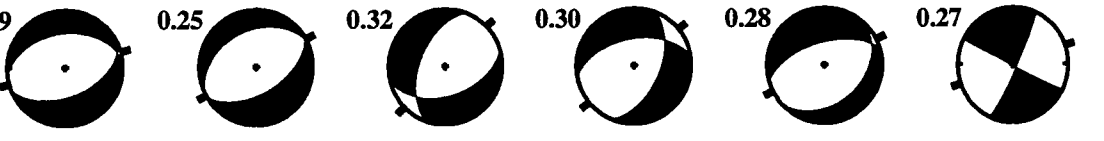

0.20

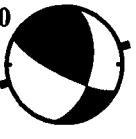

Right-lateral opening shear mechanisms

0.15 0.21 0.20 0.28 0.25 0.11

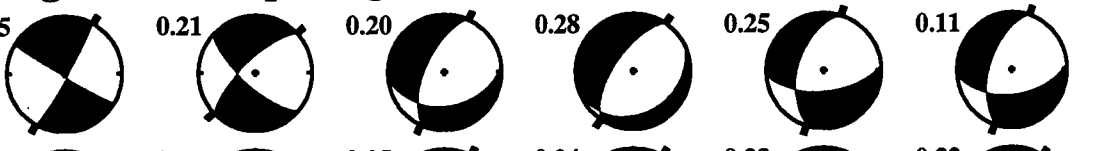

0.23 0.21 0.25 0.24 0.23 0.22

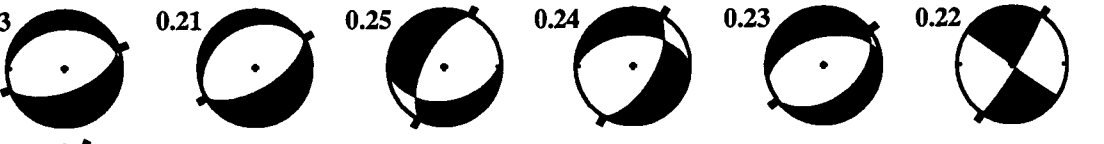

0.17

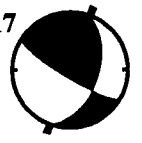

Left-lateral opening shear mechanisms

0.15 0.21 0.20 0.28 0.25 0.11

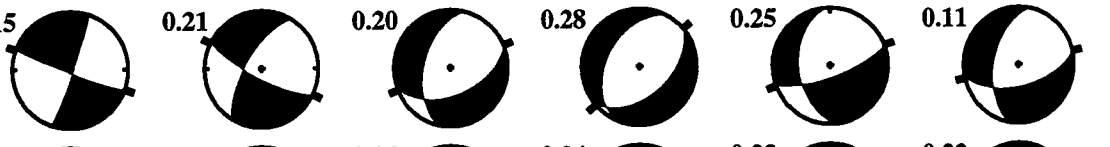

0.23 0.21 0.25 0.24 0.23 0.22

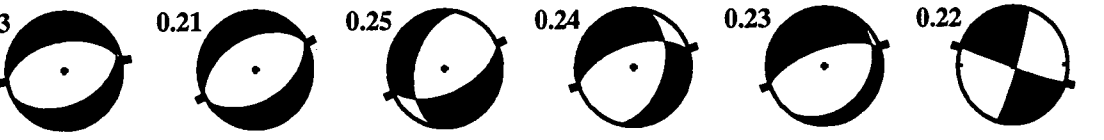

0.17

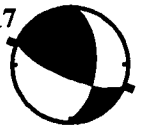

General moment tensors

Group GRN.S

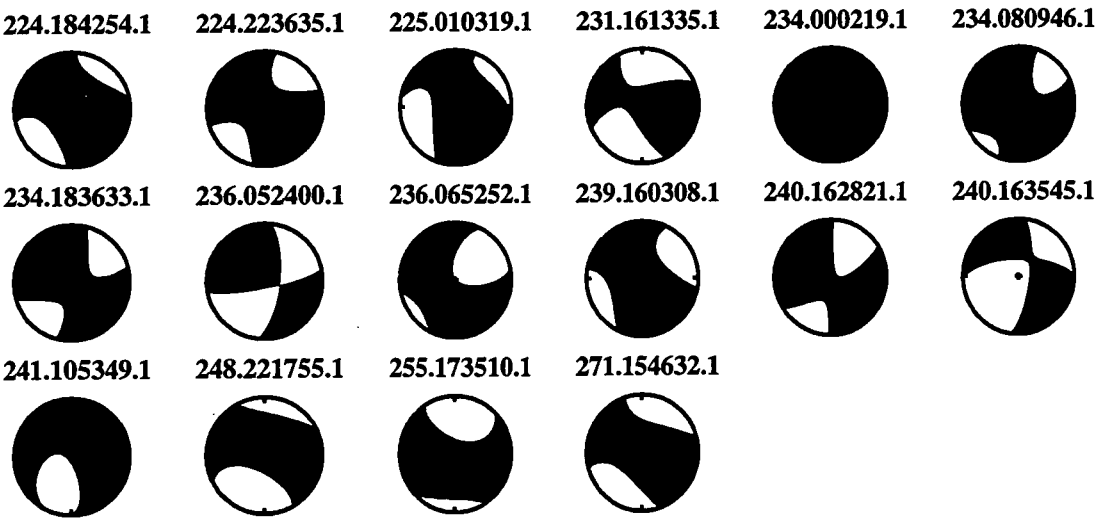

Combined tensile-shear mechanisms

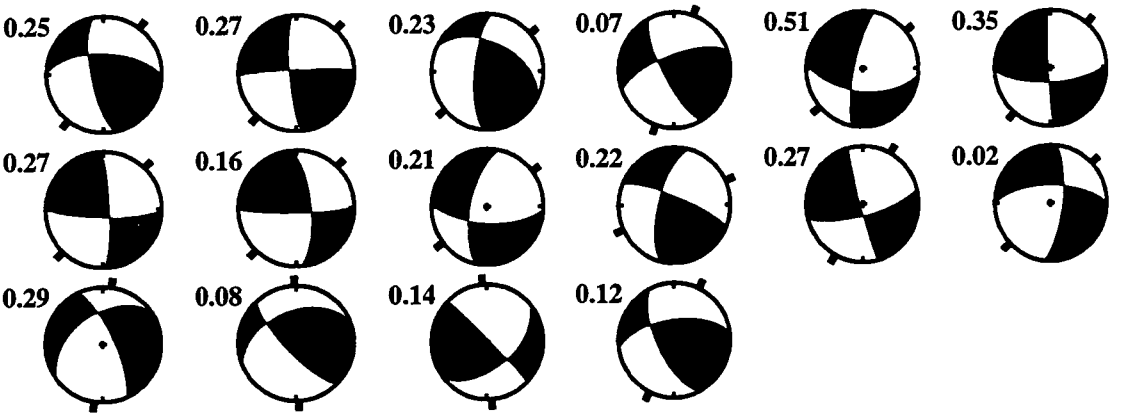

Right-lateral opening shear mechanisms

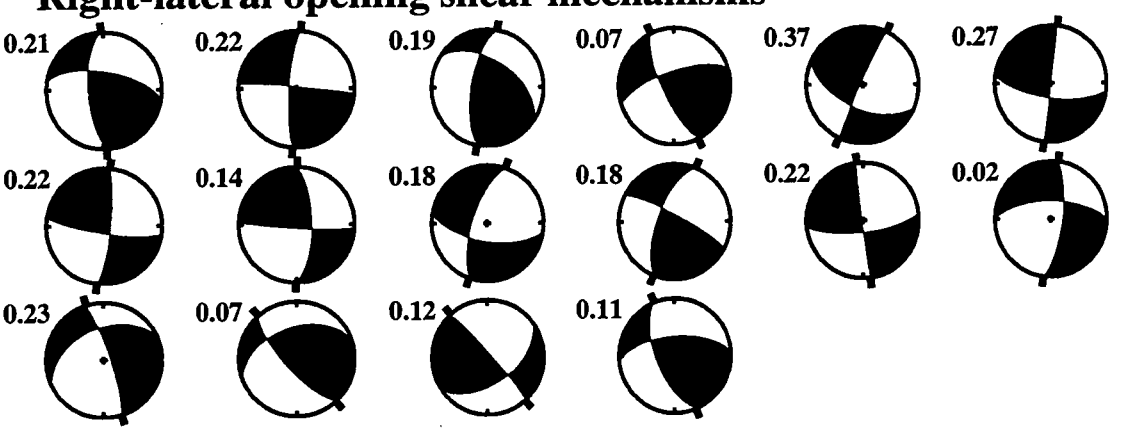

Left-lateral opening shear mechanisms

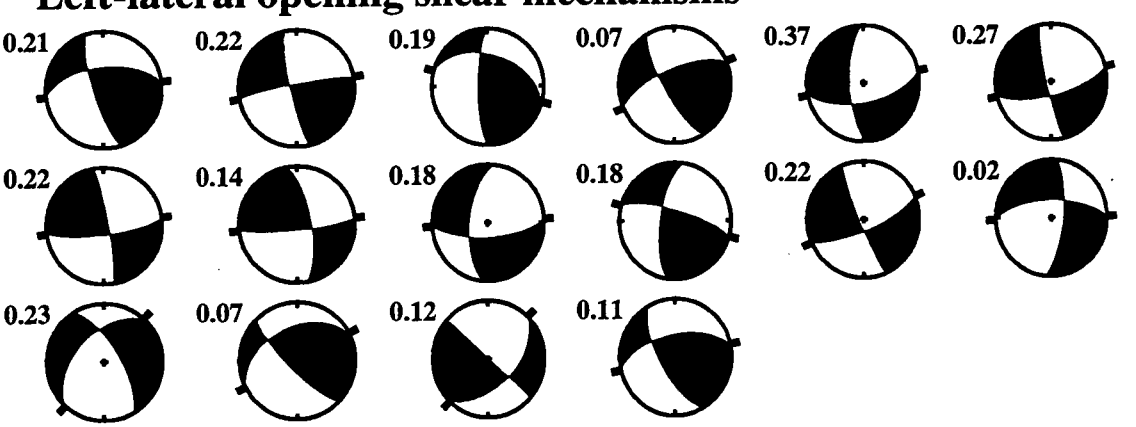

General moment tensors — Group KLM.N

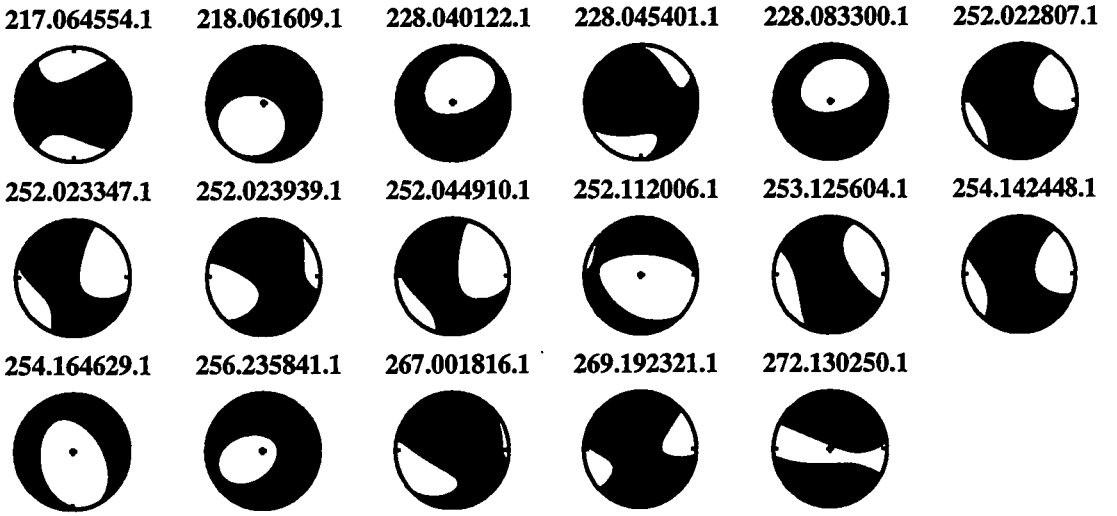

Combined tensile-shear mechanisms

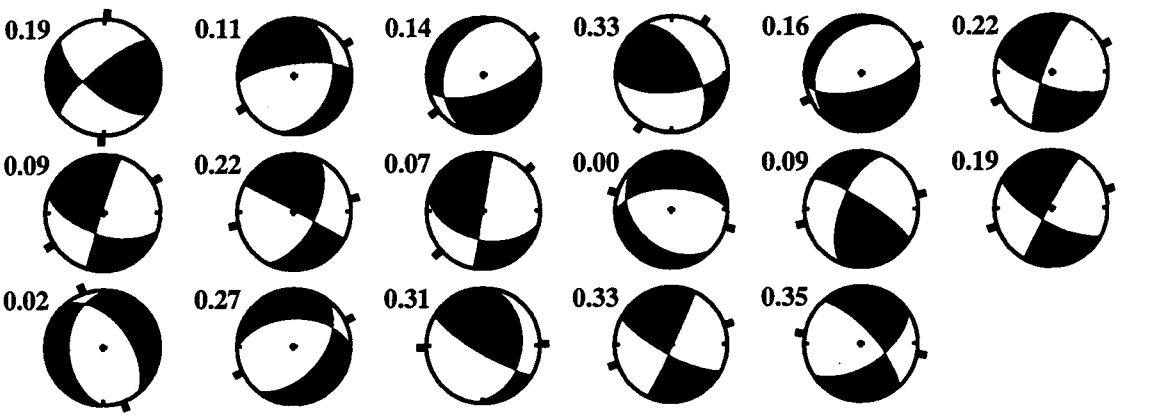

Right-lateral opening shear mechanisms

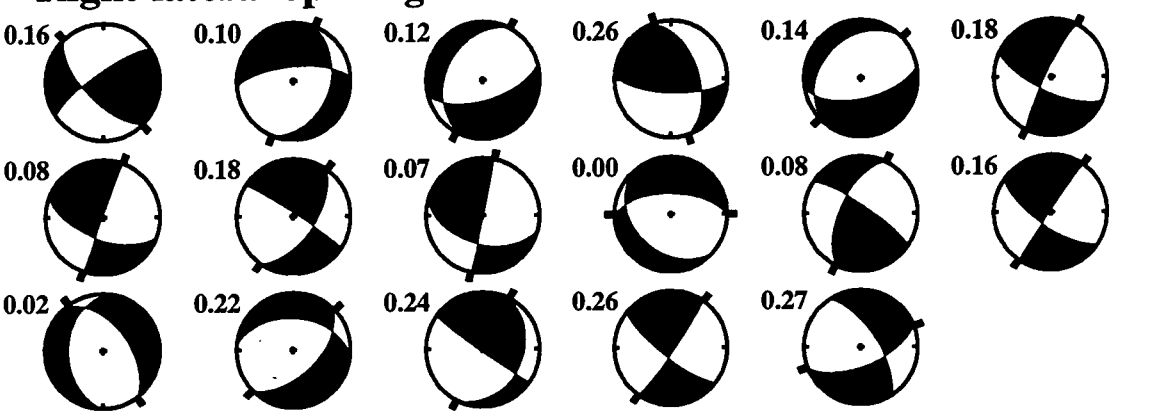

Left-lateral opening shear mechanisms

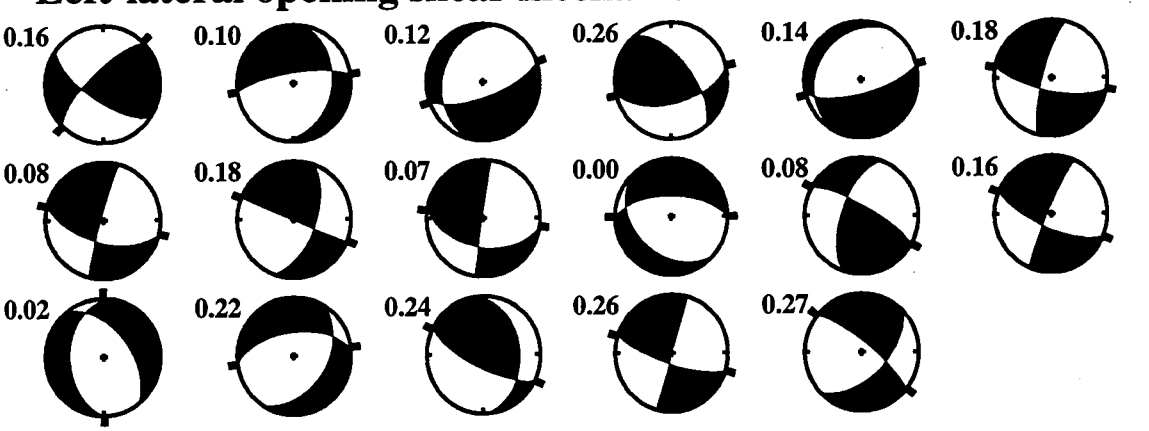

General moment tensors

Group KLM.S

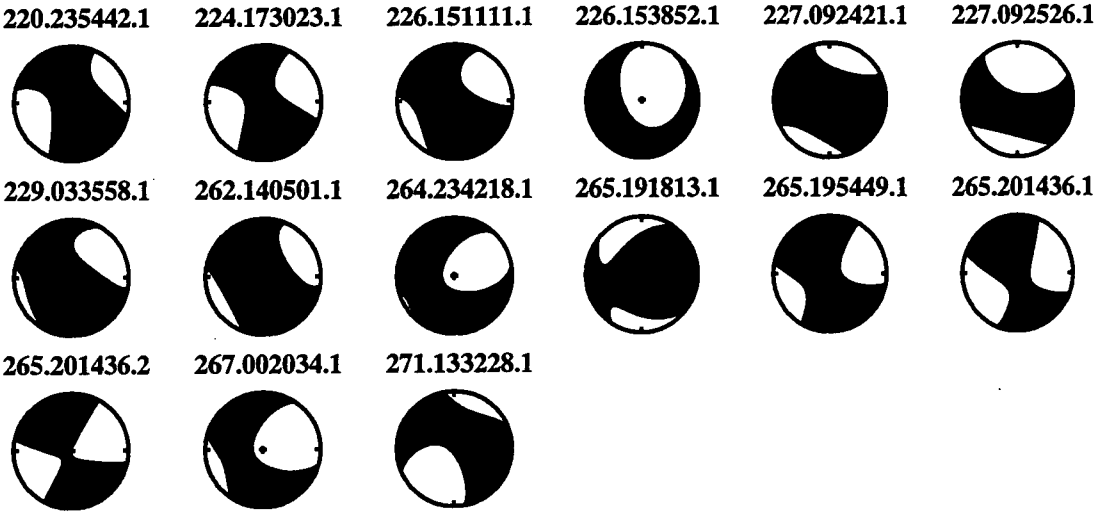

Combined tensile-shear mechanisms

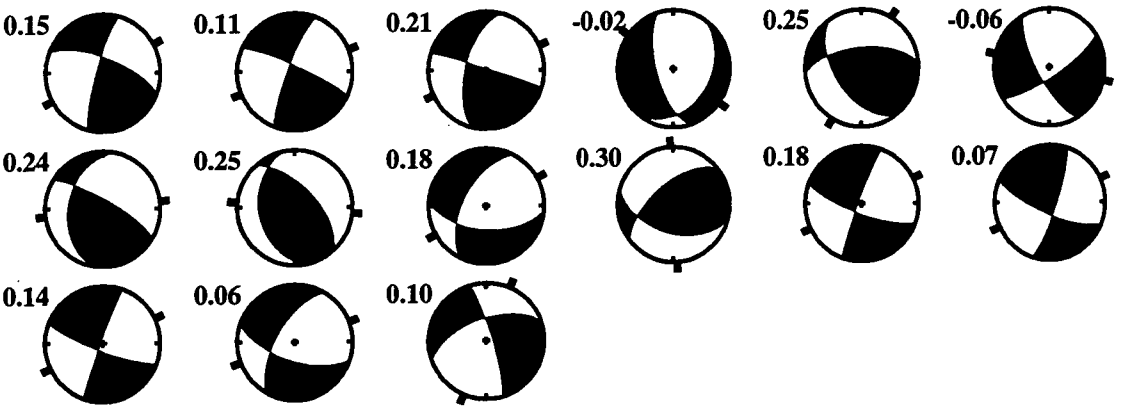

Right-lateral opening shear mechanisms

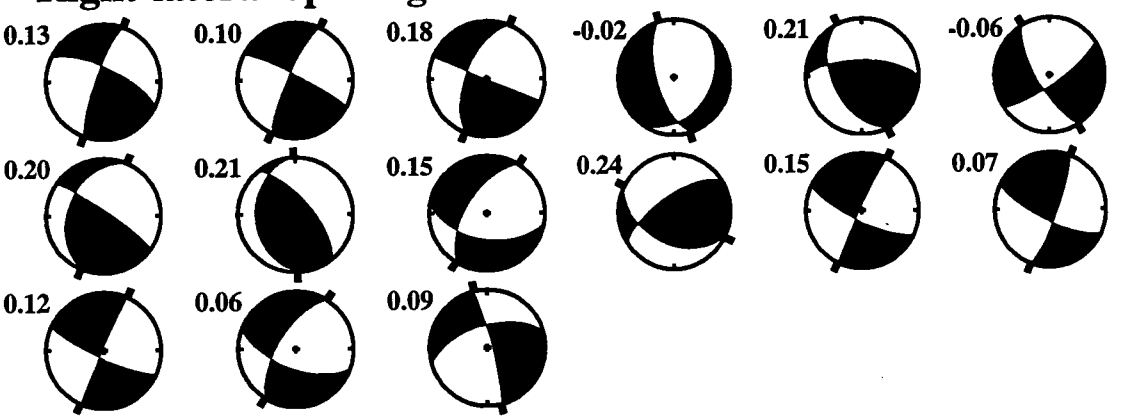

Left-lateral opening shear mechanisms

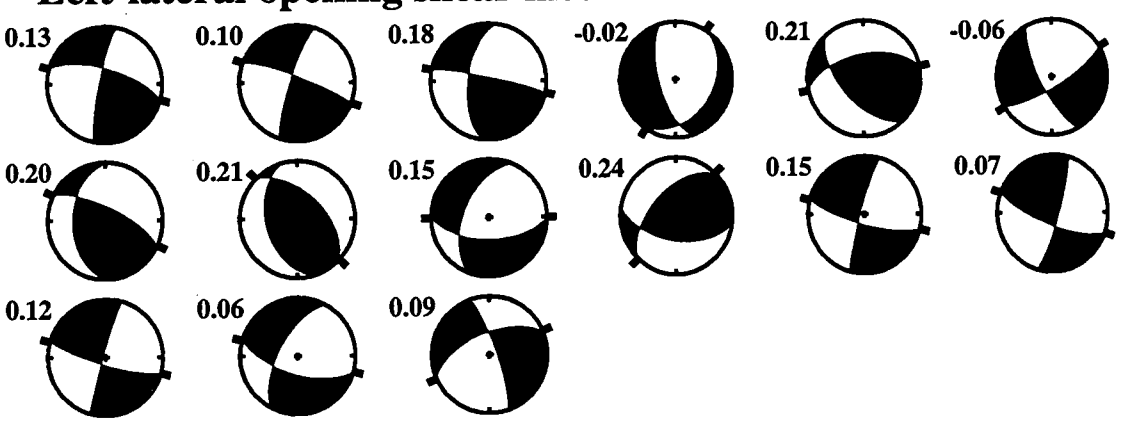

General moment tensors

Groups NW NES OLF

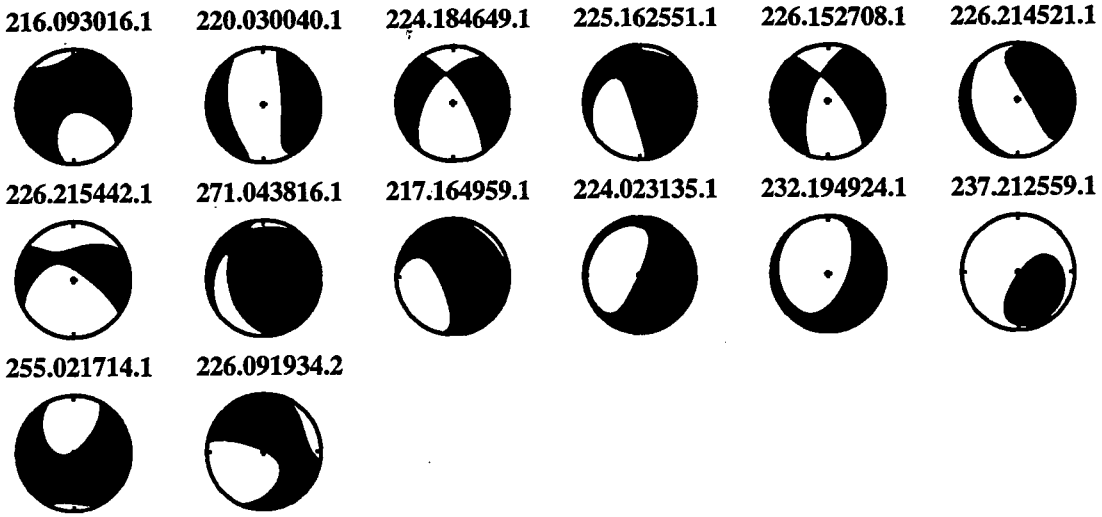

Combined tensile-shear mechanisms

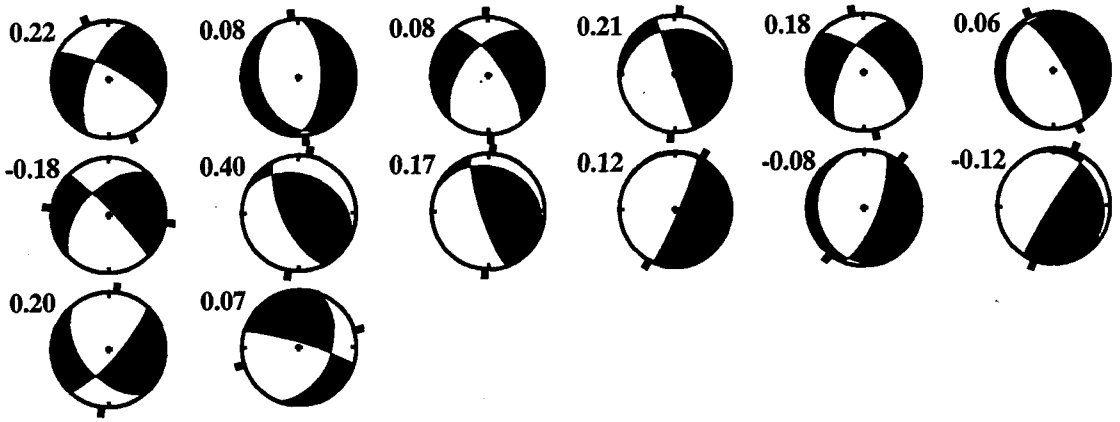

Right-lateral opening shear mechanisms

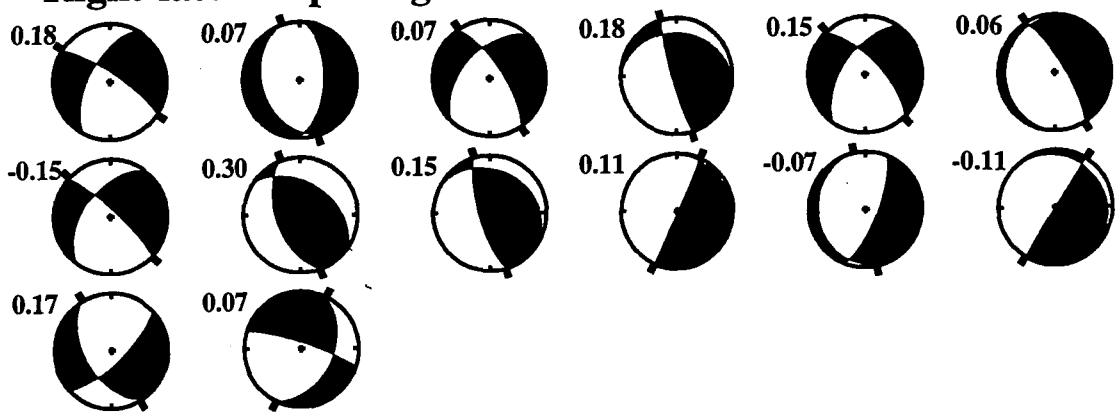

Left-lateral opening shear mechanisms

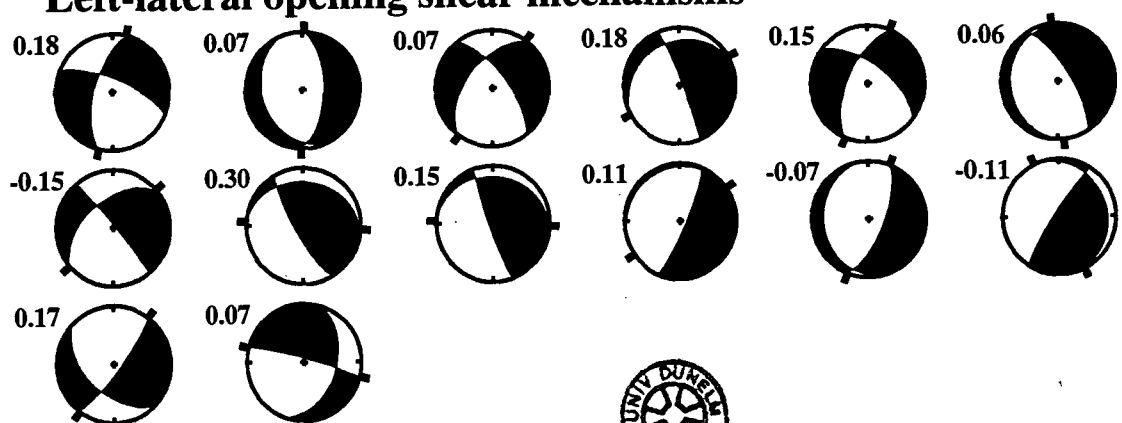

Three-dimensional v_p and v_p/v_s structure of the Hengill Triple Junction and geothermal area, Iceland, and the repeatability of tomographic inversion

G. R. Foulger and A. D. Miller

Dept. Geological Sciences, University of Durham, U.K.

B. R. Julian and J. R. Evans

Branch of Seismology, U.S. Geological Survey, Menlo Park, California

Abstract. We investigate the crustal structure of the Hengill triple junction in southwestern Iceland, applying tomographic methods to local earthquake data recorded in two field experiments with different network geometries and instrumentation. Data from the two experiments enable us to derive three-dimensional models of the compressional-wave speed v_p and the wave-speed ratio v_p/v_s. Well resolved high-v_p bodies correlate with sites of gabbroic intrusions. A small reduction in v_p/v_s associated with the high-temperature part of the geothermal area is probably due to mineral alteration or supercritical fluids. The RMS difference between the two v_p models, about 0.26 km s^{-1}, indicates the approximate repeatability that may be expected of good tomographic inversions.

Introduction

The Hengill ridge-ridge-transform triple junction area (Figure 1) contains widespread geothermal resources that are associated with continuous, small magnitude earthquake activity. This area is ideal for studying three-dimensional structure using local earthquake tomography, as earthquake activity has a broad, predictable spatial distribution, and illuminates those volumes where the strongest structural heterogeneity is expected. Two such studies of the area have been conducted, using data collected in 1981 [*Toomey and Foulger*, 1989; *Foulger and Toomey*, 1989] and in 1991. These studies were independent, and provide a rare opportunity to study the repeatability of seismic tomography.

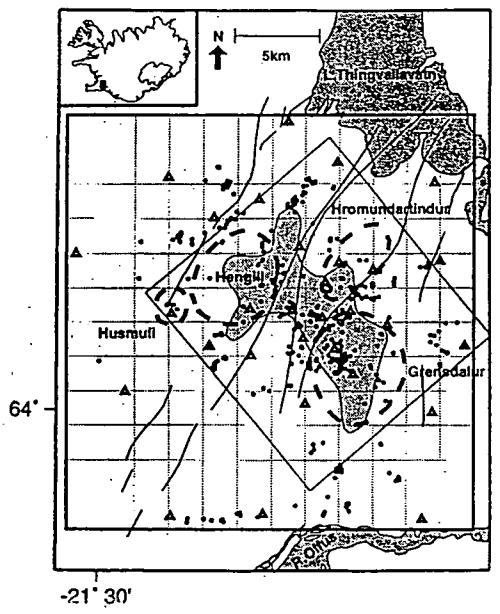

Figure 1. Map of the Hengill area, showing the main tectonic features. Dashed lines: eruptive sites of Húsmuli, Mt. Hengill, Mt. Hromundartindur, and Grensdalur. Shaded area: hot springs and fumaroles associated with the high-temperature geothermal area. Large dots: 1991 seismic stations. Small dots: 1991 earthquake epicenters. Small box: area studied using 1981 data [*Toomey and Foulger*, 1989]; large box: area studied using 1991 data and combined data. Values were computed at intersections of light grey lines. Station locations, nodal configuration, and events used for 1981 experiment are given by *Toomey and Foulger* [1989].

The 1981 Data and Inversion

In 1981, a temporary network of 23 analog seismic stations recorded 2000 locatable earthquakes [*Foulger*, 1988a;b]. *Toomey and Foulger* [1989] and *Foulger and Toomey* [1989] studied the three-dimensional variation of compressional-wave speed v_p by inverting arrival times for hypocentral parameters and crustal structure, using the SIMUL3 computer program of *Thurber* [1981; 1983]. A crustal block 14×15×6 km was parameterized using nodes spaced at intervals of 2 and 3 km horizontally and 1 km vertically. The initial starting model was obtained from preliminary test inversions. The damping was set to 2 s^2 km^{-1}, after experimenting with different values (Table 1, inversion 1).

Wave speeds in the final model differ by +20%/−47% from those in the one-dimensional starting model. The major structural features are high-v_p bodies at depths

Paper number 94GL03387
0094-8534/95/95GL-03387$03.00

Table 1. Details of the simultaneous inversions discussed in the text

Inversion Number		EQs	Shots	Stat.	Arrivals		Model Dimensions (km)	Nodes	P RMS Residual (s)	P&S RMS Residual (s)
					P	S				
1	1981 data [*Toomey & Foulger*, 1989]	158	2	20	2409	0	14 × 15 × 6	8 × 8 × 7 = 448	0.043	
2	1981 data (with outliers removed)	158	2	20	2394	0	14 × 15 × 6	8 × 8 × 7 = 448	0.022	
3	1991 data (graded inversion)	228	1	33	4748	3678	24 × 24 × 6	12 × 11 × 7 = 924	0.020	0.038
4	1991 data (one-step inversion)	228	1	33	4748	3678	24 × 24 × 6	12 × 11 × 7 = 924	0.020	0.038
5	1981 & 1991 data (graded inversion)	386	3	55	7253	3678	24 × 24 × 6	12 × 11 × 7 = 924	0.023	0.036
6	1981 & 1991 data (one-step inversion)	386	3	55	7253	3678	24 × 24 × 6	12 × 11 × 7 = 924	0.023	0.037

of 0 to 3 km beneath the Grensdalur volcano, 2 to 4 km beneath the Hromundartindur system, and 0 to 4 km beneath Húsmuli. Coherent bodies with low velocities are absent except for a small (≈ 5 km^3) body with a v_p contrast of -7% beneath the northern edge of Mt. Hengill. The high v_p bodies were interpreted as solidified gabbroic intrusions and the low v_p body as possibly a small volume of partial melt. These results agree well with geology, tectonic structure, and gravity.

An improved 1981 data set, with 15 outliers removed, was inverted using SIMULPS12 [*Eberhart-Phillips*, 1993; *Evans et al.*, 1994], a modified version of SIMUL3 that uses pseudobending ray tracing [*Um and Thurber*, 1987] and can invert both P and S-P times to obtain v_p and v_p/v_s [*Thurber*, 1993]. The results are similar, showing that the modifications to SIMUL3 have a small effect for this data set (Table 1, inversion 2).

The 1991 Field Experiment and Data

The Hengill area was revisited in 1991, using 30 stand-alone seismic stations with Mark Products model L22D 2-Hz, three-component sensors and REFTEK model 72A data loggers. Data were recorded continuously at a sampling rate of 100 Hz for two months, during which time about 4,000 earthquakes were recorded.

Arrival times for 390 earthquakes were measured with an estimated accuracy of 0.01 s for P waves and 0.02 s for S. S-wave times were picked only from horizontal components that showed clear, impulsive arrivals.

Inversion of the 1991 Data

Inversions were performed using SIMULPS12 (Table 1, inversions 3 and 4), and data from 228 well-distributed earthquakes and one explosion.

The crustal block analyzed is $24 \times 24 \times 6$ km in dimensions, and has almost three times the volume of the region studied using the 1981 data. Figure 1 shows its location and the distributions of stations and earthquakes used. A laterally homogeneous initial v_p model was obtained using the program VELEST [*Kissling et al.*, 1994]. A starting v_p/v_s ratio of 1.77 was calculated using a modified Wadati diagram [*Chaterjee et al.*, 1985].

A series of "graded inversions" was performed with the number of nodes being progressively increased to allow the wave-speed of poorly sampled volumes at the periphery of the grid to be adjusted to the best values in the early inversions [*Eberhart-Phillips*, 1993]. P and S times were used in all inversions, but the v_p/v_s model was held fixed until the final inversion, a joint inversion for v_p and v_p/v_s with a horizontal node spacing of 2 to 4 km (Table 1, inversion 3). Damping values for each inversion were obtained by analyzing "trade-off curves" of data variance reduction against model variance [*Eberhart-Phillips*, 1986]. The node spacing is the factor most affecting these curves, with the optimum v_p damping parameter decreasing from 20 s^2 km^{-1} (12 km spacing) to 5 s^2 km^{-1} (2 km spacing). However, using 5 s^2 km^{-1} in the final inversion results in large v_p oscillations in the surface layer, so 20 s^2 km^{-1} was used for all inversions. v_p/v_s damping was 2 s.

To test the stability of the procedure, we conducted a single-step inversion for v_p and v_p/v_s, starting with the same initial conditions (Table 1, inversion 4). Damping parameters were 5 s^2 km^{-1} for v_p and 2 s for v_p/v_s. The results are similar to those of inversion 3, with RMS differences of 0.12 km/s for v_p and 0.01 for v_p/v_s. Inversion 4 yielded smaller v_p variations than inversion 3, especially in the surface layer, but the final RMS data residuals are the same (Table 1).

Our data show evidence of seismic anisotropy. The S-wave travel times before inversion vary systematically with azimuth by about 4%, with the slowest waves travelling sub-parallel to the ridge (N25°E). To investigate the effect of anisotropy, we applied an empirical sinusoidal correction to the S-wave arrival times and repeated the inversion for v_p/v_s. The resulting model differs only slightly from that obtained using uncorrected data, indicating that anisotropy does not affect our results to first order, probably because the azimuthal ray distribution is sufficiently uniform.

The resolution was assessed using the spread function

$$\text{spread} = \left[\|R_j\|^{-2} \Sigma_k D_{jk}^2 R_{jk}^2\right]^{1/2}, \qquad (1)$$

where $\mathbf{R}$ is the resolution matrix, $\|R_j\|$ is the Euclidean (L2) norm of its jth row, and D_{jk} is the distance between the jth and kth nodes. The spread indicates how widely the wave speed is averaged to yield the nodal values. Examination of individual rows of the resolution matrix and the ray distribution suggests that nodes with spread ≤ 4 km are well resolved and involve only local averaging.

Inversion of Combined Data

We inverted a combination of the 1981 and 1991 data, using the same grid, starting velocities, and damping parameters as with the 1991 data. The less accurate 1981 data were given half weight. Figure 2 shows the models resulting from the one-step inversion of the combined data set (Table 1, inversion 6). The graded inversion gives a marginally better data fit (Table 1, inversion 5), but has large v_p variations (up to +22%) in the surface layer.

Results

The v_p and v_p/v_s models obtained are insensitive to starting model, event set, grid configuration and inversion strategy. v_p varies laterally by -10% to $+12\%$ from its average value within each layer. The major v_p structures are high wave-speed (up to +12%) bodies near the extinct Grensdalur volcano at depths of 1 to 4 km, under the southern part of the Hromundartindur volcanic system at 2 to 4 km, and beneath the Húsmuli basalt shield at 0 to 3 km. At lower v_p contrasts ($\sim +2\%$) these bodies form a single zone oriented parallel to the spreading direction and traversing all three volcanic systems. No major low v_p bodies were imaged.

The ratio v_p/v_s varies by $\pm 4\%$ throughout the area. The most coherent anomaly involves low v_p/v_s at 0 to 2 km depth, and correlates closely with areas of hot springs and fumaroles (Figure 2). The mean v_p/v_s is 1.77, and shows no variation from the surface to 6 km.

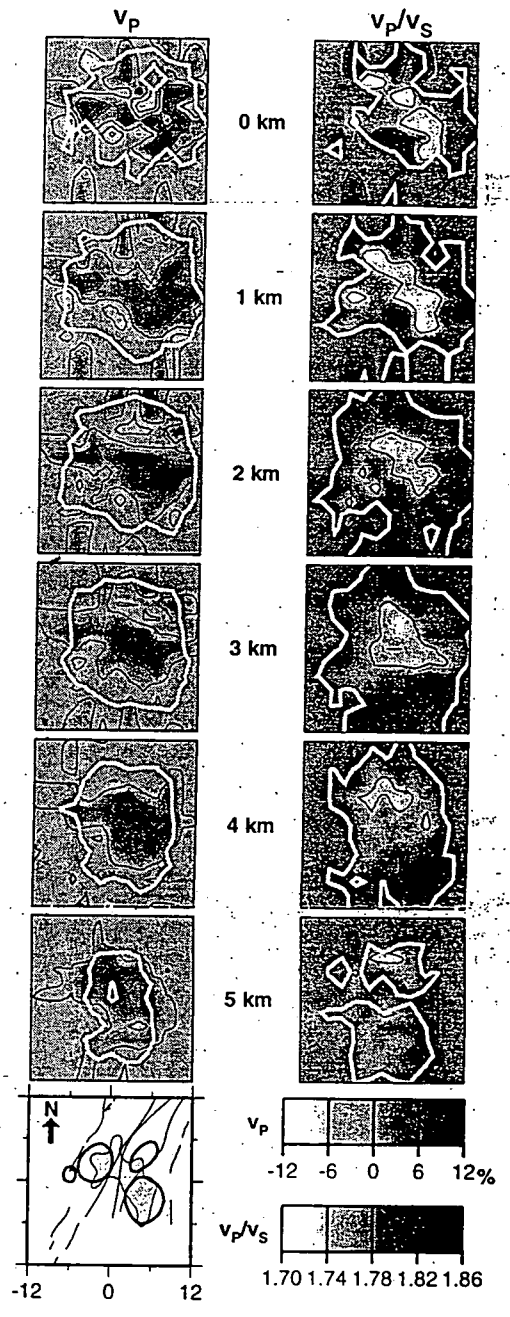

Figure 2. Horizontal cross sections of v_p and v_p/v_s structure obtained from 1981 and 1991 data (Table 1, inversion 6). For v_p, percentage difference from mean value in each layer is shown. Areas inside white lines are well resolved (*spread* < 4 km). Schematic tectonic features shown in Figure 1 are indicated at bottom left.

Interpretation

We interpret high v_p bodies within the volcanic complex as gabbro intrusions that were formerly the sources or conduits for surface volcanism.

The main factors affecting the ratio v_p/v_s are saturation [*Nur*, 1987], porosity, crack geometry and lithology. v_p/v_s commonly decreases with depth in situ [e.g., *Walck*, 1988; *Thurber and Atre*, 1993] because the closing of cracks affects v_s more than v_p. We find a mean v_p/v_s of 1.77 in all layers, a high ratio which suggests little tendency for cracks to close with depth above 6 km in the Hengill area.

The v_p/v_s variation of $\pm 4\%$ is much smaller than that found in other areas using local earthquake tomography [*Walck*, 1988; *Thurber and Atre*, 1993] and Wadati diagrams [*Chatterjee et al.*, 1985]. This suggests that there are only small variations in saturation and porosity across the region, and that the lithologies present have similar v_p/v_s ratios. No high v_p/v_s anomaly is observed, confirming that large volumes of partial melt are absent in the upper 6 km. The clear correlation of low v_p/v_s with the high-temperature geothermal area shows that it is a real feature related to the shallow part of the reservoir, possibly caused by alteration of rock to hydrated clay minerals, or changes in saturation or pore fluid temperature.

Comparing Results from the Separate and Combined Data Sets

In the Hengill area, a unique situation exists where two independent tomographic inversions have been conducted, along with a final combined inversion. The 1981 and 1991 data comprise separate events measured on different seismic networks, the crustal block was parameterized differently, and somewhat different inversion methods were used. The earlier inversion was for v_p only, so v_p/v_s cannot be compared between the two solutions.

The overall pattern of anomalies found in the two inversions is similar. High-v_p bodies are located beneath the Grensdalur and Hromundartindur systems and Húsmuli. The low-v_p body beneath the northern part of Mt. Hengill was not detected in the second inversion, so its existence is questionable.

The amplitudes of the v_p anomalies found using the 1991 data are smaller than those for the 1981 data, probably due to the larger errors in the 1981 data. Anomaly patterns agree better than absolute velocities. The RMS difference between v_p in the models is 0.26 km s^{-1}. It is slightly smaller (0.19 km s^{-1}) if variations from the mean in each layer are compared. This is about three times larger than the RMS difference between models obtained using the 1991 data set and different inversion strategies. Comparing the differences between the models with the calculated uncertainties of the 1981 model suggests that the statistical uncertainty underestimates the repeatability of v_p by a factor of about 5, a higher value than the factor of 2 estimated from quasi-empirical testing for the relationship between model uncertainty and accuracy by *Thurber* [1981].

Acknowledgments. This work was supported by a USGS G. K. Gilbert Fellowship, NERC Grant GR9/134, NERC Geophysical Equipment Loan 328/0990, and a loan of digital seismic equipment from IRIS/PASSCAL. A.D.M. is supported by a NERC Ph.D. studentship. H.M. Iyer, A.M. Pitt and R. Nowack gave helpful reviews. Data analysis was assisted by the GMT mapping software [*Wessel and Smith*, 1991].

References

Chaterjee, S. N., A. M. Pitt, and H. M. Iyer, v_p/v_s ratios in the Yellowstone National Park Region, Wyoming, *J. Volcanol. Geoth. Res.*, *26*, 213-230, 1985.

Eberhart-Phillips, D., Three-dimensional velocity structure in the northern California coast ranges from inversion of local earthquake arrival times, *Bull. Seismol. Soc. Am.*, *76*, 1025-1052, 1986.

Eberhart-Phillips, D., Local tomography: earthquake source regions, in *Seismic Tomography: Theory and Practice*, eds. H. M. Iyer and K. Hirahara, Chapman and Hall, 613-643, 1993.

Evans, J. R., D. Eberhart-Phillips, and C. H. Thurber, User's manual for SIMULPS12 for imaging v_p and v_p/v_s, a derivative of the Thurber tomographic inversion SIMUL3 for local earthquakes and explosions, *U.S. Geol. Surv. Open File Rep.*, *94-431*, 142 pp., 1994.

Foulger, G. R., The Hengill triple junction, SW Iceland: 1. Tectonic structure and the spatial and temporal distribution of local earthquakes, *J. Geophys. Res.*, *93*, 13,493-13,506, 1988a.

Foulger, G. R., The Hengill triple junction, SW Iceland: 2. Anomalous earthquake focal mechanisms and implications for process within the geothermal reservoir and at accretionary plate boundaries, *J. Geophys. Res.*, *93*, 13,507-13,523, 1988b.

Foulger, G. R. and D. R. Toomey, Structure and evolution of the Hengill-Grensdalur central volcano complex, Iceland: Geology, geophysics and seismic tomography, *J. Geophys. Res.*, *94*, 17,511-17,522, 1989.

Kissling, E., W. L. Ellsworth, D. Eberhart-Phillips, and U. Kradolfer, Initial reference models in local earthquake tomography, *J. Geophys. Res.*, *99*, 19,635-19,646, 1994.

Nur, A., Seismic rock properties for reservoir descriptions and monitoring, in *Seismic Tomography*, G. Nolet (ed.), D. Reidel Pub. Co., Holland, 203-237, 1987.

Thurber, C. H., *Earth structure and earthquake locations in the Coyote Lake area, central California*, Ph.D. thesis, Massachusetts Institute of Technology, Cambridge, MA., 332 pp, 1981.

Thurber, C. H., Earthquake locations and three-dimensional crustal structure in the Coyote Lake area, central California, *J. Geophys. Res.*, *88*, 8226-8236, 1983.

Thurber, C. H., Local earthquake tomography: velocities and v_p/v_s-theory, in *Seismic Tomography: Theory and Practice*, eds. H. M. Iyer and K. Hirahara, Chapman and Hall, 563-583, 1993.

Toomey, D. R. and G. R. Foulger, Application of tomographic inversion to local earthquake data from the Hengill-Grensdalur central volcano complex, Iceland, *J. Geophys. Res.*, *94*, 17,497-17,510, 1989.

Um, J. and C. H. Thurber, A fast algorithm for two-point seismic ray tracing, *Bull. Seismol. Soc. Am.*, *77*, 792-786, 1987.

Wessel, P. and W. H. F. Smith, Free software helps map and display data, *EOS Trans. AGU*, *72*, 441, 445-446, 1991.

J. R. Evans and B. R. Julian, U.S. Geological Survey, 345 Middlefield Road, Mail Stop 977, Menlo Park, CA 94025 (e-mail: evans or julian@andreas.wr.usgs.gov).

G. R. Foulger and A. D. Miller, Dept. Geological Sciences, University of Durham, U.K. (e-mail: g.r.foulger or a.d.miller@durham.ac.uk).

(received June 14, 1994; revised October 31, 1994; accepted November 2, 1994.)

NON-DOUBLE-COUPLE EARTHQUAKES II. OBSERVATIONS

Angus D. Miller[1,2], G. R. Foulger[1,2] and Bruce R. Julian[2]

[1] Department of Geological Sciences
University of Durham
Durham, DH1 3LE
UK

[2] U. S. Geological Survey
345 Middlefield Road, MS 977
Menlo Park, CA 94025
USA

Submitted to Reviews of Geophysics

Abstract. Most seismological analyses represent earthquakes by pairs of force couples with vanishing net torque ("double couples", or DCs, which correspond to shear motion on planar faults) but observations of increasing resolution now commonly identify radiation patterns that depart from this model. In many cases, these effects are small and are probably caused by departure from idealized shear-faulting geometry (fault curvature, for example), but some observations are radically inconsistent with shear faulting and indicate that fundamentally different earthquake processes occur in nature. Seismic waves excited by advective processes, such as landslides and volcanic eruptions, are consistent with net forces rather that DCs, in accordance with theoretical predictions. Some volcanic earthquakes also have single-force mechanisms, probably because of advection of magmatic fluids. "Explosion" earthquakes at Sakurajima volcano, Japan, have mechanisms consistent with tensile crack propagation to the surface and advection of gasses and ejecta into the atmosphere. Some earthquakes in volcanic areas, such as the Tori Shima earthquake of 13 June 1984 in the Bonin arc, the Barbarbunga, Iceland, earthquakes of 1977 to 1993, and the Long Valley caldera, California, earthquakes of May 1980, have mechanisms close to pure compensated linear-vector dipoles (CLVDs). These may be caused by rapid intrusions, probably of gas-rich magma, although simultaneous slip on multiple shear faults cannot, in theory, be ruled out. Many shallow earthquakes in volcanic/geothermal areas (notably in Iceland) and in mines have mechanisms with isotropic components, involving volume changes of either explosive or implosive polarity. These mechanisms are consistent with mixed-mode failure, involving simultaneous shear and tensile faulting. In geothermal areas, high-pressure, high-temperature fluids may facilitate crack opening at depth. In mines, tunnels may act as closing cavities. Data from submarine mid-ocean ridges are not yet adequate to determine whether non-DC earthquakes, similar to those in Iceland, occur at the oceanic spreading plate boundary also, although this is likely because the two environments are similar. Deep-focus earthquakes occur within zones of polymorphic phase transformations in the upper mantle, at depths where stick-slip instability cannot occur. Nevertheless, they do not involve volume changes resolvable by current seismological techniques. They do, however, have a tendency toward deviatoric (volume conserving) non-DC mechanisms, possibly a result of simultaneous shear slip on differently-oriented faults. Current theory attributes deep earthquakes to "transformational shear faulting", facilitated by phase changes in small "anti-cracks" in the same way that formation of ordinary shear faults is facilitated by tensile micro-cracks. It is not clear why this process should favor simultaneous shear faulting. Automatic moment-tensor catalogs routinely report statistically-significant non-DC components for large earthquakes from all over the world. However, automatic solutions are subject to large uncertainties and detailed re-examination of individual events is required to confirm such results.

1. INTRODUCTION

More than a century ago, *Gilbert* [1884] inferred that earthquakes are caused by faulting, and observations of surface breaks accompanying several earthquakes in India and Japan in the late 19th century supported this inference [*Richter*, 1958]. Observations of the 1906 San Francisco, California earthquake by G. K. Gilbert, H. F. Reid and others [*Lawson*, 1908; *Reid*, 1910] led to the formulation of the elastic rebound theory, which still forms the fundamental basis for understanding earthquake source processes. Subsequently, numerous earthquakes accompanied by visible fault motion established the connection between the two phenomena beyond reasonable doubt [*e.g.*, *Richter*, 1958].

A much larger body of evidence connecting earthquakes with faulting comes from instrumental observations of seismic waves. In theory, compressional waves radiated by shear slip on a fault have a four-lobed pattern, with adjacent lobes alternating in polarity. This pattern, and the entire static and dynamic field of motion caused by a shear fault, is identical to that produced in an unfaulted medium by a distribution over the fault surface of pairs of force couples, arranged so that their net torque vanishes. Seismologists usually specify earthquake mechanisms in terms of equivalent force systems, and shear-fault mechanisms are called "double couples" (DCs). Shida first recognized four-lobed P-wave polarity distributions in 1917 [*Kawasumi*, 1937], although controversy about the underlying theory persisted for decades. Instrumental determination of earthquake mechanisms became reliable in the 1960s, with advances in seismological theory and the introduction of a global network of standardized instruments that returned large amounts of data of unprecedentedly high quality. Fault-orientation and slip-direction determinations for thousands of earthquakes are now available, and these have played a central role in advancing understanding of tectonic processes [*e.g.*, *Isacks et al.*, 1968].

The hypothesis that earthquake source mechanisms are DCs has been so widely accepted as to have been treated as a fundamental law by many seismologists. However, the subject has never been entirely free of some controversy. Surface faulting does not always accompany large earthquakes, and it has been suggested that faulting is merely an effect of ground shaking rather than the cause. *Ishimoto* [1932] suggested that earthquakes are caused by subterranean magma motion, and Japanese seismologists attempted during the 1920s and 1930s to distinguish between the quadrantal radiation pattern expected for shear faulting and the conical pattern thought to correspond to rapid intrusion of magma into a crack [*Aki*, 1979]. *Evison* [1963] argued that faulting is a form of earthquake damage, reasoning that sliding friction would require impossibly large shear stresses at depth, and proposed instead that earthquakes are caused by rapid polymorphic phase transformations. When it was discovered that the upper mantle contains major structural discontinuities caused by polymorphic phase transformations, experimental attempts were made to detect volume changes in earthquakes [*e.g. Benioff*, 1963; *Gilbert and Dziewonski*, 1975], but the results were inconclusive. *Robson et al.* [1968] revived Ishimoto's idea and suggested that extensional failure, facilitated by magma, causes some earthquakes. On the whole, however, potential non-DC earthquake mechanisms have been given little attention because the DC model has adequately explained most seismic observations.

To a large extent, however, the success of the DC model has been a consequence of limitations in data quantity and quality. Recent improvements in seismological instrumentation and analysis techniques have now convincingly identified earthquakes whose radiated waves are incompatible with DC force systems, and thus with shear faulting. Well-constrained non-DC earthquakes have been observed in many environments, including particularly volcanic and geothermal areas, mines and deep subduction zones. This paper reviews these observations. A companion paper [*Julian et al.*, 1995a, hereinafter called Paper I] reviews the relevant seismic source theory and describes proposed source processes for non-DC earthquakes.

2. DESCRIBING NON-DC EARTHQUAKES

Earthquake mechanisms are most often determined from compressional-wave polarities, under the assumption that the mechanism is a DC (Paper I, section 3.1). Polarity observations are plotted on the "focal sphere", an imaginary sphere surrounding the earthquake focus, and orthogonal "nodal" planes sought that separate compressions and dilatations. For a shear fault, one of these nodal planes represents the fault. The assumptions that the nodal surfaces are planar and mutually orthogonal narrows the range of feasible solutions and makes possible interpretation using simple graphical methods. For general non-DC sources, however, the nodal surfaces are not necessarily planes, the range of possible interpretations is much wider, and manual solution is impractical. In other words, the rejection of the DC constraint on interpretations greatly exacerbates the classical inverse problem of earthquake mechanism determination.

To surmount this problem, and to resolve general non-DC source mechanisms, it is almost always necessary to use other data than just P-wave polarities, such as wave amplitudes. Virtually any kinds of seismic waves may be used, and they may be analyzed by various methods (Paper I, section 3.2). Notable among these are methods that invert amplitude ratios, to reduce the effects of wave-propagation anomalies (Paper I, section 3.2.1) and waveform-inversion methods, which can determine temporal variations in the source mechanism.

Non-DC source mechanisms are almost always expressed as symmetric moment tensors, which can be decomposed in a variety of ways to facilitate comprehension (Paper I, section 2.5). Here, we divide a moment tensor into a volumetric and a deviatoric part (Paper I, equation 22) and describe the departure of the deviatoric part from a DC by the parameter

$$\epsilon \triangleq \frac{-m_1'}{|m_3'|},$$

where the principal moments of the deviatoric part of the moment tensor are arranged so that $|m_1'| \le |m_2'| \le |m_3'|$. ϵ is zero for a DC, and ± 0.5 for a "compensated linear-vector dipole" (CLVD).

The equivalent force system of an earthquake cannot uniquely identify the physical source process. The force system is a phenomenological description of the source, and is all that can be determined from seismological observations, but different physical interpretations are generally possible. For example, a DC could correspond either to shear slip on a planar fault or to opening of a tensile crack and simultaneous closing of an orthogonal crack (or to many other things). In discussing earthquake focal mechanisms, geology, rock physics, and other non-seismological disciplines therefore play essential roles.

3. OBSERVATIONS OF NON-DC EARTHQUAKES

3.1 Landslides and volcanic eruptions

Landslides and volcanic eruptions can have equivalent force systems that include single forces, and are more general than moment tensors (Paper I, section 4.1). The mechanisms of landslides should, in theory, also include net torques (asymmetric moment tensors) [*Takei and Kumazawa*, 1994] but such models have not yet been applied to seismic data.

3.1.1 Mount St. Helens, Washington state

The Mount St. Helens eruption of 18 May 1980 was accompanied by a massive landslide on the north slope of the volcano [*Voight et al.*, 1981]. Many long- and intermediate-period seismic stations recorded the event, including stations of the Global Digital Seismograph Network (GDSN). The observed identical polarities of P waves at some GDSN stations, along with large observed P:S amplitude ratios, is inconsistent with a DC mechanism [*Kanamori et al.*, 1984].

Two single forces can explain the long- and intermediate-period seismic waves from the eruption of Mount St. Helens (Figure 1). A near-horizontal, southward-directed force represents the landslide, and excited most of the surface-wave energy [*Kanamori and Given*, 1982; *Kanamori et al.*, 1984; *Kawakatsu*, 1989]. A vertical single force represents the eruption and explains the teleseismic P waveforms, P:S amplitude ratios, and near-field data recorded at one intermediate-period digital instrument [*Kanamori et al.*, 1984].

3.1.2 The Mantato landslide, Peru

The Mantato landslide of 26 April 1974 is one of the largest in recorded history. This rock-slide avalanche, with a volume of $\sim 10^9\ m^3$, measured more than 8 km along its longest side, and its centroid traveled 4-6 km. It excited long-period seismic waves that were recorded at 7 digital, long-period instruments at teleseismic distances [*Kawakatsu*, 1989]. A "centroid single force" (CSF) inversion (Paper I, section 3.3.2) of long-period seismic waves with frequencies between 6 and 8 mHz (periods of 167 to 125 s) yielded a near-horizontal force oriented SW, a direction consistent with the observed direction of the slide. The seismic moment is about one-fifth the expected size, suggesting either that much of the motion occurred too slowly to excite seismic waves in the frequency range of the observations or that the landslide volume has been over-estimated.

3.1.3 The Grand Banks earthquake, Canada.

The 18 November 1929 Grand Banks earthquake (M_s 7.2) generated a turbidity current that traveled 1700 km and severed 12 trans-Atlantic undersea cables [*Doxsee*, 1948; *Hasegawa and Kanamori*, 1987]. Available seismic data consist of P- and S-wave polarities and surface-wave amplitude spectra from 50 global seismic stations of widely varying instrumental response. *Hasegawa and Kanamori* [1987] considered different source types, including double couples and single forces. The best-fit model is a horizontal, north-directed force, which is consistent with a southward landslide.

3.1.4 The Kalapana earthquake, Hawaii

The 29 November 1975 Kalapana earthquake (M_s 7.1) on the island of Hawaii coincided with large-scale subsidence along a 50-km zone on the southwest flank of Kilauea volcano, with a maximum co-seismic displacement of 3 m vertically and 8 m horizontally. The earthquake caused a 15-m tsunami on nearby beaches, indicating that substantial vertical motion occurred on the sea floor also. P-wave polarities constrain one nodal surface to be approximately vertical, and initial DC interpretations involved shear slip on a near-horizontal fault [*Ando*, 1979]. However, such a mechanism is inconsistent with the Love-wave radiation pattern, which has two lobes oriented ENE and WSW. A DC mechanism has a four-lobed Love-wave radiation pattern unless the fault plane dips less than about 5° [*Eissler and Kanamori*, 1988]. An alternative shear model involves sliding on a near-horizontal fault combined with slip on multiple planes of different orientations. In this case, the additional ruptures results in Love-wave radiation that is a mixture of two- and four-lobed patterns [*Wyss and Kovach*, 1988].

Eissler and Kanamori [1987] proposed a mechanism for the Kalapana earthquake involving a single force of about 1.6×10^{15} N in the direction opposite to the observed horizontal motion. This mechanism fits the observed Love wave amplitudes much better than the DC model of *Ando* [1979] and also is consistent with observed P-wave polarities. A CSF inversion of Kalapana earthquake data [*Kawakatsu*, 1989] produced a single-force similar to that of *Eissler and Kanamori* [1987] but gave a poorer fit to the data than the Harvard CMT mechanism (a 50% reduction in variance compared with to a 66% reduction). The CMT solution is similar to the double-couple mechanism of *Wyss and Kovach*, [1988]. The source mechanism of the Kalapana earthquake thus remains ambiguous.

3.2 Volcanic and geothermal earthquakes

3.2.1 Introduction

Observations from dense local seismic networks that give good focal sphere coverage show that earthquakes in several volcanic areas have non-DC mechanisms.

3.2.2 The Reykjanes Peninsula, southwest Iceland

A few earthquakes recorded at the Reykjanes Peninsula, SW Iceland, in an experiment in 1972 have non-DC P-wave polarity distributions with small dilatational fields [*Klein et al.*, 1977]. These events occurred within a large earthquake swarm that was recorded by 23 temporary stations. Most of the P-wave polarity distributions are consistent with DC mechanisms of normal and strike-slip type, compatible with the extensional tectonics of the region. The non-DC earthquakes had mostly compressional P-wave first motions, and the dilatational fields occupied less than half of the focal spheres. They were clustered in a small volume where seismicity was relatively low, and were intermingled spatially with DC events. This intermingling suggests that the non-DC mechanisms probably are not artifacts of propagation or instrumental effects. A source mechanism involving a tensile-faulting component could explain the observations [*Klein et al.*, 1977].

3.2.3 The Hengill-Grensdalur volcanic complex, southwest Iceland

The Hengill-Grensdalur volcanic complex in southwest Iceland is a rich source of non-DC earthquakes [*Foulger and Long*, 1984; *Foulger*, 1988b]. The area comprises an extensive high-temperature geothermal field, an active volcanic system and two essentially extinct systems (Figure 2a). Small-magnitude earthquakes occur continuously within the geothermal field.

Of several thousand earthquakes recorded by a 23-station temporary network in 1981, the mechanisms of 178 events were relatively well constrained by P-wave polarities [*Foulger*, 1988b] and half of these are incompatible with DC mechanisms. Their dilatational fields typically occupy considerably less than half of the focal sphere, which suggests that their mechanisms have explosive volumetric components. DC and non-DC earthquakes are spatially intermingled, so the non-DC observations probably are not artifacts of propagation or instrumental effects.

Mechanisms derived from P-wave polarities may be in error if the assumed directions of rays leaving the hypocenter are inaccurate, as can happen if structural heterogeneity is not correctly accounted for. The Hengill-Grensdalur earthquakes provide an unusually good opportunity to estimate this type of bias because high-quality, three-dimensional crustal models, derived by seismic tomography, are available [*Toomey and Foulger*, 1989; *Foulger et al.*, 1995]. Numerical ray-tracing using such models [*Foulger and Julian*, 1993] shows that errors in inferred ray directions can be as large as 35°, with the largest effect caused by bias in estimated focal depths, rather than the direct effects of refraction. These errors cannot, however, explain the non-DC earthquake mechanisms of the Hengill-Grensdalur earthquakes. When the data are mapped onto the focal

sphere using three-dimensional ray tracing, the number of events with non-DC focal mechanisms remains high.

In 1991 a second deployment in this area, of 30 three-component digital instruments, obtained P and S-wave amplitudes and waveforms, which provide greater constraint on the earthquake mechanisms. Inverting amplitude ratios by linear programming (Paper I, section 3.2.1) confirms that many earthquakes have substantial explosive volumetric components (Figure 2b) [*Julian and Foulger*, 1995]. Of 98 carefully studied earthquakes with moment magnitudes in the range 1.1 to 3.75, 72 have ε values greater than 0.1.

The non-DC earthquake mechanisms from the Hengill-Grensdalur area are consistent with simultaneous tensile and shear faulting (Paper I, section 4.3.4), with vertical tensile faults striking approximately parallel to the local ridge direction [*Miller et al.*, 1994]. An alternative kinematic possibility is oblique opening on ridge-parallel vertical faults. These inferred orientations of tensile cracks are consistent with the inferred stress field in the area, which is thought to involve ridge-normal extension, as this ridge segment has not spread for at least two centuries. The calculated mechanisms imply that about 30% of the moment release in these earthquakes occurs as tensile faulting.

Foulger and Long [1984] and *Foulger* [1988b] suggest that non-DC earthquakes at Hengill-Grensdalur are caused by thermal stresses induced in the heat source of the geothermal area as it is cooled by circulating ground water (Figure 2c). The regional extensional stress field, together with the availability of high-pressure geothermal fluids, enables tensile-mode failure to occur.

3.2.4 The Krafla volcanic system, north Iceland

Non-DC earthquakes also occur in the Krafla volcanic system in north Iceland. This system underwent a major dike-intrusion episode between 1975 and 1984, involving crustal rifting of several meters [*Björnsson*, 1985]. In 1985, a temporary network of 28 vertical-component seismometers recorded earthquakes for three months [*Foulger et al.*, 1989]. The earthquakes occurred continuously in time and most were clustered in the two geothermal areas within the system. *Arnott and Foulger* [1994a, b] used numerical ray tracing in a tomographically-derived three-dimensional model to determine hypocentral locations and to map P-wave polarity observations onto focal spheres. The focal depths of the earthquakes at Krafla were unexpectedly shallow and thus focal-sphere coverage sufficiently good to distinguish between DC and non-DC mechanisms was obtained for only a few events. Nevertheless, five events have polarity distributions incompatible with DC mechanisms, and four of these have significant volumetric components (two implosive and two explosive). Figure 3 shows a well constrained implosive example.

It is thought that, as in the Hengill-Grensdalur area, earthquakes in the Krafla system are caused mainly by thermal stresses induced by cooling of geothermal heat sources by ground water. However, the stress field at Krafla is inferred to have only a small deviatoric component, on the basis of the unsystematic orientations of DC-earthquake principal axes [*Arnott and Foulger*, 1994b], a state that was probably caused by the recent rifting [*Foulger and Long*, 1992]. Such a stress field is compatible with the occurrence of implosive and explosive volumetric earthquakes together.

3.2.5 Mid-ocean ridges (MORs)

The seismic and volcanic processes observed in Iceland have long been assumed to be similar to those at submarine spreading plate boundaries, and the recent discovery of many large geothermal areas along the MOR system suggests that small non-DC geothermal earthquakes may occur on

MORs also. Unfortunately, studying small MOR earthquakes is hindered by a lack of data, as currently deployed stations on land record MOR earthquakes well only for $m_b > 4.5$. For smaller earthquakes, the difficult and expensive deployment of ocean-bottom seismometers (OBSs) or hydrophones (OBHs) is necessary. Several OBS experiments on different sections of the MOR system have investigated small earthquakes and earthquake swarms, but none has involved enough stations to allow accurate determination of focal mechanisms. For example, a microearthquake monitoring experiment at the Mid-Atlantic Ridge in 1982 recorded a maximum of 10 P-wave first motions per earthquake [*Toomey et al.*, 1985, 1988]. Orthogonal nodal planes are consistent with the P-wave polarities for all these earthquakes, although for some events DC mechanisms require the assumption that large areas of the focal sphere devoid of data are dilatational. Rapid technological developments in ocean-bottom geophysical instrumentation may soon provide data to resolve the question of whether small non-DC earthquakes occur on the MOR.

3.2.6 The Geysers geothermal area, northern California

For more than a decade, large-scale steam mining has induced thousands of small earthquakes per month at The Geysers geothermal area in northern California. P-wave polarities for these earthquakes obtained from the permanent seismometer network of the U. S. Geological Survey (USGS) in the area usually allow DC interpretations [*Eberhart-Phillips and Oppenheimer*, 1984; *Oppenheimer*, 1986], although in some cases the polarities are all the same and polarity fields devoid of data must be assumed.

More comprehensive data, however, show that many Geysers earthquakes have explosive non-DC mechanisms. Figure 4 shows P- and SH-wave polarities and amplitude ratios for three earthquakes obtained in April 1991 from a dense local seismometer network that included 15 temporary three-component digital stations as well as stations of the permanent networks of the USGS and the UNOCAL Corporation. The focal-sphere positions of the observations are computed by ray tracing in the three-dimensional model of *Julian et al.* [1995b]. The earthquakes of 21 and 26 April have non-DC mechanisms involving volume increases and the earthquake of 17 April has a mechanism close to a DC.

3.2.7 Miyakejima, Izu islands

Many non-DC earthquakes with P-wave polarities that were either all dilatational or all compressional accompanied the 1983 eruption of Miyakejima volcano, in the Izu islands south of Honshu, Japan (Figure 5a,b). The earthquakes were recorded by 16 local short-period instruments [*Shimizu et al.*, 1987; *Ueki et al.*, 1984]. One area, close to the eruptive fissures produced many earthquakes with only dilatational P waves. The P waves from earthquakes in a second area, along the caldera rim, were all compressional. The earthquakes radiated significant S waves, however, so their mechanisms were not purely isotropic.

The observed P-wave polarities and P- and SV-wave amplitudes are compatible with sources involving combined tensile and shear faulting (Paper I, section 4.3.4). A kinematic model with tensile faults striking approximately N40°E, parallel to the eruptive fissures, fits data from both the implosive and explosive earthquakes. This interpretation is supported by the observation that many open cracks formed along the fissures prior to the eruption. An intrusion at the caldera rim could have caused these cracks to open and the explosive earthquakes. Closing of racks during and after the eruption, as the magma pressure decreased, is the most probable explanation for the dilatational earthquakes.

3.2.8 The Unzen volcanic region, western Kyushu, Japan

A magnitude 3.2 earthquake on 13 May 1987, 10 km beneath the Unzen volcanic region in western Kyushu, Japan, had compressional P-wave polarities at 23 out of 24 local seismic stations, which were well distributed on the focal sphere (Figure 5c) [*Shimizu et al.*, 1988; *Shimizu*, personal communication, 1988]. The kinematic tensile-shear fault model proposed for the Miyakejima earthquakes (section 3.2.7, above, and Paper I, section 4.3.4) can fit the observed polarities and P:SV amplitude ratios, with opening on an east-striking nearly vertical tensile fault accompanied by minor slip on a vertical shear fault. The orientation of the tensile fault is compatible with the stress orientation implied by N-S spreading in the Unzen graben.

3.2.9 Sakurajima Volcano, southern Kyushu, Japan

The andesitic Sakurajima volcano has been active continuously since 1955, with frequent eruptions and earthquakes of various empirically recognized types [*Iguchi*, 1994]. The volcano is monitored by a high-quality local network with eight seismographs, six of which have three components, as well as tiltmeters, extensometers, acoustic sensors, and video cameras. "A-type" earthquakes occur mainly outside the main magma conduit, excite both P and S waves, and have polarity and amplitude distributions consistent with DC mechanisms. They are probably caused by shear faulting. All the other types of earthquakes occur 2 to 3 km beneath the eruptive crater, and have identical polarities at all stations, inconsistent with DC mechanisms. "BL-type" earthquakes occur in swarms when the volcano is active. "BH-type" events are deeper, excite higher-frequency waves, and tend to occur when the volcano has been dormant for a few months. "Explosion" earthquakes accompany crater eruptions that radiate spectacular visible shock waves into the atmosphere [*Ishihara*, 1985]. BH-type and explosion earthquakes have entirely compressional P-wave polarities, whereas BL-type earthquakes have either entirely compressional or entirely dilatational polarities. S waves from BH, BL, and explosion earthquakes are vertically polarized.

There have been two recent determinations of focal mechanisms for Sakurajima earthquakes, but the results are inconsistent. *Uhira and Takeo* [1994] inverted waveforms from two explosion earthquakes, using three-component seismograms from three local stations evenly spaced around the crater at distances from 3 to 10 km. Figure 6 shows the derived moment-tensor time functions for one earthquake, which is consistent with deflation of a north-striking vertical crack (Paper I, section 4.3). The result for the other earthquake is similar except that the M_{xx} and M_{yy} components are about equal, indicating a source with azimuthal symmetry (two or more cracks with different strikes?). Rapid deflation of vertical cracks might rapidly expel gas and excite the observed atmospheric shock waves that accompany explosion earthquakes. Vertical forces accompanying the earthquakes, which would be expected consequences of eruption (Paper I, section 4.1.2) are consistent with the observations, but cannot be resolved well. *Iguchi* [1994] inverted P-wave amplitudes recorded at 8 stations within 5 km of the crater to obtain "moment acceleration" ($\ddot{\mathbf{M}}$) tensors for five explosion earthquakes, seven BL earthquakes, seven BH earthquakes, and two A earthquakes. The observed amplitudes were corrected for site effects using empirical factors determined from observations of teleseisms. The results for BH, BL, and explosion earthquakes are dominated by the vertical dipole components, as might be expected for inflation of horizontal cracks. If the reasons for the differences between the results of these two studies can be determined, the results are likely to greatly clarify our understanding of processes within Sakurajima.

3.2.10 Long Valley Caldera, California

Four earthquakes with $M_L > 6$, at least two of which had non-DC mechanisms, occurred near Long Valley caldera, eastern California, on 25 and 27 May 1980 (Figure 7). Open surface rupture

on cracks striking NNW-SSE, and parallel normal faulting with downthrow to the ENE, accompanied these earthquakes. The region had been dormant for decades until the M_L 5.7 "Wheeler Crest" earthquake of 4 October 1978, which was followed during the following two years by increasing numbers of small-magnitude earthquakes (Figure 7). Geodetic measurements made in the summer of 1980 showed that the caldera floor had been uplifted by as much as 20 cm, in a pattern consistent with inflation of a magma chamber under the caldera [*Rundle and Hill*, 1988]. Earthquakes and deformation have continued to the present, at gradually diminishing rates.

Unusually numerous and diverse seismic data are available for the large 1980 earthquakes, and they have been analyzed independently by a variety of methods. These data include polarities of short- and long-period P waves [*Cramer and Toppozada*, 1980; *Ryall and Ryall*, 1981; *Given et al.*, 1982; *Julian*, 1983; *Julian and Sipkin*, 1985], long-period P waveforms [*Barker and Langston*, 1983; *Julian and Sipkin*, 1985] and surface-wave amplitudes and initial phases [*Given et al.*, 1982; *Ekström and Dziewonski*, 1983, 1985]. The results of the analyses are consistent in requiring similar approximately deviatoric, non-DC mechanisms with large CLVD components for the first and third events[1]. The 1978 Wheeler Crest earthquake, which began the whole episode of unrest, is smaller and its mechanism is harder to resolve, but it also appears to have a similar mechanism with a large CLVD component [*Ekström and Dziewonski*, 1983; 1985]. The non-DC earthquakes occurred at widely separated locations, surrounding the DC event 2, suggesting that their mechanisms are not artifacts of wave-propagation or receiver effects.

At three stations to the northeast, near a nodal surface, short-period instruments show compressional first motions for the largest event and long-period instruments show dilatations [*Wallace et al.*, 1982]. Similar observations are not uncommon in seismology, and are expected consequences of spatial or temporal source complexity. For the Long Valley earthquakes, the significance of frequency-dependent first motions is unclear. They might be caused by complex shear faulting [*Wallace et al.*, 1982] or by propagating magma-filled cracks, with the initial compressional motions excited by tensile cracking, and later dilatations caused by pressure decreases in the cracks [*Aki*, 1984].

The source processes of these unusual earthquakes remains uncertain [*Wallace*, 1985]. Any isotropic (volumetric) components in the mechanisms are unresolvably small, and thus the events could, in theory, result from complex shear faulting (Paper I, section 4.2). The decomposition of a deviatoric moment tensor into two DCs is non-unique (Paper I, section 2.5), so many combinations of shear fault geometries and relative moments are theoretically possible, and indeed many mutually incompatible suggestions have been made [*Barker and Langston*, 1983; *Wallace et al.*, 1982; *Lide and Ryall*, 1984]. The complex shear-faulting hypothesis is contradicted by the finding of *Julian and Sipkin* [1985] that the largest event can be resolved into three sub-events, but that these all have similar, non-DC mechanisms. This finding contrasts with results from most complex earthquakes, which have DC sub-events (section 3.3.1).

Alternatively, the non-DC Long Valley earthquakes may have been caused by tensile faulting at high fluid pressure [*Julian*, 1983; *Julian and Sipkin*, 1985]. In this case, the volumetric component expected for a tensile fault (Paper I, section 4.3) must be compensated by fluid (CO_2, other gasses, or magma) flowing into the opening crack. The rather tentative available models of seismic-wave radiation in such processes do not seem to support this possibility quantitatively [*Chouet and Julian*, 1985].

[1] Given et al. [1982] modified a pure CLVD mechanism found for the first event to make it DC, arguing that some components of the mechanism are poorly resolved by long-period surface waves (Paper I, section 3.4.3).

3.2.11 Tori Shima, Izu-Bonin arc

An anomalous shallow earthquake of M_S 5.6 occurred on 13 June 1984 near Tori Shima island, located in the Izu-Bonin arc south of Honshu, Japan [*Kanamori et al.*, 1993]. This earthquake generated much larger tsunamis than would be expected from its magnitude [*Satake and Kanamori*, 1991] and produced anomalous seismic radiation nearly lacking in horizontally polarized shear (SH) motion and little azimuthal variation in the waves excited. Love-wave amplitudes were negligible compared with those of the Rayleigh waves, which had similar amplitudes and initial phases in all azimuths. All recorded P-wave first motions were compressional (Figure 8). These observations imply that the source was approximately symmetrical about a vertical axis, a situation that simplifies analysis (and rules out DC mechanisms).

Kanamori et al. [1993] inverted both long-period surface waves and teleseismic long-period body waves and obtained moment tensors with ε values between 0.3 and 0.4. Because the earthquake was shallow, the full moment tensor cannot be determined well (Paper I, section 3.4.3), so in most inversions moment tensors were constrained to be deviatoric. The result of one unconstrained inversion (Figure 8) indicates that the earthquake may have had a substantial volumetric component, and that the deviatoric component was close to a CLVD with its symmetry axis vertical .

Sudden horizontal intrusion of magma into ocean-floor sediments is kinematically consistent with the observations for this earthquake, and the resulting uplift of the ocean floor might explain the anomalously large tsunami. The seismic moment and source duration require the intrusion of approximately 0.02 km^3 of fluid within 10 to 40 seconds. Such a rate of intrusion may be possible for a mixture of magma and super-critical water [*Kanamori et al.*, 1993].

An alternative possibility is shear slip on a ring fault, which has a non-DC equivalent force system whose CLVD component increases with the arc spanned by faulting and decreases with fault dip (Paper I, section 4.2.1) [*Ekström*, 1994a]. For a fault dipping at 75°, the observed ε value of about 0.35 requires that the fault's strike vary by 180° or more. The required angle decreases for smaller dips, so slip on a more shallowly dipping fault, such as a cone-sheet, would not require such a large fault.

3.2.12 Bardarbunga volcano, southeast Iceland

Ekström [1994a] searched the Harvard CMT catalog for earthquakes in volcanic areas with nearly vertical CLVD-like mechanisms that might be caused by ring faulting, and found ten earthquakes world-wide, six of which occurred between 1977 and 1993 at the Bardarbunga volcano, beneath the Vatnajökull icecap in southeast Iceland. These earthquakes, of M_w 5.2 – 5.6 (M_0 = 8 – 30×10^{16} N m), have ε values between 0.36 and 0.48 (Figure 9).

Seismic observations impose constraints on the size and geometry of the hypothetical ring fault, because ε depends on the dip of the fault and the azimuthal range over which faulting occurs (i.e. the range of fault strikes). For a dip of 75°, the observed ε values require that the strike must span a range of 180° to 250°. The epicentral locations indicate that the ring has a radius of at least 10 km (Figure 9), which implies a fault length of 30 – 45 km and a scalar moment of at least 5×10^{17} N m (using empirical moment-source dimension relations [*Kanamori and Anderson*, 1975] and accounting for cancellation of moment release from different portions of the curved fault), which is larger than those observed. If the fault dips less than 60°, on the other hand, the predicted seismic moments would be consistent with those observed. Ring faults exposed in ancient calderas are usually vertical or dip steeply outwards [*e.g., Clough et al.*, 1909], which makes them inefficient generators of non-DC earthquakes. Cone sheets, which dip inward at shallow angles, have dips more consistent with those inferred.

3.2.13 "Long-period" volcanic earthquakes

Many small earthquakes in volcanic regions have spectra dominated by frequencies roughly ten times lower than ordinary shear-faulting earthquakes of comparable magnitudes. These "long-period" earthquakes are attributed to the underground movement of magmatic fluids, and are expected to have mechanisms involving net forces (Paper I, section 4.1.3).

Few analyses of long-period earthquakes have allowed for the possibility of net forces, however. A notable exception is the study by *Ukawa and Ohtake* [1987] of a long-period earthquake at Izu-Ooshima volcano, Japan. This volcano, located on a small island east of the Izu Peninsula in south-central Honshu, began a major eruption on 15 November 1986. Fifteen months earlier, on 27 August 1985, an unusual earthquake occurred about 30 km beneath the volcano. Several analog and 18 digital three-component local stations recorded the earthquake, producing a data set of unusually high quality. At all stations a monochromatic S-wave train with a dominant frequency of 1 Hz lasted for more than one minute (Figure 10a). The observed P:S amplitude ratios are small, and inconsistent with sources involving tensile cracks or oscillations of magma chambers. The S-wave polarization directions agree much better with those predicted for a force oriented north-south than with those from a DC (Figure 10b). These observations confirming the predicted net-force component of the mechanism supports the attribution of long-period earthquakes to unsteady fluid flow.

3.3 Earthquakes at mines

Deep mining strongly perturbs stresses in the surrounding rocks, reducing components normal to tunnel walls from values initially of the order of 100 MPa (1 kbar) to about 0.1 MPa (1 bar). The resulting stress differences (shear stresses) can exceed the strength of competent rocks and cause earthquakes (often called "rock bursts", "coal bumps", etc.). Mining-induced earthquakes, like natural earthquakes, have generally been attributed to shear faulting and assumed to have DC mechanisms [*McGarr*, 1987;*Wong and McGarr*, 1990], but recent studies have found clear examples with non-DC mechanisms. The first motions from such earthquakes are predominantly dilatational and clearly incompatible with orthogonal nodal planes [*e.g., Kusznir et al.*, 1984; *Rudajev and Sileny*, 1985; *Brawn*, 1989; *Wong et al.*, 1989; *Wong and McGarr*, 1990; *Feignier and Young*, 1992; *McGarr*, 1992a, b, 1993; *Stickney and Sprenke*, 1993; *Taylor*, 1994].

The seismic data available from mines are often of superb quality, recorded on large numbers of multi-component instruments and involving short ray paths (a few hundred meters or less) through homogeneous rock, free from the effects of rock weathering that degrade surface observations. Thus data from mines provide some of the highest-quality observations of non-DC earthquakes.

3.3.1 Gentry Mountain mining region, Utah

An M_L 3.5 earthquake at the Gentry Mountain mining region, Utah, 14 May 1981 had several unusual characteristics [*Taylor*, 1994]. Surface-wave amplitude and initial phases require an implosive volumetric component [*Patton and Zandt*, 1991] and the earthquake excited small surface waves with high-frequency spectral characteristics similar to explosions in the area. This event coincided with a large room collapse underground at the Gentry Mountain Mine, and was modeled as a tabular excavation collapse at 200 m depth [*Taylor*, 1994].

3.3.2 Couer d'Alene mining district, Idaho

During a 15-station seismic monitoring experiment at the Couer d'Alene mining district, Idaho, 21 earthquakes that had at least six identifiable first motions were recorded (Figure 11) [*Stickney*

and Sprenke, 1993]. Ninety percent of the observed P-wave first motions were dilatational. Ten of these earthquakes have P-wave polarity distributions inconsistent with orthogonal nodal planes.

3.3.3 Underground Research Laboratory, Manitoba

An experiment involving excavation of a 3.5-meter wide tunnel in unfractured, homogeneous granite at the Underground Research Laboratory in Manitoba, Canada, triggered many non-DC earthquakes [*Feignier and Young*, 1992]. The tunnel is surrounded by a network of 16 triaxial accelerometers, and hypocenter locations have an estimated accuracy of 0.5 m. *Feignier and Young* [1992] calculated moment tensors for 33 earthquakes in the moment-magnitude range -2 to -4 that occurred during a 24-hour period immediately after the tunnel was lengthened by 3 m. They classified them as tensile, implosive or shear events. All 12 tensile events occurred above the tunnel, close to an area of breakout on the tunnel roof, and had parallel T axes. The T axes lie in the σ_1-σ_3 plane, and are perpendicular to the outline of the breakout zone, suggesting that the earthquakes were caused by the breakout. Most of the six implosive earthquakes occurred in front of the active face. Shear events had volumetric:deviatoric moment ratios of less than 30%.

3.3.4 Westdriefontein, South Africa

Brawn [1989] calculated higher-degree moment tensors (Paper I, section 2.2.1) for four mining-induced earthquakes at a depth of 2.2 km in Westdriefontein, South Africa. He applied a maximum entropy method to the initial sections of the P waveforms recorded at up to 22 geophones in the mine to calculate the first three degrees of the moment tensor. This gives information about the spatial and temporal variation of moment release as rupture proceeds. Three of the mechanisms were similar, and indicated shear failure occurring away from the mining tunnels. The method is sensitive enough to detect that the shear failure was preceded by a high-frequency, short-duration failure, probably the initiation of rupture. This initial moment release corresponds to the first P-wave pulse, lasts for less than a millisecond, and is followed by weaker shear failure of longer duration. The fourth earthquake, located within five meters of an active tunnel, had a mechanism that implied two different modes of failure on the same plane, oriented normal to the tunnel. The proposed process involves shear slip along a pre-existing fracture, which simultaneously propagated into intact rock by tensile failure.

3.3.5 Witwatersrand , South Africa

Earthquakes occur frequently near the deep mines in the Witwatersrand gold fields in S. Africa [*McGarr*, 1992a, b, 1993]. Using data from both surface stations and temporary underground stations, well distributed throughout a small volume of essentially homogeneous rock, that operated in this area from 1986 to 1989, *McGarr* [1992b] inverted the polarities and amplitudes of near- and far-field P and S-waves (Paper I, sections 3.1.3, 3.2) (Figure 12a) to obtain moment tensors for 10 earthquakes located within 150 m of the tunnels, at depths of 2 to 3.3 km. The mechanisms are of two distinct types. Seven involve large volumetric decreases, and have their most negative principal moments oriented approximately vertically (Figure 12b). All the principal moments are negative, so all P-wave first motions are dilatational and these events resemble the "implosive" earthquakes of *Feignier and Young* [1992]. The moment tensors of the other three earthquakes have insignificant volumetric components and are consistent with shear faulting. The implosive events probably are caused by shear faults intersecting tunnels. The volume of the tunnel decreases suddenly as a result of the earthquake, which causes the implosive moment tensor component. The shear events occur on faults that do not intersect tunnels [*McGarr*, 1993]. The bi-modal distribution of observed volumetric moments is unexplained.

3.4 Other shallow earthquakes

3.4.1 Evidence for fault-normal motion

Unlike the planar idealizations used in mathematical analysis, real fault surfaces are rough, so "shear" slip is expected to involve some amount of motion normal to faults. Furthermore, motion occurs normal to even planar faults in laboratory experiments on stick-slip sliding in foam rubber (Paper I, section 4.4.3). Kinematically, fault-normal motion is equivalent to tensile faulting (Paper I, section 2.3.2). There is some evidence that such motion occurs in many earthquakes.

Haskell [1964] found that P:S amplitude ratios at high frequency are usually larger than those expected for shear faulting, and suggested that this indicates fault-normal motion caused by the roughness of natural fault surfaces. High P:S ratios might also be caused by anelastic attenuation (which affects shear waves more than compressional waves) or S-to-P mode conversion, but the observed effect is too large to be explained entirely by propagation effects. The theoretical P:S energy ratio for fault-normal motion is about ten times greater than for shear faulting, so only a small amount of fault-normal motion is needed to explain the observed ratios.

High P:S amplitude ratios at frequencies above 10 Hz were measured for local earthquakes at the Guerrero accelerometer array, Mexico [*Castro et al.*, 1991]. The ratio varies greatly for different source-station pairs but on average is far higher than expected for a DC source. *Castro et al.* [1991] show that the ratio varies even for events at similar distances from a single station. These observations cannot be explained by attenuation effects alone, and must be at least partly due to a source effect.

3.4.2 Complex shear faulting

If two or more shear-faulting earthquakes occur nearly simultaneously, or if the fault orientation or slip direction changes as faulting proceeds, the overall mechanism of the resulting composite event can have a non-DC component (Paper I, section 4.2), although some practically important cases, such as conjugate faulting, give DC composite mechanisms. The moment tensor for such an earthquake can, however, never have a volumetric component. Non-DC mechanisms attributable to complex faulting are rather common, especially for deep-focus earthquakes (section 3.5.3).

For example, *Sipkin* [1986a], in a study of the M_L 6.5 Coalinga, California earthquake of 2 May 1983, found that constraining the moment tensor components to be similar functions of time produces a spurious non-DC result. If this constraint is removed, the derived moment tensor varies significantly with time and corresponds to a DC that rotates slightly during rupture propagation.

The M_S 6.8 Armenia earthquake of 7 December 1988, which has an ϵ value of -0.20 in the Harvard CMT catalog, appears to result from multiple shear faulting. The teleseismic body waveforms are complex for an event of this size, and aftershock locations suggest variations in fault orientation (Figure 13). Detailed moment tensor analysis using broad-band and long-period records resolved three strike-slip DC sub-events of approximately equal size in the first 20 seconds of rupture [*Pacheco et al.*, 1989]. Analysis of a longer interval suggests that an additional dip-slip event occurred about 30 s after the initial rupture [*Kikuchi et al.*, 1993]. The sum of these four separate DC mechanisms is similar to the non-DC Harvard CMT solution.

3.4.3 Large earthquakes at MORs

Large, normal-faulting MOR earthquakes recorded teleseismically often have P-wave polarity distributions with reduced dilatational fields and non-orthogonal nodal surfaces [*e.g., Sykes*, 1967]. These are, however, probably artifacts of near-source wave-propagation effects. Because MOR

earthquakes are very shallow, the direct (P) and surface-reflected (pP and sP) phases arrive nearly simultaneously, and interference between them can reverse the apparent polarities for certain take-off angles [*Hart*, 1978; *Trehu et al.*, 1981].

Huang et al. [1986] inverted long-period teleseismic P and SH waveforms from 14 large earthquakes on MOR crests and obtained DC mechanisms consistent with normal faulting. Inversions of the surface waves from some of the same, and other, earthquakes are also consistent with normal faulting [*Weidner and Aki*, 1973; *Trehu et al.*, 1981] although such data have less resolving power than long-period body waves because MOR earthquakes are shallow (Paper I, section 3.4.3).

In apparent disagreement with this, the moment tensors of large MOR earthquakes in the Harvard CMT catalog have systematically positive ε values averaging 0.057. These mechanisms are consistent with combined normal and strike-slip faulting [*Kawakatsu*, 1991a]. Such a combination of DCs can explain 70% of the well-constrained non-DC moment tensors for earthquakes in the Harvard catalog from "well-behaved" MOR segments, *i.e.*, those located away from continental margins [*Frohlich*, 1994].

3.4.4 A 57-km deep earthquake in the Kanto district, Honshu, Japan

A well recorded magnitude 4.6 earthquake on 10 February 1987 beneath the Kanto district, Japan, had a P-wave polarity distribution that is highly inconsistent with a DC interpretation (Figure 14) [*Hurukawa and Imoto*, 1993]. Dilatational arrivals cover most of the focal sphere, which is well sampled by over 40 stations in Japan. P-wave polarities are consistent with conical nodal planes with an apex angle of about 78°, which imply that the source has an implosive isotropic component (the apex angle for a CLVD is 109.47°). This earthquake occurred within the subducting Philippine Sea plate at 57 km depth. Observations of nearby events, including a magnitude 3.9 aftershock, are compatible with DC mechanisms, which suggests that this anomalous mechanism is not an artifact of the wave-propagation effects. *Hurukawa and Imoto* [1993] suggested that the earthquake was caused by a combination of an implosive phase transformation in an "anti-crack" and shear faulting.

3.5 Deep-focus earthquakes

3.5.1 Introduction

As functions of depth, both the frequency of earthquake occurrence and the rate of seismic moment release have bi-modal distributions, with activity below about 350 km much greater than would be expected from extrapolation of shallow-earthquake trends (Figure 15). Earthquakes at these depths occur only in subduction zones, where slabs of lithosphere sink into the mantle. The minimum in activity at intermediate depths was once attributed to changes from tension to compression within slabs, but extensive data on earthquake focal mechanisms now contradict this hypothesis in many subduction zones [*Green and Houston*, 1995]. The deep earthquake region coincides closely with the "transition zone" of the upper mantle, where polymorphic phase transformations in olivine produce two rapid increases in seismic-wave speeds (the 400- and 670-km "discontinuities"). Earthquakes cease near 680 km, the base of the transition zone, even though the lithosphere apparently penetrates deeper, at least in some places. Phenomenologically, deep earthquakes differ in several respects from shallow ones. They produce fewer aftershocks. They have shorter rise times and durations for events of the same magnitude [*Vidale and Houston*, 1993] and they have more symmetrical source time functions (intermediate and shallow earthquakes tend to have moment release concentrated in the early portion of the source-time function) [*Houston and*

Vidale, 1994]. The largest deep earthquakes tend to occur in regions that are otherwise relatively inactive. There is usually no obvious spatial relationship between a deep earthquake and its aftershocks [*Frohlich and Willemann*, 1987; *Willemann and Frohlich*, 1987], and neither aftershocks nor rupture sub-events cluster preferentially along nodal planes of deep main shocks, although hypocenters of smaller earthquakes (not aftershocks) near major earthquakes are sometimes aligned [*Giardini and Woodhouse*, 1984; *Lungren and Giardini*, 1992]. All these facts suggest that deep and shallow earthquakes involve different physical processes.

The physical causes of deep earthquakes has posed an enigma since they were first recognized in the 1920s. Stick-slip frictional instability, to which shallow earthquakes are attributed, is inhibited by pressure, and plastic flow in minerals is enhanced by temperature, so stick-slip is not expected to operate below about 30 km in normal areas. Unusual conditions such as low temperature or high pore-fluid pressure might extend this limit to 100 km or so in subduction zones, but not to the depths of almost 700 km to which earthquakes persist. Some other kind of instability must cause deep earthquakes. Processes that have been considered include plastic instabilities, shear-induced melting, and polymorphic phase transformation [*Green and Houston*, 1995]. A recently recognized variant of the last process, "transformational faulting" (Paper I, section 4.6.1), has dominated recent experimental and theoretical work on deep earthquakes.

3.5.2 Volume changes

The cessation of deep earthquakes at the bottom of the upper mantle transition zone near 680 km (Figure 15) suggests that they may involve polymorphic phase transformations, but no experiments have yet convincingly resolved volume changes associated with them. One of the earliest moment-tensor inversions of seismic data, applied to normal modes of the Earth [*Gilbert and Dziewonski, 1975*], gave large precursory volume changes about 100 seconds before the deep $M_0 = 7 \times 10^{20}$ N m 1963 Peru-Bolivia earthquake of 15 August 1963 and the $M_0 = 2 \times 10^{21}$ N m Colombian earthquake of 31 July 1970, but these may have been artifacts of laterally inhomogeneous structure [*Okal and Geller*, 1979]. Studies of more recent large earthquakes, based on more numerous and higher-quality data, have not detected volume changes. For example, high-quality observations of the $M_0 = 3 \times 10^{21}$ N m Bolivian deep earthquake of 9 June 1994, discussed more fully below, show no evidence a substantial volumetric component [*Hara et al.*, 1994; *Ekström*, 1994b]. Analysis of the waveforms of long-period body waves of 19 deep earthquakes by *Kawakatsu* [1991b] showed that their volumetric components are statistically insignificant (<10% of the seismic moment). *Stimpson and Pearce* [1987] inverted P, pP and sP amplitude ratios (Paper I, section 3.2.1) to determine moment tensors for three deep earthquakes in the Sea of Okhotsk in a search for volume changes, but found no evidence of departure from DC mechanisms.

3.5.3 Deviatoric non-DC mechanisms

Deep earthquakes do, however, have systematically large non-DC components, even though these do not involve significant volume changes. In other words, deep earthquakes have larger CLVD components than shallow ones (Figure 16). The size of CLVD components may increase systematically with depth and with event magnitude [*Houston*, 1993], but these conclusions are uncertain. *Kubas and Sipkin* [1987] reported a strong positive correlation between CLVD components and magnitudes for deep earthquakes in the Nazca Plate subduction zone, but could not find a similar relationship elsewhere. The CLVD components of deep-earthquake moment tensors determined using different inversion schemes and data sets often agree well [*Kuge and Kawakatsu*, 1993], which suggests that these components are not artifacts of particular methods.

Non-DC components of deep-focus earthquakes may be partially artifacts of unmodeled path effects. Subduction zones, where deep earthquakes occur, have higher seismic-wave speeds than the surrounding mantle, because they are cooler than and compositionally different from it. Numerical simulation of the effects of a high-velocity slab on seismic waves shows that spurious non-DC components can be introduced into derived mechanisms if wavelengths are smaller than the slab thickness [*Tada and Shimazaki*, 1994].

The lack of large volume changes in deep earthquakes is compatible with complex shear faulting (Paper I, section 4.2), and detailed waveform analysis resolves some deep non-DC earthquakes into DC sub-events. For example, the January 1, 1984, South of Honshu deep earthquake has two prominent P-wave arrivals, consistent with DC sources of different orientations [*Kuge and Kawakatsu*, 1990, 1992]. Commonly the DC sub-events share a principal axis that lies within the dipping slab [*Kuge and Kawakatsu*, 1993]. Eighty percent of the deep earthquakes in the Harvard CMT catalog that have large non-DC components and small standard errors are consistent with pairs of DC earthquakes with particular orientations thought to be realistic (caused, for example by down-dip compression and slab bending) [*Frohlich*, 1994].

Glennon and Chen [1995] used P and SH waveforms to model the mechanisms of eight deep earthquakes in the northwestern Pacific, six of which showed evidence of rupture propagation, usually on sub-horizontal planes. For most events, the estimated sub-horizontal rupture plane fits within the predicted thickness of the metastable olivine wedge at depth.

The $M_0 = 3 \times 10^{21}$ N m (M_w 8.3) Bolivian earthquake of June 9, 1994 is the largest deep earthquake yet observed, and provides the best data available from a deep earthquake. It occurred at a depth of 636 km in a region of the Nazca Plate subduction zone characterized by anomalous deep seismicity [*Okal et al.*, 1994]. Independent analyses of body and surface waves give similar mechanisms, corresponding to slip on a nearly horizontal, 40-50 km long fault [*e.g., Kikuchi and Kanamori*, 1994; *Silver et al.*, 1995], with no significant volume change [*Hara et al.*, 1994; *Ekström*, 1994b]. The inferred source dimensions greatly exceed the theoretical thickness of the hypothesized wedge of metastable olivine at 630 km (less than 10 km). Thus the fault must extend outside the cold core of the subducting slab. The earthquake had relatively few aftershocks, but they were close to the inferred main-shock rupture plane. Some aftershocks occurred outside the hypothesized metastable wedge.

The deep Bolivian earthquake produced several new proposals for deep earthquake mechanisms [*Houston*, 1994]. The earthquake rupture may have begun as transformational faulting within the metastable wedge, and then extended out of it, possibly facilitated by shear melting [*Kanamori*, personal communication].

3.6 Non-DC earthquakes in moment tensor catalogs

Moment tensors for large earthquakes are now computed routinely (Paper I, section 3.3.2). The Harvard Centroid Moment Tensor (CMT) catalog is the most complete, containing over 11,000 events that occurred between 1978 and 1994 [*e.g. Dziewonski et al.*, 1987]. Of these, hundreds of events have large and statistically-significant non-DC components. These events occur in all tectonic environments and geographic areas [*Frohlich*, 1994].

There can be large discrepancies between the non-DC components for the same earthquake in the Harvard and U. S. Geological Survey (USGS) catalogs (Figure 17), with $|\varepsilon|$ from the USGS catalog systematically smaller than from the Harvard catalog [*Sipkin*, 1986b]. Different data are used for the two catalogs (Paper I, section 3.3.2), so some differences in the results are to be

expected. Comparison of the two catalogs gives information on their reliabilities, and indicates that uncertainties are larger than the formal statistical error estimates.

There is an inverse correlation between ε and scalar moment for shallow thrust-faulting earthquakes in the Harvard catalog [*Kuge and Lay*, 1994b], but surface waves are used only for events with moments larger than about 10^{18} N m [*Dziewonski and Woodhouse*, 1983], so this correlation may be an artifact of the inversion process. It may also reflect the effect of noisy seismograms. For realistic station distributions and for certain DC source mechanisms, the addition of random noise with a standard deviation of 10% to seismograms can produced $|\varepsilon|$ values as large as 0.3 [*Satake* , 1985].

The most reliable non-DC moment tensors are those that are reproducible using different methods and different data sets, such as that of the Tori Shima earthquake (section 3.3.10) and some deep earthquakes (section 3.2.11) [*Kuge and Kawakatsu*, 1993].

4. DISCUSSION

The term "non-double-couple" is uninformative and negative, expressing merely what these earthquakes are not, and implying that they deviate from some standard. The observations now available make it clear that the term actually encompasses several physical phenomena, although our understanding of them is still highly incomplete. Furthermore, theoretical considerations and recent laboratory experiments hint that such processes may be intrinsic in the nucleation and continuation of predominately-shear earthquakes also. Attention to non-DC processes is likely to become increasingly important as the quality of seismic data, the power of analytical methods, and the sophistication of our understanding of earthquake processes continue to increase.

Even "common" shear-faulting earthquakes have small non-DC components, because of departures from ideal geometry such as fault curvature and roughness, and variations in slip direction. Furthermore, the formation of shear faults is thought to involve tensile micro-cracking, though this has not yet been detected by seismological methods.

Some kinds of events, such as landslides and volcanic eruptions, involve advection and require source representations more general than moment tensors, including net forces (section 3.1). In theory, landslides require net torques also, although no analyses to date have included these. Doing so might help to resolve inconsistencies such as that between seismological and field observations for the Mantato landslide.

A disproportionate fraction of non-DC earthquakes occur in volcanic and geothermal areas. Some, such as the Tori Shima earthquake (section 3.3.10), the Barbarbunga earthquakes (section 3.6.3), and the Long Valley caldera earthquakes (section 3.3.9), have mechanisms close to pure CLVDs and may be caused by rapid intrusions, probably of gas-rich magma, although ring faulting or simultaneous slip on multiple shear faults cannot be ruled out, in theory. Other earthquakes in volcanic and geothermal areas (sections 3.3.2, 3.3.3, 3.3.4, 3.3.6, 3.3.7, 3.3.8, 3.3.9) and mines (section 3.3) have mechanisms with isotropic components, involving volume increases or decreases, which are consistent with mixed-mode failure, involving simultaneous shear and tensile faulting. In geothermal areas, high temperature/pressure geothermal fluids may provide mobile material to fill cavities and enable tensile cracks to form and remain open at depths of several km. At mines, tunnels may act as cavities that can close seismically. Data from MORs are not yet adequate to determine whether small, non-DC earthquakes occur there also, although the resemblance of geologic processes and structures on MORs to those in Iceland makes this likely. Some volcanic earthquake mechanisms include net forces (sections 3.2.9, 3.2.13), indicating that these events

involve the advection of magmatic fluids. Future analyses of volcanic earthquake mechanisms must allow for possible net force components if the source processes are to be fully understood.

Stick-slip sliding instability cannot operate beneath about 300 km depth. This fact, and various empirical seismological differences, suggest that deep- and shallow-focus earthquakes involve different physical processes. Moreover, seismic data indicate that deep-focus earthquakes do not involve significant volume changes, even though they occur within the transition zone, a region of polymorphic phase transformations in the upper mantle. They do, however, have larger CLVD components, on average, than shallow earthquakes. Mechanisms of this type are consistent with simultaneous shear slip on differently oriented faults. Current theory attributes deep earthquakes to "transformational shear faulting", facilitated by phase changes in small "anti-cracks" in the same way that formation of ordinary shear faults is facilitated by tensile micro-cracks. It is not yet clear, however, why anti-cracks should favor simultaneous shear faulting.

ACKNOWLEDGMENTS

We thank ? and ? for critically reviewing the manuscript and suggesting improvements. This research was supported by a G. K. Gilbert Fellowship from the U. S. Geological Survey and NERC grants *, * and *. A. D. Miller was supported by a NERC Ph.D. studentship.

REFERENCES

Aki, K., Evolution of quantitative models of earthquakes, *SIAM-AMS Proc., 12*, 43-58, 1979.

Aki, K., Evidence for magma intrusion during the Mammoth Lakes earthquakes of May 1980, and implications of the absence of volcanic (harmonic) tremor, *J. Geophys. Res., 89*, 7689-7696, 1984.

Ando, M., The Hawaii earthquake of November 29, 1975; Low dip angle faulting due to forceful injection of magma, *J. Geophys. Res., 84*, 7616-7626, 1979.

Arnott, S. K. and G. R. Foulger, The Krafla spreading segment, Iceland: 1. Three-dimensional crustal structure and the spatial and temporal distribution of local earthquakes, *J. Geophys. Res., 99*, 23801-23825, 1994a.

Arnott, S. K. and G. R. Foulger, The Krafla spreading segment, Iceland: 2. The accretionary stress cycle and non-shear earthquake focal mechanisms, *J. Geophys. Res., 99*, 23827-23842, 1994b.

Barker, J. S. and C. A. Langston, A teleseismic body wave analysis of the May, 1980 Mammoth Lakes, California earthquakes, *Bull. Seismol. Soc. Am., 73*, 419-434, 1983.

Benioff, H., Source wave forms of three earthquakes, *Bull. Seismol. Soc. Am., 53*, 893-903, 1963.

Bergman E. A. and S. C. Solomon, Earthquake swarms on the mid-Atlantic ridge- Products of magmatism or extensional tectonics?, *J. Geophys. Res., 95*, 4943-4965, 1990.

Björnsson, A., Dynamics of crustal rifting in NE Iceland, *J. Geophys. Res., 90*, 10151-10162, 1985.

Brawn, D. R., A maximum entropy approach to underconstraint and inconsistency in the seismic source inverse problem; Finding and interpreting seismic source moments, Ph.D thesis, University of the Witwatersrand, Johannesburg, 163 pp., 1989.

Castro, R. R., J. G. Anderson and J. N. Brune, Origin of high P/S spectral ratios from the Guerrero Accelerograph array, *Bull. Seismol. Soc. Am., 81*, 2268-2288, 1991.

Chouet, B., Sources of seismic events in the cooling lava lake of Kilauea Iki, Hawaii, *J. Geophys. Res., 84*, 2315-2330, 1979.

Chouet, B. and B. R. Julian, Dynamics of an expanding fluid-filled crack, *J. Geophys. Res., 90*, 11187-11198, 1985.

Clough, C. T., H. B. Maufe and E. B. Bailey, The cauldron-subsidence of Glen Coe, and the associated igneous phenomena., *Q. J. Geol. Soc. London, 65*, 611-678, 1909.

Cramer, C. H. and T. R. Toppozada, A seismological study of the May 1980, and earlier earthquake activity near Mammoth Lakes, California, *California Division of Mines Geological Special Report, 150*, 91-130, 1980.

Doxsee, W. W., The Grand Banks earthquake of November 18, 1929, *Publ. Dom. Observ., 7*, 323-335, 1948.

Dziewonski, A. M. and J. H. Woodhouse, An experiment in the systematic study of global seismicity: Centroid-moment tensor solutions for 201 moderate and large earthquakes of 1981, *J. Geophys. Res., 88*, 3247-3271, 1983.

Dziewonski, A. M., G Ekström, J. E. Franzen and J. H Woodhouse, Centroid-moment Tensor solutions for January-March 1986, *Phys. Earth. Planet. Inter., 45*, 1-10, 1987.

Eberhart-Phillips, D., and D. H. Oppenheimer, Induced seismicity in the Geysers geothermal area, California, *J. Geophys. Res.,, 89*, 1191-1207, 1984.

Eissler, H. K. and Kanamori, H., A single-force model for the 1975 Kalapana, Hawaii, earthquake, *J. Geophys. Res.*, 92, 4827-4836, 1987.

Eissler, H. K. and Kanamori, H., Reply, *J. Geophys. Res., 93*, 8083-8084, 1988.

Kanamori, H., G. Ekström, A. Dziewonski, J. S. Barker and S. A. Sipkin, Seismic radiation by magma injection - An anomalous seismic event near Tori Shima, Japan, *J. Geophys. Res.*, *98*, 6511-6522, 1993.

Kawakatsu, H., Centroid single force inversion of seismic waves generated by landslides, *J. Geophys. Res.*, *94*, 12363-12374, 1989.

Kawakatsu, H., Enigma of earthquakes at ridge-transform fault plate boundaries. Distribution of non-double couple parameter of Harvard CMT solutions, *Geophys. Res. Lett.*, *18*, 1103-1106, 1991a.

Kawakatsu, H., Insignificant isotropic component in the moment tensor of deep earthquakes, *Nature*, *351*, 50-53, 1991b.

Kawasumi, H., An historical sketch of the development of knowledge, *Bureau Central Seismologique Intern. Publ. Ser. A, Fasc. 15*, 2nd part, 258-330, 1937.

Kikuchi, M., and H. Kanamori, The mechanism of the deep Bolivian earthquake of June 9, 1994, *EOS Trans. AGU*, *75*, 465, 1994.

Kikuchi, M., H. Kanamori and K. Satake, Source complexity of the 1988 Armenian Earthquake: Evidence for a slow after-slip event, *J. Geophys. Res.*, *98*, 15797-15808, 1993.

Klein, F. W., P. Einarsson and M. Wyss, The Reykjanes Peninsula, Iceland, earthquake swarm of September 1972 and its tectonic significance, *J. Geophys. Res.*, *82*, 865-887, 1977.

Kubas, A. and S. A. Sipkin, Non-double-couple earthquake mechanisms in the Nazca Plate subduction zone, *Geophys. Res. Lett.*, *14*, 339-342, 1987.

Kuge, K. and H. Kawakatsu, Analysis of a deep non-DC earthquake using very broad band data, *Geophys. Res. Lett.*, *17*, 227-230, 1990.

Kuge, K. and H. Kawakatsu, Deep and intermediate depth non-double couple earthquakes-Interpretation of moment tensor inversions using various passbands of very broadband seismic waves, *Geophys. J. Int.*, *111*(3), 589-606, 1992.

Kuge, K. and H. Kawakatsu, Significance of non-double couple components of deep and intermediate earthquakes: Implications from moment tensor inversions of long period seismic waves, *Phys. Earth. Planet. Inter.*, *75*, 243-266, 1993.

Kuge, K. and T. Lay, Data-dependent non-double-couple components of shallow earthquake source mechanisms: effects of waveform inversion instability, *Geophys. Res. Lett.*, *21*, 9-12, 1994b.

Kusznir, N. J., N. H. Al-Singh and D. P. Ashwin, Induced-seismicity generated by longwall coal mining in the North Staffordshire coal field, U. K., in: N. C. Gay and E. H. Wainwright (eds.), Rockbursts and seismicity in mines, *S. African Inst. Mining and Metallurgy Symp. Ser.* no. 6, 153-160, 1984.

Lawson, A. C., The California Earthquake of April 18, 1906. *Report of the State Earthquake Investigation Commission, Volume I*, Carnegie Institution, Washington D. C., 451 pp., 1908.

Lide, C. S. and A. S. Ryall, Relationship between aftershock locations and mechanisms of the May, 1980 Mammoth Lakes earthquakes, In: Active Tectonic and Magmatic Processes Beneath Long Valley Caldera, Eastern California, *U. S. Geol. Surv. Open File Report* , *84-939*, 440-452, 1984.

Lungren, P. R. and D. Giardini, Seismicity, shear failure and modes of deformation in deep subduction zones, *Phys. Earth. Planet. Inter.*, *74*, 63-74, 1992.

McGarr, A., Seismic moments and volume changes, *J. Geophys. Res.*, *81*, 1487-1494, 1976.

McGarr, A., An implosive component in the seismic moment tensor of a mining-induced tremor, *Geophys. Res. Lett.*, 19, 1579-1582, 1992a.

McGarr, A., Moment tensors of 10 Witwatersrand mine tremors, *Pure Appl. Geophys.*, *139*, 781-800, 1992b.

McGarr, A., Factors influencing the strong ground motion from mining-induced tremors, *Proc. 3rd Int. Symp. Rockbursts and Seismicity in Mines*, Kingston, Ontario, 1993.

Miller, A. D., B. R. Julian and G. R. Foulger, Well constrained non-double-couple earthquakes at the Hengill geothermal area, SW Iceland, *EOS Trans. AGU*, *75*, 446, (abstract), 1994.

Okal, E. A. and R. J. Geller, On the observability of isotropic sources: the July 31, 1970 Colombian earthquake, *Phys. Earth Planet. Inter.*, *18*, 176-196, 1979.

Okal, E. A., E. R. Engdahl, S. H. Kirby and W.-C. Huang, Deep South American earthquakes: the general context of the large 09 June 94 Bolivia shock, an extraordinary event in an extraordinary Wadati-Benioff Zone, *EOS Trans. AGU*, *75*, 465, (abstract), 1994.

Oppenheimer, D. H., Extensional tectonics at the Geysers geothermal area California, *J. Geophys. Res.*,, *91*, 11463-11476, 1986.

Pacheco, J. F., C. H. Estabrook, D. W. Simpson and J. L. Nabelek, Teleseismic body wave analysis of the 1988 Armenian earthquake, *Geophys. Res. Lett.*, *16*, 1425-1428, 1989.

Patton, H. J. and G. Zandt, Seismic moment tensors of Western U. S. Earthquakes and implications for the tectonic stress field, *J. Geophys. Res.*, *96*, 18245-18259, 1991.

Reid, H. F., The California Earthquake of April 18, 1906. *Report of the State Earthquake Investigation Commission, Volume II: The Mechanics of the Earthquake*, Carnegie Institution, Washington D. C., 192 pp., 1910.

Richter, C. F., *Elementary Seismology*, Freeman, San Francisco, 1958.

Robson, G. R., K. G. Barr and L. C. Luna, Extension failure: An earthquake mechanism, *Nature*, *218*, 28-32, 1968.

Rudajev V. and J. Sileny, Seismic events with non-shear components: II Rockbursts with implosive source component, *Pageoph.*, *123*, 17-25, 1985.

Rundle, J. B. and D. P. Hill, The geophysics of a restless caldera- Long Valley, California, *Ann. Rev. Earth Planet. Sci.*, *16*, 251-71, 1988.

Ryall, A. and F. Ryall, Spatial temporal variations in seismicity preceding the May 1980, Mammoth Lakes, California, earthquakes, *Bull. Seismol. Soc. Am.*, *71*, 747-760, 1981.

Satake, K., Effects of station coverage on moment tensor inversion, *Bull. Seismol. Soc. Am.*, *75*, 1657-1667, 1985.

Satake, K. and H. Kanamori, Abnormal tsunamis caused by the June 13 1984 Tori Shima, Japan, earthquake, *J. Geophys. Res.*, *96*, 19933-19939, 1991.

Shimizu, H., S. Ueki and J. Koyama, A tensile-shear crack model for the mechanism of volcanic earthquakes, *Tectonophysics*, *144*, 287-300, 1987.

Shimizu, H., N. Matsuwo and S. Ohmi, A non double-couple seismic source: Tensile-shear crack formation in the Unzen Volcanic Region, *Seismol. Res. Lett.*, *59*, 5, 1988.

Silver, P. G., S. L. Beck, T. C. Wallace, C. Meade, S. C. Meyers, D. E. James and R. Kuehnel, Rupture characteristics of the deep Bolivian earthquake of 9 June 1994 and the mechanism of deep-focus earthquakes, *Science*, *268*, 69-73, 1995.

Sipkin, S. A., Interpretation of non-double couple earthquake mechanisms derived from moment tensor inversion, *J. Geophys. Res.*, *91*, 531-547, 1986a.

Sipkin, S. A., Estimation of earthquake source parameters by the inversion of waveform data: Global seismicity 1981-1985, *Bull. Seismol. Soc. Am.*, *76*, 1515-1541, 1986b.

Stickney, M. C. and K. F. Sprenke, Seismic events with implosional focal mechanisms in the Couer d'Alene mining district, northern Idaho, *J. Geophys. Res.*, *98*, 6523-6528, 1993.

Stimpson I. G. and R. G. Pearce, Moment tensors and source processes of three deep Sea of Okhotsk earthquakes, *Phys. Earth. Planet. Inter.*, *47*, 107-124, 1987.

Ekström, G., Anomalous earthquakes on volcano ring-fault structures, *Earth Planet. Sci. Lett.*, *128*, 707-712, 1994a.

Ekström, G., Teleseismic analysis of the great 1994 Bolivia earthquake, *EOS Trans. AGU*, *75*, 465 (abstract), 1994b.

Ekström, G. and A. M. Dziewonski, Moment tensor solutions of Mammoth Lakes earthquakes, *EOS Trans. AGU*, *64*, 262 (abstract), 1983.

Ekström, G. and A. M. Dziewonski, Centroid-moment Tensor solutions for 35 earthquakes in Western North America (1977 to 1983), *Bull. Seismol. Soc. Am.*, *75*, 23-39, 1985.

Evison, F. F., Earthquakes and faults, *Bull. Seismol. Soc. Am.*, *53*, 873-891, 1963.

Feignier, B. and R. P. Young, Moment tensor inversion of induced microseismic events: Evidence of non-shear failures in the -4<M<-2 moment magnitude range, *Geophys. Res. Lett.*, *19*, 1503-1506, 1992.

Foulger, G. R., Hengill Triple Junction, SW Iceland. 1. Tectonic structure and the spatial and temporal distribution of local earthquakes, *J. Geophys. Res.*, *93*, 13493-13506, 1988a.

Foulger, G. R., Hengill Triple Junction, SW Iceland. 2. Anomalous earthquake focal mechanisms and implications for processes within the geothermal reservoir at accretionary plate boundaries, *J. Geophys. Res.*, *93*, 13507-13523, 1988b.

Foulger, G. R. and R. E. Long, Anomalous focal mechanisms: Tensile crack formation on an accreting plate boundary, *Nature*, *310*, 43-45, 1984.

Foulger, G. R. and R. E. Long, Non-double couple earthquake focal mechanisms and the accretionary tectonic cycle, in: Gasparini, P., Scarpa, R. and Aki, K. (Eds.) Volcanic Seismology, *IAVCEI Proceedings in Volcanology*, *3*, Springer-Verlag, pp. 223-234, 1992.

Foulger, G. R. and B. R. Julian, Non-double-couple earthquakes at the Hengill-Grensdalur Volcanic Complex, Iceland: Are they the artifacts of crustal heterogeneity?, *Bull. Seismol. Soc. Am.*, *83*, 38-52, 1993.

Foulger, G. R., R. E. Long, P. Einarsson and A. Björnsson, Implosive earthquakes at the active accretionary plate boundary in Northern Iceland, *Nature*, *337*, 640-642, 1989.

Foulger, G. R., A. D. Miller, B. R. Julian and J. E. Evans, Three-dimensional V_P and V_P/V_S of the Hengill triple junction and geothermal area, Iceland, and the repeatability of tomographic inversion, *Geophys. Res. Lett.*, *22*, 1309-1312, 1995.

Frohlich, C., Where do "sweet" earthquakes occur?- characteristics of well-determined deviatoric non-double-couple earthquake sources, *Pageoph.*, submitted, 1994.

Frohlich, C. and R. J. Willemann, Aftershocks of deep earthquakes do not occur preferentially on nodal planes of focal mechanisms, *Nature* , *329*, 41-42, 1987.

Giardini, D. and J. H. Woodhouse, Deep seismicity and modes of deformation in the Tonga subduction zone, *Nature, 307*, 505-509, 1984.

Gilbert, F., and A.M. Dziewonski, An application of normal mode theory to the retrieval of structural parameters and source mechanisms from seismic spectra, *Philos. Trans. R. Soc. London Ser. A*, *278*, 187-269, 1975.

Gilbert, G. K., A theory of the earthquakes of the Great Basin, with a practical application, *Am. J. Sci.*, *XXVII*, 49-54, 1884.

Given, J. W., T. C. Wallace and H. Kanamori, Teleseismic analysis of the 1980 Mammoth Lakes earthquake sequence, *Bull. Seismol. Soc. Am.*, *72*, 1093-1109, 1982.

Glennon, M. A. and W.-P. Chen, Ruptures of deep-focus earthquakes in the north-western Pacific and their implications on seismogenesis, *Geophys. J. Int.*, *120*, 706-720, 1995.

Green, H. W. III, and H. Houston, The mechanics of deep earthquakes, *Annu. Rev. Earth Planet. Sci.*, *23*, 169-213, 1995.

Hara, T., K. Kuge and H. Kawakatsu, The determination of moment tensor of the 1994 Bolivia deep earthquake using various datasets of seismic waves at very broadband frequency, *EOS Trans. AGU*, *75*, 465 (abstract), 1994.

Hart, R. S., Body wave studies of the September 1969 North Atlantic Ridge earthquake, *EOS Trans. AGU*, *59*, 1135 (abstract), 1978.

Hasegawa, H. S and H. Kanamori, Source mechanism of the magnitude 7.2 Grand Banks earthquake of November 1929: Double couple or submarine landslide?, *Bull. Seismol. Soc. Am.*, *77*, 1984-2004, 1987.

Haskell, N. A., Total energy and energy spectral density of elastic wave radiation from propagating faults, *Bull. Seismol. Soc. Am.*, *54*, 1811-1841, 1964.

Houston, H., The non-double-couple component of deep earthquakes and the width of the seismogenic zone, *Geophys. Res. Lett.*, *20*, 1687-1690, 1993.

Houston, H., Deep quakes shake up debate, *Nature*, *372*, 724, 1994.

Houston, H. and Vidale, J., The temporal distribution of seismic radiation during deep earthquake rupture, *Science*, *265*, 771-774, 1994.

Huang, P. Y., S. C. Solomon, E. A. Bergman and S. L. Nabelek, Focal depths and mechanisms of Mid-Atlantic Ridge earthquakes from body waveform inversion, *J. Geophys. Res.*, *91*, 579-598, 1986.

Hurukawa, N. and Imoto, M., A non double-couple earthquake in a subducting oceanic crust of the Philippine Sea plate, *J. Phys. Earth*, *41*, 257-269, 1993.

Iguchi, M., A vertical expansion source model for mechanisms of earthquakes originating in the magma conduit of an andesitic volcano, Japan, *Bull. Volcanol. Soc. Japan*, *39*, 49-67, 1994.

Isacks B., J. Oliver and L. R. Sykes, Seismology and the new global tectonics, *J. Geophys. Res.*, *73*, 5855-5899, 1968.

Ishihara, K., Dynamical analysis of volcanic explosion, *J. Geodynamics*, *3*, 327-349, 1985.

Ishimoto, M., Existence d'une source quadruple au foyer sismique d'apres l'etude de la distribution des mouvements initiaus des secousses sismiques, *Bull. Earthquake Res. Inst. Univ. Tokyo*, *10*, 449-471, 1932.

Julian, B. R., Evidence for dyke intrusion earthquake mechanisms near Long Valley Caldera, California, *Nature*, *303*, 323-325, 1983.

Julian, B. R. and S. A. Sipkin, Earthquake processes in the Long Valley Caldera Area, California, *J. Geophys. Res.*, *90*, 11155-11169, 1985.

Julian, B. R. and G. R. Foulger, Moment tensors from linear inversion of body-wave amplitude ratios: Powerful constraints on earthquake mechanisms, *Bull. Seismol. Soc. Am.*, submitted, 1995.

Julian, B. R., A. D. Miller and G. R. Foulger, Non-double-couple earthquakes I. Theory, *Rev. Geophys.*, 1995a (this volume).

Julian, B, R., A. Ross, G. R. Foulger, and J. R. Evans, Three-dimensional seismic image of a geothermal reservoir: The Geysers, California, *Geophys. Res. Lett.* (submitted), 1995b.

Kanamori, H and D. L. Anderson, Theoretical basis for some empirical relations in seismology, *Bull. Seismol. Soc. Am.*, *65*, 1073-1092, 1975.

Kanamori, H and J. W. Given, Analysis of long period seismic waves excited by the May 18, 1980, eruption of Mt. St. Helens - A terrestrial monopole?, *J. Geophys. Res.*, *87*, 5422-5432, 1982.

Kanamori, H, J. W. Given and T. Lay, Analysis of seismic body waves excited by the Mount St. Helens eruption of May, 1980, *J. Geophys. Res.*, *89*, 1856-1866, 1984.

and may also include a downward force, but the relative contributions of F_z and M_{xz} cannot be resolved well. Second contractile pulse for times greater than about 8 s may not be well resolved. Coordinate axes (x,y,z) are directed (north, east, down). Solid lines: best-fit solutions; dashed lines: error bounds. [From *Uhira and Takeo*, 1994].

Figure 7. Long Valley Caldera, California, and vicinity, showing best-located earthquakes in 1980 with coda-duration magnitude > 3 and mechanisms for largest earthquakes of 1978 and 1980. WC: M_S 5.3 "Wheeler Crest" earthquake of 4 October 1978; 1: M_S 6.1 earthquake of 16:34 on 25 May 1980; 2: M_S 6.0 earthquake of 19:45 on 25 May 1980; 3: M_S 6.0 earthquake of 14:51 on 27 May 1980. Unlabelled star: $M_S \geq 6$ earthquake of 16:49 on 25 May 1980, whose mechanism cannot be determined well. The Wheeler Crest earthquake and earthquakes 1 and 3 have mechanisms with large non-DC components. Heavy line: caldera boundary. Lower hemisphere equal-area projections, with fields of compressional P-wave polarity shaded. [From *Julian and Sipkin*, 1985]. Mechanism of Wheeler Crest earthquake from *Ekström and Dziewonski* [1983].

Figure 8. (a) Body waves from the 13 June 1984 Tori Shima earthquake and, for comparison, a nearby thrust-faulting earthquake in November 1983. Vertical (V), radial horizontal (R) and transverse horizontal (T) seismograms are shown for stations plotted on the lower focal hemisphere (equal-area projection) at the lower right. P and S phases are marked. The tangential records show a clear difference in P:SH amplitude ratios between the two events. All recorded P waves for the Tori Shima earthquake had compressional first motions. Δ : epicentral distance; ϕ : epicenter-to-station azimuth. [From *Kanamori et al.*, 1993]. (b) Decomposition of strongly non-DC focal mechanism of *Kanamori et al.* [1993].

Figure 9. Map showing Harvard CMT focal mechanisms of earthquakes at Bardarbunga volcano, southeast Iceland, from Ekström [1994a]. Also shown are the southeast coast of Iceland and the outline of the Vatnajökull icecap.

Figure 10. Top: examples of vertical-component seismograms from the long-period earthquake of 27 August 1985 beneath Izu-Ooshima volcano, Japan. Note nearly sinusoidal wave trains of long duration. Bottom: Polarization directions of S waves. (a) best-fit model, a single force oriented to the north, (b) best-fit double couple. The sums of squared residuals ("SSR"), mean residuals ("Av. of Ri") and standard deviations ("STD") of the fits to polarization directions are shown for each solution. Shading show the range of axis positions for SSR < 30 rad^2. Lower hemisphere equal-area projections. [From *Ukawa and Ohtake*, 1987].

Figure 11. Earthquakes with predominantly dilatational P-wave polarities from the Cour d'Alene mining district, northern Idaho. Solid circles: compressional polarities; open circles: dilatations. Upper focal hemispheres are shown in equal-area projection. From *Stickney and Sprenke* [1993].

Figure 12. Near-field seismograms and derived moment tensor for a non-DC mining earthquake in the Witwatersrand gold fields, South Africa. (a) Three-component displacement seismograms (doubly integrated accelerograms) from stations HMN and HBF. The phases P, near-field S (nf), S to P conversion (SP), S, and surface-reflected S (R) are shown. [From *McGarr*, 1992b]. (b) Decomposition of the moment tensor derived by *McGarr* [1992b] from the seismograms in (a) into

volumetric (implosive) and deviatoric components. Numbers: principal moments in units of 10^{14} N m. Trends and plunges of associated principal axes are (281°, 10°), (12°, 4°), and (122°, 79°).

Figure 13. Map showing complex-shear-faulting interpretation of M_S 6.8 Armenian earthquake of 7 December 1988, from *Pacheco et al.* [1989]. First sub-event, north of town of Spitak, was followed within 20 seconds by events 17 km to the southeast and 38 km to the west. Diamonds: towns; dots: aftershocks; thin dashed line: trace of fault observed on LANDSAT images; Heavy dashed line: inferred fault position at depth of aftershocks.

Figure 14. P-wave polarities for the magnitude 4.6 non-DC earthquake of 10 February 1987 in the Kanto district, Japan. Nodal surfaces shown are for a "conical type" mechanism with an apex angle of 78°, which corresponds to a mechanism with both implosive isotropic and CLVD components. Open circles: dilatational polarities; filled circles: compressions. Different symbol sizes indicate data from different networks. Upper focal hemisphere is shown in equal-area projection. [From *Hurukawa and Imoto*, 1993].

Figure 15. Distribution of seismic moment release with depth for worldwide earthquakes from 1980 to 1989 inclusive. Activity below about 300 km is much greater than predicted by extrapolated trend from shallower events. Data from Preliminary Determination of Epicenters (PDE) catalog of the U. S. Geological Survey, with moments M_0 (N m) derived from magnitudes using the empirical relation $M_0 = 9.1 + 1.5M$.

Figure 16. Observed distributions of ε, which measures the relative contribution of CLVD components to mechanisms, for shallow and deep earthquakes in the Harvard CMT catalog between 1 January 1977 and 31 May 1994. Deep earthquakes have systematically more negative values.

Figure 17. Comparison of the non-DC components of earthquakes in the Harvard CMT catalog and the USGS moment tensor catalog. (a) ε values for 1418 events between January 1980 and May 1994 that are in both catalogs. (b) and (c) Histograms of ε for the same data set. There is no clear correlation between the ε values in the two catalogs.

Sykes, L. R., Mechanism of earthquakes and nature of faulting on mid-ocean ridges, *J. Geophys. Res.*, *72*, 2131-2153, 1967.

Tada, T. and K. Shimazaki, How much does a high-velocity slab contribute to the apparent non-double-couple components in deep-focus earthquakes?, *Bull. Seismol. Soc. Am.*, *84*, 1272-1278, 1994.

Takei, Y., and M. Kumazawa, Why have the single force and torque been excluded from seismic source models?, *Geophys. J. Int.*, *118*, 20-30, 1994.

Taylor, S. R., False alarms and mine seismicity: An example from the Gentry Mountain Mining Region, Utah, *Bull. Seismol. Soc. Am.*, *84*, 350-358, 1994.

Toomey, D. R., S. C. Solomon, G. M. Purdy and M. H. Murray, Microearthquakes Beneath the median valley of the Mid-Atlantic Ridge near 23N: Hypocenters and focal mechanisms, *J. Geophys. Res.*, *90*, 5443-5458, 1985.

Toomey, D. R., S. C. Solomon and G. M. Purdy, Microearthquakes Beneath the median valley of the Mid-Atlantic Ridge near 23N: Tomography and tectonics, *J. Geophys. Res.*, *93*, 9093-9112, 1988.

Toomey, D. R. and G. R. Foulger, Inversion of local earthquake data from the Hengill-Grensdalur Central Volcanic complex, Iceland, *J. Geophys. Res.*, *94*, 17497-17510, 1989.

Trehu, A. M., J. L. Nabelek and S. C. Solomon, Source characterization of two Reykjanes Ridge earthquakes: Surface waves and moment tensors; P waveforms and non-orthogonal nodal planes, *J. Geophys. Res.*, *86*, 1701-1724, 1981.

Ueki, S., H. Shimizu, J. Comm and A. Takagi, Seismic activity following the 1983 eruption of Miyakejima, in: The 1983 eruption of Miyakejima, *Bull. Volcanol. Soc. Japan, Series II*, *29*, S81-S100, 1984.

Uhira, K. and M. Takeo, The source of explosive eruptions of Sakurajima volcano, Japan, *J. Geophys. Res.*, *99*, 17775-17789, 1994.

Ukawa, M. and M. Ohtake, A monochromatic earthquake suggesting deep-seated magmatic activity beneath the Izu-Ooshima volcano, Japan, *J. Geophys. Res.*, *92*, 12649-12663, 1987.

Vidale, J. E. and H. Houston, The depth dependence of earthquake duration and implications for rupture mechanisms, *Nature*, *365*, 45-47, 1993.

Voight, B., H. Glicken, R. J. Janda, and P. M. Douglass, Catastrophic rockslide avalanche of May 18, in The 1980 Eruptions of Mount St. Helens, Washington, edited by P. W. Lipman and D. R. Mullineaux, *U. S. Geol. Surv. Prof. Pap.*, *1250*, 347-377, 1981.

Wallace, T., A Re-examination of the moment tensor solutions of the 1980 Mammoth Lakes earthquakes, *J. Geophys. Res.*, *90*, 11171-11176, 1985.

Wallace, T., J. Given and H. Kanamori, A discrepancy between long- and short-period mechanisms of earthquakes near the Long Valley Caldera, *Geophys. Res. Lett.*, *9*, 1131-34, 1982.

Weidner, D. J. and K. Aki, Focal depth and mechanisms of mid-ocean ridge earthquakes, *J. Geophys. Res.*, *78*, 1818-1831, 1973.

Willemann, R. J. and C. Frohlich, Spatial patterns of aftershocks of deep focus earthquakes, *J. Geophys. Res.*, *92*, 13927-13943, 1987.

Wong, I. G. J. R. Humphrey, J. A. Adams and W. J. Silva, Observations of mine seismicity in the Eastern Wasatch Plateau, Utah, U.S.A.: A possible case of implosional failure, *Pageoph.*, *129*, 369-405, 1989.

Wong, I. G. and A. McGarr, Implosional failure in mining-induced seismicity: A critical review, In: C. Fairhurst (Editor), *Rockbursts and Seismicity in Mines*, Bakema, Rotterdam, 45-51, 1990.

Wyss M. and R. L. Kovach, Comment on "A single-force model for the 1975 Kalapana, Hawaii, Earthquake" by Holly K. Eissler and Hiroo Kanamori, *J. Geophys. Res.*, *93*, 8078-8082, 1988.

FIGURE CAPTIONS

Figure 1. Equivalent-force model of the 18 May 1980 eruption of Mount St. Helens, Washington state, derived from seismic-wave observations by *Kanamori et al.* [1984]. Left: time line showing the sequence of events reconstructed from photographic and other observations. Center: vertical force caused mainly by the eruption, which consists of two major pulses, each composed of sub-events. Positive values indicate downward force. Right: horizontal force caused mainly by the landslide. Positive (southward) forces indicate acceleration of the slide, and negative values indicate deceleration.

Figure 2. (a) Map of the Hengill-Grensdalur volcanic complex, SW Iceland. Dashed lines: areas of maximum volcanism within the three volcanic systems. Solid lines: fissure zones. Dots: hot springs and fumaroles. Inset shows location of the area within Iceland, and its relationship to the mid-Atlantic ridge ("MAR") and neovolcanic zones of Iceland (shaded) [From *Foulger*, 1988a]. (b) P-wave polarities plotted on upper focal hemispheres in stereographic projection for representative earthquakes recorded in 1991. Solid circles: compressions; open circles: dilatations. These polarity patterns cannot be fit with orthogonal nodal planes, even after local structural heterogeneity has been accounted for. The nodal surfaces are calculated by inverting P and S-wave polarities and amplitude ratios [From *Foulger and Julian*, 1993]. (c) Schematic illustration of the process of tensile cracking by thermal stresses caused by convective cooling of rocks at the heat source of a geothermal system [From *Foulger*, 1988b].

Figure 3. Observed P-wave polarities for a non-DC earthquake on 6 August 1985 at the Krafla volcano, northeast Iceland, after *Arnott and Foulger* [1994b]. Open circles: dilatational polarities; Filled circles: compressions. Nodal surfaces shown are for most explosive mechanism consistent with observations, which is still strongly implosive. Upper focal hemisphere is shown in equal-area projection.

Figure 4. Focal mechanisms of two non-DC earthquakes (top and middle rows) and one DC earthquake (bottom row) at The Geysers geothermal area, northern California. Dates and origin times are given at left. Left column: P-wave polarities; middle column; SH-wave polarities; right column, P:SH-wave amplitude ratios. Open symbols: dilatational polarities; filled symbols: compressions. Squares: lower-hemisphere observations plotted at their antipodal points. Amplitude ratios are represented using scheme of *Julian and Foulger* [1995], with directions of small arrows giving theoretical ratios, and line segments indicating ranges compatible with observations. Upper focal hemispheres are shown in equal-area projection.

Figure 5. P-wave polarities for three non-DC earthquakes at volcanic regions in Japan. (a) and (b): earthquakes at Miyakejima Island in 1983. Solid circles: compressions; open circles: dilatations. Upper focal hemispheres are shown in equal-area projection. [From *Shimizu et al.*, 1987]. (c) Earthquake of 13 May 1987 in the Unzen volcanic region. Upper hemisphere is shown in equal-area projection. Triangles: compressions; circles: dilatations. [From *Shimizu, unpublished manuscript*, 1987].

Figure 6. Mechanism of "explosion" earthquake of 14 November 1986 at Sakurajima volcano, Kyushu, Japan. Mechanism is roughly consistent with deflation of a north-striking vertical crack,

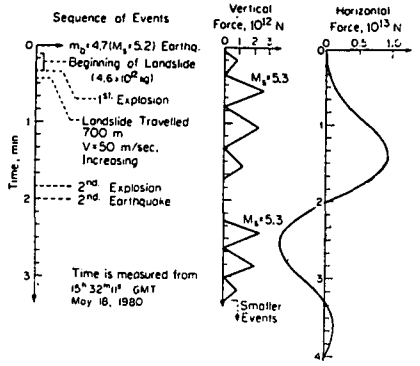

Fig. 1

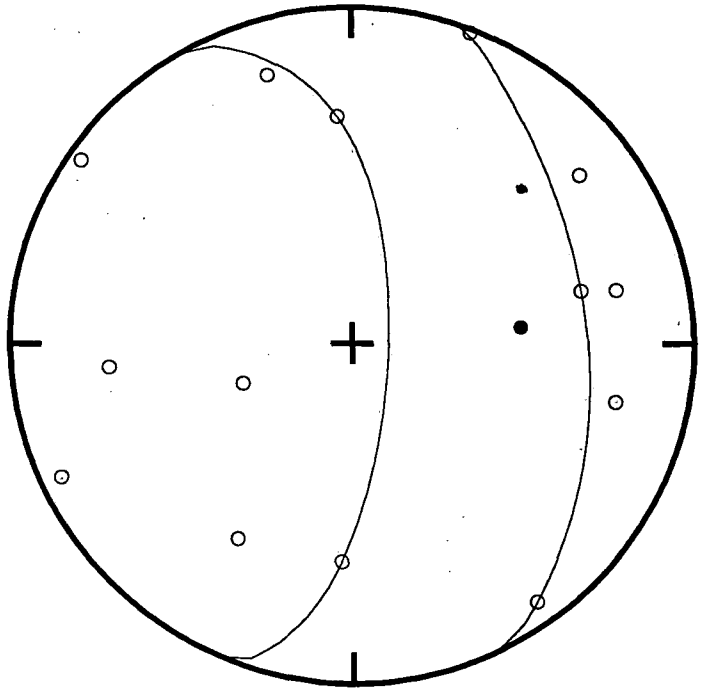

Fig. 3

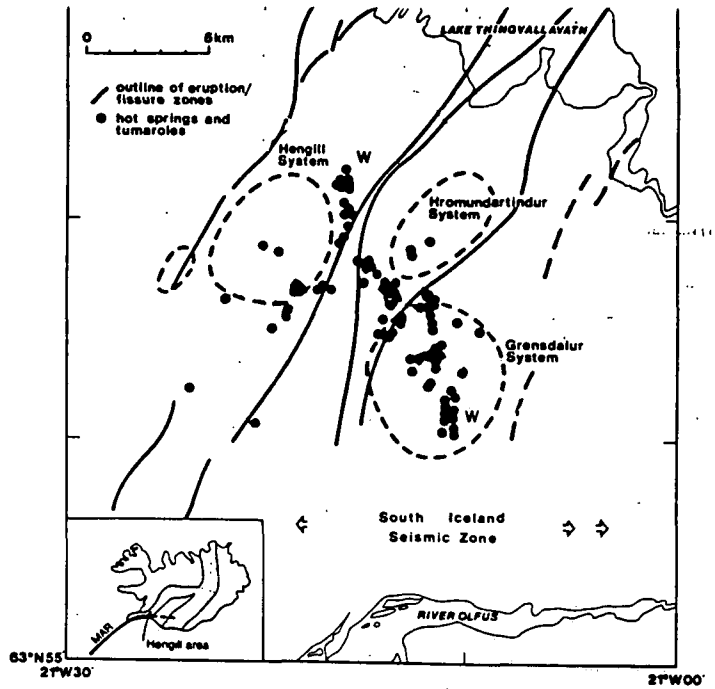

(b)

910813 0902

910915 0741

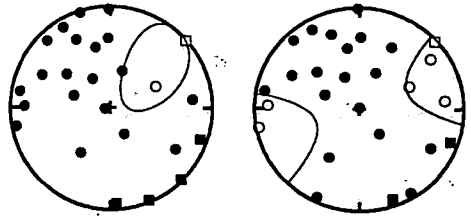

(c)

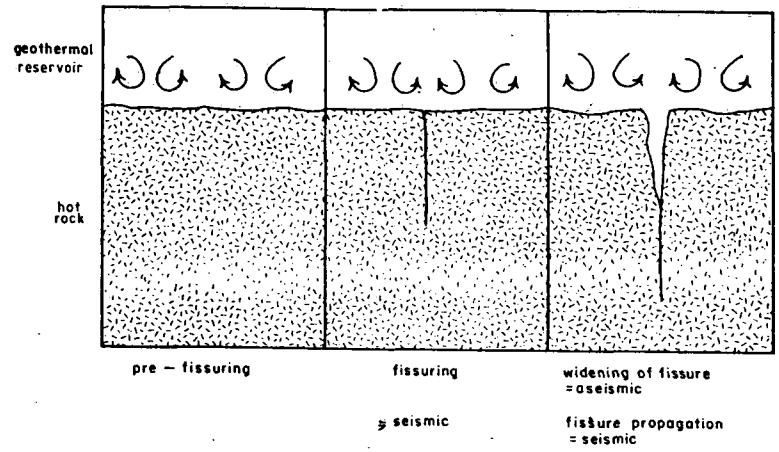

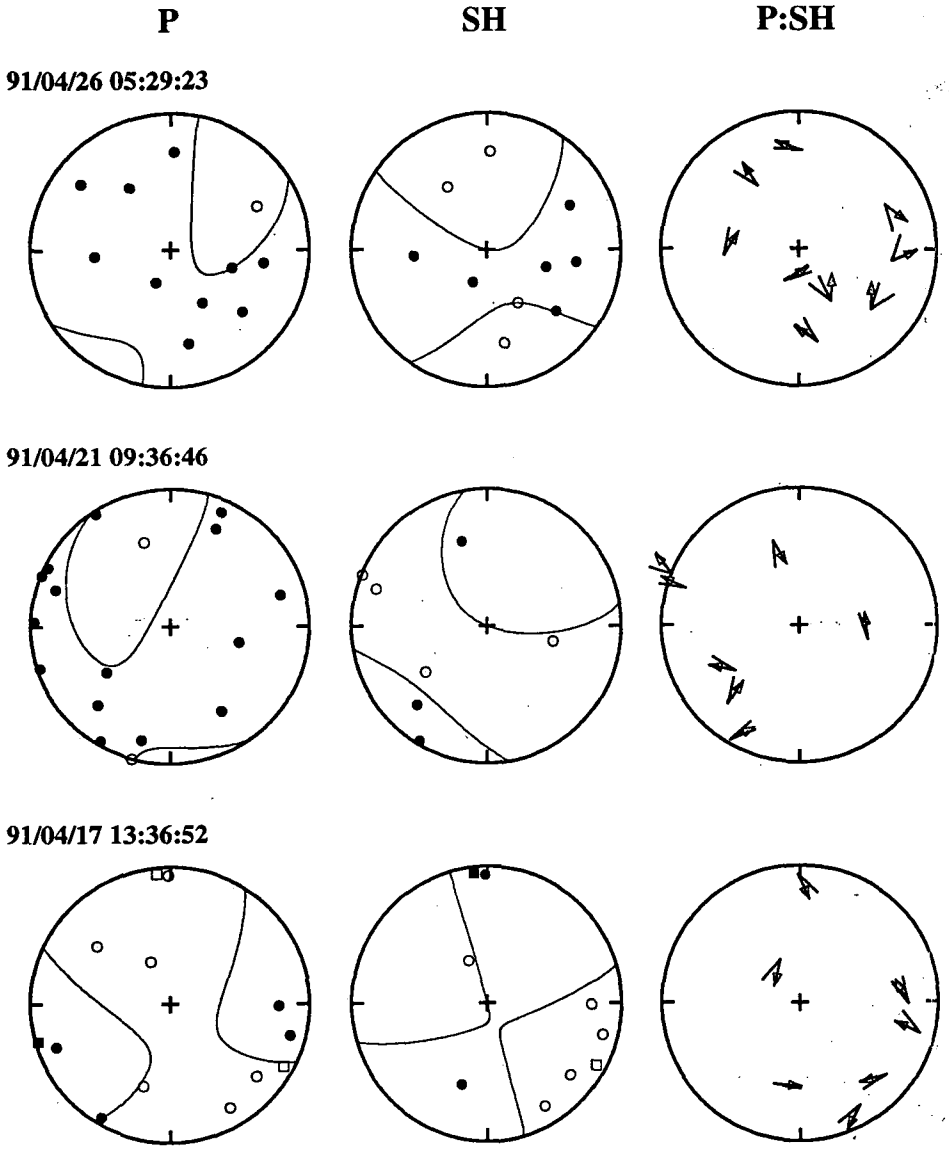
P
SH
P:SH
91/04/26 05:29:23
91/04/21 09:36:46
91/04/17 13:36:52

Fig. 4

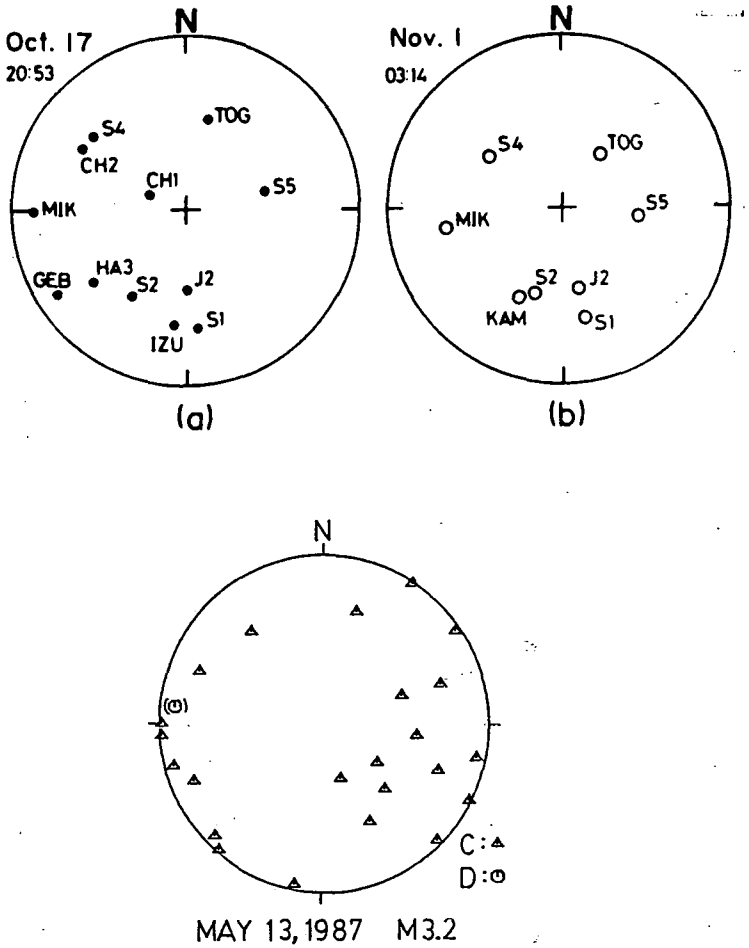
Oct. 17
20:53
N
S4
TOG
CH2
CH1
S5
MIK
GEB
HA3
S2
J2
S1
IZU
(a)
Nov. 1
03:14
N
S4
TOG
MIK
S5
S2
J2
KAM
S1
(b)
N
C:
D:
MAY 13, 1987 M3.2

Fig. 5

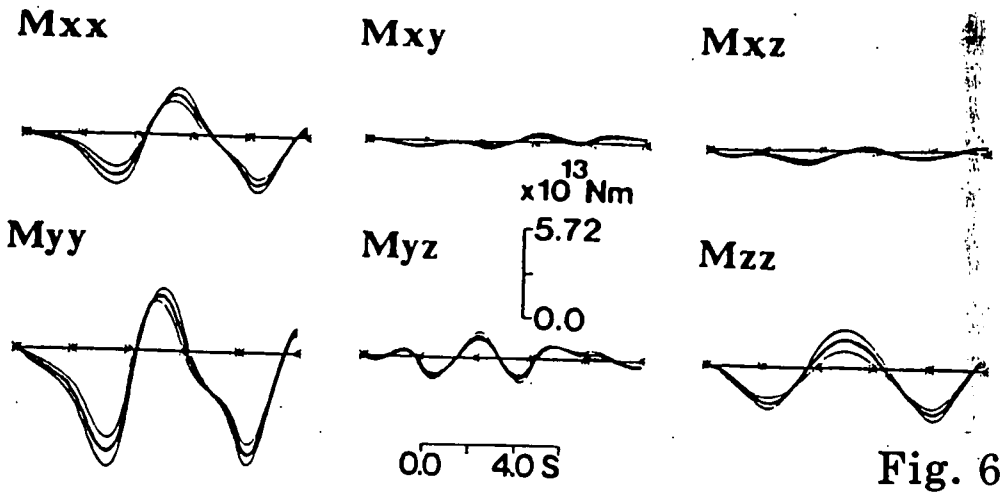

Fig. 6

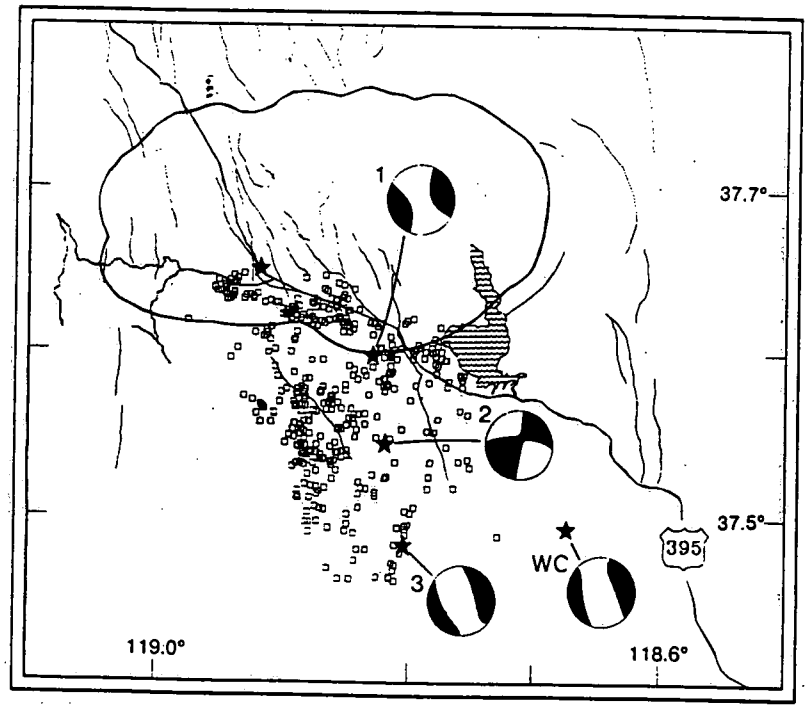

Fig. 7

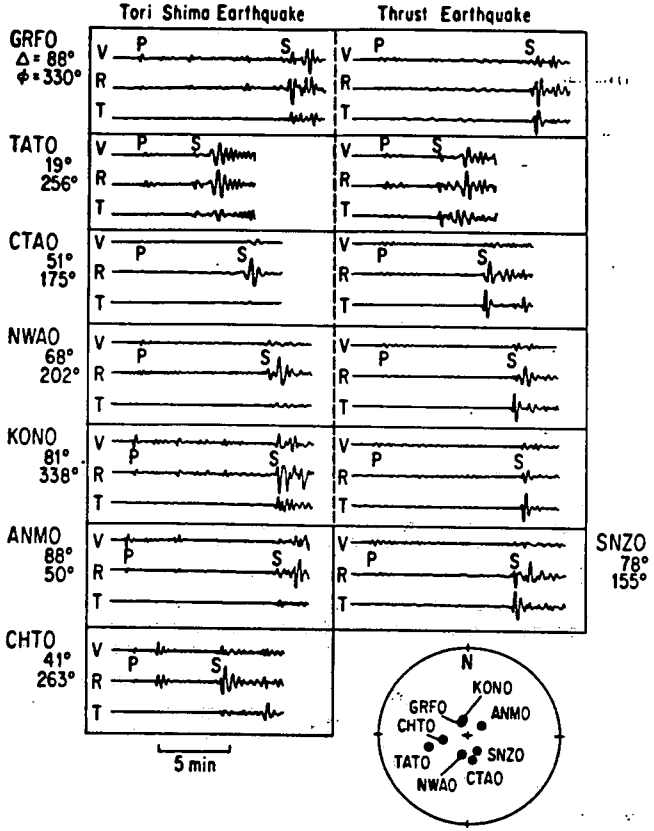

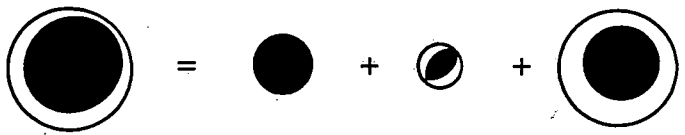

Fig. 8

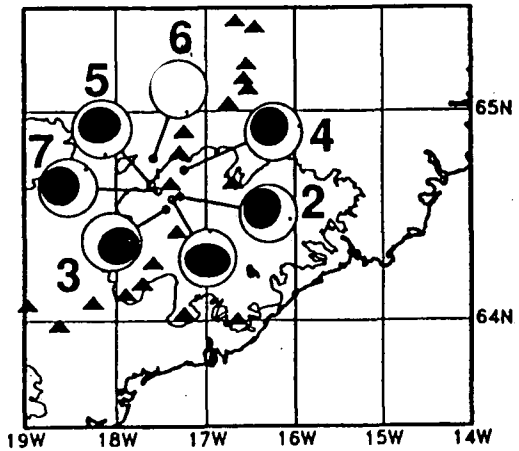

Fig. 9

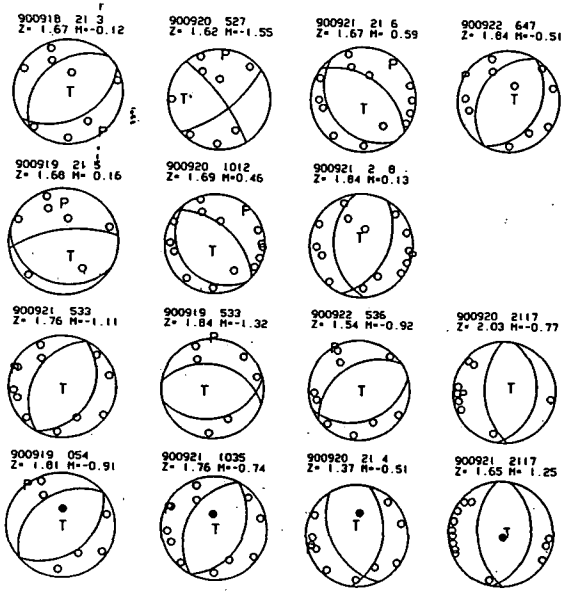

Fig. 11

Fig. 10

(a)

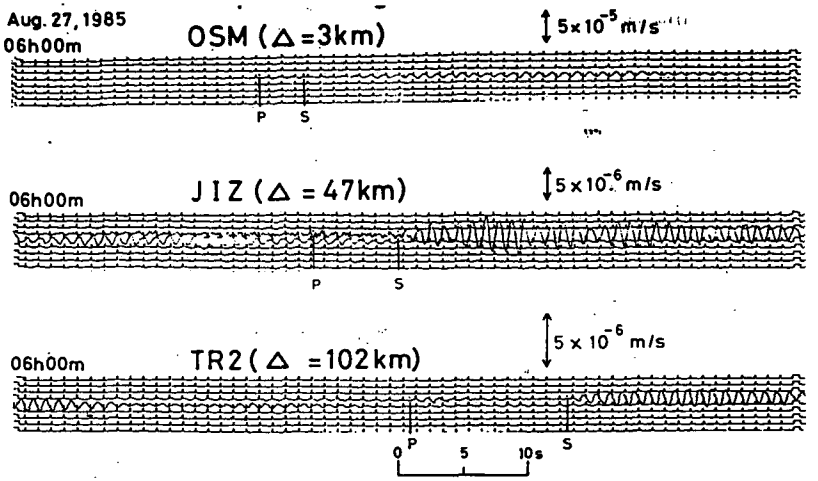

(b)

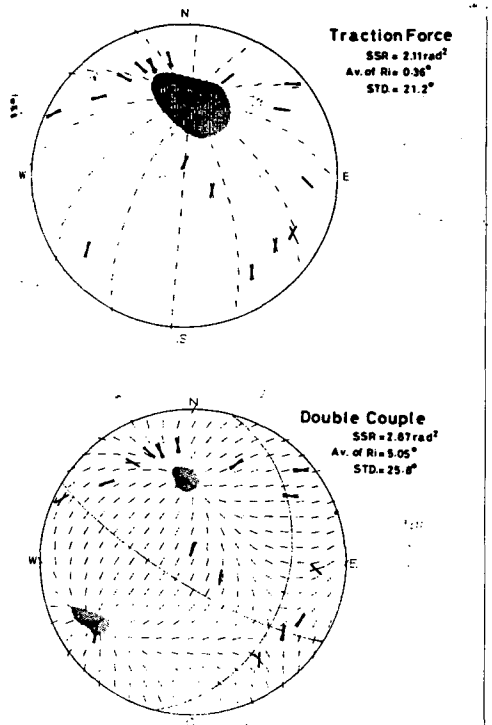

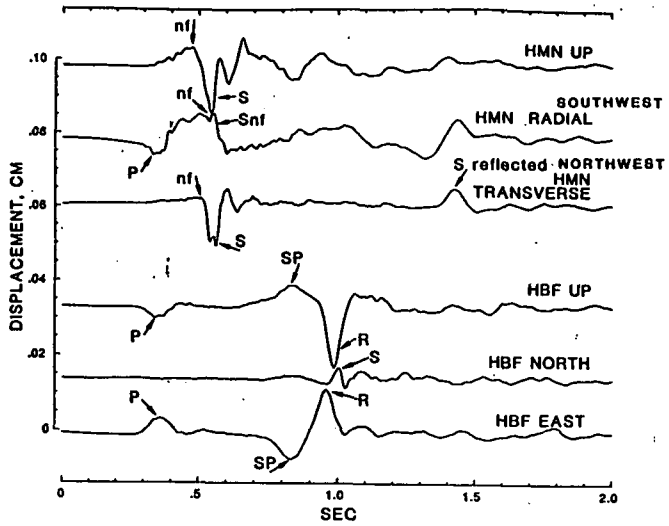

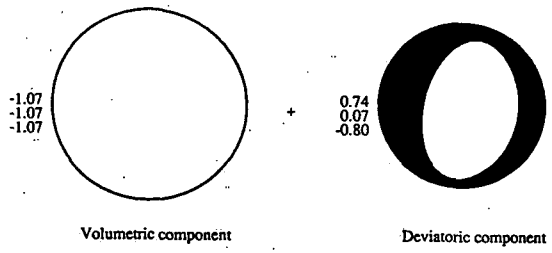

Fig. 12

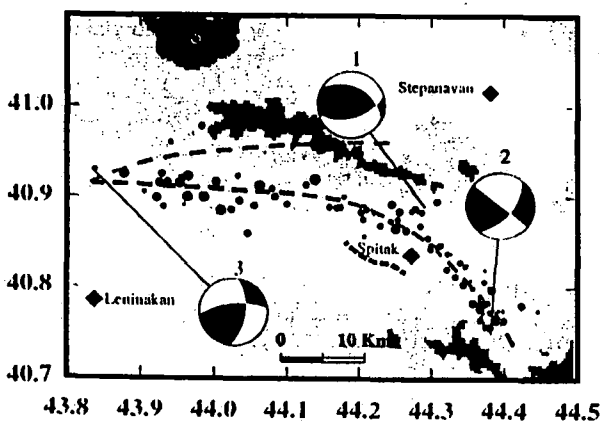

Fig. 13

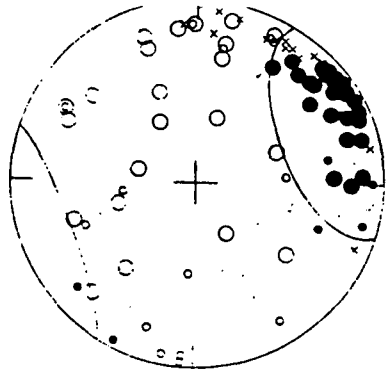

Fig. 14

1980-1989

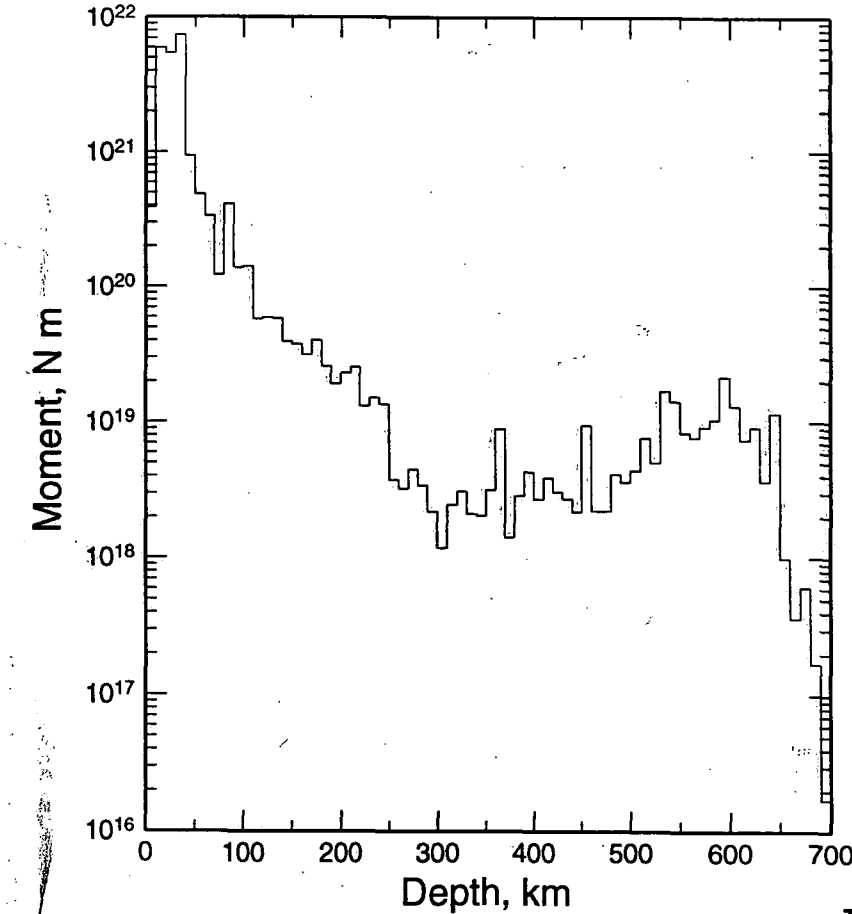

Fig. 15

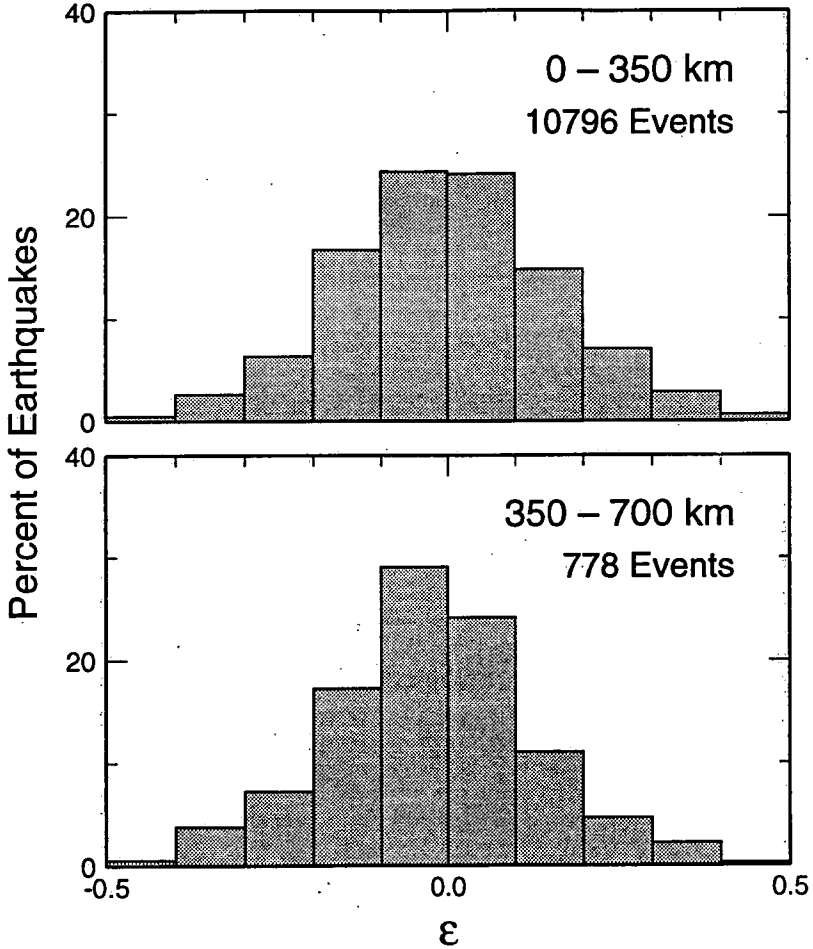
0 – 350 km
10796 Events
350 – 700 km
778 Events
Percent of Earthquakes
40
20
0
-0.5
0.0
0.5
ε

Fig. 16

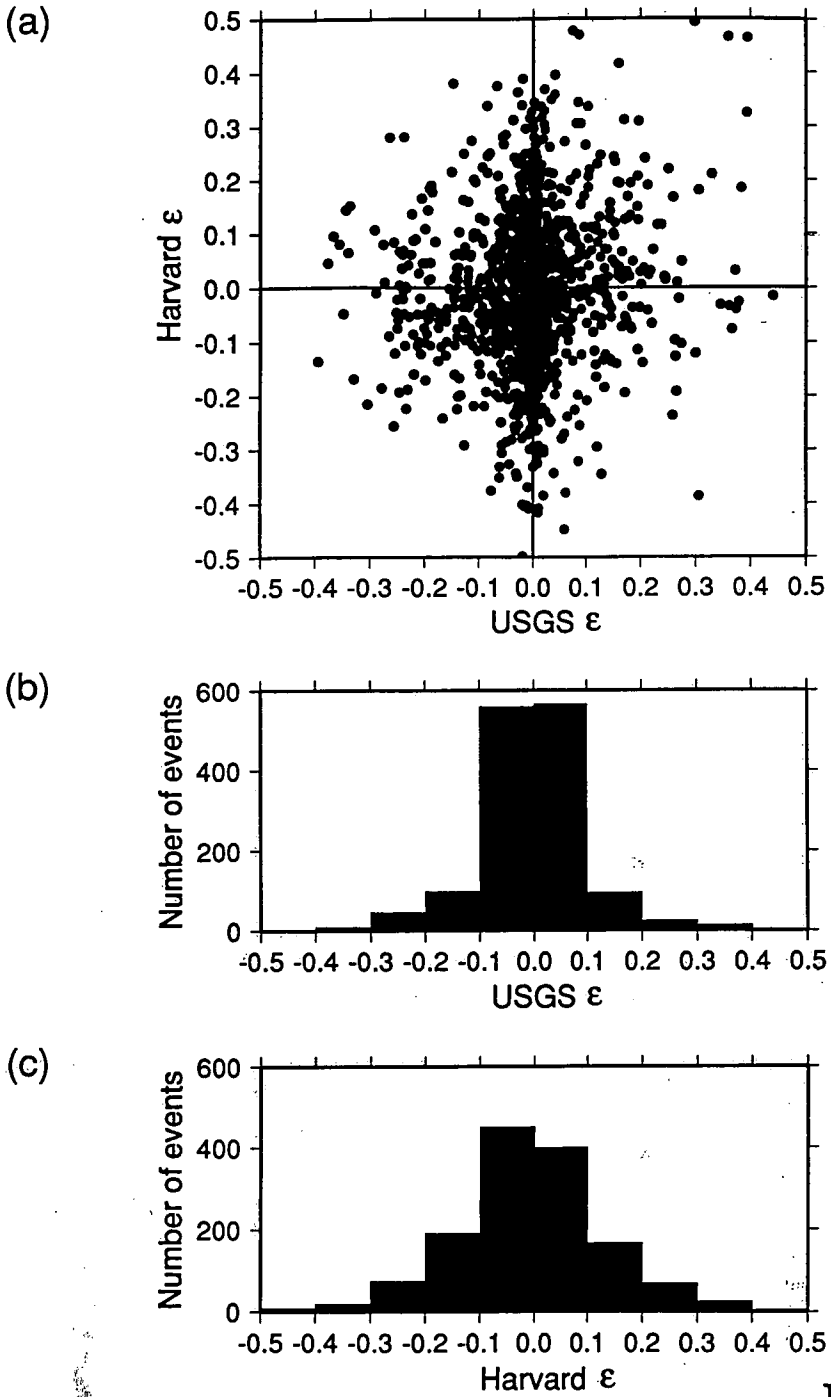
(a)
Harvard ε
USGS ε
(b)
Number of events
USGS ε
(c)
Number of events
Harvard ε
600
400
200
0
-0.5 -0.4 -0.3 -0.2 -0.1 0.0 0.1 0.2 0.3 0.4 0.5

Fig. 17